AD-780 608

# PREDICTION METHODS FOR AIRCRAFT AERODYNAMIC CHARACTERISTICS

Advisory Group for Aerospace Research
and Development
France

1974

**U.S. Department of Commerce**
**National Technical Information Service**
**NTIS**

AD-780 608

AGARD-LS-67

AGARD-LS-67

# AGARD

ADVISORY GROUP FOR AEROSPACE RESEARCH & DEVELOPMENT

7 RUE ANCELLE 92200 NEUILLY SUR SEINE FRANCE

⑮

## AGARD LECTURE SERIES No. 67

on

# Prediction Methods for Aircraft Aerodynamic Characteristics

```
(AGARD-LS-67)  PREDICTION METHODS FOR                N74-26445
AIRCRAFT AERODYNAMIC CHARACTERISTICS                 THRU
(Advisory Group for Aerospace Research               N74-26455
and)  349 p HC $20.50                                Unclas
                                          H2/02      42168
```

RECEIV...
NASA ...

NORTH ATLANTIC TREATY ORGANIZATION

REPRODUCED BY
NATIONAL TECHNICAL
INFORMATION SERVICE
U.S. DEPARTMENT OF COMMERCE
SPRINGFIELD, VA. 22161

**DISTRIBUTION AND AVAILABILITY
ON BACK COVER**

316

AGARD-LS-67

NORTH ATLANTIC TREATY ORGANIZATION

ADVISORY GROUP FOR AEROSPACE RESEARCH AND DEVELOPMENT

(ORGANISATION DU TRAITE DE L'ATLANTIQUE NORD)

AGARD Lecture Series No.67

# PREDICTION METHODS FOR AIRCRAFT AERODYNAMIC CHARACTERISTICS

The material in this book has been assembled to support a Lecture Series under the sponsorship of the von Kármán Institute, the Fluid Dynamics Panel and the Consultant and Exchange Programme of AGARD, presented in Brussels on 13–17 May, 1974.

I

## THE MISSION OF AGARD

The mission of AGARD is to bring together the leading personalities of the NATO nations in the fields of science and technology relating to aerospace for the following purposes:

- Exchanging of scientific and technical information;
- Continuously stimulating advances in the aerospace sciences relevant to strengthening the common defence posture;
- Improving the co-operation among member nations in aerospace research and development;
- Providing scientific and technical advice and assistance to the North Atlantic Military Committee in the field of aerospace research and development;
- Rendering scientific and technical assistance, as requested, to other NATO bodies and to member nations in connection with research and development problems in the aerospace field;
- Providing assistance to member nations for the purpose of increasing their scientific and technical potential;
- Recommending effective ways for the member nations to use their research and development capabilities for the common benefit of the NATO community.

The highest authority within AGARD is the National Delegates Board consisting of officially appointed senior representatives from each member nation. The mission of AGARD is carried out through the Panels which are composed of experts appointed by the National Delegates, the Consultant and Exchange Program and the Aerospace Applications Studies Program. The results of AGARD work are reported to the member nations and the NATO Authorities through the AGARD series of publications of which this is one.

Participation in AGARD activities is by invitation only and is normally limited to citizens of the NATO nations.

The content of this publication has been reproduced
directly from material supplied by AGARD or the authors.

Published May 1974

533.65 : 533.6.015.8 : 533.6.07

PRECEDING PAGE BLANK NOT FILMED

*Printed by Technical Editing and Reproduction Ltd*
*Harford House, 7–9 Charlotte St, London. W1P 1HD*

# PREFACE

In 1972 an AGARD-VKI Lecture Series was held on "Aircraft Performance Prediction Methods and Optimization" (AGARD LS-56), which concentrated mainly on the prediction of aircraft range/radius, airfield and manoeuvre performance; aero-dynamic aspects were reviewed only briefly in the time then available. The Fluid Dynamics Panel of AGARD therefore recommended a complementary Lecture Series on "Prediction Methods for Aircraft Aerodynamic Characteristics". This LS-67 has again been co-sponsored by the Fluid Dynamics Panel and the von Karman Institute for Fluid Dynamics, and implemented by the Consultant and Exchange Programme of AGARD together with VKI. Professor John Sandford, the VKI Coordinator, warrants special mention for his technical assistance and local organisation of the Short Course, held at the VKI from 13 to 17 May, 1974.

The aim here is to provide primarily an up-to-date account and authoritative appraisal of methods of prediction of aerodynamic characteristics for both combat and transport aircraft (excluding rotorcraft), over conditions ranging from low speeds (CTOL, RTOL, STOL) through subsonic/transonic to supersonic speeds (climb, cruise, manoeuvre, descent). Aircraft lift and drag estimation methods are analysed along with related aerodynamic optimisation techniques, taking into account practical methods for wing/body aerodynamic design and boundary-layer flow treatments. The prediction and implications of special aerodynamic characteristics associated with engine installation and external store effects are examined, relevant stability/control needs are reviewed, and some aircraft noise restraints on aerodynamic design are noted.

The nine main lecturers in particular deserve much appreciation for their extensive efforts and cooperation, in providing such valuable studies and preparing such comprehensive lecture notes for advance publication. Finally, our acknowledgements are due to the official and private organisations through whose help and courtesy it was possible to offer appropriate technical experts as lecturers.

John Williams
Lecture Series Director

December 1973

# LIST OF SPEAKERS

Lecture Series Director
Mr J.Williams
Deputy Chief Scientific Officer
Aerodynamics Department
Royal Aircraft Establishment
Farnborough, Hants
United Kingdom

Mr J.B.Berry
Aircraft Research Association Ltd
Bedford
United Kingdom

Mr G.M.Bowes
Unit Chief
Aerodynamics Staff
Boeing Commercial Airplane Company
Renton, Washington
USA

Mr J.G.Callaghan
Section Manager
High Lift Technology Development
Aerodynamics Subdivision
Douglas Aircraft Company
McDonnell Douglas Corporation
3855 Lakewood Boulevard
Long Beach,
California 90846
USA

Mr D.N.Foster
Royal Aircraft Establishment
Bedford
United Kingdom

Mr J.E.Jenkins
Air Force Flight Dynamics Laboratory
Wright Patterson Air Force Base
Dayton, Ohio
USA

Mr C.S.Leyman
Chief Aerodynamicist (Concorde)
and
Mr T.Markham
Assistant Chief Aerodynamicist (Concorde)
British Aircraft Corporation (C.A.D.)
Filton House, Filton
Bristol
United Kingdom

Mr J.Leynaert
Head, Applied Aerodynamics Division
ONERA
92320 Châtillon
France

Mr W.Loeve
Head, Scientific Services
National Aerospace Laboratory
Anthony Fokkerweg 2
Amsterdam
The Netherlands

Ph.Poisson-Quinton
Adjoint au Directeur Scientifique Central
ONERA
France

Mr J.Steinheuer
Research Scientist
Institut für Aerodynamik der DFVLR
Braunschweig
Germany

## CONTENTS

Page

PREFACE iii

LIST OF SPEAKERS iv

Reference

GENERAL TECHNICAL INTRODUCTION
by J.Williams 1

AERODYNAMIC PREDICTION METHODS FOR AIRCRAFT AT LOW SPEEDS WITH MECHANICAL HIGH LIFT DEVICES
by J.G.Callaghan 2 ✓

A REVIEW OF THE LOW-SPEED AERODYNAMIC CHARACTERISTICS OF AIRCRAFT WITH POWERED-LIFT SYSTEMS
by D.N.Foster 3 ✓

AIRCRAFT LIFT AND DRAG PREDICTION AND MEASUREMENT
by G.M.Bowes 4 ✓

PREDICTION OF SUPERSONIC AIRCRAFT AERODYNAMIC CHARACTERISTICS
by C.S.Leyman and T.Markham 5 ✓

APPRAISAL OF WING AERODYNAMIC DESIGN METHODS FOR SUBSONIC FLIGHT SPEED
by W.Loeve 6 ✓

BOUNDARY-LAYER CALCULATION METHODS AND APPLICATION TO AERODYNAMIC PROBLEMS
by J.Steinheuer 7 ✓

ENGINE INSTALLATION AERODYNAMICS
by J.Leynaert 8 ✓

EXTERNAL STORE AERODYNAMICS FOR AIRCRAFT PERFORMANCE PREDICTION
by J.B.Berry 9 ✓

STABILITY AND CONTROL IMPLICATIONS ON AIRCRAFT PERFORMANCE PREDICTION AND OPTIMIZATION (Provisional Summary only)
by J.E.Jenkins 10 ✓

AIRCRAFT PERFORMANCE CONSIDERATIONS FOR NOISE REDUCTION
by J.Williams ~~11~~ ✓

APPLICATION OF GROUND FACILITIES FOR FLIGHT AERODYNAMIC PERFORMANCE PREDICTION
by Ph.Poisson-Quinton ~~12~~ ✓

N74-26446

# GENERAL TECHNICAL INTRODUCTION

by

JOHN WILLIAMS
(Lecture Series Director)

## 1 ORIGIN AND PURPOSE OF LECTURE SERIES 67

In April 1972, I had the privilege and pleasure of being Technical Director of the AGARD-VKI Lecture Series entitled

"Aircraft Performance - Prediction Methods and Optimisation";

Also subsequently of editing the lecture notes provided by the authors together with some additional 'seminar' contributions, for publication as AGARD LS-56 (March 1973).

The formulation and assessment of methods for the prediction and optimisation of the mission flight capabilities for both combat and transport aircraft, assuming known aircraft characteristics, were presented in the first three papers of LS-56:-

(1) Range and Radius-of-Action Performance. (R K Page, MOD(PE)/UK)

(2) Airfield Performance (J Williams, RAE/UK)

(3) Flight Manoeuvre and Climb Performance (H Friedel, Dornier/Germany).

Related engine performance aspects and aircraft design synthesis considerations were then covered by two complementary papers:-

(4) Engine Selection (J F Dugan, NASA/USA)

(5) Parametric and Optimisation Techniques (R E Wallace, Boeings/USA)

However, as regards methods for the estimation of airframe aerodynamic characteristics, the time then available permitted only brief mention of some of the problem areas in the above five papers, supplemented by a review of some fundamental aspects in a special paper:-

(6) Aerodynamic Coefficients (C Lievens, STAe/France)

Consequently, AGARD-VKI agreed to arrange the present Lecture Series 67 (May 1974), devoted to methods for the prediction and optimisation of aerodynamic characteristics for the estimation and evaluation of the flight performance of combat and transport aircraft. The treatments given are primarily illustrated in terms of the following applications:-

Combat and Transport aircraft types with turbo-jet or turbo-fan engines;

CTOL, RTOL and STOL modes of airfield operation;

Transit Operational Conditions relating to climb, cruise, manoeuvre, loiter and descent relevant to typical combat or transport missions;

Airspeeds ranging from low to high subsonic and through transonic to supersonic, as appropriate.

Naturally, much of the technical background is also of considerable interest for aircraft outside the foregoing spectrum, either with other modes of propulsion (eg propellers/rotors, rocket), or with other modes of operation (eg VTOL, Hypersonic cruise), though any airframe characteristics particular to such modes are not dealt with specifically here.

The major targets of the present lecture series might reasonably be summarised as follows, with special reference of course to aircraft aerodynamic characteristics.

(i) To critically review available prediction/optimisation methods and associated aerodynamic data, particularly with a view to clarifying recent aerodynamic advances.

(ii) To formulate more comprehensive frameworks for the analysis and synthesis of aerodynamic data, so that the latter can be more readily appreciated and more readily applied for aircraft design purposes.

(iii) To assess the major deficiencies in the state of knowledge on aerodynamic characteristics, and to suggest appropriate aerodynamic research and development studies bearing in mind possible future aircraft requirements.

(iv) To indicate the most profitable steps towards complementary systematic utilisation of and further improvement of theoretical treatments, ground-based testing facilities and flight-testing techniques for the reliable prediction of aircraft aerodynamic characteristics.

Obviously, it would be unrealistic for us to claim that any of these goals could be achieved to our satisfaction by this lecture series alone. However, I hope that these published papers, together with the supplementary contributions and seminar discussions, will provide a reasonably comprehensive basis, stimulate further evaluation of many of the issues raised, and encourage useful exchanges of relevant information and ideas.

## 2 OVERALL TECHNICAL CONSTRAINTS ON PREDICTION

Apart from the problems arising due to limitations of aerodynamic knowledge, as will be discussed in later papers, the aircraft engineer is continually faced with enormous difficulties in predicting and guaranteeing the aerodynamic characteristics of new projects to the definition levels and time-scales demanded, and of course in specifying optimum aircraft configurations. His problems are usually aggravated by a variety of complementary factors over which he may not have direct control. For example:-

(i) Estimates of performance, for conventional configurations at least, are usually expected to be given to much higher levels of accuracy and confidence than previously, to reduce any shortfall in ultimate aircraft performance and minimise development costs.

(ii) Improvements in aircraft performance or mission effectiveness are invariably required, often with reduced or only small increase in operational costs, to ensure aircraft competitiveness on entry into service and throughout subsequent developments.

(iii) There is often a tendency towards introducing a wider range of speed/altitude requirements for greater mission effectiveness or flexibility; thus the aircraft design cannot be biased so heavily towards one or two predominant aerodynamic conditions, or estimations for off-design conditions allowing extensive flow separations or/and severe shocks become important.

(iv) From time-to-time, new engine/airframe concepts have to be explored and optimised, simultaneously taking into account possible new operational capabilities and novel aircraft control techniques. Here, the possible significant errors in accuracy of prediction need to be well appreciated, particularly for comparative assessments with competitive conventional designs.

(v) Leglislation becomes steadily more severe and complex towards ensuring greater environmental improvements (safety, noise, etc) which can apply extra constraints or imply extra guarantees.

(vi) The interplay between an increasingly large number of design parameters and diverse performance requirements necessitates careful and wide-ranging aerodynamic studies, not only with a view to optimisation for operational cost effectiveness, but also in order to assess sensitivities to possible later deviations in practice from the original technical assumptions and the mission specification.

(vii) Production demands for simplified aircraft component shapes usually lead to complex airflow conditions at some part of the mission. Also the provision of acceptable airflow conditions over the mission usually requires complex tailoring of the aircraft configurations or sometimes more complex variable geometry, eg variable sweep as well as leading-edge and trailing-edge devices.

(viii) It is invariably assumed that engine development or a new generation of engines can be relied on to provide significant improvements in aircraft performance. But these have to be ensured when the engine is integrated in the airframe - without unacceptable conflicting penalties on either the engine or airframe performance characteristics. In some cases variable geometry of the engine exits and/or intakes will be essential.

This list does not represent more than a few of the general constraints and needs of project studies, but it is important that their existence and nature should be appreciated by the research worker desiring practical application of his results, not merely by those directly engaged on specific project estimates.

## 3 PROJECT STAGES AND PREDICTION METHODS

The aerodynamic prediction and design capabilities which can be exploited for aircraft project work will vary widely, according to the evolutionary or revolutionary nature of the particular aircraft project. For example, there will obviously be great differences in R & D time-scales and efforts required to produce reliable estimates for aircraft with:-

> an unconventional layout based on relatively new concepts and relying on substantial applications of new advanced technology, so as to ensure an outstanding step forward in operational capability;

as compared with

> a more conventional layout and the employment of well-tried component design techniques, towards producing more quickly a more straightforward replacement aircraft with worthwhile but smaller advantages; or perhaps making use of advances in design technology only when improvements in overall economics rather than flight performance could be guaranteed.

Practical methods for the prediction of aerodynamic characteristics often need to utilise simple analytical frameworks based on good aerodynamic understanding. These frameworks lead to formulae incorporating logical empirical factors, whose values are derived by correlation of available experimental data from model and full-scale tests, and by interpretation of comprehensive theoretical treatments and computations for more idealised or special cases. Early on in the project studies, ab-initio predictions without special confirmatory experiments may have to be attempted. However, some experimental data (force measurements and corresponding flow conditions) should be made available as soon as possible on models partly representative of the configuration for which predictions have to be made. Then, the analytical framework and the associated formulae can be adjusted to fit the experimental results, taking into account differences between model and full-scale, in test configurations and in possible flow conditions. The importance of assessing possible aerodynamic prediction errors throughout, and of appreciating the possible sensitivity of aircraft performance estimates to these, cannot be overemphasised. Such aspects will be raised as appropriate in the subsequent papers.

The levels of sophistication and reliability of the prediction methodology needed will vary significantly also according to the stages reached in the development of the particular aircraft project and in the associated military or civil requirements. For preciseness, I shall refer here only to a few technical design stages and conveniently related milestones; the choice and nomenclature should be regarded simply as a personal preference for the present discussion.

First, a Feasibility Stage or exploratory design study period can follow directly as a response to an outline operational requirement and market appraisal, all of which should be accompanied or even preceded by an assessment of the status of relevant technology. Quick approximate estimates,for a range of sketch-designs of the aircraft and often for wide-ranging parametric studies,are primarily needed during the feasibility stage. Sometimes, generalised aerodynamic data from somewhat similar configurations may be available, or some crude models may be tested quickly. Nevertheless, even at this stage, as later, progress towards a systematic and consistent approach for prediction should be attempted, which could be incorporated early on into computer programs for aircraft design and optimisation. Also feasible aerodynamic targets and realistic contingency limits will need to be declared, for a variety of alternative designs, including comparisons of possible developments of existing aircraft as well as completely new types.

The results of such feasibility studies need to include not only comparison of technical solutions to meet the outline operational requirement and some variations, but also indications of relative time-scales and costs. Thereby, the relative cost-effectiveness of alternative proposals can be assessed, to allow a full and relatively-firm version of the operational requirement to be formulated and issued by the appropriate customer.

A Project Definition Stage can follow next, for detailed engineering studies on one or two projected aircraft types, whose main features have been agreed between the customer and the contractor against a full operational requirement. These definitive project studies must examine in depth tbe vital characteristics and technical problems of the aircraft design, so as to reach a complete aircraft specification and provide detailed statements on performance, development and production time-scales, and costs. Thus, during this project definition stage, all the major aerodynamic characteristics must be thoroughly investigated and any problems shown to be tractable within the allowable time-scale and costs. The performance estimates must be continually refined and updated, taking due account of the possible occurrence (or control) of degradations associated with practical aircraft design needs and with expected manufacturing standards. This process of thorough technical validation and carefully considered modifications requires intensive R & D work on selected main aspects, using models generally representative of the preferred designs for both experimental and theoretical investigations. In particular, areas of doubt in the analytical frameworks and in the formulae for the prediction of the aerodynamic characteristics must be clarified and quantified, or removed, while specific estimates must be substantiated for the performance of the aircraft major components and for the definitive aircraft as a whole.

Such project definition studies should enable a practical compromise to be decided on which is a near-optimum but retains some flexibility, and a formal specification for the aircraft to be agreed, bearing in mind also any further operational and market developments which have arisen in the meantime. The go-ahead for pre-production engineering development, at least as far as construction of the prototype batch, may then be given; preferably with minimum risk as regards unforeseen changes in the operational requirement, so as to preclude unaccounted delays and any major cost increases not associated with the original technical specification.

During the Engineering Development Stage even more representative model studies should be undertaken, especially with a view to checks against the flight experiments on the prototype aircraft; so as to ensure early rectification of any design defects and thereby expedite the final tailoring at full-scale, to meet or even surpass guaranteed performance predictions over the whole flight envelope. Towards the end of this stage, at least, improved analytical frameworks and prediction formulae should be derived on the light of the whole R & D work to date. These should be collocated to the measured prototype performance at carefully-selected and well-understood test conditions, with due allowance for possible errors in the measured test data. Estimates of mean performances and tolerances for the production aircraft will now have to be declared, taking into account the expected standards of production quality control. Moreover, from the R & D experience gained, the project staff should have begun already to attempt confident predictions of worthwhile improvements for later production batches, and to explore possibilities for future aircraft development; naturally, taking advantage also of the results from the flight certification and clearance trials when available.

## 4 TECHNICAL SCOPE

The individual topics of this lecture series, on prediction methods for aircraft aerodynamic characteristics, could have been selected in a variety of ways and the choice provided an interesting mental exercise at the start. The present arrangement seemed to offer a logical aerodynamic choice to cover reasonably the flight speed range and operational modes for both transport and combat aircraft. Additionally, it facilitated early agreement by some official and industrial establishments within NATO to provide acknowledged experts, not only with up-to-date special knowledge of their selected topic, but also with considerable interest and experience in some of the others. This should prove an extra asset for the two half-day discussion seminars arranged towards the middle and end of the week of lecture presentations. Indeed, we should express our appreciation to AGARD-VKI and to the contributing technical organisations, for meeting the demand to have eight appropriate lecturers attend from Europe and three from America.

The first pair of Lectures (L.2 and L.3), directly following this introduction, are complementary in considering the prediction of aircraft aerodynamic characteristics at low flight speeds, relating primarily to airfield performance for CTOL, RTOL and STOL operation. For convenience of presentation, the individual lectures are divided as follows:-

(L.2) Low Speed with Mechanical High-Lift Devices (J G Callaghan, Douglas/USA)

(L.3) Low Speed with Powered Lift Systems (D N Foster, RAE/UK)

Some appreciation is needed at the outset of the most predominant aerodynamic coefficients, along with the significant levels of accuracy of prediction and production targets, in relation to the airfield performance capabilities required; see AGARD LS-56, Paper 2. This can be illustrated quickly though qualitatively from typical first-order relations, here excluding thrust deflection considerations for simplicity, for some specific airfield performance capabilities such as the Take-off distance $S_{TO}$, Climb-out angle $\gamma_{TO}$, Landing distance $S_L$, and Approach speed $V_A$.

Thus:-

$$S_{TO} \approx K_{TO} \cdot (W/S) \cdot (W/T) \cdot (1/C_{Lu});$$

$$\gamma_{TO} \approx (T/W) - (C_D/C_L);$$

$$V_A \approx K_A \cdot (W/S)^{\frac{1}{2}} \cdot (1/C_{Lu})^{\frac{1}{2}};$$

$$S_L \approx K_L \cdot (W/S) \cdot (1/C_{Lu}).$$

The values of the factors K can vary according to the class of aircraft (transport or combat), their mode of operation (CTOL/RTOL or STOL) and the particular airfield environment; while of course the installed thrust/weight ratio (T/W) and wing loading (W/S) will vary from aircraft to aircraft.

However, the sensitivities of airfield performance capabilities, to the 'trimmed' aircraft values of the appropriate usable lift coefficient $C_{Lu}$ (with adequate safety margins) and of the appropriate attainable lift/drag ratio $C_L/C_D$, are clearly important. For example, prediction errors (eg overestimation) of the values of these aerodynamic coefficients can lead to 'proportional' errors (eg degradation) of the corresponding airfield performance capabilities in practice; or, alternatively, if the airfield performance has to be achieved without further aircraft modification, then the allowable aircraft weights and hence disposable loads are modified (eg reduced). The aircraft lift and drag coefficients at low speeds can also have much wider implications, as discussed later; eg in respect of possible reduction of aircraft noise annoyance, and for search/rescue/loiter capabilities.

The second pair of lectures (L.4 and L.5) are concerned primarily with the prediction of aircraft aerodynamic characteristics for typical transit conditions at either subsonic or supersonic flight speeds.

(L.4) Subsonic Speed - (G M Bowes, Boeing, USA)

(L.5) Supersonic Speed - (C S Leyman and T Markham, BAC/UK)

As previously, the significance of predominant aerodynamic coefficients in respect of relevant flight performance capabilities can again be illustrated quickly, though only qualitatively, by inspection of 'proportional' changes given by some simple first-order relations; AGARD LS-56 (Papers 1 and 3) gives more elaborate formulae. For example, the Range factor $dR/dW_F$ and the Endurance factor $dt/dW_F$, ie the instantaneous rates of increase in still-air range R and endurance t with use of fuel weight $W_F$, are simply:-

$$(dR/dW_F) \approx (1/W) \cdot (V/c) \cdot (C_L/C_D),$$

$$(dt/dW_F) \approx (1/W) \cdot (1/c) \cdot (C_L/C_D);$$

in steady level flight at aircraft weight W, airspeed V, and thrust specific fuel consumption c. Moreover, especially for combat aircraft, there is a need to estimate and optimize the Specific Excess Power or the instantaneous rate of increase of energy height $[h + (V^2/2g)]$ with time. As a first approximation:-

$$d[h + V^2/2g)]/dt \approx V\,[(T/W) - (C_D/C_L)]$$

Also, the attainable normal acceleration capability ng in steady horizontal turns can be given (without thrust limitation) by:-

$$n \approx (\gamma p/2) \cdot M^2 \cdot (S/W) \cdot C_{Lu},$$

where here $C_{Lu}$ must be limited to ensure an adequate buffet margin at Mach number M and atmospheric pressure-height p.

For these and many other relevant flight performance capabilities, particular flight conditions may be prescribed (eg Mach number, altitude and temperature) or flight profile optimization may be sought subject to certain limiting constraints. However, from such simple relations, the justification for improvements in and accurate predictions of at least $C_L/C_D$, $C_{Lu}$ and $C_D$ under relevant aircraft performance conditions can again be broadly argued. I envisage that the subsequent Lecturers will comment on and illustrate typical practical aspects, more specifically and in more depth with respect to their own particular topics.

It is important to recall at this stage that aerodynamic lift and drag predictions for practical aircraft cannot usually be divorced from examination of other aerodynamic characteristics; such as those associated with stability and control, engine installation and external stores, as will be discussed in later lectures. More generally, other aircraft design disciplines also cannot be ignored; such as those associated with aeroelasticity, airworthiness, weight, complexity, overall cost-effectiveness and time-scales for development. For example, two of the classical 'Bêtes noires' of project development are excess drag and weight growth, which in many respects can prove interdependent and of course are frequently subject to snowball (boule-de-neige) effects.

The third pair of Lectures (L.6 and L.7) review in detail aerodynamic flow prediction at subsonic flight speeds, including consideration of conditions where local transonic flows can occur on the airframe surfaces:-

(L.6) Wing Aerodynamic Design Methods - (W Loeve, NLR/Netherlands)

(L.7) Boundary-Layer Calculation Methods - (J Steinheuer, DFVLR/Germany)

As regards supersonic flight speeds, it should be noted that relevant methods for wing aerodynamic design and drag estimation are discussed in the earlier lecture L.5 by Leyman and Markham. The potentialities and limitations of the treatments reviewed in relation to flight at either subsonic or supersonic speeds should be well worth appreciation by aerodynamicists concerned with project development, as well as those interested primarily in research.

The final trio of published lectures (L.8, L.9, L.10) are devoted to three special topics, each of which is sometimes treated perhaps too casually in early aerodynamic studies of basic airframe performance, but whose implications on aerodynamic performance predictions and design can be significant even at the feasibility stage of project studies and over much of the flight envelope.

(L.8) Engine Installation Aerodynamics (J Leynaert, ONERA/France);

This lecture reviews techniques for the theoretical design, optimisation and experimental investigation of engine air-intakes, afterbodies and jet nozzles. Special attention is given to the need for careful and consistent evaluation of thrust and drag terms, and of the engine intake and exit flow conditions which are directly relevant to prediction of engine performance characteristics (net thrust, specific fuel consumption, etc).

(L.9) External Store Aerodynamics (J B Berry, ARA/UK);

This analyses the effects of external stores on the aerodynamic characteristics of aircraft, discussing in particular the prediction of incremental drag due to various practical types of store installation. It should be emphasised that the drag contribution of installed external stores is usually significant and often a limiting factor in the performance of strike/fighter aircraft, so reliable predictions and possible means of reduction are clearly important even at the project feasibility stage.

(L.10) Stability and Control Implications (J E Jenkins, WPAFB/USA);

This should clarify the primary ways in which stability and control considerations can influence the aircraft design and performance predictions, along with the possible trade-offs between inherent airframe characteristics and flight control system complexity (CCV aspects) for aircraft performance optimisation. Aerodynamic data prediction requirements from such stability and control viewpoints also should be noted.

Two supplementary presentations (L.11 and L.12) already planned, summaries of which are published here, take as their subjects:-

(L.11) Aircraft Performance Considerations for Noise Reduction (J Williams, L S Director);

(L.12) Application of Ground Facilities for Flight Aerodynamic Performance Predictions
(Ph Poisson-Quinton, ONERA/France).

Other contributions from attendees are also welcomed, as time permits, to take advantage of any appropriate specialised knowledge.

Most of the lectures published here contain extensive lists of reports for further reference on the particular topics. At this stage, therefore, perhaps I need mention only three existing sets of papers also of general use for aerodynamic predictions.

1) The Royal Aeronautical Society Data Sheets and Transonic Data Memoranda.
2) The USAF Stability and Control Datcom.
3) The AGARD Conf Proc 124 on 'Aerodynamic Drag'.

N74-26447

# AERODYNAMIC PREDICTION METHODS FOR AIRCRAFT AT LOW SPEEDS WITH MECHANICAL HIGH LIFT DEVICES

by

J. G. Callaghan, Section Manager
High Lift Technology Development, Aerodynamics Subdivision
Douglas Aircraft Company, McDonnell Douglas Corporation
3855 Lakewood Boulevard, Long Beach, California 90846

## 1.0 SUMMARY

The subject paper will discuss in some detail a survey of present methodology used for the estimation of low speed aerodynamic characteristics of aircraft with mechanical high lift systems. While this methodology is applicable to a large variety of aircraft with unpowered high lift systems, the emphasis will be on transport type aircraft. Prediction methods empirically derived from experimental data, as well as more sophisticated theoretical methods will be discussed. Correlations of calculated results with both wind tunnel and flight measurements will be presented.

To place the current state of the art of methodology into proper perspective, a critical review of areas of both strength and weakness will be presented, with emphasis on future requirements. Within this context, the particular need for methods to estimate the high lift characteristics of aircraft with thin, highly swept, low aspect ratio wings, such as supersonic transport configurations will be reviewed.

## 2.0 INTRODUCTION

The accurate estimation of the low speed aerodynamic characteristics of aircraft with mechanical high lift systems is dependent on a wide spectrum of methods ranging from sophisticated three-dimensional analytical tools to highly empirical formulations, and in some instances, to a total dependence on the wind tunnel. The ability to accurately estimate the low speed characteristics with an attendant high degree of confidence is fundamental to the success of any program involving the development of a new airplane. This is manifest in two ways: firstly, if flight measurements reveal deficiencies relative to the guaranteed performance, costly flight development programs may result, and indeed may result in re-design and re-manufacturing problems. Secondly, an established high degree of confidence in analytical estimation techniques reduces the dependence on extensive wind tunnel test programs. For typical jet transport aircraft, this testing will run into thousands of wind tunnel test hours (References 1 and 2). Because of the limitations of estimation methods, testing to some extent will always be required because the aerodynamic characteristics must be established as thoroughly as possible before flight. It is, however, desirable to continue development of improved methodology, which departs from empiricism and approaches the problem from a more fundamental sense. This will invariably provide more firm guidelines for improving the design of high lift systems.

The high lift prediction methods to be discussed in the present paper are to a large extent those associated with predicting low speed characteristics of large transport aircraft, such as that shown in Figure 1, as this represents the experience of the author and his colleagues. Many of the methods, however, particularly the more fundamental ones, have applications to a wide variety of aircraft. It is the intent of this paper to present a general assessment of prediction methods, rather than to provide a methods handbook. In particular, to the extent possible, these methods will represent the best available analytical tools in the present state-of-the-art, rather than the less rigorous methods sometimes used for advanced design trade studies.

The characteristics whose estimation will be addressed are those in the longitudinal mode which are required to determine takeoff, climbout, approach, and landing performance. In general, the present state-of-the-art permits reasonably accurate estimation of the low speed characteristics, as must be evidenced in part by the many successful transport aircraft in service today. There are, however, many characteristics which cannot be assessed by estimation methods and, therefore, require wind tunnel measurements.

Fundamental to the ability of any method to accurately predict aerodynamic characteristics is the degree to which the flow over the appropriate geometry is analytically modeled. The non-aerodynamic shapes which may be introduced by the deflection of the high lift system greatly compound this problem as is evidenced by the example of Figure 2. The flow can be analytically modeled to varying degrees within the present state-of-the-art to a relatively high degree of accuracy in two dimensions and to a lesser extent in three dimensions.

The type of methods generally available to estimate low speed aerodynamic characteristics can be roughly placed in four different categories:

- Three-Dimensional Analytical Techniques - In general, the applicable three-dimensional methods are limited to estimating those characteristics wherein viscous considerations are small, and are necessarily neglected. These methods range from simple lifting line theories to more sophisticated lifting surface theories and to full lifting potential flow solutions. Such methods find applicability in estimating lift and pitching moment characteristics in regions below the stall in the absence of flow separation.
- Two-Dimensional Analytical Techniques - Highly sophisticated methods are within the state-of-the-art for calculating two-dimensional characteristics, including both potential flow and viscous flow solutions for multi-element airfoils of arbitrary shape. To a limited extent some techniques are available for modeling separated flow regions. In general, these methods depend on a certain degree of empiricism for adjusting the resulting two-dimensional section

characteristics to three dimensions.

- Empirical Methods - Many characteristics to be estimated, such as maximum lift coefficient, do not presently lend themselves to analytic treatment. In these instances empirical techniques must be utilized. In some cases there exists a theoretical basis for the empiricism and, indeed, in other instances it is whatever seems to make the method work.
- Experimental Methods - In many instances there are not even suitable empirical relationships for estimating certain characteristics, in which case the wind tunnel must be utilized. Typical of these problem areas are the estimation of drag increments for high lift devices, and interference effects.

The shortcoming of empirical techniques is primarily that they are limited to providing characteristics only for those geometries upon which the empiricism is based. This introduces possible errors for new geometries which depart from the empirical base. An additional deficiency of empirical techniques is that they may not necessarily contribute to a more fundamental understanding of the associated flow phenomenon, and subsequently to improved designs. A shortcoming exists even with more sophisticated empirical methods in that the estimation of certain characteristics, such as maximum lift with high lift devices extended relies on a component buildup which does not allow for possible interference effects between components.

In the process of estimating aerodynamic characteristics, one finds a wide variety of methods available. In the selection of an appropriate lifting surface theory, for example, there are those formulated by Woodward, Giesing, Lamar and Margason, and Martin (References 3 thru 6 respectively). A similar situation exists in two-dimensional methods for multi-element airfoils such as those by Bhateley, Goradia, and Callaghan and Beatty (References 7, 8, and 9). All of these clearly have their advantages and their limitations. The particular ones addressed in the subsequent discussion reflect the experience of the author and his colleagues at the Douglas Aircraft Company; similar applications of these various methods beyond this experience could be and, indeed, probably have been made.

In the ensuing discussion certain of the methods will be referred to several times, in that they have application in many areas. For example, in the instance of the Giesing vortex lattice lifting surface theory, this program finds application in determining lift curve slope, lift increment due to flap deflection, span load distribution, and pitching moment characteristics. In other instances wherein methods have limited application, or in fact where no methods exist, little can be said.

The methods to be addressed are those which are applicable to the estimation of lift and drag characteristics for a complete airplane configuration with leading and trailing edge devices extended. Methods for estimating pitching moment characteristics will also be discussed in that the resulting trim effects must be considered as to their impact on lift and drag.

In order to appreciate the significance of the various characteristics whose estimation will be discussed, some review of the pertinent airplane performance characteristics will be beneficial at this point. Figure 3 presents a schematic of a representative takeoff profile as dictated by Federal Aviation Agency requirements. Certain speeds of significance are indicated in the figure and are defined below.

The rotation speed, $V_R$, is the speed at which the pilot begins to rotate the aircraft to attain the liftoff attitude and must not be less than 5% above the air minimum control speed, $V_{MC}$. The latter speed is determined by the minimum speed at which directional control can be maintained in the event of failure of the most critical engine. The liftoff speed, $V_{LO}$, is the speed at which the airplane becomes completely airborne and must be at least 5% above the minimum unstick speed. The minimum unstick speed, $V_{MU}$, is the minimum speed that the aircraft can be made to liftoff without hazard and continue takeoff. This speed is determined by flight tests as shown in Figure 4. The takeoff safety speed, $V_2$, must not be less than 1.2 times the stall speed, $V_S$, or less than 1.1 times the minimum control speed; the $V_2$ speed is necessarily at least as fast as the $V_{LO}$ speed and is, therefore, at least 5% above the minimum unstick speed. Further, the $V_2$ speed must be such that a minimum climb gradient (approximately 3% depending on the number of engines) can be maintained in the event of engine failure.

These speeds and the resulting takeoff field length are directly related to the lift coefficient attainable at a given attitude, and to the maximum lift coefficient. The climb gradient is strongly dependent on the lift-to-drag ratio in the climbout configuration.

The takeoff field length is determined by several criteria, one of which is shown in Figure 3. This is the so called critical engine out takeoff distance which is the distance from start of takeoff to a point 35 feet above the runway at the $V_2$ speed, assuming an engine failure to be recognized at the decision speed, $V_1$.

A representative takeoff field length performance plot is shown in Figure 5 for an airplane in the 500,000 lb. takeoff gross weight class; the increase in slope at the higher gross weight results from the second segment limiting weight. For a given thrust level (T), the gross weight (W) is reached beyond which the required engine-out climb gradient cannot be met; in order to increase the takeoff gross weight, the lift-to-drag ratio (L/D) must be increased. This can be brought about by a reduction in flap setting which will have an attendant lift coefficient decrease which results in some increase in field length. The sensitivity of field length to lift coefficient can be seen in the figure; for the range of gross weights which are not second segment limited, the change in field length is directly related to lift coefficient. This follows from consideration of the generalized takeoff parameter:

$$\text{takeoff field length} = f\left[\frac{(W/S)}{(T/W)\ \rho\ C_L}\right]$$

where S, $\rho$, and $C_L$ are wing area, density, and lift coefficient respectively.

For example, for a 10,000-foot field length, a four percent increase in $C_{L_{MAX}}$ is worth a 400-foot reduction in field length. This may seem like a relatively insignificant change in performance.

However, if viewed from the standpoint of weight, the impact is more significant. For this fixed field length, the 4% improvement in maximum lift coefficient increases the takeoff gross weight by 10,000 pounds, which is equivalent to about fifty passengers! In the region where the airplane has become second segment limited, the performance is basically insensitive to a $C_L$ change. This results from the limiting region being basically an envelope; any increase in $C_L$ would result in a decrease in L/D, which would violate the second segment constraint.

The sensitivity of the takeoff performance to drag is shown in Figure 6, again for an airplane in the 500,000 pound takeoff gross weight class. For the weight region wherein the airplane is not climb gradient limited, the field length is relatively insensitive to changes in drag. However, there is an extreme sensitivity once the configuration becomes gradient limited. The climb gradient $\gamma_z$ is

$$\gamma_z = \frac{T}{W} - \frac{1}{L/D} ,$$

and is on the order of 3% for a one-engine out configuration. In the non-limiting weight region, a 10% increase in drag is equivalent to roughly 5,000 pounds (25 passengers) for a fixed field length. second segment limited condition, this increase in drag could be equivalent to as much as 20,000 or roughly 100 passengers.

Examination of the landing performance reveals a similar picture in that landing field length sensitivity is directly related to $C_L$ changes. The sensitivity to drag is quite small unless the airplane is limited by approach climb requirements which is a go-around requirement with all engines operating. For most transport aircraft, this is generally not a limiting condition.

Another important airplane parameter which can be quite sensitive to the aerodynamic characteristics is that of noise during takeoff and landing. Basically there are three requirements to be met:

- Sideline Noise - Measured on the ground approximately one quarter mile from the centerline of the takeoff path.
- Takeoff Noise - Measured 3.5 nautical miles from brake release, which may include a throttle cut prior to this point provided minimum altitude and climb gradient requirements can be met.
- Landing Noise - Measured on approach with the airplane in the landing configuration on a 3° glide slope approximately 400 feet in the air.

The permissible noise levels for these various criteria are dependent on the gross weight of the airplane but cannot exceed 108 EPNdB. The noise level is directly related to the thrust of the engines, which is in turn related to the drag level of the aircraft. There is, however, a noise floor, which is established by the basic power-off aerodynamic noise of the vehicle. This aerodynamic noise floor is below the noise level of current large transport aircraft. The sensitivity of noise to drag characteristics can be seen in Figure 7 for a representative approach condition with the airplane in the landing configuration. For this particular geometry, approximately three percent of airplane drag is equivalent to one EPNdB.

Consideration of the above discussion indicates a strong sensitivity of takeoff and landing performance to the pertinent lift and drag characteristics. In order to meet performance guarantees, it is desirable to provide estimates of aerodynamic characteristics that have a tolerance level that is on the order of one percent. With these demands on accuracy, one is then faced with applying the most sophisticated estimation methods which the present state-of-the-art will permit. The ensuing discussion will review these methods insofar as the prediction of the lift, drag, and pitching moment characteristics are necessary for the determination of takeoff and landing performance.

The special problems of determining characteristics from wind tunnel and flight measurements will also be addressed. In addition, some discussion will present the correlation between estimated characteristics and flight measurements, and the correlation between wind tunnel characteristics and flight measurements.

Finally, an assessment of the present state-of-the-art will be made to review those areas where particular development work is required. Some assessment will also be made of the particular problems associated with estimating characteristics for highly swept, low aspect ratio, thin wings such as those on supersonic transport configurations. A review of the promising theoretical techniques presently under development for application in addressing the full three-dimensional viscous problem will be addressed.

It is to be noted that throughout the discussion of the various aerodynamic prediction methods, the use of the terminology "lift", "drag", and "pitching moment" will, for convenience, be used interchangeably with "lift coefficient", "drag coefficient", and "pitching moment coefficient", respectively. Further, lower case letters will be utilized to designate section characteristics, and upper case letters will be utilized to designate three dimensional characteristics.

## 3.0 AERODYNAMIC PREDICTION METHODS

### 3.1 Lift Characteristics

It can be stated that the estimation of lift characteristics do, in general, lend themselves better to analytic treatment than the drag characteristics. In general, for transport aircraft, the drag forces are an order of magnitude smaller than the lift, in that one is dealing with lift-to-drag ratios on the order of ten. The various strong three dimensional analytical methods which are available provide good accuracy in regions where viscous effects do not dominate the flow field. The analytical techniques available for estimation which include viscous effects are generally restricted to two-dimensional unseparated flows, with empiricism required for adjusting to three dimensions, though certain three dimensional approaches under development appear promising and will be discussed at the close of the paper. However, in the case of maximum lift, empirical techniques must be utilized.

### 3.1.1 Lift Curve Slope

Lift curve slope may be determined from empirical relationships, or more desirably from appropriate lifting surface theories. The empirical relationships require a knowledge of the defining airfoil section properties; these section properties, in turn, may be determined from empirical relationships or from sophisticated two-dimensional potential flow and viscous solutions. The theoretical section lift curve slope, $c_{l_\alpha}$, may be determined from the relationship given in Reference 10:

$$c_{l_\alpha} = 6.28 + 4.7\left(\frac{t}{c}\right)\left(1 + .00375\ \phi_{TE}\right) \qquad \text{(per radian)}$$

where $\phi_{TE}$ is the total trailing edge angle in degrees and t/c is the airfoil thickness-to-chord ratio. The theoretical lift curve slope is shown in Figure 8; since this level is relatively insensitive to trailing edge angle, a value of 20°, representing the upper limit of the method was used for the slope shown in Figure 8. Viscous effects will bring about a reduction in lift curve slope relative to this theoretical level. This results from the decambering effect due to the presence of the boundary layer displacement thickness. As obtained from Reference 10, this viscous effect has been correlated with Reynolds number and trailing edge angle and is shown in Figure 8.

A much greater degree of accuracy in determining section characteristics can be obtained by the application of sophisticated potential flow solutions of the type described in References 7, 8, and 9. The theoretical method described in Reference 9 can compute the high lift characteristics of multi-element airfoils of arbitrary shape operating in a viscous incompressible fluid in the absence of flow separation. This approach combines a geometry definition routine, a potential flow solution based on a surface source distribution, and a finite-difference boundary layer routine to accomplish the analysis. The geometry routine smooths and spaces the body coordinates for input to the potential flow program. The boundary layer characteristics are then calculated from the resulting potential flow pressure distribution and an equivalent inviscid body is formed by the addition of the boundary layer displacement thickness to the original body. These coordinates are then used to calculate a new pressure distribution for the equivalent body. This process is repeated until convergence is achieved. Experience has shown that satisfactory convergence can be achieved after two or three iterations. Figure 9 illustrates the computational process. A representative pressure distribution calculated by this method is compared to an experimentally measured one in Figure 10 at an angle of attack of 10°. The corresponding lift curve, for both the inviscid and the viscous solution is presented in Figure 11. As can be seen, the viscous solution is in very close agreement with the experimentally measured value in terms of both angle of zero lift and lift curve slope, until close to stall. It is significant that for this case, only one iteration was required, that is, two potential flow solutions and one boundary layer solution.

The section lift characteristics, derived by either the empirical relationship, or more sophisticated solutions may be corrected to three dimensions by the method given in Reference 10. For straight tapered wings, this three dimensional correction is presented in Figure 12 as a function of wing aspect ratio, midchord sweep angle, Mach number, and section lift curve slope.

In contrast to techniques for calculating lift curve slope which rely on empiricism and on a knowledge of the defining airfoil characteristics, are the various available lifting surface theories, (References 3, 4, 5, and 6). The vortex lattice approach of Reference 4 represents the wing by a network of small horseshoe vortices distributed in both chordwise and spanwise directions. The strengths of the individual vortices are determined by applying the wing boundary condition at as many points on the wing as there are vortices. A system of simultaneous equations is then solved to determine the horseshoe-vortex strength. The fuselage is represented by a line of doublets on the fuselage axis and a non-planar doublet sheet to represent the wing image system, with the boundary condition being that the flow does not penetrate the fuselage surface. The ability of this type of lifting surface theory to accurately describe lift characteristics is shown in Figure 13, which presents a correlation of the calculated and experimentally measured span loading in the presence of wing mounted nacelles and external flap hinge fairings for a 35° swept wing-fuselage combination.

Comparisons of lift curves as calculated by the referenced method with experimentally measured values are presented in Figures 14 and 15 for the DC-9 and DC-10 airplanes respectively. The rather close agreement in both cases between experimental and calculated values is somewhat remarkable. This results from two simplifications in the approach which are compensating to a certain degree. The neglect of any viscous effects in the analysis tends to over-predict the lift curve slope, as previously mentioned in the discussion on section characteristics. Conversely, the exclusion of thickness effects tends to underpredict the lift curve slope. The contribution of the fuselage to the lift curve slope is shown in Figure 15; excluding the fuselage lift underpredicts the total level by a significant amount.

### 3.1.2 Clean Wing Maximum Lift

The basic approach to the estimation of airplane maximum lift with high lift devices deflected is a linear buildup of the maximum lift for the clean wing and of the increments of maximum lift due to the leading and trailing edge high lift devices. The determination of clean wing maximum lift coefficient is dependent on a knowledge of the spanwise lift characteristics of the clean wing and of the maximum lift of the various airfoil sections which define the wing. The general procedure for calculating wing $C_{L_{MAX}}$ is predicated on the assumption that when any given section first reaches its section maximum lift coefficient, the complete wing has reached $C_{L_{MAX}}$. This is basically a practical definition, in that once any single section has stalled, the subsequent flow separation spreads and the wing loses its usefulness as a lifting surface (Reference 11). This approach was originally intended to apply to unswept wings, but has been carried through to application to wings with moderate sweep. Clearly a point is reached for highly swept wings, particularly with low thickness ratios when this approach can no longer be applicable.

A variety of approaches exists for estimating the values of section maximum lift coefficient for defining airfoils. The optimum approach is to have two-dimensional wind tunnel test data available for the desired sections. This is, of course, not always possible. There are several empirical approaches which provide varying degrees of accuracy. In addition, some promising approaches to analytically calculating section $c_{l_{max}}$ will be reviewed.

The first method to be considered is that of Loftin (Reference 12). Perhaps the best overview regarding this method is Loftin's own comment ".... an approximate method for estimating the effect of airfoil section on the maximum lift coefficient has been developed. It should perhaps be pointed out in the beginning that this method most certainly cannot be justified from first principles; however, it did seem to offer at least a rough guide to the manner in which a thin airfoil should be designed to give a high maximum lift coefficient." Loftin assumed that at a section lift coefficient, $c_l$, of 0.1 less than $c_{l_{max}}$, the boundary layer separation point was between the 90% and 100% chord stations. The value of the parameter $(P_2 - P_1)/q_1$, where $P_1$ is the minimum pressure near the leading edge, $P_2$ is the pressure at the 90% chord station, and $q_1$ is the dynamic pressure at the peak evaluated at $c_l = (c_{l_{max}} - 0.1)$ was taken to be indicative of critical conditions necessary for the complete separation corresponding to maximum lift. The correlation was carried out for conventional NACA airfoils based on Theodorsen potential flow pressures and experimental $c_{l_{max}}$ test data. The critical value of the parameter was determined to be 0.885 for values of $c_{l_{max}} \approx 1.5$, as shown by the data of Figure 16.

It is emphasized that the application of Loftin's approach is limited to moderately thin airfoils exhibiting leading edge stall, with nominal or preferably no trailing edge separation. Misapplication of Loftin's criterion may result in significant errors in $c_{l_{max}}$ estimation as indicated in Figure 17. As can be seen, this approach works reasonably well for thickness ratios up to about ten percent, but departs substantially from the test data for the thicker sections.

A second, more flexible, empirical method is that of the USAF stability and control DATCOM (Reference 10). In DATCOM, the section $c_{l_{max}}$ is determined by use of the relationship:

$$c_{l_{max}} = (c_{l_{max}})_{base} + \Delta_1 c_{l_{max}} + \Delta_2 c_{l_{max}} + \Delta_3 c_{l_{max}}$$

where $(c_{l_{max}})_{base}$ is the basic uncambered airfoil $c_{l_{max}}$ at $R_N = 9 \times 10^6$, and $\Delta_1$, $\Delta_2$, and $\Delta_3$ are $c_{l_{max}}$ corrections for camber, thickness, and Reynolds number, respectively.

The various components of $c_{l_{max}}$ are presented as functions of a parameter $\Delta Y$ which is the difference in ordinates (% chord) of the upper surface of an airfoil between the 0.15% and 6% chord stations. Moreover, $\Delta Y$ is based on the uncambered airfoil having the same thickness distribution as the airfoil under consideration. The accuracy of this method may be assessed by examining Figure 18 which correlates calculated and experimental $c_{l_{max}}$ values for a wide range of airfoils.

More sophisticated analytical methods are currently under development which show considerable promise of addressing the problem in a more fundamental manner. One such approach is presented in Reference 13, based on a so-called "free-streamline" approach. In this method, the separation point on the upper surface is determined by a suitable boundary layer routine operating on a velocity distribution which has been corrected for viscous effects. Vortices are distributed around the airfoil surface except in the region between the upper surface separation point and the trailing edge. A single source is used inside the body to give an outflow in the separated region producing a free streamline. The Kutte condition is then satisfied by forcing the pressures to be equal at the lower surface trailing edge and the upper surface separation point. A sample calculation for $c_{l_{max}}$ from this reference is presented in Figure 19; while there is a well defined break in the lift curve which is in agreement with the experimental value of $c_{l_{max}}$, the analytical solution shows a continuing increase in lift after this break.

A second analytical method is that developed by Jacob (Reference 14) and later modified by Beatty (Reference 15). This method simulates the airfoil by a distribution of vortices around the surface contour. A separation point is chosen and an angle of attack assumed. From the separation point to the trailing edge, a source distribution is placed which emits flow and thus simulates the separated region shape as shown in Figure 20. The edge of this region is determined by using a streamline analysis and satisfying the boundary condition of constant pressure at points, A, B, and C. From this model a pressure distribution is generated which is then analyzed by an appropriate boundary layer routine. If the boundary layer routine predicts separation at the assumed separation location then the case is done. If, however, separation is calculated either before or after the assumed separation point, then the angle of attack is changed and a new pressure distribution generated. This procedure is repeated until an angle is found which will move the calculated separation point to the same location as the assumed separation point. The applicability of this method can be seen from the lift curve in Figure 21; while the calculated value is approximately eight percent higher than the experimental value, a very definite round-over in the lift curve is evident.

Given that the section maximum lift coefficients for the defining airfoils are determined by an appropriate method, an accurate knowledge of the spanwise lift distribution is then required. Historically, the ability to calculate span loading has been limited to simple lifting line concepts, wherein the wing lift is considered to be concentrated in a single lifting line at the wing quarter chord, and requires that the induced local flow be parallel to the local chord at a specified location, usually chosen as the three-quarter chord line. Lifting line theories can, in fact, provide a good description of span loading for wings of moderate sweep and aspect ratio. The main shortcoming of the lifting line approach is the inability to accurately simulate highly cambered wings, such as those with trailing edge flaps deflected. These problems have been overcome to a considerable extent with so called lifting surface theories such as the vortex lattice theory discussed in some detail in the previous section.

Given the spanwise lift distribution, the wing maximum lift is then determined to the first order by the section maximum lift characteristics of the defining airfoils. The wing maximum lift coefficient is that value at which the local lift coefficient at any point along the span first reaches the value of the section maximum lift coefficient along the span.

It is again emphasized that this approach is basically sound for unswept wings and loses validity as sweep is increased. This is complicated by strong induced camber effects along the span; the induced effects tend to increase the effective camber inboard, and decrease it outboard, with a resulting departure from two-dimensional characteristics on more highly swept wings. A strong additional complicating factor is the effect of the spanwise gradient on the boundary layer. The addition of nacelles, pylons, and planform discontinuities can also change the characteristics from those predicted.

In spite of all the ostensible shortcomings of this approach to estimating maximum lift, experience has shown that for configurations with moderate sweep, it does in fact work quite well. Figure 22 illustrates the application of the method for calculating the maximum lift coefficient of a wing-fuselage combination with a 24° swept wing. The section maximum lift characteristics were calculated by the method of Reference 12 indicating a total wing $C_{L_{MAX}}$ of 1.51. This compares favorably with a wind tunnel measured value of 1.5. Figure 23 illustrates the application of the method for calculating the maximum lift coefficient of a wing-fuselage combination with a 35° swept wing. The section maximum lift characteristics were calculated for the defining airfoil sections by the method of Reference 10 for a free stream Reynolds number of $6 \times 10^6$ per foot. The local spanwise lift first achieves maximum lift at a total wing $C_L$ of 1.26. The measured $C_{L_{MAX}}$ for the configuration was 1.25.

### 3.1.3 Lift Increment at Low Angle of Attack due to Trailing Edge Flaps

The increment in lift at low angles due to the deflection of trailing edge flaps, $\Delta C_{L_F}$, sometimes referred to as flap effectiveness, is dependent on the section lift increment due to flap deflection, as determined by most methodologies. As will be discussed subsequently, lifting surface theories can be applied to determine flap effectiveness for moderate flap deflections.

The method of Reference 16 relies on a knowledge of the section flap effectiveness, and is given by

$$\Delta C_{L_F} = \Delta c_{l_f} \left(\frac{C_{L_\alpha}}{c_{l_\alpha}}\right) \left[\frac{\alpha_\delta \; C_L}{\alpha_\delta \; c_l}\right] K_b$$

where

| | |
|---|---|
| $\Delta c_{l_f}$ | is the section lift increment due to flap deflection. |
| $C_{L_\alpha}$ | is the lift-curve slope of the unflapped wing. |
| $c_{l_\alpha}$ | is the section lift-curve slope of the basic airfoil. |
| $\frac{\alpha_\delta \; C_L}{\alpha_\delta \; c_l}$ | is the ratio of the three-dimensional flap-effectiveness parameter to the two-dimensional flap-effectiveness parameter, obtained from Figure 24 as a function of wing aspect ratio and the theoretical value of $(\alpha_\delta)_{c_l}$. The theoretical value of $(\alpha_\delta)_{c_l}$ is obtained from the inset chart of the figure, and is a function of flap chord ratio, $c_f/c$. |
| $K_b$ | is the flap-span factor obtained from Figure 25. (Note: $\eta$ is the flap span station expressed as a fraction of wing semi-span. |

A variety of ways exist for determining the section lift increment due to flap deflection. Reference 10 provides the relationship

$$\Delta c_{l_f} = c_{l_\alpha} \; \alpha_\delta \; \delta_f$$

where $c_{l_\alpha}$ and $\alpha_\delta$ are as defined previously and $\delta_f$ is the flap deflection. The change in angle due to flap deflection parameter, $\alpha_\delta$, is given in Reference 10 for a variety of flap configurations, all empirically derived from experimental data. In general, this approach provides an accurate description of flap effectiveness when combined with the three-dimensional relationship. As obtained from Reference 10, the agreement between calculated and experimentally measured flap effectiveness is seen to be reasonably good, as shown in Figure 26.

The limitation of the empirical approach described above is that the finer details of the flap geometry cannot be taken into consideration. This shortcoming can be circumvented by the availability of two-dimensional wind tunnel data for the appropriate flap geometry, or by the application of sophisticated two-dimensional potential flow and boundary layer solutions such as that of Reference 9 as previously discussed. The ability of such a program to accurately describe the flow characteristics over arbitrary multi-element airfoils is shown in Figure 27 for a slatted airfoil with and without a double slotted trailing edge flap. As addressed to the particular problem of determining flap effectiveness, the purely inviscid solution may be applied up to moderate flap deflections to provide a very accurate representation of section flap effectiveness. This can be seen in Figure 28 which compares the potential flow solution flap effectiveness with two-dimensional experimental values for three different double slotted flap geometries. At the higher flap deflections, the viscous effects become more predominant resulting in an optimistic prediction of flap effectiveness. Iterating on the boundary layer solution would result in closer agreement with the experimental values. At the lower flap deflections, while the viscous effects are significant with regard to absolute level of lift, they are of second order effect with regard to a difference in lift, such as the case of flap lift increment.

The application of lifting surface theories can in many instances provide a good direct estimate of three-dimensional flap effectiveness. Such an approach cannot, of course, consider the mutual interference effects of a multi-element flap, or the viscous and thickness effects; however, a careful tailoring of the camber distribution used in a lifting surface theory to represent the actual flap can give a good measure of flap effectiveness when the section properties are not known a priori. The Giesing vortex lattice lifting surface theory (Reference 4) calculations of flap effectiveness are compared in Figure 29 to the experimentally measured values for the DC-9 airplane, and in Figure 30 for the DC-10 airplane indicating good agreement.

### 3.1.4 Maximum Lift Increment due to Trailing Edge Flaps

The estimation of the maximum lift increment due to trailing edge flap deflection is based on purely empirical approaches. The additional lift increment at angles of attack prior to stall brought about by the increase in camber due to trailing edge flaps is readily amenable to analytic treatment until viscous effects dominate the flow as is the case at maximum lift. The addition of trailing edge flaps alters the pressure distribution over an airfoil to the extent that for a given level of lift, the leading edge is unloaded, and the aft section loading is increased, relative to the unflapped airfoil. The maximum lift then occurs when the leading edge becomes loaded to the extent that flow separation occurs there, or when the adverse pressure gradient on the flap itself becomes too severe for negotiation by the boundary layer.

To analytically address this problem is difficult enough for two-dimensional sections. Present two-dimensional boundary layer techniques can accurately predict the flow separation point on the multi-element airfoils given a good description of the potential flow (Reference 9), provided that the viscous flow over a given element is not influenced by the merging of wakes from forward elements. This in itself is not adequate to estimate the maximum lift for airfoils with multi-element high lift systems. The separated wake flow must be analytically modeled so that, as the separation progresses, the lift can be calculated to the point that it no longer increases with angle of attack. As previously discussed, some wake modeling methods have been developed for single element airfoils which appear promising. At present, however, this type of approach for multi-element airfoils is at best in the embryonic stage. These problems are greatly complicated by three-dimensional effects. No techniques presently exist for calculating flow characteristics over swept wings with multi-element high lift systems exhibiting separated flow.

For these reasons the calculation of flap maximum lift increment depends entirely on empirical techniques, which in turn depend on a knowledge of the two-dimensional section characteristics with flaps deflected. The one general method in widespread usage is that of Reference 10. This empirical relationship provides the section maximum lift increment $\Delta c_{l_{max}}$ for plain, split, and slotted flaps as

$$\Delta c_{l_{max}} = K_1 K_2 K_3 \left(\Delta c_{l_{max}}\right)_{base}$$

where $\Delta c_{l_{max\,base}}$ is the section maximum lift increment for a 25-percent chord flap and is dependent on the type of flap and the thickness of the defining airfoil. The factors $K_1$, $K_2$, and $K_3$ account for the effects of flap chord, flap deflection, and flap motion. The accuracy of this approach can be gleaned from Figure 31. As can be seen, the general trend is good, although significant errors can be realized in some instances.

An approximate level of flap maximum lift increment can be obtained from thin airfoil theory considerations. According to thin airfoil theory (Reference 17) the loading at the leading edge of a cambered airfoil is the same as that of an uncambered airfoil at a lift coefficient higher by the amount of one-half the increment in lift due to flap deflection, for vanishingly small flap chord ratios. This implies that, for airfoils whose maximum lift is controlled by leading edge stall, that the flap maximum lift increment is equal to one-half the lift increment provided at constant angle of attack for small flap chords. This increment becomes smaller as the flap chord ratio increases. Thickness effects will, of course, serve to increase this level above that given by thin airfoil theory. This can be seen by examination of the correlation shown in Figure 32 for experimental data measured from five different double slotted flap arrangements for a 9% thick airfoil, each with a chord ratio of approximately 35%. According to thin airfoil theory, the maximum lift increment should be approximately 40% of the lift increment at constant angle of attack; however, due to thickness effects this level is more nearly 60%. Reference 18 carries this approach a step further to account for finite thickness of the airfoil.

The section value of flap maximum lift increment is then used to calculate the three-dimensional value, $\left(\Delta C_{L_{MAX}}\right)_{FLAP}$ by the relationship

$$\left(\Delta C_{L_{MAX}}\right)_{FLAP} = \Delta c_{l_{max}} \left(\frac{S_{w_f}}{S_w}\right) K_\Lambda$$

where $\frac{S_{w_f}}{S_w}$ is the ratio of the wing area affected by the trailing edge flap to the total wing area. The factor $K_\Lambda$ is empirically derived to account for the effects of wing sweep and is given by

$$K_\Lambda = \left[1 - .08 \cos^2(\Lambda_{c/4})\right] \cos^{3/4} \Lambda_{c/4}.$$

In the final analysis, the best assessment of three-dimensional maximum lift increment due to flap deflection lies in measurements in the wind tunnel.

### 3.1.5 Maximum Lift Increment due to Leading Edge Devices

The increase in maximum lift due to leading edge devices results from establishing flow conditions which permit the airfoil to go to a higher angle of attack before stall occurs. The estimation of this maximum lift increment again resorts to empiricism, particularly for adjusting the section values to the three-dimensional ones. The estimation of the section value does, however, lend itself to a certain amount of analytical treatment. Roshko, in Reference 17, proposes a method based on the assumption that for airfoils exhibiting leading edge stall, the pressure distribution at the leading edge is the same at stall regardless of the camber. This implies that the stagnation point location is at the same location in all cases and the pressure distribution around the nose is a function only of stagnation point location. From thin airfoil theory considerations, for an uncambered airfoil, the flow comes smoothly onto the airfoil at zero degrees angle of attack. At other angles, a singularity develops at the nose. For a cambered airfoil, the flow will come smoothly onto the nose at some other angle, in general different from zero. This angle is called the ideal angle of attack. Roshko proposes that the change in maximum lift due to change in leading edge camber, i.e., leading edge device, is entirely due to the change in ideal angle brought about by the camber. This is to say that the pressure distribution at the nose on the uncambered airfoil at the stall angle will now occur at an angle of attack higher than this by the change in ideal angle due to camber. Simple thin airfoil theory considerations provide this change in ideal angle of attack, and the corresponding change in maximum lift. A correlation of the maximum lift increment calculated by this method with experimental values is shown in Figure 33 for a thin airfoil with a 15% chord nose flap, showing reasonable agreement up to about 25° deflection of nose flap.

The above approach cannot, of course, be applied with any degree of confidence for airfoils with multi-element leading edge devices such as a slat. Another approach is suggested, using the criteron that the ultimate maximum lift achievable is limited by exceeding supersonic flow locally on the nose of the airfoil. This is not to say that this will always be the case. Indeed, in the three-dimensional situation many complex factors enter into the control of maximum lift. It is rather suggested that the highest achievable level of maximum lift will be limited by exceeding sonic flow locally but could, of course, be below this due to other factors. Observations of two-dimensional wind tunnel test data seem to support this, as can be seen in Figure 34. The minimum pressure coefficient, $C_p$, measured at the leading edge at $c_{l_{max}}$ is shown for several values of $c_{l_{max}}$. These points represent geometries with several flap deflections and different leading edge devices, and some geometries with no leading edge device. As can be seen, the values are all very close to the critical value corresponding to the free stream Mach number of 0.2 in the wind tunnel. It should be recognized that the pressure gradients at the nose for these high lift conditions are very steep, with significant pressure changes occurring over distances that are on the order of the size of the pressure orifice; this causes some difficulty in extremely accurate pressure measurements, though it is reasonable to assume that the flow is near sonic in all cases.

The flow phenomenon which produces this limiting condition by slightly exceeding the sonic condition is unclear. It may perhaps be due to the formation of weak shocks during deceleration from supersonic flow; this may be sufficient to cause flow separation due to the pressure jump across the shock, imposed on an already severe adverse gradient.

Assuming that the critical value of pressure coefficient can be used as a guideline for maximum lift, sophisticated potential flow solutions can be utilized to calculate the maximum lift increment due to leading edge devices. The potential flow solution is calculated for a variety of lift coefficients for the high lift geometry (i.e., flapped airfoil) both with and without leading edge device, and the difference in lift coefficient at which the critical $c_p$ is reached for the two geometries is a measure of the maximum lift increment for the leading edge device.

A comparison of the calculated maximum lift increment using this approach based on the method of Reference 9, and experimental values for an airfoil with a double slotted flap deflected 5°, for several leading edge slat deflections is shown in Figure 35. While the predicted value is generally above the experimental level, it is interesting to note that the shapes of the two curves are very similar. The probable reason for the overprediction at the lower slat deflection angles is that the control of stall is dominated by trailing edge separation rather than conditions at the leading edge. As the slat deflection is increased, the control of stall is determined by leading edge conditions, giving closer agreement between the measured and calculated values.

For full span slats on three-dimensional wings, the primary parameter affecting the maximum lift increment would appear to be the wing sweep, with slat performance decaying roughly with the square of the cosine of the sweep angle. This is indicated by the accumulation of slat performance data shown in Figure 36. An empirical approach for estimating slat maximum lift increment, $\Delta C_{L_{MAX}\,SLAT}$, for full span slats would then be simply

$$\Delta C_{L_{MAX}\,SLAT} = \left(\Delta c_{l_{max}}\right)_{slat} K_{\Lambda}$$

where $\Delta c_{l_{max}\,slat}$ is the appropriate section value and $K_{\Lambda}$ is the empirical factor shown in Figure 36 to account for sweep.

It is important to note that significant reductions in this performance can be brought about by interruptions in the leading edge by nacelles and pylons. This effect must be assessed by appropriate three-dimensional wind tunnel tests.

### 3.1.6 Total Configuration Maximum Lift

As can be evidenced by the previous discussions, the estimation of airplane maximum lift is generally based on a linear buildup of the various airplane components contributing to the maximum lift, such as clean wing, leading edge devices, and trailing edge flaps, and the horizontal tail load required to trim the pitching moment at maximum lift. In general, this approach works reasonably well, as can be seen in Figure 37 which compares estimated and flight measured values of maximum lift for a variety of airplanes for different flap settings, both with and without leading edge devices.

While the agreement between measured and calculated $C_{L_{MAX}}$ is generally good for those configurations shown, it is not to say that the approach of using a linear buildup is not without its disadvantages. To a large extent, the methods which estimate these characteristics are empirical in nature. This can lead to obvious difficulties for advanced concepts which have geometries departing from those upon which the empirical data is based. Further, complicating interference effects may be introduced which can only be determined from wind tunnel tests of the appropriate geometry.

### 3.1.7 Lift in Ground Effect

During the portions of the takeoff and landing when the airplane is in proximity to the ground, it will experience a change in lift characteristics; at a given geometric angle of attack, the lift will be higher or, at a given level of lift, the effective angle of attack will be lower, at least up to a certain point. The incremental angle of attack decrease due to ground effect can be predicted by Prandtl's multi-plane interference factors as applied to ground operation by Wieselsberger (Reference 19). The mathematical model in this method is formed by two horseshoe vortices representing the real wing and an image located twice the ground height below the wing to form a ground plane streamline. The lifting line theory treatment is simplified to evaluate only the induced vertical velocity at the real wing due to the image wing trailing vortices. A comparison of wind tunnel measured angle of attack changes for several flap deflections with that predicted by the method of Reference 19 is shown in Figure 38. As can be seen, the method does reasonably well in the linear portion, but departs from the data in the higher lift coefficient range. The method of Tani (Reference 20) attempts to refine the approach by including the effect of the bound vortex in the image system, which accounts for the longitudinal velocity induced at the real wing and the resulting circulation change, as well as the induced effects due to the image trailing vortices. The agreement is reasonably good in the linear range, and it attempts to calculate the non-linear effects, but overpredicts the magnitude of the change. Accurate lift predictions are required in ground effect up to the ground angle limit for $V_{MU}$ estimation as this has a direct effect on the takeoff field length as previously discussed. As noted in the figure, the representative lift coefficient for $V_{MU}$ is well into the non-linear region where the methods become unreliable. As a result, empirical methods, or more preferably, wind tunnel ground effect tests of the configuration are required. A more sophisticated treatment of the local induced velocity at the wing is required, which should include the effects of camber as modified by viscous effects.

No consideration is given to ground effect on maximum lift since this is demonstrated only in free air, and the takeoff speeds are at least twenty percent above the speeds corresponding to those at maximum lift.

### 3.2 Drag Characteristics

The accurate estimation of airplane drag characteristics is considerably more difficult than that of the lift characteristics. This is primarily due to the flow being dominated by viscous effects; with the single exception of the inviscid contribution to the drag due to lift, no viscous aspects of the problem are currently amenable to analytical treatment. The zero lift parasite drag computations for the clean configuration are empirically built up from sound two-dimensional analytical considerations; no such analytical treatment is available for multi-element high lift systems.

The problem is complicated by the presence of many non-aerodynamic shapes when a high lift system is deflected, such as flap structural tracks, screw jacks, linkages, and open cavities in flap wells. This is compounded by the presence of highly three-dimensional flows at high lift coefficients, in both the viscous and inviscid sense. For these reasons, the estimation of the parasite drag contribution due to high lift device drag is strongly dependent on experimental data.

### 3.2.1 Clean Configuration Drag

A good approximation to a clean configuration (high lift systems retracted) low speed drag polar is that represented by the classical parabolic polar

$$C_D = C_{D_o} + \frac{{C_L}^2}{\pi A\!R e}$$

where $C_{D_o}$ is the drag at zero lift, and $\frac{C_L^2}{\pi A\!R e}$ is the lift dependent drag. In the strict sense, the drag polars are not parabolic; in the practical sense, however, this representation is a reasonable one. This can be seen from the representative DC-10 flight measured polar shown in Figure 39, which indicates that the drag due to lift is linear with $C_L^2$ throughout the range of lift coefficients.

The zero-lift parasite drag with the high lift system retracted is estimated by empirical methods which rely heavily on wind tunnel and flight test data gathered during previous transport development programs. The basic equivalent parasite drag for the individual airplane components is defined as

$$\left(C_{D_o}\right)_{COMP} = C_f \; K \; \frac{S_{wet}}{S_{ref}}$$

where $C_f$ is the flat plate skin friction coefficient, including the effects of roughness, and $K$ is a form factor which accounts for the effects of thickness, supervelocities, and pressure drag. $S_{wet}/S_{ref}$ is the ratio of wetted area to the reference area.

The flat plate skin friction coefficients can be obtained from Reference 21 for fully turbulent flow and are based on the characteristic length of each component. The characteristic length for a body (fuselage, nacelle) is the overall length and for aerodynamic surfaces (wing, tail, and pylon) it is the exposed mean aerodynamic chord. Roughness effects are due to excrescences such as protruding rivets, steps, gaps, and bulges in the skin, etc., which result from typical manufacturing procedures. This is accounted for (Reference 21) by an equivalent roughness. This equivalent roughness has been determined by equating the flight test zero lift parasite drag for the DC-8, DC-9, and DC-10 to a detailed estimate of the parasite drag and solving for roughness. This value has been determined to be 0.00095 inch and is, within the accuracy of the flight data, a constant value.

The form factor for aerodynamic surfaces is a function of average thickness ratio and of the sweep of the surface, and may be determined from Reference 22, or appropriate two- and three-dimensional wind tunnel data. The form factor for aerodynamic bodies is a function of overall body fineness ratio and may also be determined from Reference 22 or appropriate wind tunnel data.

In addition to the basic form drag of the nacelles there may be base drag due to the design requirements in stowing the thrust reverser. The appropriate base drag coefficients can be obtained from Reference 23. An additional miscellaneous excrescence drag is due to protuberances such as light and antenna fairings, drain masts, probes, unavoidable mismatches, holes, airconditioning system, etc. which all aircraft are required to have. Experience at Douglas based on a detailed analysis of the DC-8, DC-9, and DC-10 aircraft has shown this drag increment to be a constant percentage (~8%) of the basic parasite drag.

The zero-lift wing twist drag can be obtained analytically from an appropriate lifting surface theory such as the Giesing Vortex Lattice program (Reference 4).

The representation of the drag due to lift for the parabolic polar is

$$C_{D_i} = \frac{C_L^2}{\pi ARe}$$

where 'e' is the so-called airplane efficiency factor which accounts for the departure of lift dependent drag from that due to elliptic loading and for the variation of parasite drag with lift. The induced drag may be written as the sum of an inviscid contribution and a viscous contribution

$$C_{D_i} = \left(C_{D_i}\right)_{\text{inviscid}} + \left(C_{D_i}\right)_{\text{viscous}}.$$

The inviscid contribution may be determined from appropriate methods, such as those of References 3 through 6 or 24. The viscous contribution to the induced drag must necessarily be empirically determined from experimental data. The parasite drag is lift dependent due to the thickening of the boundary layer as the pressure gradients increase with increasing lift, and is assumed to be linear with lift coefficient squared:

$$\left(C_{D_i}\right)_{\text{viscous}} = KC_L^2.$$

The total lift dependent drag may then be written as

$$C_{D_i} = \left(C_{D_i}\right)_{\text{inviscid}} + KC_L^2 = \frac{C_L^2}{\pi ARe}$$

from which

$$e = \frac{1}{\pi AR\left[\frac{\left(C_{D_i}\right)_{\text{inviscid}}}{C_L^2} + K\right]}$$

where $\frac{\left(C_{D_i}\right)_{\text{inviscid}}}{C_L^2}$ is merely the slope of the calculated inviscid drag polar.

The parameter 'K' has been empirically determined from available flight measured low speed drag polars and found to be primarily a function of wing sweep. Applying this empirically determined viscous contribution, with the appropriate value of the inviscid drag polar slope to the above relationship, the value of 'e' was calculated for a variety of configurations, and is compared to the flight measured values, as shown in Figure 40. As can be seen, the agreement is generally good. It is again emphasized that the parabolic polar is an approximation, as flight measured polars indicate some distortion from this. Given that enough carefully measured flight polars were available for a variety of configurations one could undoubtedly arrive at additional empirical relationships to account for this. It is, however, far more desirable to continue development of three-dimensional viscous analytical tools which can provide a more fundamental approach to the solution of the problem.

### 3.2.2 Drag due to Trailing Edge Flaps

The drag increment due to the deflection of trailing edge flaps results from both a parasite drag increase and an increase in induced drag. The parasite drag increment due to the deflection of trailing edge flaps presents one of the more challenging low speed characteristics to estimate. As previously mentioned, the non-aerodynamic shapes such as the flap actuating structure which become exposed when the flaps are deflected creates a very complex flow picture which is at best, difficult to assess. This is over and above the consideration that no three-dimensional viscous analytical tools are available to provide a firm theoretical foundation for estimating the drag due to flaps.

There are, however, several promising two-dimensional techniques which can assess the viscous solution of arbitrary multi-element airfoils, such as References 7, 8, 9, and 25. These approaches are, however, limited in their ability to calculate drag. Goradia, in Reference 8, using an integral boundary layer solution, accounts for the presence of the wake from a forward element. This approach provides good correlation with experimentally measured boundary layer characteristics, though the reference does not provide any correlations with measured drag data. Similarly, References 7 and 9, while providing very good agreement with experimentally measured pressure distributions and lift and pitching moment characteristics, have not addressed the drag problem.

A first order approach utilizing the potential and viscous solutions for multi-element airfoils, is to separately apply to each element the method of Squire and Young (Reference 26) which requires a knowledge of the momentum thickness and the potential flow velocity at the trailing edge. This approach works quite well for single element airfoils (Reference 27). It does not, however, lend itself to multi-element airfoils, partly because it does not consider the complex merging effects that occur with the boundary layers of the various elements. More fundamental than this may be that the underlying assumptions to the method are violated in the presence of the asymmetrical and highly curved wake associated with multi-element airfoils under high lift conditions. In the final analysis, the true solution to calculating the drag for multi-element airfoils must lie in extending the calculation downstream into the wake, and determining the velocity distribution in that region.

One is left, then, with a dependence on experimental data for calculating the parasite drag of trailing edge flaps. References 10 and 28 provide experimentally derived section parasite drag increments for relatively simple flaps, such as split flaps and single slotted flaps but do not provide data for more sophisticated double and triple slotted flaps, such as those currently in wide usage on transport aircraft. There are various ways of correcting this section data to three-dimensional values to adjust to part span levels, such as given in Reference 28. Where previously established section data do not provide levels of flap parasite drag for more sophisticated trailing edge flaps, this level must be extracted from three-dimensional data for similar geometry.

The induced drag increment due to the deflection of trailing edge flaps results from the distortion in span loading at a constant lift coefficient, that is, a twist drag increment. This increment is far more amenable to analytic treatment than is the case for the parasite drag increment. The difficulty is that the determination of this increment has no testability; that is, it cannot be determined per se from experimental measurements since any three-dimensional drag increment due to flap deflection includes both the parasite and induced drag contributions.

The assumption must, therefore, be that if the span loading can be accurately calculated, then the resulting induced drag is implicitly correct. The various lifting surface theories can be applied to accurately calculate the span loading for clean wings with no flaps. This task requires considerably more care in the case of large flap deflections. Given that an accurate representation of the effective camber line can be made, good agreement between calculated and measured span loadings can be achieved using methods such as the vortex lattice lifting surface theory of Reference 4. Figure 41 shows such a correlation for a part-span double-slotted flap deflected 50°, indicating good agreement. In principal then, the resulting induced drag increment due to the distortion of the loading over and above the basic clean wing loading will be the appropriate value.

The total flap drag increment is then

$$\Delta C_{D_{FLAP}} = \left(\Delta C_{D_P}\right)_{FLAP} + \left(\Delta C_{D_i}\right)_{FLAP}$$

where $\left(\Delta C_{D_P}\right)_{FLAP}$ is the section value adjusted for span and $\left(\Delta C_{D_i}\right)_{FLAP}$ is the value of induced drag due to span loading distortion.

### 3.2.3 Drag due to Leading Edge Devices

The estimation of the drag increment due to leading edge devices is as difficult, if not more so, than that of the trailing edge flaps. In attempting to analytically calculate the section parasite drag of a leading edge slat by the Squire-Young method, based on the potential flow and viscous solutions from the method of Reference 9, which do not consider the possibility of separated flow on the slat lower surface, one finds even more disparity between theory and experiment as shown in Figure 42. A secondary message to this figure might be noteworthy to the designer, in that the theoretical level might represent something of a lower bound of drag to strive for as a goal.

The very wide variety of leading edge device geometries which can be used for improving low speed characteristics, such as slats, slots, and leading edge flaps, makes it difficult to lend even an empirical approach to the estimation process. One is then left with an almost complete dependance on experimental data to estimate the drag increment resulting from a leading edge device.

### 3.2.4 Miscellaneous Drag

Several additional considerations of drag must be made prior to arriving at the total drag characteristics for any airplane in the high lift configuration. There are several increments of drag which must be included for landing or rejected takeoff calculations, such as drag due to spoilers and landing gear. Within the experience of this author, no methods as such exist for calculating this type of drag increment. Both of these examples are strongly configuration dependant; spoiler drag, for example, is not only dependent on the type of spoiler but the type of trailing edge flap system as well. This results from the spoilers seperating the flow over the flaps, and increases with increasing flap deflection for a fixed spoiler geometry as can be seen in Figure 43, for example, from the spoiler drag increment for the DC-9 airplane as measured in the wind tunnel. The level of drag due to spoilers for no flap deflection could probably be estimated from simple considerations of the drag of flat plates normal to the flow. This is, however, only a small portion of the total drag due to spoilers at high flap deflections. Additional contributions to the spoiler drag result from changes in the induced drag characteristics due to distortion in the span loading, and due to the fact that the spoiler is operating in an increasingly higher velocity field as flap deflection is increased. The drag increment due to spoilers is best obtained from wind tunnel data.

This is similarly true with the drag increment due to landing gear. References such as 22 can be used to estimate the parasite drag of wheels, struts, cavities, doors, etc. However, the drag increment may vary with flap deflection, depending on the relationship of the gear geometry to the flap system. Presumably this results from the downwash field induced by the flaps. This can be seen in Figure 44 for the experimentally measured landing gear drag increment for the DC-8 airplane; this same trend of decreasing drag increment with increasing flap deflection is also evident on the DC-9 and DC-10 aircraft.

Two other drag contributions must be considered for the low speed performance calculations which result from balancing the forces and moments on the airplane, that of longitudinal trim, and that of lateral-directional trim in the instance of a thrust loss due to engine failure.

The balance of forces and moments to be considered for the longitudinal trim case is shown in the force diagram of Figure 45. This results in a change to the total airplane drag due to the load carried on the horizontal tail. The trim drag increment is made up of three main components, which are, for a fixed level of airplane lift coefficient: 1) the change in the airplane tail-off induced drag due to the lift on the horizontal tail, 2) the induced drag of the horizontal tail, and 3) the drag (or thrust) increment due to rotation of the tail lift vector which results from inclination of the local onset flow in the presence of the wing downwash field.

The level of trim drag increment is primarily dependant on the airplane tail length, the amount of static margin, and the amount of high lift system employed. In general, the amount of uncertainty introduced will be dependant on the accuracy of determining the pitching moment and the downwash at the tail. Figure 46 provides an indication of the sensitivity of the trim drag increment to these parameters for a typical transport airplane trimmed in a climbout configuration. As can be seen, the trim drag represents roughly five percent of the total airplane drag at the $V_2$ condition. For this particular case, the trim drag is relatively insensitive to accuracy in pitching moment, there being less than one quarter of one percent change in airplane drag for a 10% change in pitching moment. However, it is evident that the trim drag has considerable sensitivity to the downwash accuracy, in that an uncertainty of .5° can result in a one percent change in total airplane drag. The significance here is that the downwash should best be determined from wind tunnel tests, since there are no suitably accurate methods for predicting the strong 3-D effects which can be encountered in the high lift configuration.

The balancing of forces and moments to be accomplished in the event of an engine failure is shown in Figure 47. This must be considered in takeoff computations as the airplane must be able to continue a takeoff in the event of engine failure at a speed equal to or greater than the decision speed, as previously discussed in the introduction. Balancing the resulting asymmetry will result in an incremental drag.

The loss of an engine as shown in Figure 47 will introduce a yawing moment due to the thrust asymmetry and the windmilling jet drag on the engine which has been shut down. This yawing moment can be balanced by side force due to sideslip and rudder deflection. This net side force can then be balanced by varying amounts of bank angle; however, the airplane will generally be flown with wings level (0° bank angle) which will then require some sideslip. The sideslip and rudder deflection produce a rolling moment which must be balanced by deflection of ailerons and/or spoilers. The net result of the loss of an engine which produces an asymmetric thrust is that the airplane must be balanced in yawing moment, side force and rolling moment. This results in drag increments due to sideslip, rudder and aileron (and/or spoiler) deflections, windmilling engine drag, and, if the airplane is not flown wings level, there will be a slight increment in induced drag due to increased angle of attack to maintain level flight.

Clearly the estimation of these forces is not a simple matter. There are empirical methods dependent on gross parameters such as tail length and engine moment arm, which suffice for preliminary design work. For a more careful analysis, however, the lateral and directional characteristics must be known from wind tunnel measurements. A representative drag increment due to engine out condition is shown in Figure 48 as determined from wind tunnel measured characteristics, for a range of sideslip angles. The various components of the total drag increment are also shown in the figure. For the particular geometry represented here, the drag increments due to rudder deflection and sideslip dominate the picture as contrasted to the various other increments; this picture will, of course, vary for different configurations.

### 3.2.5 Drag in Ground Effect

During the course of ground takeoff acceleration, or deceleration during landing when the airplane is in proximity to the ground, it experiences a reduction in induced drag. This results from a reduction of the downwash from the lifting field of . . wing. The methods of Wieselsberger (Reference 19) and Tani (Reference 20) previously discussed can be applied with good success to the estimation of the drag reduction. A comparison of the estimations using both these methods is shown in Figure 49 with experimentally measured data for a configuration with flaps retracted and slats extended. As can be seen, the theories do a reasonable job of estimating the induced drag reduction. In addition to these two methods, a calculation is shown based on the vortex lattice lifting surface theory of Giesing (Reference 4) for the wing and its image. As can be seen, there is essentially no difference between the lifting surface and the simple lifting line concepts. An additional correlation is shown in Figure 50 for several flapped configurations using the method of Reference 19 for ground heights encompassing the range of angles of attack tested. Again, good agreement is shown in the linear region beyond which the method overpredicts the drag reduction. As previously discussed, the sensitivity of takeoff field length to drag is rather small, except in those cases wherein the airplane is second segment climb limited, which is determined by drag out of ground effect.

### 3.2.6 Total Configuration Drag

The buildup of the total drag of the complete airplane polar in the high lift configuration is assumed to be a component buildup referenced to the clean configuration; the total drag is then

$$C_D = C_{D_o} + \frac{C_L^2}{\pi A e} + \Delta C_{D_{FLAP}} + \Delta C_{D_{SLAT}} + \Delta C_{D_{TRIM}} + \Delta C_{D_{GEAR}}$$

where $C_{D_o}$ is the clean configuration drag at zero lift, and 'e' is the efficiency factor for the clean configuration. This is an artificial approach in the sense that the clean configuration would not be flown at the same lift coefficients as those of the airplane in the high lift case. However, experience with the DC-8, DC-9, and DC-10 transport aircraft has shown that this represents a reasonably accurate method for estimating the high lift configuration drag characteristics. This process is illustrated in Figure 51 which shows the buildup of the various components of drag which comprise the drag polar for the landing configuration. As noted in the figure, this type of buildup does not imply that the slope of the polar in the high lift configuration is the same as that of the clean configuration. In general, the high lift system will, of course, improve the flow quality in that flow separation is reduced and additional leading edge suction is recovered so that the effective 'e' of the polar is higher in the high lift case than that of the clean configuration. This is manifest in the estimation process in that the flap and slat drag increments are dependent on lift coefficient.

The polar shown in Figure 51 is for a landing case with landing gear down. High lift polars for other configurations can be built up in a similar manner, incorporating other drag increments such as that due to spoiler deflection, engine out drag, or drag in ground effect, as appropriate. Correlations of polars estimated in this manner with both wind tunnel measurements and flight measurements will be presented in subsequent discussions.

### 3.3 Pitching Moment Characteristics

Pitching moment characteristics enter into airplane performance in both a direct way and an indirect way. The direct way is with regard to the flying qualities of the airplane, particularly in the stall and post-stall regimes. The indirect way is the manner in which pitching moment characteristics must be balanced to provide longitudinal trim for the airplane, and the resulting effect on trimmed lift and drag characteristics. For the present discussion, the concern will not be with flying qualities, but rather with the determination of the magnitude of pitching moment characteristics for assessing trimmed characteristics.

Pitching moment coefficient is a difficult parameter to determine since it requires an accurate description of the chordwise loading across the span of a configuration, as well as fuselage effects. Applicable methods consist of empirical approaches, lifting surface theories, and full three-dimensional lifting potential flow solutions.

Reference 10 provides an empirical approach for calculating pitching moment characteristics for configurations with and without high lift devices. This procedure is based on an availability of appropriate section pitching moment characteristics; the section characteristics can be determined with reasonable accuracy for arbitrary high lift geometries by a suitable two-dimensional potential and viscous flow solution such as Reference 9 as was previously shown in Figure 27. Due to a lack of experience with this approach by the author and his colleagues, no evaluation of it can be presented.

Representative available lifting surface theories are the vortex lattice theory (Reference 4) which has been discussed previously, and the elementary vortex distribution method (EVD) of Reference 29. The finite element EVD method was originally developed for powered lift systems but has proven to be a valuable analytical tool for wings with unpowered high lift systems as well. In this approach, the wing is represented by a sheet of infinitesimal horseshoe vortices located on their horizontal projection plane. The boundary condition to be satisfied is one of tangential flow on the wing surface. The Kutta condition is satisfied by requiring the vortex strength at the trailing edge to be zero. The formulation of this method consists of dividing the wing planform into a set of rectangular boxes, upon which a composite set of elementary vortex distributions is constructed at any given spanwise station. The chordwise vortex distribution will primarily consist of a series of triangular elements.

The ability of both the EVD and vortex lattice lifting surface theories to accurately calculate the details of chordwise loading is shown in Figure 52, which compares calculated and experimentally measured chordwise pressure distributions at two spanwise stations on a planar wing at 4° angle of attack. It would appear that both methods provide equivalent levels of accuracy in terms of good agreement with experimental results. However, as shown in Figure 53, this accuracy is not carried through to the ability to estimate pitching moment characteristics. While both methods provide agreement with the level of pitching moment at zero $C_L$, the slope of the curve is only in fair agreement according to the vortex lattice theory, and less so for the EVD method.

A fully three-dimensional lifting potential flow solution can provide a good representation of pitching moment characteristics for a wing alone geometry, as shown in Figure 54. The method of Reference 30 was used to calculate the pitching moment characteristics for a planar swept wing, and indicates good agreement with experimental data in the range of lift coefficients wherein viscous effects are not significant. However, as shown in Figure 55, the agreement is rather poor for a swept wing with a fuselage. It is not understood whether this results from numerical accuracy problems, or whether it is due to the possibility of strong viscous flow effects over the fuselage.

The difficulty of applying the various analytical tools with any confidence is compounded for configurations with high lift devices deflected. In general, within the lifting surface theories, the fuselage is represented by either slender body theory considerations, or by semi-infinite fuselages; wing body interference effects, present in the clean configuration as well, present possible additional inaccuracies in the high lift case. In addition, the lifting surface theories are generally linearized so that integrations for force coefficients are conducted in a horizontal plane which includes only vertical components; thus when a flap is deflected, the component of moment due to the force acting in a horizontal plane is not included. Further, viscous considerations such as large parasite drag components on highly deflected flaps can introduce significant errors.

The results of the application of the vortex lattice lifting surface theory (Reference 4) to a swept wing fuselage combination is shown in Figure 56, comparing calculated and experimental pitching moment increment due to flap deflection. As can be seen, the calculated value is in error by a factor of two, probably due to the reasons cited above. A comparison between experimental and calculated pitching moment is shown in Figure 57 for a complete airplane with flaps deflected 20°, utilizing the method of EVD (Reference 29). In this instance, the agreement is seen to be relatively good in terms of slope and level. To some extent, however, this must be fortuitous, since the calculated value was for wing alone and includes no fuselage effects.

In the event that detailed pitching moment characteristics are required, three-dimensional wind tunnel testing must be conducted. At best the various analytical tools can provide some indication of the level of pitching moment, but the strong viscous effects which determine stability characteristics can only be determined experimentally.

## 4.0 WIND TUNNEL MEASUREMENTS

In the final analysis, the low speed high lift characteristics for a given new configuration must be measured in an appropriate wind tunnel to provide the high level of confidence necessary for the initiation of a production program. This permits the designer to verify the estimated characteristics, and to identify and correct potential problem areas which could not be accounted for in the estimation process.

### 4.1 Two-Dimensional Wind Tunnel Testing

While the wind tunnel remains as the single device which can best simulate aerodynamic characteristics, considerable care must be exercised to insure that the desired flow conditions are properly simulated. The complete airplane characteristics must be simulated utilizing a three-dimensional scale wind tunnel model; however, increasing use is given to determining certain component characteristics by utilizing two-dimensional wind tunnels. The advantages are basically due to the wind tunnel model simplicity and associated reduction in cost as compared to three-dimensional models. Further, the results need not be oriented towards a specific configuration, but rather may be applicable to any one of a variety of configurations. Indeed, as pointed out several times in the previous discussion, many estimation methods are strongly dependent on a knowledge of two-dimensional characteristics with empirical corrections to three-dimensions.

A representative low speed two-dimensional wind tunnel currently in use is the McDonnell Douglas facility shown in Figure 58. The model is mounted between two parallel floor-to-ceiling inserts that provide a two-foot two-dimensional test section. This type of testing has certain associated difficulties, the single most difficult problem being the assurance of achieving two-dimensional flow. Departure from two dimensionality can result from two possible sources: external bracketry attaching the high lift system to the model, and, far more significantly, wall boundary layer separation. The former problem can be minimized by relatively large span models and aerodynamically clean bracketry, or may be eliminated altogether by having the high lift system support internal to the walls.

The wall boundary layer separation results from the inability of the tunnel boundary layer to negotiate the severe adverse gradients imposed on the wall by the lifting field of the model. The resulting wall boundary layer separation induces significant three dimensionality in the model flow field. Wall boundary layer control is necessary to minimize this problem either by blowing (Reference 31) or by suction as used in the McDonnell Douglas facility (Reference 32). The importance of applying wall boundary layer control can be seen in Figure 59 for a high lift configuration. The lack of wall suction results in both a significant loss in lift and in non-linear lift characteristics. In addition, the pressure distribution across the span of the vane and flap is highly three dimensional in the absence of the suction. The application of localized wall suction provides a reasonably good level of two-dimensionality across the span of the various model components.

Two additional problem areas associated with two-dimensional testing techniques are possible floor and ceiling flow separation, and the measurement of drag. According to Reference 31, the floor and ceiling separation can be avoided by roughly following the criterion that $c_l(\frac{c}{h})<2$, where c/h is the model chord to tunnel height ratio. This indicates that for chord to height ratios of about one fourth, values of lift coefficient as high as eight can be tolerated without floor or ceiling flow separation. With regard to the measurement of drag, the boundary layer control in the wall introduces significant tares in the drag force direction which are difficult to measure; this usually results in the requirement that drag be measured by a downstream wake survey, using one of the various methods reviewed in Reference 33.

Incorporation of the proper wall interference corrections (Reference 34) and attention to these various problem areas can result in highly accurate two-dimensional measurements over complex high lift shapes with several elements. This was previously demonstrated by the close correlation between theoretically calculated and experimental two-dimensional high lift characteristics discussed, for example, in relationship to Figures 27 and 28.

### 4.2 Three-Dimensional Wind Tunnel Testing

The problem of insuring proper flow simulation for three-dimensional testing becomes correspondingly more complex than in two dimensions, resulting from a desire to correct the tunnel data to full scale flight conditions. The jet boundary corrections normally applied are those of Reference 35 to account for the presence of the wind tunnel boundaries on the model flow field.

The model support system used in conventional wind tunnel testing will interfere with the free air flow about the model. Interference tares must be obtained to account for this effect. The interference tares of a typical model support system can be found by using the procedure given in Reference 36, and illustrated in Figure 60. In this method the aerodynamic characteristics with model upright and inverted with image system installed (Runs 2 and 3 in Figure 60) are used to establish the degree of flow angularity present in the tunnel. The average of the characteristics obtained for these two configurations will correct for this angularity. The difference between these average coefficients, and those obtained from the model inverted with no image system (Run 1) will then represent the complete interference tare correction to account for both angularity and support system interference. This tare correction will then be applied to the data obtained from the model run in the normal upright position, which is Run 4 in Figure 60. It should be noted that to accomplish the interference tare analysis correctly, tares should be generated for each major configuration tested.

The most significant parameter of concern in low speed high lift wind tunnel testing is Reynolds number. In order to simulate flight conditions, a Reynolds number as high as is practicable is desired. Ordinary Reynolds number effects on skin friction due to Reynolds number differences between tunnel test and flight can be readily accounted for. However, there are other significant, and well known Reynolds number effects due to flow separation which cannot be analytically accounted for. A classic example of this is the Reynolds number effect on maximum lift, as shown in Figure 61, for a representative high lift configuration. For this particular geometry, there is about a .13 difference in $C_{L_{MAX}}$ over the range of Reynolds numbers tested. Experience has shown to a large extent that the $C_{L_{MAX}}$ values measured at Reynolds numbers of about $6 \times 10^6$ agree reasonably well with flight. The drag measurements at various Reynolds numbers are shown by the representative data of Figure 62 for both a takeoff and a landing configuration. The difference in drag due to Reynolds numbers effects is significantly more than that due to skin friction; it is, in fact, due to premature flow separation. At lift coefficients which represent climbout conditions, the difference between low Reynolds number levels and that obtained at high Reynolds number represents approximately 4% of the total airplane drag. At the higher Reynolds numbers e.g. between 4.0 and $6.0 \times 10^6$, the differences are attributable to Reynolds number effects on skin friction, and can be accounted for. This effect is even more dramatic for a high lift configuration representative of a landing geometry, as shown in Figure 62. Clearly, the adjustment to the data for calculable Reynolds number effects will produce minimum error at the highest possible test Reynolds number.

In summary, then, to produce an accurate level of high lift configuration drag characteristics, the data must be corrected for wall effects, support strut interference, and adjusted for Reynolds number differences between tunnel and flight, and finally, trimmed to flight c.g. locations. The significance of these effects on representative takeoff lift-to-drag ratio characteristics is shown in Figure 63. As shown, these various effects are not small. The largest adjustment is that due to wall effects, being approximately 12% at representative climbout $C_L$. The remaining adjustments account for an additional reduction such that in going from raw tunnel data to flight simulated levels, an adjustment in access of 20% is required. Considerable care must be exercised to insure that these various adjustments are correctly applied if one is to have confidence in properly simulating full scale levels.

How, then, do these measured characteristics compare to those estimated? From the drag standpoint, the low speed polars as estimated and measured for the DC-10 transport are compared in Figure 64 for representative takeoff and approach configurations. The estimates of these drag characteristics were obtained by a component buildup for the basic clean airplane and high lift system, as previously discussed. The values were obtained from the NASA 12-foot Pressure Wind Tunnel at Ames Research Center. The various adjustments as discussed above were applied to these data. As can be seen, both polars are in remarkably close agreement with the tunnel measurement. The estimated level for the approach conditions has a slightly different slope than the measured level, and is higher by approximately one percent in drag. Estimated polars for various other flap deflections showed similar correlations in that the estimates were in close agreement with the high Reynolds number levels as measured and accordingly corrected to full scale.

This is not to imply that one can always confidently expect close agreement between the tunnel measurements and estimates. The maximum lift coefficients through the range of flap deflections were estimated for the DC-10 by the component buildup previously discussed. In addition, an estimate for a degradation in $C_{L_{MAX}}$ due to nacelle and pylon interference was applied. Subsequent high Reynolds number wind tunnel testing showed, however, that at higher flap deflections, the nacelle interference effects were higher than originally estimated, resulting in a $C_{L_{MAX}}$ for the landing configuration which was lower than estimated, as shown in Figure 65. This condition led to the wind tunnel development of the nacelle strakes, a feature unique to the DC-10 (Reference 37). The principle of the strake is shown in Figure 66; as the angle of attack increases a vortex is shed from the strake and flows over the wing. As the wing approaches stall, this vortex moves close to the wing upper surface, and acts as an energy transport device with the free stream air. This results in delay of the flow separation which originates in this region without the strakes. The effect of the strakes can be seen in Figure 65, which shows the level of $C_{L_{MAX}}$ to be equal to or higher than the original estimate.

The wind tunnel can, then, provide verification of estimated characteristics, and identify problem areas which can be rectified at an early date. This requires careful attention to the adjustment of the tunnel data to proper full scale conditions, and testing at as high a Reynolds number as is practicable. In the final analysis it is the flight characteristics which determine the success of an airplane. A discussion of certain pertinent problem areas in flight measurements, and correlation between flight measurements with estimated and wind tunnel measured characteristics follows.

## 5.0 FLIGHT TEST MEASUREMENTS

The performance demonstrated in flight determines the degree of success of an airplane regardless of the estimated or wind tunnel measured characteristics. The commercial aircraft certification requirements dictate an extensive flight program to demonstrate compliance with FAA regulations; however, the performance items demonstrated are usually not sufficient for the acquisition of the highest quality aerodynamic data. The additional time and funds required for more suitable flight testing can be judged to be too prohibitive since these data are not directly applicable to certified performance. Another possible source of lift and drag data is from prototype and development flight test programs which are conducted to obtain a preliminary assessment of the performance. If the aircraft is performing as expected and no improvement devices are being tested, the development phase may be considerably shortened. The aircraft lift and drag must then be extracted from the certification performance data with supplementation from development flight testing.

### 5.1 Lift Characteristics

The minimum flying speed ($V_{min}$) from which $C_{L_{MAX}}$ is determined, is extracted from a time history trace of velocity for the various high lift configurations, an example of which is shown in Figure 67. The FAA requirements dictate that $V_{min}$ be demonstrated at a rate of entry into the stall of one knot per second. Several entry rates are flown for each high lift geometry and the $C_{L_{MAX}}$ at the one knot per second entry rate is determined accordingly as shown in Figure 68. The $V_{min}$ value of $C_{L_{MAX}}$ is, however, not purely aerodynamic since complicated inertial effects are involved in its demonstration. These $C_{L_{MAX}}$ values cannot then be compared directly with estimated or wind tunnel predictions which are based on a steady state (1-g) stall condition. The 1-g value can be obtained from the flight data by establishing the break in the normal acceleration time history trace as shown in Figure 67. In a fashion similar to the $V_{min}$ $C_{L_{MAX}}$, the 1-g $C_{L_{MAX}}$ can be determined for various entry rates, although experience has shown that the effect of entry rate on 1-g $C_{L_{MAX}}$ is usually negligible.

Complete free air lift curves below stall can be derived from either steady state speed power points, or from the speeds established through the performance of a $V_{min}$ maneuver. Because of its highly dynamic nature the evaluation of lift from the $V_{min}$ maneuver requires accurate measurement of equivalent airspeed, normal and axial accelerations, ambient conditions, angle of attack, gross weight and center of gravity location. In addition to the above parameters, the effects of idle thrust, aeroelasticity, and transitory trim and control inputs must be recognized. Representative complete lift curves derived from both $V_{min}$ maneuvers and level flight data are presented in Figure 69 for two different flap settings. The $C_{L_{MAX}}$ values shown are the 1-g values. As can be seen, the lift curves can be reasonably well established in this manner, though some scatter exists, varying from about one percent at $C_{L_{MAX}}$ to two percent at the lower angles.

In addition to the flight curves shown in Figure 69, the high Reynolds number wind tunnel derived lift curves are presented. The general qualitative character of the wind tunnel lift curves is in good agreement with the flight levels though some differences are to be seen. There is some loss in slope at the higher angles for both flap settings. In addition, for the higher flap setting, the tunnel level of

$C_{L_{MAX}}$ is lower than that measured in flight by about five percent. From these trends, one might conclude that this is a Reynolds number effect, though there is no way to firmly ascertain this. While the wind tunnel provides good agreement in general with flight, the tunnel values must always be viewed with some judgement as to their absolute levels.

Lift chracteristics in ground effect, with landing gear just touching the runway, are usually extracted from minimum unstick speed ($V_{MU}$) or variable pitch attitude maneuvers. Constant pitch attitude liftoff maneuvers have also been flown at angles of attack lower than for $V_{MU}$ in an effort to obtain more stable data. In obtaining lift characteristics in proximity to the ground, the effects of wind, thrust, and pilot trim inputs are also accounted for. The lack of an airspeed system which accurately measures airspeed relative to the air in ground effect with high pitch attitude is still a major problem in data acquisition. A correlation between flight measured and estimated lift curves in ground affect for a transport airplane in a takeoff configuration is shown in Figure 70. The estimated curve is based on a free air flight curve, corrected for ground effect by applying wind tunnel measured increments. The flight measured level was obtained from several constant pitch attitude flight points. As can be seen in Figure 70, the in-ground effect lift curve is well defined, with a scatter band of slightly over one percent, and is in good agreement with the estimated value.

## 5.2 Drag Characteristics

The low speed out-of-ground effect drag characteristics can be obtained from either engine-out climb data or if available from stabilized level flight speed-power points. The engine-out climb data contain measurement errors associated with transients in thrust, airspeed, altitude, temperature, and wind, in addition to the trim drag due to asymmetric thrust. This trim drag may be removed by subtracting wind tunnel measured trim drag increments from the flight test drag level. As can be seen from the data for the various polars in Figure 71, the scatter band can amount to as much as 5% for drag data obtained in this fashion.

Figure 72 presents several polars obtained from stabilized level flight. These data were corrected for accelerations or altitude changes which occurred during data acquisition. As can be seen, the drag data obtained in this manner exhibit significantly less scatter than those obtained from the engine-out climb maneuvers, being in general on the order of one percent.

The measurement of low speed drag in ground effect has met with limited success primarily due to the fact that steady maneuvers have not been obtained in ground effect. Ground effect data are acquired from zero angle of attack ground acceleration runs and at liftoff. The influence of the rolling coefficient of friction during the ground acceleration is much stronger than the drag for dynamic pressures at and below liftoff speed. The dynamics at liftoff introduce a large degree of uncertainty which is compounded by the uncertainty in lift measurement. In any event, this particular characteristic has a relatively small effect on the takeoff ground roll, and is not a characteristic that is demonstrated for certification.

The previous discussion has elaborated on the various problems associated with acquiring good quality flight test drag polars. A similar discussion was presented in Section 4.0 with regard to wind tunnel data. How then, do wind tunnel and flight measured polars compare after one has exercised the greatest possible care in insuring high quality data? Two representative comparisons are shown in Figure 73 for the DC-10 transport aircraft with two different flap settings. The tunnel data were obtained from high Reynolds number wind tunnel tests and adjusted to full scale levels as previously discussed. For the lower flap deflection, it can be seen that the wind tunnel is in very good agreement with the flight measurement throughout the range of lift coefficients. On the other hand, for the higher flap setting, a difference in slope for the polars is observed, in that the tunnel measurement indicates a slightly lower drag due to lift than measured in flight. As previously discussed, the wind tunnel levels of drag are quite sensitive to tunnel wall corrections and to system support interference tares; these effects could be the cause of the slight discrepancy in the slope of the polars. At any rate, this discrepancy is small, and for this particular comparison the polars cross at the $C_L$ of interest, the $C_L$ for $V_2$ speed. It is the general experience at the Douglas Aircraft Company that for transport aircraft, the high Reynolds number derived low speed high lift drag polars are in good agreement with flight measurements, indicating that the wind tunnel provides a very good indication of the drag characteristics to be expected in flight.

The final accounting occurs when the correlations between orginal estimated characteristics and flight measurements are made. If the original estimation is made based on high Reynolds number wind tunnel measurements, a high chance for success is indicated. This is in general not always the case. Considerable wind tunnel development work may occur after a guarantee is made on an airplane, such that the performance characteristics may be based on estimation methods such as those previously discussed. Severe penalties may be imposed if guaranteed performance is not met; on the other hand, having too much conservatism built into the predictions could result in underselling the potential of the aircraft, or in fact, penalizing it unnecessarily due to over-design. It is desired to provide an estimate which will in the end agree very closely with the final flight demonstration.

Comparisons are made in Figure 74 of estimated and flight measured polars for the DC-10. The estimated polars were built up entirely by the previously discussed methods. For the lower flap setting, the estimated level is in good agreement throughout the range of lift coefficients with a slight amount of conservatism in the estimate amounting to about one percent at the $C_L$ for $V_2$ speed. For the higher flap setting, the polars have slightly different slopes such that the estimate has overpredicted the drag at lower $C_L$'s and underpredicted at the higher $C_L$'s . The difference at the $C_L$ for $V_2$, is however, negligible.

## 6.0 ASSESSMENT OF PRESENT STATE-OF-THE-ART

From the previous discussion concerning the various methods available for estimating airplane characteristics, it becomes clear that a wide range of methods exist from full three-dimensional analytical tools to two-dimensional ones with empirical adjustments to three dimensions, purely empirical approaches, and in some instances no method beyond direct application of the wind tunnel data available for the appropriate geometry. A summary of the various types of available methods is shown in Figure 75. In general, it can be concluded that the full analytical treatment of low speed high lift characteristics does not presently exist. A large portion of the high lift characteristics is strongly dominated by viscous effects, such as the parasite drag increments due to high lift system deflection, and more particularly, maximum lift.

What then, do we presently have? The area of high lift characteristics most amenable to analytic treatment is the lift prior to stall. This is basically because for well designed high lift systems there is no flow separation and viscous effects do not dominate the flow picture. For these cases, inviscid representation of the flow provide a reasonable approximation; the slight viscous effects in the absence of flow separation are compensated in lifting surface theories by some extent due to the neglect of thickness effects. It has been shown that sophisticated lifting surface theories can do a reasonable job of predicting lift curve slope, and the lift increment at constant angle of attack due to flap deflection. With regard to the latter characteristics, far more sophisticated two-dimensional approaches can be brought to bear on the problem. Potential flow solutions exist which can calculate the exact potential flow for multi-element airfoils of arbitrary shape. Appropriate boundary layer solutions are available which can modify the potential flow solutions for viscous effects, in the absence of separated flow regions. While these methods provide quite remarkable levels of accuracy for a variety of high lift geometries, they are limited to two-dimensional flows, and therefore require a certain degree of empiricism to adjust to three dimensions. This capability provides a good degree of accuracy in estimating lift increment due to flap deflection.

The various lifting surface theories can also be applied with some success to the estimation of pitching moment characteristics. The pitching moment at zero lift and the slope of the pitching moment curve can be estimated with reasonable accuracy for the clean configuration, although the inability to accurately treat fuselage effects can cause a loss in accuracy. Depending on the extent to which the lifting surface theory can provide details of the chordwise pressure distribution, the pitching moment due to flap deflection can be estimated, though with limited success. The various lifting surface theories provide a good description of the span loading characteristics of wings with flaps deflected, and with fuselage effects. This implies that the resulting calculated induced drag with flaps deflected is then correct.

What then are the shortcomings of present methodology? The determination of the drag increments (aside from induced drag) due to high lift devices is presently dependent either on highly empirical techniques, or in some instances, directly on the wind tunnel. It is doubtful that this problem will ever be completely amenable to analytic treatment, due to the many non-aerodynamic shapes present in the flow with lift devices extended. However, the development of fully three-dimensional boundary layer solutions should lend a sound analytical backing to the estimation process. A further benefit of the availability of such a method is the provision of a more fundamental understanding of the associated flow phenomenon which must ultimately lead to improved high lift system design.

Much the same situation exists with regard to the estimation of maximum lift coefficient. There is some soundness to the estimation process for the maximum lift for the basic wing, though this must be fortuitous to some extent. The ability to analytically calculate the maximum lift for wings with arbitrary multi-element high lift systems depends again on the development of full three dimensional viscous tools. The problem does not stop here, however. Analytical modeling must be developed for separated flow regions, since maximum lift will frequently occur with significant amounts of flow separation present on the geometry. At present, this is a formidable enough task for two dimensions, and it seems reasonable to assume that the solution for arbitrary three-dimensional wings will be correspondingly more difficult.

Many highly complex problems such as Mach number effects and interference effects do not seem amenable to analytic treatment in the near future. In the final analysis one must resort to the wind tunnel for a realistic assessment of the magnitude of these effects. Experience has shown that low speed high lift characteristics, including interference effects can be assessed in the wind tunnel, provided the Reynolds number is sufficiently high. On the contrary, low Reynolds number testing may give misleading characteristics.

A particular problem area which was not addressed in the main text of the paper concerns the lack of availability of analytical tools for estimating low speed high lift characteristics of low aspect ratio highly swept thin wings associated with configurations such as supersonic transport aircraft. Experimental studies (References 38, 39) have shown that even at low angles of attack, the flow over such wings separates from the leading edge and rolls up into spiral vortex sheets, as shown in the sketch of Figure 76. As discussed in Reference 39, flow attachment lines have been observed inboard of the vortex sheets and indicate that the air is drawn over the vortex sheets and accelerated downward. The result of this flow phenomenon is a strong departure from characteristics predicted by ordinary inviscid considerations. The presence of the vortices induce strong local suction peaks which result in an increase in lift, usually referred to as vortex lift, relative to that predicted by linear theory. This increase in lift can be equivalent in magnitude to the basic potential flow lift, as shown in Figure 76 for a 75° swept sharp leading edge delta wing. This drastic change in loading can significantly alter the pitching moment characteristics depending on the wing geometry. The increase in lift may be desirable in some instances to help offset the low lift curve slope associated with low aspect ratio wings; there is, however, an attendant increase in drag due to the loss of leading edge suction resulting from the leading edge separation. The magnitude of this drag increment can be seen in Figure 77, obtained from Reference 40, for a 60° delta wing. The drag due to lift, $\Delta C_D$, as experimentally measured is compared to the theoretical upper and lower bounds of drag due to lift. The lower bound, 100% leading edge suction, results from drag due to lift for an elliptic loading and is

$$\Delta C_D = \frac{{C_L}^2}{\pi A\!\!\!R}$$

The upper bound is for the complete loss of leading edge suction; in this instance the resultant force acts normal to the zero lift line of the wing, or in the case of a flat wing, normal to the surface, and so the drag is simply

$$\Delta C_D = C_L \tan \alpha \, .$$

The experimental drag lies in between these boundaries, indicating that there is a significant loss of leading edge suction.

A very simple approach to calculating the lift and drag characteristics in the presence of leading edge vortex flow was postulated by Polhamus (Reference 38). The basic assumption of the method is that the presence of vortex flow creates a force normal to the wing chord which is equal in magnitude to the leading edge suction force which is predicted by potential flow theory. Underlying this is the basic assumption that the total force acting on the wing associated with the pressures required to maintain the equilibrium of the flow over the separated spiral vortex sheet is essentially the same as the leading edge suction force associated with the leading edge pressures required to maintain attached flow around a leading edge radius. The flow pattern in both cases is somewhat similar, except that for the sharp leading edge-separated flow condition, the force acting on the wing will act primarily on the upper surface rather than on the leading edge. Bhateley, et al, Reference 41, have extended this concept to wings of more complex planform by assuming the normal force introduced by a separated tip vortex on the side of a wing with a finite tip is identical to the tip suction force on that side.

The application of this remarkably simple so called "leading edge suction analogy" leads to a very good accuracy in estimating the lift and drag characteristics for flat wings with sharp leading edges. The resulting estimated lift and drag characteristics, for example, for an aspect ratio 2.0 delta wing are seen to be in good agreement with experimental values, as seen in Figure 78. At the very high angles of attack, the test values of lift are seen to ultimately fall below the predicted levels. This results from a breakdown of the vortex flow, which is initiated at some point in the wake downstream of the wing trailing edge, and moves forward as the wing angle of attack is increased.

The shortcoming of this "leading edge suction analogy" method is that it is limited to wings with sharp leading edges, and zero twist and camber. In general, wings associated with supersonic transport configurations will be highly twisted and cambered from supersonic cruise drag minimization considerations and, from low speed considerations, will possess some leading edge camber and radius, either inherently, or as a result of mechanical devices. Depending on the requirements, there may be trailing edge flaps introducing additional camber. The presence of a finite leading edge radius may permit the attainment of partial leading edge suction. An additional limitation, whether for plane or cambered surfaces is that the chordwise distribution of the analogous leading edge vortex normal force is not known; this limits the application of the approach in computing pitching moment characteristics. An assessment was made of the applicability of this method to wings with twist and camber, and with non-zero leading edge radii.

To accomplish this assessment, the low speed characteristics of a highly cambered 72° swept low aspect ratio wing-fuselage combination were calculated and compared to experimentally measured results. The basis of the potential flow solution is the vortex lattice lifting surface theory of Lamar and Margason (Reference 5). In this scheme up to 120 horseshoe vortices are used to describe the wing-fuselage-tail lifting system. The configuration is divided into a number of panels (one horseshoe vortex per panel) and the distribution of horseshoe vortex strength is calculated to satisfy a no-flow condition through the mean line of the configuration at the 3/4 chord point on the median of each panel. This distribution of circulation along with the calculation of leading-edge suction permits the calculation of lift, drag, and pitching moments.

The calculated and experimental results are shown in Figures 79 and 80 for a clean configuration and a high lift configuration respectively. The associated wing planform and paneling used in the lifting surface theory are shown as inset sketches. To simulate the flaps in the Lamar Margason program, the camberline slopes of several panels were adjusted to represent the deflected flaps. As the spanwise positioning of the paneling did not exactly coincide with that of the flaps, paneling was utilized to provide equivalent area and span of the actual flaps.

The calculated characteristics are presented both with and without vortex lift. As can be seen in Figure 79, the initial lift curve slope for the purely inviscid case is in reasonable agreement with the experimental results; however, the experimental data rapidly depart from the linear characteristics, exhibiting a classical example of leading edge vortex formation. The addition of the calculated vortex lift increment to the inviscid level provides remarkably good agreement with the experimental level. The experimental drag at zero lift has been added to the calculated drag due to lift in both cases for comparative purposes. The exclusion of any leading edge vortex effects results in a drag due to lift considerably less than the experimental level as would be expected since this represents only the inviscid induced drag for the appropriate loading. Adjusting the drag level to the zero leading edge suction level according to the leading edge suction analogy results in closer agreement with experiment. The calculated level is somewhat higher than experiment which may be due to the maintenance of some leading edge suction, or may be due in part to the inability of the method to establish the direction in which the analogous leading edge suction force, and the associated drag, is acting for highly twisted and cambered surfaces.

Because the leading edge suction analogy does not provide any details about the chordwise distribution of the flow, the moment calculations are necessarily shown only for the inviscid solution. As can be seen at the lower lift coefficient, the slope of the calculated moment curve is in fair agreement with the experimental level, although the level of zero lift pitching moment is in rather poor agreement.

Similar comments apply to the correlation shown in Figure 80 for the flaps deflected case. In general, there is a larger departure of the calculated level from the experimental values than for the no-flaps case. This may, in part, be due to the flap paneling approximation in the vortex-lattice wing model, but more significantly is probably due to the inability of the leading-edge suction analogy to handle cambered and twisted surfaces. Another primary problem with the leading-edge suction analogy is that it is directly related to the level of lift present in the system. That is, the actual intent of the analogy was for application to sharp leading edges, so that full loss of leading-edge suction occurs at the onset of any lift, however small. No provision is allowed for maintenance of a substantial portion of leading-edge suction as in the case of cambered leading edges.

The inability of various methods to accurately calculate the drag due-to-lift is graphically presented in Figure 81. For this summary the relatively simple case of a clean wing with no leading or trailing edge high lift devices was utilized, which is the same geometry as that in Figure 79. The upper chart presents, for convenience, the classical upper and lower boundaries of full and zero leading-edge suction respectively. As seen, through the high $C_L$ range, most of the leading-edge suction has been lost. Various analytical solutions are presented in the lower figure; the leading-edge suction analogy provides the closest agreement with experiment. The near field solution was obtained from Reference 3, using the lifting surface theory of Woodward; it would be expected that this calculated drag would be substantially lower than the experimental level, which is clearly not the case. This is due to an inability of the Woodward solution to completely describe the leading edge suction peak, with a consequent overly pessimistic near-field solution to the drag. The Trefftz plane solution was obtained utilizing the span loading from the Woodward program. One additional level is shown using an airplane efficiency factor, 'e' of 0.8. This value was calculated from the empirical method previously discussed. Clearly none of these approaches provide any high degree of accuracy for calculating drag due-to-lift.

In order to address this problem in the analytical sense, fully three-dimensional potential and viscous flow tools are needed. The tools for calculating three-dimensional lifting potential flow characteristics for arbitrary configurations already exist in the state-of-the-art; the Douglas three-dimensional lifting Neumann program (Reference 42) is an example of this type of method. The three-dimensional Neumann program is an exact method since no approximations are made in the basic formulation as is done in both small-perturbation and lifting surface theories. This approach consists of representing the configuration by appropriately distributed panels. The configuration is separated into various sections such as wing, fuselage, horizontal and vertical tail, which can be designated lifting or non-lifting; i.e., a fuselage is assumed to be non-lifting while wings, tails, etc. are considered lifting. The elements which make up the sections are then used to locate distributions of sources and doublets to generate the desired potential flow solutions. Each lifting section must, in addition, have an associated semi-infinite wake.

The extent to which this potential flow method can describe the local details of the flow on a highly swept wing is indicated in Figures 82 and 83, utilizing experimentally measured surface pressures on the 72° swept wing of Reference 43.

Figure 82 presents a correlation of the measured and theoretically calculated pressure distributions at a relatively low angle of attack prior to the onset of any flow separation. The character of the pressure distribution is represented quite well by the Neumann potential flow solution, particularly on the outer panel wherein the leading edge is highly loaded. It is noted that the mid-span station has not been represented in the immediate vicinity of the leading edge, as contrasted to the other stations. This may be due to the formation of a local separation bubble and subsequent reattachment, or it may be that a more accurate paneling representation of the leading edge is required. In contrast to this correlation is one presented in Figure 83 at a high angle of attack wherein viscous effects are predominant. On the inboard end, the level of loading is seen to be reduced relative to the potential flow solution even though the flow has not separated. This is due to the decambering effect resulting from the boundary layer displacement thickness, which increases with increased loading. On the outboard end of the inner panel, a drastic departure of the flow from that predicted by the potential flow solution is evident. This is very clearly due to the formation of the leading-edge vortex, centered about 20% aft of the leading edge. The departure from potential flow is even more evident on the outer panel. The vortex flow is strongly evident on the inner portion of the panel, and complete flow separation is present on the outer portion.

An attempt to analytically model the flow pattern such as that shown in Figure 83 presents a formidable challenge to the theoretician. This requires a fully three-dimensional boundary layer method, which coupled with the existing potential flow solution can provide the initial key to the problem, namely to establish the conditions which cause the flow to breakdown at the leading edge. Once this phenomenon is understood, then analytical methods must be developed to model the vortex flow and the separated flow.

The development of analytical techniques to determine high lift characteristics in the presence of vortex flow will serve two strong purposes. Firstly, the lack of even sound empirical techniques currently results in a strong dependence on wind tunnel data for estimating these characteristics; the availability of suitable analytical tools will reduce this dependence. Secondly, the methodology will provide a more fundamental understanding of the leading edge vortex flow phenomenon, which can lead to improving the design of leading edge devices.

It appears that the assessment of the state-of-the-art of estimating low speed airplane characteristics whether for supersonic transport configurations or more current aircraft, reveals that significant improvements in sophistication in the future will be strongly dependent on development of fully three-dimensional viscous analytical tools. In effect, this desired goal is one of achieving a mathematical wind tunnel. The potential flow solution for arbitrary three-dimensional lifting geometries is basically within the state-of-the-art. The three-dimensional boundary layer solution is less than complete at this point.

In many instances the potential flow solution can provide a good representation of the three-dimensional flow field. In other instances, the viscous effects will predominate the flow picture and ignoring these effects will significantly overpredict the characteristics, as shown, for example, in Figure 84 which presents a comparison between an inviscid span loading and an experimentally measured one for a 45° swept wing. While the full three-dimensional viscous solution is not yet available, a somewhat crude attempt to adjust the inviscid pressures for the effects of viscosity was made. This was done by utilizing a blowing technique in the potential flow solution to simulate the effect of adding the boundary layer displacement thickness to the basic wing geometry. This approach was crude in the sense that the boundary layer displacement thickness used in the analysis was obtained from a two-dimensional method. As can be seen in Figure 84, the agreement between calculated and experimentally measured spanwise and chordwise loading along the entire span was substantially improved, even by this approximate viscous correction.

In the final analysis, of course, the full three-dimensional boundary layer equations must be solved. Certain special cases of this have already been solved, such as the boundary layer equations for small cross flow (Reference 44). In this approach the boundary layer equations are solved along a streamline (Figure 85). The coordinate system is an orthogonal one formed by the inviscid streamlines and their orthogonal trajectories on the surface. As seen in Figure 85, the projection of the free-stream velocity vector on the surface is aligned with the surface coordinate x. The velocity component along the z-axis, referred to as the cross-flow velocity, is zero at the edge of the boundary layer. For a three-dimensional flow, the velocity vector at any y-location in the boundary-layer differs in direction from the freestream vector when both are projected on the surface, in which case the crossflow velocity w within the boundary-layer differs from zero, except at the wall. For the special case of small crossflow the solution of the three-dimensional boundary layer equations can be simplified by assuming that the crossflow terms and the lateral derivatives are small relative to the streamwise terms. These equations can be readily solved using numerical techniques given in Reference 45. This small crossflow solution, while relatively new, should find accurate application in boundary layer solutions for wings of moderate sweep and high aspect ratio.

Eventually, this approximate solution will be replaced by a new three-dimensional boundary layer routine currently under development by Dr. Cebeci (Reference 46). This new method will make none of the simplifying assumptions made in the small crossflow solution, and will actually solve the complete three-dimensional boundary layer equations.

The solution of the various two- and three-dimensional inviscid and viscous flow problems have been made possible by the advent of new numerical techniques such as those of Cebeci and Keller (Reference 45), coupled with major advancements in computer technology. Until recently, computing times would have been prohibitive for many of these problems, whereas today, calculation times are small enough to permit these complex programs to be used as every day design tools for aerodynamic designers.

In addition to the mathematical complexities which must be overcome in order to develop complete three-dimensional flow solutions, the problem of associated computing costs is also relevant. It is granted that the enormously increased capacity of modern digital computers has permitted the solution of problems which a decade or so ago could not be solved. The indications are that computers in the future will be even faster. However, these faster computers are more costly, and the unit cost per given solution may not necessarily be reduced. An indication of the cost of computerized solutions for different inviscid flow solutions can be seen in Figure 86. The cost is presented as a function of the complexity of the program; simple lifting line methods which define a wing surface with very few elements are virtually insignificant in cost. However, full three-dimensional potential flow solutions requiring one thousand or more elements may become quite expensive. Indeed, it can be envisioned that three-dimensional viscous flow solutions for several flow conditions, could result in computer costs which are of the same order of magnitude as an appropriate wind tunnel test.

Neither the computer nor the wind tunnel will replace each other; it is rather that increasingly sophisticated methods requiring more complex computer programs will serve to reduce the reliance on the wind tunnel and at the same time provide more fundamental understanding of the flow phenomenon. In the final analysis, it is the combined application of all of these tools, coupled with sound judgement by the engineer, which provides the most realistic estimation of low speed aerodynamic characteristics.

## 7.0 REFERENCES

1. Bates, R. E.: Progress on the DC-10 Development Program. AIAA Paper No. 69-830, July 1969.

2. Harvey, S. T.; and Norton, D. A.: Development of the Model 727 Airplane High Lift System. SAE Paper S408, 21 April 1964.

3. Woodward, F. A.; Tinoco, E. N.; and Larsen, J. W.: Analysis and Design of Supersonic Wing-Body Combinations, Including Flow Properties in the Near Field. NASA CR-73106, August 1967.

4. Giesing, J. P.: Lifting Surface Theory for Wing-Fuselage Combinations. Rep. DAC-67212, Vol. 1, Douglas Aircraft Company, August 1968.

5. Margason, R. J.; and Lamar, J. E.: Vortex-Lattice Fortran Program for Estimating Subsonic Aerodynamic Characteristics of Complex Planforms. NASA TN D-6142, February 1971.

6. Martin, G. H.: Vortex Collocation Lifting Surface Theory for Subsonic Compressible, Potential Flow. Lockheed-Georgia Company ER 8814, 1967.

7. Bhateley, I. C.; and Bradley, R. G.: A Simplified Mathematical Model for the Analysis of Multi-Element Airfoils Near Stall. Presented at AGARD Meeting "The Fluid Dynamics of Aircraft Stalling," Lisbon, Portual, April 1972.

8. Stevens, W. A.; Goradia, S.H.; and Braden, J. A.: Mathematical Model for Two-Dimensional Multi-Component Airfoils in Viscous Flow. NASA Contractor Report CR-1843, July 1971.

9. Callaghan, J. G.; and Beatty, T.D.: A Theoretical Method for the Analysis and Design of Multi-Element Airfoils. Journal of Aircraft, Vol. 9, No. 12. December 1972, pp. 844-848.

10. USAF Stability and Control DATCOM: Mcdonnell Douglas Corporation, revised February 1972.

11. Kuethe, A. M.; and Schetzer, J. D.: foundations of Aerodynamics. New York, John Wiley & Sons, Inc., 1955.

12. Loftin, L. K.; and von Doenhoff, A. E.: Exploratory Investigation at High and Low Subsonic Mach Numbers of Two Experimental 6-Percent-Thick Airfoil Sections Designed to Have High Maximum Lift Coefficients NACA RM L51F06, 14 December 1951.

13. Bhateley, Ishwar C.; and McWhirter, Jack W.: Development of Theoretical Method for Two-Dimensional Multi-Element Airfoil Analysis and Design. Air Force Flight Dynamics Laboratory Report AFFDL-TR-72-96 Part 1, August 1972.

14. Jacob, K.: Theoretical Calculation of Pressure Distributions and Force Coefficients for Arbitrary Airfoils in Incompressible Flow with Separation. Douglas Aircraft Company Report No. MDC-J0656, Translated from Aerodynamische Versuchsanstalt Gottingen AVA 67A 62 by A. D. Gordon, March 1970.

15. Beatty, T. D.: Prediction of Flows with and without Partial Separation. Masters Thesis presented to the Department of Mechanical Engineering, California State University, Long Beach, July 1972.

16. Lowry, J. G.; and Polhamus, E. C.: A Method for Predicting Lift Increment due to Flap Deflection at Low Angles of Attack in Incompressible Flow. NACA TN 3911, 1957.

17. Roshko, A.: Computation of the Increment of Maximum Lift due to Flaps. Douglas Aircraft Report SM-23626. July 13, 1959.

18. McRae, D. M.: Aerodynamics of Mechanical High Lift Devices. AGARD Lecture Series No. 43, "Assessment of Lift Augmentation Devices," 1971.

19. Wieselsberger, C.: Wing Resistance Near the Ground. TM No. 77, NACA, 1922.

20. Tani, Itiro; Taima, Masao; and Simidu, Sodi: The Effect of Ground on the Aerodynamic Characteristics of a Monoplane Wing. Report No. 156 (Vol. XIII, 2), Aero. Res. Inst., Tokyo Imperial University, September 1937.

21. Clutter, D. W.: Charts for Determining Skin Friction Coefficients on Smooth and on Rough Flat Plates at Mach Numbers up to 5.0 with and without Heat Transfer. Douglas Report ES29074, April 15, 1959.

22. Hoerner, S. F.: Fluid Dynamic Drag. Published by Author, 1958.

23. Stoney, W. E.: Collection of Zero Lift Drag Data on Bodies of Revolution from Free Flight Investigations. NASA TN 4201, January 1958.

24. Anderson, R. F.: Determination of the Characteristics of Tapered Wings. NACA Report 572, 1936.

25. Irwin, H. P. A. H.: A Calculation Method for Two-Dimensional Turbulent Flow over a Slotted Flap. RAE Technical Report 72124, 1967.

26. Squire, H. B.; and Young, A. D.: The Calculation of the Profile Drag of Aerofoils. ARC R&M 1838, 1938.

27. Cebeci, T.; and Smith, A. M. O.: On the Calculation of Profile Drag of Airfoils at Low Mach Numbers. Journal of Aircraft, Vol. 5, No. 6, November - December 1968.

28. Royal Aeronautical Society Data Sheets.

29. Lopez, M. L.; and Shen, C. C.: Recent Developments in Jet Flap Theory and its Application to STOL Aerodynamic Analysis. AIAA Paper No. 71-578, June 1971.

30. Friedman, D. M.: A Three-Dimensional Lifting Potential Flow Program. Douglas Aircraft Company Report MDC J6182-01. (To be published).

31. Van den Berg, B.: Some Notes on Two-Dimensional High Lift Tests in Wind Tunnels. AGARD Lecture Series No. 43, 1971.

32. Morrison, Myron E.: Two-Dimensional Channel Insert in the McAir Low Speed Wind Tunnel. McDonnell Engineering Laboratories Paper presented at the Subsonic Aerodynamic Testing Association Meeting, Ottawa, Canada, May 1970.

33. Zwaaneveld, J.: Comparison of Various Methods for Calculating Profile Drag from Pressure Measurements in the Near Wake at Subcritical Speeds. AGARD Conference Preprint No. 124.

34. Allen, H. Julian; and Vincenti, Walter G.: Wall Interference in a Two-Dimensional Wind Tunnel with Consideration of the Effect of Compressibility. NACA Report No. 782, 1944.

35. Sivells, James C.; and Salmi, Rachel M.: Jet Boundary Correction for Complete and Semispan Swept Wings in Closed Circular Wind Tunnels. TN 2454, 1951.

36. Millikan, C. B.; Smith, J. E.; and Bell, R. W.: High Speed Testing in the Southern California Cooperative Wind Tunnel. Journal of the Aeronautical Sciences, February 1948.

37. Bates, R. E.: DC-10 Design Development. Presented to ATA Engineering Maintenance Conference, Douglas Aircraft Company Paper 5996, December 1971.

38. Polhamus, E. C.: A Concept of the Vortex Lift of Sharp Edge Delta Wings Based on a Leading Edge Suction Analogy. NASA TN D3767, December 1966.

39. Polhamus, E. C.: Prediction of Vortex-Lift Characteristics by a Leading-Edge Suction Analogy. Journal of Aircraft, Volume 8, No. 4, April 1971.

40. Polhamus, E. C.: Application of the Leading Edge Suction Analogy of Vortex-Lift to the Drag due-to-Lift of Sharp-Edge Delta Wings. NASA TN D-4739, August 1968.

41. Bradley, R. G.; Smith, C. W.; Bhateley, I. C.: Vortex Lift Prediction for Complex Wing Planforms. AIAA Engineering Note, Journal of Aircraft, Vol. 10, No. 6, June 1973.

42. Hess, John L.: Calculation of Potential Flow about Arbitrary Three-Dimensional Lifting Bodies. Douglas Aircraft Report MDC J5679-01, October 1972. Prepared under NASC Contract N00019-71-C-0524.

43. Lamar, John E.; and McKinney, Wayne L.: Low-Speed Static Wind-Tunnel Investigation of a Half-span Fuselage and Variable-Sweep Pressure Wing Model. NASA TN D-6215, August 1971.

44. Cebeci, Tuncer; Mosinskis, G. J.; and Kaups, Kalle: A General Method for Calculating Three-Dimensional Incompressible Laminar and Turbulent Boundary Layers. I. Swept Infinite Cylinders and Small Cross Flow. Douglas Aircraft Report No. MDC J5694, November 1972. Prepared under NSRDC Contract No. N00014-72-C-0111.

45. Keller, H. B.; and Cebeci, T.: Simple Accurate Numerical Methods for Boundary Layers. I. Two-Dimensional Laminar Flows. Proceedings of the Second International Conference on Numerical Methods in Fluid Dynamics, Lecture Notes in Physics, Vol. 8, Springer-Verlag, New York, 1971.

46. Cebeci, Tuncer; Kaups, Kalle; Mosinskis, G. J.; and Rehn, J. A.: Some Problems of the Calculation of Three-Dimensional Boundary Layer Flows on General Configurations, NASA Report CR2285, July 1973.

## 8.0 ACKNOWLEDGEMENT

The subject matter of this paper extends over a wide spectrum of disciplines within low speed aerodynamics, and thereby represents contributions on the part of several colleagues. The author wishes to acknowledge the contributions of T. D. Beatty in the more theoretically oriented aspects of the paper, J. T. Callaghan and P. M. Minor in the wind tunnel and flight test discussions, and A. W. Ebeling for her suggestions regarding the broad outline of the paper. Particular appreciation is expressed to Alice Morgan for her highly efficient performance in the typing of this paper.

LIFT SYSTEM

FIGURE 1. DC-10 TRANSPORT IN HIGH-LIFT CONFIGURATION

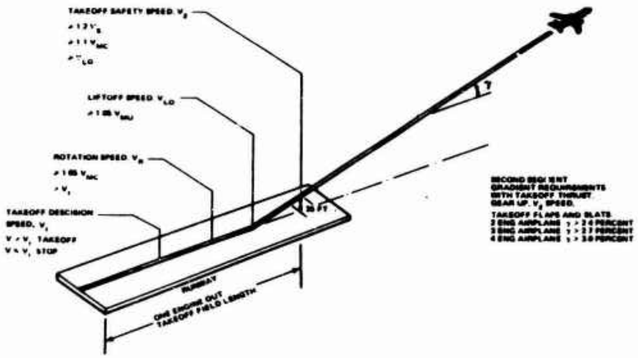
TAKEOFF SAFETY SPEED $V_2$
$\geq 1.2 V_S$
$\geq 1.1 V_{MC}$
$\geq V_{LO}$
LIFTOFF SPEED $V_{LO}$
$\geq 1.05 V_{MU}$
ROTATION SPEED $V_R$
$\geq 1.05 V_{MC}$
$\geq V_1$
TAKEOFF DESCISION SPEED, $V_1$
$V \geq V_1$ TAKEOFF
$V < V_1$ STOP
35 FT
γ
RUNWAY
ONE ENGINE OUT TAKEOFF FIELD LENGTH
SECOND SEGMENT GRADIENT REQUIREMENTS WITH TAKEOFF THRUST GEAR UP, $V_2$ SPEED.
TAKEOFF FLAPS AND SLATS
2 ENG AIRPLANE $\gamma > 2.4$ PERCENT
3 ENG AIRPLANE $\gamma > 2.7$ PERCENT
4 ENG AIRPLANE $\gamma > 3.0$ PERCENT

FIGURE 3. TAKEOFF DEFINITIONS

FIGURE 2. STRUCTURAL COMPLEXITIES OF HIGH-LIFT SYSTEM

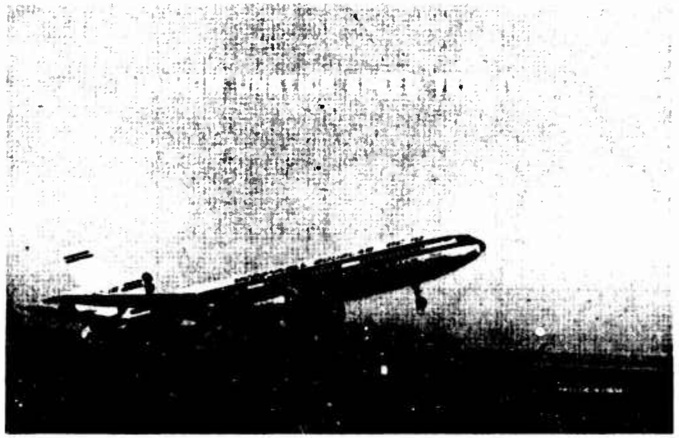

FIGURE 4. MINIMUM UNSTICK SPEED DEMONSTRATION

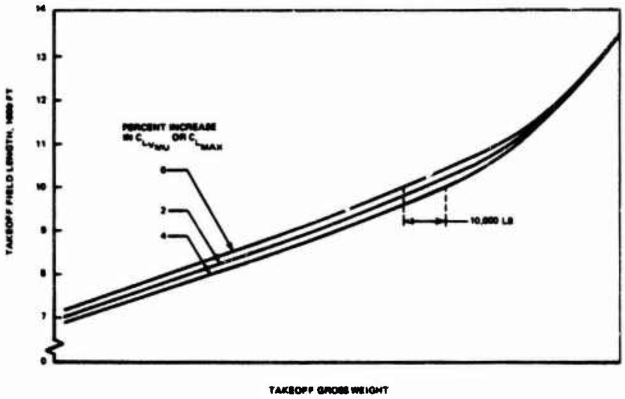

FIGURE 5. SENSITIVITY OF TAKEOFF FIELD LENGTH TO CHANGES IN LIFT

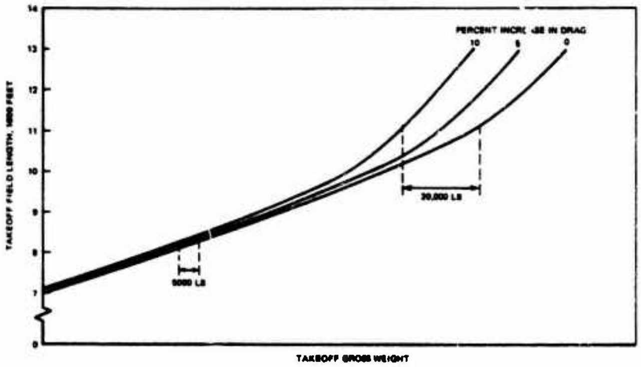

FIGURE 6. SENSITIVITY OF TAKEOFF FIELD LENGTH TO CHANGES IN DRAG

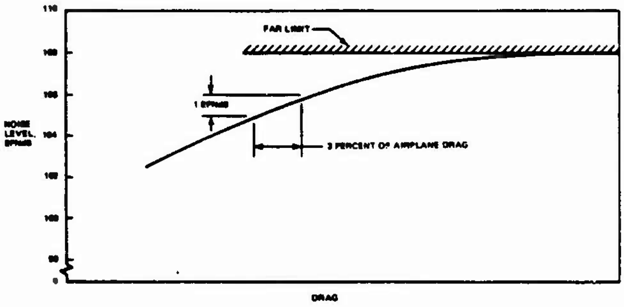

FIGURE 7. EFFECT OF DRAG ON APPROACH NOISE LEVEL

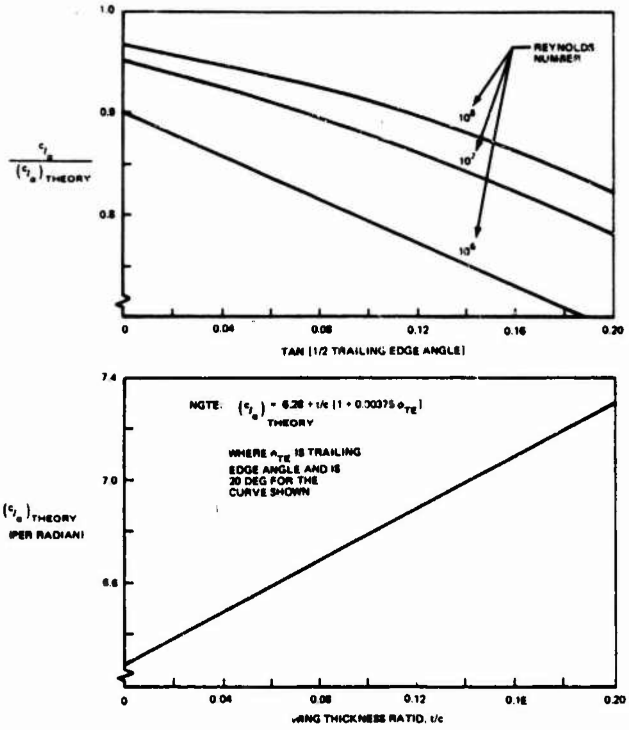

FIGURE 8. TWO-DIMENSIONAL LIFT-CURVE SLOPE

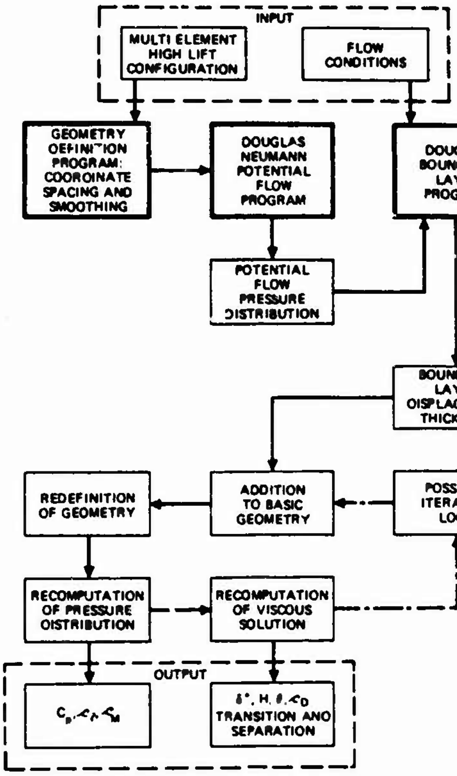
INPUT
MULTI ELEMENT HIGH LIFT CONFIGURATION
FLOW CONDITIONS
GEOMETRY DEFINITION PROGRAM: COORDINATE SPACING AND SMOOTHING
DOUGLAS NEUMANN POTENTIAL FLOW PROGRAM
DOUGLAS BOUNDARY LAYER PROGRAM
POTENTIAL FLOW PRESSURE DISTRIBUTION
BOUNDARY LAYER DISPLACEMENT THICKNESS
REDEFINITION OF GEOMETRY
ADDITION TO BASIC GEOMETRY
POSSIBLE ITERATIVE LOOP
RECOMPUTATION OF PRESSURE DISTRIBUTION
RECOMPUTATION OF VISCOUS SOLUTION
OUTPUT
$C_p, C_l, C_M$
$\delta^*, H, \theta, C_D$
TRANSITION AND SEPARATION

FIGURE 9. FLOW DIAGRAM OF COMPUTER PROGRAM FOR MULTI ELEMENT AIRFOIL DESIGN AND ANALYSIS METHOD (MADAAM)

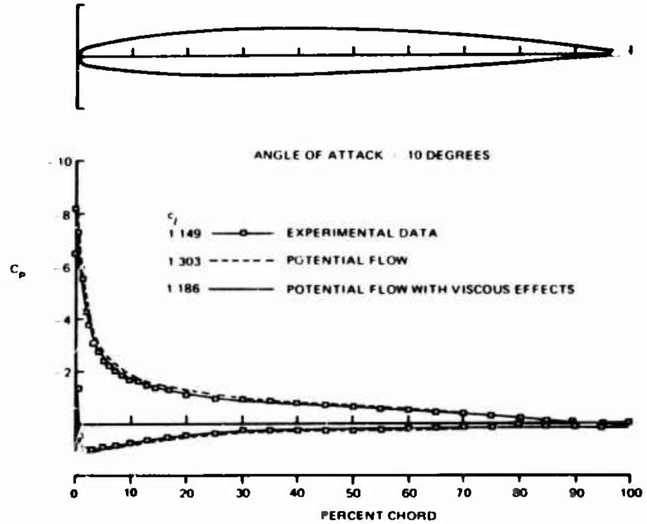

FIGURE 10. COMPARISON OF EXPERIMENTAL AND CALCULATED PRESSURE DISTRIBUTIONS FOR SINGLE ELEMENT AIRFOIL

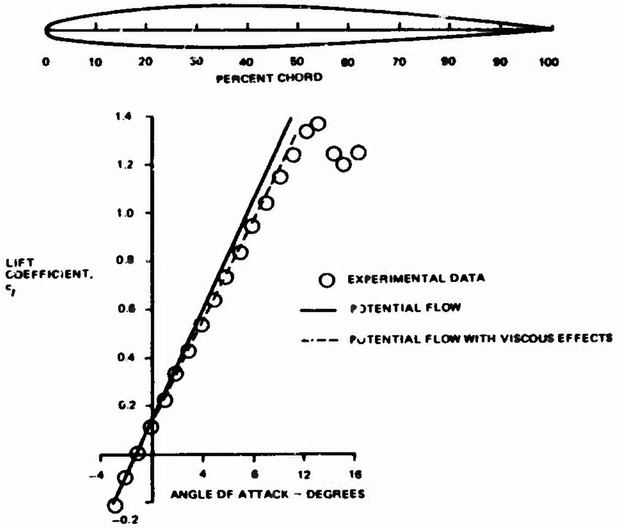

FIGURE 11. COMPARISON OF EXPERIMENTAL AND CALCULATED LIFT CURVES FOR SINGLE ELEMENT AIRFOIL

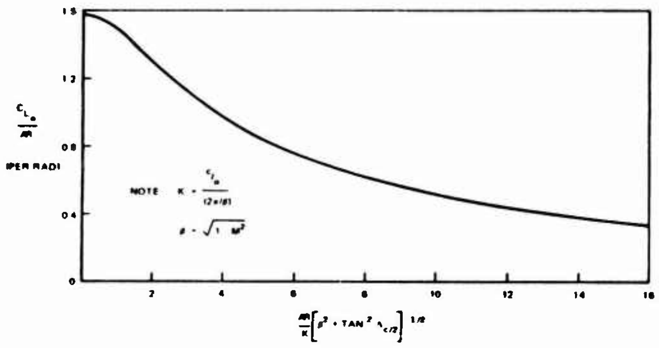

FIGURE 12. SUBSONIC WING LIFT – CURVE SLOPE

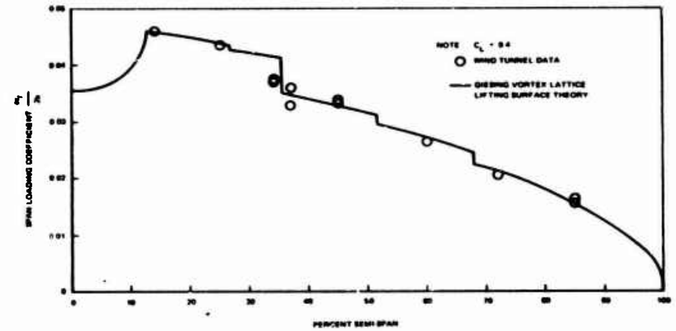

FIGURE 13. SPAN LOADING DISTRIBUTION ON 35-DEGREE SWEPT WING FUSELAGE COMBINATION WITH NACELLES, PYLONS AND FLAP HINGE FAIRINGS

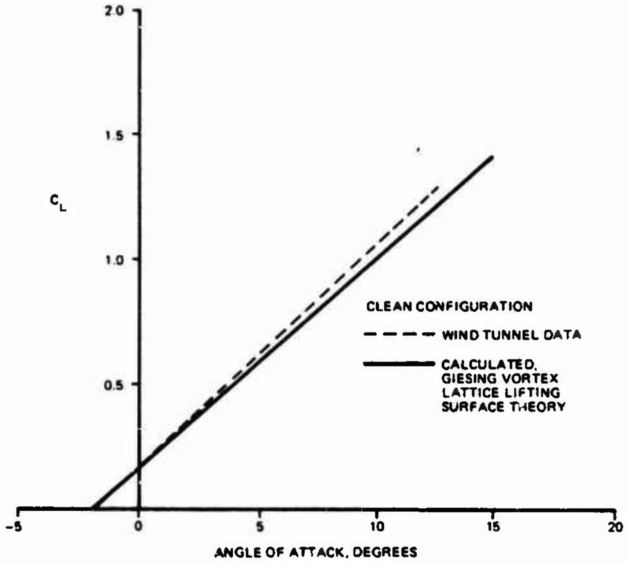

FIGURE 14. COMPARISON OF CALCULATED AND EXPERIMENTAL LIFT CURVES, MODEL DC-9

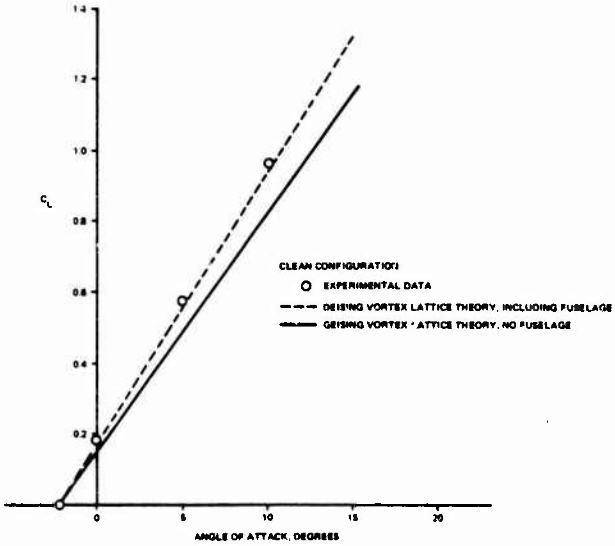

FIGURE 15. COMPARISON OF CALCULATED AND EXPERIMENTAL LIFT CURVES, MODEL DC-10

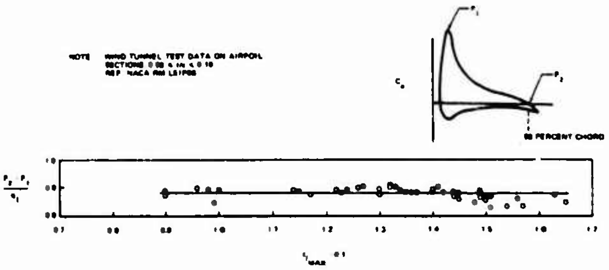

FIGURE 16. CORRELATION OF PRESSURE-RECOVERY PARAMETER FOR LOFTIN SECTION $c_{l_{MAX}}$ CRITERION

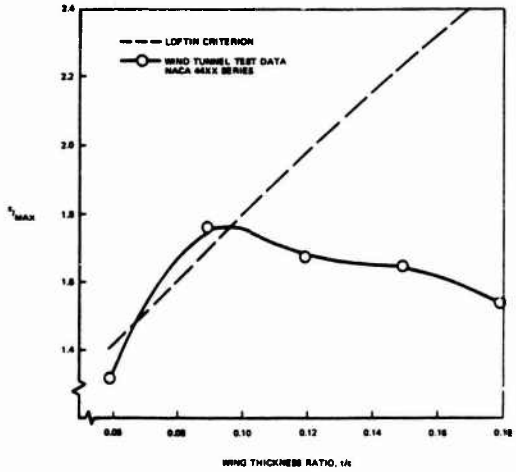

FIGURE 17. COMPARISON OF EXPERIMENTAL AND CALCULATED SECTION $c_{l_{MAX}}$ USING LOFTIN CRITERION FOR NACA 44XX AIRFOIL SERIES

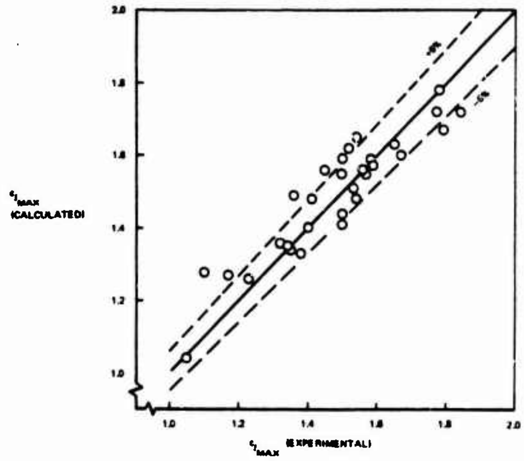

FIGURE 18. COMPARISON OF EXPERIMENTAL AND CALCULATED VALUES OF $c_{l_{MAX}}$ USING DATCOM

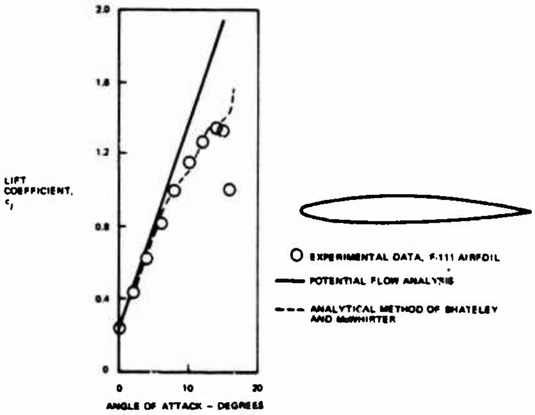

FIGURE 19. COMPARISON OF EXPERIMENTAL AND ESTIMATED LIFT CURVES USING METHOD OF BHATELEY AND McWHIRTER

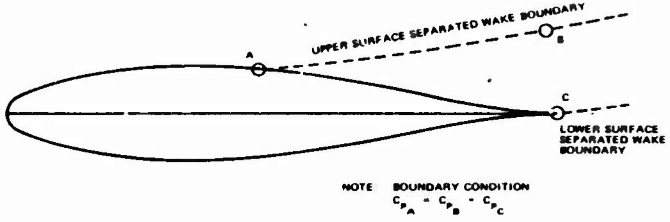
UPPER SURFACE SEPARATED WAKE BOUNDARY
A
B
C
LOWER SURFACE SEPARATED WAKE BOUNDARY
NOTE BOUNDARY CONDITION $C_{p_A} = C_{p_B} = C_{p_C}$

FIGURE 20. SEPARATED WAKE MODEL BOUNDARY CONDITIONS, AFTER JACOB

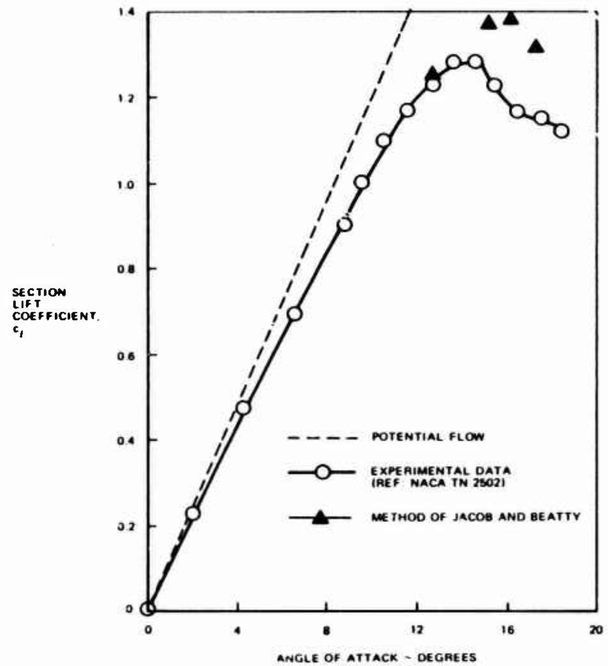

FIGURE 21. COMPARISON OF EXPERIMENTAL AND CALCULATED LIFT CURVES FOR NACA $63_2$–018 AIRFOIL, USING METHOD OF JACOB AND BEATTY

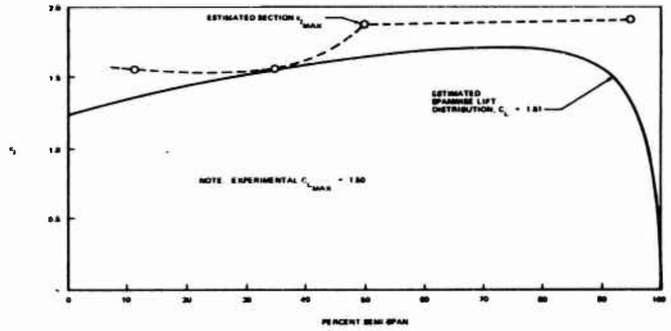

FIGURE 22. ESTIMATED $C_{L_{MAX}}$ FOR 24-DEGREE SWEPT WING-FUSELAGE COMBINATION

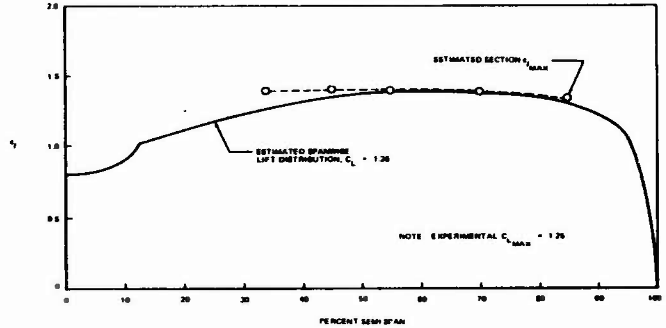

FIGURE 23. ESTIMATED $C_{L_{MAX}}$ FOR 35-DEGREE SWEPT WING-FUSELAGE COMBINATION

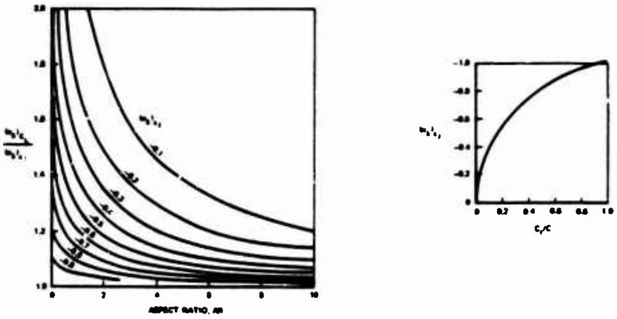

FIGURE 24. FLAP-CHORD FACTOR FROM DATCOM

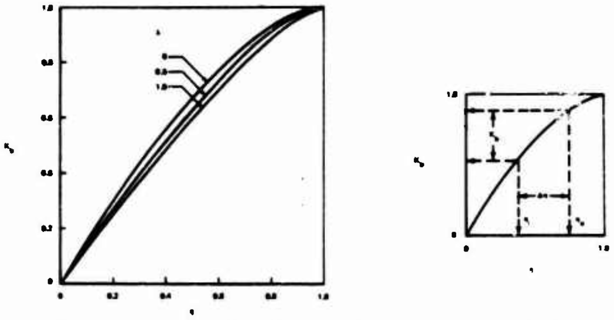

FIGURE 25. SPAN FACTOR FOR PART-SPAN FLAPS

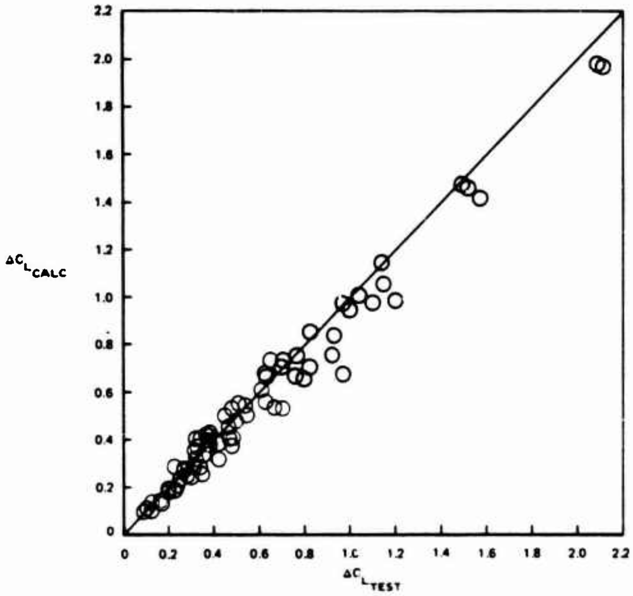

FIGURE 26. COMPARISON OF EXPERIMENTAL AND CALCULATED VALUES OF THREE-DIMENSIONAL LIFT INCREMENT DUE TO FLAP DEFLECTION

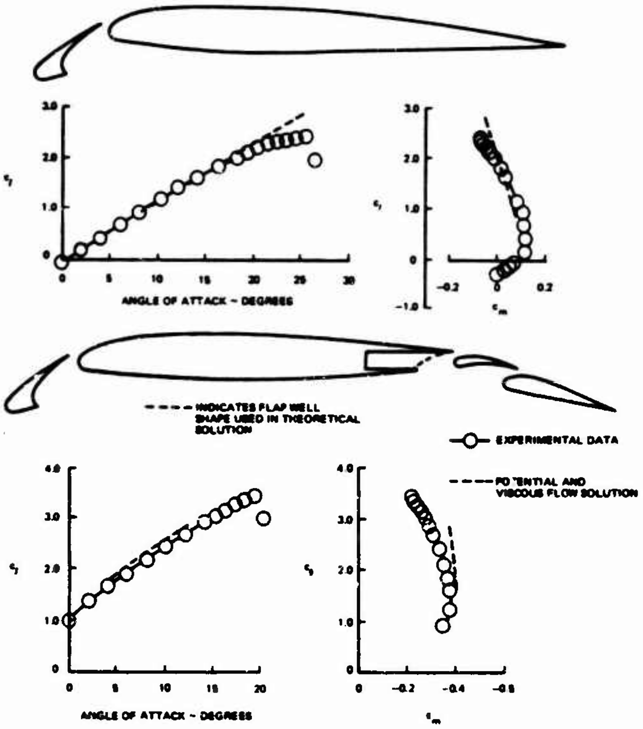

FIGURE 27. COMPARISON OF EXPERIMENTAL AND CALCULATED SECTION CHARACTERISTICS FOR SLATTED AIRFOIL WITH TRAILING EDGE FLAP AT 0-DEG AND 15-DEG DEFLECTION

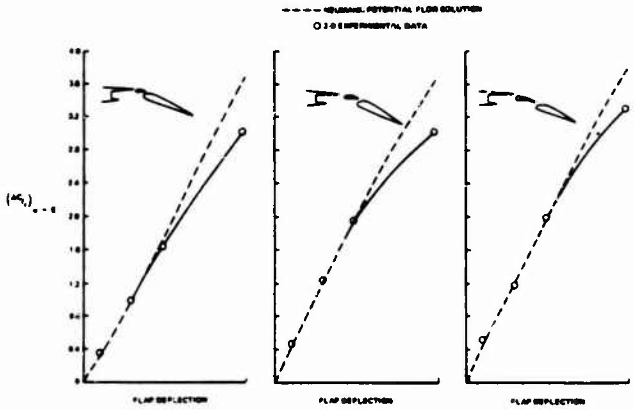

FIGURE 28. COMPARISON OF EXPERIMENTALLY MEASURED AND POTENTIAL FLOW LIFT INCREMENT DUE TO FLAP DEFLECTION FOR THREE DOUBLE SLOTTED FLAPS

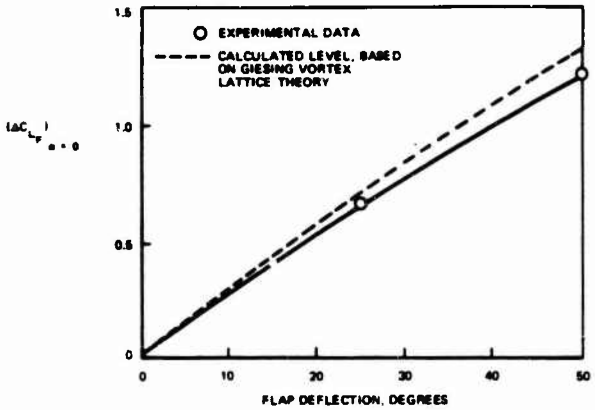

FIGURE 29. COMPARISON OF EXPERIMENTAL AND CALCULATED LIFT INCREMENT DUE TO FLAP DEFLECTION FOR MODEL DC-9

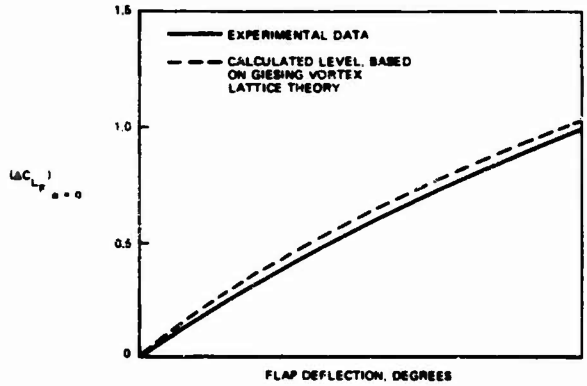

FIGURE 30. COMPARISON OF EXPERIMENTAL AND CALCULATED LIFT INCREMENT DUE TO FLAP DEFLECTION FOR MODEL DC-10

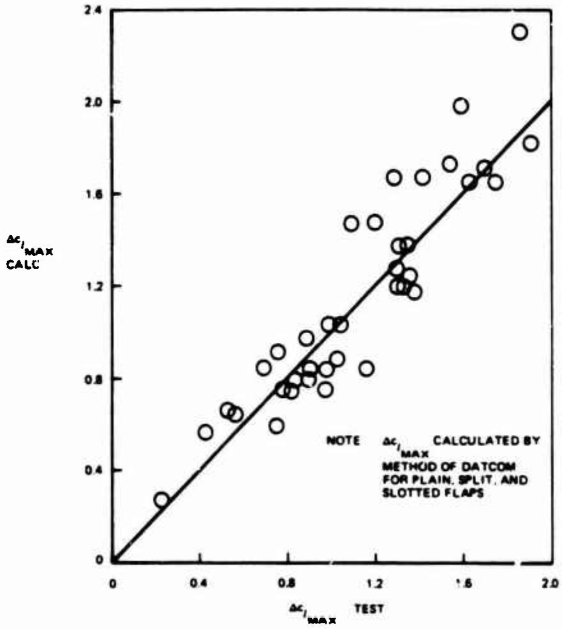

FIGURE 31. COMPARISON OF EXPERIMENTAL AND CALCULATED SECTION $c_{l_{MAX}}$ INCREMENTS DUE TO THE DEFLECTION OF TRAILING EDGE FLAPS

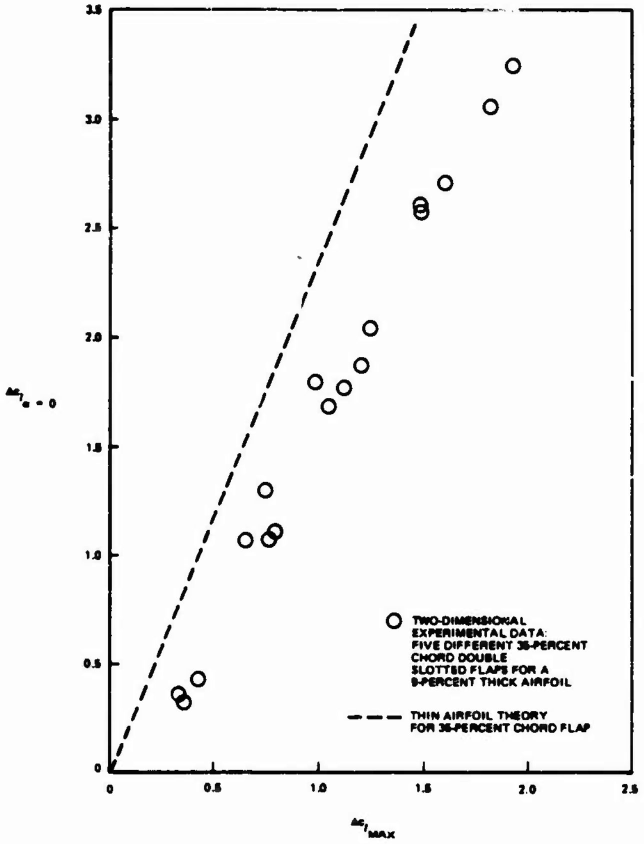

**FIGURE 32.** RELATIONSHIP OF DOUBLE SLOTTED FLAP SECTION LIFT INCREMENT AT CONSTANT ANGLE OF ATTACK AND MAXIMUM LIFT INCREMENT

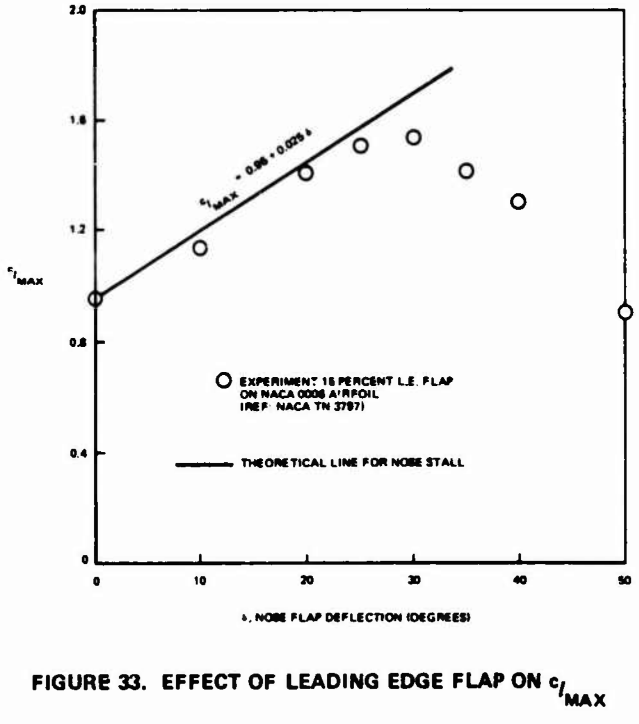

**FIGURE 33.** EFFECT OF LEADING EDGE FLAP ON $c_{l_{MAX}}$

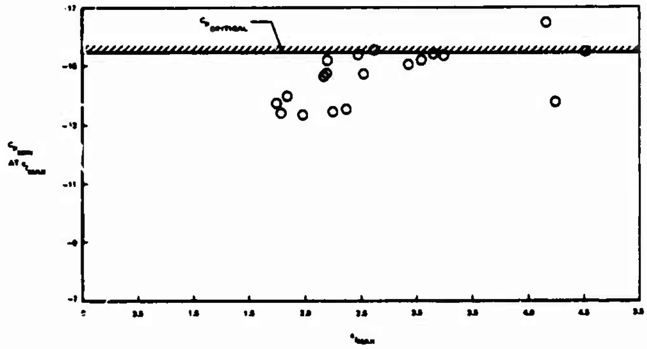

FIGURE 34. EXPERIMENTALLY MEASURED LEADING EDGE MINIMUM PRESSURE COEFFICIENT AT $c_{l_{MAX}}$ FOR A VARIETY OF TWO-DIMENSIONAL HIGH-LIFT CONFIGURATIONS

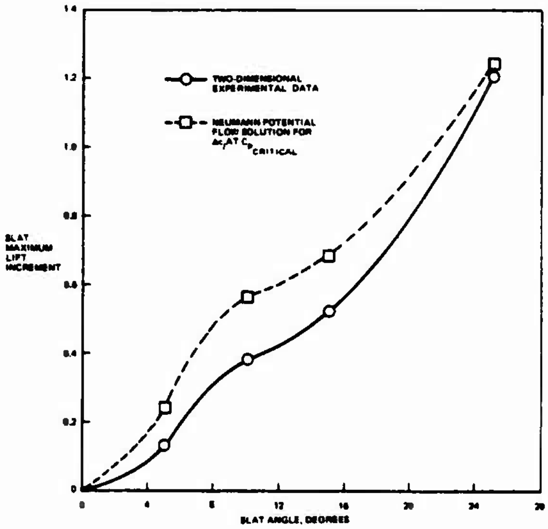

FIGURE 35. COMPARISON OF MEASURED AND ESTIMATED SLAT MAXIMUM LIFT INCREMENTS

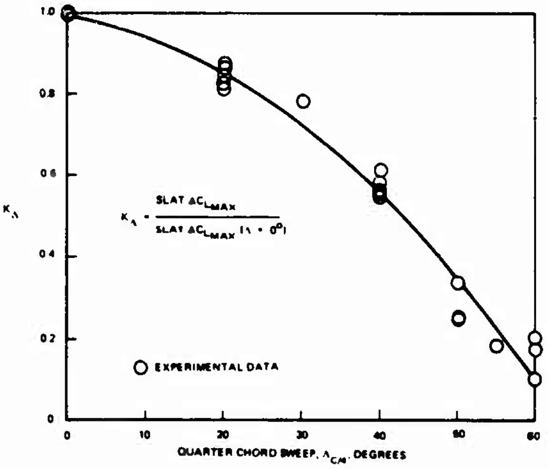

FIGURE 36. SWEEP CORRECTION FACTOR FOR LEADING EDGE SLAT MAXIMUM LIFT INCREMENT

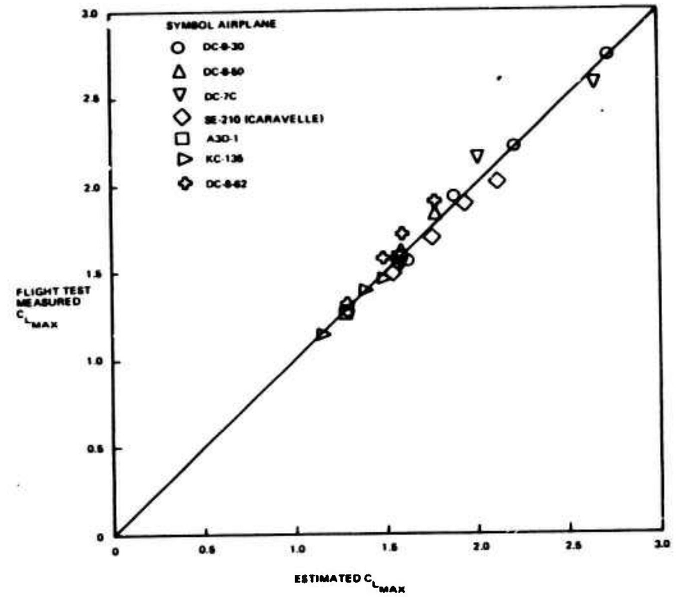

FIGURE 37. COMPARISON OF FLIGHT TEST AND ESTIMATED AIRPLANE MAXIMUM LIFT COEFFICIENTS

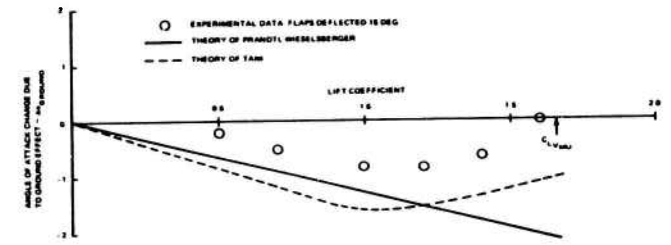

FIGURE 38. COMPARISON OF ESTIMATED AND WIND TUNNEL MEASURED ANGLE OF ATTACK CHANGE DUE TO GROUND EFFECT

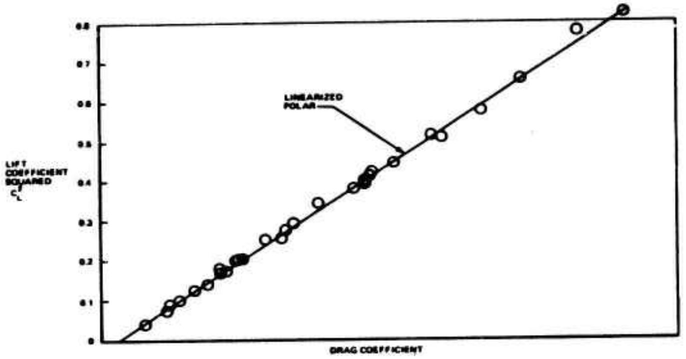

FIGURE 39. CLEAN CONFIGURATION FLIGHT POLAR FOR MODEL DC-10

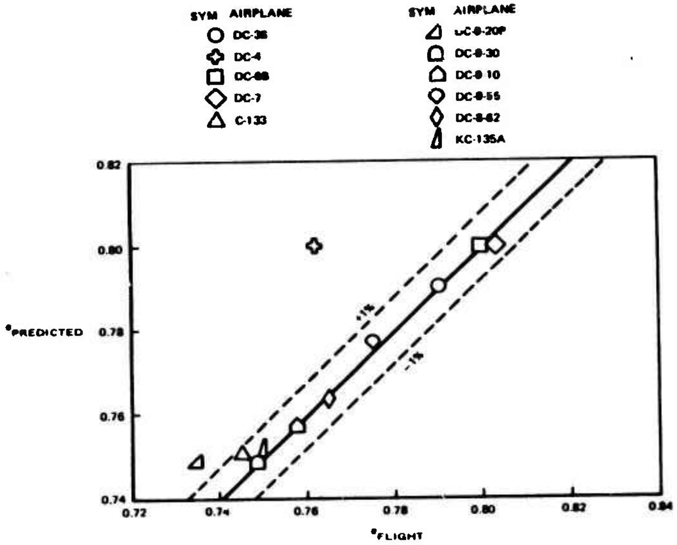

FIGURE 40. COMPARISON OF FLIGHT AND ESTIMATED AIRCRAFT EFFICIENCY FACTOR, e

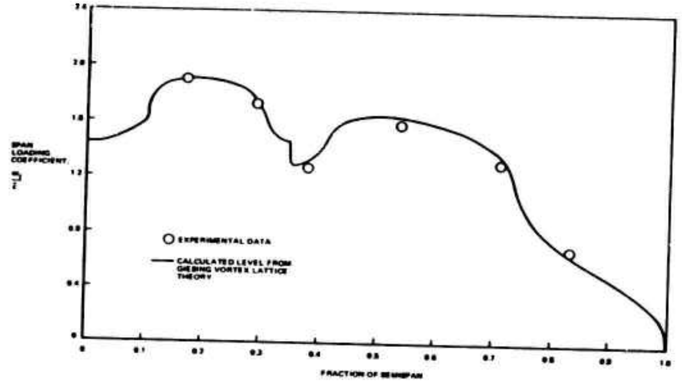

FIGURE 41. COMPARISON OF EXPERIMENTAL AND CALCULATED SPAN LOADING FOR MODEL DC-10 WITH FLAPS DEFLECTED 50 DEGREES

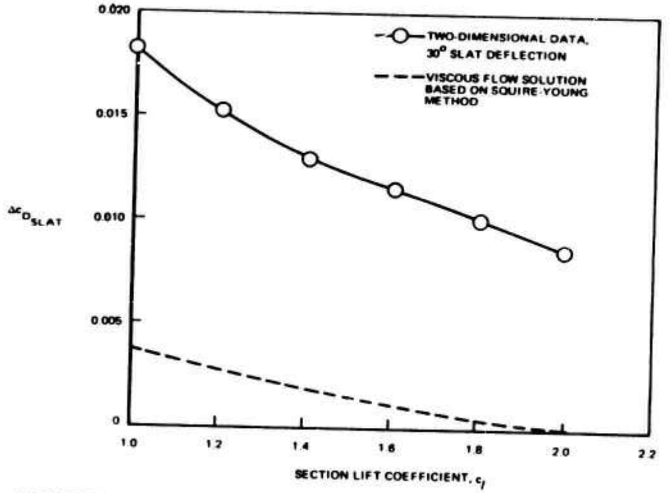

FIGURE 42. COMPARISON OF CALCULATED AND EXPERIMENTAL DRAG INCREMENT DUE TO SLAT DEFLECTION

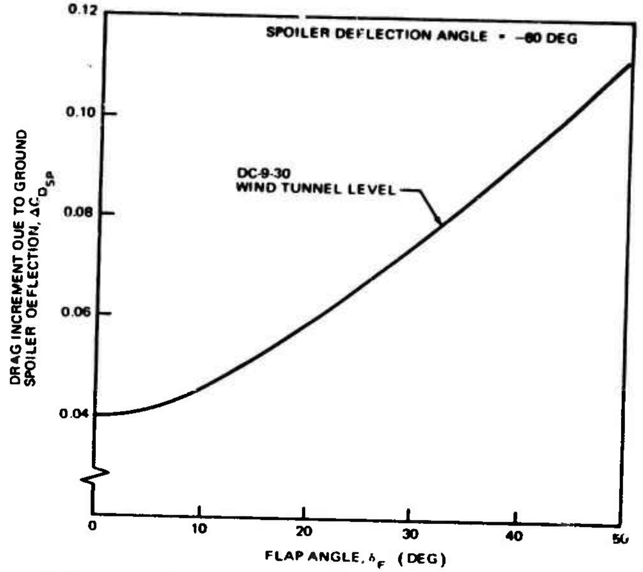

FIGURE 43. EXPERIMENTALLY MEASURED GROUND SPOILER DRAG INCREMENT

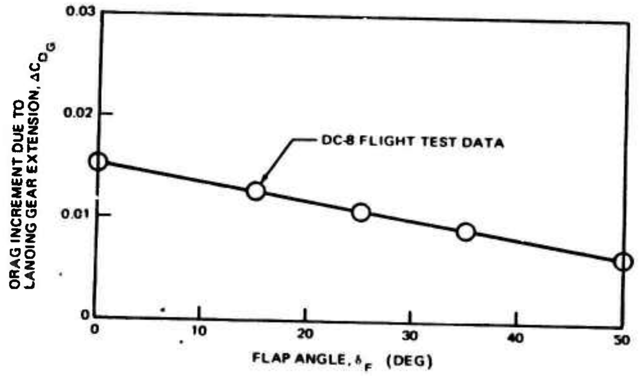

FIGURE 44. FLIGHT MEASURED LANDING GEAR DRAG INCREMENT

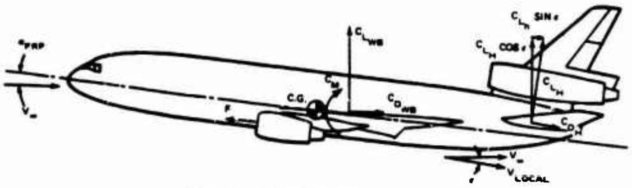
$\alpha_{FRP}$
$V_\infty$
$C_{L_{WB}}$
$C_M$
C.G.
F
$C_{D_{WB}}$
$C_{L_H}$ SIN ε
$C_{L_H}$ COS ε
$C_{L_H}$
$C_{D_H}$
$V_\infty$
$V_{LOCAL}$
ε

| | |
|---|---|
| $C_{L_{WB}}$ | WING BODY LIFT COEFFICIENT |
| $C_{D_{WB}}$ | WING BODY DRAG COEFFICIENT |
| $C_{L_H}$ | HORIZONTAL TAIL LIFT COEFFICIENT, NORMAL TO $V_{LOCAL}$ |
| $C_{D_H}$ | HORIZONTAL TAIL DRAG COEFFICIENT, PARALLEL TO $V_{LOCAL}$ |
| ε | DOWNWASH ANGLE |

**FIGURE 45. AIRPLANE FORCES FOR STATIC LONGITUDINAL FLIGHT**

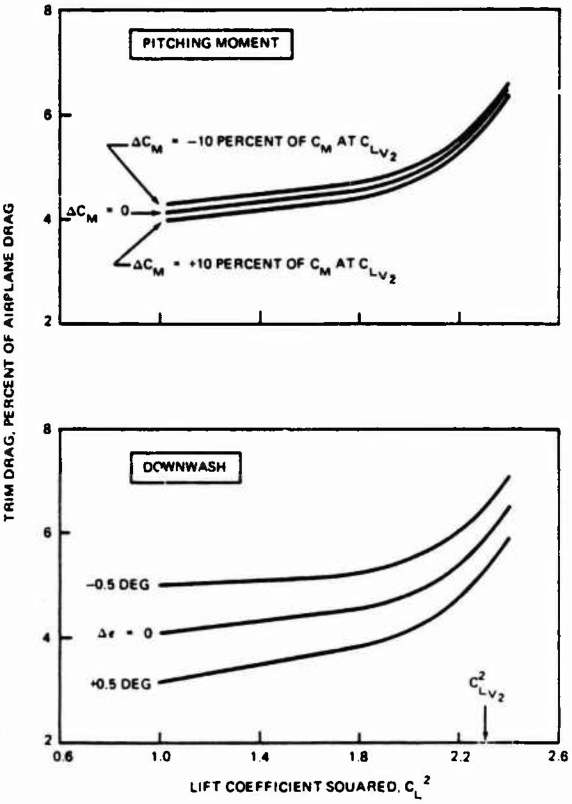

**FIGURE 46. SENSITIVITY OF TRIM DRAG TO PITCHING MOMENT AND DOWNWASH**

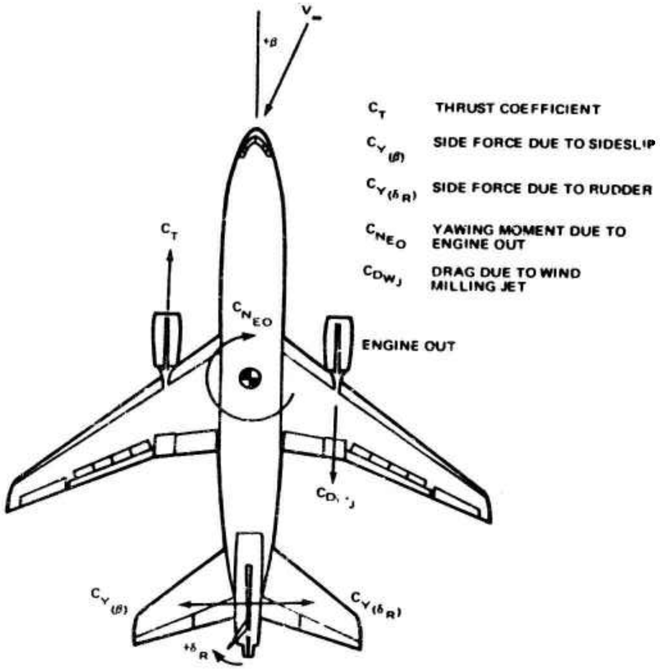
$V_\infty$
$+\beta$
$C_T$ THRUST COEFFICIENT
$C_{Y(\beta)}$ SIDE FORCE DUE TO SIDESLIP
$C_{Y(\delta_R)}$ SIDE FORCE DUE TO RUDDER
$C_{N_{EO}}$ YAWING MOMENT DUE TO ENGINE OUT
$C_{DW_J}$ DRAG DUE TO WIND MILLING JET
$C_T$
$C_{N_{EO}}$
ENGINE OUT
$C_{DW_J}$
$C_{Y(\beta)}$
$C_{Y(\delta_R)}$
$+\delta_R$

FIGURE 47. LATERAL-DIRECTIONAL ASYMMETRY DUE TO ENGINE-OUT CONDITION

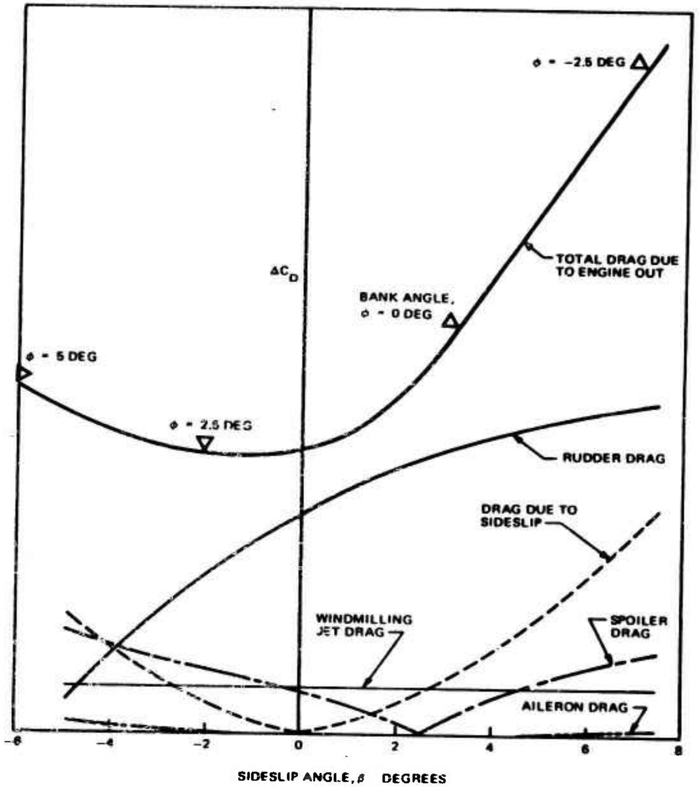

FIGURE 48. DRAG INCREMENTS RESULTING FROM BALANCING LATERAL-DIRECTIONAL ASYMMETRY DUE TO ENGINE OUT AT $C_L$ FOR $V_2$ SPEED

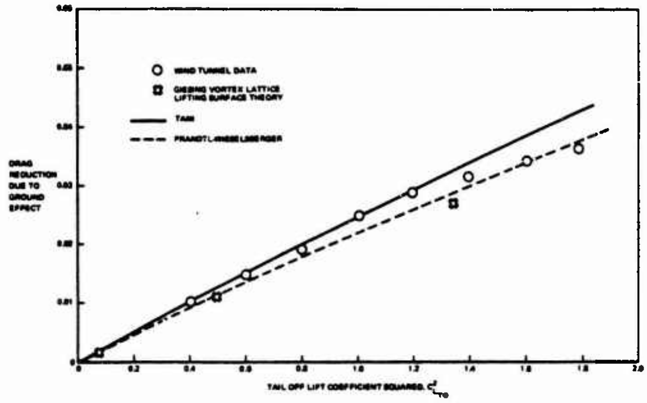

FIGURE 49. COMPARISON OF ESTIMATED AND WIND TUNNEL DRAG REDUCTION DUE TO GROUND EFFECT – FLAPS UP

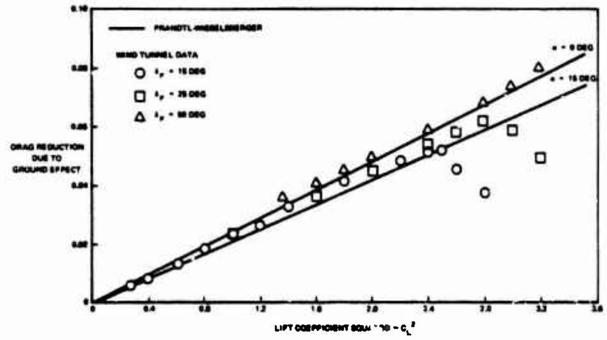

FIGURE 50. COMPARISON OF ESTIMATED AND WIND TUNNEL DRAG REDUCTION DUE TO GROUND EFFECT – FLAPS DEFLECTED

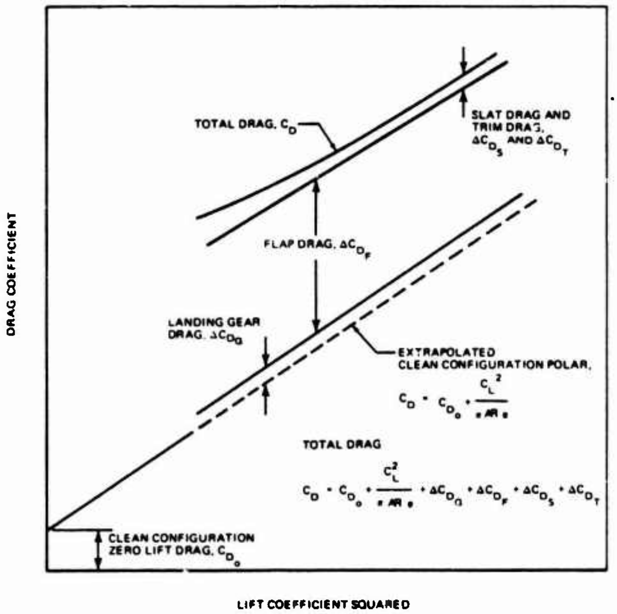
TOTAL DRAG, $C_D$
SLAT DRAG AND TRIM DRAG, $\Delta C_{D_S}$ AND $\Delta C_{D_T}$
FLAP DRAG, $\Delta C_{D_F}$
LANDING GEAR DRAG, $\Delta C_{D_G}$
EXTRAPOLATED CLEAN CONFIGURATION POLAR,
$C_D = C_{D_0} + \frac{C_L^2}{\pi AR e}$
TOTAL DRAG
$C_D = C_{D_0} + \frac{C_L^2}{\pi AR e} + \Delta C_{D_G} + \Delta C_{D_F} + \Delta C_{D_S} + \Delta C_{D_T}$
CLEAN CONFIGURATION ZERO LIFT DRAG, $C_{D_0}$
DRAG COEFFICIENT
LIFT COEFFICIENT SQUARED

FIGURE 51. BUILDUP OF DRAG POLAR FOR HIGH-LIFT CONFIGURATION

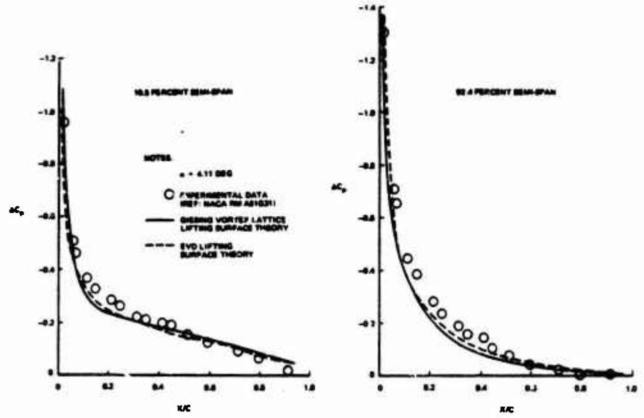

FIGURE 52. COMPARISON OF CALCULATED AND EXPERIMENTAL CHORDWISE LOADINGS ON A 45-DEGREE SWEPT PLANAR WING USING LIFTING SURFACE THEORIES

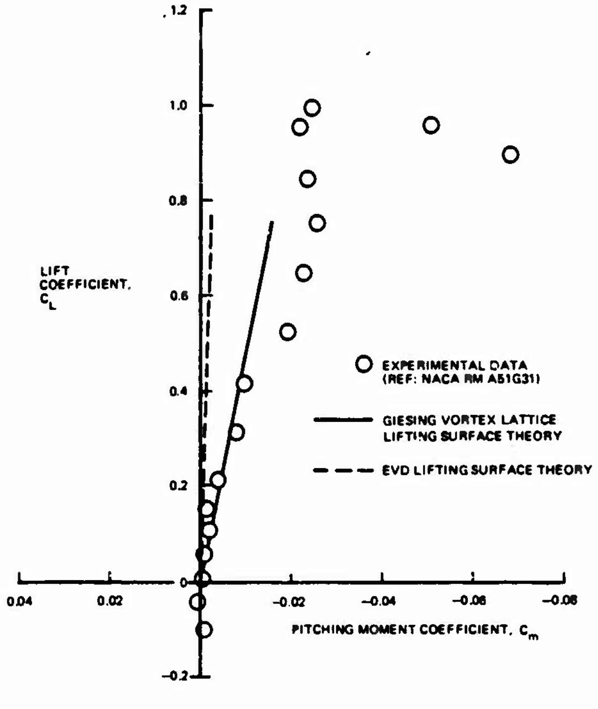

FIGURE 53. COMPARISON OF CALCULATED AND EXPERIMENTAL PITCHING MOMENT CHARACTERISTICS FOR A 45-DEGREE SWEPT PLANAR WING USING LIFTING SURFACE THEORY

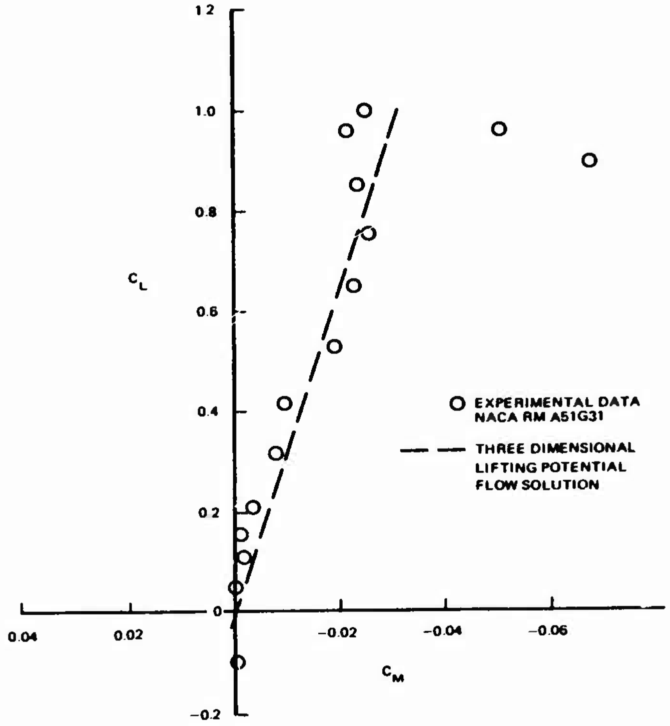

FIGURE 54. COMPARISON OF CALCULATED AND EXPERIMENTAL PITCHING MOMENT CHARACTERISTICS FOR A 45-DEGREE SWEPT PLANAR WING, USING THREE-DIMENSIONAL LIFTING POTENTIAL FLOW SOLUTION

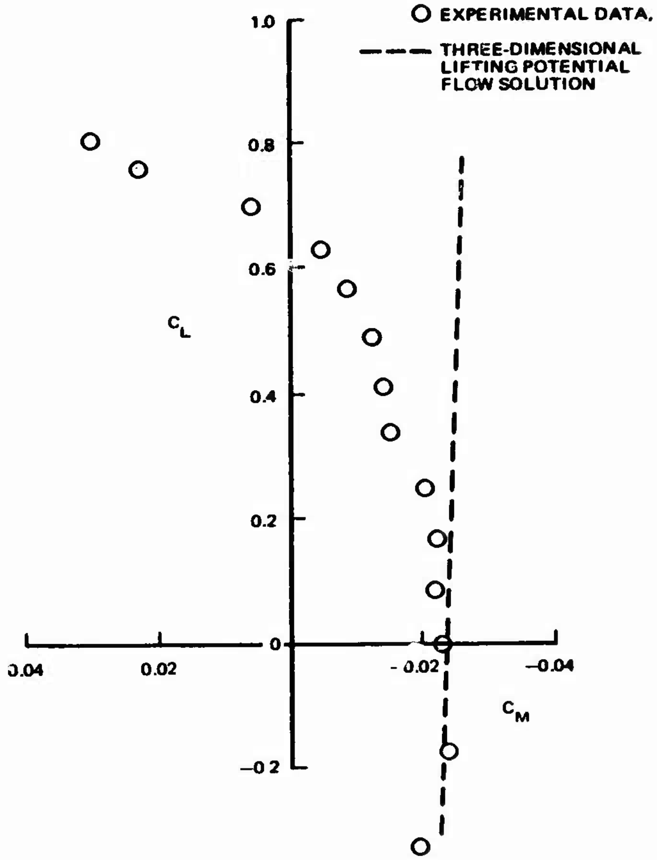

FIGURE 55. COMPARISON OF CALCULATED AND EXPERIMENTAL PITCHING MOMENT CHARACTERISTICS FOR A 35-DEGREE SWEPT WING FUSELAGE COMBINATION, USING THREE-DIMENSIONAL LIFTING POTENTIAL FLOW SOLUTION

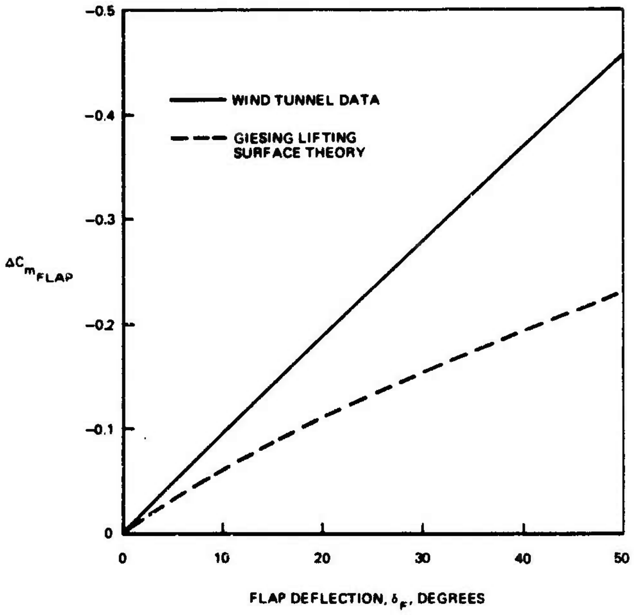

FIGURE 56. COMPARISON OF EXPERIMENTAL AND THEORETICAL INCREMENTAL PITCHING MOMENT DUE TO FLAP DEFLECTION FOR A SWEPT WING-FUSELAGE CONFIGURATION

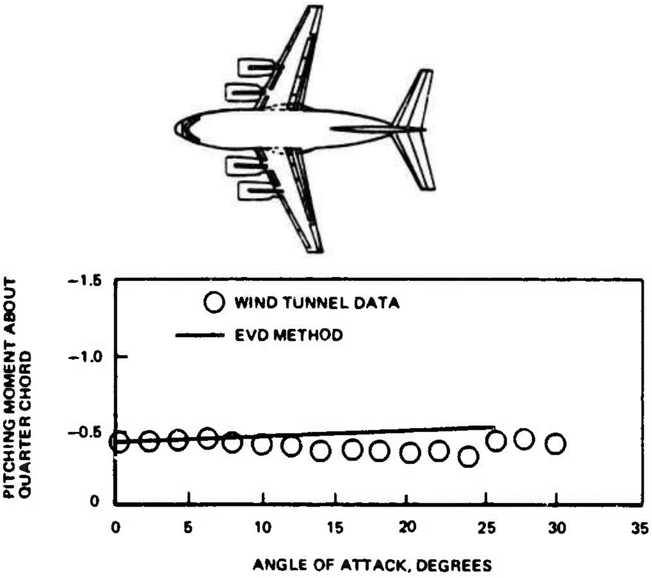

FIGURE 57. COMPARISON OF EXPERIMENTAL AND ESTIMATED PITCHING MOMENT CHARACTERISTICS, FLAP DEFLECTED 20 DEGREES

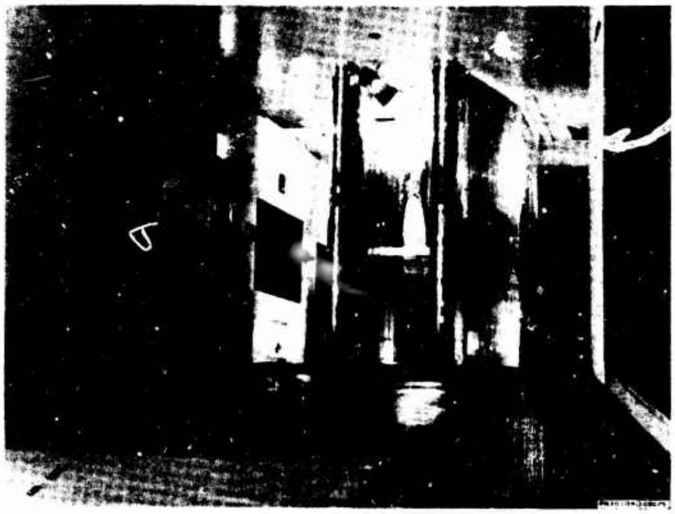

FIGURE 58. MCDONNELL DOUGLAS TWO-DIMENSIONAL HIGH-LIFT WIND TUNNEL FACILITY

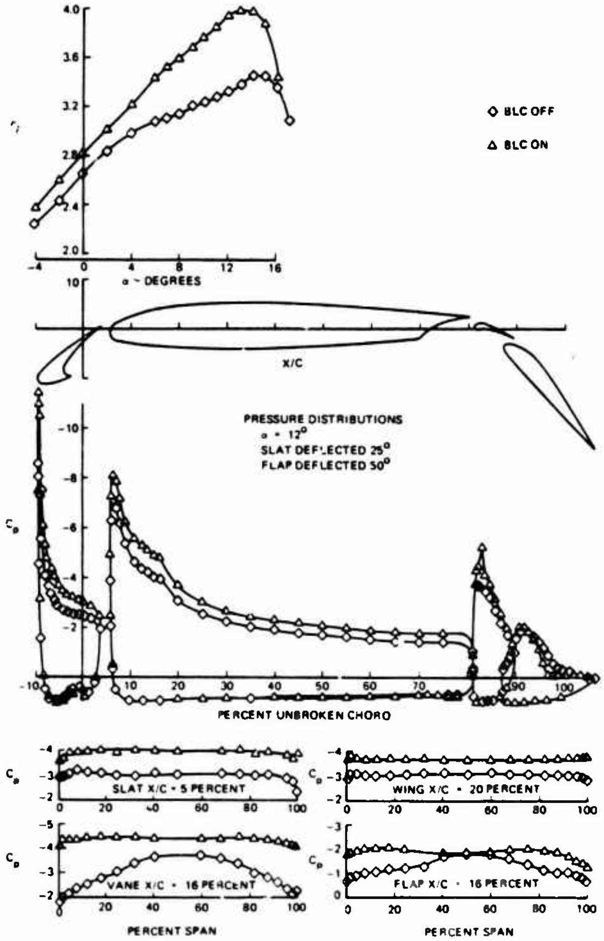

FIGURE 59. EFFECT OF WIND TUNNEL WALL BOUNDARY LAYER CONTROL ON TWO-DIMENSIONAL LIFT CHARACTERISTICS

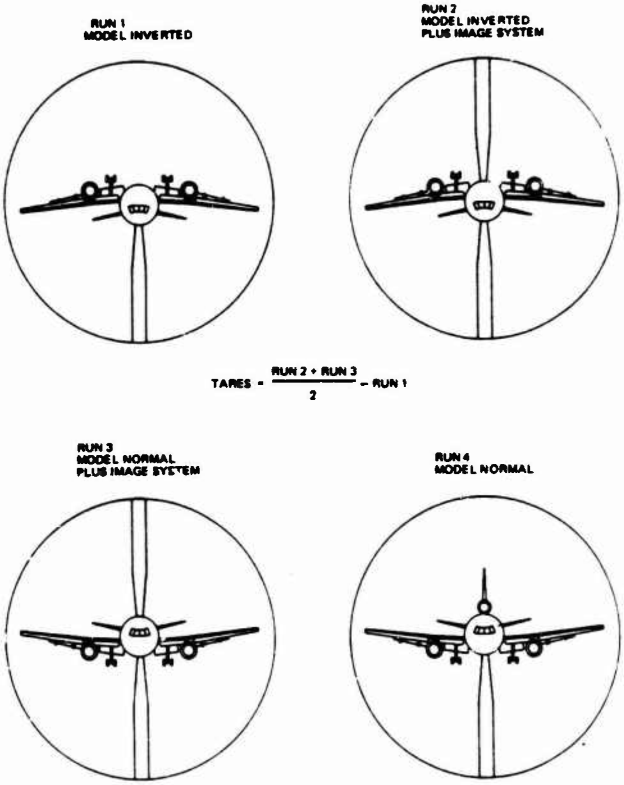
RUN 1
MODEL INVERTED
RUN 2
MODEL INVERTED
PLUS IMAGE SYSTEM
TARES = (RUN 2 + RUN 3)/2 − RUN 1
RUN 3
MODEL NORMAL
PLUS IMAGE SYSTEM
RUN 4
MODEL NORMAL

FIGURE 60. WIND TUNNEL TARE PROCEDURE FOR SUPPORT MOUNTED MODEL

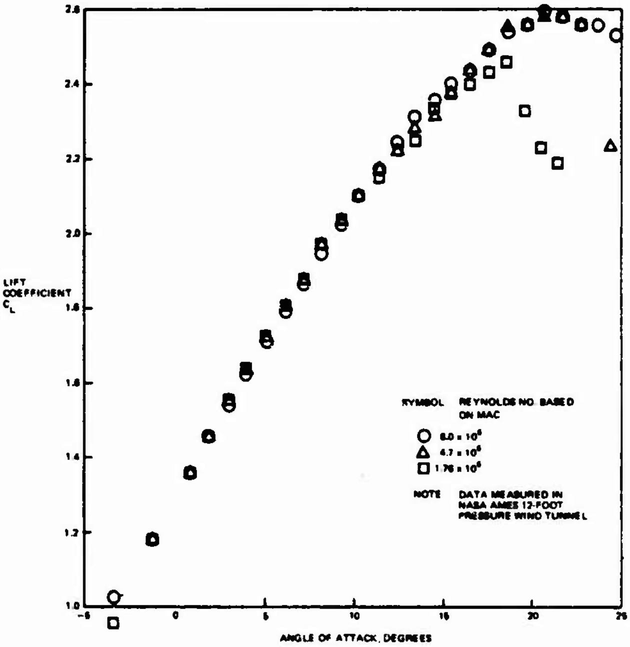

FIGURE 61. EFFECT OF REYNOLDS NUMBER ON LIFT CHARACTERISTICS, $\delta_F$ = 50 DEGREES

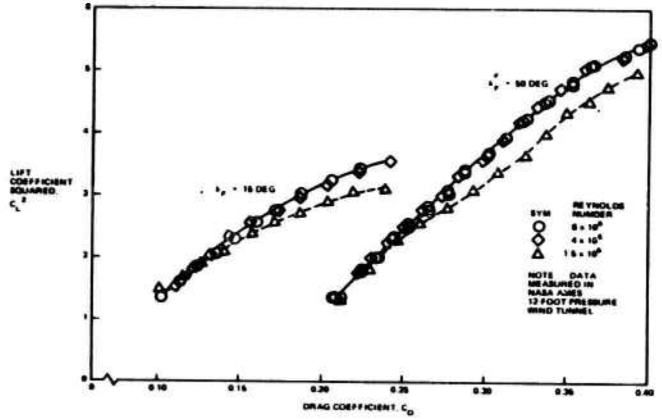

FIGURE 62. EFFECT OF REYNOLDS NUMBER ON DRAG POLAR, FLAPS DEFLECTED

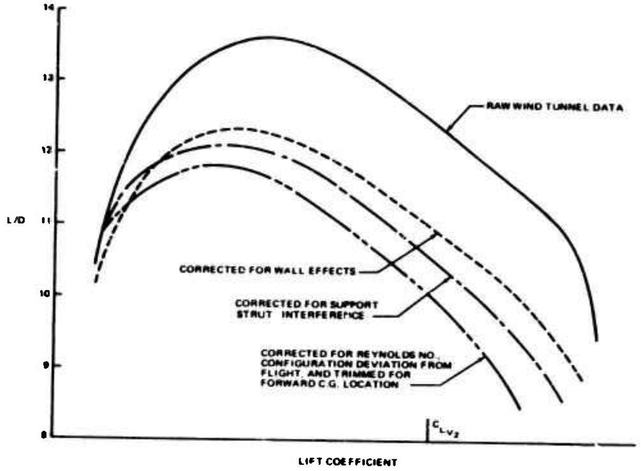

FIGURE 63. ADJUSTMENT OF WIND TUNNEL DATA TO FULL-SCALE LEVEL FOR MODEL DC-10, TAKEOFF CONFIGURATION

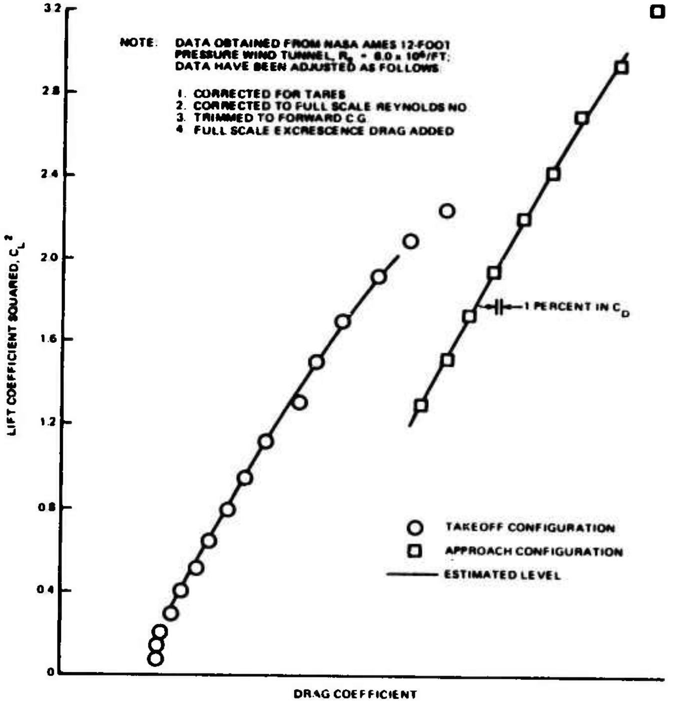

NOTE: DATA OBTAINED FROM NASA AMES 12-FOOT PRESSURE WIND TUNNEL, $R_N$ = 6.0 × $10^6$/FT; DATA HAVE BEEN ADJUSTED AS FOLLOWS:

1. CORRECTED FOR TARES
2. CORRECTED TO FULL SCALE REYNOLDS NO
3. TRIMMED TO FORWARD C.G.
4. FULL SCALE EXCRESCENCE DRAG ADDED

FIGURE 64. COMPARISON OF ESTIMATED AND HIGH REYNOLDS NUMBER WIND TUNNEL LOW-SPEED DRAG POLARS FOR MODEL DC-10

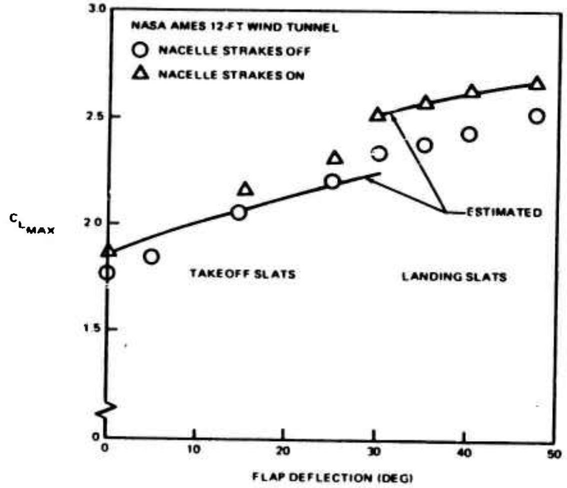

FIGURE 65. EFFECT OF NACELLE STRAKES ON $C_{L_{MAX}}$ FOR MODEL DC-10

FIGURE 66. VORTEX SHEDDING FROM DC-10 NACELLE STRAKE

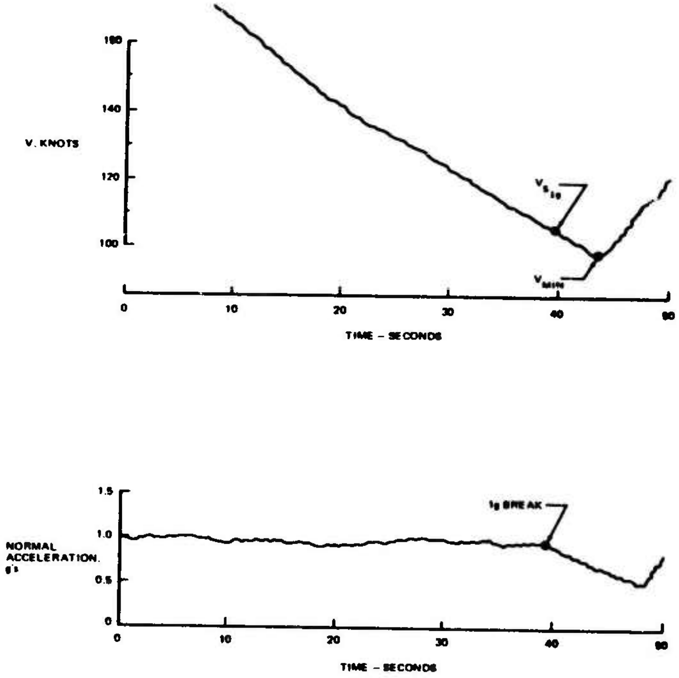

FIGURE 67. FLIGHT DETERMINATION OF MINIMUM FLYING SPEED ($V_{MIN}$) AND 1g STALL SPEED ($V_{S_{1g}}$)

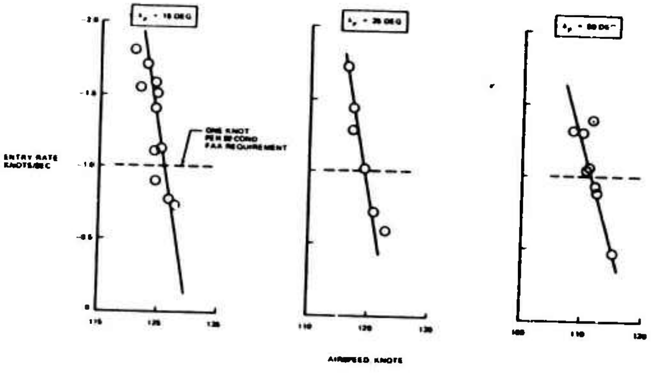

FIGURE 68. EFFECT OF ENTRY RATE ON MINIMUM FLYING SPEED, $V_{MIN}$

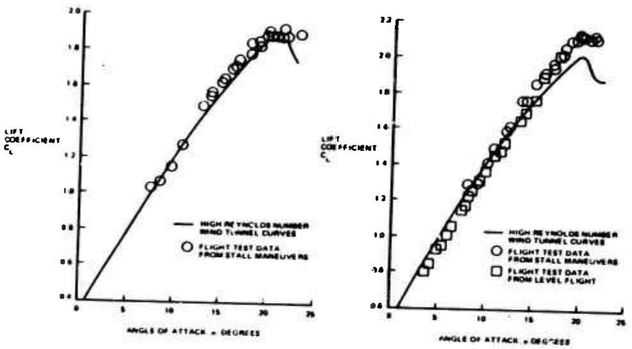

FIGURE 69. COMPARISON OF WIND TUNNEL AND FLIGHT TEST LIFT CURVES FOR TWO DIFFERENT FLAP DEFLECTIONS, MODEL DC-10

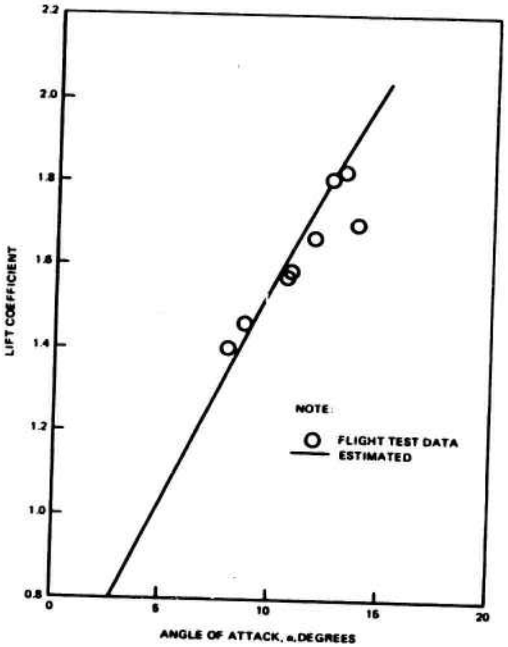

FIGURE 70. COMPARISON OF FLIGHT TEST AND ESTIMATED LIFT IN GROUND EFFECT FOR AIRCRAFT WITH SLATS AND FLAPS DEFLECTED

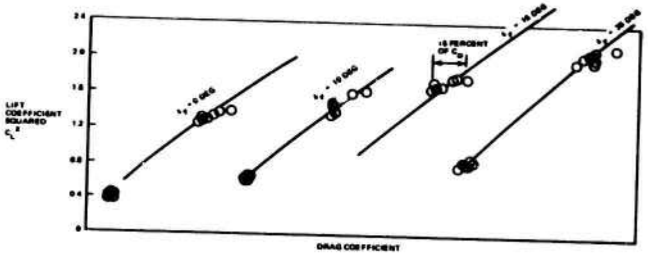

FIGURE 71. LOW-SPEED DRAG POLARS MEASURED FROM CLIMB MANEUVERS

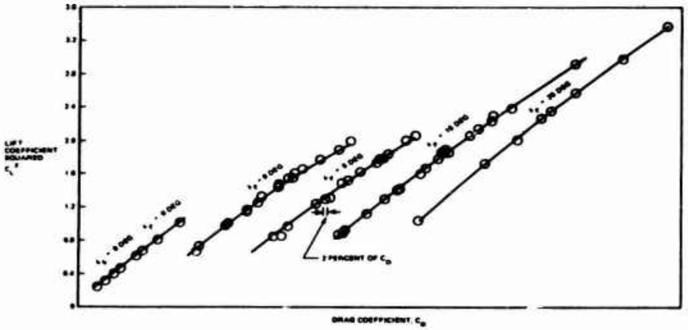

FIGURE 72. LOW-SPEED DRAG POLARS MEASURED FROM LEVEL FLIGHT

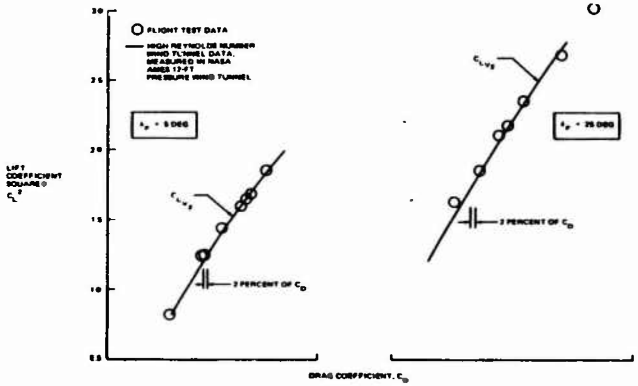

FIGURE 73. COMPARISON OF FLIGHT AND WIND-TUNNEL LOW-SPEED DRAG POLARS FOR MODEL DC-10

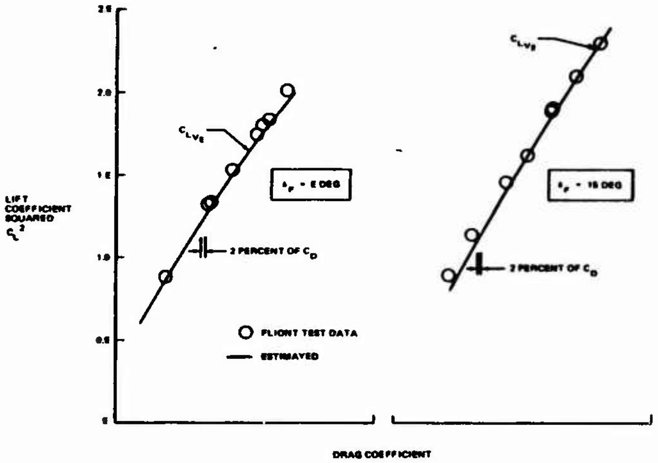

FIGURE 74. COMPARISON OF FLIGHT AND ESTIMATED LOW-SPEED DRAG POLARS FOR MODEL DC-10

| ANALYTICAL STATUS | TYPE OF METHOD | APPLICATION |
|---|---|---|
| FIRM ANALYTICAL FOUNDATION IN THREE DIMENSIONS | • 3-D LIFTING POTENTIAL FLOW SOLUTION<br>• LIFTING SURFACE THEORIES | LIFT AND PITCHING MOMENT CHARACTERISTICS WHERE VISCOUS EFFECTS ARE NEGLIGIBLE |
| FIRM ANALYTICAL FOUNDATION IN TWO DIMENSIONS INCLUDING VISCOUS EFFECTS: REQUIRES EMPIRICISM TO ADJUST TO THREE DIMENSIONS | • MULTI-ELEMENT AIRFOIL ANALYSIS METHODS<br>• FINITE DIFFERENCE BOUNDARY LAYER SOLUTIONS | • LIFT AND PITCHING MOMENT CHARACTERISTICS WITH VISCOUS EFFECTS PRIOR TO FLOW SEPARATION<br>• CLEAN CONFIGURATION SKIN FRICTION |
| EMPIRICAL TECHNIQUES COMBINING ANALYTICAL TOOLS AND EXPERIMENTAL DATA | • $C_{L_{MAX}}$ OF CLEAN CONFIGURATION<br>• $C_{L_{MAX}}$ INCREMENT OF HIGH LIFT DEVICES<br>• DRAG OF HIGH LIFT DEVICES | |
| FULL RELIANCE ON EXPERIMENTAL DATA | • INTERFERENCE EFFECTS<br>• REYNOLDS NUMBER EFFECTS<br>• MACH NUMBER EFFECTS<br>• CHARACTERISTICS OF HIGH LIFT SYSTEMS DEPARTING FROM EMPIRICAL DATA BASE | |

FIGURE 75. ANALYTICAL STATUS OF METHODS FOR ESTIMATING HIGH-LIFT CHARACTERISTICS

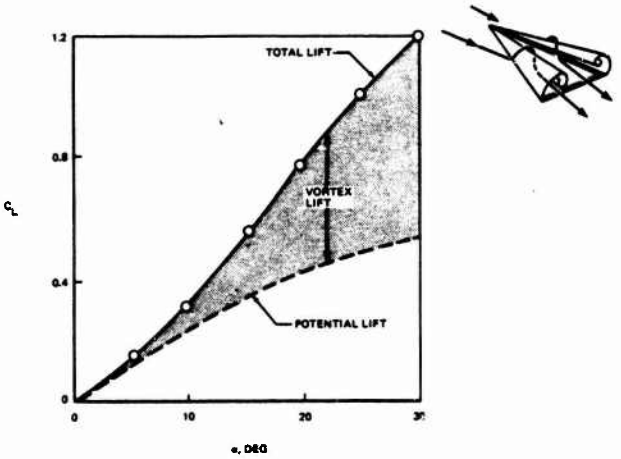

FIGURE 76. ILLUSTRATION OF THE VORTEX LIFT FOR A 75-DEGREE DELTA WING

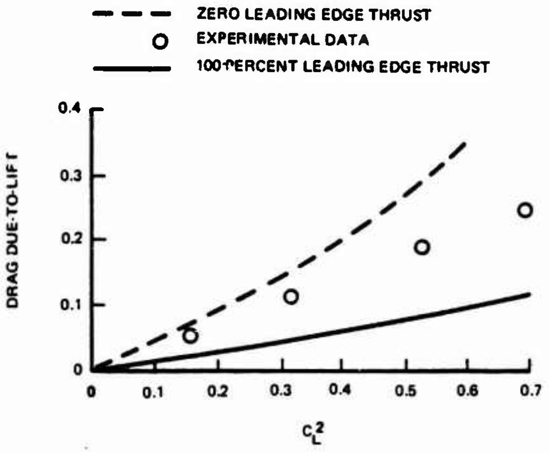

FIGURE 77. DRAG DUE-TO-LIFT FOR A 60-DEGREE DELTA WING

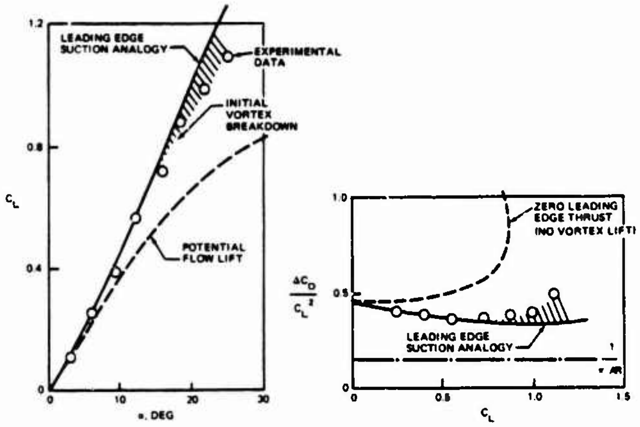

FIGURE 78. COMPARISON OF EXPERIMENTAL AND CALCULATED LIFT AND DRAG CHARACTERISTICS FOR ASPECT RATIO 2 DELTA WING, USING POLHAMUS LEADING EDGE SUCTION ANALOGY

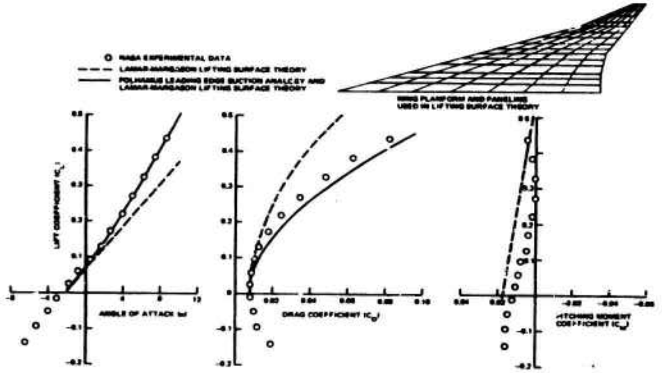

FIGURE 79. COMPARISON OF CALCULATED AND EXERIMENTAL LOW-SPEED AERODYNAMIC CHARACTERISTICS FOR 72-DEGREE SWEPT WING – FUSELAGE COMBINATION – FLAPS UP (LAMAR-MARGASON PROGRAM)

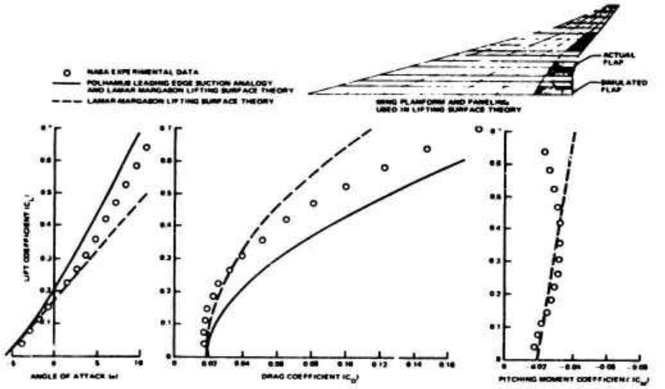

FIGURE 80. COMPARISON OF CALCULATED AND EXPERIMENTAL LOW-SPEED AERODYNAMIC CHARACTERISTICS FOR 72-DEGREE SWEPT WING – FUSELAGE COMBINATION – FLAPS DEFLECTED 15 DEGREES (LAMAR-MARGASON PROGRAM)

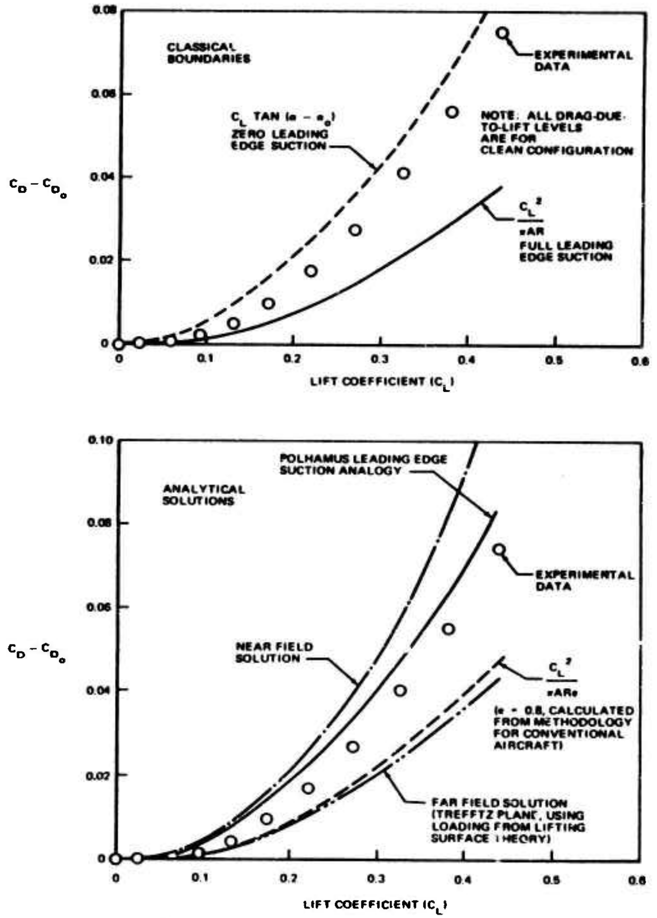

FIGURE 81. A COMPARISON BETWEEN CALCULATED AND EXPERIMENTAL DRAG DUE-TO-LIFT FOR 72-DEGREE SWEPT WING – FUSELAGE COMBINATION

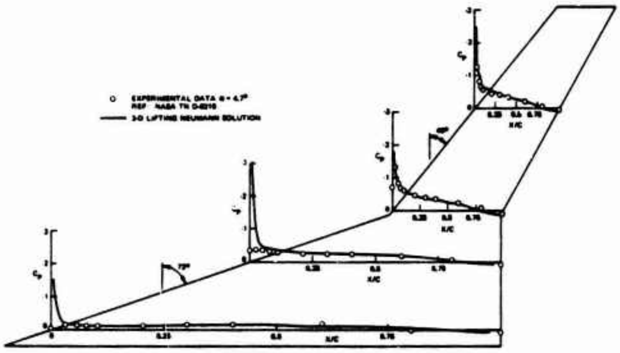

FIGURE 82. COMPARISON OF CALCULATED AND EXPERIMENTALLY MEASURED PRESSURE DISTRIBUTIONS FOR A 72-DEGREE SWEPT WING: α = 4.7 DEGREES

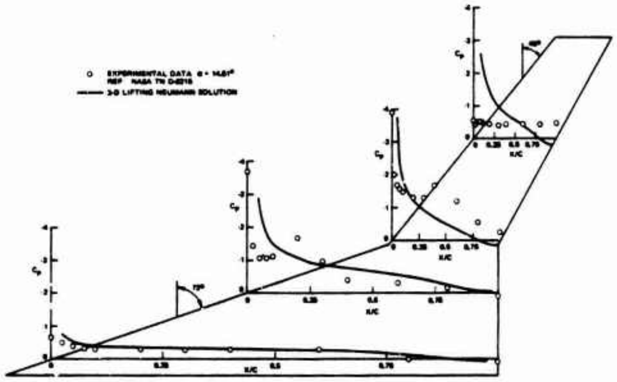

FIGURE 83. COMPARISON OF CALCULATED AND EXPERIMENTALLY MEASURED PRESSURE DISTRIBUTIONS FOR A 72-DEGREE SWEPT WING: α = 14.61 DEGREES

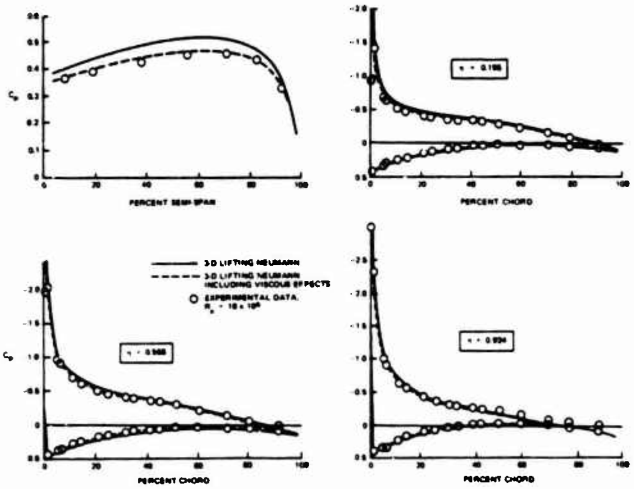

FIGURE 84. COMPARISON OF CALCULATED AND EXPERIMENTAL LOADINGS ON A 45-DEGREE SWEPT TAPERED WING AT 8-DEGREE ANGLE OF ATTACK

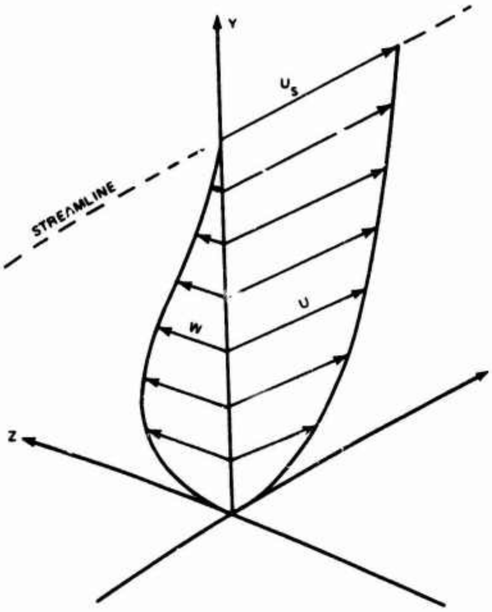
Y
U_S
STREAMLINE
U
W
X
Z

FIGURE 85. THREE-DIMENSIONAL BOUNDARY LAYER PROFILE ALONG A STREAMLINE

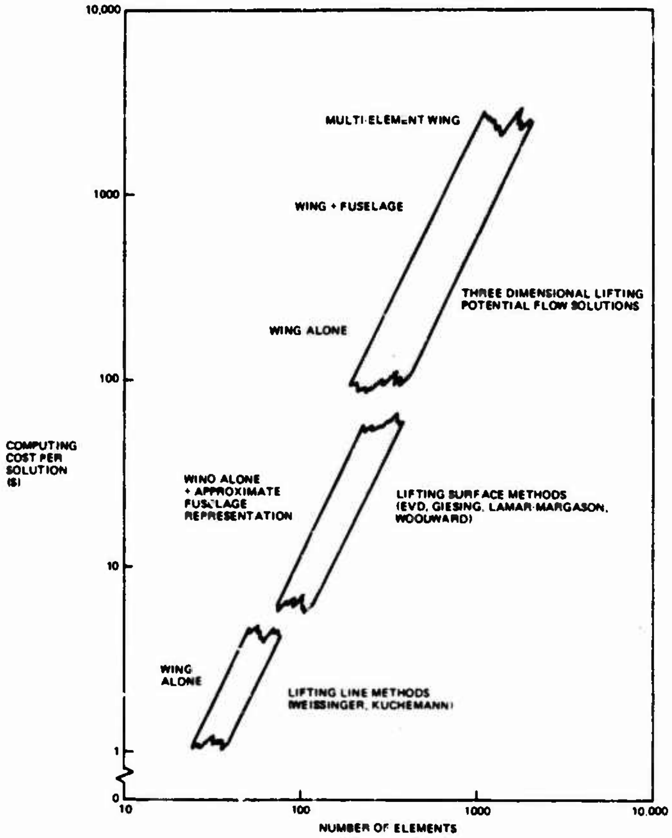

FIGURE 86. COMPUTING COST FOR THREE-DIMENSIONAL POTENTIAL FLOW SOLUTIONS

N74-26448

# A REVIEW OF THE LOW-SPEED AERODYNAMIC CHARACTERISTICS OF AIRCRAFT WITH POWERED-LIFT SYSTEMS

D N FOSTER, ROYAL AIRCRAFT ESTABLISHMENT, BEDFORD, ENGLAND

## SUMMARY

The aim of this paper is to review the aerodynamic characteristics of a number of different configurations of fixed-winged aircraft with powered-lift systems, but excluding those configurations employing direct jet-lift, and to discuss methods of predicting these characteristics. Detailed consideration is given to aircraft employing boundary-layer control, and with jet-flaps, the latter involving internal blowing, external blowing from underwing and overwing engines, and augmentor systems. The paper also includes a discussion of spanwise blowing and other specialised devices.

Wherever possible, comments have been made on the aerodynamic characteristics in ground effect as well as in free air. Some aspects of the noise problem which are directly related to the particular powered-lift system under discussion have been highlighted.

## LIST OF SYMBOLS

| | |
|---|---|
| AR | wing aspect ratio |
| $a_1$ | wing lift-incidence curve slope in inviscid flow |
| b | wing span |
| $C_{BLC}$ | momentum coefficient, based on local conditions at slot exit |
| $C_D$ | drag coefficient |
| $C_{D_i}$ | theoretical lift-dependent drag coefficient |
| $C_{D_W}$ | drag coefficient derived using wake-survey technique |
| $C_{D_o}$ | boundary-layer drag coefficient |
| $\Delta C_{D_p}$ | increment in lift-dependent drag coefficient due to part-span flaps |
| $C_J$ | overall jet momentum coefficient, including turning and spreading losses (external-flow jet-flap) and augmentation effects (augmentor systems) |
| $C_L$ | lift coefficient |
| $C_{LP_\alpha}$ | lift coefficient resulting from pressures induced by angle of incidence |
| $C_{LP_{\delta_J}}$ | lift coefficient resulting from pressures induced by jet deflection |
| $C_{L_{TRIM}}$ | trimmed lift coefficient |
| $\Delta C_{L_g}$ | increment in lift coefficient due to ground effect |
| $\Delta C_{L_{max}}$ | increment in maximum lift coefficient |
| $\Delta C_{L_{TRIM}}$ | increment in trimmed lift coefficient |
| c | wing chord |
| $\bar{c}$ | wing mean chord |
| $c_f$ | rear flap chord |
| $c_{LE}$ | nose flap chord |
| $\Delta C_{L_\infty}^*$ | increment in lift coefficient in two-dimensional inviscid flow |
| $C_l$ | rolling moment coefficient |
| $C_{l_\beta}$ | rolling moment derivative due to angle of sideslip |
| $C_{l_{\dot\beta}}$ | rolling moment derivative due to rate of change of angle of sideslip |
| $C_m$ | pitching moment coefficient |
| $C_{n_r}$ | yawing moment derivative due to yawing velocity |
| $C_{n_\beta}$ | yawing moment derivative due to angle of sideslip |
| $C_{n_{\dot\beta}}$ | yawing moment derivative due to rate of change of angle of sideslip |
| $C_p$ | static-pressure coefficient |
| $C_{p_s}$ | static-pressure coefficient at slot exit |
| $C_Q$ | quantity flow rate coefficient $= M/\rho_\infty V_\infty S$ |
| $C_{Q_a}$ | quantity flow coefficient for attached flow |
| $C_T$ | thrust coefficient |
| $C_{TG}$ | gross-thrust coefficient |
| $C_X$ | axial force coefficient |
| $C_\mu$ | blowing momentum rate coefficient at slot $= MV_J/\frac{1}{2}\rho_\infty V_\infty^2 S$ |
| $C_{\mu_a}$ | blowing momentum coefficient for attached flow |
| $C_{\mu_{eff}}$ | effective blowing momentum coefficient leaving wing trailing edge |
| $C_{\mu_N}$ | blowing momentum coefficient at nose flap |
| $C_{\mu_R}$ | blowing momentum coefficient at rear flap |
| D | drag force |
| d | diameter of hole in suction surface |
| F | aspect-ratio conversion factor for lift |
| h | height of mean quarter-chord point above ground |
| $h_n$ | width of slot nozzle |
| $K_1$ | wing lift-dependent drag factor |
| $K_L$ | part-span flap lift factor |
| L | lift force |
| $L_R$ | lift ratio = lift in ground effect/lift in free air |
| l | distance from mean quarter-chord point of wing to mean quarter-chord point of tailplane |
| M | blowing or suction mass flow rate |
| $M_\infty$ | free-stream Mach number |
| $\dot{m}$ | augmentor mass flow rate |
| P | supercirculation factor for lift |
| PR | nozzle pressure ratio |

| | |
|---|---|
| $R$ | radius of flap knuckle |
| $R_E$ | Reynolds number |
| $r$ | thrust recovery factor |
| $S$ | wing area |
| $S_f$ | wing area corresponding to spanwise extent of flap |
| $T_o$ | static thrust force |
| $t$ | wing thickness |
| $U$ | cylinder peripheral velocity |
| $V_J$ | jet velocity |
| $V_\infty$ | free-stream velocity |
| $x$ | distance measured along chord from wing leading edge |
| $y$ | distance measured along span from fuselage centre line |
| $z$ | distance from top of fuselage to mean quarter-chord point of tailplane |
| $\alpha$ | angle of incidence |
| $\beta$ | angle of sideslip |
| $\delta_a$ | deflection angle of aileron |
| $\delta_f$ | deflection angle of flap |
| $\delta_{f1}, \delta_{f2}$ | deflection angle of fore and rear flap |
| $\delta_J$ | deflection angle of jet |
| $\delta_N$ | deflection angle of nose flap |
| $\delta_R$ | deflection angle of rear flap |
| $\epsilon$ | downwash angle |
| $\Lambda$ | sweepback angle |
| $\lambda$ | wing taper ratio |
| $\kappa, \nu$ | part-span conversion factors for lift |
| $\rho_\infty$ | free-stream flow density |
| $\phi$ | thrust augmentation ratio |

SUPERSCRIPT ' signifies that value is appropriate to sectional conditions

SUFFIX $\infty$ signifies that value is appropriate to two-dimensional flow conditions

## 1 INTRODUCTION

There are a wide variety of methods by which the power of a gas turbine engine can be made to interact with the flow around a wing to increase the circulation lift on the wing. Power may be extracted from the engine in the form of shaft drive, as a flow of air to or from the compressors, or by direct utilisation of the efflux of the engine. Some of these methods, which form the basis of this paper, are shown on Figure 1. It will be noted that blowing systems predominate over suction systems, reflecting the fact that this is where the main interest has been in recent years.

The systems which require the least power to be extracted from the engine are those which aim to achieve boundary-layer control; that is to suppress separations of the boundary layer which would otherwise occur on leading- or trailing-edge flaps. The flaps are generally of the plain variety, hinged about a point on the lower surface of the wing. Boundary-layer control may be achieved by blowing through a spanwise slot in a downstream direction tangential to the local wing surface either ahead of, or within the flap knuckle, Figure 1(a); the high energy flow re-energises the existing boundary layer, and enables it to negotiate the strongly adverse pressure gradients which exist around the flap knuckle. The air required for blowing may be obtained from the compressor of the main propulsion engine. Alternatively boundary-layer control may be achieved using suction to remove part or all of the existing boundary layer, so that a new boundary layer is created which is able to negotiate the adverse pressure gradients. In practice this is realised either by suction through a slot in the wing surface ahead of the flap knuckle, or by suction through a porous area, Figure 1(b). Power for the suction plant may be obtained by a shaft offtake from the engine. Other systems to achieve boundary-layer control, which have not been subjected to such extensive experimental and theoretical investigations, include the rotating cylinder flap, in which the flap knuckle is replaced by a cylinder which, if rotated sufficiently rapidly, increases the speed and hence the energy of the boundary layer to the point at which it is able to negotiate the adverse pressure gradients. Spanwise blowing from an orifice in the side of the fuselage, in contrast to the chordwise blowing shown on Figure 1(a), has also been considered.

Commensurate with the low power requirements of boundary-layer control systems is a limit on the maximum increase of lift that they can produce, corresponding approximately to the lift that the wing would produce in an inviscid fluid. The system employing internal blowing, Figure 1(a), is however, capable of yielding steadily increasing values of lift when the momentum of the jet is increased. This occurs because the jet is then strong enough to sustain a pressure difference across itself, and can be considered to affect the flow around the wing as if it were a physical extension of the trailing-edge flap, resulting in an increment to the circulation lift which is several times the vertical component of the jet momentum. Whilst theoretically the full jet momentum should be recovered as thrust, in practice the thrust recovery appears to lie between this value and the horizontal component of the jet momentum. The loss of thrust that this implies, together with the losses in the ducting between the engine and the slot, make up the power requirements of this, the jet-flap system. Although it has been discussed above in relationship to blowing over a trailing-edge flap, the increase in circulation (supercirculation effect) resulting from the jet sheet will, of course, exist even if the jet emerges from the trailing edge of the wing, and a number of schemes have been proposed based on this concept.

In order to achieve very high lift coefficients using the internal-flow jet-flap scheme, large quantities of air must be ducted to the blowing slot, with attendant ducting problems. These problems are avoided in external-flow jet-flap schemes, which may be realised either with the engine mounted under the wing, Figure 1(c), or above the wing, Figure 1(d). When mounted under the wing, the engine is positioned close to the wing lower surface, and is sometimes fitted with a target-type deflector to ensure that a large proportion of the efflux strikes the lower surface of the flaps, which are generally of the double or triple slotted variety. The efflux of the engine is deflected downwards by the lower surface of the flap, and also spreads spanwise along the flap before being discharged from the flap trailing edge, so that a jet sheet is formed with a span much greater than the diameter of the nacelle. Some flow also reaches the slot or slots in the flap, and is turned around the leading edge of the flap to flow along its upper surface, resulting in boundary-layer control for the flow on the flap upper surface. In general, the efflux flow leaves the flap trailing edge in a direction inclined to the longitudinal plane of symmetry, and as only the component of the efflux momentum in the direction of the plane of symmetry contributes to the thrust experienced by the wing and nacelle, the turning process itself results in the major portion of the thrust loss and of the power absorbed by this system.

The turning process for the configuration with the engine installed above the wing, Figure 1(d), is rather different, relying on the Coanda effect. The upper surface of the flap is therefore smooth, with no slots, and with as large a radius of curvature as possible. In order to obtain effective turning the efflux from the engine must be made to attach itself to the upper surface of the wing, and this may be achieved either by deflecting the efflux downwards by a deflector, or by discharging through a rectangular nozzle. If the turning is effective the jet remains compact with little or no spreading, and the turning losses can be lower than for the underwing engine. As before, the engine efflux produces a boundary-layer control effect on the flap upper surface, and is discharged as a jet-sheet from the trailing edge, but of a smaller span than for the underwing engine configuration.

The use of injectors to augment the thrust available has found application in the augmentor wing and injector wing, Figures 1(e) and 1(f). In the augmentor wing the primary flow is discharged from a spanwise slot into a duct formed by separating the upper and lower halves of the flap. A Coanda surface at the leading edge of the lower surface of the flap causes the jet to turn through the deflection angle of the flap. A slot in the lower surface of the flap just aft of the Coanda surface results in the jet becoming detached from the remainder of the lower surface, in order to reduce the losses incurred when a high velocity jet passes over a fixed surface. The upper half of the flap provides the upper wall of the mixing duct, and a slot just aft of the intake results in the boundary layer which has developed on the upper surface of the intake being drawn into the mixing duct, so that a new boundary layer is formed on the downstream element of the upper surface, which is able to negotiate the adverse pressure gradients on this surface. The mixed primary and induced flows are discharged from the trailing edge of the duct as a thick jet sheet, resulting in the wing experiencing supercirculation lift. The power requirements of the system are those associated with producing and ducting the primary air at a pressure sufficiently high to make the injector operate effectively.

For configurations requiring lift at very low speeds it may be preferable to discharge the efflux of an injector from the lower surface of the wing, Figure 1(f), rather than through the flap. At very low speeds the net thrust vector should then pass through the aircraft centre of gravity, whilst at higher speeds the mixed efflux will act in a manner of a jet sheet, though of lower effectiveness than for a jet discharged at the wing trailing edge.

The aerodynamic characteristics of these systems, and the methods available for their prediction, will now be considered.

## 2 BOUNDARY-LAYER CONTROL

The aerodynamic aspects of boundary-layer control by blowing or suction were admirably analysed by Williams and Butler in 1963[1]; some subsequent RAE research was summarised by Williams in 1966[2]. The intention here is therefore to consider primarily the experimental data and theoretical methods which have been published since then.

### a) BOUNDARY-LAYER CONTROL BY CHORDWISE BLOWING

The methods proposed by Williams and Butler[1] for the estimation of lift and drag are given in Appendix A. Naturally, the situation for which analysis of the relationship between the aerodynamic characteristics of the flow and the power expended by the boundary-layer control system is simplest occurs in the flow around a two-dimensional wing. Tests[3] were conducted by the RAE on a model wing having the cross-section shown in Figure 2, and mounted between the roof and floor of a wind tunnel. The large chord of the model enabled detailed pressure distributions to be measured around the centre-line of the model, and from this data the lift of the wing section could be obtained. The drag of the wing section was measured by the wake survey method using a rake of total pressure and static pressure tubes mounted approximately one chord downstream of the model. Measurements were obtained for a range of trailing-edge flap deflections and blowing momentum, in conjunction with both an undeflected and deflected leading-edge flap, the latter having a blowing slot at the flap knuckle.

As the aim of boundary-layer control is to eliminate flow separations, when the boundary-layer control system is operating effectively the flow around the wing section should correspond closely to that in inviscid flow, with, possibly, allowances for the development of the attached boundary-layer. The recent advances in methods[4,5] of calculating the flow around wing sections have allowed the lift coefficient for the wing to be calculated in incompressible flow in free air, in compressible flow in free air, and in incompressible flow in the presence of the wind-tunnel walls. Whilst the true situation, that of a compressible flow in the presence of the wind-tunnel walls, cannot strictly be computed, Figure 3 shows that the effect of compressibility is small but that, for the size of model considered here, the presence of the tunnel walls does affect the lift. It is therefore reasonable to compare the lift curve calculated for incompressible flow in the presence of the wind-tunnel walls with the experimental lift curves measured for a range of blowing conditions, and this has been carried out in Figure 4. The experimental lift curve slopes are lower than the inviscid value, so that the momentum coefficient to achieve the inviscid lift increases with angle of incidence. Figure 5 shows the measured and theoretical pressure distributions agree very well, except near the flap knuckle where the contour considered is of necessity different from the actual contour. Figure 6 shows results of measurements of the sectional drag by the wake survey technique. When a line corresponding to the values of the angle of incidence and momentum coefficient at which the inviscid lift coefficient was achieved is superimposed on the carpet it is seen to be close to zero wake drag throughout.

It appears, therefore, that when the inviscid lift and inviscid pressure distribution are achieved sensibly zero wake drag results; it remains to calculate the momentum coefficient to produce these conditions. Thomas[6] was, perhaps, the first to suggest a method of predicting the momentum coefficient for attached flow, the method being based on the measured effect of a jet on the development of a viscous layer in a small adverse pressure gradient. Gartshore and Newman[7,8] reviewed a number of integral methods, and considered that more flexibility was required in the definition of the velocity profile than had been given in the previous methods. They therefore proposed a method in which the profile was defined by four independent parameters. By integrating the momentum equation over four different intervals in the viscous layer, equations can be derived for these four parameters in terms of the shear stress at the four positions in the layer. The values of the shear stress have been derived from empirical correlations with velocity profile parameters or their derivatives.

Using this method it is possible to predict the minimum momentum coefficient to produce attached flow just to the trailing-edge of the wing section. It has been applied to the inviscid flow pressure distributions calculated for the RAE wing, with the upstream boundary layer being calculated as follows; the method of Thwaites[9] for the laminar boundary layer; a number of transition criteria or Horton's[10] laminar bubble method to determine the end of the development of the laminar layer; and Green's[11] method for the turbulent boundary layer. Figure 7 shows the results of these calculations compared with values of the momentum coefficient to achieve the inviscid lift coefficient derived from experimental measurements as on Figure 4. The momentum coefficient is seen to be underestimated for both flap angles considered, although the errors reduce as the lift coefficient increases at the high flap deflection. This is somewhat surprising, as Gartshore has pointed out[8] that whilst the assumed velocity profile, which contains only one inflexion from a maximum velocity, is a reasonable representation of the measured profile for small flap deflections, at the higher flap deflections a second inflexion resulting from a minimum velocity is also found in the velocity profile, and so the basic flow model is unrepresentative.

More recently, Levinsky and Yeh[12], in their study of circulation control by a Coanda Jet, have extended Gartshore and Newman's method to include curvature and induced pressure gradient effects. They have made estimates for the RAE wing at one angle of incidence and two flap deflections, and their results have been added to Figure 7. It can be seen that their estimate is an improvement on the Gartshore and Newman value at the low flap angle, but not at the high flap angle. Perhaps the finite-difference method of Dvorak[13], which can consider velocity profiles with both maxima and minima, or with maxima only, will prove to provide the accuracy of prediction being sought. Nevertheless it is to be hoped that, even if the absolute values of the momentum coefficient predicted are incorrect, the Gartshore-Newman method will correctly reflect the effect of changes of the aerofoil pressure distribution resulting from changes in the radius of curvature of the flap knuckle. Figure 8 shows that doubling the knuckle radius produces a very marked (and worthwhile) reduction of the momentum coefficient to produce attached flow, but that further increase of radius does not have a large effect on the attachment momentum coefficient. It is possible that advantage can be taken of the large initial reduction by using the RAE Variable Aerofoil Mechanism[14] to give a knuckle with an increased radius of curvature. The advantage of blowing from a slot in the knuckle, rather than in the shroud, was discussed by Williams and Butler[1].

Finally before leaving considerations of sectional properties, it should be noted that there are circumstances in which, as the jet velocity is of the same order as the freestream velocity, the momentum coefficient is inadequate as a correlating parameter. Early analysis of some low-pressure blowing experiments by NASA[15] and NPL[1] suggested that a local momentum coefficient $C_{BLC}$, defined in relation to conditions at the slot exit, would be a better correlating parameter, and recent systematic data published by Engler and Williams[16], Figure 9, confirms this.

Turning to the application of boundary-layer control to complete aircraft, Eyre and Butler[17] carried out systematic tests on a complete model of a transport aircraft having an aspect ratio 8.0 wing with 28° sweep-back on the leading edge, Figure 10. The wing section was the same as on the two-dimensional model shown on Figure 2. The effect of deflection of the leading-edge flap, both with and without blowing at the knuckle, was investigated, and the increases of maximum lift coefficient are summarised on Figure 11, together with theoretical estimates based on an extension of the method given in a paper considering external-flow jet-flaps[18]. The theory assumes that the maximum lift coefficient is defined by a leading-edge stall, and the experimental measurements with the leading-edge flap undeflected suggest that this condition is approached for blowing momenta over the trailing-edge flap greater than 0.1. The measurements made with the leading-edge flap deflected but unblown suggest that at high values of trailing-edge blowing momentum, the increment in maximum lift coefficient will be slightly greater than that given by the simple theory, whilst blowing at the flap knuckle gives a further increase in the maximum lift coefficient.

However the increase in maximum lift coefficient is only one aspect of the performance of the high-lift system. Eyre and Butler noted that with the leading-edge flap undeflected substantial reductions in stalling incidence resulted from the application of trailing-edge blowing, and that the onset of the stall was sudden and accompanied by considerable buffeting; there was a large loss of lift post-stall with a pronounced pitch-up. Deflection of the leading-edge flap increased the stalling incidence, Figure 12, but the post-stall lift losses and pitch-up effects were aggravated. Blowing at the knuckle of the deflected leading-edge flap also resulted in an increase of the stalling incidence, Figure 12, and reduced the spanwise rate of spread of the separated flow region. However the basic pattern of the stall progression persisted, and there were still fairly severe lift-losses and pitch-up.

In an attempt to further reduce the rate of spread of the flow separations and alleviate the severity of the stall the inboard 25% of each leading-edge blowing slot was sealed, restricting the blowing to the outer 75% of the exposed span. The leading-edge flaps were, however, still deflected over the whole of their span. Figure 13 shows that some reduction of maximum lift coefficient resulted from this reduction of the spanwise extent of the blowing, but that pitch-up was effectively removed. It therefore appeared that this simple modification was sufficient to enable acceptable stalling characteristics to be achieved, and that by optimising the spanwise distribution of blowing it is possible that the penalty incurred on the maximum lift coefficient could be reduced.

A second beneficial feature of leading-edge flap deflection appeared on examination of the drag polars (Figure 12). The linear portion of the curve for the undeflected leading-edge flap corresponds to a lift-dependant drag factor of 1.28, being typical of values measured for a wing of this planform with highly-loaded flaps. When the leading-edge flap was deflected, with or without blowing, the lift-dependant drag factor decreased to 1.18, reflecting the improvement in the condition of the boundary layer below the stall. This low value appeared to be insensitive to the angle of deflection of the trailing-edge flap, or to the value of the blowing momenta at the leading- or trailing-edge flaps.

Measurements made with the tailplane showed that the downwash angle increased linearly with angle of incidence up to the stall, with a slope of approximately 0.3. Above the stall, the configuration with full-span blowing at the leading-edge indicated a marked increase in the downwash angle, resulting in a decrease in stability. For the configuration with part-span blowing, the downwash angle decreased beyond the stall, yielding an increase in stability. Variation of tailplane height did not change the slope of the downwash ~ angle of incidence curve below the stall and changed the absolute value of the downwash angle by less than 2° for the full range of tailplane heights. Near the stall, however, the tail position affected the angle of incidence at which the stabilising effect commenced, the angle of incidence increasing with tail height.

Interpretation of the measurements of the lateral characteristics made with this model are made difficult by the use of a flat-plate fin, installed primarily to carry the tailplane. However one basic feature found was that the magnitude of lift losses due to sideslip were greater for the high-lift wing than for the plain wing, resulting in appreciably larger negative values for $\ell_v$.

This model was subsequently tested over a moving ground belt, at one fixed height, $h/\bar{c} = 1.2$, to determine the effect of ground proximity. Figure 14 compares lift curves measured in free air, and in ground effect, for leading- and trailing-edge flaps deflected and blown[19]. It can be seen that both the lift at a given angle of incidence, and the maximum lift coefficient, have been reduced by the presence of the ground. An attempt to model theoretically this situation was made using the vortex-ring method of Maskew[20]. In this method, the lifting effect of the wing is represented by a series of quadrilateral vortex-rings situated on the mean-line of the aerofoil section. It is possible therefore to represent highly-deflected flaps, and the method has the facility to allow the trailing vortices to roll up. Calculations have been made for the wing of the model, assuming that the blowing momentum is just sufficient to produce attached flow over the wing. The lift curves are shown on Figure 15, which also indicates that the effect of wake roll-up, although more marked for the wing in ground effect, is nevertheless small. Figure 16 shows that the theory does give a reasonable indication of the fractional change in lift due to ground effect.

Accompanying the reduction of lift was a reduction of drag, such that at an equal value of the lift coefficient the drag in ground effect was 25% less than that in free air. The main effect on pitching moment was a constant positive increment without change of slope. However the normal variation of downwash angle with angle of incidence was almost completely suppressed in ground effect.

Use of boundary-layer control at the leading-edge of a wing was also investigated by Butler[21] for a rather different situation. Here the half model tested (Figure 17) was of a strike aircraft with a thin wing section (typically 8%) and under the constraint that the leading-edge arrangement must be fixed, and with a shape dictated by high-speed requirements. A range of positions of the leading-edge blowing slot was considered, and it was found (Figure 18) that the expected increase of effectiveness was not achieved when the position of the blowing slot was moved forward from 1½% chord to ½% chord. Further increase of blowing momentum at ½% chord also resulted in a reduction of the maximum lift coefficient, instead of the expected increase. Reduction of the tunnel airspeed, Figure 19, did however result in an increase of maximum lift coefficient to a level well above that achieved with the slot at 1½% chord. It would appear that the reduced effectiveness of blowing at ½% chord resulted from an adverse interaction of the jet, at approximately sonic velocity, with an external flow which is also locally at a near-sonic velocity due to the high circulation resulting from blowing over the flap.

A second effect noted in these tests is the favourable influence of leading-edge blowing on the effectiveness of blowing over trailing-edge flaps, so that for the same total blowing momentum very similar lift increments at zero incidence are achieved by blowing at the trailing-edge flap with no leading-edge blowing, or by subdividing the blowing, Figure 20. Obviously, at higher angles of incidence the advantage lies in blowing at the leading-edge. This effect was also found by Lohr[22] on a rectangular wing between endplates

b) BOUNDARY-LAYER CONTROL BY SPANWISE BLOWING

The use of spanwise blowing over flaps to increase the lift of a wing has been discussed by Dixon[23]. Air is discharged in a spanwise direction from a nozzle located in the side of the fuselage just above deflected flaps, Figure 21. The jet impinges on the flap upper surface and spreads spanwise over the flap, eventually turning to be discharged from the trailing edge of the flap in a near streamwise direction. During this process freestream air is entrained and turned to flow sensibly parallel to the flap upper surface. It is the downward motion of the large mass of entrained air that results in the increase of lift.

The effectiveness of spanwise blowing has been compared with that of conventional chordwise blowing by tests on a model of an F-8J Crusader Aircraft[23]. Due to differences of scale between the spanwise blowing model and the chordwise blowing model there were differences in the unblown datum values, and so the results are best compared on a lift-increment basis, although the lower Reynolds number may still favour the spanwise blowing. Figure 22 shows that although chordwise blowing is more effective at zero angle of incidence, increase of angle of incidence reduces the difference until at an angle of incidence of 12° the performance of the two systems is virtually identical. It was also found that the thrust recovery was about the same for the two systems.

Reverting to Figure 21, it can be seen that the jet rolled up into a strong vortex very soon after leaving the outboard tip of the flap, and that a smaller contra-rotating vortex sprang from the flap-fuselage junction. These vortices produced much larger downwash angles at the tailplane of the model than were measured for chordwise blowing, by a factor that may be as large as 3. Dixon comments that to obtain the same static stability with spanwise blowing as is obtained for chordwise blowing, it will be necessary to choose a higher position for the tailplane. If this is found to be acceptable, spanwise blowing offers potentially large savings in weight, cost and complexity.

### c) BOUNDARY-LAYER CONTROL BY SUCTION

Although boundary-layer control by suction has not actually been applied to a production aircraft, it has some attractions for civil aircraft. The discussion of British and American work presented by Williams and Butler[1] concluded that, if the available compressor bleed and the associated thrust losses were restricted, area suction could be competitive, and perhaps, superior, to blowing. If, for example, a reasonably well-designed multi-nozzle ejector pump system was fed with air from the engine-compressor, the bleed quantity to provide area suction could be as little as one quarter that required for direct slot-blowing. The suction installation would be more complex, but the weight penalty would not necessarily be higher, and would in any case be small. Williams and Butler also concluded that a wide range of porous materials were then available, which were satisfactory from aerodynamic, structural and non-clogging aspects.

Area suction research did, in fact, continue at RAE until about 1966[2]. In particular a series of tests were performed at RAE[24] on a model large enough to accommodate practical perforated suction surface arrangements with simple internal wing ducts. The model, Figure 23, was fitted with extending-chord trailing-edge flaps, and suction was applied at the knuckle of a deflected leading-edge flap. The variation of the minimum suction rate required to suppress the natural stall at a given angle of incidence, with angle of incidence, was measured for a range of suction surfaces (Figure 24). The lowest suction rates corresponded to the surface with the largest open-area ratio, whilst at a given open-area ratio, there was no significant effect of variation of perforation size over the range of hole diameters tested.

One potential problem area for systems involving boundary-layer control by suction is the effect of atmospheric conditions, and in particular flight through rain. The RAE model was therefore tested in conjunction with a "rain gun"[25], which generated a rain-like distribution of droplets in the wind tunnel airstream by means of an oscillating water spray. Three combinations of flow rate and jet nozzle size were tested to give concentrations approximating to light, moderate and very heavy rain. The effect of simulating rainfall was measured for the wing with a smooth contour, and also with a downward step ahead of the flap knuckle of a magnitude equal to that which might exist in a practical configuration. Figure 25 shows that some scatter occurred in the measurements, but that the increase of the minimum suction rate due to rain was much less than that due to the surface discontinuity.

### d) BOUNDARY-LAYER CONTROL BY ROTATING CYLINDER FLAPS

The use of a rotating cylinder at the hinge of a plain flap to apply boundary-layer control to the flow around the region of high curvature was first suggested by Professor Alvarez-Calderon[26]. Subsequently large scale models were tested by NASA[27,28] in the AMES 40ft x 80ft wind tunnel. Both models incorporated propellers, and extensive tests were conducted to determine the efficiency with which the rotating cylinder turned the propeller slipstream. For compatibility with the remainder of this paper, comments will be restricted to the zero propeller thrust condition.

The first model tested[27] had a wing of fairly low aspect ratio (3.6). The tests established that the rotating cylinder was an effective and efficient device for boundary-layer control. The correlating parameter was the ratio of the peripheral velocity of the cylinder to the freestream velocity. At low values of the velocity ratio, the flow over the surface of the flap was separated. As the velocity ratio was increased, the separated area of the flap was reduced and then finally removed. Further increases in velocity ratio resulted in only very small increases of lift. The velocity ratio for attached flow was found to depend only on flap deflection, and to be independent of the angle of incidence and of the actual value of the free-stream velocity. The power required was found to be proportional to the cube of the freestream speed; thus the rotating cylinder is most attractive for aircraft designed for very low approach speeds. The effect of moving the position of the effective hinge point of the flap is shown on Figure 26; there is only a small difference in lift, and drag, but a considerable reduction of the nose-down pitching moment.

The second model tested[28] used the same rotating cylinder, but in conjunction with a wing of larger aspect ratio (5.4). The change of aspect ratio did not affect the lift performance greatly, but as it is similar to that of a wing with boundary-layer control by chordwise blowing[29], comparisons of power requirements are possible. For similar flap deflections, and a maximum lift coefficient of 4.0, the rotating cylinder flap requires only 21% of the power required for blowing boundary-layer control, for an airspeed of 40kt; if the airspeed rises to 80kt the rotating cylinder flap requires 43% of the power required for blowing boundary-layer control and so still provides a worthwhile saving.

Thus if the mechanical complexity of the rotating cylinder flap is acceptable it offers the prospect of achieving boundary-layer control with a reduction of power compared to a system employing blowing, and of generating smaller nose-down pitching moments than blowing systems, with its consequential effect on tail size.

## 3 INTERNAL-FLOW JET-FLAP

### a) BLOWING OVER TRAILING-EDGE FLAPS

The aerodynamic characteristics of the internal-flow jet-flap were analysed by Williams, Butler and Wood[30] in 1961, and by Williams[2] in 1966. Again the basic estimation methods are given in Appendix A. Since that time a greater effort would seem to have been applied to the development of theoretical methods than to experimental studies.

Although the method of Spence[31,32], to predict the lift coefficient on a two-dimensional aerofoil section with a jet-flap, has shown good agreement with experimental results up to large jet deflections, the assumption that the vortex distribution representing the jet is placed along a line passing through the aerofoil trailing-edge in the direction of the undisturbed flow would suggest that the method is strictly applicable only to small jet deflection angles, and to small blowing rates, so that the jet path is shallow. Attempts have therefore been made[33,34] to derive theories which do not have this restriction, by placing a vortex distribution along the jet path and along the aerofoil chord[33] or aerofoil surfaces[34]. Iterations are then carried out between the vortex distributions and the jet path until the radius of curvature of the jet at any given point, deduced from the flow field induced by the vortex distribution, is compatible with the assumed strength of the jet vorticity at that point. Published results for one method[33] indicated that the lift of the aerofoil, and to a lesser extent, the jet path, was strongly dependent on the number of vortices representing the aerofoil. A comparison with the predictions of Spence's method suggested similar values for the lift curve slope, and, perhaps surprisingly, higher values of lift at a given angle of incidence and jet deflection, at low values of momentum coefficient, but tending to the Spence value at high values of the momentum coefficient.

In the calculation of the characteristics of the three-dimensional jet-flap wing, the classical theory of Maskell and Spence[35] is strictly only applicable to a wing of elliptic planform, with no camber and twist, and having an elliptic distribution of blowing momentum. Lissaman[36] has generalised the method of Maskell and Spence to consider straight, uncambered wings of arbitrary planform and twist, and with arbitrary distributions of blowing. An interesting result given by his method, and shown on Figure 27, is that whilst the pressure lift due to flap deflection varies with momentum coefficient in much the same way for large aspect ratios (of the order 10), as for small aspect ratios (of the order 4), the pressure lift due to angle of incidence is almost independent of momentum coefficient for the small aspect ratio. This result, which is, perhaps, of more significance to the external-flow jet-flap than the internal-flow jet-flap, would indicate that the effect of blowing for a small aspect ratio wing would be to yield an increment in lift coefficient almost independent of angle of incidence.

Theories having somewhat similar principles, that of applying the two-dimensional characteristics of jet-flap aerofoils along a lifting line, have been proposed by Lopes and Shen[37] and Gielow[38].

Das[39] developed a lifting surface theory based on Multhopp's method, in which the vortex distribution along the wing chord was represented by the sum of the first three terms in Birnbaum's expression for the chordwise vortex distribution of a two-dimensional thin aerofoil, each with unknown coefficients, and the first three terms of Spence's two-dimensional jet-flap theory, again with unknown coefficients. By making several approximations, the number of independent coefficients were reduced to three, so that the boundary conditions need be satisfied at only three points along the chord: at one-quarter chord, three-quarters chord, and infinity downstream. The spanwise stations considered by the method are specified by the method employed by Multhopp in the spanwise integration of the downwash integral. Whilst being suitable for wings with full-span flaps, the spanwise distribution of stations is in general less satisfactory for wings with part-span flaps. Das[40] also measured the chordwise and spanwise pressure distributions over a number of rectangular wings of varying aspect ratio, and a comparison of the spanwise distribution of lift due to angle of incidence and due to flap deflection, as measured, and as predicted by Das's theory, is shown on Figure 28. It can be seen that Das's method correctly represents the loading due to flap deflection, but underestimates the loading due to angle of incidence.

A more general lifting surface theory has been developed by Shen et al[41] at McDonnell Douglas, known as the Elementary Vortex Distribution Method. The trace of the wing and the jet in the plane of the free-stream is divided into a number of small rectangular elements. Elementary Vortex Distributions are now distributed over one or two of these elements, and overlap chordwise, to produce a piecewise linear and continuous vortex distribution in the chordwise sense, but a piecewise constant and discontinuous distribution in the spanwise sense. Different types of Elementary Vortex Distributions are used to ensure the correct behaviour close to the leading edge and to a flap hinge; at infinity downstream; and over the wing and jet away from the leading edge, flap hinge and infinity downstream. The strengths of these Elementary Vortex Distributions are derived by applying the boundary conditions at one point in each element, normally the centre of the element. The results of applying this theory to Das's wing are also shown in Figure 28, where it can be seen that the method produces an improved estimate of the loading due to angle of incidence, but overestimates slightly the loading due to flap deflection.

The McDonnell-Douglas method has also been applied to the complete model representing a jet-flap aircraft, Figure 29, tested by Butler et al[42]. Two sets of estimates are shown: one for the thin wing, and one for the thick wing, obtained by increasing the circulation part of the lift by a factor $(1 + t/c)$, as first suggested by Spence[31], and subsequently confirmed theoretically by Lissaman[36]. The theory with thickness correction is seen to be in good agreement with the measured lift-incidence variation, except at the highest angles of incidence where, perhaps, non-linear effects should have been included. The effect of the thickness correction on the pitching-moment curve is less than on the lift curve, but still results in better agreement between theory and experiment. The remaining discrepancy is thought to have resulted from treating the wing-fuselage combination as an isolated wing with a part-span flap, so ignoring the interference lift on the fuselage[43]. The theory can, of course, only predict the lift-dependent drag $C_{Di}$, and this has been included on the drag polar. Also shown is the difference $C_D - C_{Di}$, which represent the boundary-layer drag. Intuitively, this might not be expected to vary very rapidly with lift, and this is indeed the case, suggesting that the lift-dependent drag has been predicted correctly.

Wind tunnel tests on this model were performed in conjunction with a moving-belt rig[44], to supplement the data obtained previously with a fixed ground board[42]. Due to the particular installation of the moving-belt rig, the model had to be mounted inverted, in contrast to its normal upright position, and some interference was encountered between the strut, through which air passed to the model, and the flow around the root of the wing. As a consequence only the increments due to belt velocity are considered valid, and these have been applied to the data measured with the model in an upright position over a fixed ground board, to give the comparison shown on Figure 30. In the absence of jet impingement the effect of ground proximity on lift is small, and midly favourable. Subsequent to jet impingement, ground effect became progressively less favourable, until the wing stalled. It was found that the stall resulted from leading-edge separations, in contrast to the flap-shroud separation which initiated the stall in free-air.

In the absence of jet impingement the effect of ground proximity was to cause a reduction in drag (or an increase in thrust) relative to free-air conditions; subsequent to jet impingement the fall-off of lift is accompanied by an increase of drag. The tendency to pitch-up subsequent to jet impingement, found in earlier tests with a fixed ground board, was absent in the tests with the moving-belt rig. As with the high aspect-ratio model with flaps having boundary-layer control, the normal variation of downwash angle with angle of incidence was almost completely suppressed in ground effect.

A wider ranging investigation of the effect of ground proximity on the characteristics of a wing with an internal-flow jet-flap was carried out by Turner[45]. He tested an unswept rectangular wing at various heights above a moving-belt rig, with a small-chord flap at a range of deflection angles and with various momentum coefficients. Apart from some small favourable effects measured at small flap deflection angles, the effect of ground proximity was almost uniformly unfavourable on lift. Typical results are shown on Figure 31, which indicates that the ground effect depends primarily on the lift in free air, but that there is also a small dependence on the flap deflection.

The RAE jet-flap model was the subject of an experiment to measure the yaw-damping derivative $n_{\dot{\psi}}$,using the free-oscillation technique[46]. The separate effects of wing, fin, tailplane and fuselage were measured, and it was found that the latter gave a large and unpredicted destabilising contribution, while damping due to the fin was smaller than the estimated value. Explorations of the flow fields around the rear fuselage and fin suggested that these unexpected features resulted from the presence of wing-root vortices, whose strength increased with the high values of lift coefficient associated with jet-flap configurations, and which rolled up more rapidly at high-lift.

Extensive flight tests were carried out by BAC and RAE on the BAC-Hunting 126 jet-flap research aircraft,[2,47] and it has recently been tested in the NASA AMES 40ft x 80ft wind tunnel[48,49]. Comparisons between flight and tunnel measurements are made difficult by the fact that whereas the wind tunnel tests were conducted at a fixed windspeed and hence constant momentum coefficient, the flight tests[50] were made at constant engine rpm and varying airspeed, and hence varying momentum coefficient. The comparisons shown on Figure 32 show the values of the lift coefficient measured in flight compared with values interpolated from wind tunnel results, for the flight angle of incidence and momentum coefficients. Among the factors which may contribute to the difference is the quality of the position errors applied to the airspeed, as these were established at the higher airspeeds and extrapolated to the lower speeds; the fact that, due to the uncertainties of establishing wind-tunnel wall corrections for powered-lift models, the tunnel results have not been corrected for tunnel wall effects, and the fact that the wind tunnel tests were made at a fixed tail setting whereas the flight results are, of course, under trimmed conditions.

It should finally be mentioned that tests in an anechoic chamber at zero forward speed[51] have shown that the internal-flow jet-flap exhibits a much lower noise characteristic than the external-flow jet-flap or the augmentor flap scheme.

## b) BLOWING AT THE TRAILING-EDGE OF UNCONVENTIONAL WING SECTIONS

Lock and Albone[52] reviewed the data which exists on the use of the jet-flap concept at high subsonic speeds, and considered that it offered sufficient promise of improving the cruise performance and buffet margin to merit further research. Wind tunnel tests in this speed range were reported by Englar[53], who compared the performance of three aerofoils with different forms of trailing-edge blowing, Figure 33. The values of lift coefficient measured, Figure 34, suggested that the performance of an aerofoil with blowing from the lower surface was exceeded by that of an aerofoil with blowing from the upper surface over a curved trailing edge.

Consideration of this and other wind tunnel tests, and of arguments similar to those presented by Lock and Albone, has led to the suggestion of the use of a new type of aerofoil section, termed the Power Profile[54], Figure 35. Jets emerge from the slots above and below the control surface, and flow around the control surface to coalesce into a single jet flowing downstream. By varying the position of the control surface the width of the upper and lower slots may be changed simultaneously. This in turn changes the direction of the final single jet and thus the lift on the aerofoil, so that lift can be varied at a constant angle of incidence and momentum coefficient. Thus in addition to offering benefits in terms of better cruise and buffeting performance, high values of lift coefficient will be available at low speed in a manner which allows rapid changes to be made, suggesting that improvements in ride quality may be achieved through gust alleviation.

## 4 EXTERNAL-FLOW JET-FLAP

## a) ENGINES INSTALLED UNDER THE WING

This concept,originated by NASA, has been the subject of intensive study experimentally, and a wide variety of theoretical methods have been proposed by which the performance may be predicted. One obvious starting point lies in the methods developed for internal-flow jet-flaps[30]. The question then arises of the magnitude, distribution across the span, and deflection of the momentum leaving the trailing edge of the flap. Perry[18] assumed that the magnitude and direction of the momentum flux under forward speed conditions was the same as that measured under static conditions, and that it was sufficient theoretically to represent the non-uniform spanwise distribution by a uniform distribution of momentum over that part of the flap span thought to be affected by the jet sheet. Based on measured values of the static turning efficiency and static turning angle, and including allowances for non-linear effects at large flap angles and momentum coefficients, Perry obtained reasonable agreement between measured and predicted lift increments. However when he attempted to utilise this approach to analyse longitudinal forces, he found that it was not possible to obtain a satisfactory correlation of measured and predicted forces, and that it was necessary to revert to treating the flap as a simple thrust deflector and including the effect of supercirculation only in the calculation of the lift-dependent drag. Even with this limitation the method is restricted in the range of configurations to which it could be applied, since the effect of the position and orientation of the nacelle on the static turning parameters could not be predicted.

Ashill[55] has recently extended this approach by developing a semi-empirical method of predicting the static turning efficiency and static turning angle, based on an extensive series of static tests[56]. Using, as in the Perry method, the classical theory for jet-flap wings due to Maskell and Spence[35], and incorporating allowances for non-linear effects at large flap angles, and for the effect of the boundary layer on the flap upper surface at low momentum coefficients, Ashill has incorporated his predicted static turning parameters to give a better prediction of the lift coefficients measured in a NASA test[57] than could be obtained by the Perry method (Figure 36). Ashill followed Perry in predicting the longitudinal force using the thrust-deflector analogy; as Figure 37 shows, providing that a suitable value is assumed for the boundary-layer drag of the area of the wing external to the jet sheet, satisfactory agreement can be achieved between the predicted and measured values. The agreement between the predicted and measured values of the pitching-moment coefficient are, perhaps, less good (Figure 38) but this may be because the effect of the fuselage on the pitching moment is not adequately represented by the theory.

The Douglas Elementary Vortex Distribution method for the prediction of the characteristics of wings with internal-flow jet flaps has been applied[41] to an external-flow jet-flap configutation, by using an estimate of the turning efficiency, turning angle, and spanwise spreading of the engine exhaust derived from static measurements. Figure 39 shows that reasonable agreement is obtained for lift and pitching moment, and also for drag, if a suitable value of the boundary-layer drag is included.

All the above methods rely on static measurements to indicate the magnitude and direction of the momentum flux leaving the trailing-edge of the flap. Recent experiments at RAE Bedford have confirmed that forward speed has only a small effect on the turning and spreading process, but it is possible that a development of a theoretical method similar to that proposed by Shollenberger[58], in which both the wing and the jet are represented by singularity panels, and the spanloading and jet shape undergo an iterative process until they are compatible, will remove this dependence on static measurements in prediction methods.

Smith[57] has studied the effect of the size of the high-lift devices experimentally, using the unswept model shown in Figure 40, to test four flap configurations. As might be expected, Figure 41 shows that the configuration with the largest chord produced the most lift, and that with the smallest chord the least lift. For a given flap chord it appeared to be most advantageous to have a small vane and a forward slot; the configuration with an aft slot appearing to suffer from relatively poor turning performance. Different leading-edge devices were also tested on this model. At a moderate value of the momentum coefficient ($C_{TG} = 2.75$), increasing the chord of the leading-edge slat from 19% chord to 25% chord only resulted in an increase of the lift coefficient measured above the stall, and, as again might be expected, leading-edge slats were more effective than the leading-edge flaps formed by sealing the slots of the slats. In tests on a model similar to that shown in Figure 42(a), at a rather higher Reynolds number, Parlett, Smith and Megrail[59] showed that a leading-edge slat of 25% chord had some advantages over a 15% chord slat in terms of the angle of incidence at the stall and the break in the lift-curve slope. A leading-edge flap of larger chord (30% chord) was also tested, but was found to be inferior to the slats.

Smith[60] used the half model tested previously with various high-lift devices[57], Figure 40, to investigate the effect of wing aspect ratio, flap span, and engine position. He found that there was only a small loss of the trimmed lift coefficient when the wing aspect ratio was reduced from 7.0 to 5.25, but a much greater loss occurred when the same fractional reduction was applied to the flap span only, indicative of the lateral extent of the spreading of the engine exhaust. At a given overall momentum coefficient, a configuration with two engines located close to the fuselage had about the same longitudinal aerodynamic characteristics as a configuration with four engines located uniformly over the span of the wing.

Loss of thrust from one engine has a profound effect on lift, drag and pitch trim; in general the reduction in lift due to an inboard engine failure is greater than that due to an outboard engine failure[57,60]. Account must be taken of these longitudinal effects in defining safe flight speeds at high lift, but a potentially more difficult problem exists in the lateral characteristics, where the out-of-balance rolling moments generated at low angles of incidence by the loss of lift are magnified at higher angles of incidence by the engine-failed wing stalling first. Parlett, Smith and Megrail[59] showed that some of the earlier measurements of the out-of-balance rolling moment on a swept-wing configuration may have been pessimistic due to their low Reynolds number, and that the use of a large chord slat reduced the magnitude of the rolling moment. As an alternative[61] blowing at the leading-edge can be used to reduce the lift loss at the stall. However for this model the largest reduction of the out-of-balance rolling moment occurred when the engine arrangement was changed from the spread-out configuration of Figure 42(a) to the clustered arrangement of Figure 42(b), as is shown on Figure 43(a)[62]. For this model the change was accompanied by a loss of all-engines performance, both in terms of drag at a given lift coefficient, and of maximum lift coefficient, Figure 43(b).

A considerable effort has been devoted to a study of the lateral control devices required to trim the out-of-balance rolling moment. Parlett and Shivers[63] showed, for a model with an unswept wing and clustered engines, that conventional ailerons and spoilers, even when at large deflection angles, Figure 44(a) could only provide lateral trim up to an angle of incidence of 13° compared with the stalling angle of incidence of 22°. Moreover, deflection of the spoilers incurred a reduction of lift coefficient of the order of 0.45 through the incidence range. These tests suggested that a conventional rudder was sufficient to produce trim in yaw, but later tests on the model with engines spaced across the span of the wing, Figure 42(a), indicated that the conventional rudder was not sufficient to restore directional trim after an engine failure. These tests also showed that conventional wing spoilers at a large deflection (60°), combined with a small-chord spoiler on the flap itself, could produce roll trim up to stalling angle of incidence (22°), Figure 44(b) but with a decrement of approximately 1.0 in lift coefficient. Use of differential flap setting could not give roll trim up to the stalling angle of incidence, and produced large adverse yawing moments. Freeman, Parlett and Henderson[62] investigated the effectiveness of ailerons with large differential deflections, (60°), in conjunction with blowing over the deflected aileron, on the model with clustered engines, Figure 42(b), but found, Figure 44(c), that this was only effective at low angles of incidence. Further investigations will therefore be necessary before an adequate lateral control system can be defined.

Perry[18], in his review of the data available in 1970 on the external-flow jet-flap, noted that large reductions in the downwash factor occurred with increasing momentum coefficient. Parlett et al[64] investigated a range of fore-and-aft and vertical positions of the tailplane of a four-engined model, Figure 45, and concluded that if the tailplane were to retain even a minimal effectiveness at high momentum coefficients it must be located at least 1.5 to 2 wing chords above the fuselage.

Measurements of static and dynamic stability derivates were made by Freeman, Grafton and D'Amato[65] for the swept-wing model with engines spaced across the span, Figure 42(a). Figure 46 shows that increase of momentum coefficient increased the positive dihedral effect ($-C_{\ell_\beta}$), but reduced the directional stability ($+C_{n_\beta}$). Increase of momentum coefficient also increased the damping in roll ($-(C_{\ell_p} + C_{\ell_{\dot\beta}} \sin \alpha)$); the yaw damping ($-(C_{n_r} - C_{n_{\dot\beta}} \cos \alpha)$) was approximately independent of the momentum coefficient.

Vogler[66] compared a high-wing and a low-wing model with the engines spread out across the span both in and out of ground effect. He found that, at a given angle of incidence, the high-wing configuration had between 5% and 7% more lift than the low-wing configuration, probably due to the end-plate effect of the fuselage. The low-wing configuration in general produced lower nose-down pitching moments, especially at low flap deflections. With the low-wing configuration it was possible to have the tailplane closer to the fuselage than for the high-wing configuration without loss of tailplane power. The effect of ground proximity on lift, Figure 47, was similar for both the high-and low-wing at the same ground-clearance height. However for the same undercarriage height the low-wing configuration will suffer approximately twice the loss of lift as the high-wing configuration. Gratser and Mahal[67] have shown that this increased adverse ground effect will have a marked effect on the ability of the aircraft to execute a flare, since the lift increment required to flare may not be obtainable at a practical attitude. There are thus very powerful arguments for the adoption of a high wing.

One particular disadvantage of the underwing external-flow jet-flap concept in respect of its use for civil aircraft lies in the noise it generates. Experiments[68] have shown that impingement of the jet on the flap leading edge and the flow leaving the flap trailing edge add to the noise of the basic jet an amount which increases with flap angle, giving an increase of some 10dB for the landing flap setting. In an attempt to reduce the impingement noise, a "daisy" nozzle was added to an engine exhaust stream to reduce the velocity of the flow at the flaps[69]. Although a reduction of 35% of velocity was measured, and the impingement noise reduced, the daisy nozzle had a higher noise level than the basic conical nozzle, and so showed no net advantage.

It has been assumed that the aerodynamic behaviour depends only on momentum of the jet, but it may be that, as with boundary-layer control, at the low values of the ratio of jet velocity to external flow velocity which would result from using such a device to reduce the jet velocity, the momentum coefficient is not the correct correlating parameter.

### b) ENGINES INSTALLED OVER THE WING

There is a potential advantage in installing the engines over the wing, as the wing will provide some acoustic shielding. However some of this advantage is eroded when the engine exhaust is utilised to give powered lift. In order to allow the engine exhaust to be turned around the flap knuckle, and to be discharged from the trailing edge of the flap, it must attach itself to the wing ahead of the flap knuckle. This may be done either by directing the efflux from a conventional circular nozzle onto the wing surface by a deflector at the nozzle exit, or by discharging the efflux through a rectangular or semi-circular nozzle. Both methods result in scrubbing noise[70] being generated at the wing surface, and being convected in the exhaust to the flap trailing edge.

The utilisation of the Coanda effect to turn the jet implies that the upper surface of the wing joins the upper surface of the flap smoothly, with no slots or gaps. Such a wing and flap configuration is not an effective one outside the region of influence of the engine exhaust, so that either the flap must revert to a conventional slotted flap outside this region, or boundary-layer control by blowing must be employed to maintain attached flow, as was the case in the only wind tunnel test for which data has so far been published[71]. The process of turning a jet by the Coanda effect depends on the pressure ratio of the jet, and its thickness relative to the radius of curvature around which it is turning. When turning is successfully accomplished it occurs with little or no spanwise spreading of the jet, and so can yield higher values of turning efficiency than are obtained for the engine-under-the-wing concept. On the other hand, the lack of spreading minimises the spanwise extent of the wing influenced by the jet. Nevertheless, the data so far published for the model shown in Figure 48 suggested that at a given engine momentum coefficient the over-wing-engine produces somewhat more lift at a given drag coefficient than the under-wing-engine, Figure 49. The pitching moment curves indicate that the over-wing engine configuration had slightly more instability than the under-wing engine configuration, and, taking into account the fact that the over-wing engine produced more lift, this implies that the centre-of-pressure for the over-wing engine was more forward than for the under-wing engine. This may be a direct reflection of the fact that the under-wing engine configuration employs a double-slotted flap with significant rearward extension.

## 5 AUGMENTOR SYSTEMS

### a) BLOWING THROUGH FLAPS

The prediction of the characteristics of an augmentor wing with blowing through a divided trailing-edge flap, Figure 50, requires a method of estimating the performance of the injector system, and of calculating the aerodynamic loading on the wing, accounting for the sink effect of the flow entrained into the injector, and the jet-flap effect of the thick jet emerging from the trailing edge of the flap. Whittley[72], the originator of the scheme at De Havilland (Canada), has indicated that a theory has been developed for the performance of an injector system with non-uniform inlet and exit velocity profiles. Difficulties were, however, encountered in applying this theory to predict the effect of forward speed on the performance of the injector system, as the exit profile is modified from the static distribution by forward speed effects. Chan[73] has analysed the flow around a thin aerofoil with a jet-flap and a sink located at the hinge of the flap. He found that suction into the injector system can induce an additional lift on the aerofoil, this additional lift decreasing slightly as the jet momentum increases. Recent analysis of the effect of thick jets[55] suggests that the correlating parameter $C_\mu$ should be replaced by $C_\mu - 2t_J/c$, where $t_J$ is the thickness of the jet. In view of these effects, the comparison shown on Figure 51 between experimental results, and the predictions of the McDonnell-Douglas Elementary Vortex Distribution Method[41], assuming a thin jet having the measured static thrust modified to allow for the flow of boundary-layer-control air, is surprisingly good.

The static performance of an augmentor wing with the primary nozzle in the form of a thin slot[74] is summarised in Figure 52. Analysis of measurements made on a quasi-two-dimensional model showed that the effective augmentation ratio decreased from a static value of 1.30 to 1.21 at forward speed. This resulted from a combination of the effect of forward speed on the characteristics of the injector, and from incomplete thrust recovery, but it was not possible to isolate the individual contributions.

Following early Canadian two-dimensional tests, the major part of the wind tunnel data for complete models with this powered-lift system has been obtained in the AMES 40ft x 80ft wind tunnel[75,76] using the models illustrated in Figure 53. A particular feature of this system[77] is that the flow induced by the injector system provides a powerful control on the flow at mid chord, and tends to limit the spanwise spread of the stall. This is illustrated by the well-rounded maximum which occurred in the lift curves for both the unswept and swept wings, Figure 54. For the straight wing the initial breakdown of the flow occurred at the wing root, and a small increase of the maximum lift coefficient was obtained by blowing through a slot on the upper surface of the fuselage in line with the leading edge of the wing. In the case of the swept wing the wing root was less heavily loaded, and although separations still occurred in this region as the stall was approached, a fuselage boundary-layer control slot could not influence the progression of the stall.

Both models were tested with highly-deflected ailerons having boundary-layer control by blowing in order to achieve as uniform a spanwise lift distribution as possible. However it was found, Figure 55, that a reduction of the deflection of the ailerons had only a small effect on the maximum lift coefficient, but markedly reduced the nose-down pitching moment below the stall, and the post-stall pitch-up.

An internal flow system such as the augmentor wing (or the internal-flow jet-flap) allows the possibility of cross-ducting the flow bled from the engines, so that engine failure will not cause assymetric loadings, as occurs for the external-flow jet-flap. The augmentor also provides a ready means of providing lateral control moments independent of forward speed. This is achieved using the "augmentor choke", Figure 50, a flap in the trailing-edge portion of the injector system which can partially choke the exit. Tests[75] showed that it produces changes in rolling moment which are almost independent of the lift coefficient, with only a small penalty in the maximum lift coefficient, Figure 56.

Measurement of ground effect on these models has been made only with a fixed ground board[78]. The results, Figure 57, show that both the lift curve slope and the maximum lift coefficient are reduced as ground clearance is reduced, but the effects shown may be exaggerated by the presence of the boundary layer which develops on the fixed ground board.

One disadvantage of the augmentor-wing configurations so far discussed lie in the noise they generate, typically some 115PNdB at a 500ft sideline compared with a goal of 95PNdB for commercial aircraft. The Boeing Company have investigated[79] alternative forms of nozzles to the slot nozzle, Figure 58. The multirow lobe nozzle with a "screech eliminator" in a lined augmentor has actually demonstrated the objective 95PNdB sideline noise. Figure 59 shows that, for a given thrust coefficient, the aerodynamic performance of the slot and lobe nozzles are approximately the same.

Boeings compared the effect of forward speed on the axial force, at a given lift coefficient and primary nozzle momentum coefficient, for two augmentor configurations with that for an internal-flow jet-flap having the same flap chord ratio, Figure 60. Whilst the axial force for the jet flap is essentially invariant with airspeed, the values for the augmentor configurations vary markedly with airspeed, and are more negative (higher thrust). The shape of the axial force curve is well reproduced by the curve of the sum of the ram drag and the augmented thrust. The difference between the axial force and the sum of the ram drag and augmented thrust is independent of airspeed, and, as static values of the thrust augmentation factor and entrainment ratio (as Figure 52) have been used in this calculation, this is taken to imply that the characteristics of the injector system are not affected by forward speed.

### b) BLOWING THROUGH THE WING

Quinn[80,81] has considered the application of injectors to aircraft requiring VTOL capability, where in the absence of forward speed there can be no circulation induced on the wing by the jet. The necessity of making the thrust vector pass through, or very near to the centre of gravity, then suggests that the injectors should be mounted in the wing, in contrast to their installation in the flap for a purely STOL application. Figure 61 shows such an installation with two spanwise rows of injectors; the intake and exit doors are arranged to deflect the thrust vector for transitional flight.

At zero forward speed the injector is the sole source of lift; a high thrust augmentation ratio is therefore essential. Installation within the wing results in a minimum length being available for mixing, whereas the achievement of high values of thrust augmentation has in the past required large mixing lengths. A special form of primary nozzle, known as the hypermixing nozzle, has therefore been developed with the aim of promoting rapid mixing. The nozzle, Figure 62, is subdivided into a number of segments, and each segment imparts a transverse velocity to the flow of opposite sense to that imparted by its neighbouring segments. As a result vortices are set up at the junction of adjacent segments, which entrain additional fluid and accelerate the spreading of the primary jet.

A large scale model of a single channel was tested statically to determine the effect of mixing length, diffuser length, and of the ratio of the exit area to the area of the mixing section. Subsequently a four channel model powered by a turbofan engine was tested; Figure 63 shows the level of thrust augmentation achieved, and the fact that the multi-channel results are in good agreement with the single channel data measured earlier. Figure 64 shows that with forward speed, the lift component of thrust is augmented by circulation lift, whilst the axial component of thrust is opposed by the momentum drag. An analysis of the stability and control of an aircraft with this form of thrust augmentation[82] has indicated that the aircraft could perform a stable and controlled transition manoeuvre provided that the static thrust-weight ratio was of the order of 1.3.

## 6 ACKNOWLEDGEMENT

The author acknowledges the permission of Her Britannic Majesty's Stationery Office to reproduce the paper, which is British Crown Copyright.

## APPENDIX A

## EQUATIONS FOR LIFT AND DRAG COEFFICIENTS DUE TO WILLIAMS ET AL[1,30]

### A.1. LIFT

Classical jet-flap theory suggests that the lift coefficient $C_{L_\infty}$ for a two-dimensional thin flat plate at an angle of incidence $\alpha$, with blowing over a hinged flap of chord ratio $c_f/c$, such that the jet is discharged with a deflection $\delta_J$, and with an effective momentum coefficient at the trailing edge of the flap $C'_{\mu_{eff}}$, is given by[31]

$$C_{L_\infty} = \delta_J \left(\frac{\partial C_L}{\partial \delta_J}\right)_\infty + \alpha \left(\frac{\partial C_L}{\partial \alpha}\right)_\infty \qquad \text{A.1}$$

The derivatives $\left(\frac{\partial C_L}{\partial \delta_J}\right)_\infty$ and $\left(\frac{\partial C_L}{\partial \alpha}\right)_\infty$ have been derived by numerical analysis, and for blowing at the wing trailing edge ($c_f/c = 0$) it has been found that they can be expressed as

$$\left(\frac{\partial C_L}{\partial \delta_J}\right)_\infty = \left[4\pi C'_{\mu_{eff}} \left(1 + 0.151\, {C'_{\mu_{eff}}}^{\frac{1}{2}} + 0.139\, C'_{\mu_{eff}}\right)\right]^{\frac{1}{2}}$$

$$\left(\frac{\partial C_L}{\partial \alpha}\right)_\infty = 2\pi \left(1.0 + 0.151\, {C'_{\mu_{eff}}}^{\frac{1}{2}} + 0.219\, C'_{\mu_{eff}}\right) \qquad \text{A.2}$$

For a thin wing of aspect ratio AR with a full-span jet-flap the derivatives $\left(\frac{\partial C_L}{\partial \delta_J}\right)_{AR}$ and $\left(\frac{\partial C_L}{\partial \alpha}\right)_{AR}$ are obtained by multiplying the two-dimensional values by the factor $F(AR, C'_{\mu_{eff}})$ which can be written as

$$F(AR, C'_{\mu_{eff}}) = \frac{AR + \frac{2C'_{\mu_{eff}}}{\pi}}{AR + 2 + 0.604\, {C'_{\mu_{eff}}}^{\frac{1}{2}} + 0.876\, C'_{\mu_{eff}}} \qquad \text{A.3}$$

For a wing of thickness-chord ratio $t/c$ having a part-span flap corresponding to a fraction $S_f/S$ of the wing area, a more general expression for the lift was given as

$$C_L = F\left[\left(1 + \frac{t}{c}\right)\left\{\kappa\, \delta_J \left(\frac{\partial C_L}{\partial \delta_J}\right)_\infty + \nu\alpha \left(\frac{\partial C_L}{\partial \alpha}\right)_\infty\right\}\right] - \frac{t}{c}\, C_{\mu_{eff}} (\delta_J + \alpha) \qquad \text{A.4}$$

where

$$\kappa = \frac{S_f}{S}; \quad C_{\mu_{eff}} = C'_{\mu_{eff}} \frac{S_f}{S}; \quad \nu = \frac{S_f \left(\frac{\partial C_L}{\partial \alpha}\right)_\infty + (S - S_f) \left(\frac{\partial C_L}{\partial \alpha}\right)_{\infty,\, C'_{\mu_{eff}} = 0}}{S \left(\frac{\partial C_L}{\partial \alpha}\right)_\infty} \qquad \text{A.5}$$

With slot blowing at the knuckle of a deflected trailing-edge flap the effective momentum coefficient $C'_{\mu_{eff}}$ can reasonably be taken as the excess jet momentum over that required to achieve attached flow, ie $C'_\mu - C'_{\mu_a}$.

For a wing with boundary-layer control, the effective momentum coefficient $C'_{\mu_{eff}}$ is small, and the value of $\left(\frac{\partial C_L}{\partial \alpha}\right)_{\infty,\, C'_{\mu_{eff}}}$ does not differ significantly from the attached flow value $\left(\frac{\partial C_L}{\partial \alpha}\right)_{\infty,\, C'_{\mu_{eff}} = 0}$. The effect of boundary-layer control may be considered to be confined to producing a lift increment $\Delta C_L$, which is independent of the angle of incidence, and from equations A.3 and A.4 can be written as

$$\Delta C_L = \frac{AR}{AR + 2}\left(1 + \frac{t}{c}\right) \kappa\, \delta_J \left(\frac{\partial C_L}{\partial \delta_J}\right)_\infty \qquad \text{A.6}$$

The term $\frac{AR}{AR + 2}\left(1 + \frac{t}{c}\right)$ has been replaced by $\frac{a_1}{2\pi}$ where $a_1$ is the lift-curve slope of the thick, finite aspect ratio wing in inviscid flow. For these configurations an improved estimate of the part-span factor $\kappa$ has been obtained from the Roy Ae Soc Data Sheets, and designated $K_L$. Finally the two-dimensional lift increment has been written as a small perturbation of the two-dimensional lift increment for attached flow $\Delta C^*_{L_\infty}$, so that equation A.6 is, for boundary-layer control by blowing

$$\Delta C_L = \frac{a_1}{2\pi} K_L\, \Delta C^*_{L_\infty}\, P_{C'_{\mu_{eff}}} \qquad \text{A.7}$$

with

$$P_{C'_{\mu_{eff}}} = \frac{\left(\frac{\partial C_L}{\partial \delta_J}\right)_{\infty,\, C'_{\mu_{eff}}}}{\left(\frac{\partial C_L}{\partial \delta_J}\right)_{\infty,\, C'_{\mu_{eff}} = 0}} \qquad \text{A.8}$$

## A.2. DRAG

Classical jet-flap theory indicates that the drag coefficient of a wing of aspect ratio AR with a full-span jet-flap is given by[35]

$$C_D = \frac{C_L^2}{\pi AR + 2C'_{\mu_{eff}}} - C'_{\mu_{eff}} \qquad A.9$$

More generally this has been written as

$$C_D = C_{D_o} + \frac{K_1 C_L^2}{\pi AR + 2C'_{\mu_{eff}}} - r C'_{\mu_{eff}} \qquad A.10$$

where $C_{D_o}$ represents the boundary-layer drag of surfaces not subject to the jet-flap effect; the term $K_1$ allows for departures from elliptic loading for the basic unblown wing, and r allows for incomplete thrust recovery due to mixing and turning losses.
For a part-span flap equation A.10 was extended to become

$$C_D = C_{D_o} + \frac{K_1 C_L^2}{\pi AR + 2C_{\mu_{eff}}} + \Delta C_{D_p} - r C_{\mu_{eff}} \qquad A.11$$

with $\Delta C_{D_p}$ representing the increase in lift-dependent drag arising from the change of spanwise load distribution.

For wings with boundary-layer control, and small values of $C_{\mu_{eff}}$, equation A.11 has been simplified, to become

$$C_D = C_{D_o} + \frac{K_1 C_L^2}{\pi AR} + \Delta C_{D_p} - \cos \delta_f C_{\mu_{eff}} \qquad A.12$$

It was noted that the experimental values of $\Delta C_{D_p}$ were greater than the estimated values by a factor of up to 2.

## REFERENCES

1 J Williams, S F J Butler. Aerodynamic aspects of boundary-layer control for high-lift at low-speeds. AGARD Report 414 (1963).

2 J Williams. Recent basic research on V/STOL aerodynamics at RAE. Zeit fur Flugwiss 14 Heft 6 (1966).

3 J A Lawford, D N Foster. Low-speed wind-tunnel tests on a wing section with plain leading- and trailing-edge flaps having boundary-layer control by blowing. R&M No 3639 (1970).

4 C C L Sells. Plane subcritical flow past a lifting aerofoil. RAE TR 67146 (1967).

5 J L Hess, A M O Smith. Calculation of potential flow about arbitrary bodies. Progress in Aeronautical Sciences, Vol 8, Pergamon Press, London (1966).

6 F Thomas. Investigations into increasing the lift of wings by boundary-layer control through blowing. RAE Library Translation 1267 (1967). From: Untersuchungen Über die Erhöhung des Auftriebes Von Tragflügeln Mittels Grenzschichtbeeinflussung durch Ausblasen. Z Flugwiss 10, No 2, 46-65 (1962).

7 I S Gartshore, B G Newman. The turbulent wall jet in an arbitrary pressure gradient. Aero Quarterly Vol 20, p 65 (1969).

8 I S Gartshore. Predictions of the blowing required to suppress separation from high-lift aerofoils. AIAA Paper No 70-872 (1970).

9 B Thwaites (Ed). Incompressible aerodynamics. Clarendon Press (1960).

10 H P Horton. A semi-empirical theory for the growth and bursting of laminar separation bubbles. ARC CP No 1073 (1967).

11 J E Green. Application of Head's entrainment method to the prediction of turbulent boundary-layer and wakes in compressible flow. RAE TR 72079 (1972).

12 E S Levinsky, T T Yeh. Analytical and experimental investigation of circulation control by means of a turbulent Coanda jet. NASA CR-2114 (1972).

13 F A Dvorak. Calculation of turbulent boundary-layers and wall jets over curved surfaces. AIAA Journal Vol 11 No 4 (1973).

14 G F Moss, A B Haines, R Jordan. The effect of leading-edge geometry on high-speed stalling. Paper No 13 of AGARD CP 102 "Fluid Dynamics of Aircraft Stalling" (1972).

15 M W Kelly. Analysis of some parameters used in correlating blowing-type boundary-layer control data. NACA RM A56F12 (1956).

16 R J Engler, R M Williams. Test techniques for high lift two-dimensional airfoils with boundary-layer and circulation control for application to rotary wing aircraft. Canadian Aeronautics and Space Journal Vol 19 No 3 (1973).

17 R C W Eyre, S F J Butler. Low speed wind tunnel tests on an AR8 swept wing subsonic transport research model with BLC blowing over nose and rear flaps for high-lift. RAE TR 67112 (1967).

18 D H Perry (with an Appendix by D N Foster). A review of some published data on the external-flow jet-augmented flap. ARC CP No 1194 (1972).

19 S F J Butler, R C W Eyre. Unpublished data on subsonic transport research model.

20 B Maskew. Calculation of the three-dimensional potential flow around lifting non-planar wings and wing-bodies using a surface distribution of vortex-rings. Loughborough University of Technology Report TT 7009 (1970).

21 S F J Butler. Low-speed wind-tunnel tests on a sweptback wing model (Buccaneer Mark I) with blowing at the wing leading edge and blowing over the flaps and drooped ailerons. R&M No 3655 (1971).

22 R Lohr. Increase in maximum lift of a rectangular wing in ground effect by combined blowing at the wing nose and trailing edge flap.
RAE Library Translation No 1270 (1967).
From:
Erhöhung des Maximalauftriebes eines Rechteckflügels in Bodennähe Durch Kombiniertes Ausblasen an der Flügelnase und an der Hinterkantenklappe.
DLR FB 64-02 (1964).

23 C J Dixon. Lift and control augmentation by spanwise blowing over trailing edge flaps and control surfaces.
AIAA Paper No 72-781 (1972).

24 S F J Butler, J A Lawford. Low-speed wind-tunnel tests on a wing-fuselage model with area suction through perforations at the leading-edge flap knee. R&M 3640 (1970).

25 M H L Waters, L J Warren. Tests in the RAE blower tunnel of the air blast system for TSR 2 windscreen rain clearance.
RAE Report Mech Eng 25 (1963).

26 A Alvarez-Calderon, F R Frank. A study of the aerodynamic characteristics of a high-lift device based on a rotating cylinder and flap.
Stanford University Technical Report RCF-1 (1961).

27 J A Weiberg. Large-scale wind-tunnel tests of an airplane model with two propellers and rotating cylinder flaps.
NASA TN D-4489 (1968).

28 J A Weiberg, S O Dickinson. Large-scale wind-tunnel tests of an airplane model with four propellers and rotating cylinder flaps. NASA TN D-5742 (1970).

29 J A Weiberg, C A Holzhauser. Large-scale wind-tunnel tests of an airplane model with an unswept, tilt wing of aspect ratio 5.5 and with four propellers and blowing flaps. NASA TN D-1034 (1961).

30 J Williams, S F J Butler, M N Wood. The aerodynamics of jet flaps.
R&M 3304 (1961).

31 D A Spence. The lift coefficient of a thin jet-flapped wing. Proc.Roy.Soc.(London) Vol 238 pp 46-58 (1956).

32 D A Spence. The lift of a thin aerofoil with a jet-augmented flap.
Aero Quart.9 pp 287-299 (1958).

33 A C Herold. A two-dimensional, iterative solution for the jet flap.
NASA CR-2190 (1973).

34 N D Halsey. Two-dimensional non-linear jet-flap potential flow method.
Unpublished McDonnell Douglas Report.

35 E C Maskell, D A Spence. A theory of the jet flap in three dimensions.
Proc.Roy.Soc. Vol 251 pp 407-425 (1959).

36 P B S Lissaman. Analysis of high-aspect-ratio jet-flap wings of arbitrary geometry.
NASA CR-2179 (1973).

37 M L Lopez, C C Shen. Recent development in jet flap theory and its application to STOL aerodynamic analysis.
AIAA Paper 71-578 (1971).

38 R C Gielow. Performance prediction and evaluation of propulsion-augmented high lift systems for STOL aircraft.
AIAA Paper 71-990 (1971).

39 R Das. Tragflächentheorie für Tragflugel mit Strahlklappen. Jahrbuch der Wissenschaftlichen Gesellschaft für Luftfahrt pp 112-133 (1960).

40 R Das. Theoretische und Experimentelle Untersuchungen an Tragflügeln endlicher Spannweite mit Strahlklappen.
DFIR FB-64-40 (1964).

41 C C Shen, M L Lopez, N F Wasson. A jet-wing lifting surface theory using elementary vortex distributions. AIAA Paper 73-652 (1973).

42 S F J Butler, M B Guyett, B A Moy. Six component low-speed tunnel tests of jet-flap complete models with variation of aspect ratio, dihedral and sweepback, including the influence of ground proximity.
R&M 3441 (1961).

43 D N Foster. Exploratory low-speed tunnel tests of part-span flap and fuselage effects on a high-lift wing. RAE TR 65288 (1965).

44 S F J Butler, B A Moy, G D Hutchins. Low-speed tunnel tests of an AR 9 jet-flap model, with ground simulation by moving-belt rig. Tech Note Aero 2957 (1964).

45 T R Turner. Wind-tunnel investigation of an unswept airfoil with a 0.098 chord blowing flap. NASA TM X-2675 (1972).

46 A P Cox, S F J Butler. Low-speed wind tunnel measurements of damping in yaw ($n_{\dot{\psi}}$) on an AR 9 jet-flap complete model.
ARC CP No 869 (1967).

47 K D Harris. The Hunting H126 jet-flap research aircraft.
AGARD Lecture Series 43 (1971).

48 T N Aiken, A M Cook. Results of full-scale wind tunnel tests on the H 126 jet-flap aircraft. NASA TN D-7252 (1973).

49 J Cowper. Report on H 126 Ames tunnel tests. HSA (Brough) Note YAD 3083 (1970).

50 P L Bisgood. Data from RAE flight tests of H 126 aircraft.

51 F W Gibson. Noise measurements of model jet-augmented lift systems.
NASA TN D-6710 (1972).

52 R C Lock, C M Albone. Note on the use of a jet flap for lift augmentation at high-subsonic speeds, with suggestions for further research.
Unpublished MOD Report (1971).

53 R J Englar. Two-dimensional transonic wind tunnel tests of three 15-percent thick circulation control airfoils. NSRDC Technical Note AL-182 (1970).

54 A B Bauer. A new family of airfoils based on the jet-flap principle. McDonnell-Douglas Report MDC-J5713 (1972).

55 P R Ashill. A theoretical and experimental investigation of the external-flow jet-augmented flap. AGARD CP No 135 (1973).

56 P R Ashill, S F Mansfield. Note on some exploratory tests on a swept wing with an external-flow jet-augmented flap. RAE TR 72192 (1972).

57 C C Smith. Effect of engine position and high lift devices on aerodynamic characteristics of an external-flow jet-flap STOL model. NASA TN D-6222 (1971).

58 C A Shollenberger. A three-dimensional wing/jet interaction analysis including jet distortion influences. AIAA Paper No 73-655 (1973).

59 L P Parlett, C C Smith, J L Megrail. Wind-tunnel investigations of effects of variations in Reynolds number and leading-edge treatment on the aerodynamic characteristics of an externally blown jet-flap configuration. NASA TN D-7194 (1973).

60 C C Smith. Effect of wing aspect ratio and flap span on aerodynamic characteristics of an externally blown jet-flap STOL model. NASA TN D-7205 (1973).

61 L T Goodmanson, L B Gratzer. Recent advances in aerodynamics for transport aircraft. AIAA Paper No 73-9 (1973).

62 D C Freeman, L P Parlett, R L Henderson. Wind-tunnel investigation of a jet transport airplane configuration with an external-flow jet flap and inboard pod-mounted engines. NASA TN D-7004 (1970).

63 L P Parlett, J P Shivers. Wind-tunnel investigation of an STOL aircraft configuration equipped with an external-flow jet flap. NASA TN D-5364 (1969).

64 L P Parlett, D C Freeman, C C Smith. Wind-tunnel investigation of a jet transport airplane configuration with high thrust-weight ratio and an external-flow jet flap. NASA TN D-6058 (1970).

65 D C Freeman, S B Grafton, R D'Amato. Static and dynamic stability derivatives of a model of a jet transport equipped with external-flow jet-augmented flaps. NASA TN D-5408 (1969).

66 R D Vogler. Wind-tunnel investigation of a four-engine externally blowing jet-flap STOL airplane model. NASA TN D-7034 (1970).

67 L B Gratzer, A S Mahal. Ground effects in STOL operations. AIAA Paper No 71-579 (1971).

68 W A Olsen, R G Dorsch, J H Mills. Noise produced by a small-scale, externally blown flap. NASA TN D-6636 (1972).

69 T W Putnam, P L Lasagna. Externally blown flap impingement noise. AIAA Paper No 72-664 (1972).

70 U Von Glahn, M Reshotko, R Dorsch. Acoustic results obtained with upper-surface-blowing lift-augmentation systems. NASA TM X-68159 (1972).

71 A E Phelps. Low-speed wind-tunnel investigation of a semispan STOL jet transport wing-body with an upper surface blown jet flap. NASA TN D-7183 (1973).

72 D C Whittley. Some aspects of propulsion for the augmentor-wing concept. AGARD CP No 91 (1971).

73 Y Y Chan. The lift on a two-dimensional Augmentor wing. NRC Report LR-523 (1969).

74 T N Aiken. Advanced augmentor-wing research. NASA TM X-62,250 (1972).

75 D G Koenig, V R Corsiglia, J P Morelli. Aerodynamic characteristics of a large scale model with an unswept wing and augmented jet flap. NASA TN D-4610 (1968).

76 M D Falarski, D G Koenig. Aerodynamic characteristics of a large scale model with a swept wing and augmented jet flap. NASA TM X-62029 (1971).

77 D C Whittley. The aerodynamics of high lift illustrated by augmentor-wing research. Paper No 72-20 presented at Anglo-American Aeronautical Conference (1971).

78 M D Falarski, D G Koenig. Longitudinal aerodynamic characteristics of a large-scale model with a swept wing and augmented jet flap in ground effect. NASA TM X-62174 (1972).

79 J V O'Keefe, G S Kelley. Design integration and noise studies for jet STOL aircraft. NASA CR 114471 (1972).

80 B Quinn. Compact ejector thrust augmentation. Journal of Aircraft Vol 10 No 8 (1973).

81 B Quinn. Compact thrust augmentors for V/STOL aircraft. AGARD CP No 135 (1973).

82 G Kurylowich, J M Martin. An analysis of the stability and control characteristics of an ejector wing V/STOL during transition. AFFDL-TR-72-37 (1973).

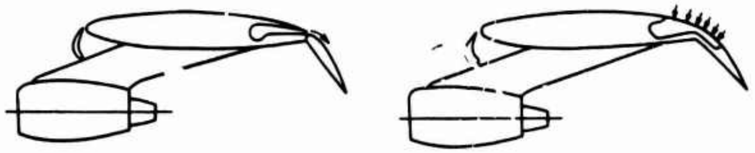

a BLOWING

b SUCTION

INTERNAL - FLOW SYSYEMS

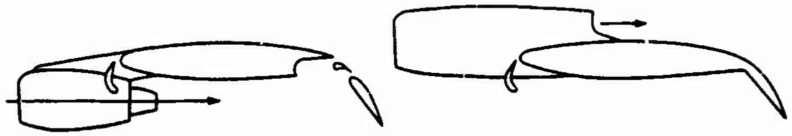

c ENGINES INSTALLED UNDER WING

d ENGINES INSTALLED OVER WING

EXTERNAL - FLOW SYSTEMS

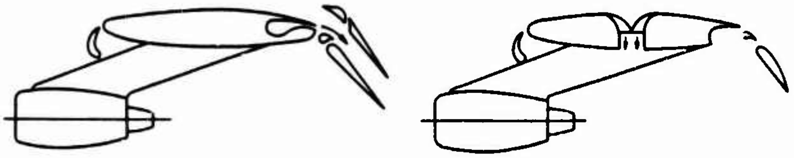

e AUGMENTOR WING

f INJECTOR WING

AUGMENTOR SYSTEMS

FIG. 1 POWERED - LIFT SYSTEMS

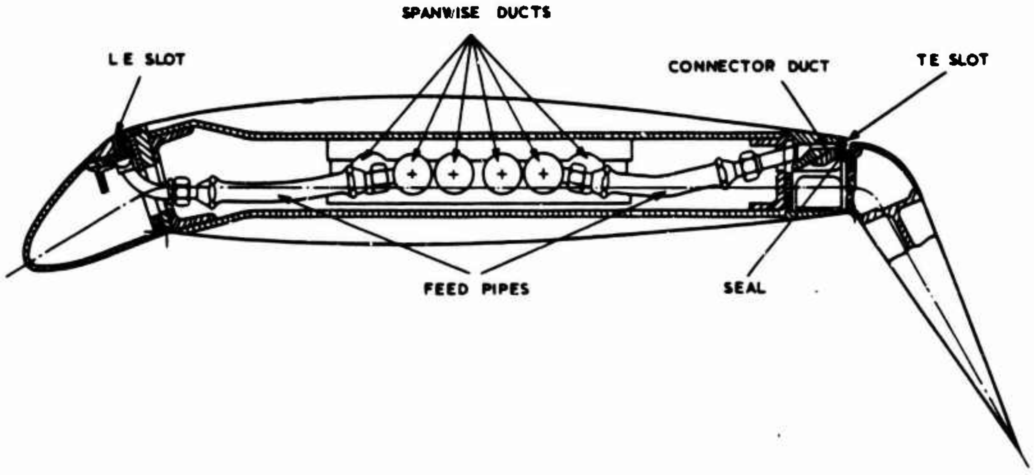
SPANWISE DUCTS
L E SLOT
CONNECTOR DUCT
TE SLOT
FEED PIPES
SEAL

FIG. 2 TYPICAL SECTION OF RAE TWO - DIMENSIONAL MODEL

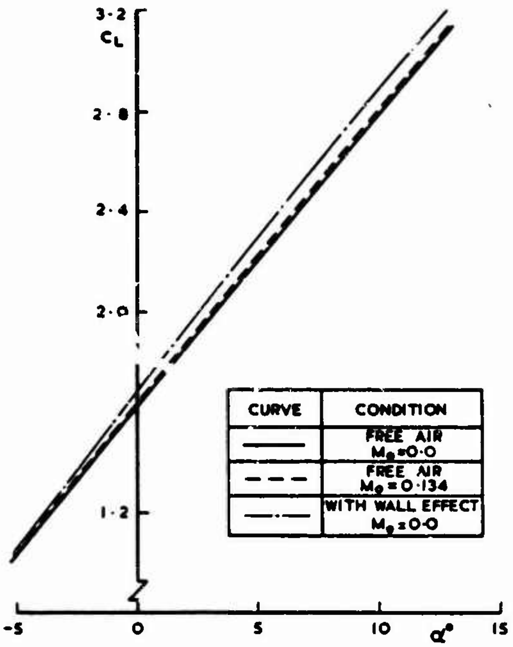

FIG.3 THEORETICAL EFFECT OF ANGLE OF INCIDENCE ON LIFT

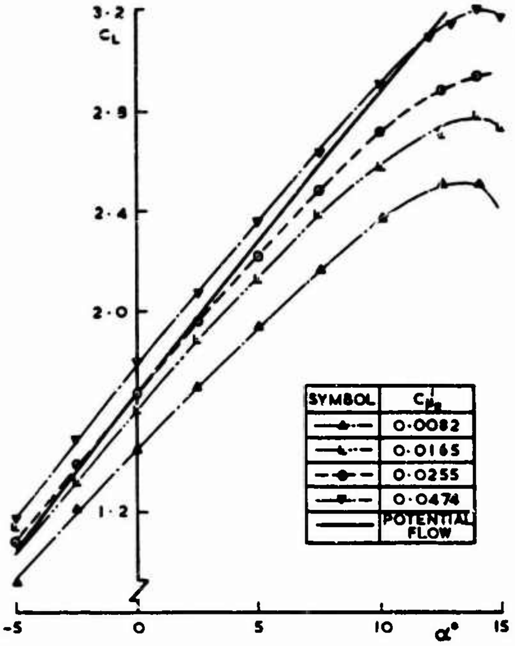

FIG.4 EXPERIMENTAL EFFECT OF ANGLE OF INCIDENCE ON LIFT

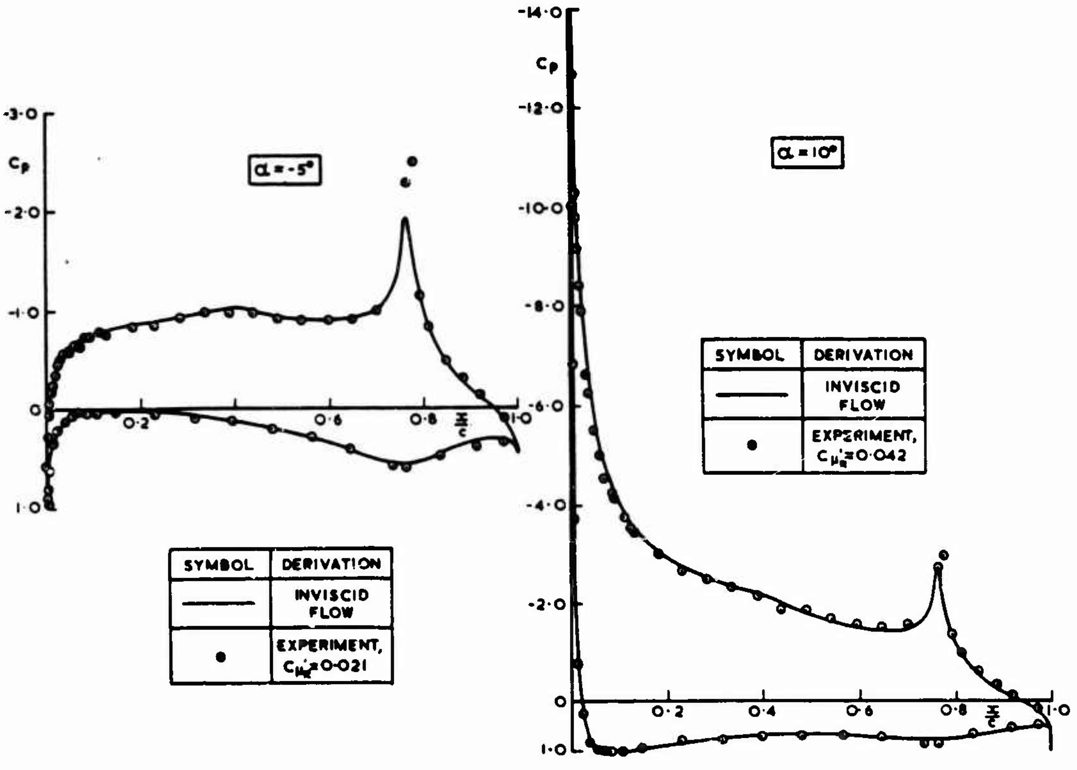

FIG.5 COMPARISON OF THEORETICAL AND EXPERIMENTAL PRESSURE DISTRIBUTIONS

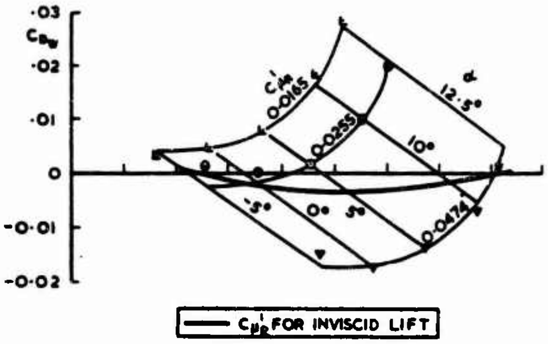

FIG.6 VARIATION OF WAKE DRAG WITH MOMENTUM COEFFICIENT AND ANGLE OF INCIDENCE

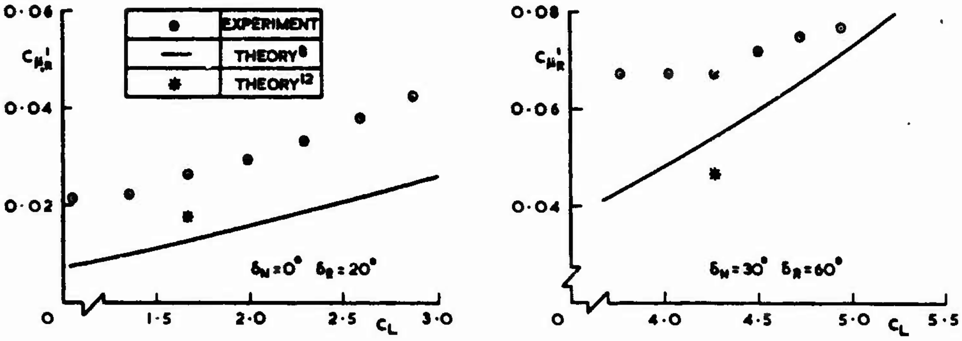

FIG.7 COMPARISON OF PREDICTED AND MEASURED VALUES OF THE MOMENTUM COEFFICIENT TO GIVE THE INVISCID LIFT

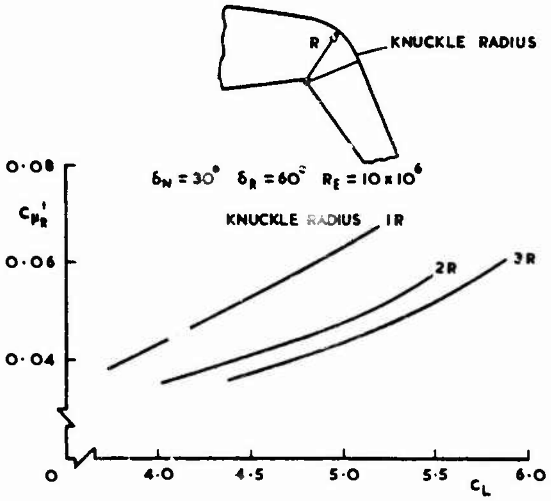

FIG.8 THEORETICAL EFFECT OF INCREASING KNUCKLE RADIUS

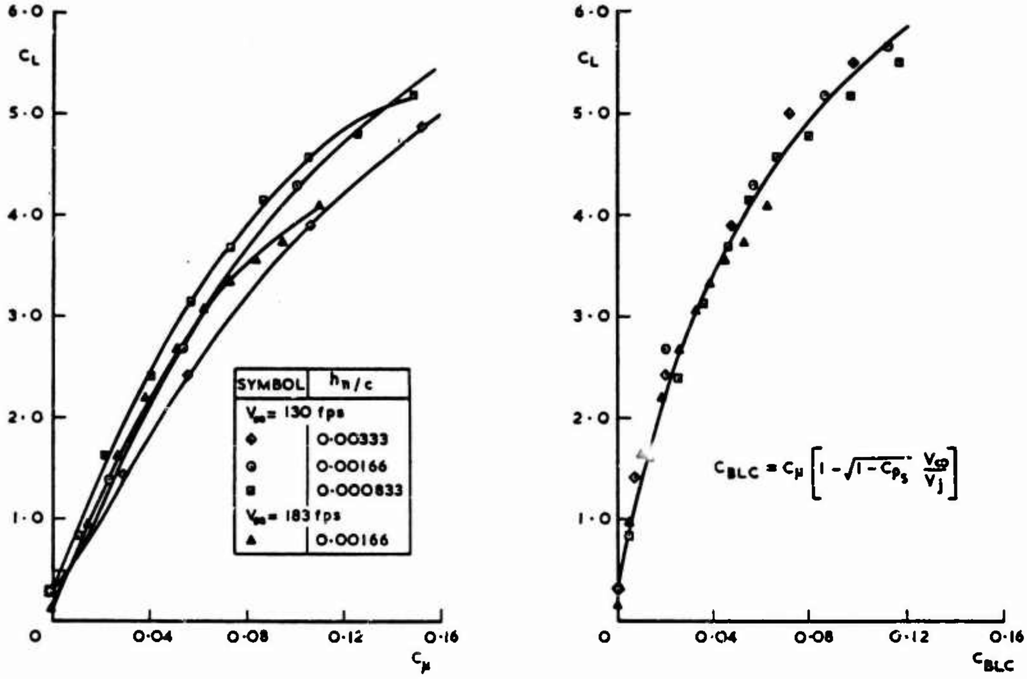

FIG. 9 COMPARISON OF $C_\mu$ AND $C_{BLC}$ AS CORRELATING PARAMETERS

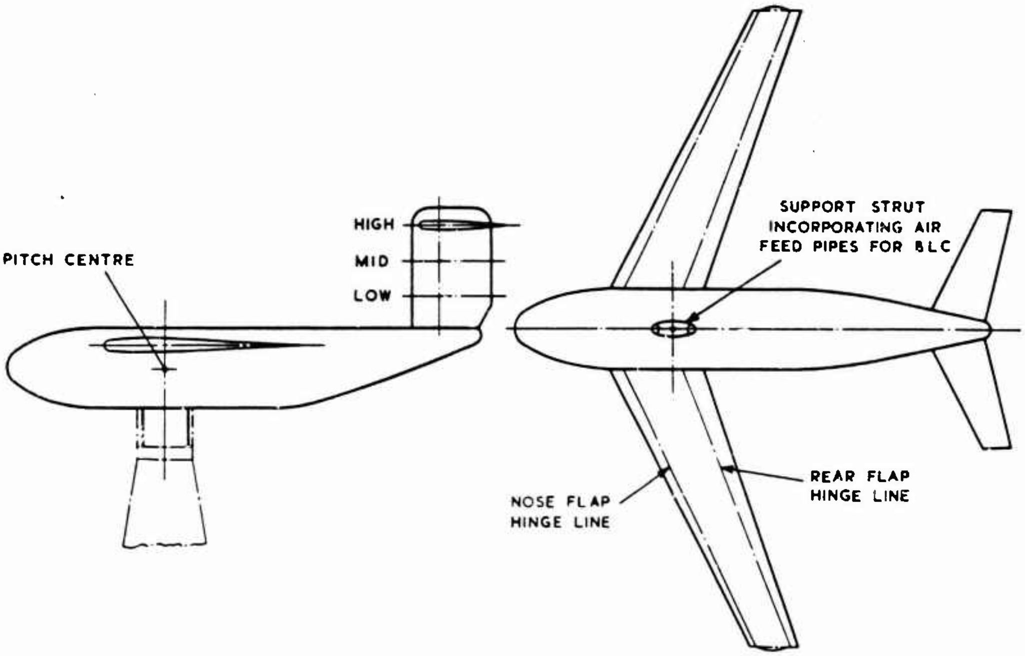
PITCH CENTRE
HIGH
MID
LOW
SUPPORT STRUT INCORPORATING AIR FEED PIPES FOR BLC
NOSE FLAP HINGE LINE
REAR FLAP HINGE LINE

FIG. 10 GENERAL ARRANGEMENT OF SUBSONIC TRANSPORT MODEL

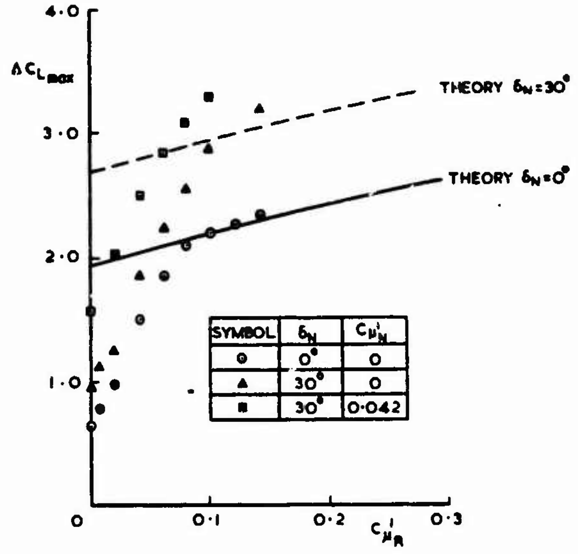

FIG.11 EFFECT OF DEFLECTION OF THE LEADING-EDGE FLAP, AND BLOWING AT THE FLAP KNUCKLE, ON INCREASES OF MAXIMUM LIFT

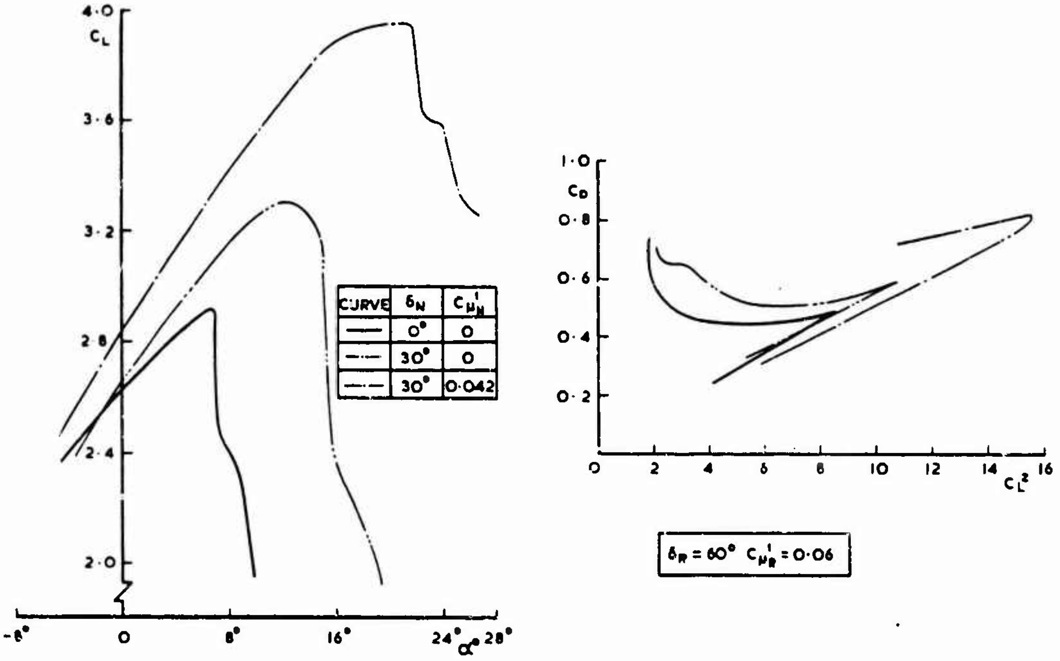

FIG.12 EFFECT OF DEFLECTION OF THE LEADING-EDGE FLAP, AND BLOWING AT THE FLAP KNUCKLE, ON LIFT AND DRAG CURVES

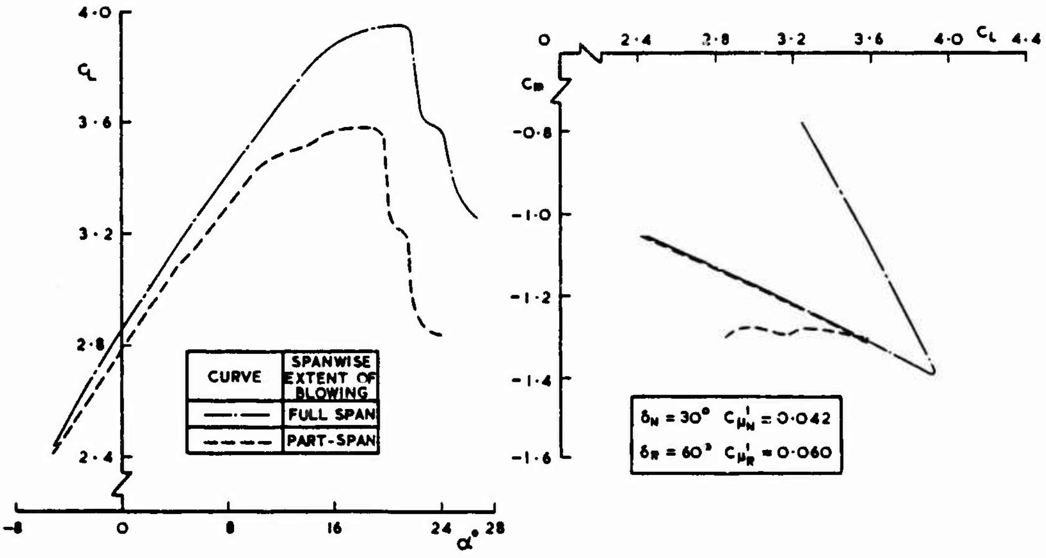

FIG.13 EFFECT OF SPANWISE EXTENT OF BLOWING AT LEADING EDGE ON LIFT AND PITCHING MOMENT CURVES

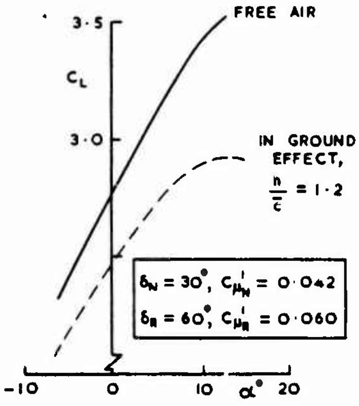

FIG.14 EXPERIMENTAL LIFT CURVES, IN AND OUT OF GROUND EFFECT

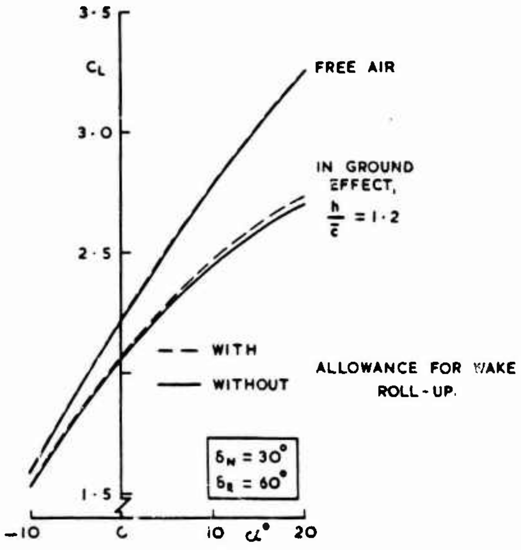

FIG.15 INVISCID LIFT CURVES, IN AND OUT OF GROUND EFFECT

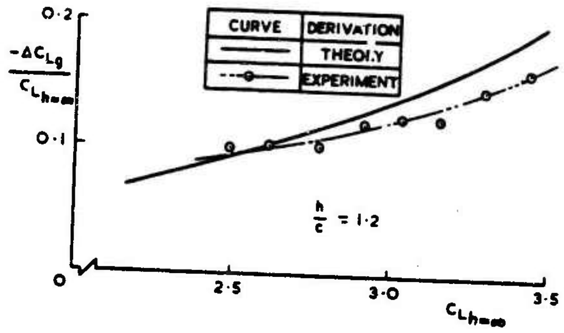

FIG.16 THEORETICAL AND EXPERIMENTAL EFFECT OF GROUND PROXIMITY ON LIFT

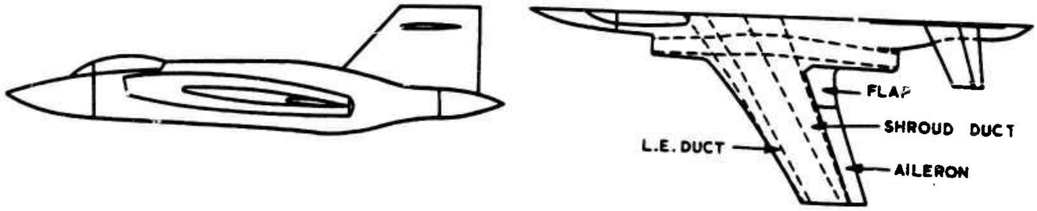
FLAP
SHROUD DUCT
L.E. DUCT
AILERON

FIG.17 GENERAL ARRANGEMENT OF BUCCANEER HALF MODEL

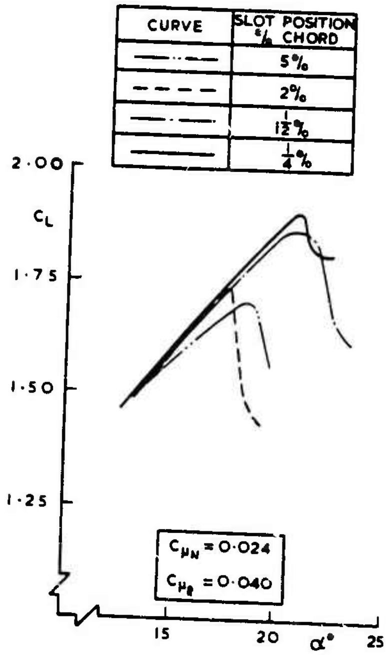

FIG.18 EFFECT OF POSITION OF BLOWING SLOT ON LIFT CURVES

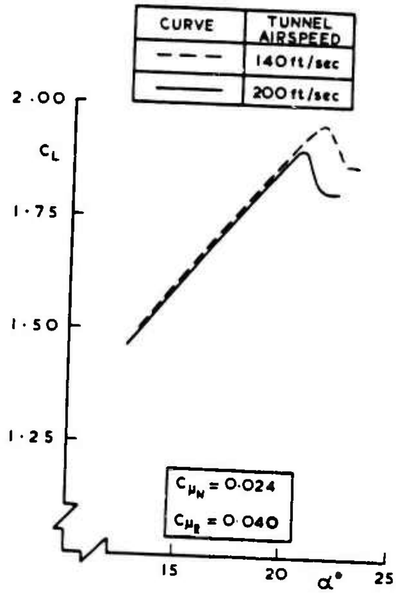

FIG.19 EFFECT OF TUNNEL AIRSPEED ON EFFECTIVENESS OF BLOWING AT $\frac{1}{4}$% CHORD POSITION

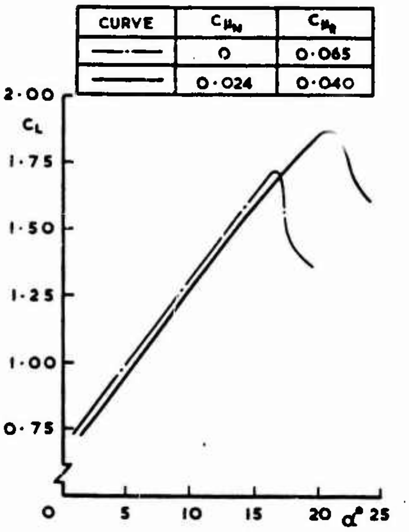

FIG. 20 COMPARISON OF BLOWING AT TRAILING-EDGE ONLY AND AT LEADING- AND TRAILING-EDGE, ON LIFT CURVES

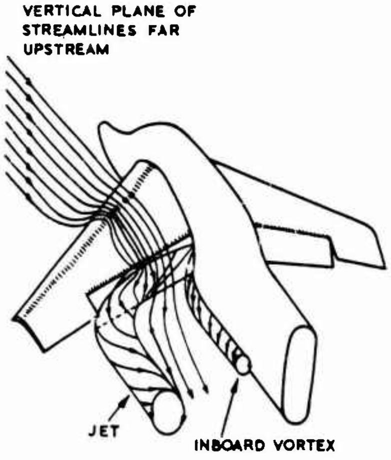
VERTICAL PLANE OF STREAMLINES FAR UPSTREAM
JET
INBOARD VORTEX

FIG. 21 SUGGESTED FLOW PATTERN ASSOCIATED WITH SPANWISE BLOWING

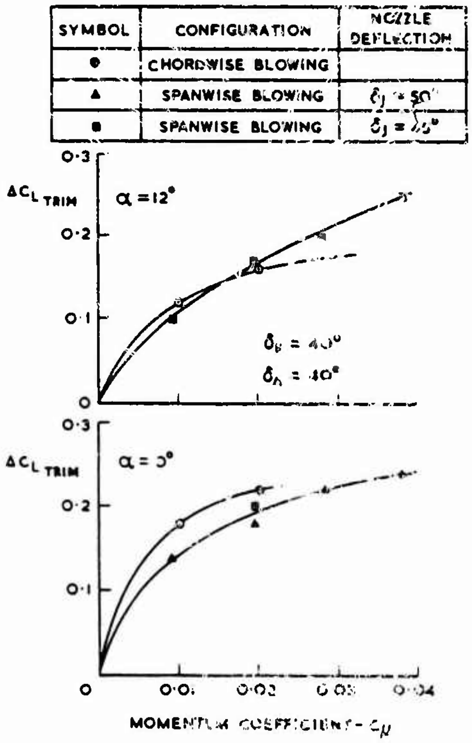

FIG. 22 COMPARISON OF CHORDWISE AND SPANWISE BLOWING

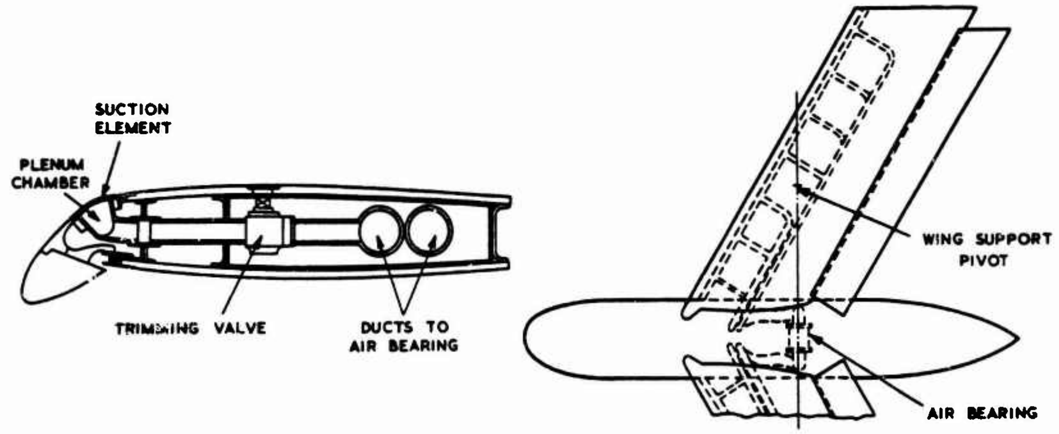
SUCTION ELEMENT
PLENUM CHAMBER
TRIMMING VALVE
DUCTS TO AIR BEARING
WING SUPPORT PIVOT
AIR BEARING

FIG. 23 GENERAL ARRANGEMENT OF MODEL WITH LEADING-EDGE FLAP SUCTION

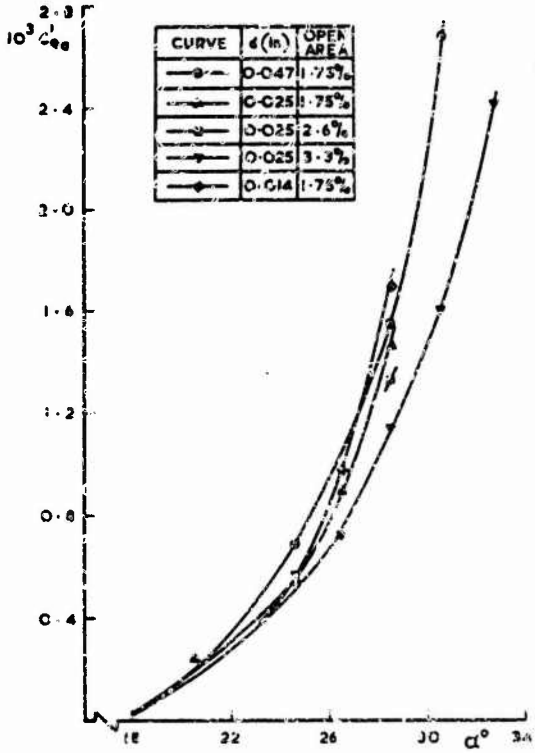

FIG. 24 EFFECT OF SUCTION ARRANGEMENT ON ATTACHMENT FLOW COEFFICIENT

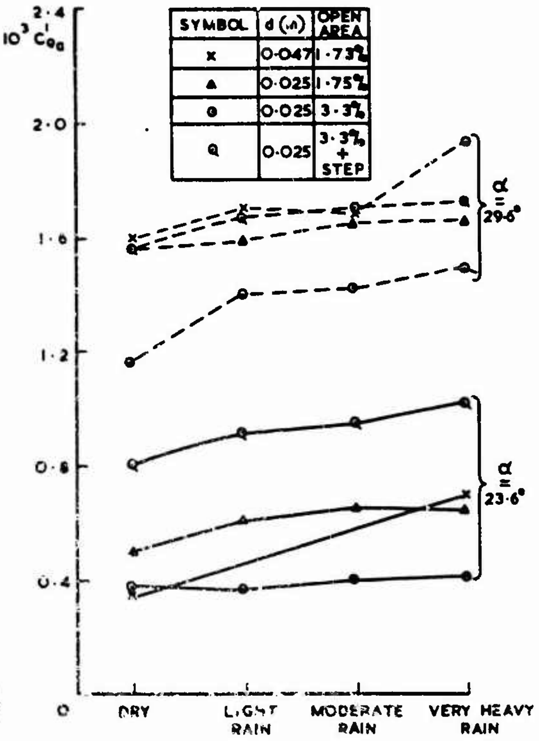

FIG. 25 EFFECT OF RAIN ON ATTACHMENT FLOW COEFFICIENT

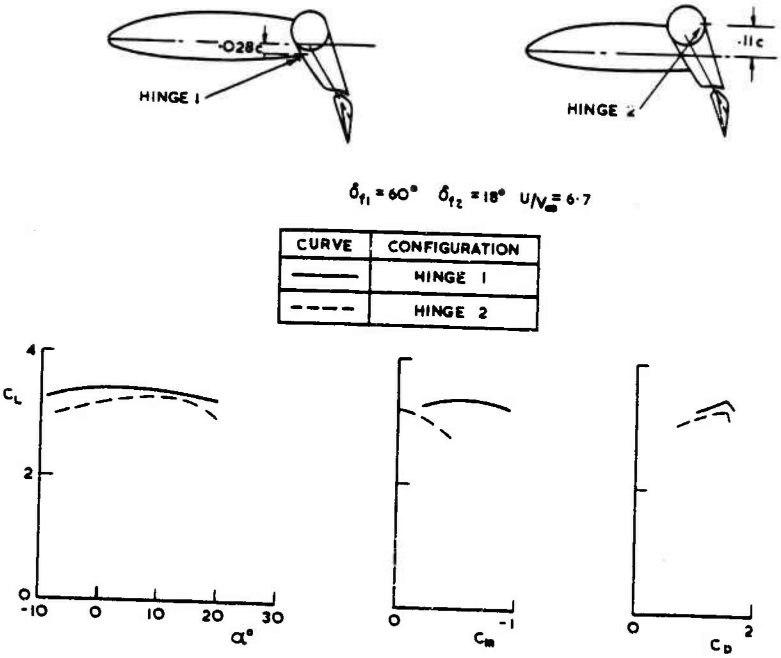

FIG.26 EFFECT OF HINGE POSITION ON AERODYNAMIC CHARACTERISTICS OF ROTATING CYLINDER FLAPS

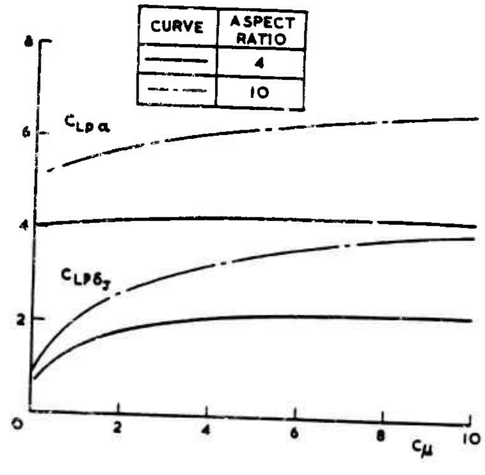

FIG.27 VARIATION OF PRESSURE LIFT DUE TO ANGLE OF INCIDENCE, AND DUE TO FLAP DEFLECTION, WITH MOMENTUM COEFFICIENT

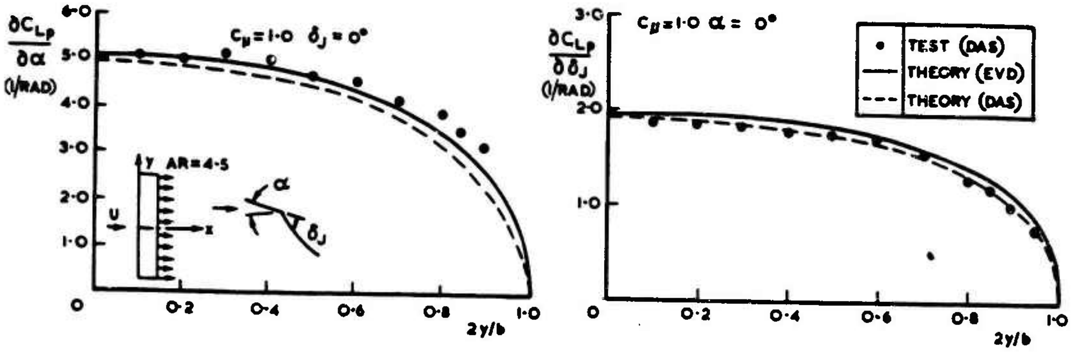

FIG.28 COMPARISON OF SPANWISE LOAD DISTRIBUTION DUE TO INCIDENCE AND BLOWING AS MEASURED AND AS PREDICTED BY TWO THEORIES

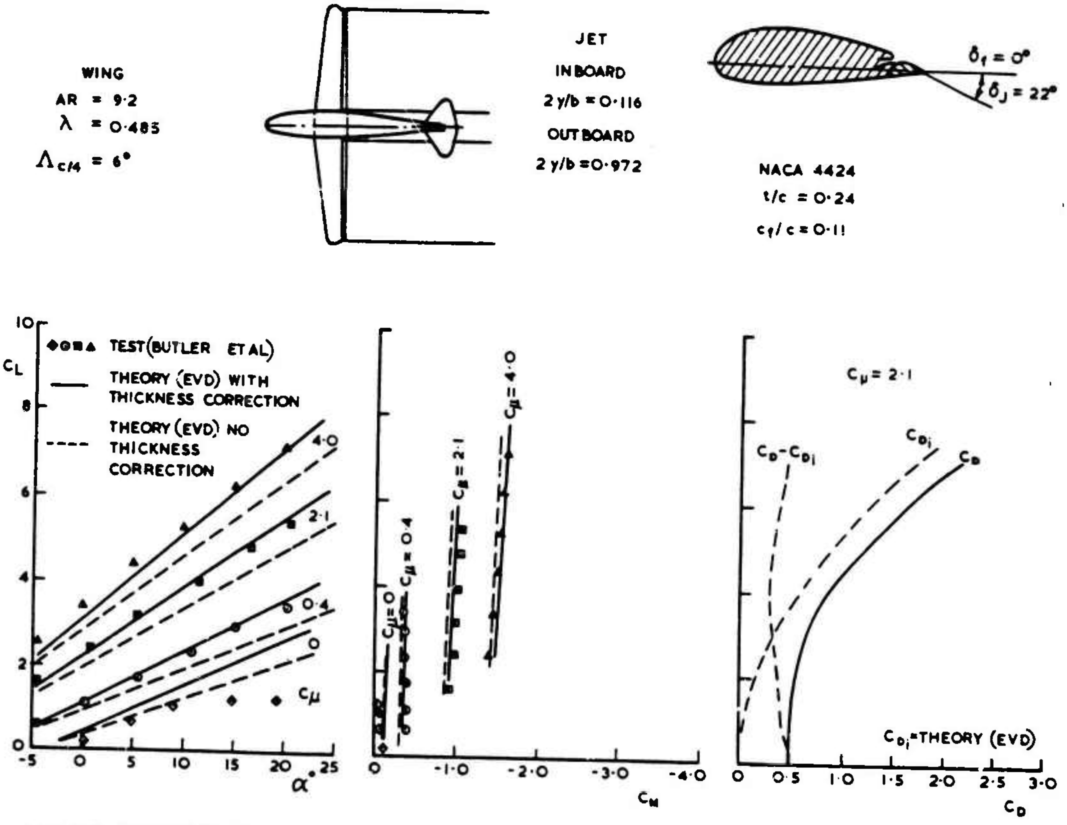

FIG.29 COMPARISON OF THEORETICAL AND EXPERIMENTAL CHARACTERISTICS OF MODEL OF JET-FLAPPED AIRCRAFT

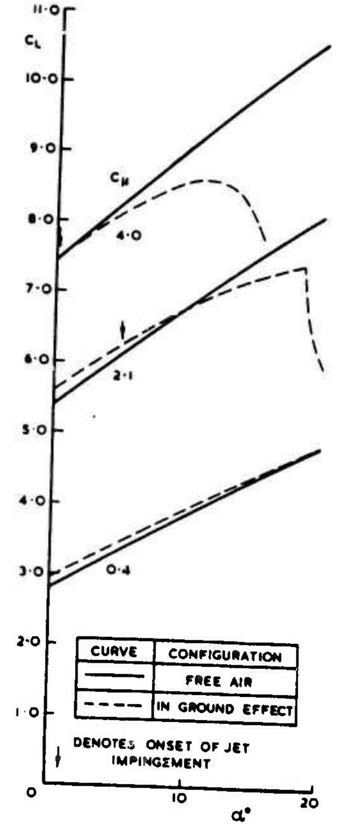

FIG. 30 EFFECT OF GROUND ON LIFT CURVES FOR JET-FLAP MODEL JET ANGLE 50°; $h/\bar{c}$ = 1·5

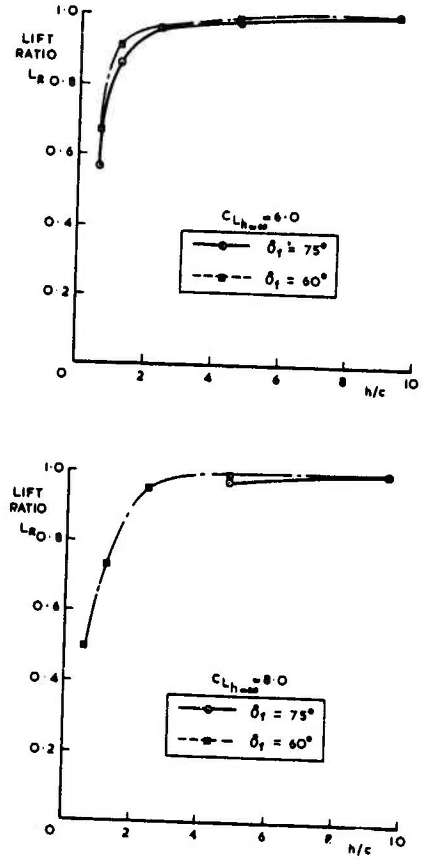

FIG. 31 VARIATION OF LIFT RATIO WITH HEIGHT, FREE-AIR LIFT COEFFICIENT, AND FLAP ANGLE

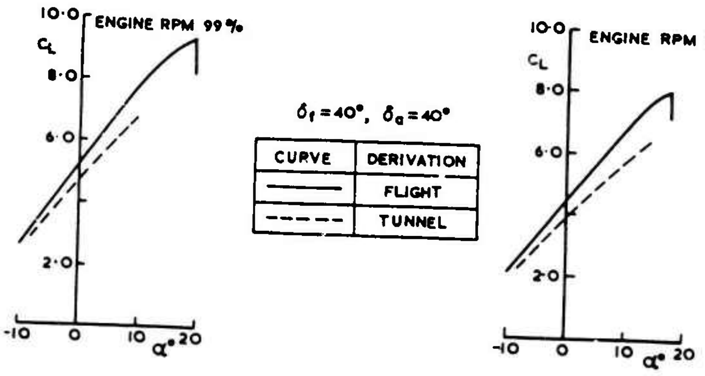

FIG. 32 COMPARISON OF LIFT CURVES FOR HUNTING 126 JET-FLAP AIRCRAFT, AS MEASURED IN TUNNEL AND FLIGHT

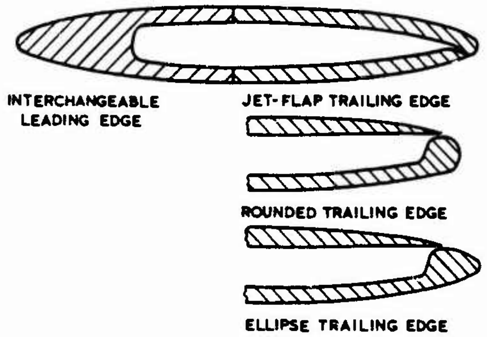
INTERCHANGEABLE LEADING EDGE
JET-FLAP TRAILING EDGE
ROUNDED TRAILING EDGE
ELLIPSE TRAILING EDGE

FIG.33 TRAILING-EDGE BLOWING MODELS TESTED AT TRANSONIC SPEEDS

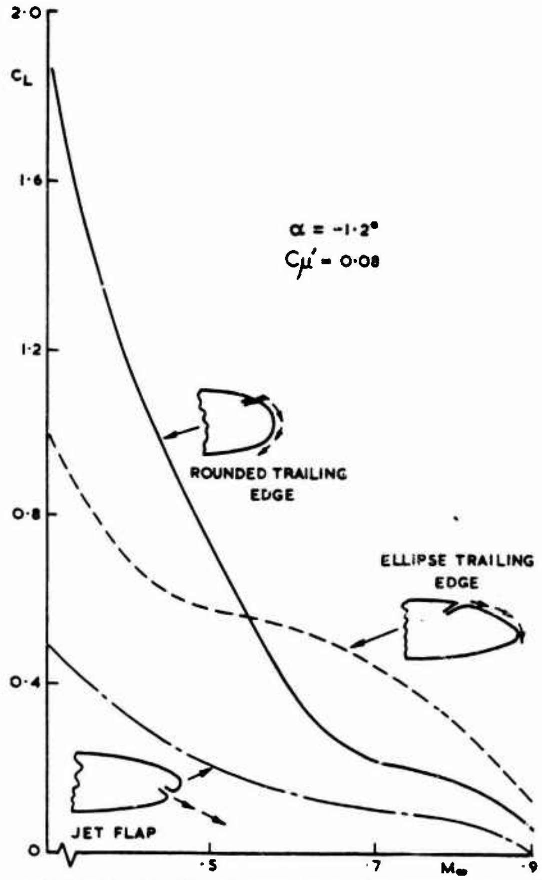

FIG.34 EFFECT OF MACH NUMBER ON LIFT

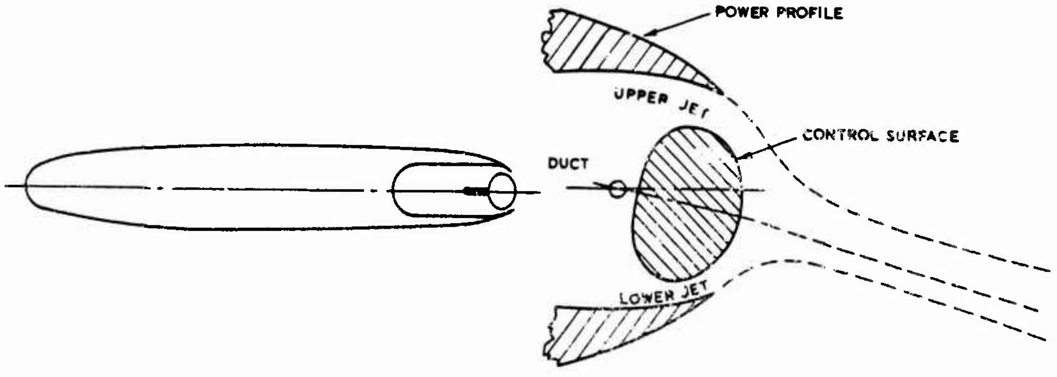
POWER PROFILE
UPPER JET
CONTROL SURFACE
DUCT
LOWER JET

a POWER PROFILE

b DETAILS OF CONTROL SURFACE AND JET FLOW

FIG.35 PROPOSED WING SECTION WITH TRAILING-EDGE BLOWING

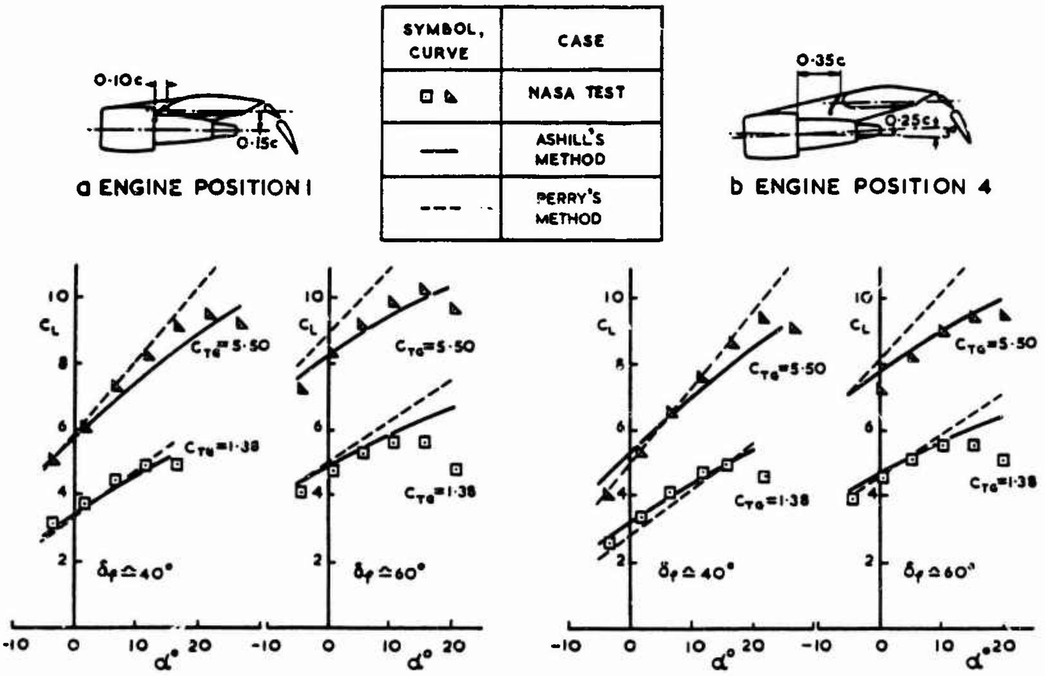

FIG.36a&b COMPARISON BETWEEN WIND-TUNNEL TEST-DATA AND TWO ESTIMATION METHODS

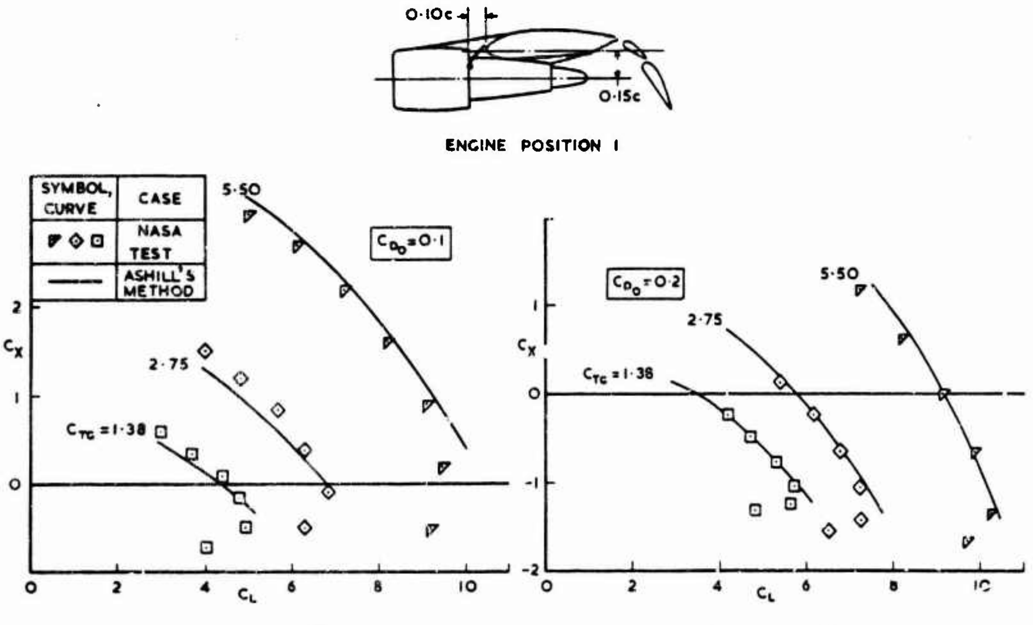

a $\delta_f \simeq 40°$ b $\delta_f \simeq 60°$

FIG.37a&b LONGITUDINAL FORCE PLOTTED AGAINST LIFT: COMPARISON BETWEEN WIND-TUNNEL RESULTS AND THRUST-DEFLECTOR THEORY

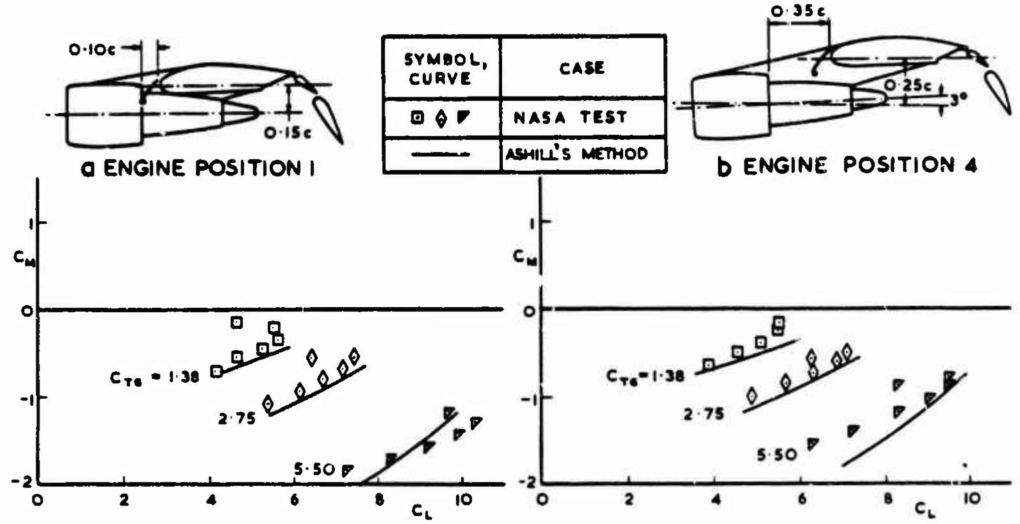

| SYMBOL, CURVE | CASE |
|---|---|
| □ ◊ ▼ | NASA TEST |
| —— | ASHILL'S METHOD |

FIG.38 a & b EFFECT OF THRUST ON PITCHING MOMENT ∿ LIFT CURVES: COMPARISON BETWEEN WIND-TUNNEL RESULTS AND METHOD OF ASHILL

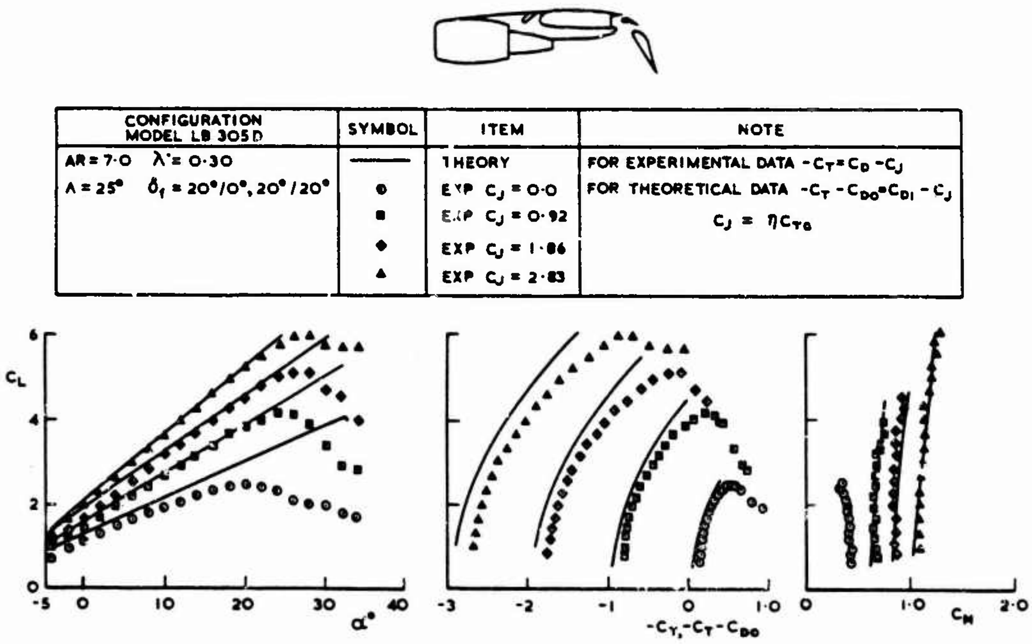

| CONFIGURATION MODEL LB 305D | SYMBOL | ITEM | NOTE |
|---|---|---|---|
| AR = 7·0 $\lambda' = 0{\cdot}30$ | —— | THEORY | FOR EXPERIMENTAL DATA $-C_T = C_D - C_J$ |
| $\Lambda = 25°$ $\delta_f = 20°/0°, 20°/20°$ | ● | EXP $C_J = 0{\cdot}0$ | FOR THEORETICAL DATA $-C_T - C_{DO} = C_{DI} - C_J$ |
| | ■ | EXP $C_J = 0{\cdot}92$ | $C_J = \eta C_{TO}$ |
| | ◆ | EXP $C_J = 1{\cdot}86$ | |
| | ▲ | EXP $C_J = 2{\cdot}83$ | |

FIG.39 COMPARISON OF PREDICTIONS OF DOUGLAS EVD THEORY WITH EXPERIMENTAL VALUES

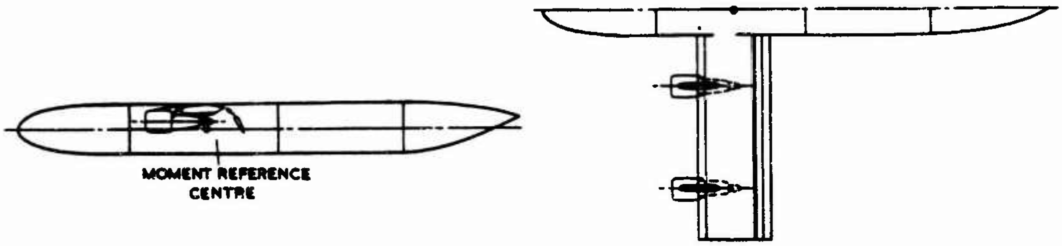
MOMENT REFERENCE
CENTRE

FIG.40 MODEL USED TO TEST EFFECT OF DIFFERENT HIGH-LIFT DEVICES

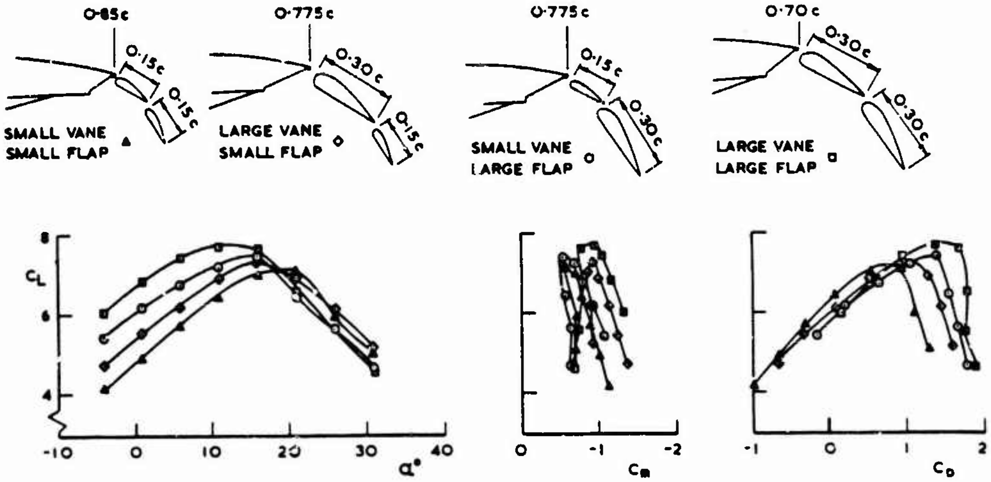

FIG.41 EFFECT OF FLAP CONFIGURATION ON AERODYNAMIC CHARACTERISTICS

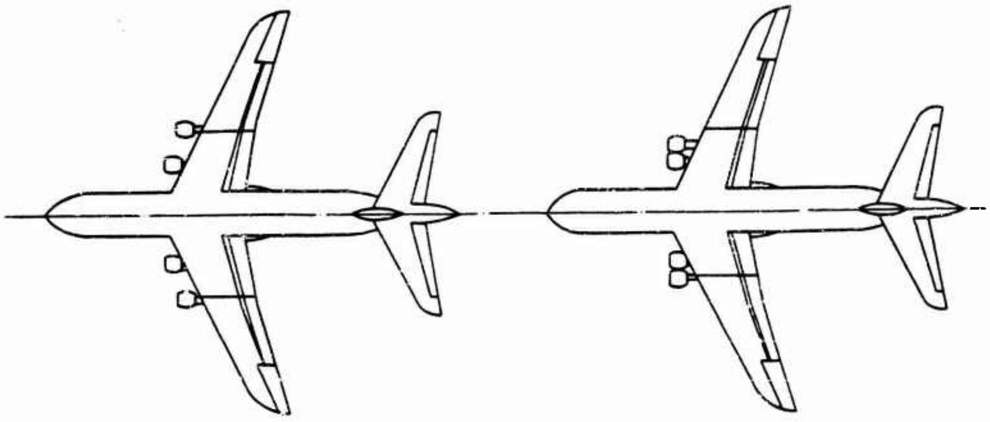

a SPREAD OUT

b CLUSTERED

FIG. 42 ENGINE ARRANGEMENTS TESTED

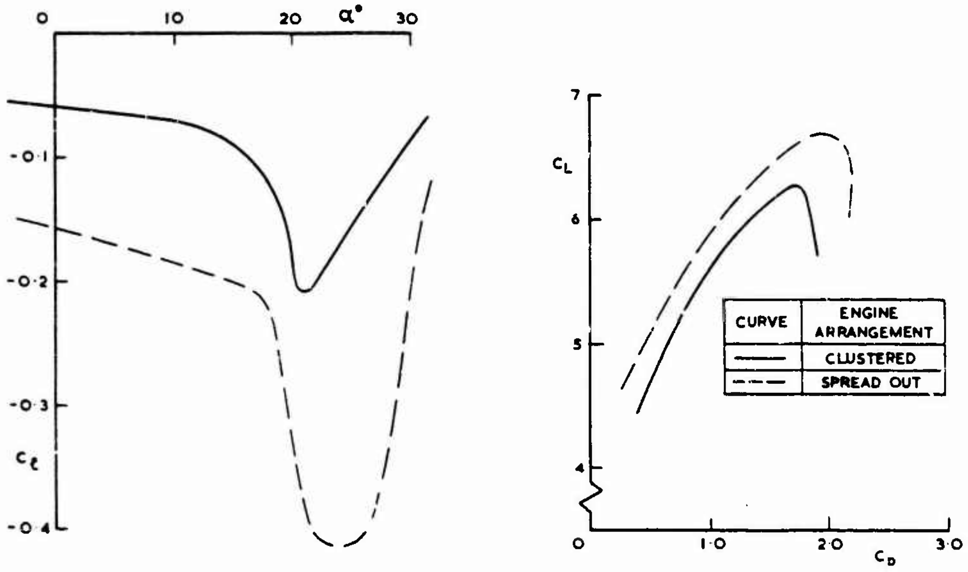

a ROLLING MOMENT AFTER ENGINE FAILURE

b ALL ENGINES OPERATING CHARACTERISTICS

FIG. 43 EFFECT OF ENGINE ARRANGEMENT ON ROLLING MOMENT AFTER ENGINE FAILURE, AND ON LIFT-DRAG POLARS

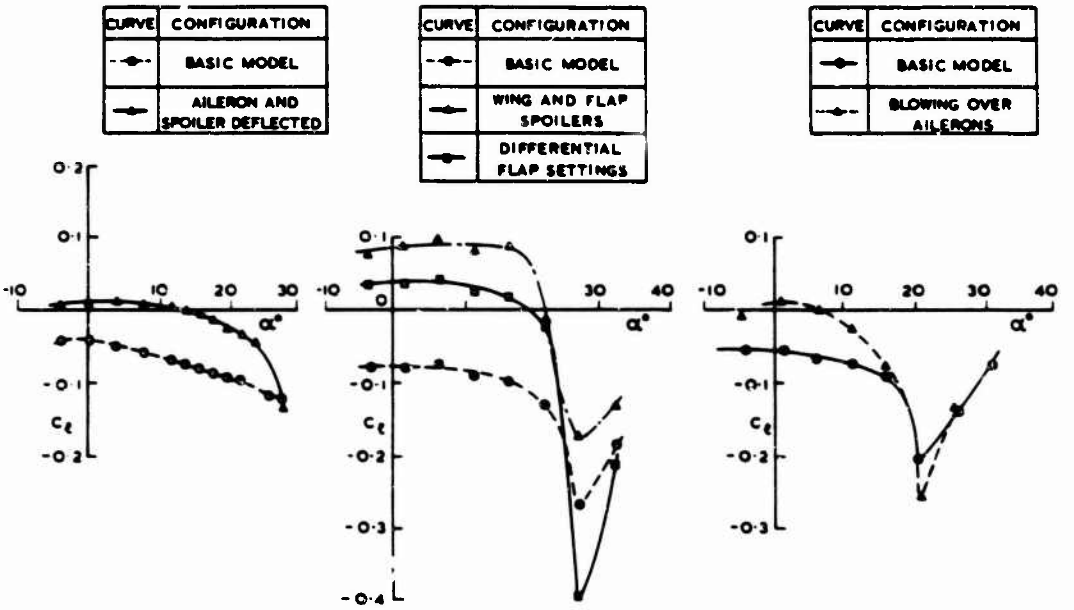

a EFFECT OF CONVENTIONAL LATERAL CONTROL DEVICES

b EFFECT OF FLAP SPOILERS AND DIFFERENTIAL FLAP SETTINGS

c EFFECT OF ASYMMETRIC BLOWING OVER DEFLECTED AILERON

FIG. 44 EFFECT OF LATERAL CONTROL DEVICES ON ROLLING MOMENTS AFTER ENGINE FAILURE

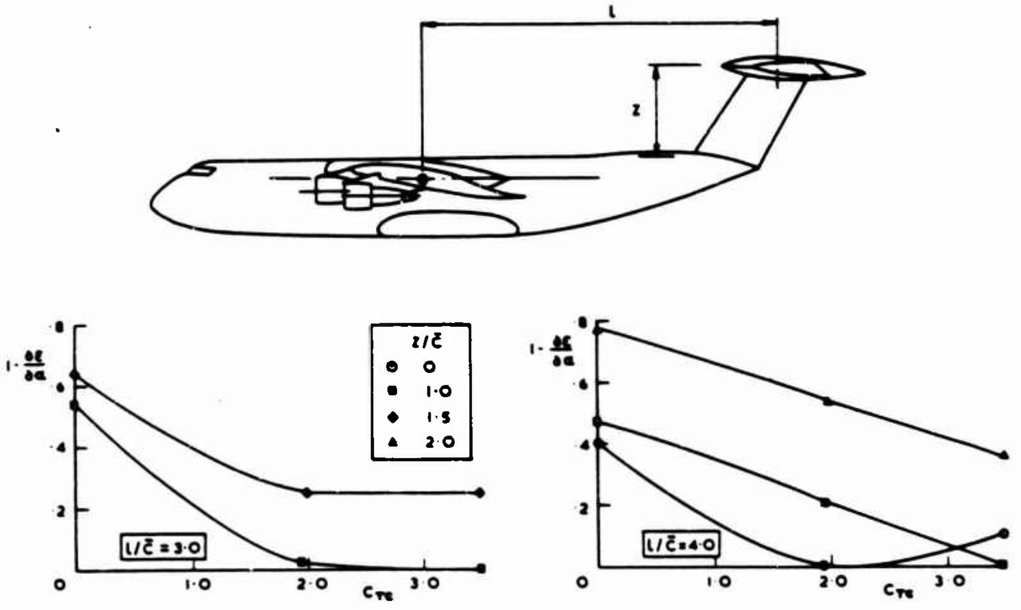

FIG. 45 EFFECT OF POSITION OF TAILPLANE ON DOWNWASH FACTOR

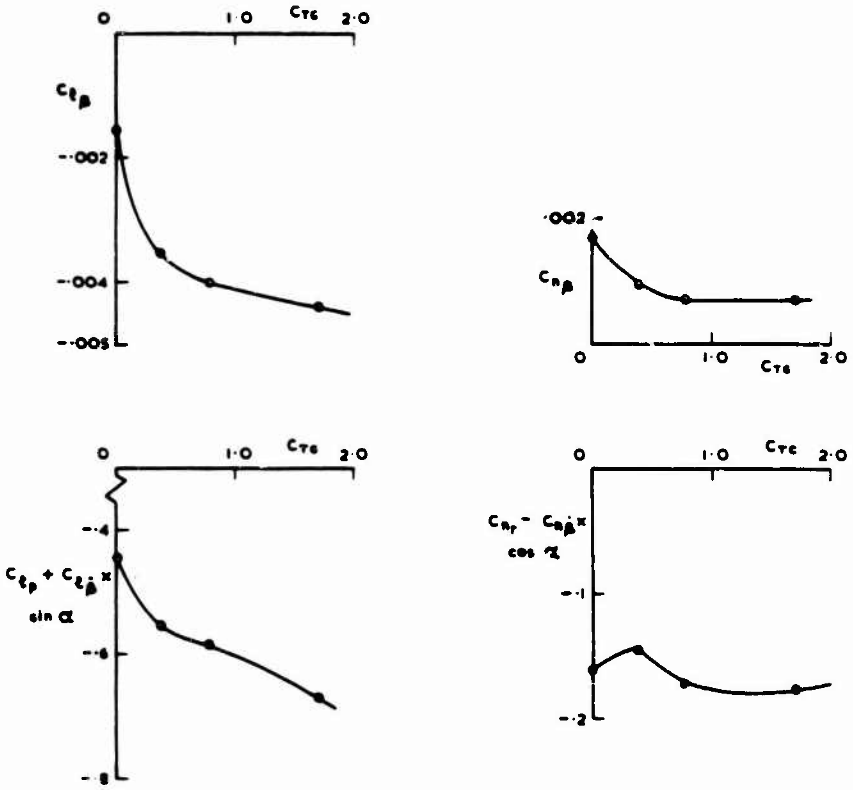

FIG. 46 EFFECT OF THRUST ON LATERAL STATIC AND DYNAMIC DERIVATIVES AT A LOW ANGLE OF INCIDENCE

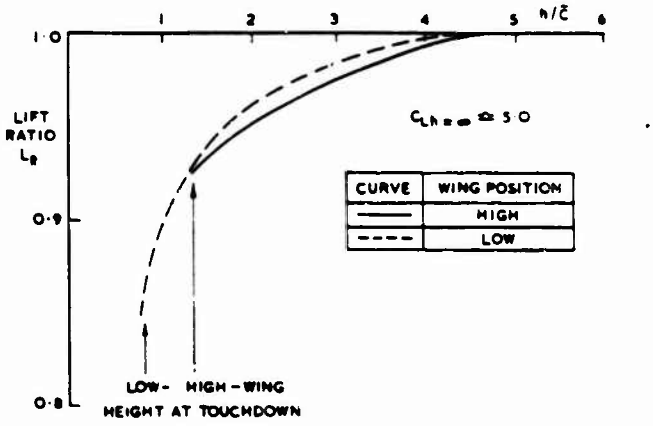

FIG. 47 EFFECT OF WING HEIGHT ON GROUND EFFECT

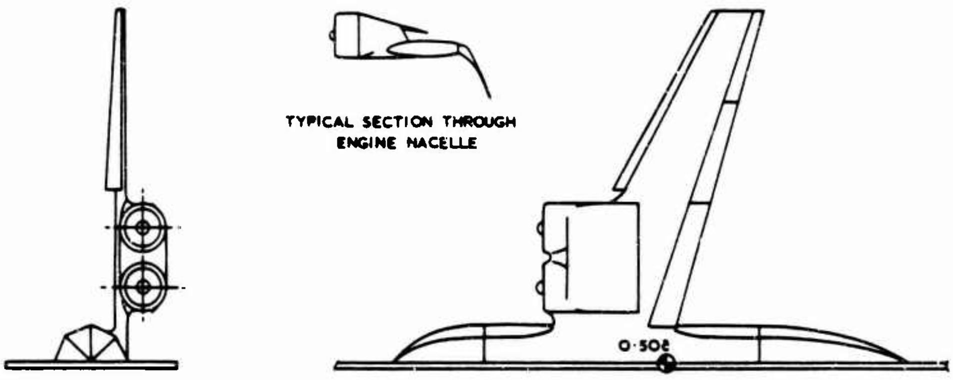
TYPICAL SECTION THROUGH ENGINE NACELLE
0·50c̄

FIG.48 MODEL TESTED WITH ENGINES MOUNTED OVER THE WING

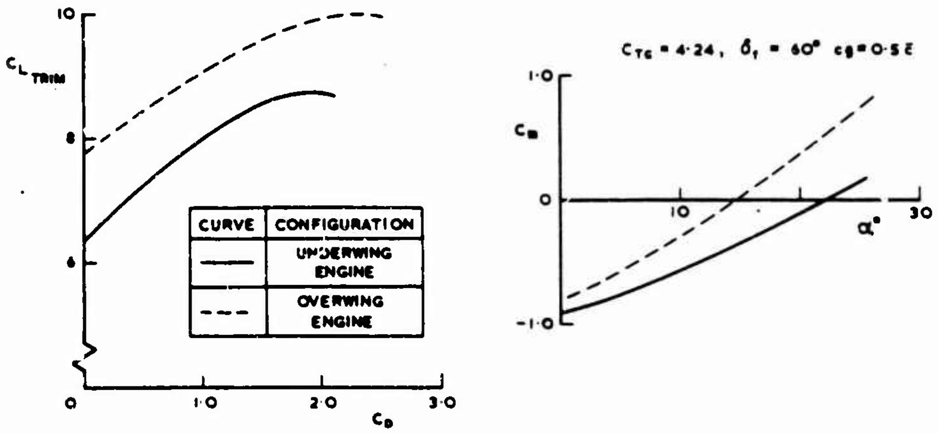

FIG.49 COMPARISON OF CHARACTERISTICS OF OVERWING AND UNDERWING EXTERNAL-FLOW JET-FLAP

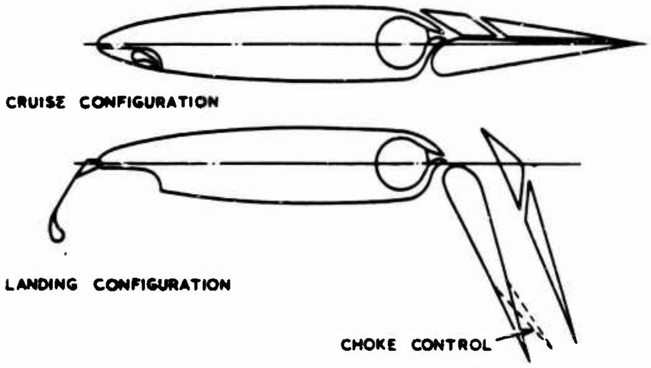
CRUISE CONFIGURATION
LANDING CONFIGURATION
CHOKE CONTROL

FIG. 50 AUGMENTOR WING SECTION

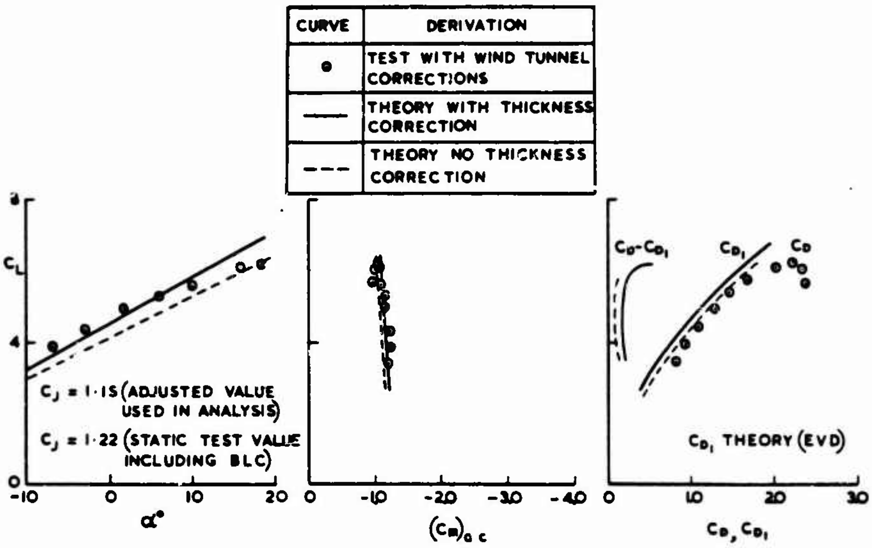

| CURVE | DERIVATION |
|---|---|
| ● | TEST WITH WIND TUNNEL CORRECTIONS |
| ——— | THEORY WITH THICKNESS CORRECTION |
| - - - | THEORY NO THICKNESS CORRECTION |

FIG. 51 COMPARISON OF PREDICTIONS OF DOUGLAS EVD METHOD WITH EXPERIMENTAL RESULTS

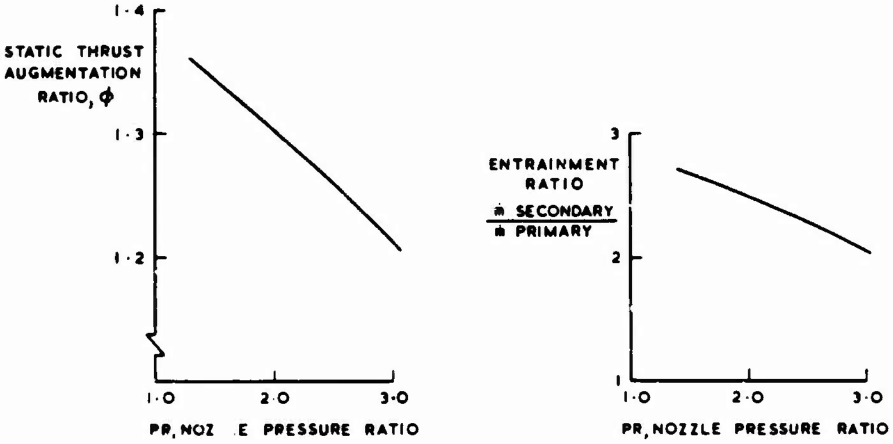

FIG. 52 STATIC CHARACTERISTICS OF A SLOT NOZZLE

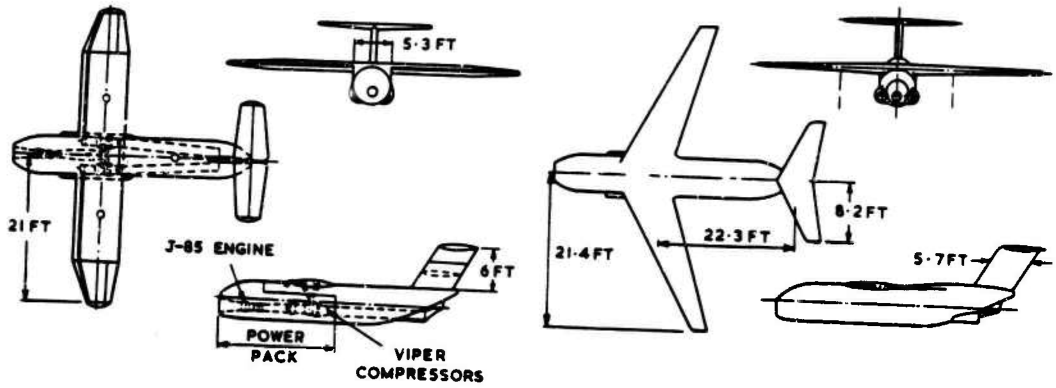
5·3 FT
21 FT
J-85 ENGINE
6 FT
POWER PACK
VIPER COMPRESSORS
8·2 FT
22·3 FT
21·4 FT
5·7 FT

FIG. 53 UNSWEPT AND SWEPT MODELS TESTED BY NASA

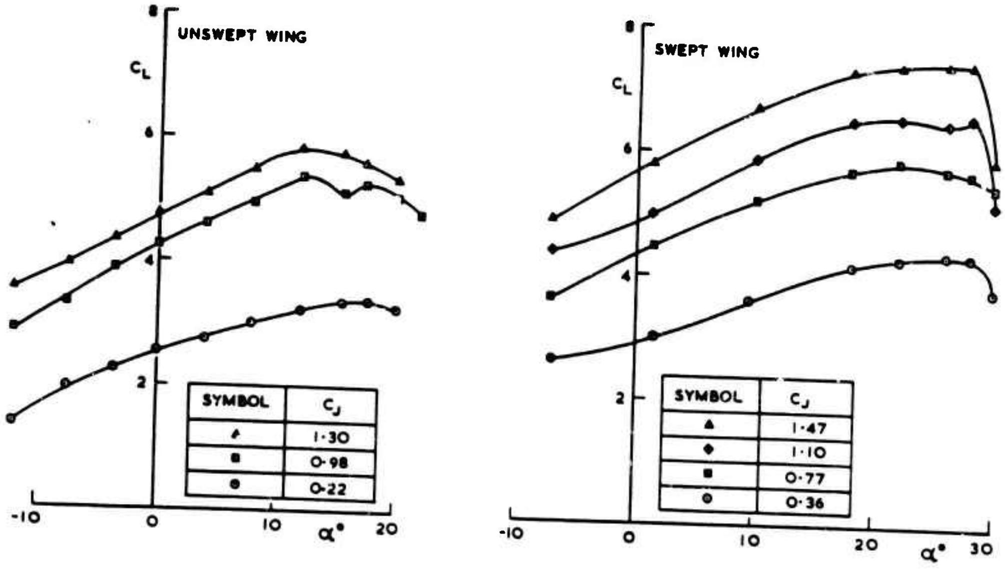

FIG. 54 COMPARISON OF LIFT CURVES FOR UNSWEPT AND SWEPT WING

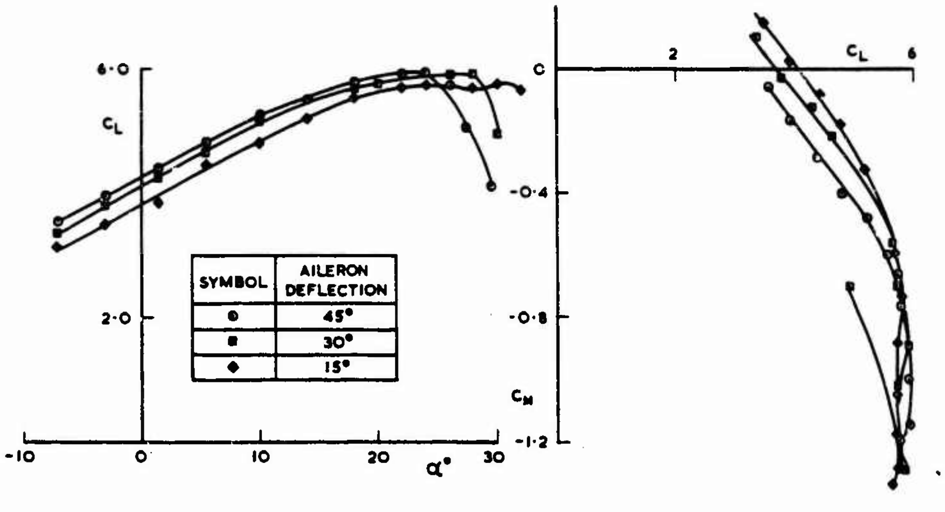

FIG.55 EFFECT OF SYMMETRICAL AILERON DEFLECTION ON LIFT AND PITCHING MOMENT CHARACTERISTICS

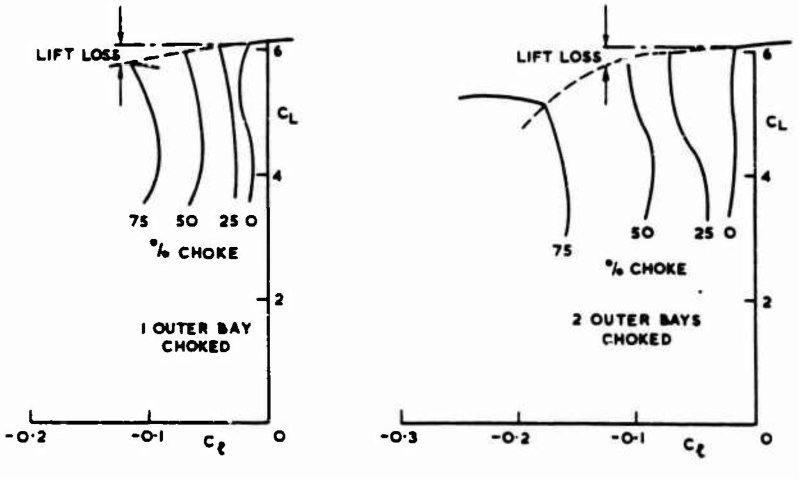

FIG.56 EFFECT OF AUGMENTOR CHOKE ON ROLLING MOMENT

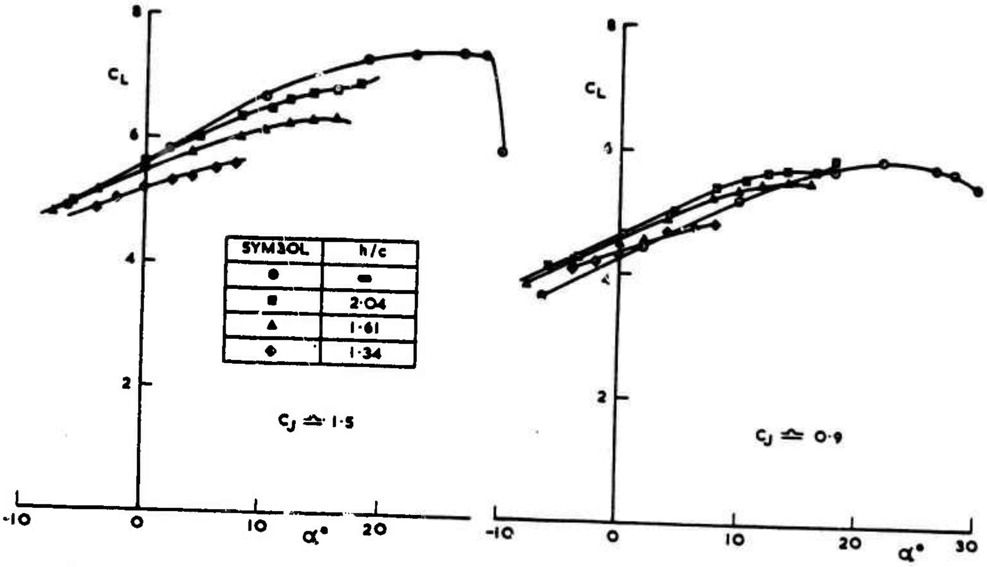

FIG. 57 EFFECT OF GROUND PROXIMITY ON LIFT CURVES FOR MODEL WITH SWEPT WING

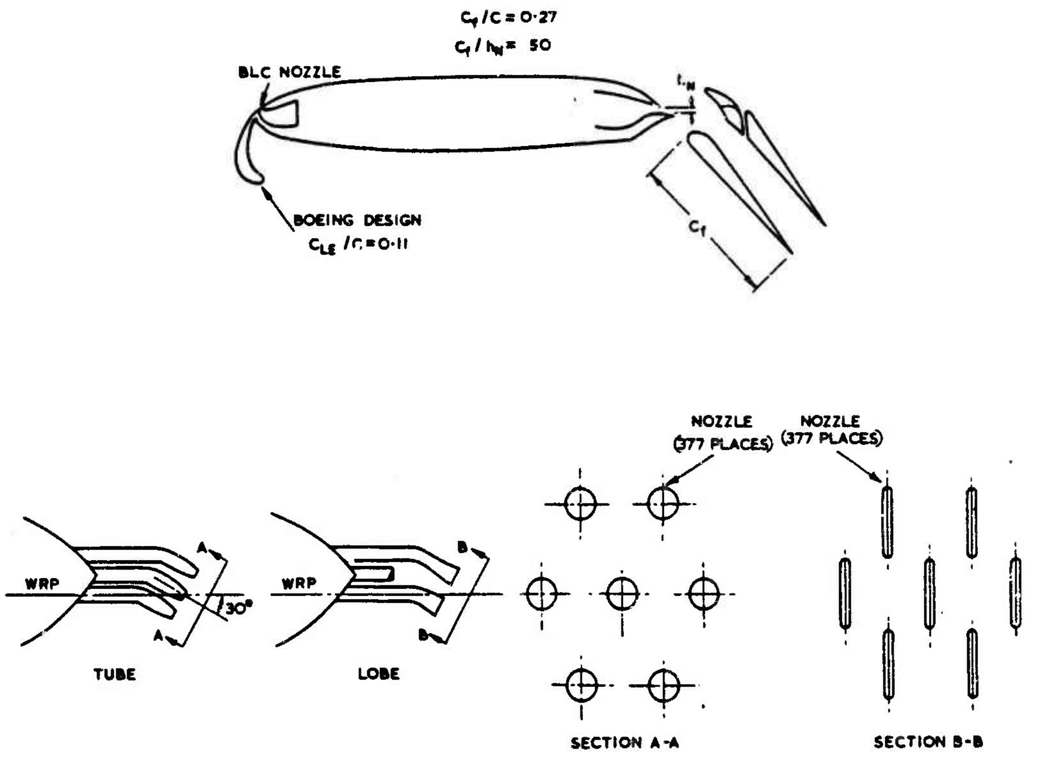
$C_f/C = 0.27$
$C_f/t_N = 50$
BLC NOZZLE
$t_N$
BOEING DESIGN
$C_{LE}/C = 0.11$
$C_f$
NOZZLE (377 PLACES)
NOZZLE (377 PLACES)
A
B
WRP
30°
WRP
TUBE
LOBE
SECTION A-A
SECTION B-B

FIG.58 WING SECTION AND NOZZLE SHAPES TESTED BY BOEING

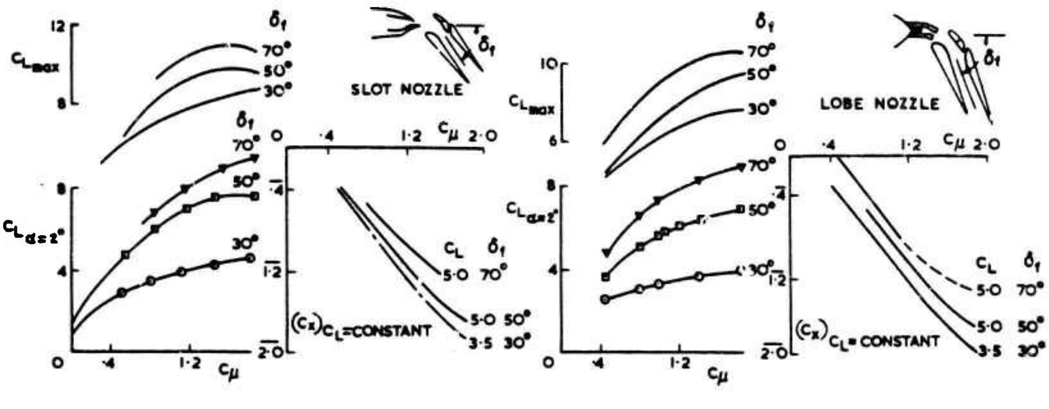

FIG.59 COMPARATIVE PERFORMANCE OF SLOT AND LOBE NOZZLES

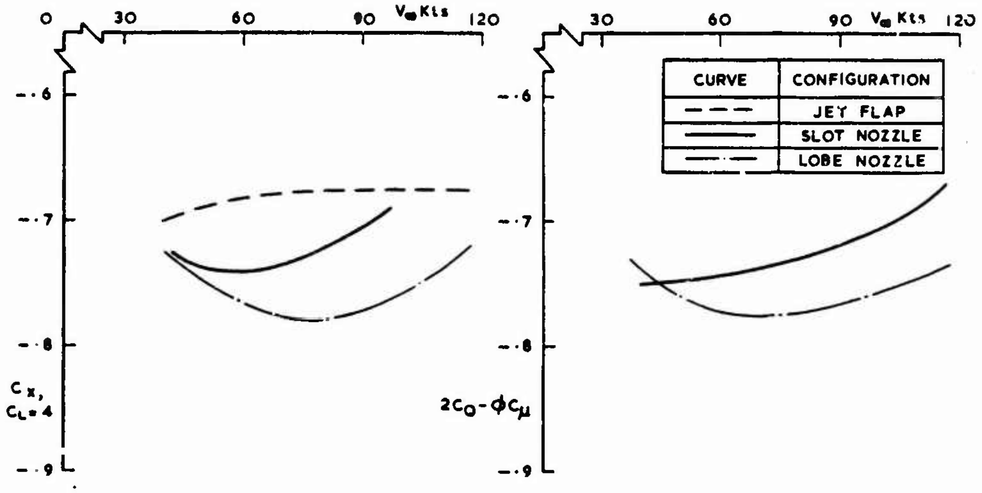

FIG.60 EFFECT OF FORWARD SPEED AT CONSTANT $C_\mu$

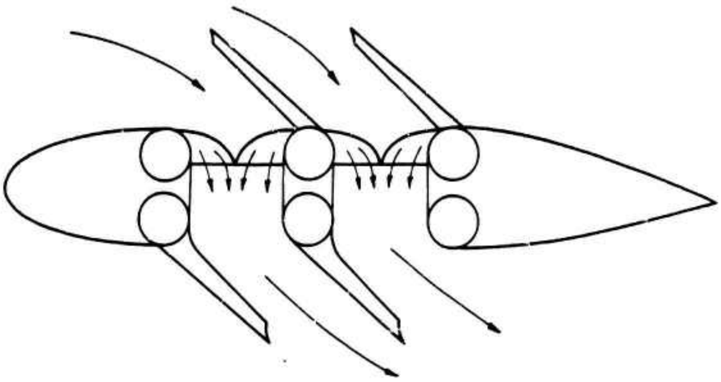

FIG.61 GENERAL ARRANGEMENT OF INJECTOR WING

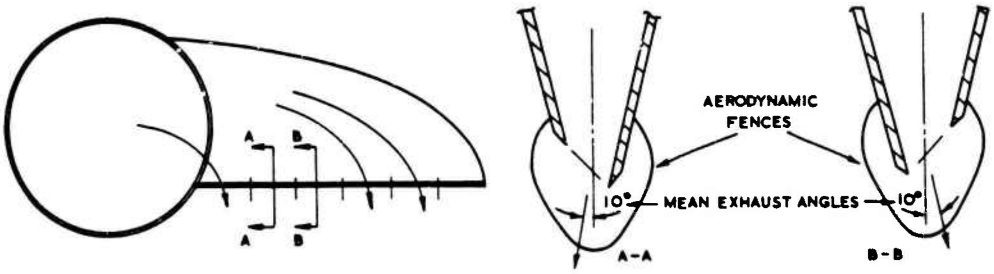
A
B
A
B
AERODYNAMIC
FENCES
10°
MEAN EXHAUST ANGLES
10°
A-A
B-B

a DETAILS OF INJECTOR NOZZLE

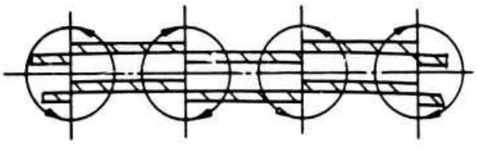

b FLOW DOWNSTREAM OF NOZZLE

FIG.62 DETAILS OF INJECTOR NOZZLE AND FLOW MODEL

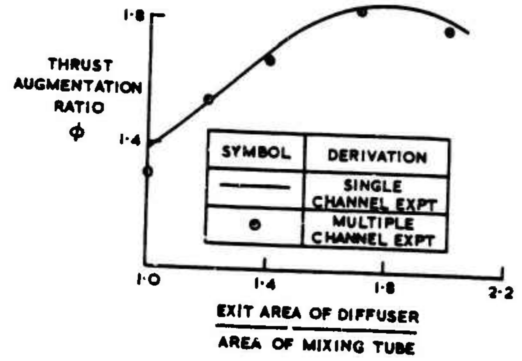

FIG. 63 COMPARISON OF THRUST AUGMENTATION RATIO MEASURED IN TWO EXPERIMENTS

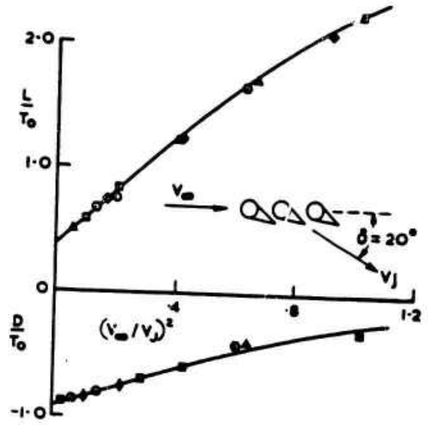

FIG. 64 EFFECT OF FORWARD SPEED ON LIFT AND DRAG

N74-26449

# AIRCRAFT LIFT AND DRAG PREDICTION AND MEASUREMENT

by

G. M. Bowes*

## ABSTRACT

Techniques for predicting and measuring lift and drag relationships for subsonic cruise flight are described. The status of this drag methodology is reviewed. Recent presentations on the subject are referenced and incorporated into an overall summary describing current capabilities for developing the basis of aircraft performance predictions. The role of the wind tunnel in airplane design and development is discussed, and the importance of flight test measurements of specific range and engine parameters is emphasized. Theoretical developments for three-dimensional design and lift/drag predictions are described. The accuracy with which the drag levels of a new design can be determined is examined.

Examples of specialized wind tunnel and flight investigations into the airflow and pressures on localized portions of an airplane are presented.

## INTRODUCTION

Airplanes have become more efficient with time. Using the subsonic transport as an example, the 1973 airplane offers

- Longer Range
- Higher Speed
- More Passengers

while offering more comfort, reliability, safety, and less community noise. Some of these trends in performance are shown on Figure 1, commencing with the 707 and DC-8 intercontinental models.

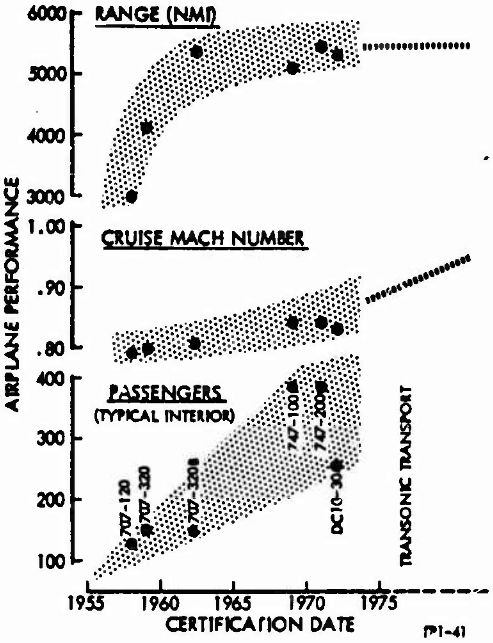

Figure 1: AIRPLANE DESIGN TRENDS
(LONG RANGE TRANSPORTS)

---

* Unit Chief, Aerodynamics Staff, Boeing Commercial Airplane Company, Renton, Washington.

The improvement in efficiency may be evaluated in various ways. One basic parameter would consider the productivity of the airplane (payload x range) per pound of fuel. Figure 2 shows that the most modern transports are about 30% more efficient at a given payload fraction than the smaller, older long range aircraft.

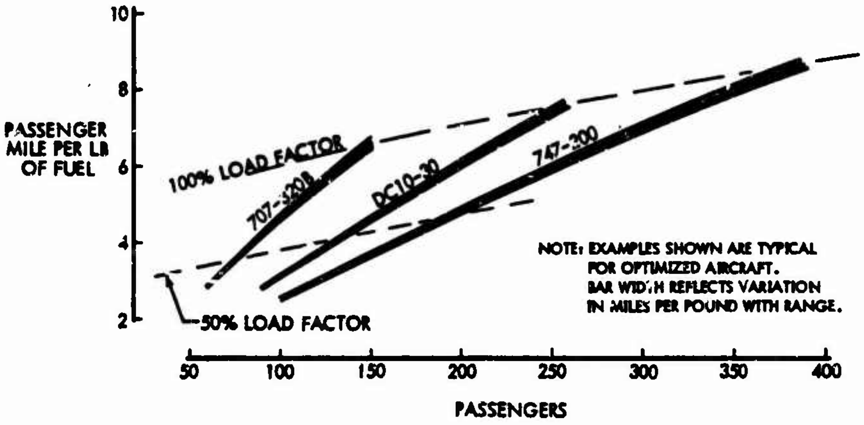

NOTE: EXAMPLES SHOWN ARE TYPICAL FOR OPTIMIZED AIRCRAFT.
BAR WIDTH REFLECTS VARIATION IN MILES PER POUND WITH RANGE.

Figure 2: PRODUCTIVITY PER POUND OF FUEL

These achievements result from advances in aircraft technology, particularly in the fields of aerodynamics, propulsion design, and structural design. With regard to aerodynamic technology, a brief historical review illuminates the gains which have been offered to the airplane designer. The Boeing B-47 was the first successful application of the theory of wing sweep to a "long range" design. It involved significant advances into new technical areas of aerodynamics, structures, and flight controls. The L/D levels and cruising speed regime of the B-47 are shown on Figure 3 as an initial reference for subsonic swept wing aircraft. This airplane represented a definite advance in speed for bomber aircraft - it outflew the P-80 fighter used as a pace/chase aircraft - and the range exceeded the program requirements.

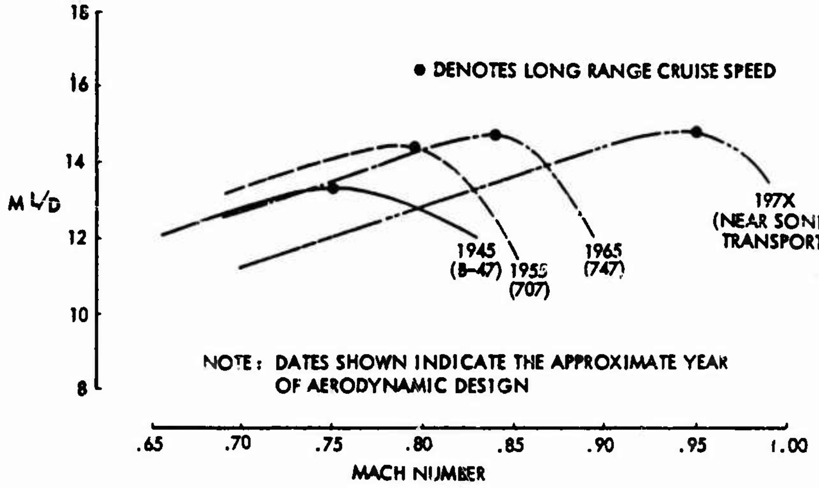

NOTE: DATES SHOWN INDICATE THE APPROXIMATE YEAR OF AERODYNAMIC DESIGN

Figure 3: AERODYNAMIC TECHNOLOGY DEVELOPMENT

The B-47's success was due in large measure to a significant forward step in design technology - the high aspect ratio swept back wing being one of the more obvious and significant features of this airplane - and it had the benefit of full scale experimental prototype flight testing which is necessary to fully exploit such major gains. The 707 and DC-8 transports, characterized on Figure 3 by the curve labeled "1955" were developed from a technology base established by the B-47 (Reference 1). The wings of these transport aircraft were basically derived from the NACA 6-series airfoils. Variation in airfoil thickness ratio, camber, and twist across the span of the wing was included in these designs to optimize cruise L/D. However, the design methodology was largely an evolutionary process based upon experimental results; final wing shapes incorporated modifications developed in the wind tunnel in order to correct or improve specific concern areas.

More advanced theoretical tools, which provided a better understanding of the airflow over the upper surface at supercritical Mach numbers led to the airfoils employed on wings applied to the current wide bodied transports, illustrated by the L/D levels labeled "1965" on Figure 3. These wings were also developed largely by experimental procedures, but with a much deeper theoretical understanding of the two-dimensional characteristics of the airfoils. The Vickers VC-10 was perhaps one of the first airplanes for which three-dimensional theoretical wing design studies were developed (References 2 and 3). The goal of determining the shape of a wing which will develop a specified pressure distribution in three-dimensional compressible flow has not yet been fully achieved and is discussed in more detail later in this paper.

The final curve shown on Figure 3 indicates an optimistic potential for further improvement to airplane design using current advances in aerodynamic technology. One study of potential designs and the aerodynamic characteristics of aircraft incorporating these higher speed features is provided in Reference 4. Such designs take maximum advantage of advanced transonic airfoils, wing sweep, and overall configuration definition to satisfy area rule constraints.

These data show the progressive improvements in aerodynamic design which have been achieved in response to continuous competitive pressures demanding performance gains. The major technical advance has involved the control of the drag due to supercritical flow over the wing by reducing the shock strength or by delaying its formation to higher free stream Mach numbers. Both speed and range increases have been important. An increase in one of these items at the expense of the other has not been considered as a viable trade. Whether these requirements will persist in the future is an interesting question. In view of the trends now evident on fuel availability and cost, new economic factors may well impact these design criteria such that different aerodynamic goals will become apparent for the next generation of aircraft.

Developments in aerodynamics as summarized above were motivated by several different forces, of which the competitive drive was a major factor. In the course of these competitions, the ability of the designer to promise a performance capability and of the airplane to meet this promise has been a dominant factor in success or failure of individual programs. The purpose of this paper is to review significant elements in the prediction and measurement of the aerodynamic contribution to the range equation, studying the subject primarily from the standpoint of cruise drag of subsonic long range aircraft.

There is a vast body of literature on the subject of "drag". Predictive processes are well known and have been documented rather thoroughly in textbooks and in lectures. There are many experts, both within and outside the industry. Nevertheless, the subject remains open for discussion, and this suggests that the science, or art of performance prediction still has room for improvements. The technology of airplane design is not static, and the introduction of new configurations operating in areas of fluid dynamics not completely understood has brought additional uncertainties into drag prediction and measurement.

In recent years, improvements in theoretical methods of analysis and in test facilities (both full scale and model scale) have brought the basic methodology of drag prediction to an advanced state. This is not to say that prediction accuracies are necessarily adequate, but rather to suggest that the uncertainties and their sources are more readily identifiable. With these advances in mind, and in view of the large amount of drag methodology reports in the literature, this paper does not provide another detailed description of the method for developing a lift-drag polar by the traditional approach, but rather gives an overview to the subject and highlights areas currently of interest.

References are made throughout these notes to some of the recent presentations relative to the basic topic. One of the more significant collection of papers is contained in the publication of the 1973 AGARD Fluid Dynamics Panel conference on "Aerodynamic Drag" held in Izmir, Turkey in April (Reference 5).

To summarize this introduction, a few statements are offered below as to the status of drag methodology.

- Drag prediction methods derive their validity from both direct and deduced drag measurements. These measurements are expressed in an overall airplane drag polar as the end product, based upon flight tests, and are supplemented by various flight test and wind tunnel measurements of component configuration items.

- The most accurate drag predictions require extensive use of the wind tunnel. In addition, configurations which involve different and novel aerodynamic features or which expand the known and proven flight envelope may require new wind tunnel techniques to insure an understanding of the fluid flow effects.

- Theoretical tools do not exist which by themselves permit the calculation of a drag polar for a subsonic airplane; however, the application of theory to fundamental fluid dynamic flow problems can be very significant to the timely development of configuration design and is useful for critical analysis.

- The determination of interference effects by the proper simulation of propulsion system interaction with the flow field around the aircraft is recognized as a major requirement for improved accuracy of lift and drag prediction.
- A bookkeeping system identifying and accounting for all engine and airframe contributions to "drag" is necessary, together with a terminology used and understood by the propulsion specialist as well as the aerodynamicist.

## DRAG PREDICTION METHODS

### TRADITIONAL METHODS

The most widely used approach to drag prediction is essentially an empirical analysis process which relies heavily on previous experience. This traditional approach (References 6, 7 and 8) considers the zero lift profile drag of each major component of the aircraft, establishes a subcritical polar shape and lift coefficient at which minimum profile drag occurs, and adds drag due to lift. Interference effects, if any, are judged and compressibility drag rise characteristics are assigned. The result is a lift drag polar with typical elements in simplified form shown on Figure 4.

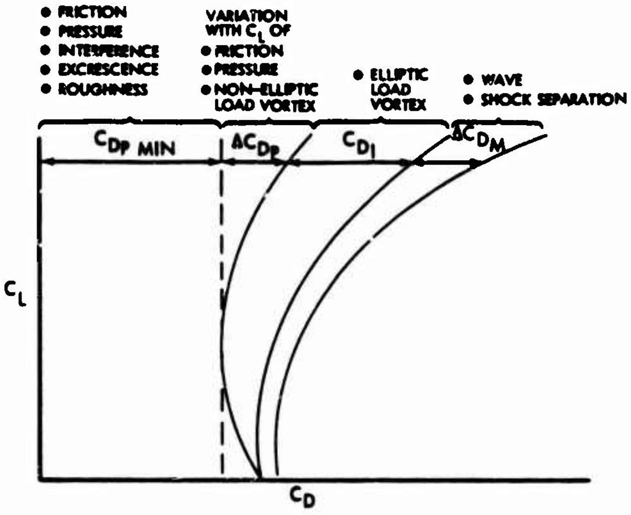

Figure 4: DRAG BUILDUP BY ANALYSIS

These drag elements can be conveniently organized into the familiar equation for drag of subsonic airplane:

$$C_D = \underbrace{C_{D_{pmin}} + \Delta C_{D_p} + \frac{C_L^2}{\pi AR}}_{\text{Subcritical Polar}} + \underbrace{\Delta C_{DM}}_{\text{Compressibility Effects}} \qquad (1)$$

The airplane drag is thus identified for purposes of prediction and analysis by three major items.

- Minimum Profile Drag
- Subcritical Lift Dependent Drag
- Compressibility Drag

In addition, there may be thrust-dependent terms. These are discussed in succeeding paragraphs.

$C_{D_{pmin}}$ is the minimum profile drag as identified at a given Reynolds number and does not change with lift coefficient. It includes both friction and pressure drag.

$\Delta C_{D_p}$ includes the remainder of the friction and pressure drag. This term varies with lift coefficient and reflects wing section camber, non-elliptic span loading and other configuration items producing vortex drag.

$C_{D_i}$ is the elliptical vortex drag under subcritical conditions. A good wing design should approach this elliptic loading at the design condition. Identification of areas on the airplane producing unwanted friction or pressure drag increases due to lift can be quickly made by assigning a 100% efficiency factor to the wing induced drag (or a different level if logical), and analyzing the other airplane components accordingly.

$\Delta C_{D_M}$ is identified as a coefficient which varies with Mach number and lift coefficient. It may also vary due to the changes in the air flow accompanying thrust changes.

These simple classifications provide a logical framework within which drag prediction and measurement can be organized. The use of any prediction program depends upon the level of accuracy desired, the firmness of the airplane definition, and the analysis tools available. For preliminary design feasibility studies, the above model can be applied in a simple "add up the increments" manner; but for an authoritative prediction on a well defined airplane a careful and thorough appraisal must be made not only of each individual element of the configuration but also of the aerodynamic interaction of each part of the configuration. The simplified representation of the drag components given by equation (1) above is rapidly expanded into more complex terms when serious design efforts get launched. This process, as currently applied in industry, will call upon the use of all the tools available to the aerodynamicist: historical data, empirical factors, wind tunnel data, and theoretical analyses. The manner in which these resources are used to blend together into a prediction is subject to the experience of the design team, the degree to which the configuration resembles previous models, and the amount of proprietary experimental data available to the engineer. Norton (Reference 6) discussed the application of this traditional approach to the estimation and analysis of airplane drag. Concern was expressed for the heavy reliance of the methodology upon "empirical data or empirical explanation of flow processes." This concern is still valid.

## ESTIMATION ACCURACY

Each manufacturer has a methodology by which a thorough drag estimate is made. The state-of-the-art is a dynamic one, and improvements and additions to the methodology are constantly being made. There is no single, industry-wide handbook for such predictions, and any attempt to produce a universal process would require flexibility and provision for updating. However, there are several basic sources of fundamental information on component drag levels and estimation processes such as Hoerner (Reference 9), the Royal Aeronautical Society Data Sheets (Reference 10) and the USAF DATCOM (Reference 11). The proof of these methods lies in analysis of flight data, in which comparisons against the estimates are made and further refinements to the estimation elements are developed. Very few reports are published which attempt to reflect the total comparison between prediction and test. One reason is that such an effort must be done in considerable detail to be worthwhile, and this requires adequate flight data and expert technical attention. The results, whether good or bad, are highly proprietary and become a significant part of a company's "know how".

A chart is shown on Figure 5 showing components of a drag polar for which a relatively high degree of prediction confidence is believed to exist, and also components for which the drag estimation process has proven to show a higher degree of uncertainty. Confidence in the estimated drag polar will therefore vary for different flight speeds, i.e., the profile drag level is usually predictable with much more accuracy than is the drag rise. Experience has shown that of all the configuration items, the propulsion system installation can be the most troublesome and is the source of large errors in drag estimation. Particular care must be taken in identifying the potential interference effects due to the engine installation and the associated thrust effects.

Several reports recently published have discussed the ability to assess full scale drag components, particularly profile drag. References 12, 13 and 14 provide comparisons between flight test and predictions, and provide supporting evidence for the data shown on Figure 5. A more detailed discussion of estimation accuracy is provided in the concluding section of this paper.

## THEORETICAL METHODS

Theoretical programs are available to calculate the subcritical lift and drag, based upon potential flow theory applied to a given geometry of a wing or other airplane components. However, these programs will not account for the interaction in the boundary layer with intersections such as at the wing-body juncture or with local flow changes such as produced by body upsweep. These programs can compute subcritical wing or body pressure distributions, and methods are emerging which will improve on the present process of empirical adjustment to these pressures for the supercritical case. This is discussed in detail in a later section of this paper. In the main, the role of theoretical programs to date has been to provide valuable data on subcritical flow pressure fields and gradients, which, when tempered with corrections derived from experience, result in a more rapid convergence of the best aerodynamic design.

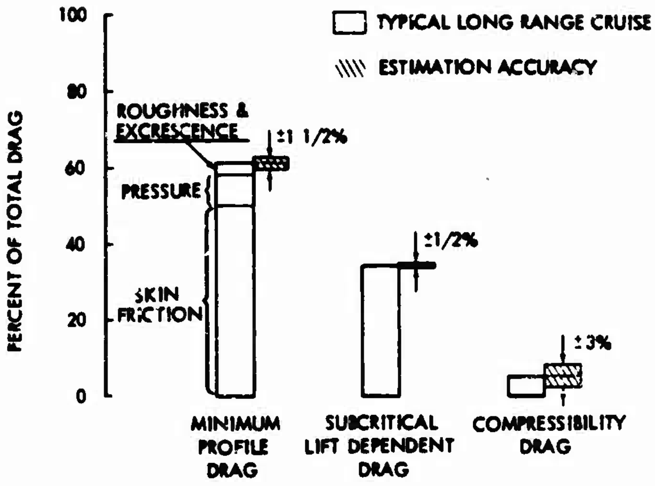

**Figure 5: DRAG SOURCE AND ESTIMATION ACCURACY (LONG RANGE TRANSPORTS)**

At this point, the use of integrated computerized design programs for more rapid analysis might be proposed. The computer is very helpful in comparing designs, analyzing missions, and providing comparative performance data which suggest optimum trends. However, there are no computer programs which can accurately construct the total airplane subcritical (not to mention transonic) polar based only upon a geometry definition, nor can the computer optimize the geometry to correct "deficiencies" which it might discover. As stated in Reference 15, "a comprehensive general theoretical drag prediction framework suitable for all the main current classes of military and civil aircraft is certainly not likely to be feasible for some time to come." Neither does an adequate empirical base exist for the computerized construction of a drag polar. Hodges in Reference 16 recognizes the need for additional data to establish generalized but accurate predictions for some configuration items. Also, there is a lack of knowledge on the way to sum individual component data for configuration items which are mounted at various incidence angles to each other, or which may involve interaction effects, or which involve significant vortex drag at zero lift such as a cambered, twisted wing.

## WIND TUNNEL DATA

The wind tunnel is an indispensable tool for developing forecasts for full scale aerodynamic characteristics as well as for configuration design optimization. Ideally, wind tunnel results are used to modify previously established data from flight tests of similar configurations. In this manner, some of the more obscure sources of drag can be observed directly at model scale, such as non-elliptic vortex drag which may come from unsuspected components of the aircraft, or interference effects due to the configuration arrangement, or to thrust effects. Decisions can then be made as to the full scale characteristics which should be predicted.

The wind tunnel is the only experimental way in which the drag "buildup" can be accomplished, and it is thus an integral part of the eventual analysis of the flight polar. The effect of Mach number and Reynolds number on the lift and drag, and in fact most if not all of the configuration items which have an impact on the relationship between lift, drag, and angle of attack are most easily and accurately observed by wind tunnel tests. For instance, the effect of span loading changes due to wing flexibility, or the variation and level of trim drag at various Mach numbers or airplane center of gravity positions is usually determined in the wind tunnel. These comments are directed strictly at the question of drag measurement, and do not credit the major effort of basic configuration development and refinement for which the wind tunnel is also extremely valuable. In addition, the wind tunnel is applied to specific diagnostic flow studies aimed at improving the L/D of the aircraft, as discussed in a later section of this paper. Finally, the wind tunnel is also used to provide flow visualization studies which have become an essential part of the airplane design effort (particularly the wing) and the concurrent drag analysis. An intelligent, confident forecast of the airplane performance cannot be made without this integration of information of all types from the wind tunnel - pressure data, force data, flow visualization studies - together with maximum correlation with full scale results on similar configurations.

Results from the wind tunnel are sometimes applied to full scale predictions without the benefit of baseline data from flight tests on a similar model. In this case, heavy reliance must be placed on the corrections which must be applied to remove the "tares" from the wind tunnel data due to tunnel and support interferences. Greater risks are assumed with respect to polar shape and drag rise characteristics than in the case where the major scale effect can be attributed largely to minimum profile drag.

## THRUST - DRAG BOOKKEEPING

One of the areas of drag prediction which may bring a large amount of uncertainty is the determination of the contribution of the propulsion system to the drag of the aircraft. This has historically been a cause for concern, particularly on those airplanes with a close coupled or highly integrated propulsion system. Interactions at the inlet or the nozzle produced by the changes of airflow accompanying thrust changes require careful testing in the wind tunnel in order to predict the proper thrust minus drag. It is necessary that a clearly defined bookkeeping system be established in order to translate the ideal thrust as quoted by the engine manufacturer and the "power off" wind tunnel data into accurate flight predictions. The first requirement is to establish which terms will be included in the propulsion system definition and which will be classified as drag. One approach taken by The Boeing Company for subsonic commercial aircraft in which thrust interaction is a significant variable, is to construct a drag polar at a given Mach number in accordance with the following equation:

$$C_D = C_{D_{REF}} + \Delta C_{D_{INLET}} + \Delta C_{D_{THRUST}} \qquad (2)$$

where

$C_{D_{REF}}$ = Full scale projection of drag, lift, moments, including corrections for $R_N$, excrescences, etc. The basis is unpowered, flow-nacelle wind tunnel model tests.

$\Delta C_{D_{INLET}}$ = Incremental forces due to variable inlet velocity ratio, determined experimentally.

$\Delta C_{D_{THRUST}}$ = Incremental forces due to fan or primary exhaust flow, measured in the wind tunnel using powered nacelles.

The boundary between thrust and drag is established as a surface occurring on the wind tunnel model nacelles along the inlet stream tube, around the fan cowl (if a short duct installation) and along an arbitrary fan or primary exhaust stream tube. This is illustrated in Figure 6 for an underwing and also for an overwing engine installation.

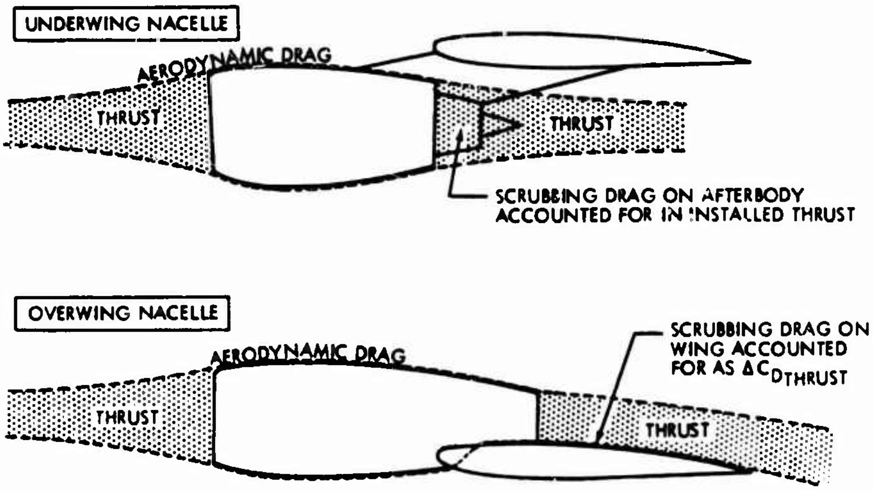
UNDERWING NACELLE
AERODYNAMIC DRAG
THRUST
THRUST
SCRUBBING DRAG ON AFTERBODY ACCOUNTED FOR IN INSTALLED THRUST
OVERWING NACELLE
AERODYNAMIC DRAG
THRUST
THRUST
SCRUBBING DRAG ON WING ACCOUNTED FOR AS $\Delta C_{D_{THRUST}}$

Figure 6: DRAG AND THRUST INTERFACE

The reference configuration for the polar construction is an unpowered model with flow-through nacelles. Powered nacelles are then tested, and the incremental exhaust thrust effects are obtained using the ram pressure ratio of the flow-through nacelles as a base. These results are shown schematically on Figure 7 . The nacelles may be either the "blown" type or the fully powered engine simulator type shown on Figure 8. If blown nacelles are used, additional tests are required to determine the effect of mass flow on the inlet drag, which is assumed to be independent of the exhaust flow conditions. The engine simulator combines the inlet and exhaust thrust effects into one setup and more correctly simulates the boundary layer characteristics between the wing and nacelle. A detailed description of testing with these small, high speed turbines is available in Reference 17.

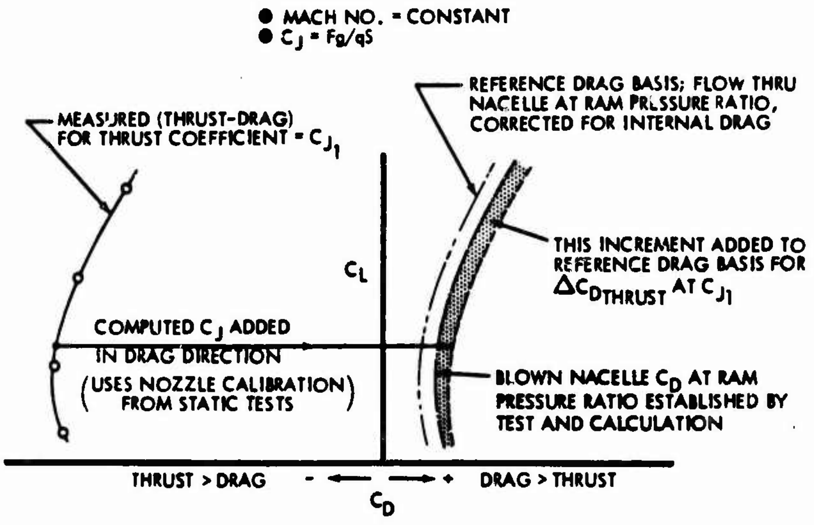
● MACH NO. = CONSTANT
● $C_J = F_g/qS$
MEASURED (THRUST-DRAG) FOR THRUST COEFFICIENT = $C_{J_1}$
REFERENCE DRAG BASIS; FLOW THRU NACELLE AT RAM PRESSURE RATIO, CORRECTED FOR INTERNAL DRAG
$C_L$
THIS INCREMENT ADDED TO REFERENCE DRAG BASIS FOR $\Delta C_{D_{THRUST}}$ AT $C_{J1}$
COMPUTED $C_J$ ADDED IN DRAG DIRECTION
(USES NOZZLE CALIBRATION FROM STATIC TESTS)
BLOWN NACELLE $C_D$ AT RAM PRESSURE RATIO ESTABLISHED BY TEST AND CALCULATION
THRUST > DRAG
- ← → +
DRAG > THRUST
$C_D$

Figure 7: THRUST - DRAG BOOKKEEPING

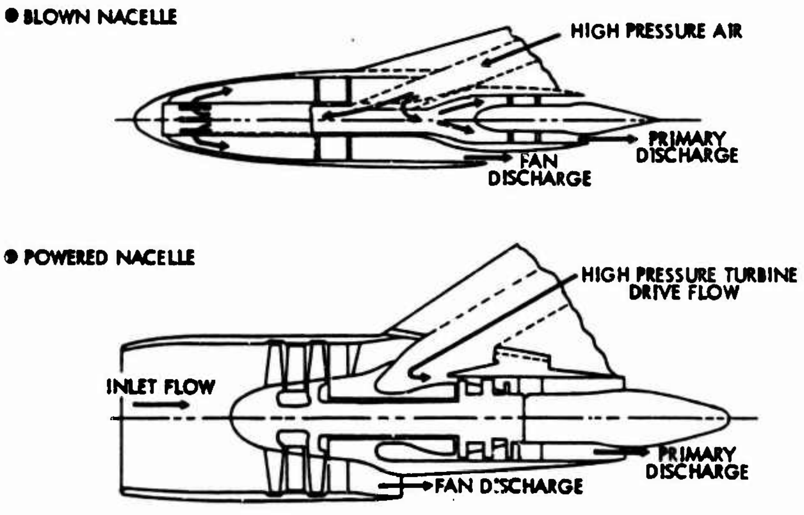
● BLOWN NACELLE
HIGH PRESSURE AIR
PRIMARY DISCHARGE
FAN DISCHARGE
● POWERED NACELLE
HIGH PRESSURE TURBINE DRIVE FLOW
INLET FLOW
PRIMARY DISCHARGE
FAN DISCHARGE

Figure 8: ENGINE SIMULATORS

Force accounting using this logic is summarized on Figure 9 which shows how the unpowered wind tunnel model and the uninstalled engine data are modified to provide full scale performance predictions in accordance with results from wind tunnel tests described above. Where the variation of thrust level is not a powerful factor in the drag level at a given Mach number, as is the case with most of today's transports, corrections for thrust can be synthesized into the force data so that slightly modified drag rise characteristics are developed, i.e., $\Delta C_{D_{THRUST}}$ is treated as a function only of Mach number. However, if there are significant thrust effects on drag, lift, and other forces at a given Mach number, the eventual data presentation is a series of curves as shown on Figure 10 . Other components of the force data are also impacted by thrust effects and are presented as shown on Figure 11 .

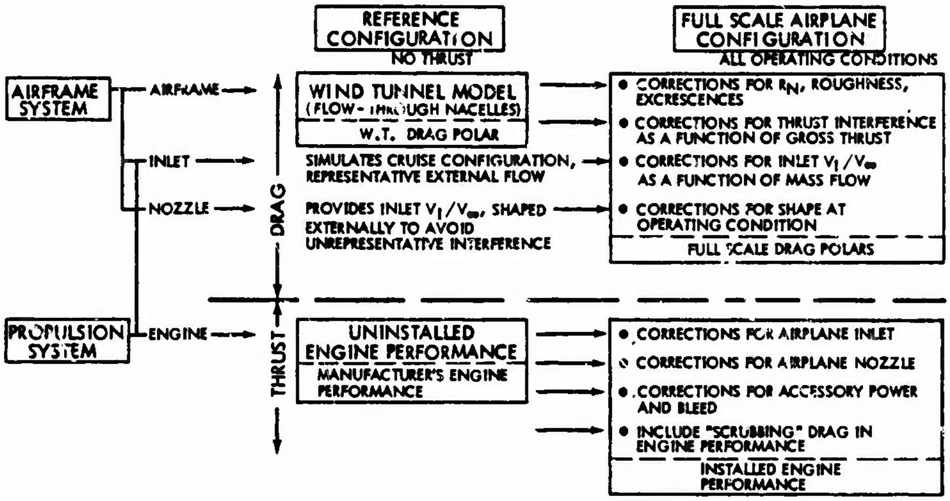
REFERENCE CONFIGURATION
NO THRUST
FULL SCALE AIRPLANE CONFIGURATION
ALL OPERATING CONDITIONS
AIRFRAME SYSTEM
AIRFRAME
INLET
NOZZLE
DRAG
WIND TUNNEL MODEL (FLOW-THROUGH NACELLES)
W.T. DRAG POLAR
SIMULATES CRUISE CONFIGURATION, REPRESENTATIVE EXTERNAL FLOW
PROVIDES INLET $V_I/V_\infty$, SHAPED EXTERNALLY TO AVOID UNREPRESENTATIVE INTERFERENCE
• CORRECTIONS FOR $R_N$, ROUGHNESS, EXCRESCENCES
• CORRECTIONS FOR THRUST INTERFERENCE AS A FUNCTION OF GROSS THRUST
• CORRECTIONS FOR INLET $V_I/V_\infty$ AS A FUNCTION OF MASS FLOW
• CORRECTIONS FOR SHAPE AT OPERATING CONDITION
FULL SCALE DRAG POLARS
PROPULSION SYSTEM
ENGINE
THRUST
UNINSTALLED ENGINE PERFORMANCE
MANUFACTURER'S ENGINE PERFORMANCE
• CORRECTIONS FOR AIRPLANE INLET
• CORRECTIONS FOR AIRPLANE NOZZLE
• CORRECTIONS FOR ACCESSORY POWER AND BLEED
• INCLUDE "SCRUBBING" DRAG IN ENGINE PERFORMANCE
INSTALLED ENGINE PERFORMANCE

Figure 9: FORCE ACCOUNTABILITY WITH THRUST EFFECTS

$$\bullet\ C_{D_{A/P}} = C_{D_{REF}} + \Delta C_{D_{INLET}} + \Delta C_{D_{\substack{THRUST\\EFFECTS}}}$$

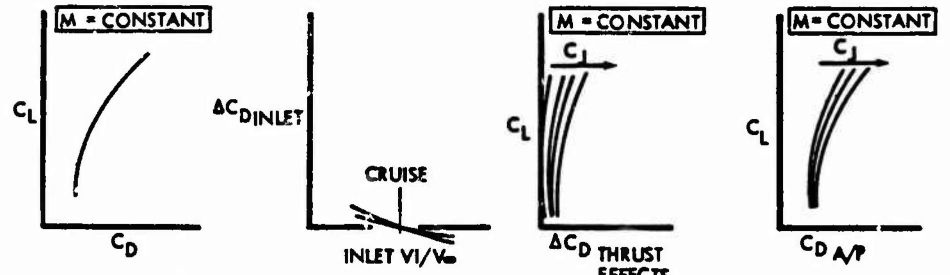

- WIND TUNNEL DATA CORRECTED FOR WALL EFFECTS, ETC.
- CRUISE INLET VELOCITY RATIO
- NACELLE INTERNAL DRAG REMOVED

- VARIABLE INLET MASS FLOW TESTING

- INCREMENTS DUE TO BLOWING WITH RESPECT TO RAM PRESSURE RATIO CONDITIONS

- INCLUDES THRUST EFFECTS

Figure 10: DRAG POLAR BUILDUP PROCEDURE

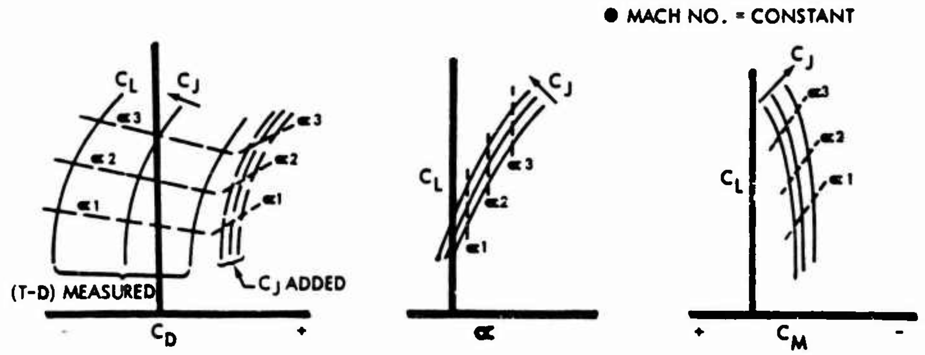

Figure 11: THRUST INTERACTION ACCOUNTABILITY ON AIRPLANE FORCE DATA

There are several advantages to the above method for bookkeeping thrust and drag. With regard to the engine data, the method minimizes changes to the performance developed by the engine manufacturer, principally translating the data to the airplane installed nacelle configuration. The method puts the responsibility for designing to minimize thrust interference effects on the aerodynamicist, where it belongs; and it retains a large degree of flexibility for performance calculations in the initial design stages when the engine type, size, and location is in a study phase and the degree of thrust accountability is only vaguely known.

The above paragraphs offer a status review of the topic of drag prediction methods. These methods have been well documented and are being applied intensively. What is not easily available is an index to the success of these predictions. The answer to this question is a highly qualified one, and since it may perhaps involve a legal as well as a technical concern, the data is understandably hard to come by. However, there are occasional press reports of technical problems in military or commercial aircraft which quote large deficiencies in range or speed. The claimed performance of the sales brochures is not always verified when actual operating performance becomes known. There is little argument with the conclusion that continued effort and better results for drag prediction is desirable. However, the question is not confined to lift and drag, since the ultimate deficiency is measured in range, altitude, or speed. This brings the engine performance and technical definition clearly into the equation, and leads to a logical discussion in the next section of performance assessment in flight.

## FLIGHT TEST PERFORMANCE MEASUREMENTS

In the end result, the measure of drag estimation is reflected in the performance of the aircraft rather than by agreement with predicted coefficients. The operator observes directly the range, speed, or similar items for which he has particular requirements. The L/D of the aircraft is not normally listed in a management summary of the aircraft when a competitive evaluation is being made; nor is it an item for which a direct reading is acquired in flight testing. Instead, the observed items consist of terms such as airspeed, fuel flow, and engine parameters. It is interesting to look at the basic data acquired by Charles Lindbergh in his flight testing of the Spirit of St. Louis, in preparation for the first nonstop airplane flight between the continents of America and Europe. Basic data upon which his flight was predicted (Reference 18) is illustrated in Figure 12 .

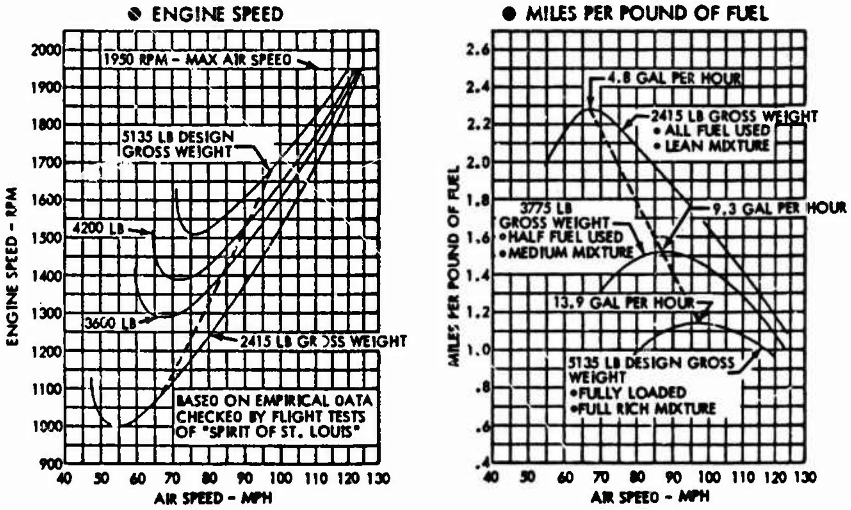

Figure 12: FLIGHT TEST DATA ("SPIRIT OF ST. LOUIS")

Lindbergh was not concerned so much with the drag polar as with the miles per pound of fuel, the speed at which the optimum fuel mileage would occur, the engine rpm for these conditions, and of course the total fuel available. Test data were obtained during "acceptance" flights in San Diego and the transcontinental "proving" flights to New York City. The fact that the performance confirmed the designer's estimates established confidence for his solo flight across the Atlantic. The record flight performance comfortably exceeded the predictions (the airplane landed with 85 gallons of gasoline remaining out of the original 450 gallons, enough fuel to have flown another thousand miles).

A major purpose of the predictive drag polar is its function in the development of airplane performance charts over a wide range of flight conditions. In discussing the accuracy with which such predictions can be made, a number of qualifications must be described. For this part of the discussion, let it be assumed that the time and activity span commences with the date of first flight and ends with airworthiness certification of the airplane. The technical problem is clear - the configuration is defined and built, the engineering staff presumably has the full knowledge of the impact on performance of all the configuration changes which have been made, and (at least within the aircraft company), therefore the compliance to be measured refers to a carefully developed prediction.

Significant events which take place in this time period are shown on Figure 13 . A typical flight test program for a new commercial transport in the United States covers a period of nine to ten months, involving four to five aircraft with a total test time of about 1500 flight hours. The initial test period of four to five months allows for basic data acquisition on the various systems (including the power plant), plus enough performance data to know whether the airplane and its systems are operating close to or far off from predictions, and whether these misses are positive or negative. On a successful program, enough favorable signals on the aircraft are acquired, including substantiation of structural integrity and handling quality criteria, to proceed with the rigorous certification program under the auspices of the government airworthiness agency. Meanwhile, additional aircraft are coming down the production line at an accelerating rate. Any changes found necessary in the test airplanes must be incorporated in the certified configuration and in all the production aircraft. At the time of certification, as many as 25 to 30 airplanes may be in final assembly or on the field waiting for delivery. This is not the time period when the aerodynamicist is writing a comprehensive paper on comparisons between flight test and wind tunnel predictions!

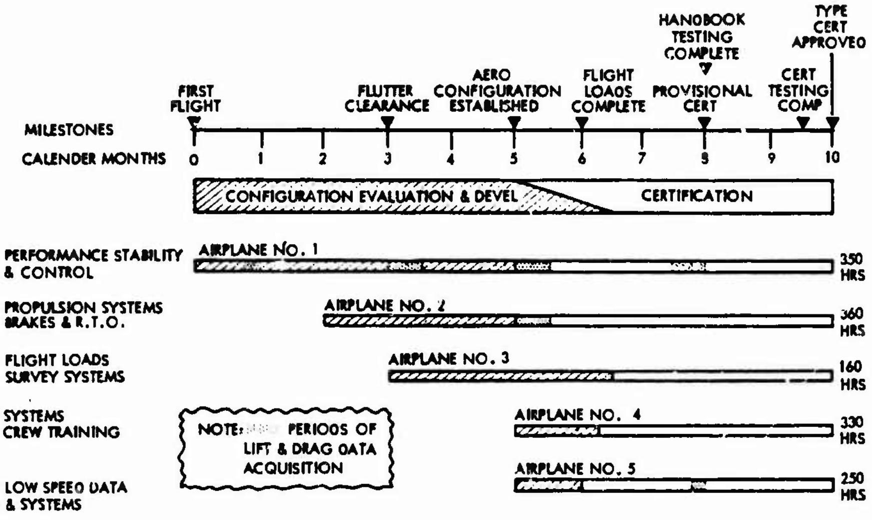

Figure 13: FLIGHT TEST PROGRAM MILESTONES

## FLIGHT TEST MEASUREMENT ACCURACY

The performance testing for which the basic engine and airframe characteristics are defined consist of about 70 to 80 hours of flight time, usually concentrated on one airplane and a selected set of calibrated engines. About two-thirds of this time is devoted to cruise performance, and the remainder on the takeoff and landing configuration. These data will be used to modify estimated data already published in the operator's flight handbook and to establish levels used in showing compliance with guarantees, and to provide assurance of climbout and approach performance for certification purposes. To achieve maximum accuracy, a limited amount of carefully flown test data is acquired for flight conditions considered most representative or critical. These test data are then expanded analytically to cover the entire range of conditions for which the airplane is to be used. It is impossible in this limited time period to obtain meaningful flight test trends over a sufficient range of variables such as Reynolds number, altitude, weight, airplane c.g., etc., as the sole source of information from which to provide corrective trends. Therefore, wind tunnel data and theory are used to modify and normalize the flight data. This is necessary because in some cases of testing to establish trends, the experimental scatter with limited data is large enough to obscure the trend, and there is dubious validity to a literal fairing of such data.

Boeing experience shows that flight testing has been unrewarding when it involves items such as trim drag and Reynolds number which are predicted by the wind tunnel or theory to have a small slope. Best results are obtained by identifying the normal operating conditions, testing under these conditions, and then reproducing these observations into the flight handbook charts with a minimum of correction. Some spot checking of extremes in the operating envelope is necessary in order to provide the widest range of observations, to insure that "flat" trends in the normal operating environment are innocuous, and to prepare for later development of the aircraft into areas originally thought unlikely.

Any generalized statement that the flight test has confirmed the drag prediction within ( ) percent needs qualification to be technically meaningful; furthermore, to offer evidence as to the degree with which one or two elements of the drag estimation process agree with predictions must be considered within the context of the total airplane/engine performance results. Such an analysis must also develop an estimate of drag on each element of the configuration and provide an assessment of all portions of the aerodynamic terms entering into the construction of the drag polar.

It is believed that the following accuracies in measurement important to the definition of performance of several variables can be achieved:

Table 1: FLIGHT TEST MEASUREMENT ACCURACIES

| DATA SOURCE | MEASUREMENT ERROR Miles/Lb | MEASUREMENT ERROR Thrust |
|---|---|---|
| ● One Flight | ± 1.5% | ± 2.0% |
| ● Several Flights | ± 1.0% | ± 1.5% |
| ● Several Airplanes | ± 0.5 to 1.0% | ± 1.0% |

The results of tests on five separate Boeing 747's are shown on Figure 14 . It can be seen that the maximum deviation of data from faired curves on a given airplane is ± [illegible] and that the majority of test points fall within 0.5% of the faired curves. In comparison, data acquired in 1962 for the 707 are shown on Figure 15 , and show a scatter of ± [illegible]% for a given airplane.

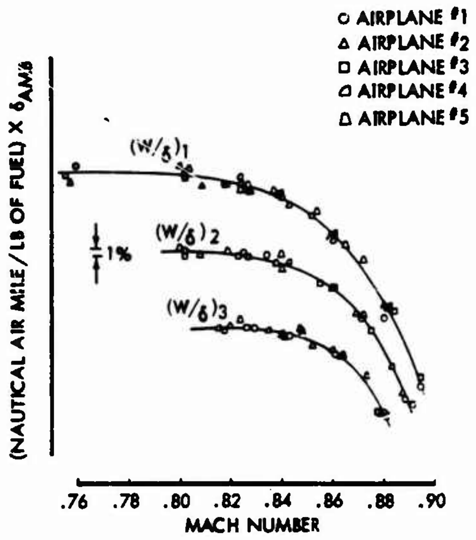

Figure 14: BOEING 747 FLIGHT TEST DATA

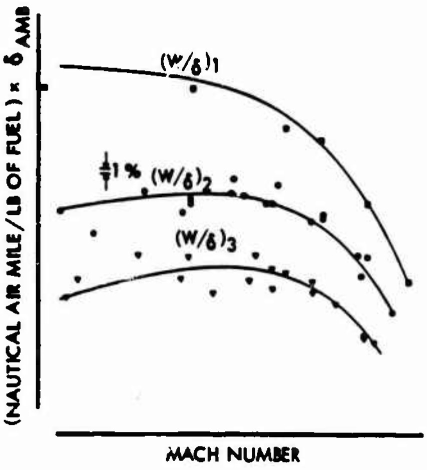

Figure 15: BOEING 707 FLIGHT TEST DATA

These data show the progress which has been achieved in measurement accuracy due to the introduction of better recording instrumentation, new techniques for onboard computing and analysis, improved calculation processes, and the use of the inertial navigator and autopilot for improved steady state flight test conditions.

In addition to these conclusions, it is believed that, by extensive testing of calibrated engines and flight nozzles, the engine performance as measured in a test cell using the engine manufacturer's inlet and nozzle can be "tracked" to the installed flight test performance with an accuracy of ± 1% of thrust and fuel flow using level, steady flight techniques.

## METHODS OF PERFORMANCE TESTING

Flight test performance measurements may be obtained from steady-state, level flight recordings in which stabilized levels of thrust, fuel flow, airplane speed and altitude, and other variables are obtained; or by non-steady maneuvers which rely more heavily on measurements of longitudinal and normal acceleration and angle of attack to compute lift and drag. Both methods require the determination of thrust from engine parameters. The steady-state procedure is more time consuming, but it produces the greatest accuracy (least scatter) and most correctly simulates the actual operating conditions of a long range transport. This method develops the best data to correlate predictions from wind tunnel lift/drag polars and establishes a solid basis for resolving the basic range parameter - miles per pound - into the components of airframe drag and engine thrust/fuel flow. On the other hand, a greater volume of lift/drag data can be acquired from acceleration or deceleration tests, or in carefully flown wind-up turns or roller coaster maneuvers. These data provide a statistical quantity which tends to offset the slightly greater inaccuracy of a given point. The non-steady maneuvers may be used to supplement steady state base points in some cases, or can be used as incremental data from the baseline conditions, and thereby efficiently fill in the grid of lift/drag characteristics. This is particularly true early in a flight test program where it is desirable to establish firmly and confidently the engine and airframe performance, but where this item is only one of many essential tests competing for priority.

Whatever method or combinations of methods employed, it is mandatory that the inflight, installed engine performance be determined and reconciled with the engine manufacturer's data, and with the drag polar established for the airplane. This may seem so obvious and elementary that it need not be mentioned; but when it is necessary to commit to and verify guaranteed performance to levels within 5%, a one or two percent vagueness in specific fuel consumption or drag is intolerable. Furthermore, as a production program matures, and later improved versions of the engine are made available, the proof of one or two percent gains in s.f.c. must be measured in flight test. This requirement for careful resolution of fuel mileage data emphasizes the value of steady tests in the cruise configuration, since these tests provide the best concurrent measurement of drag and fuel flow.

The accuracy of representative performance data from Boeing steady-state tests was summarized on Table 1 and in Figure 14 . An example of data acquired on the B737 airplane by the non-steady acceleration technique is shown on Figure 16 . A comprehensive description of these methods applied to a Grumman F-14 fighter was recently presented (Reference 14) and this paper suggested that the following accuracies on thrust (drag) have been achieved:

| Type of Testing | Data Scatter-Drag Definition |
|---|---|
| ● Steady State Level Flight | ± 1% (concurs with Boeing experience) |
| ● Quasi-steady | ± 4% subsonic, ± 2% M = 2.0 |
| ● Dynamic | ± 4% subsonic, ± 2% M = 2.0 |

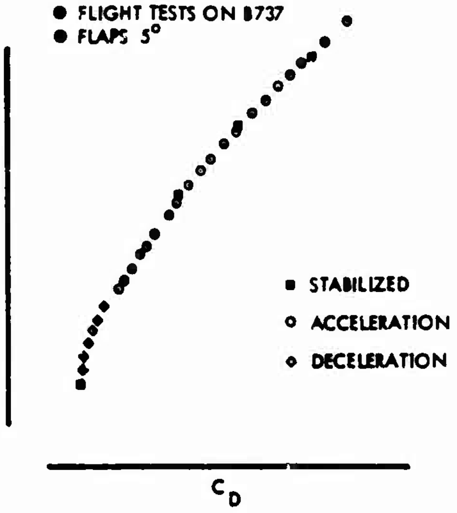

Figure 16: COMPARISON OF FLIGHT TEST TECHNIQUES

In order to achieve this level of accuracy and minimum random data scatter, the flight test technique at The Boeing Company requires onboard real-time monitoring of the data. Sensitive instrumentation of engine and airframe parameters is required. A trailing cone is used for the reference static pressure, which is recorded on a quick developing direct readout oscillograph along with airspeed, total air temperature, and ground speed from the Inertial Navigation System (INS). Tests are flown at several levels of weight and altitude ($W/\delta$) with the pilot adjusting the thrust to an estimated level for the condition, and holding altitude with the autopilot. Both the pilot and the engineers monitor critical items such as speed, acceleration, or engine parameters. Data samples are taken during the test condition. A successful test including stabilized fuel flow readings is held "on condition" for about five minutes. Several sample calculations of $C_L$ and $C_D$ are made, providing confidence that the eventual final reduced data will be satisfactory. A recent improvement to data reduction has been to utilize the INS ground speed as the source of the energy correction rather than the true airspeed. In this manner, accelerations caused by changes in the velocity of the air mass are accounted for.

These tests are performed early in the flight test program, and as mentioned previously are used to support guarantee compliance or for airworthiness certification. At times these comprehensive tests are supplemented by additional flights on later production models. A recent description of DC-10 flight testing of this nature was published in Reference 19 and is partially quoted below:

"...before production deliveries begin, all airlines fly one aircraft to check cruise performance at a number of points (altitude and speed) selected by the carrier.

"ZK-NZL had a ramp weight of 208,480 kg (459,700 pounds) for its performance flight. The takeoff-center of gravity was at 25 percent chord. Usable fuel was 63,000 kg (138,915 pounds). Zero fuel weight for the flight was 66,000 kg (147,700 pounds). Because the aircraft was empty, except for a small instrument package and several temporary seats for the flight observers, a large amount of ballast, weighing 28,200 kg (62,181 pounds) had to be carried in the hold to bring the weight to a high W/delta value.

"The points to be checked on the ANZ DC-10 were as follows:

| Altitude (Ft) | Mach No. | W/delta (Millions) |
|---|---|---|
| ● 33,000 | 0.82<br>0.83<br>0.84 | 1.2 |
| ● 35,000 | 0.82<br>0.83<br>0.84 | 1.8 |
| ● 37,000 | 0.82<br>0.83<br>0.84 | 1.9 |

"The aircraft sailed easily up to the test altitude out of Long Beach, California, with the characteristic smoothness and low noise level of the wide-bodied jets, to look for the smooth air that is essential for accurate plots. With the correct altitude and Mach number reading on the normal flight instruments, the aircraft was placed in the hands of the autopilot for a straight and level run lasting for a minimum of three minutes for each run. The small onboard digital recorder was activated for each run. The package had a 125-channel capacity but only a fraction was used to record the full data required, including $N_1$ rpm and fuel flow on all three engines, plus altitude, airspeed and air temperatures. Data reduction is performed on the ground in Long Beach in the elaborate computer facility built for DC-10 flight test, where results can be rapidly machine-processed for examination on large cathode ray tube displays. As a double check on fuel usage, the fuel tanks are dipped for their contents after the flight is over.

"Flying the nine points as tabled was predicted to take about four hours..."

## DRAG REDUCTION AND PERFORMANCE IMPROVEMENT

Almost every airplane program is subjected, in respective order, to three major drives: weight reduction, drag "clean-up", and cost reduction. In addition, there of course is a program for obtaining more thrust and less fuel flow from the engine.

The initiation of these improvements suggests that most manufacturers instill an optimistic and positive approach into their engineering staffs. In any event, the weight reduction program is initiated during the final stages of design and initial assembly, at a time when it is obvious as to the first airplane's weight status. The drag clean-up starts shortly after the performance flight tests produce data in which all of the answers on range appear to be on the low side of the prediction. The cost reduction program is initiated when the corrective action from the weight and drag reduction programs become apparent. The drag clean-up may be inspired by a failure to meet predicted performance levels (regardless of the engine performance) or by a demand to improve performance in order to achieve further competitive advantages.

A listing of items which are normally inspected and sometimes modified in a clean-up campaign are:

- ●Seals - Leading edge devices
  - Controls
  - Landing gear doors
- ●Skin Joints - Steps, chamfering, gaps
- ●Rivets - Properly installed in critical areas
- ●"Holes" - Correct manufacture and operation of valves, inlets, exhausts, vents, etc.
- ●Rigging - All movable surfaces checked, especially on the wing
- ●Faired Surfaces - Nacelle struts, wing-body joints, stabilizer "elephant ears"

These items, if not designed or installed correctly, can easily account for a degradation of 5% of the airplane drag. Large losses can occur in critical areas such as the wing leading edge, where all movable devices must be carefully faired and sealed. Pumping of air through wing, body, and empennage cavities can also cause measurable losses.

Not listed above was the propulsion system, which includes the inlet, thrust reverser, and sound suppressor. Experience has shown that losses due to leakage through seals in these systems, or by poor model scale measurement of drag around the nacelle afterbody, can cause significant errors in prediction of airplane profile drag or drag rise. For instance, on the 707 Intercontinental airplanes with the P&W JT4A or JT3C engines, a major effort was expended to measure the drag in flight tests on several configurations of the sound suppressor/thrust reverser. The basic propulsion pod drag without SS/TR devices had been well established by analysis of the military KC-135 airplane performance. It was determined that the 707 drag could be improved by as much as 3% by covering and sealing the reverser cascades, and that improvements in the tubular sound suppressor could offer another 1.5% drag reduction. In a later investigation, modification of the fuselage contours above and aft of the pilot's windows, and improvement of the air conditioning inlet and exhaust controls, were tested. These items were thought to afford a potential of one to three percent reduction in drag, but it proved difficult to record significant differences consistently, and it was concluded that the changes would be of relatively small benefit and could only be made at considerable cost. An improved scheduling of the inlet and exhaust controls for the air conditioning system was developed.

In cases where a drag clean-up of relatively minor items is unnecessary or of minimum benefit, more major configuration changes of benefit to cruise L/D can be applied to the aircraft. These are sometimes incorporated into a model improvement program. Some examples of these changes as applied to commercial transports include:

- ●Revised wing tips
- ●Revised wing leading edges
- ●Revised nacelle or nacelle strut lines

This type of modification usually comes after the initial design is well understood and in some cases when a new set of goals for the design is established. Response to these opportunities by such modifications has allowed the original aircraft to grow in performance capability and thereby achieve a level of efficiency far surpassing the original point designs.

A brief look at the history of the range performance levels on the 707 and DC-8 series of aircraft is interesting in this regard. These models furnished the first major competitive efforts in the long range subsonic jet class; the original versions barely met the goal of transatlantic operation. With help from the engine manufacturers, and with aerodynamic development, these aircraft rather quickly met demands for range and payload satisfactory for nonstop operation between the U.S. and the Orient, and from interior Europe to the U.S. West Coast. A comparison of the range factor levels achieved by these series is shown on Figure 17 , derived from published airline data, company technical papers, and news releases such as that in References 20 and 21. The total improvement from the initial 707-120 model to the current 707-320B Advanced model is 35%, of which approximately 19% was due to changes to the engine and the remainder, 16%, is credited to the airframe. Likewise, on the DC-8, a gain of about 20% in aerodynamic efficiency between the initial and final series aircraft can be attributed to aerodynamic changes.

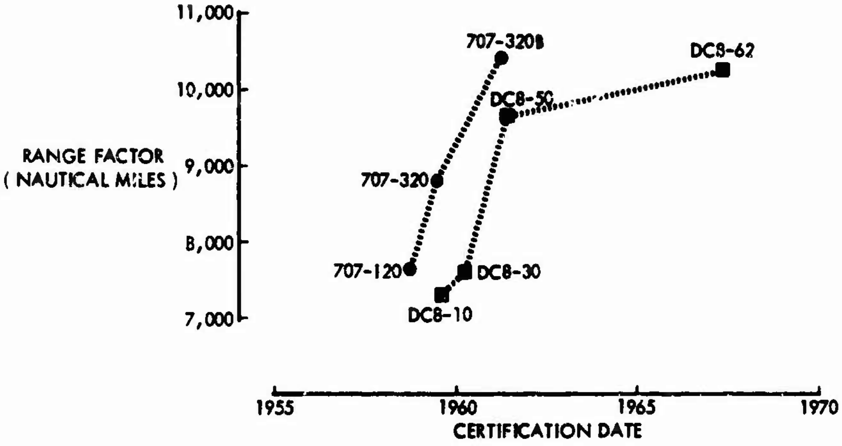

Figure 17: PRODUCT DEVELOPMENT

Configuration changes are also developed in flight tests in order to correct aerodynamic characteristics affecting stability, control, or buffet limits. These changes may bring an accompanying drag reduction as a side benefit. For example, the use of vortex generators to eliminate a premature localized separation due to boundary layer thickening in either subcritical or supercritical flow conditions may result in a lower drag level and/or a higher airplane critical Mach number as well as improved buffeting or stability characteristics.

In summary, drag improvement efforts on long range subsonic aircraft can offer potential benefits as follows:

| | |
|---|---|
| ● Cleanup | 5% |
| ● Propulsion installation changes, including struts, sound suppressor, and thrust reverser and nacelle lines | 5% |
| ● Wing leading edge and tip | 10% |
| ● Miscellaneous - cab contours, fairings, body changes | 3% |

## FLOW DIAGNOSTIC STUDIES IN FLIGHT

Flow diagnostic studies play an important role in the determination of flow conditions in localized areas on the airplane, and in understanding the fundamental aerodynamic properties of the airplane. If problems are believed to exist, the objectives of such studies are to examine the flow conditions at certain critical points of the airplane, identify problem areas where improvements can be made, and then to evaluate the effectiveness of fixes or refinements designed to resolve the problems. The flow diagnostic studies are also useful for checking the validity of theoretical or experimental drag prediction methods which, in turn, benefits the design of future airplanes.

The techniques of in-flight flow diagnostic work are similar to those used in the wind tunnel. These include surface static pressure surveys and wake or boundary layer total pressure surveys as well as flow visualization.

Static pressure surveys are often made with a multi-tube plastic belt which is temporarily attached to the airframe by an adhesive. This approach eliminates the necessity of making pressure taps in the airframe, which is not only expensive and undesirable, but simply inadmissible in some areas (such as the spar box). Total pressure surveys are performed with the aid of fixed pitot rakes or remote controlled traversing pitot probes. Flow visualization is most often done by tufts, but other techniques based on dye injection, or sublimation, have also been successfully applied.

The Boeing Company has developed a new and unique precision flow measuring instrument for diagnostic studies on aircraft in flight (References 22 and 23). The Boeing Airborne Traversing Probe acquires data in two or three dimensional flow fields with far greater accuracy and detail than possible with conventional fixed probes or pitot rakes.

The concept of this instrument and its three principal modes of operation are shown in Figure 18. The probe consists of four main components: 1) flow sensors, 2) rotating arm, 3) drive unit, and 4) mounting base. The flow sensors are mounted on an arm attached to a rotating shaft whose axis is approximately parallel with the flow direction. During operation the probe travels along a circular arc in a plane normal to the flow. The probe location relative to the airplane is determined from the measurement of the angular position of the shaft by a high precision photoelectric encoder. A single probe with pitot-static and flow direction sensors may be used for surveying boundary layers and wakes in quasi two dimensional flows such as on wings, tail surfaces, etc. A multiple probe rake may be used in three dimensional flows that are typical at intersections, jet mixing regions, etc. Several mounting options and adjustment provisions permit the installation of the instrument at practically any part of an airplane. A wide variety of sensor systems may be used, which gives a great versatility to the instrument.

A specific application of the Boeing Airborne Traversing Probe is described in the next paragraphs. This is a typical example of how flow diagnostic studies may aid in the verification of drag methodology.

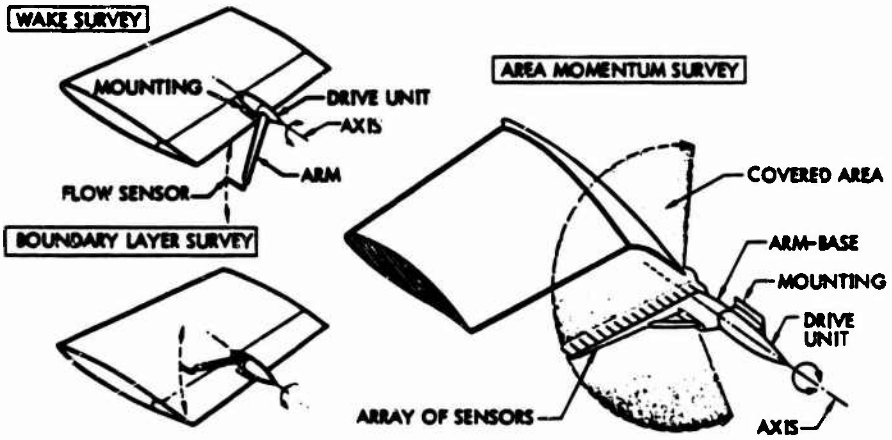

Figure 18: AIRBORNE TRAVERSING PROBE CONCEPT AND CONFIGURATIONS

## WING SECTION PROFILE DRAG MEASUREMENTS ON THE BOEING 727

A flight test program was carried out on the Boeing 727 airplane to determine the drag characteristics of the outboard wing airfoil section. The purpose of obtaining these data was to compare the actual full scale flight drag of a wing section with predictions extrapolated from wind tunnel data or from theoretical methods. The tests include wake, boundary layer and pressure distribution measurements at the 62 percent semi-span location (see Figure 19).

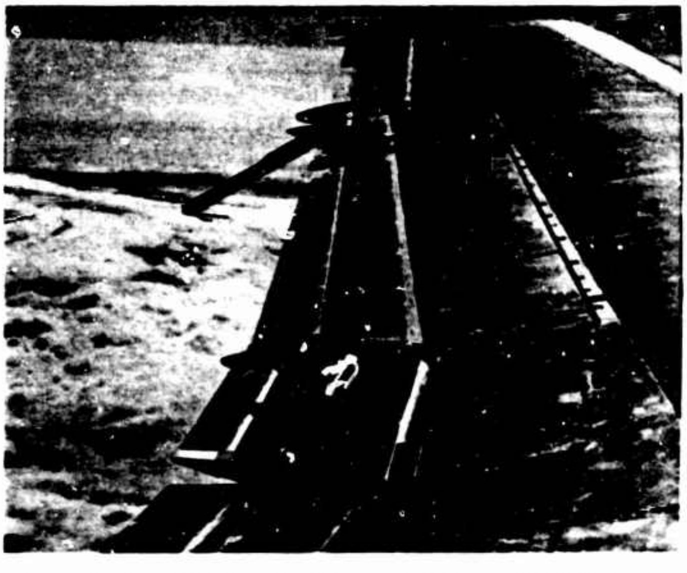

Figure 19: TRAVERSING PROBE INSTALLATION ON THE BOEING 727

The principal results of these tests were the following:

- The section drag characteristics, derived from wake survey data, showed close resemblance to the complete airplane's drag characteristics. The variation of section drag with $C_L$, for example, was nearly the same as $C_D - C_{D_i} = f(C_L)$ for the airplane. Also, the drag divergence points (M at $\frac{dC_D}{dM} = .10$) for the airfoil section and for the airplane were very close, although the airplane's drag rise curve had somewhat more creep (see Figure 20 ). This indicates that the airplane's drag characteristics in this particular case are dominated by the behavior of the outboard wing. Thus, using the outboard wing section for checking out the validity of prediction techniques may be regarded as a viable approach.

- The measured minimum section profile drag at M = .73 was about 15 percent higher than predicted from wind tunnel test data for a smooth airfoil. The wind tunnel data used in this correlation were also from wake surveys on the 727 wing. The data were adjusted to fully turbulent flow and extrapolated to flight Reynolds numbers. This quite sizeable difference between the measured and extrapolated values of $C_{d_{min}}$ has been attributed to surface roughness and excrescences on the airplane wing, although the 15 percent increase in wing section profile drag is larger than traditionally allotted in airplane drag estimates. The wing section where this survey was performed was inspected and had numerous steps and bumps due to control devices and manufacturing tolerances which would account for this local level of excrescence drag. This is not representative of the entire wing surface.

- Correlations between flight test and predictions based on wind tunnel data are shown in Figure 21 showing the wing section drag polar at M = .73 and section drag rise at $C_l = .3$. The predictions represent the traditional approach: the lift dependent part of the section profile drag, $\Delta C_{d_p}$, and compressibility drag increment, $\Delta C_{D_M}$, measured in the wind tunnel were added to the minimum section profile drag at full scale Reynolds number. Since the flight test data covering the M = .73 drag polar does not correspond to a constant Reynolds number, an adjustment of these data is necessary to make a valid comparison with wind tunnel results.

  This adjustment results in a rotation, i.e., an opening, of the flight polar, which now shows clearly lower $\Delta C_{d_p}$ values than the prediction from wind tunnel data. The different polar shapes, however, can be explained by the relatively thicker boundary layer on the wind tunnel model which results in an apparent increase of the form drag. This example illustrates the dependence of the $\Delta C_{D_p}$ term on Reynolds number.

  The correlation between the measured and predicted section drag rise characteristics as shown in Figure 21 is considered quite good, although the prediction is somewhat optimistic. There could be several reasons for this, such as: 1) Reynolds' number effects on $\Delta C_{d_M}$ (rearward shift of transition on the model with increasing Mach number, more favorable shock/boundary layer interaction on the model, etc.), 2) increase of excrescence drag with increasing Mach number, or 3) differences in local loading between the airplane and the model due to aeroelastic effects.

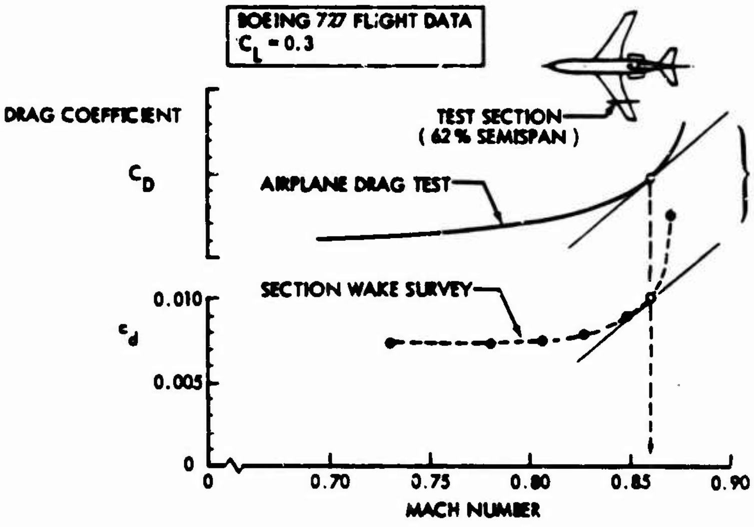

Figure 20: WING SECTION AND AIRPLANE DRAG RISE COMPARISON

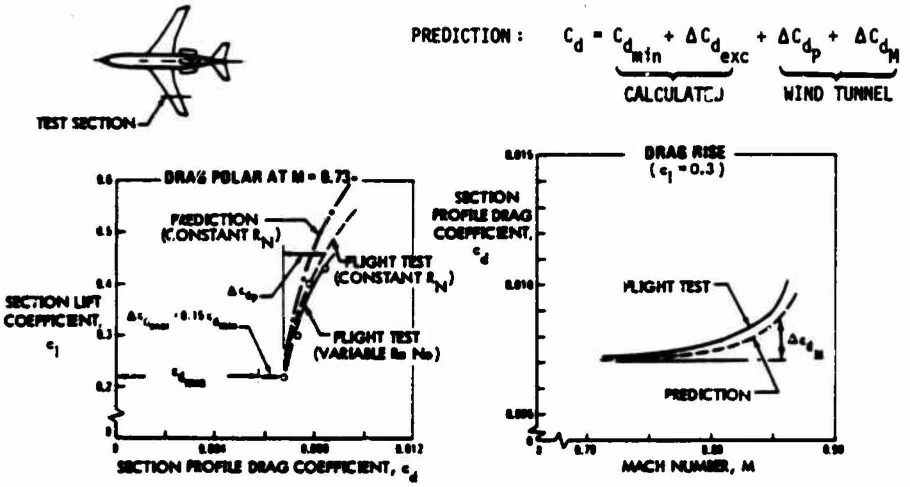

Figure 21: FLIGHT VS. PREDICTED SECTION PROFILE DRAG

## MEASUREMENT OF SPECIFIC RANGE

In the opening paragraphs of this section, an emphasis was placed upon the importance of the primary variables measured in performance, particularly miles per pound of fuel. Most of the above discussions have been concerned with drag, an inferred quantity, and it is usually assumed that accuracy in the determination of this item is equivalent to a corresponding accuracy in range performance. This is only true if a conscious effort is made to "close the loop" and reduce a given set of data simultaneously for both airframe and engine performance. In this era of specialists, attention is sometimes focussed on separate, isolated studies of interesting flight data. This may occur easily if the comparison models for engine and airframe are different, and independent efforts for correlation of flight data with "wind tunnel" or "engine specification" are undertaken. The resolution of total thrust minus drag and specific range must be a coordinated effort and is successfully completed only when both the airframe and propulsion system performance levels are established.

This process, as pursued by The Boeing Company, is illustrated by the diagram on Figure 22 . The first comparison to be made involves a look at several items - the specific range as measured directly - and also the component elements of airframe and engine performance. The result of the independent airframe and engine performance analyses will produce a set of curves which, when re-combined, will usually offer a slightly different grid of specific range than obtained directly from the flight data points. Iterative adjustments to all of the curve fairings are then applied in order to arrive at the most acceptable final performance levels.

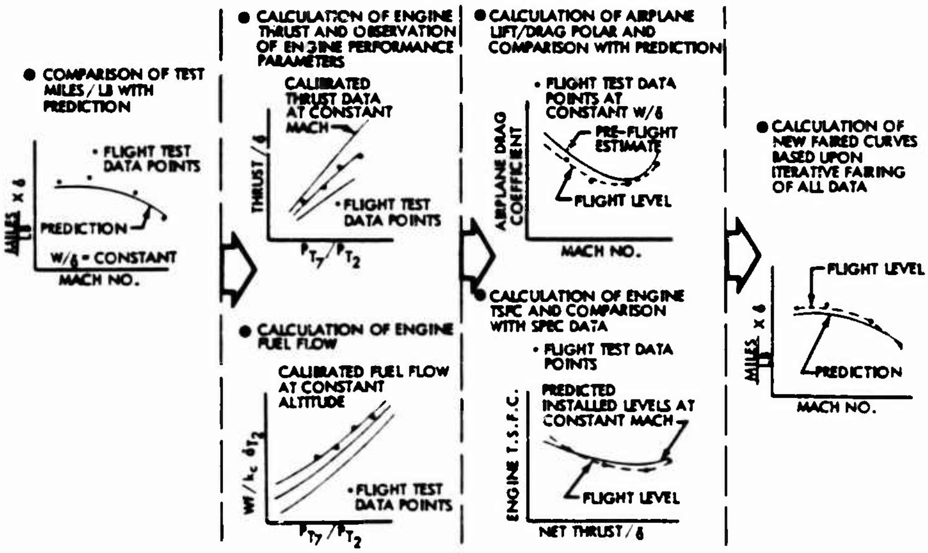
● COMPARISON OF TEST MILES / LB WITH PREDICTION
• FLIGHT TEST DATA POINTS
PREDICTION
W/δ = CONSTANT
MILES/LB × δ
MACH NO.
● CALCULATION OF ENGINE THRUST AND OBSERVATION OF ENGINE PERFORMANCE PARAMETERS
CALIBRATED THRUST DATA AT CONSTANT MACH
THRUST / δ
• FLIGHT TEST DATA POINTS
$P_{T_7}/P_{T_2}$
● CALCULATION OF ENGINE FUEL FLOW
CALIBRATED FUEL FLOW AT CONSTANT ALTITUDE
$W_f/k_c\,\delta_{T_2}$
• FLIGHT TEST DATA POINTS
$P_{T_7}/P_{T_2}$
● CALCULATION OF AIRPLANE LIFT/DRAG POLAR AND COMPARISON WITH PREDICTION
• FLIGHT TEST DATA POINTS AT CONSTANT W/δ
PRE-FLIGHT ESTIMATE
AIRPLANE DRAG COEFFICIENT
FLIGHT LEVEL
MACH NO.
● CALCULATION OF ENGINE TSFC AND COMPARISON WITH SPEC DATA
• FLIGHT TEST DATA POINTS
PREDICTED INSTALLED LEVELS AT CONSTANT MACH
ENGINE T.S.F.C.
FLIGHT LEVEL
NET THRUST / δ
● CALCULATION OF NEW FAIRED CURVES BASED UPON ITERATIVE FAIRING OF ALL DATA
FLIGHT LEVEL
PREDICTION
MILES/LB × δ
MACH NO.

Figure 22: DEVELOPMENT OF AIRPLANE POLAR AND ENGINE PERFORMANCE

# WIND TUNNEL TECHNIQUES

The wind tunnel can be considered an analog computer designed to simulate the flow field about an airplane in free flight. Actually, since many large wind tunnels are directly connected to a digital computer, such an installation represents a hybrid computer system. The digital portion of this system controls tunnel conditions and data acquisition. It also reduces the data and corrects them for imperfections in simulation of the airplane flow field in the wind tunnel. At the same time, the computer provides a real time display of the test results, a capability which greatly enhances the decision making process of the aerodynamicist. The reduction of the data acquired in the tunnel consists of the following three steps:

(1) Processing of the signal output of balances, pressure transducers, thermocouples, etc., to obtain the true forces and pressures acting at the model.

(2) Correction of the forces measured to account for the differences between the flow field in the tunnel and the flow field in free flight.

(3) Extrapolation of the free air model data to the flight regime of the full scale airplane.

Signal processing needs no discussion here, although the importance of on-line data reduction and display is sometimes overlooked. Development testing in the ultimate sense consists of a series of rejections and refinements until either the optimum design is determined or a time-limited selection is made.

With respect to Item (2) above, three types of corrections are required: a) corrections to account for imperfections of the flow in the test section, b) corrections to account for the effect of the limited size of the test section (tunnel wall corrections), and, (c) corrections to account for the effects of the model suspension system (aerodynamic interference, elastic deflections). The first correction includes the static pressure calibration, tunnel.bouyancy, and upflow; the second item includes the effect of the tunnel velocity profile and tunnel porosity. The third item presents the more difficult problem, that of identifying and adjusting for the effects of the model suspension system.

## MODEL SUSPENSION EFFECTS

A significant amount of uncertainty of the drag measurements is introduced by the model suspension system. Some of the more common suspension methods are shown in Figure 23 . Each of the different mounting systems introduces a different set of upflow and buoyancy corrections due to its own pressure field and due to obstruction of part of the wind tunnel cross-section. In addition, viscous drag is generated at the intersection between the model and its mounting. At higher Mach numbers the interference between the model and its mounting system can lead to large errors in the determination of drag divergence Mach number if appropriate corrections are not applied.

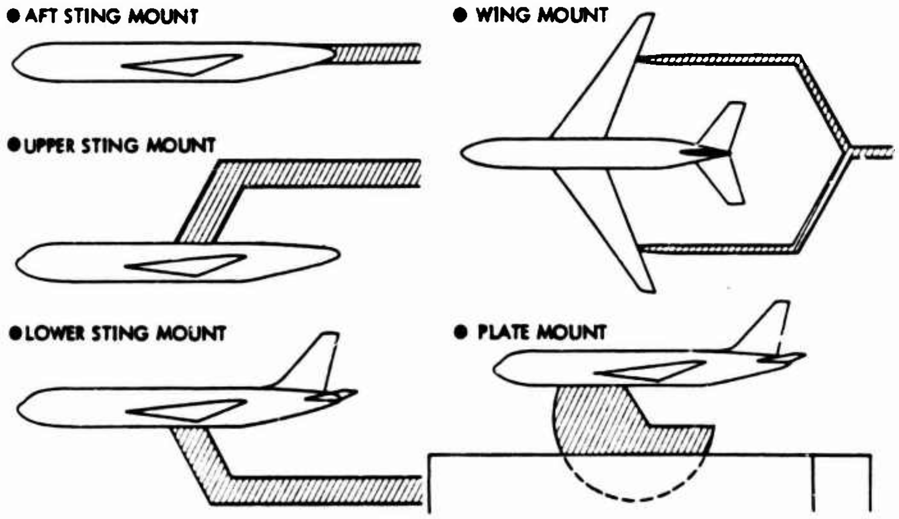

Figure 23: TYPICAL MODEL SUSPENSION SYSTEMS

Some special problems require unique mounting systems. For example, a double sting, if the flow properties at the fuselage aft end have to be investigated, or a floor-mounted half model for large scale wing-nacelle installation evaluation. A fairly recent development is the use of a magnetic suspension system. The model is held and stabilized by a strong magnetic field without any mechanical connections. This promising method, however, is still in the developmental stage and has not been used in airplane configuration development.

Support system interference effects can be determined by flying various combinations of model supports and dummy struts with the model upright and inverted (Reference 24). However, there always exists some uncertainty since the support corrections have to be determined as the small difference between two large numbers. These corrections may noticeably change both the incompressible polar shape and the compressibility drag increments.

## TRIP STRIP APPLICATION

Due to the large difference in Reynolds number between wind tunnel and flight, there is a considerable difference in the boundary layer development on the model components, thereby creating some obvious variations in aerodynamic forces. Most noticeable is a change in drag level and a significantly higher maximum lift coefficient achievable in the case of the full scale airplane. While the boundary layer on a large aircraft is nearly always fully turbulent, extensive regions of laminar flow may exist on a wind tunnel model flown at low Reynolds numbers. The size of the laminar flow regions depend on many factors such as streamwise pressure distribution, the surface quality of the model and the free stream turbulence in the tunnel flow. Small changes in any of these items can significantly affect the size of areas with laminar boundary layer flow, and thus model drag.

Standard practice in the past has been to use a forward trip at 5% to 10% chord in order to simulate full scale turbulent flow and thereby more confidently adjust the wind tunnel profile drag data for Reynolds number. Wing pressure distributions so obtained matched flight observations and theory, particularly for subcritical flow conditions. Furthermore, data repeatability is greatly improved when the point of transition is fixed by a forward trip strip on all model components.

The most widely used trip strip consists of a narrow band of carborundum grit. Based on data of Braslow (Reference 25), the grit size should be selected such that the Reynolds number based on local flow conditions and nominal grit height is greater than 600. Excessive grit size should be avoided to minimize the drag created by the trip strip itself. A trip strip can only be fully effective when it is placed in an area where the stability of the laminar boundary layer is already low enough so that the perturbations introduced by the trip can trigger transition. This condition is usually reached when the Reynolds number based on the length between the stagnation point and the trip location is greater than 1 x $10^5$. This condition determines the most forward trip location.

The spanwise flow component in the case of tapered swept wings causes the accumulation of boundary layer material towards the wing tip. Under those conditions, the thickness of the laminar boundary layer can locally be much larger than indicated by simple two-dimensional boundary layer theory. In fact, the boundary layer can become thick enough, that a trip sized according to Reference 25 is below the critical roughness and cannot trigger transition. The limited amount of experimental data available on this subject suggests an increase in trip size toward the tip of a swept wing as shown in Figure 24 . The effectiveness of a trip strip should always be verified by some flow visualization technique.

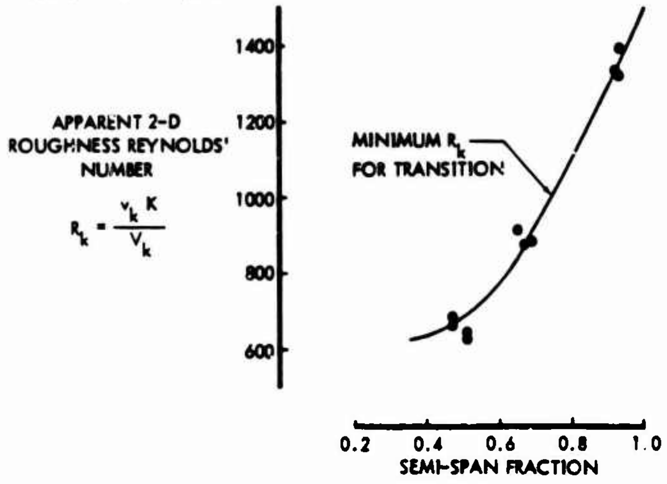

Figure 24: ROUGHNESS REYNOLDS' NUMBER FOR TRANSITION

Unlike the turbulent boundary layer, laminar boundary layers can negotiate only very weak adverse pressure gradients without separation. Therefore, it is essential that the boundary layer be fully turbulent at the location of shock wave. But on the other hand, tripping the boundary layer at a forward location will lead to unrealistically thick boundary layer at the shock which may result in a shift in the shock position or in a premature shock induced separation (Reference 26). By properly fixing the boundary layer transition point on the wind tunnel model, full scale conditions can be quite closely simulated at the usual wind tunnel Reynolds numbers. The required location of the trip strip can be predicted theoretically with acceptable accuracy by simulating the boundary layer characteristics at the airfoil trailing edge. A more expedient and practical approach for determining the location of the trip strip on a three-dimensional wing is to observe the shock pattern without tripping, and thereby select the desired location at the chosen test Mach number and angle of attack.

In summary, trip strips are essential for the proper simulation of full scale conditions on a wind tunnel model, but they must be carefully placed, considering the pressure distribution about the individual components, free stream Mach number, and the purpose of the test. Flow visualization of the wing upper surface with no trip, and with an aft trip is desirable for the determination of the extent and intensity of the shock under varying conditions of Mach number and angle of attack. Visual inspection of the shock patterns thus obtained can be a primary guide to the use of the force and pressure data. Philosophically, the data developed from the wind tunnel tests for prediction must be synthesized from forward and aft trip results, and this synthesis encompasses all speeds and lift loading conditions. Practically, a judgment must be made from limited and specific sets of data, usually selected to represent the normal, typical operating conditions.

## EXTRAPOLATION OF WIND TUNNEL RESULTS TO THE FULL SCALE AIRPLANES

Several operations are necessary to arrive at the full scale airplane drag using corrected model data as a starting point. (1) The model data must be corrected for scale effects due to the one or two orders of magnitude difference in Reynolds numbers between the model and the airplane. (2) The drag of items which cannot be simulated in model test has to be assessed. These items include surface roughness, excrescences, leakage and losses due to the air conditioning system. (3) The impact of scale effect on polar shape and drag rise must be decided. (4) Corrections for thrust effects, if any, must be applied.

Prediction of the full scale airplane drag at high subsonic Mach numbers is presently based entirely on the wind tunnel measurements of the drag increments due to compressibility. There is a definite lack of theoretical methods to reliably assess the drag rise characteristics of a complete airplane configuration, and in particular, the effects of Reynolds number on the drag rise.

## REYNOLDS NUMBER EFFECTS

For most of the transport aircraft now flying, the effects of Reynolds number upon performance in the cruise configuration has been predicted with a reasonable degree of accuracy on the basis of low Reynolds number wind tunnel data. The new generation of supercritical, aft loaded airfoil sections, however, are more sensitive to scale effects than earlier airfoils. Small changes in boundary layer displacement thickness can cause a large shift of the wing upper surface shock location, affecting both airplane drag and stability. Thus, more emphasis is now being placed on high Reynolds number wind tunnel testing. The development and application of advanced aerodynamic configuration features is difficult to achieve if the experiments do not closely simulate full scale boundary layer conditions.

## FLOW DIAGNOSTIC STUDIES IN WIND TUNNEL

The most common of the flow diagnostic type of tests is the measurement of the surface static pressure distributions. This not only gives a very good insight into the probable behavior of the model boundary layer flow, but also often permits the integration of static pressure along model components from which the acting pressure drag may be estimated.

Total pressure surveys, either in the form of boundary layer measurements on the surface of the models or in the form of wake surveys downstream of the model, also play an important role in flow diagnostic work. Several ways of measuring boundary layer characteristics are shown in Figure 25 . Because of the relatively thin boundary layers on wind tunnel models, a very high precision is required in measuring the probe position from the surface. Compactness is another very stringent requirement to eliminate unwanted interference effects due to the survey apparatus. Traversing probes are, in general, preferable over fixed pitot-rakes because of their greater data resolution capability and compactness.

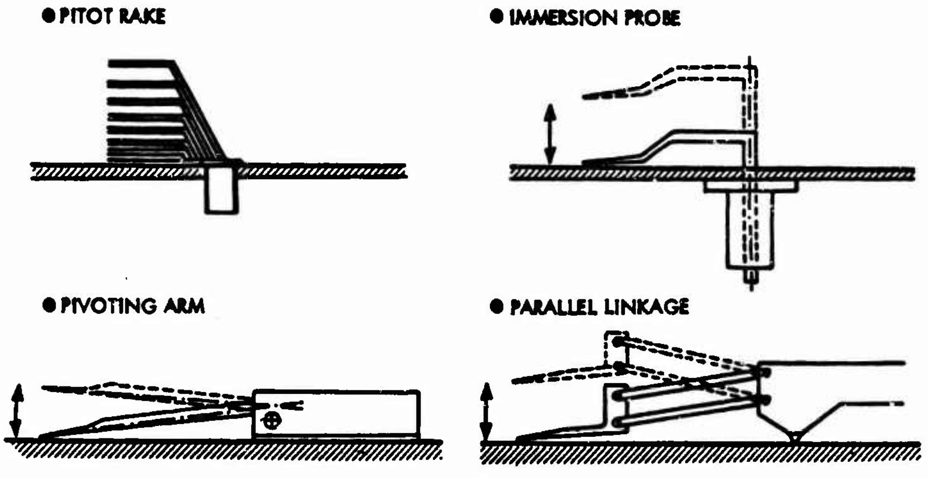

Figure 25: VARIOUS BOUNDARY LAYER SENSING DEVICES

Flow visualization techniques are of two basic kinds, such as surface flow indicators and flow field indicators. The first category includes the various evaporation, oil flow (See Figure 26 ) and tuft techniques, while the second class constitutes the shadowgraph and Schlieren type of flow visualization.

A few typical examples of flow diagnostic type wind tunnel tests will be briefly described in the forthcoming sections.

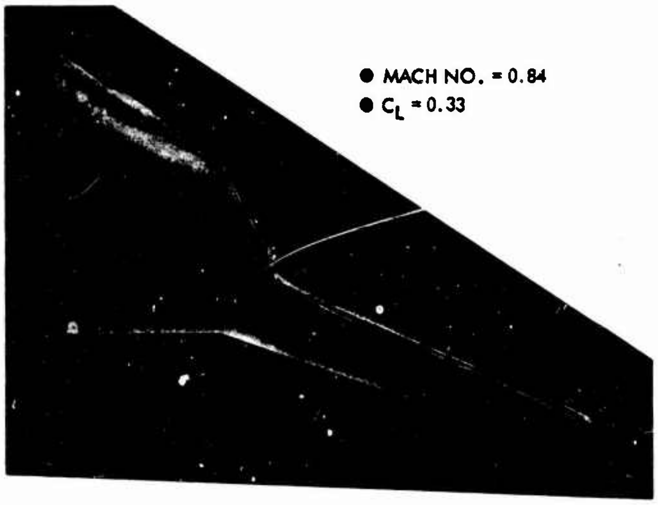

Figure 26: FLOW VISUALIZATION - OIL FLOW

## FLOW STUDIES ON A JET TRANSPORT CAB

A comprehensive investigation of the flow characteristics around the pilot cab of contemporary jet transports was made in a wind tunnel test using the Boeing 737 model (Reference 27). The purpose of the study was to broaden the understanding of the nature of flow perturbances and associated drag penalties caused by the conventional cab designs. It was hoped that this knowledge would lead to improved cab designs on future airplanes. The test program included static pressure surveys, boundary layer surveys and flow visualization beside the standard force balance data. A faired nose configuration was also tested after the basic cab for comparison purposes. The static pressure survey indicated that a sharp negative pressure peak with locally supersonic flow above M = .75 develops at the side corner post of the windshield, and high positive Cp's prevail over a large portion of the windshield and nose cone (see Figure 27). Oil flow studies showed that a strong crossflow forms ahead of the windshield which leads to flow separation and vortex shedding at the side posts of the windshield. The boundary layer surveys revealed that the momentum thickness was significantly increased in comparison with the smooth nose in the region affected by the cab, especially in the vicinity of the vortex trails shedding from the windshield (see Figure 28 ). The force balance data showed that the drag increment due to the cab was about 1% of the total drag at M = .7 and about 2.5% of that at M = .85.

On the basis of these results it was recommended that future airplanes should be designed with smoother cab contours and this inspired the development of the 747 cab, which represents a considerable improvement over the classical 707 design.

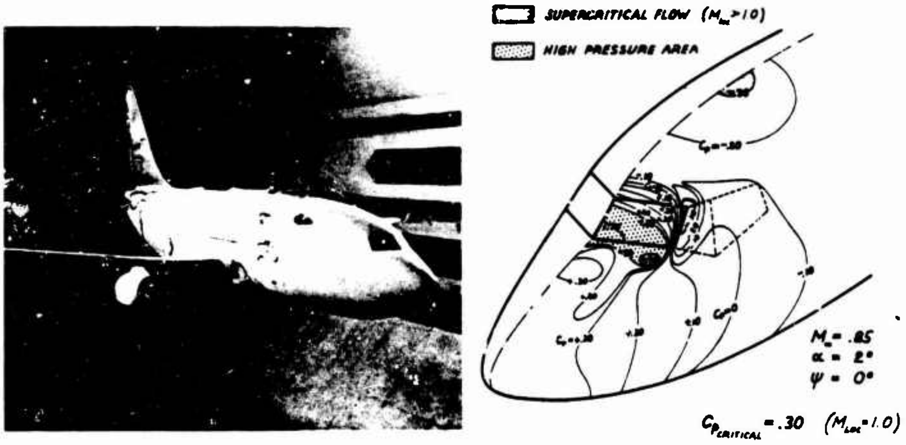
SUPERCRITICAL FLOW ($M_{loc}$>1.0)
HIGH PRESSURE AREA
$C_p$=-.30
$C_p$=+.30
$C_p$=0
$M_\infty$= .85
α = 2°
ψ = 0°
$C_{P_{CRITICAL}}$=.30 ($M_{loc}$=1.0)

ISOBARS ON THE FOREBODY

Figure 27: CAB FLOW STUDY IN WIND TUNNEL

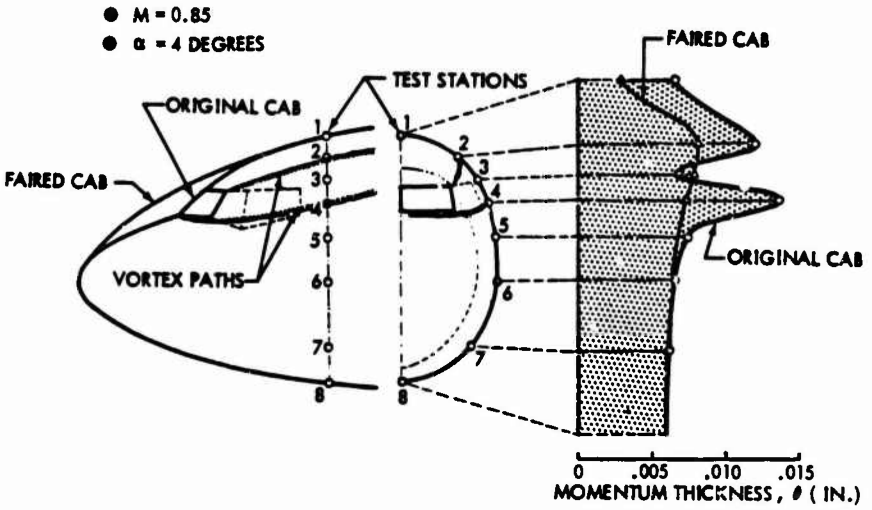
● M = 0.85
● α = 4 DEGREES
FAIRED CAB
TEST STATIONS
ORIGINAL CAB
FAIRED CAB
VORTEX PATHS
1
2
3
4
5
6
7
8
ORIGINAL CAB
0
.005
.010
.015
MOMENTUM THICKNESS, θ ( IN.)

Figure 28: EFFECT OF CAB FAIRING ON THE BOUNDARY LAYER MOMENTUM THICKNESS

## WING PROFILE DRAG MEASUREMENTS ON THE BOEING 727

A typical example of flow studies to analyze a wing design is demonstrated by tests of the Boeing 727 model. Measurements included wake traverses at nineteen locations along the span and supplementary static pressure surveys and flow visualization. The test setup is shown on Figure 29 . The main objective of the test was to determine the spanwise variation of profile drag as represented by the wake momentum loss. The results then were correlated on the one hand with theoretical calculations to verify such computation methods and, on the other hand with flight test wake drag measurements which in turn were intended to check the validity of scaling techniques, including the estimation of surface roughness and excrescences on the real wing. These correlations were described in a previous section of this paper.

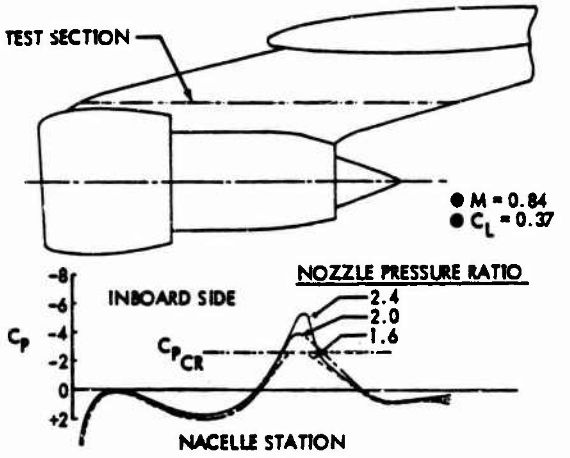

Figure 33: EFFECT OF NOZZLE PRESSURE RATIO ON STRUT PRESSURES

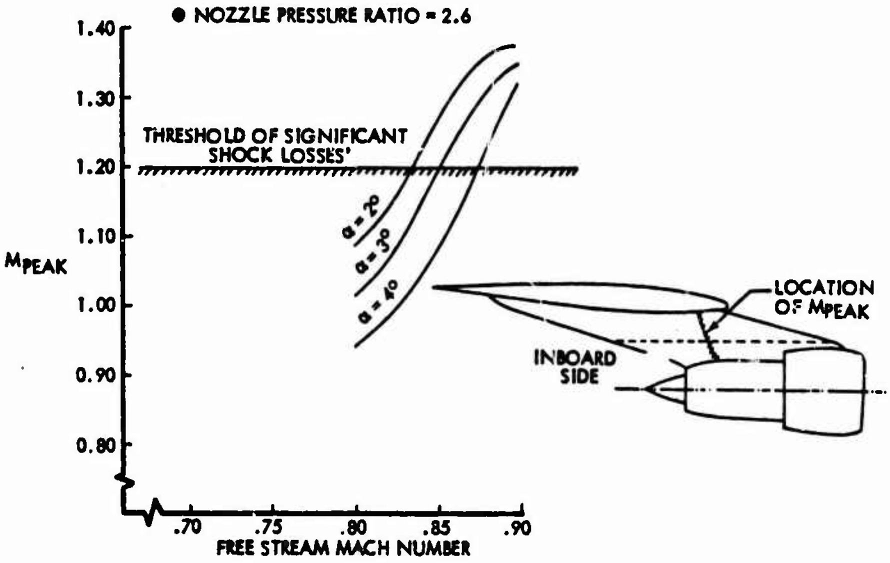

Figure 34: PEAK MACH NUMBER ON THE PYLON

## ADVANCES IN TECHNIQUES FOR ANALYTICAL LIFT AND DRAG PREDICTION

The contemporary aerodynamicist has a variety of powerful analysis tools available to him, which have altered the focus of the aerodynamicist's activity. With the traditional drag methods, the technical challenge was mainly to estimate the drag of a given configuration. But the current focus and use of the emerging analytical methods is more to design the configuration to produce the desired lift while controlling the sources of unnecessary drag. The visibility provided by modern analytical methods which permits the identification and elimination of unnecessary drag sources serves to increase the reliability of drag prediction methods. The modern analytical methods also provide a greatly expanded opportunity for the design of radically new configurations, with increased confidence in the prediction of their drag and with the need for less exploratory testing to establish initial feasibility and later design refinement. In the following discussion, the components of a complete airplane will be considered in turn: airfoils, wings, and bodies, empennages, nacelles, and finally special aspects of configuration analysis.

pages 4-25-4-26 are blank

## AIRFOILS

Current practice for the design of subsonic wings typically uses the outboard wing section as the basis for the performance characteristics of the complete wing. The sectional load and isobar pattern of the outboard wing are generally chosen to reflect known aerodynamic characteristics of associated two-dimensional airfoil sections. The outboard upper surface isobar distribution is generally embodied in the wing root region as well, and serves as a basis for tailoring the wing root geometry. Consequently, the design of an efficient subsonic wing begins with the development of suitable two-dimensional airfoil sections.

The design of two-dimensional sections in the recent past was largely based on the theoretical calculation of their pressure distributions at subcritical Mach numbers, a capability that is now routine with modern computers. Figure 35 shows a typical calculated result for an advanced, rear-loaded section. The experimental pressures are shown for comparison. The effect of the boundary layer on the pressures may also be included in such calculations, although this was not done for Figure 35 . While being very accurate at low speeds, these basically linear computational methods cannot calculate the transonic pressure distribution of the airfoil at its cruise condition. Consequently, a design process evolved based on empirical extrapolation of subcritical potential flow characteristics into the transonic regime to allow aerodynamicists to design airfoils posessing good transonic characteristics which could be applied to the outboard portion of a wing. However, the transonic lift and drag cannot be calculated directly by this process, since accurate theoretical transonic pressure distributions are ordinarily not available. Consequently, those needed performance characteristics are obtained through experimental testing of the sections designed by the theoretical/empirical approach.

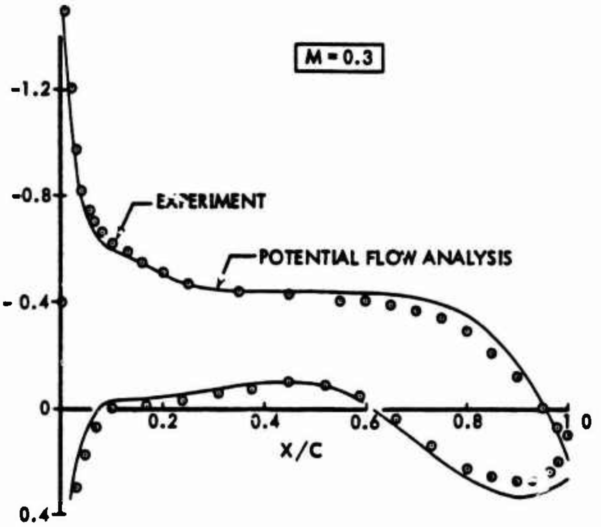

Figure 35: THEORETICAL PREDICTION OF SUBCRITICAL PRESSURES ON A TWO-DIMENSIONAL AIRFOIL

Other empirical methods have been devised that are aimed at obtaining a direct prediction of the transonic potential flow pressure distribution. An example is the procedure of Sinnott (Reference 28). Figure 36 shows the predicted transonic pressure distribution by a method similar to that of Sinnott, for the same airfoil as on Figure 35 . It is seen that the method predicts the supersonic region quite accurately, up to the point of shock impingement. Whereas the boundary layer calculation for the predicted pressures might produce an accurate estimate of skin friction, the pressure drag and lift components would be in error by a sizeable amount because of the error in shock location. Consequently this approach was generally not successful in eliminating the requirement for extensive experimental testing of two-dimensional airfoil sections.

The obvious need was for a computational procedure capable of accurately predicting the nonlinear transonic flow about an airfoil section, and there has been extensive progress in this area in recent years emanating from the work of many investigators. Developments have now reached the point where the aerodynamicist can calculate, rather routinely, the inviscid transonic pressures for an airfoil, albeit at considerable computational expense on a large computor. Figure 37 gives the predicted pressures for the same airfoil as on Figures 35 and 36 , as calculated by the method of Garabedian and Korn (Reference 29), only one of several currently in use. It is seen that the agreement between theory and experiment is excellent when proper account is taken of the boundary layer. It is also apparent that proper representation of the boundary layer and its interaction with the inviscid flow is essential in the theoretical analysis. This further capability is still in the developmental stage and cannot yet be classed as routine. Nevertheless, developmental computations, for the example shown, predict a drag of 100 counts, whereas the measured drag is 97 counts. The predicted drag is composed of skin friction and pressure drag, with the skin friction found from an integral boundary layer solution scheme with an empirical step thru the shock, and the pressure drag found by integrating the calculated pressure forces. As developments proceed, a routine analytical capability will become available to the aerodynamicist for reliably predicting the lift and drag of new transonic airfoils, and this will lead to more rapid exploration for advanced airfoil designs without the need for a comprehensive parallel testing program.

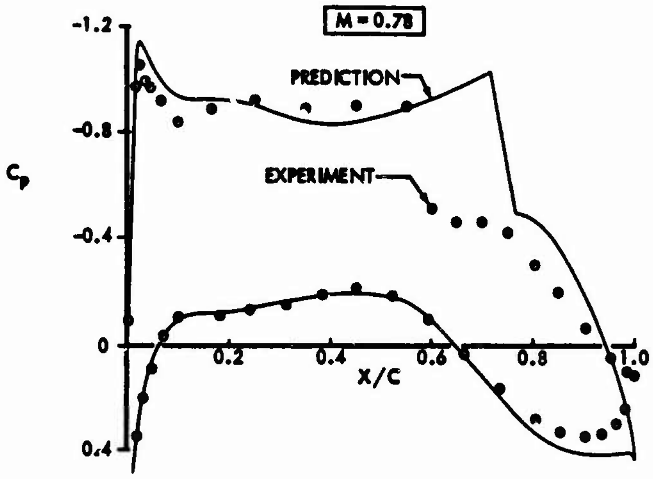

Figure 36: EMPIRICAL PREDICTION OF TRANSONIC PRESSURES ON A TWO-DIMENSIONAL AIRFOIL

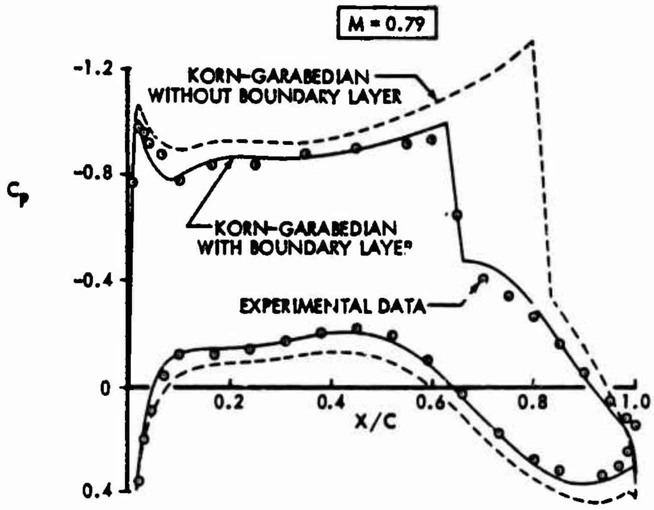

Figure 37: ANALYTICAL PREDICTION OF TRANSONIC PRESSURES ON A TWO-DIMENSIONAL AIRFOIL

## WINGS AND BODIES

With known transonic lift and drag characteristics of the airfoil as a base, and with the rules of simple sweep theory as a moderator, the aerodynamicist can approach the design of the wing and the estimation of its lift and drag with increased confidence. One procedure is as follows: the designer begins with the selection of an airfoil section that will provide the desired performance, at specified values of sweep and wing thickness based on simple sweep theory considerations. The subcritical design condition pressures (i.e., aralagous to those of Figure 35 of the airfoil) are corrected by simple sweep theory to become the upper and lower isobar design goals for the wing in the presence of the body. The governing assumption is that these subcritical isobars will develop into the same transonic pressures that were observed for the basic two-dimensional airfoil, i.e., analagous to those of Figure 36 , thus reproducing for the wing the transonic performance observed for the airfoil. Theoretical analysis and design methods are currently available for the wing-body configurations that routinely produce essentially exact solutions for subsonic inviscid flows, but with the limit that the supercritical flow regions are not correctly predicted. Figure 38 illustrates the representation provided by a theoretical analysis method typical of those in routine use, which involve surface distributions of source panels.

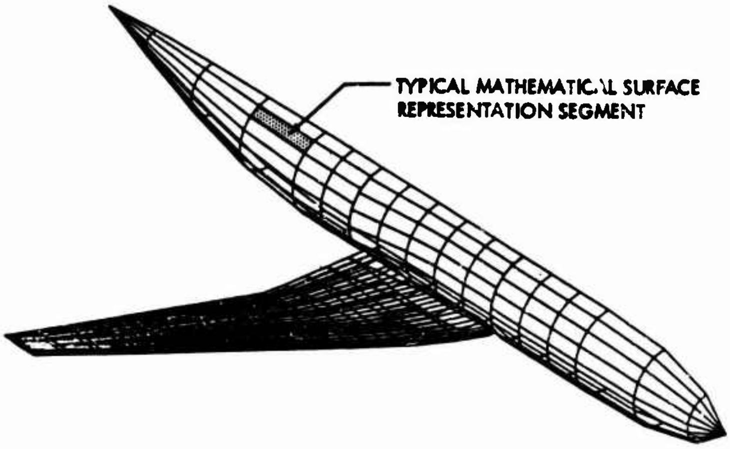

Figure 38: POTENTIAL FLOW SOURCE PANELS FOR WING-BODY SOLUTION

The first order of business for the aerodynamicist is to tailor the wing's twist, camber and thickness forms to achieve a good root isobar pattern that blends into the intended outboard isobar pattern, while producing favorable span loading distribution. This process usually involves iterative use of the theoretical design and analysis tools and leads to trades and compromises of various detailed objectives, a prime underlying objective being to prevent unwanted drag while providing the intended lift at the cruise condition and maximizing structural efficiency.

It should be pointed out that this design produces the shape of the wing at the 1-g load condition. Further steps are required to determine the required jig shape or for other flight loadings. The same analysis methods used to design the wing can be used to formulate an aerodynamic influence coefficient matrix, which, when coupled to the structural flexibility matrix, allows determination of the jig shape. In this way, the aeroelastic design cycle and the airplane performance can be controlled in a disciplined framework common to each technical area - performance, structures, and flight dynamics. The timing of the preliminary design cycle as expressed in Reference 30 can be considerably compressed with today's analytical capabilities.

Figure 39 compares various analytical and experimental results for a 30° sweep wing and body. Two wing sections are shown, one near the side of the body, and one outboard in the region of infinite yawed wing flow. The experimental pressures are predicted very well at this subcritical Mach number. The outboard section at this Mach number is also compared with the subcritical pressures for the base airfoil, after the simple sweep correction has been applied. It is seen that the wing design process has duplicated the essential features of the airfoil section on the outboard wing. Also shown is the experimental result for the wing at its cruise Mach number and the experimental result for the two-dimensional airfoil, corrected by simple sweep (Figure 40 , and it is seen that the intended cruise pressure distribution has indeed been achieved on the wing. Finally, the experimental and analytical span loads for this wing are given on Figure 41 , showing the degree of support the designer receives from current wing-body analysis methods.

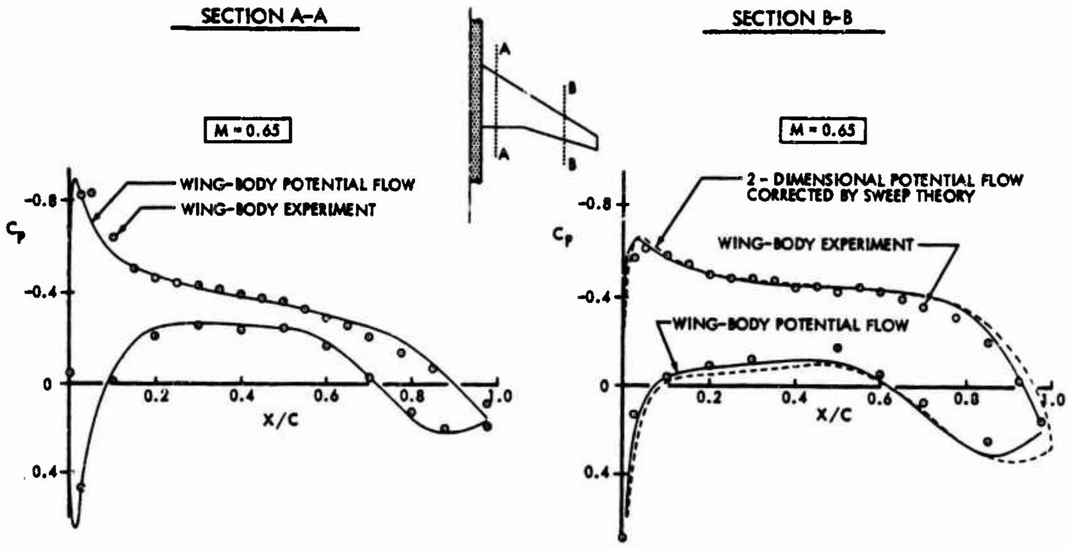

Figure 39: COMPARISON OF THEORY & EXPERIMENT FOR WING-BODY GEOMETRY

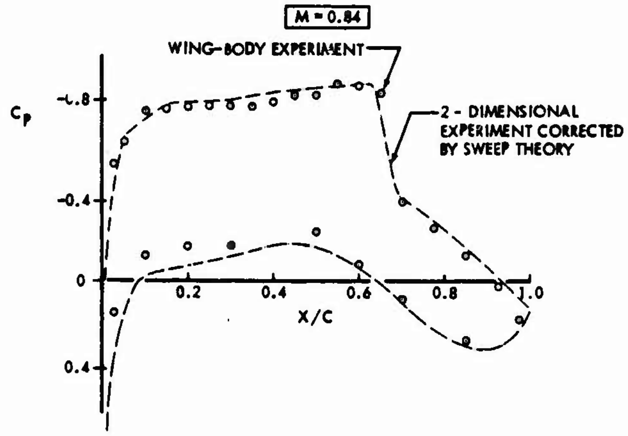

Figure 40: COMPARISON OF THEORY & EXPERIMENT FOR WING-BODY GEOMETRY (SECTION B-B)

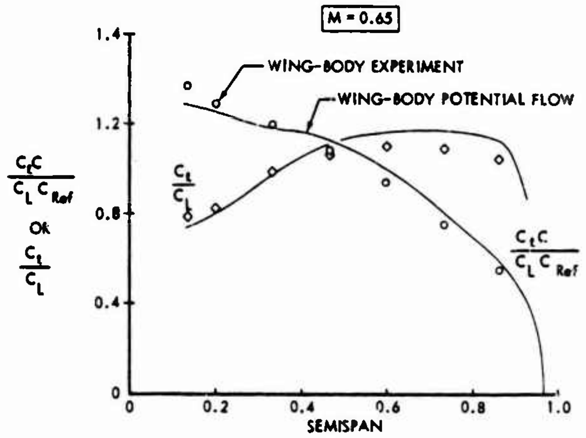

Figure 41: POTENTIAL FLOW AND EXPERIMENTAL SPAN LOADING COMPARISONS

The design and lift prediction for aircraft intended to cruise in the near-sonic speed regime pose special problems to the configurator, but can be analyzed by the aerodynamicist with the same potential flow techniques as were presented above. The special configuration problems are concerned with satisfying the requirements of sonic area ruling, including the effect of lift compensation. These will determine a body area distribution that will be consistent with the wing's thickness distribution and planform. Once the body is specified, the task of the aerodynamicist becomes as routine as for conventional subsonic transports, that is to determine the wing's twist, camber and resulting chordwise and spanwise lift distribution. Figure 42 illustrates the drag rise performance of a wing-body that was analytically designed for near-sonic speeds.

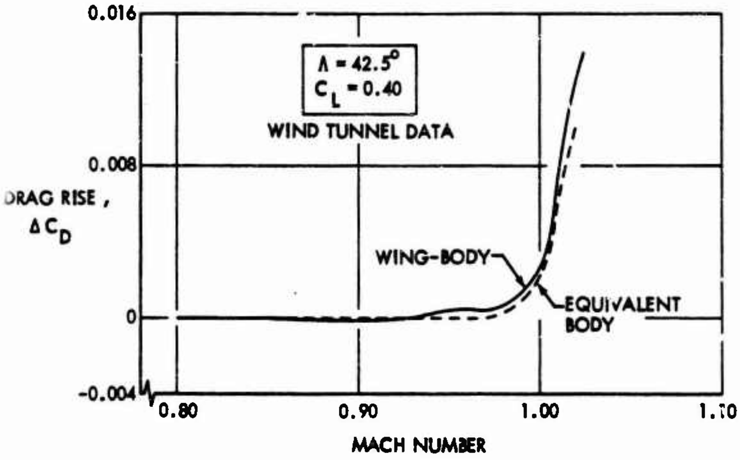

Figure 42: PERFORMANCE OF TRANSONIC WING-BODY DESIGNED WITH POTENTIAL FLOW METHODS

Taken together, Figures 39, 40 and 41 are proof that the pressures on a wing and body, and consequently the lift, can be calculated with a high degree of accuracy. This allows the drag of the wing to be approached analytically as well. With the $C_{D_p}$ drag method, the wing drag may be expressed as:

$$C_{D_{wing}} = C_{D_p} + C_{D_i} + \Delta C_{D_{interference}} + \Delta C_{D_M} \qquad (3)$$

where $C_{D_p} = C_{D_{pmin}} + \Delta C_{D_p}$

$C_{D_i}$ = induced drag, $\left( \frac{C_L^2}{\pi AR} \right)$

$\Delta C_{D_{interference}}$ = drag due to corner flows in intersection regions

$\Delta C_{D_M}$ = drag rise effect

On a component basis, the profile drag, $C_{D_p}$, is made of skin friction and pressure drag due to the boundary layer. These are both predicted by obtaining a boundary layer solution on a strip basis for the wing, using the analytical pressures, and applying the well-known Squire-Young drag formula. The deviation of induced drag from the elliptic ideal can be calculated from Trefftz plane methods, using theoretical spanwise load distributions. Figure 43 demonstrates that this procedure can accurately provide these components of the wing drag. The remaining components, $\Delta C_{D_{interference}}$ and $\Delta C_{D_M}$, must still be provided empirically. Being able to calculate analytically the major portion of the wing drag allows the aerodynamicist to more accurately estimate the lift and drag while reducing the dependence on empiricism, a particularly valuable capability when dealing with new or unusual configuration for which an experimental data base may not be available.

The pressures on the body are provided along with those for the wing by most of the present potential flow analytical methods. Local body problem areas such as aft body closure or upsweep may be evaluated on a pressure gradient criterion, but the state-of-the-art currently prohibits boundary layer calculations for a realistic body with crossflows arising from wing and local body effects. Consequently, evaluation of the total drag of the wing-body combination must still involve the application of empirical factors, with confirmation by wind tunnel tests.

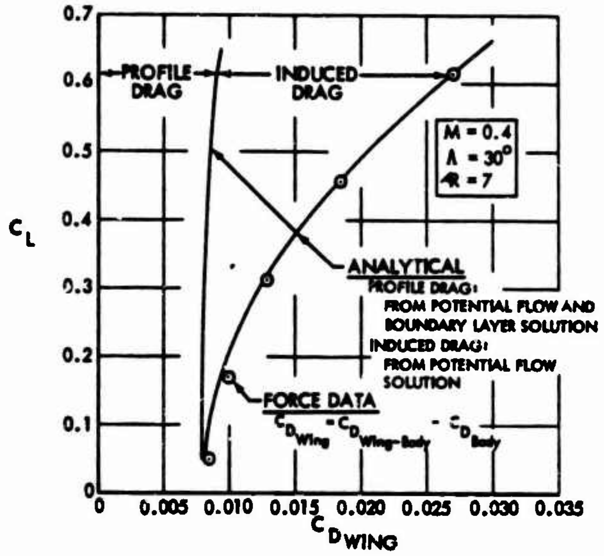

Figure 43: ANALYTICAL CALCULATION OF WING DRAG

## EMPENNAGES

The design and analysis of the empennage can be approached with these same three-dimensional potential flow analysis methods. The approach involves the theoretical design of the horizontal tail in the presence of the body, the vertical tail and the wing's downwash field. The objective is to achieve a camber, twist and thickness distribution that provide an efficient tail loading within the context of preventing undue drag while providing the required lift. Figure 44 shows examples of the twist distribution for a T-tail and a low horizontal tail both designed to have the same spanwise loading (elliptic in this example). It is noticed that an elliptically loaded tail can be far from flat, and that the twist near the fin or body is of opposite sign, depending on whether the tail is a T-tail or a low tail.

The analysis techniques used for this design provide pressures on both the vertical and horizontal tail. The boundary layer can thus be calculated and the skin friction and pressure drag obtained in a manner similar to that for the wing. Total airplane induced drag can be calculated from a Trefftz plane analysis. The interference component and drag rise component of tail drag must still be obtained by comparisons with previous designs and the application of empirical factors.

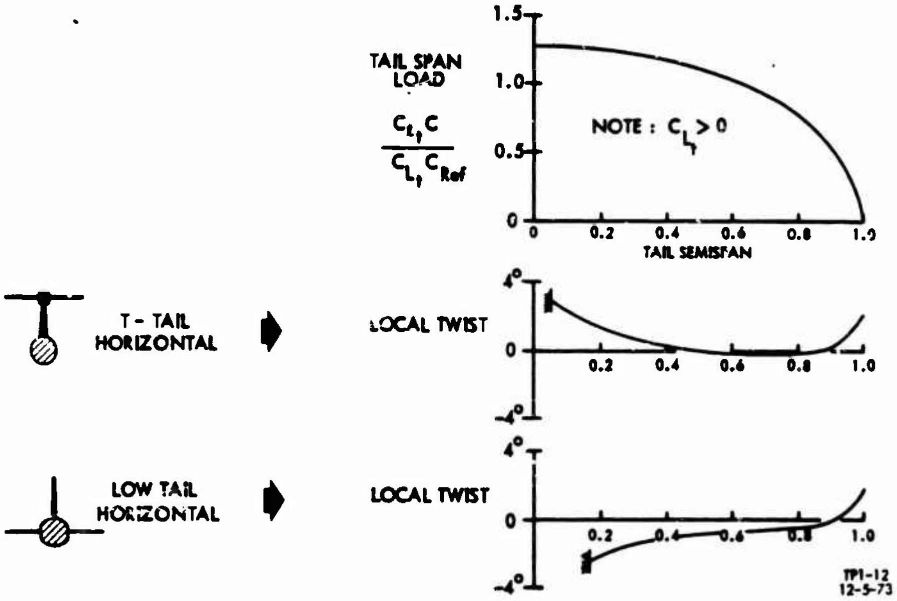

Figure 44: HORIZONTAL TAIL TWIST FOR ELLIPTICAL TAIL LOAD

## NACELLES

The remaining principal airplane component to be considered is the power plant installation. Traditionally nacelles are first optimized in isolation (axisymmetric flow) and then installed on an airplane in such a way that interference effects are minimized. Accordingly we first considered isolated techniques and then installation effects separately.

### Isolated Design

Typically nacelle design is divided into two disciplines. The first encompasses the inlet and the second the exhaust system (afterbody and plug). The inlet will be considered first. The inlet must perform well over a wide range of mass flows and Mach numbers; it must provide clean airflow to the engine while preserving good external drag characteristics. In recent years, inlet design has been approached in the same manner as airfoil design. An empirical process has evolved for designing inlet shapes at subcritical Mach numbers so as to have desirable characteristics at the cruise Mach number. The inlet wall pressure distribution can be calculated at the subcritical case and the boundary layer can be predicted. These calculations can provide an assessment of the external inlet forces for the design airflow condition.

More recently finite difference techniques have been developed which can accurately predict the inviscid transonic inlet flow. Shock waves are predicted and losses can be integrated to compute the nacelle drag rise. These methods, coupled with a boundary layer analysis, will soon reduce considerably the amount of isolated wind tunnel testing required.

The exhaust system design is perhaps harder to approach analytically and engineers have generally relied on an empirical approach. Some success however has been reported using an axisymmetric method of characteristics for the supersonic jet coupled to a subsonic potential flow analysis exterior to the jet boundary. Generally, however, the jet flow becomes subsonic and the method of characteristic marching procedure fails. Fully transonic jet computer programs are currently under development, using many of the ideas of the transonic inlet and airfoil methods, and should provide a valuable tool for afterbody design.

### Installed Design

Many a good isolated nacelle design has proven less than satisfactory when installed on a wing with a strut. This can be due to shock waves induced by wing, strut and nacelle interference as well as wing/strut/nacelle flow field effects on nacelle jet.

A traditional tool for assessing these effects is a cross sectional area plot encompassing portions of wing, strut, and nacelle. The designer tries to achieve as smooth an area distribution as possible consistent with the design constraints (e.g. flutter).

Currently more sophisticated techniques than simple area plots are available to predict interference effects. This is possible using subsonic three dimensional potential flow computer programs wherein usually some simplifying assumption is required regarding the jet boundary. Using such a program, one can examine the influence of the installation on the inlet pressure distribution as well as pressure loads likely to be imposed on jet exhaust boundary. These data coupled with previous experience provide the designer with a good assessment of expected interference effects.

Three dimensional potential flow programs also allow the designer to predict the effects of the nacelle and strut on the wing load and pressure distributions and provide an opportunity for designing the wing in the presence of nacelles and struts. Figure 45 gives an example of the wing twist modification required to preserve the isolated wing/body span load in the presence of nacelles and struts. The experimental data confirms that the twist change produced the desired effect.

The ability to predict the subcritical load for the entire geometry allows for drag improvements that would be difficult to achieve purely on an experimental basis. For instance, Figure 46 presents the span load for a wing/body with four nacelles and struts designed for minimum induced drag, which leads to side loading on the struts and corresponding small spanwise discontinuities in the load distribution on the wing. Such a design has about 1% less induced drag than an elliptically loaded wing with unloaded struts while preserving the same lift.

A second and distinctly different nacelle integration problem is the close-coupled installation. This denotes an arrangement where the nacelle produces a major perturbation on the local forces of the configuration. The production B737 nacelle and strut is an example of this type of installation, and the analytic potential flow solution is a valuable tool for giving the aerodynamicist a picture of the distribution of the total forces on the configuration. For example, Figure 47 presents the calculated velocity vectors for the B737 nacelle strut, in the presence of the nacelle, wing and body. The flow is seen to be very orderly on the strut, with no large changes in flow

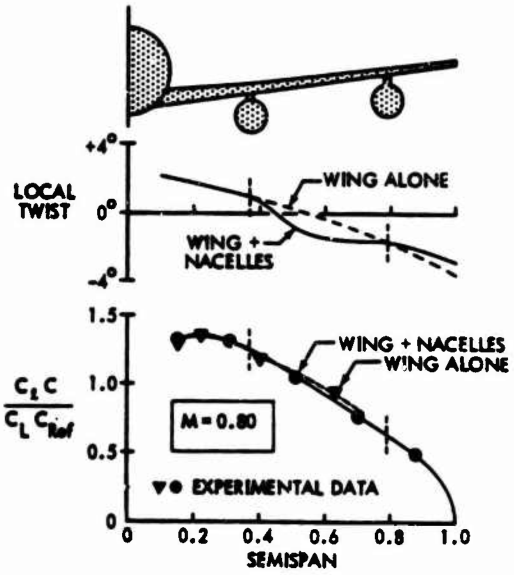

Figure 45: AERODYNAMIC EFFECT OF WING-MOUNTED NACELLES ON WING TWIST

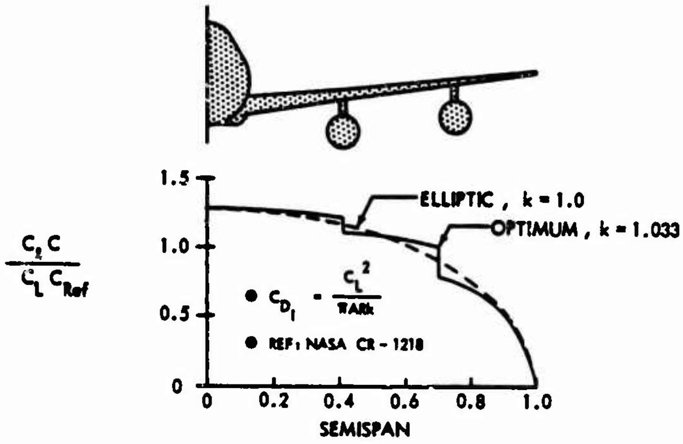

Figure 46: WING SPAN LOAD FOR MINIMUM INDUCED DRAG WITH WING-MOUNTED NACELLES

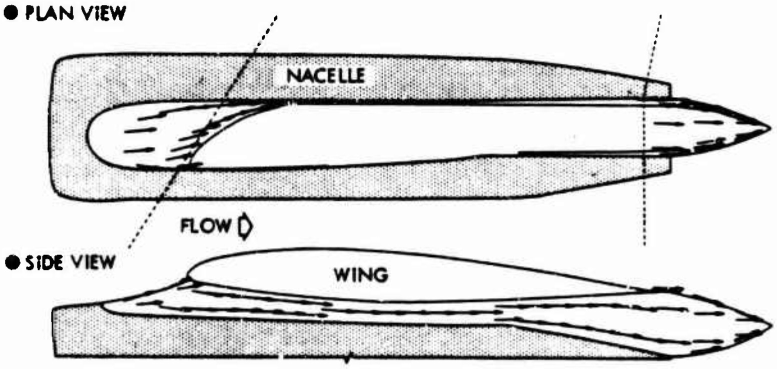
● PLAN VIEW
NACELLE
FLOW
● SIDE VIEW
WING

Figure 47: POTENTIAL FLOW VELOCITY VECTORS FOR B-737 NACELLE STRUTS

direction, which would suggest large local pressure gradients. However, Figure 48 shows the analytical prediction of span load for the wing-body and for the complete configuration, and a large effect of the nacelle installation on the wing as indicated. These figures serve to illustrate that successful integration of a close-coupled nacelle arrangement can be assisted by these analytical solutions, by giving the aerodynamicist details about the flow field that are difficult to achieve experimentally.

The local pressures can be adequately predicted for all these kinds of nacelle installations, and a good estimate of the lift can be made. In principle, it is also possible to calculate the boundary layer for the wing, strut and nacelles, then estimate the skin friction and pressure drag terms and calculate the induced drag, to get a result similar to that of Figure 43. However, for the nacelles and struts, the possibility of large crossflows is high, so that the drag is best calculated by handbook methods, using the predicted lift as a guide for the calculations.

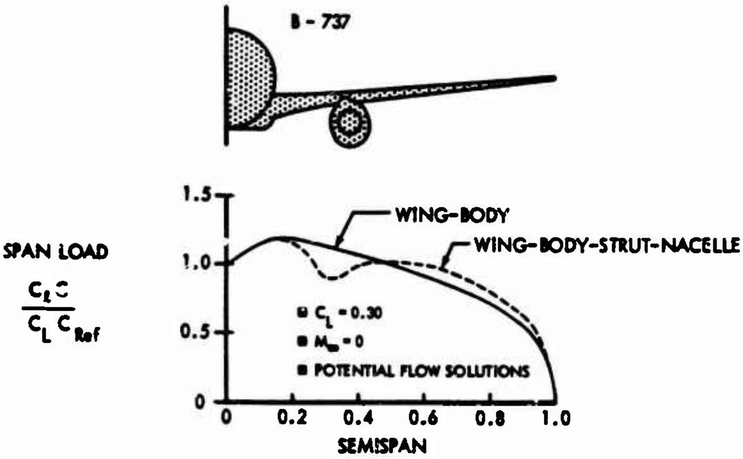

Figure 48: ANALYTICAL SPAN LOAD EFFECT OF CLOSE-COUPLED NACELLE

## APPLICATION OF THEORETICAL ANALYSIS TO CONFIGURATION DETAILS

The above discussions illustrate the manner in which theoretical design methods are being used to assist in developing a configuration. Emphasis has been placed on the insight which the current analytical techniques provide into wing design, particularly the chordwise and spanwise loading under cruise conditions. The methods are not adequate to displace either experimental methods or data banks of historical information. However, they can provide valuable support in preventing the occurrence of unnecessary drag. Two representative examples are given:

The first of these examples is the design and analysis of the shape of the pilot cabin. The experimental part of this paper shows that a flat-paned cab with sharp corners can produce one to two percent additional airplane drag, as compared to a smoother cab design. While the analytical method cannot predict the drag difference between the two designs, Figure 49 shows that the analysis process can provide guidance in the design and selection of a good cab. The figure shows a flat-paned cab to have high local pressures, sharp gradients, and extensive local supersonic flow. The curved pane cab is shown by analysis to be considerably more moderate in terms of its pressures. Intuitively, the curved-panel cab would be preferred from its potential lower drag (and lower cockpit noise levels) based on the calculated pressures.

The second example concerns the wing-body intersection, and in particular the wing root leading edge fairing into the body. Figure 50 presents the experimental result of a fairing designed with a three-dimensional potential flow analysis method (Reference 31). The objective of the design was to reduce the wing-body interference by preventing corner separation, and the analytically designed fairing is seen to prevent this separation. Again, the analysis cannot predict the drag, but instead can be used to prevent drag.

In review, the potential flow and boundary layer analysis methods available to the contemporary aerodynamicist can greatly enhance his ability to design efficient lifting geometries. In most cases, the design/analysis process provides information to help prevent excessive drag, and in some cases the actual drag can be calculated.

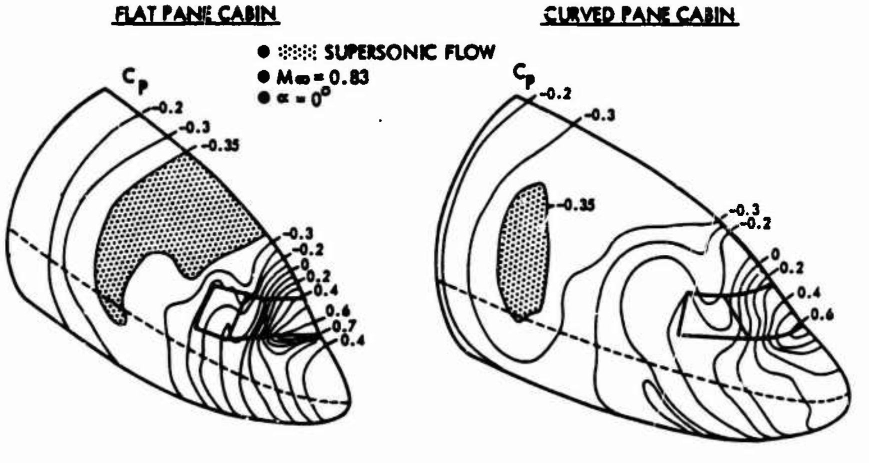

Figure 49: POTENTIAL FLOW — PILOT CABIN EVALUATION

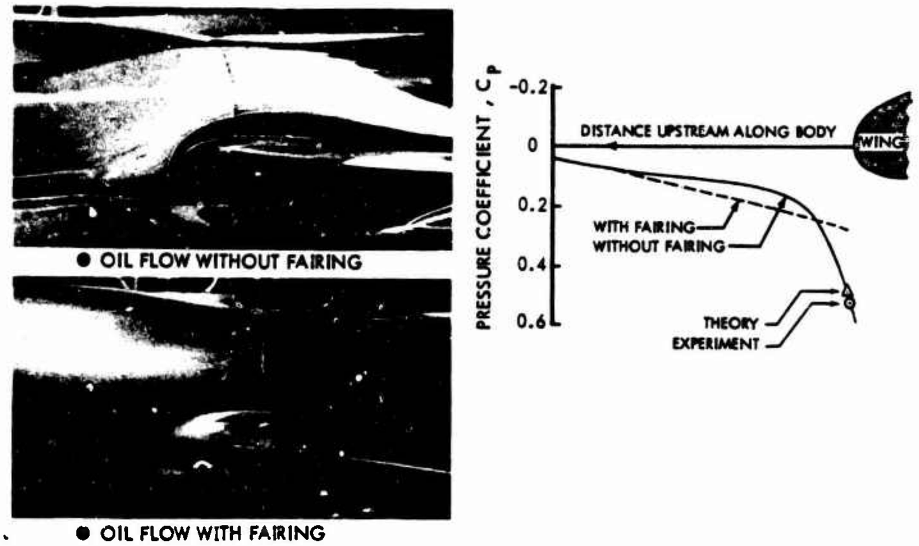

● OIL FLOW WITHOUT FAIRING

● OIL FLOW WITH FAIRING

Figure 50: DESIGN OF WING-BODY INTERSECTION FAIRING

## NEAR-TERM DEVELOPMENTS IN LIFT AND DRAG PREDICTION

The limitations of current three-dimensional theoretical analysis methods now in daily use restrict their application to Mach numbers that are low enough to exclude locally supersonic flow, and to geometries which have negligible crossflows for boundary layer predictions. In the near term, advances in analytical methods promise to place in the hands of the aerodynamicist the ability to calculate the inviscid cruise Mach number pressure distributions, and to provide limited capability for the analysis of certain classes of three-dimensional boundary layer flows. There are three distinct areas where useful near-term development is anticipated:

First, the three-dimensional mixed supersonic-subsonic pressure calculation by analysis will be a major advance in the field of wing design. Figure 51 presents a truly significant result in this direction: the first calculation of the flow about a three-dimensional wing at transonic speeds with an imbedded shock wave (Reference 32). The solution shown is for a wing with biconvex section, but the analysis method is not inherently prevented from handling the case of lifting wing with a round leading edge. In fact, Steger and Baily have calculated results for the lifting case. In addition, Jameson has recently shown a similar result for a yawed wing (Reference 33). Using past experience, these methods in improved form will be available for general use by the aerodynamicist within the next few years.

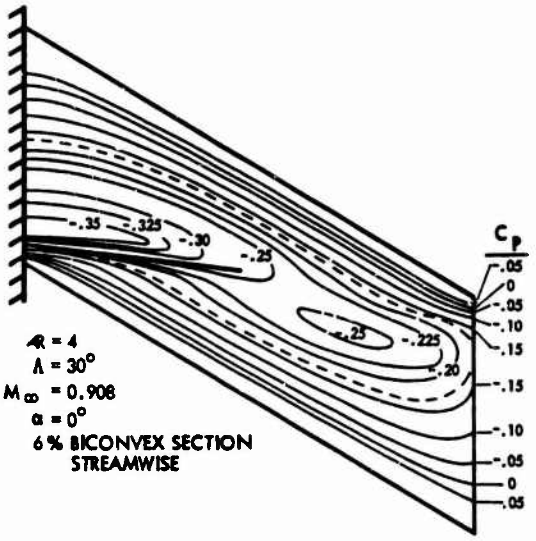

Figure 51: ISOBARS ON TRANSONIC, NONLIFTING SWEPT WING WITH EMBEDDED SHOCK

The second area of improvement will hopefully be in the prediction of the occurrence and location of off-body vortices. In particular, the vortices off a nacelle forebody or the forward fuselage have particular significance in regard to stability; the ability to calculate these vortices will allow designs that prevent or control their formation without unduly penalizing the lift.

A third area of significant payoff will be an improved capability for modeling jet effects and the interaction of a jet with the external flow about the airframe. This is becoming increasingly important in view of the trend toward close-coupled nacelle installations and the increasing dependence on theoretical analysis tools for aerodynamic design.

These added analytical capabilities will all be valuable to the aerodynamicist, and will be used as soon as they become reliable. It is difficult to guess the order of their appearance, but the calculation of surface pressures at the cruise Mach number will probably be in wide usage first, and is the one that is most needed.

# SUMMARY

Drag estimation procedures are not exact. Inaccuracies and uncertainties have been present in the past, and are still with us. There is no room for smugness on the part of any design team with regard to superior capabilities in this field of lift/drag estimation and prediction, for the record clearly shows that each configuration entails a risk. This is true not only with older designs but also with the advanced double-aisle planes now in service. Most aircraft have had their in-house program of review and improvement, with resultant changes not necessarily publicized broadly. A bit of wing tip here, a change in nacelle fairing there, a few seals in the slats - there is always a need for such corrective action.

It is difficult to offer a simple arithmetical statement as to the degree of success which an aeronautical engineer can expect relative to his prediction of drag level. In the broadest sense, the term "accuracy" must encompass all of the errors from the point when the design cycle has reached a serious status until the airplane has been flight tested and proven. The preliminary design study must be considered as the reference point for eventual judgement on program success. The initial decisions on wing area, aspect ratio, thickness ratio and the matching engine cycle and thrust requirements are determined based upon these early L/D estimates. In order to assure that the chosen propulsion system will in fact fly the airplane at its critical flight condition, an early judgement has to be made as to the lower bound of cruise L/D. On the other hand, too much conservatism will result in an inefficient engine/airplane which is not competitive.

In considering this long term overview, the designer is really faced with performance predictions which include errors from two sources:

- Errors due to lack of configuration definition
- Errors due to inaccurate methods

The prediction inaccuracies early in the program due to inadequate geometry definition are greater than inaccuracies due to methodology. An example of the progress of an airplane development and the associated trends in drag accuracy is given on Figure 52 As the design progresses, the geometry definition error washes out, and methodology error becomes most important.

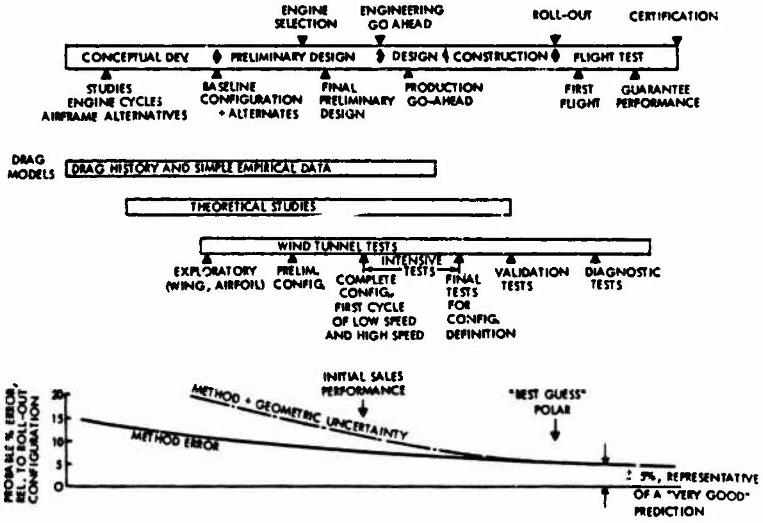
ENGINE SELECTION
ENGINEERING GO AHEAD
ROLL-OUT
CERTIFICATION
CONCEPTUAL DEV
PRELIMINARY DESIGN
DESIGN
CONSTRUCTION
FLIGHT TEST
STUDIES ENGINE CYCLES AIRFRAME ALTERNATIVES
BASELINE CONFIGURATION + ALTERNATES
FINAL PRELIMINARY DESIGN
PRODUCTION GO-AHEAD
FIRST FLIGHT
GUARANTEE PERFORMANCE
DRAG MODELS
DRAG HISTORY AND SIMPLE EMPIRICAL DATA
THEORETICAL STUDIES
WIND TUNNEL TESTS
INTENSIVE TESTS
EXPLORATORY (WING, AIRFOIL)
PRELIM. CONFIG.
COMPLETE CONFIG., FIRST CYCLE OF LOW SPEED AND HIGH SPEED
FINAL TESTS FOR CONFIG. DEFINITION
VALIDATION TESTS
DIAGNOSTIC TESTS
PROBABLE % ERROR, REL. TO ROLL-OUT CONFIGURATION
20
15
10
5
0
INITIAL SALES PERFORMANCE
"BEST GUESS" POLAR
METHOD + GEOMETRIC UNCERTAINTY
METHOD ERROR
± 5%, REPRESENTATIVE OF A "VERY GOOD" PREDICTION

Figure 52: AIRPLANE DEVELOPMENT SCHEDULE

Some allowance has to be made by the design team manager and the aerodynamics engineer for the ability of the airplane to eventually reflect the configuration upon which the early performance estimations are made. If it becomes clear that there are two non-converging designs - one on the drawing board and a different one in the books and wind tunnel models of the aerodynamicist, it is time for a new understanding. Therefore, the fairest evaluation of the lift/drag prediction capability should logically commence when the configuration is well defined and after the aerodynamicist has been able to use all of the tools described in this paper. This leads to the development of a "best guess" drag polar at the time of roll-out. This polar may not be the performance level used in brochures, but it represents the true basis upon which flight tests will later be compared. At this time, a complete drag analysis is available, with an account given for each part of the configuration and an estimate made for friction drag, induced drag, trim drag, and compressibility drag. As Butler has noted (Reference 15), "Before the first flight of the prototype, the spread of the bounds of the drag estimates should have been reduced to that associated with residual uncertainties in the interpretation or extrapolation of test data on specific experimental models, and second-order doubts about the application of prediction methods". The result is a potential error around the best guess levels which varies with Mach number as shown on Figure 53 . This curve illustrates the probability of estimating drag more accurately at the subcritical flight speeds where higher confidence exists in the ability to predict the drag components. At cruise speeds, the Mach dependent drag assumes a greater significance. The confidence band includes an allowance for errors associated not only with the prediction of the drag increment for a particular critical Mach number, but also with the prediction of the critical Mach number itself. The level of probable error is discussed in the final remarks.

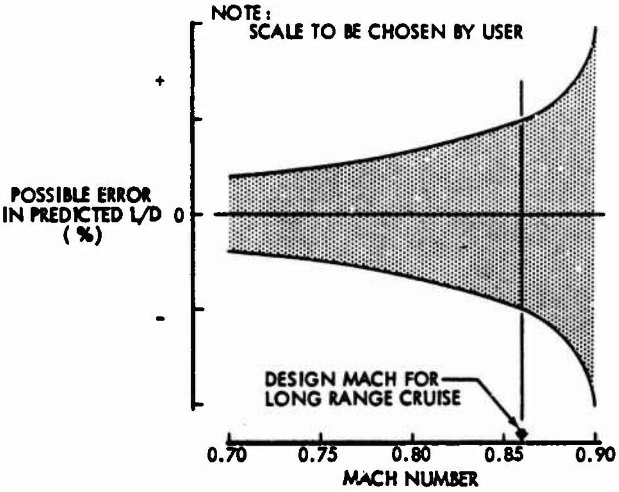

Figure 53: POSSIBLE ERROR IN PREDICTED L/D
(LONG RANGE TRANSPORT)

Attention has been directed throughout this paper to the impact of the propulsion system on estimation and design studies. This item is perhaps the single factor of most concern because of its obvious impact upon thrust/drag accountability and also due to the influence of the propulsion installation upon the wing-body drag level and drag rise. Examples of airplanes for which significant improvements in nacelle or mounting strut lines were made after initial production models were developed include the B737, the DC-8, the Super VC-10, and the Convair 990. A classic description of the approach to improving the latter airplane is reported in Reference 34 and is partially quoted as follows, "An extensive drag reduction program on the 990 was initiated . . . . consisting of three general phases: (1) exploratory flight tests, (2) an extensive engine nacelle wind tunnel investigation, and (3) development flight tests. Modifications of the following nature were established: (1) a sharper, less drooped wing leading edge, (2) a nacelle afterbody extension, (3) a wing-fuselage aft fillet redesign to more generous lines, and (4) the addition of engine nacelle and pylon fairings. The incorporation of these modifications has resulted in the achievement of cruise performance in excess of the original guarantees."

One illustration of further variations in performance levels - those determined from different series of flight tests - was presented for the DC-10 in Reference 19, which was previously quoted in the Flight Test section of this paper. The range factor comparisons are shown on Figure 54 , and these provide an insight into the differences between an estimated performance level, prior to flight, and results obtained during initial flight tests. Flight results at relatively low Mach numbers were 3½% below predictions, and results at higher speeds exceeded predictions by a similar amount. At top speeds, there was little difference. Later tests, with a small wing tip extension, showed a benefit from this change at speeds below Mach 0.83. These data illustrate some of the differences in performance levels which, although small, must be measured, analyzed, and reconciled in establishing a final level for accuracy comparisons.

Detailed, thorough flight tests from which the desirable analyses can be made for comparison with predictions are expensive, time consuming and difficult to obtain. Some of the illustrations given in this paper have resulted from cases where an obvious discrepancy in performance was evident, demanding corrective action. There are fortunately other cases in which interesting research has been undertaken which permitted comprehensive correlation between flight and predictions. Two such studies were presented in

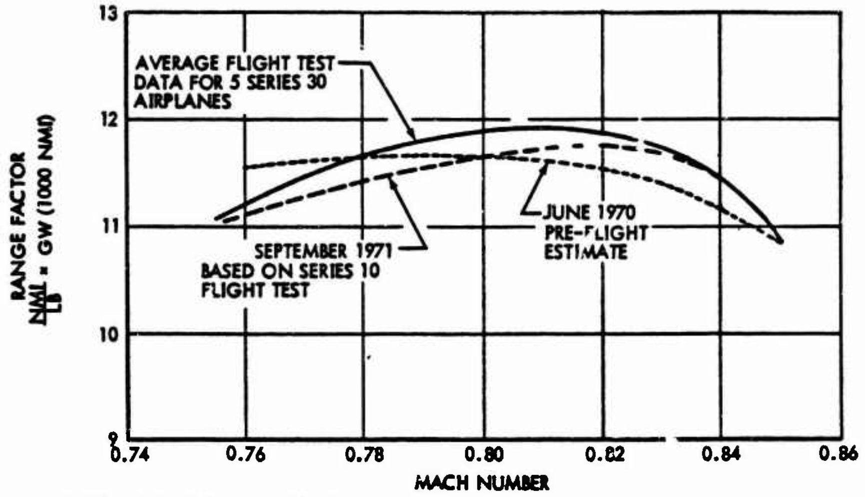

REFERENCE: INTERAVIA, JUNE 1973

Figure 54: RANGE FACTOR COMPARISON - FLIGHT TEST VS. PREDICTION (DC-10-30)

References 12 and 14. The first of these involved extensive tests and analyses on the Lockheed C-141 and C5A, supported by both company and NASA research efforts. This paper describes in detail the prediction process as employed by Lockheed, emphasizes the importance of profile drag estimation, and reflects a design philosophy which minimizes interference effects by designing for smooth area distributions. The second reference summarizes results of correlation studies on the Grumman F-14 fighter. This study likewise shows good agreement and correlation in prediction of subsonic skin friction and profile drag and drag rise. However, it is difficult to determine from these studies what the pre-flight prediction levels of either component or total airplane drag were.

With regards to the status of drag prediction methodology, Butler (Reference 15) has recommended "a more enlightened approach in which the synthesis of drag is achieved by compounding elements arising from different basic causes, associated more directly with the nature of the fluid dynamics." Butler's review also emphasizes the need for flight test anchor points for drag prediction models, discusses the potential for predictive errors even with "closely related members of a given aircraft family", and mentioned the inadequacies of analysis efforts of "prototype" flight drag data if testing is compromised by schedules and budgets. These are real concerns and apply to early production tests as well.

Theoretical methods for drag estimation are not available at this time as a replacement for experimental studies. Theoretical design methods, however, are essential to the development of a configuration and to the compression of the design cycle time span. The "synthesis" approach to drag estimation recommended by Butler will provide a framework for the introduction of advances in theoretical methods as they occur.

In conclusion, I would like to offer a rating for comment which represents a purely personal opinion as to accuracy levels which might be expected on a subsonic, swept wing commercial transport design. These figures represent the accuracy with which an aerodynamicist can estimate the L/D for use in a performance document, and assume he has for his beneficial use a series of wind tunnel tests which accurately incorporate the specific shapes of wing, body, empennage and propulsion system of the proposed design. I would suggest that, at cruise conditions, the following score should be assigned, based upon flight test results:

| L/D Level Achieved | $M_{DD}$ | Rating |
|---|---|---|
| ± 3% | ± .002 | Amazing |
| ± 5% | ± .004 | Very Good |
| ± 7% | ± .006 | Average |
| ± 10% | ± .010 | Below Average |

This table is strictly the product of the author, and does not represent any official position of the Boeing Company or the industry. While offered seriously, it must be taken with considerable reservations and qualifications. One would certainly expect a derivative model to produce a rating much higher than a new, novel, configuration. Most of the commercial aircraft flying fit within this table, it is believed. Military programs in general have been far less successful in achieving these accuracy levels. One is loath to discuss cases which have rated poorly; an example which has been well proven on the good side is the Boeing 727. This airplane demonstrated between 8 to 10% better than the best guess levels of range performance when first flown, so the airplane earns high marks, but the aerodynamicist's drag prediction rating is mediocre. As a matter of fact, a bias is generally worked into the performance quotes such that the negative signs on the error bands are most often encountered.

An observer of these thoughts on drag prediction risks might conclude that the likelihood for success on a new airplane program is very small. There is no doubt as to the large measure of risk involved, and it is true that many aircraft have performed somewhat poorly when first flown. The track record of the final product is very good, however, as described in reviewing the historical trends presented in the Introduction. The goals have been high, and achieving these goals requires a clear understanding of the design which can only be acquired by in-depth analytical and theoretical studies. Continued improvements in subsonic aerodynamic efficiency have resulted from better understanding of the fundamental nature of the fluid dynamics in the transonic speed regime. Concurrently, the task of configuration definition and drag estimation has grown more difficult, even though the tools available for analysis offer more capability - the computers, better wind tunnels, and advanced theoretical approaches. Finally, there is no substitute for large scale flight data. Any program which seeks an advantage from novel configuration features without provision for appropriate flight tests of components, prototype models, or development time on a first flight model is assuming a considerable additional risk.

# REFERENCES

1. Cook, W. H., Howell, C. S., Wimpress, J. K., "Aerodynamic Performance," pp 238 AIR SPACE AND INSTRUMENTS, Edited by Sidney Lees, Draper Anniversary Volume, 1963
2. Hay, J. A., "Vickers VC-10 Aerodynamic Design," Aircraft Engineering, June 1962
3. Pearcey, H. H., "The Aerodynamic Design of Section Shapes for Swept Wings," Second International Conference, International Council of the Aeronautical Science, September 1960
4. Goodmanson, L. T., "Transonic Transports," Astronautics and Aeronautics, Vol. 9, No. 11, November 1971
5. AGARD-CPP-124, "Aerodynamic Drag," Conference Proceedings, 1973
6. Norton, D. A., "Airplane Drag Prediction," NY Acad. Sc. Annals, 154, pp 306-328, 1968
7. Dommasch, D. D., "Airplane Aerodynamics," Pitman Publishing Corp., 1958
8. Perkins, C. D., and Gage, R. E., "Airplane Performance Stability and Control, John Wiley and Sons, 1949
9. Hoerner, S. S., Dr.-Ing., "Fluid-Dynamic Drag Theoretical, Experimental and Statistical Information, 1958
10. Royal Aeronautical Society Data Sheets (Aerodynamics)
11. USAF Stability and Control Datcom
12. Paterson, J. H., MacWilkinson, D. G., Blackerby, W. T., "A Survey of Drag Prediction Techniques Applicable to Subsonic and Transonic Aircraft Design," AGARD Conference on Aerodynamic Drag, AGARD-CCP-124, 1973
13. Pyle, J. S., Saltzman, E. J., "Review of Drag Measurements from Flight Tests of Manned Aircraft with Comparisons to Wind Tunnel Predictions," AGARD Conference on Aerodynamic Drag, AGARD-CCP-124, 1973
14. Rooney, E. C., "Development of Techniques to Measure In-Flight Drag of a US Navy Fighter Airplane and Correlation of Flight Measured Drag with Wind-Tunnel Data," AGARD Conference on Aerodynamic Drag, April 1973
15. Butler, S. F., "Aircraft Drag Prediction for Project Appraisal and Performance Estimation," AGARD Conference on Aerodynamic Drag, AGARD-CCP-124, 1973
16. Hodges, M. D., et al, Appendix to "Aircraft Drag Prediction for Project Appraisal and Performance Estimation," AGARD Conference on Aerodynamic Drag, AGARD-CCP-124, 1973
17. Welge, H. R., Ongarato, J. R., AIAA Paper No. 70-590, "Powered Engine Simulator Procedures and Experience for the DC-10 Wing Engine at High Subsonic Speeds," 1970
18. Lindbergh, Charles A., "The Spirit of St. Louis," Appendix, Charles Scribner's Sons, New York, N. Y., 1953
19. Geddes, J. Philip, INTERVIA 6-18-73, "Taking an Airliner from Certification to Airline Acceptance - the DC-10-30"
20. Dunn, Orville, R., SAE 237-A, "Flight Characteristics of the DC-8," 1960
21. Aviation Week, "DC-8-63 Range Stretch," March 13, 1967, pp 30
22. George-Falvy, D., AIAA Paper No. 71-289, "Scale Effect Studies of Airfoil Profile Drag at High Subsonic Speed," 1971
23. George-Falvy, D., "Sweeprake - A New Tool of Flow Diagnosis," Unpublished paper presented at the AIAA Pacific Northwest Section Technical Specialists Seminar, Sept. 11, 1972
24. Hammond, D. G., and Wilkerson, C., Jr., "An Evaluation of Single and Multiple Sting Support Methods to Obtain Unmodified Interference-Free Wind Tunnel Data," AIAA Paper No. 71-267, 1971
25. Braslow, A. L., Hicks, R. M., and Harris, R. V., Jr., "Use of Grit-Type Boundary Layer Transition Trips on Wind Tunnel Models," NASA TN D-3579, 1966
26. Blackwell, James A., Jr., NASA Technical Note, NASA TN D-5003 "Preliminary Study of Effects of Reynolds Number and Boundary-Layer Transition Location on Shock-Induced Separation," January 1969

27. George-Falvy, D., "An Investigation of the Flow Characteristics Around the Cab of Boeing Jet Transports," Boeing Document D6-15D06, 1966

28. Sinnott, C. G., "Theoretical Predictions of the Transonic Characteristics of Air-Foils," J. Aero/Space Sci., Vol. 29, No. 3, March 1962

29. Bayer, F., Garabedian, F., and Korn, D., "Supercritical Wing Sections," Springer-Verlog, 1972

30. Kehrer, W. T., "Design Evolution of the Boeing 27D7-3D0 Supersonic Transport," Park II, Presented at AGARD Symposium, Florence, Italy, October 1-4, 1973, 43rd Flight Mechanics Panel Meeting

31. Rubbert, P. E., and Saaris, G. R., "Review and Evaluation of a Three-Dimensional Lifting Potential Flow Analysis Method for Arbitrary Configurations," AIAA Paper No. 72-188, 1972

32. Baily, F. R. and Steger, J. L., "Relaxation Techniques for Three-Dimensional Transonic Flow about Wings," AIAA Journal, Vol. II, No. 3, pp 318-325, March 1973

33. Jameson, A., "Numerical Calculations of the Three-Dimensional Transonic Flow over a Yawed Wing,"AIAA Computational Fluid Dynamics Conference Proceedings, pp 18-26, 1973

34. Keetney, J. T., and Piszkin, S. P., "Reduction of Drag Rise on the Convair 99D Airplane," Journal of Aircraft, Jan-Feb 1964 (AIAA Preprint 63-276)

## ACKNOWLEDGEMENT

I wish to express my appreciation for broad support and assistance from many of my colleagues in the Boeing Commercial Airplane Company Aerodynamics Staff. Specific credit is due Mr. Walter Gillette and Mr. Dez George-Falvy for major contributions to these lecture notes. Mr. Gillette is responsible for most of the section entitled "Advances in Techniques for Analytical Lift and Drag Prediction". Mr. George-Falvy has been engaged for several years in fundamental aerodynamic studies involving the understanding of fluid flow, and has presented his findings in several published papers.

N74-26450

# PREDICTION OF SUPERSONIC AIRCRAFT AERODYNAMIC CHARACTERISTICS

by

C.S. Leyman Chief Aerodynamicist (Concorde)
T. Markham Assistant Chief Aerodynamicist (Concorde)

BRITISH AIRCRAFT CORPORATION (C.A.D.)
FILTON HOUSE
FILTON
BRISTOL

## SUMMARY

The paper reviews the methods currently available for the prediction of the aerodynamic characteristics of supersonic aircraft as they affect performance.

The particular problems of supersonic aircraft design are illustrated by consideration of hypothetical transport and fighter aircraft.

## INTRODUCTION

The object of this paper is to present a review of methods in current use for the prediction of the aerodynamic characteristics of supersonic aircraft.

"Aerodynamic characteristics" in this context is taken to be that collection of data which is necessary to permit the calculation of aircraft performance;that is, to say the establishment of the thrust/drag balance equations.

Because of the authors' background, the paper is necessarily biased towards those methods which have been successfully used to predict the performance of Concorde. This is deliberate, since the production of accurate performance estimates for a long range commercial supersonic aircraft is probably the most demanding in terms of precision and technique of prediction. In addition, the methods used are now thoroughly understand by four firms and two NATO governmental agencies - which of itself must be something or a record!

The paper itself is divided into six parts. Firstly the aerodynamic principles which result in the particular characteristics which make supersonic aircraft different from subsonic designs are briefly reviewed.

Next the available design methods are reviewed together with a consideration of their accuracy and suitability for the various stages of design.

The third section describes the state of the art in the estimation of parasitic drag and thrust loss due to air leakage.

The fourth section discusses the problems of estimating the installed powerplant performance. The fifth section gives a set of consistent definitions of thrust and drag and discusses the techniques.

The final section deals with the effect of the design mission on the design philosophy.

## SECTION 1

### 1.1 DRAG IN SUPERSONIC FLOW

In supersonic flow there are three basic mechanisms whereby drag is created. The first two are essentially the same as in subsonic flow namely skin friction and vortex drag. The third, unique to supersonic flow, is wave drag.

A convenient breakdown of drag from a fluid mechanics standpoint is set out in Figure 1.1. Skin friction drag, trim drag and form drag which are common to subsonic and supersonic flow are manifested by a reduction of streamwise momentum in the wake, whereas vortex drag is associated with transverse components of momentum in the wake flow. On physical grounds wave drag is most satisfactorily associated with the entropy rise across the shock waves, but this is not very useful in practice. Within the linearised theory one can calculate wave drag by considering the lateral convection of streamwise momentum. However neglecting form drag (i.e. the effects of boundary layer displacement thickness on the pressure drag) and assuming small lift forces we can identify wave drag with pressure drag (approximately) - a common assumption in the analysis of experiments.

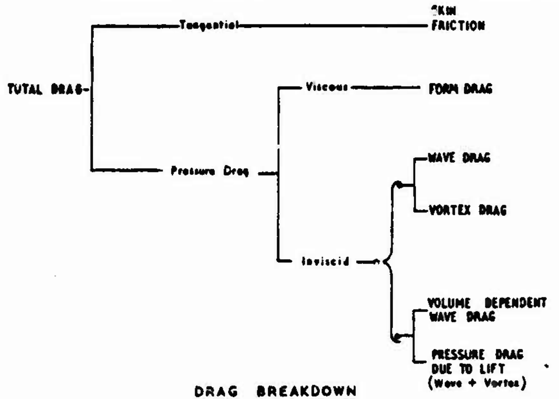

DRAG BREAKDOWN

FIG 1.1

### 1.2 WAVE DRAG

The distinction between wave drag and vortex drag becomes clearer when we attempt to calculate the drag from momentum considerations.

We surround the vehicle by a control surface (as shown in Figure 1.2) consisting of a cylindrical surface, $S_2$, of radius R closed by two end planes $S_1$, $S_3$. It should be noted that we are using wind axes (as we will do throughout).

For present purposes we assume that the radius, $R$, is very large compared with a typical dimension of the aircraft. We also assume $S_1$ and $S_3$, the end surfaces, to be placed well away from the vehicle, which, in turn, is assumed to have negligible base area.

A consideration of the momentum flow through the surfaces gives, to lowest order, the streamwise force component

$$\frac{D}{q} = \underbrace{-2\iint_{S_2} \phi_x \phi_r \, dS_2}_{\text{WAVE DRAG}} + \underbrace{\iint_{S_3} (\phi_y^2 + \phi_z^2)\, dS_3}_{\text{VORTEX DRAG}}$$

Where $q = \frac{1}{2}\rho U^2$

Here $\phi$ is the perturbation velocity potential such that $\phi_x, \phi_y, \phi_z$ and $\phi_r$ are the components of the perturbation velocity parallel to the coordinate axes and in the radial direction respectively.

As indicated the second term gives the vortex drag, which is identical to the induced drag for subsonic flow. Hence

$$\left.\frac{D}{q}\right|_{\text{VORTEX}} = \iint_{S_3} (\phi_y^2 + \phi_z^2)\, dS_3$$

$$= \frac{1}{2\pi}\int_{-s}^{s}\int_{-s}^{s} \frac{d\Gamma}{dy}\,\frac{d\Gamma}{dy_1}\,\ln|y - y_1|\,dy\,dy_1$$

where $\Gamma(y)$ is the span loading.

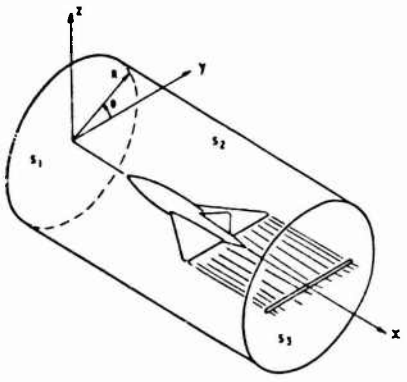

MOMENTUM CONTROL SURFACE FOR DRAG CALCULATION

FIG. 1.2

The first term is the wave drag, which in the absence of any trailing vorticity, will be equal to the pressure drag.

As indicated in Figure 1.1 the precise breakdown of the pressure drag may be achieved in different ways and we shall find breakdown into

Total Pressure Drag = Wave Drag due to Volume
+ Pressure drag due to lift

the most convenient in practice.

## SECTION 2 METHODS OF DRAG PREDICTION

### 2.1 SKIN FRICTION, FORM AND TRIM DRAG

Knowledge of skin friction is needed for three separate reasons during the cycle of design and testing :-

(i) Prediction of basic full scale skin friction during initial design.

(ii) Correction from wind tunnel model to full scale friction.

(iii) Analysis of flight test results in order to properly define drag as function of Mach number, altitude, ambient temperature, lift coefficient.

(i) requires accurate full scale friction at the key design points.

(ii) requires the correct variation of friction with Reynolds number over the relatively large range from model to full scale conditions.

(iii) requires the correct variation of friction with Reynolds number over the relatively small range of full scale Reynolds number covered at any one Mach number.

Overall in order to achieve consistency, the same theory should be used for all estimates.

On a supersonic transport the Mach number range is up to 2.2M and the Reynolds number range from less than $10^6$ on the fin of a 1/30th scale model to greater than $5 \times 10^8$ on the fuselage during initial cruise.

A method to cover a Mach range from 0 to 2.2 and a Reynolds number range up to $10^9$ is therefore required.

Unlike many other parts of theoretical aerodynamics turbulent boundary layer theory has no simple linear theory framework on which to base an approach. In fact since the subject is a mixture of theory and experiment linked through empirical relationships there is freedom in the approach to be used and a casual reader of the literature might be forgiven for believing that the number of solutions is roughly proportional to the square of the number of workers in the field.

The method given below is that which was used in the design of Concorde. Subsequent work has suggested that a marginally more correct result can be obtained by using the methods of references 2, 3 and 4 rather than ref. 1.

Turbulent Friction with Zero Heat Transfer

At the time of the initial design work (1961) there was no clear 'best method' and for convenience we chose the method described by Michel (ref. 1). This had the advantage that besides fitting the available data reasonably well it also split conveniently into two parts the one a function of aircraft geometry the other a function of the flight condition.

Reference 1 covers laminar and mixed flows but in this paper fully turbulent flow will be assumed.

Mean friction Coefficient

$$C_{F_{Mean}} = \frac{0{\cdot}0442}{R_e^{1/6}} \, f_T(M)$$

where

$$f_T(M) = \left[\frac{T_e}{T_R}\right]^{1/2} \left\{ \frac{1 + S/T_e}{\frac{T_R}{T_e} + S/T_e} \right\}^{1/6}$$

$$\frac{T_R}{T_e} = 1 + 0{\cdot}54\left\{\frac{T_p}{T_e} - 1\right\} + 0{\cdot}16\left\{\frac{T_f}{T_e} - 1\right\}$$

and

$$\frac{T_f}{T_e} = 1 + 0{\cdot}9\,\frac{\gamma - 1}{2}M^2 = 1 + 0{\cdot}18M^2$$

Where $T_e$ ambient temperature

$T_R$ reference temperature

$T_P$ skin temperature

$T_f$ skin temperature for zero heat transfer

$S$ Sutherland Constant 110.4°K

Then

$$\frac{D_F}{q} = \int C_{F_{mean}} \ell \, dy = \int \frac{\ell}{\ell^{1/6}} \, dy \left\{ \frac{0.0442}{[Re/\ell]^{1/6}} f_T(M) \right.$$

Note that $\int \ell^{5/6} dy$ depends only on aircraft geometry

and $\frac{0.0442}{[Re/\ell]^{1/6}} f_T(M)$ depends in the case of zero heat transfer only on speed, temperature and pressure

Hence the effects of geometry and flight conditions have been separated and the simplified calculation procedure mentioned above is demonstrated.

The variation of $4.42/(Re/\ell)^{1/6} \; f_T(M)$ with altitude and Mach number for an ISA atmosphere and zero heat transfer is shown on figure 2.1.

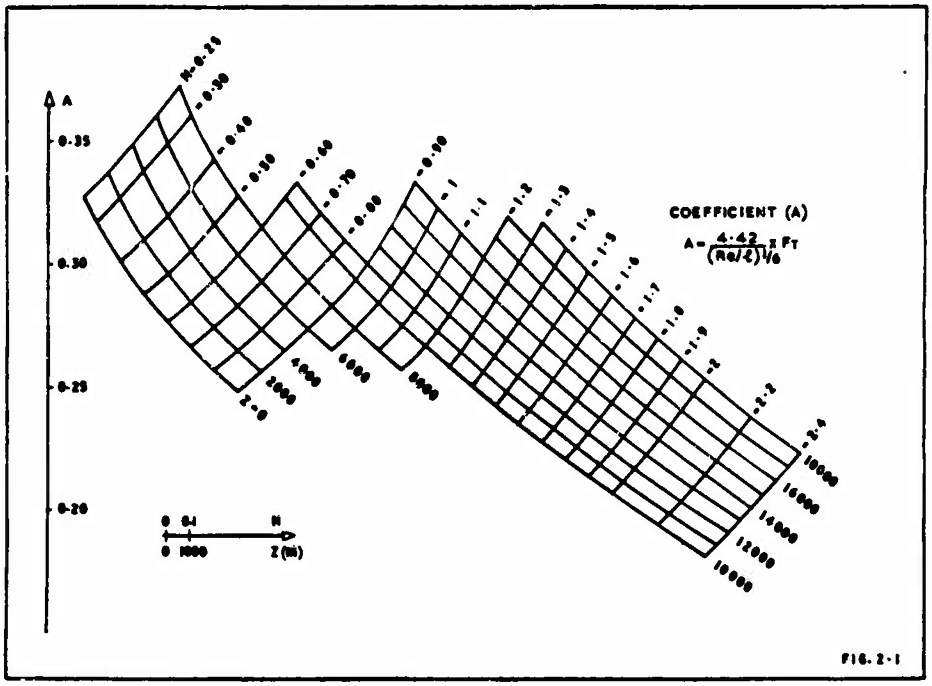

FIG. 2·1

Corrections for the effect of heat transfer

For the Mach numbers under consideration the effect of skin temperature away from the zero heat transfer case can be treated relatively crudely since the total effects of heat transfer are relatively low.

At 2.0M heat transfer causes an increase of about 1% in friction drag which is about 0.3% in total drag.

The method used has been to form $\frac{C_F - C_{F_{ZHT}}}{C_{F_{ZHT}}} = \frac{f_T(M) - f_T(M)_{ZHT}}{f_T(M)_{ZHT}}$ as a function of $\frac{T_P}{T_f}$ and M - fig. 2.2.

Then $\frac{\Delta D_F}{q} = \sum \Delta C_{F_{LOCAL}} S$ where the summation is carried out over a relatively coarse number of elements

$$\Delta C_{F_{LOCAL}} = \frac{\Delta C_F}{C_{F\ ZHT}} C_{F_{LOCAL}}$$

and

$$C_{F_{LOCAL}} = \frac{\xi}{6} C_{F_{MEAN}}$$

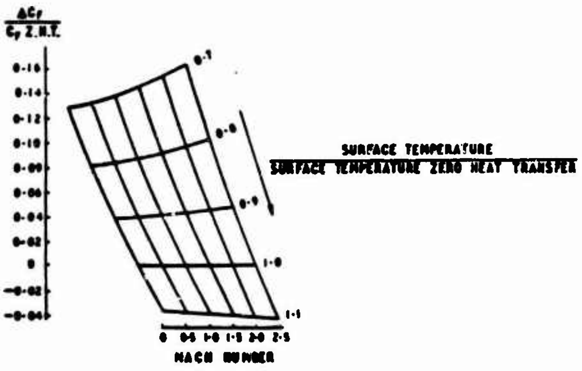

CHANGE DUE TO HEAT TRANSFER

FIG. 2.2

## Comparison with the results of other methods

Since reference 1 was published more work, both experimental and theoretical, has been carried out.

In particular Spalding and Chi (reference 2, 1964) reviewed the available experimental results and theories.

All available acceptable evidence was used to compare with twenty available turbulent boundary layer skin friction laws.

The R.M.S. error in friction coefficient ranged from 11.0% to 32.3%. A new calculation procedure was then developed based on the postulate that a unique relation exists between $C_f F_C$ and R $F_R$ where $C_f$ is the drag coefficient, R is the Reynolds number, and $F_C$ and $F_R$ are functions of Mach number and temperature ratio alone.

This new procedure then gave an R.M.S. error of 9.9%.

Winter and Gaudet (reference 3, 1970 ) report a series of skin friction measurements in the R.A.E. 8 ft. tunnel. They concluded from these and other results that for turbulent flow the mean friction coefficient on a flat plate with zero heat transfer could be written :-

Incompressible form

$$c_f^{\,i} R_{e_x}^{\,i} = 0{\cdot}7788\left[1 - 8{\cdot}353(c_f^{\,i})^{\frac{1}{2}} + 24{\cdot}16(c_f^{\,i})\right] e^{0{\cdot}537 (c_f^{\,i})^{-\frac{1}{2}}}$$

$$C_F^{\,i} R_{e_x}^{\,i} = 0{\cdot}7768\left[1 - 4{\cdot}632(C_{F_i})^{\frac{1}{2}}\right] e^{0{\cdot}537 (c_f^{\,i})^{-\frac{1}{2}}}$$

With compressibility factors

$$F_c = \frac{c_f^{\,i}}{c_f} = \frac{C_F^{\,i}}{C_F} = \left[1 + 0{\cdot}2M^2\right]^{\frac{1}{2}}$$

$$\frac{F_\delta}{F_c} = \frac{R_{e_x}^{\,i}}{R_{e_x}}$$

with

$$F_\delta = 1 + 0{\cdot}056 M^2$$

It was shown that the results from this were very similar to those of Sommer and Short (ref. 4).

A useful approximation to the above expression is

$$C_F = \frac{0{\cdot}49}{F_c} \frac{1}{\left\{\log_{10} \frac{F_\delta}{F_c} R_{e_x}\right\}^{2{\cdot}625}}$$

The results from Michel (ref. 1), Spalding and Chi (ref. 2), and Winter and Gaudet (ref. 3) are compared on figure 2.3 at both zero and 2.0M.

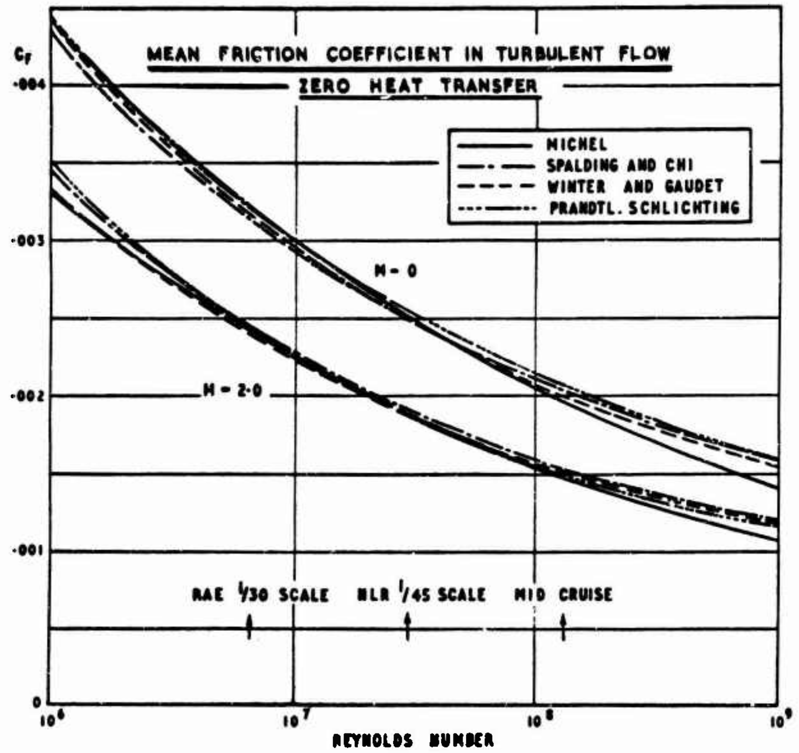

FIG. 2·3

Concentrating on 2.0M it is seen that at Mid cruise compared with reference 3 Michel under-estimates friction drag by about 2½% $C_f$ (0.8% total drag).

The aircraft drag prediction is based mainly on 1/45 scale models tested at N.L.R. For this Reynolds number Michel over-estimates by about 2½% of full scale drag.

It may be concluded that compared with reference 3, reference 1 as used for Concorde estimates, predicted :-

(i) lower aircraft drag directly by 2½% $C_F$ (0.8% Total drag)

(ii) lower aircraft drag from model data by 5% $C_F$ (1.5% Total drag)

Taking into account the R.M.S scatter of about 10% $C_F$ mentioned above and the availability of estimates, computer programmes and Flight Test results, it was never felt justifiable to change from the methods of reference 1.

Heat Transfer

Although a number of methods have been used the one most soundly based and giving best agreement with flight test measurements is based on the work of Spalding and Chi (ref. 2).

The friction coefficients discussed above have been related to the heat transfer by means of the following relationships :-

Colburn's modified Reynolds analogy $S_t = \frac{1}{2} C_f (P_r)^{-2/3}$

where $S_t = \frac{h}{C_p \rho V}$ - Stanton Number

$P_r = \frac{C_p \mu}{k}$ - Prandtl Number

$c_f$ = local skin friction coefficient

$h$ = heat transfer coefficient

$k$ = Conductivity of air

### Form Drag

On subsonic aircraft a great deal of useful work is being done on the interaction between the pressure drag and viscous drag terms. That is to say the effect of the real three-dimensional flow on skin friction and the effect of the boundary layer displacement thickness on the pressure drag and lift terms is beginning to be taken into account. During initial design on Concorde in subsonic flow simple RAeS data sheet corrections were made in the traditional manner and in supersonic flow the simple addition of wave drag and skin friction drag was used i.e. form drag was not directly estimated.

Once wind tunnel evidence was available this was the prime source of drag prediction and it was assumed that interaction effects were common to the models and the aircraft, that is to say anything above the summation of wave and friction drag was obtained from tunnel tests.

On a less slender aircraft than Concorde, say a Supersonic Strike fighter, these effects could be well worth investigating.

### Trim Drag

Trim drag is of course common to both sub and supersonic aircraft However on supersonic aircraft the aerodynamic centre moves aft as Mach number increases - very crudely this can be associated with a transfer of the lift centre from the quarter chord point to the centre of area. This means that unless special measures are taken to reduce the out of balance pitching moment the trim drag can be very significant. Suitable means of reducing trim drag could be wing camber to produce a nose up zero lift pitching moment and/or movement of the centre of gravity by fuel transfer.

There is no generally valid method of estimating trim drag as it will vary significantly with the configuration being studied. Equally there are no features of supersonic flight which require special techniques for the estimation of trim drag.

## 2.2 WAVE DRAG

### Slender Body Theory

Although most practical supersonic aircraft configurations (including Concorde) cannot be regarded as slender in the strict mathematical sense, which requires that all surfaces, including the wing leading edges make an angle with the freestream much less than the Mach angle, slender body theory proves to be a very useful tool in practice.

Indeed, the design studies that led to the Concorde configuration owe much to this relatively simple theory, in the same way that high aspect ratio subsonic aircraft rely on the mathematically similar lifting line theory.

If we consider the linearised equation for the perturbation velocity potential in supersonic flow

$$-\beta^2 \phi_{xx} - \phi_{yy} + \phi_{zz} = 0$$

and consider the flow about a body which lies well inside the Mach cone from its nose, so that near its surface

$$y^2 + z^2 = r^2 << x^2/\beta^2$$

then, in general, the variation of the potential in the $x$ direction will be negligible compared to those in directions normal to the freestream. The potential equation then reduces to the two-dimensional 'cross flow' equation

$$\phi_{yy} + \phi_{zz} = 0$$

The solution to this problem will be of the form

$$\phi(x,y,z) = \phi_1(y,z;x) + \phi_2(x)$$

where $\phi_1$ is a solution of the cross flow equation with $x$ entering only as a parameter. The second term, $\phi_2$, has to be found by matching with a solution of the full potential equation. It turns out that the major effect away from the immediate vicinity of the body is the source like flow induced by the rate of change of its cross-sectional area along its length. At a distance, then, the body looks like a line source of varying strength

$$S'(x) = \frac{dS(x)}{dx}$$

where $S$ is the body cross-sectional area distribution.

The velocity potential due to this line source is

$$\phi(x,r) = -\frac{1}{2\pi}\int_0^{x-\beta r} \frac{S'(X)\,dX}{\sqrt{(x-X)^2-\beta^2 r^2}}$$

in the vicinity of the body we take the limit of this solution as $r \to 0$ to obtain

$$\phi \sim \frac{S'(x)}{2\pi}\ln r + \phi_2(x)$$

where

$$\phi_2(x) = -\frac{1}{2\pi}\int_0^x \ln\frac{2(x-X)}{\beta}\, S''(X)\,dX$$

Note that the first term corresponds to $\phi_1(y,z;x)$ for a body of revolution, being a two-dimensional source flow. Any deviation from a circular cross-section is determined solely in the cross flow plane.

A careful application of this to the calculation of drag leads to the familiar formula for bodies

$$\frac{D}{q} = -\frac{1}{2\pi}\int_0^l\int_0^l \ln(x-x_1)\, S''(x)\, S''(x_1)\, dx\, dx_1$$

$$+\frac{1}{\pi}S'(l)\int_0^l S''(x)\ln(l-x)\,dx$$

$$-\frac{1}{2\pi}\left[S'(l)\right]^2 \ln\frac{\beta}{2} - \oint_{BASE} \phi_1 \frac{d\phi_1}{dn}\,ds + \frac{D}{q}_{BASE}$$

where $n$ is the normal to body contour at the base, and $\frac{D}{q}_{BASE}$ is the drag due to base pressure.

If the body is pointed at its base, or ends in a parallel section such that $S'(l) = 0$ then we obtain, assuming zero lift and excluding the base drag term

$$\frac{D}{q} = -\frac{1}{2\pi}\int_0^l\int_0^l \ln|x-x_1|\, S''(x)\, S''(x_1)\, dx\, dx_1$$

The similarity of this equation with that for the induced drag of a lifting line means that, just as we can calculate wing loadings for minimum induced drag, so can we determine supersonic area distributions for minimum wave drag.

A particularly useful one is the Sears-Haack distribution

$$S(x) = \frac{128\,V}{3\pi l}\left\{\frac{x}{l} - \frac{x^2}{l^2}\right\}^{\frac{3}{2}}$$

giving minimum wave drag, for a slender body of volume $V$ and length $l$ with $S'(l)$ zero, equal to

$$\frac{D}{q} = \frac{128\,V^2}{\pi\, l^4}$$

This is often taken as a standard value for such bodies to which observed values can be compared.

We shall be returning to the question of optimum bodies of revolution when we discuss numerical methods. Meanwhile, we note Lighthills result (ref. 5) for a body with a wing terminating in a trailing edge of finite span, 2s,

$$\frac{D}{q} = \frac{1}{2\pi}\int_0^l\int_0^l S''(x)S''(x_1)\ln\left|\frac{l}{x-x_1}\right|dx\,dx_1$$

$$-\frac{S'(l)}{\pi}\int_0^l S''(x)\ln\left|\frac{l}{l-x}\right|dx$$

$$+\left[S'(l)\right]^2\frac{1}{2\pi}\left[\ln\left(\frac{l}{\beta s}\right)+k\right]$$

where $k$ is a constant dependent on the spanwise distribution of trailing edge angle. A typical value of $k$ is 1.5 (uniform distribution).

The importance of this result is that by terminating the body with a finite span trailing edge we can achieve non-zero values of $S'(l)$ while still maintaining zero base area. In this way we can actually achieve lower drags than that for the Sears-Haack body.

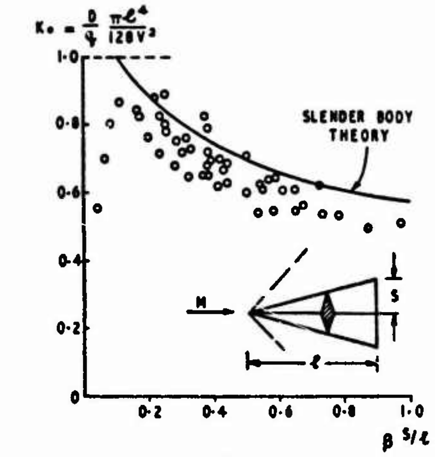

VOLUME DEPENDENT DRAG FOR DELTA WING

FIG. 2.4

Figure 2.4 illustrates the gains achieved for a delta wing with an area distribution of Lord V type. The abscissa is the "Slenderness parameter", $\beta\frac{s}{l}$ and the ordinate, $k_0$, is the ratio of the drag to that of the Sears-Haack body of the same volume and length.

i.e. $\frac{D}{q} = k_0 \frac{128\,V^2}{\pi\, l^4}$

The importance of this result is, of course, that we can achieve a lower drag for a given volume by using a wing-body than by using a body of revolution - which is rather a nice result for the designer!

When using this result the limitations of slender body theory should be borne in mind. Mathematically, this requires

$$\frac{\beta s}{l} \ll 1$$

i.e. that the configuration lies well inside the Mach cone from the nose. In practice, however, it appears that the method works quite well for $\beta\frac{s}{l}$ quite close to unity.

Whereas slender body theory has pointed the way in the development of Concorde it has been necessary to employ the full linear theory to get sensible results; the configuration is not slender at cruise Mach numbers.

Obviously, very few fighter configurations can be regarded as slender in any sense.

For wave drag due to volume however we can turn to the supersonic area rule which we discuss next.

Supersonic Area Rule

The results we have derived for the wave drag so far have been restricted to slender configurations. We shall now discuss, briefly, the calculation of the wave drag of non-slender configurations.

To do this we must return to the 'far-field' approach we used earlier to derive the drag components from momentum considerations.

The wave drag was shown to be given by

$$\frac{D}{q}_{\text{WAVE}} = -2\int_{-\infty}^{\infty} dx \int_0^{2\pi} \phi_x\,\phi_r\,R\,d\theta$$

where $R$ is the radius of the cylinder $S_2$, taken to be very large.

The velocity components $\phi_x$ and $\phi_r$ are to be determined for $r = R \to \infty$ Starting with Volterra's solution to the linearised equation for $\phi$

$$\phi(x,y,z) = -\frac{1}{2\pi}\frac{\partial}{\partial x}\iint_{\tau}\left(\frac{\partial \phi}{\partial \nu_1} - \phi\frac{\partial}{\partial \nu_1}\right) \times$$
$$\times \ln\left|\frac{x-x_1+\sqrt{(x-x_1)^2-\beta^2 r_1^2}}{\beta r_1}\right| dS$$

where $$r_1^2 = (y-y_1)^2 + (z-z_1)^2$$

$S$ is an element of the aircraft surface area

and $\nu_1$ is known as the 'co-normal'

The co-normal derivative is defined by

$$\frac{\partial}{\partial \nu_1} = \frac{-\beta^2 n_1\frac{\partial}{\partial x_1} + n_2\frac{\partial}{\partial y_1} + n_3\frac{\partial}{\partial z_1}}{\sqrt{n_1^2\beta^2 + n_2^2 + n_3^2}}$$

where ( $n_1$ , $n_2$ , $n_3$ ) are the components of the unit normal to the surface.

Lomax has shown (ref. 6) by carefully extracting the limiting values of $\phi$ , $\phi_x$ and $\phi_r$ for large radius, that the wave drag for a general configuration is given by

$$\frac{D}{q} = -\frac{1}{4\pi^2}\int_0^{2\pi} d\theta \int_{-\infty}^{\infty}\int_{-\infty}^{\infty} A''(x;\theta)\, A_1''(x_1;\theta) \ln|x-x_1|\, dx\, dx_1$$

where

$$A''(x;\theta) = S''(x;\theta) - \frac{\beta}{2} L'(x;\theta)$$
$$S''(x;\theta) = \frac{d^2}{dx^2} S(x;\theta)$$
$$L'(x;\theta) = \frac{d}{dx} L(x;\theta)$$

The quantities $S(x;\theta)$ and $L(x,\theta)$ are elemental area and force distributions determined by cutting through the configuration by a series of parallel 'Mach' planes tangent to the set of cones whose semi-included angle, with respect to the $x$ axis, is the Mach angle $\mu = \sin^{-1}\frac{1}{M}$ (Fig. 2.5).

The area $S(x;\theta)$ is that part of the Mach plane enclosed by the body projected onto a plane normal to the freestream, the plane itself cutting the axis at $x = x_1$

The force $L(x;\theta)$ is the component of the resultant force on the cut (found by integrating pressures around the cut) which acts in the plane $\theta$ = const and is normal to the freestream.

This equation gives the wave drag of any lifting or non-lifting aircraft in supersonic flow the only approximations being those basic to linearised theory.

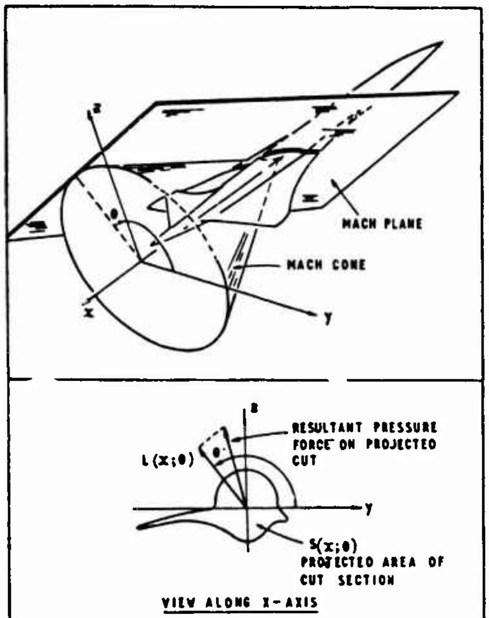
z
θ
x
y
MACH PLANE
MACH CONE
z
L(x;θ)
θ
RESULTANT PRESSURE FORCE ON PROJECTED CUT
y
S(x;θ)
PROJECTED AREA OF CUT SECTION

VIEW ALONG X-AXIS

MACH PLANES, FORCES AND AREAS USED IN SUPERSONIC AREA RULE

FIG.2.5

Obviously the application of this result requires a detailed knowledge of the disturbing object and its surface pressure distribution. If this is known then, rather than calculate the wave drag and vortex drag separately, we would simply integrate the known loading times surface slope to obtain the total pressure drag. However in certain applications we may be able to neglect (say) the force terms in relation to the area terms. For example, if one wishes to find the wave drag of a wing body combination which is symmetrical about the horizontal plane (e.g. a thin non-lifting wing mounted centrally on a body of revolution), it is not necessary to know the pressures on the wing since their contributions to the resultant forces on the cuts are negligible. Hence we would only require the pressures on the body, and in fact only the asymmetry of these pressures in the oblique planes. If the body is slender the latter effect may be assumed negligible compared to the cut area gradient and the drag equation is reduced to

$$\frac{D}{q} = \frac{1}{2\pi}\int_0^{2\pi} \frac{D}{q}(\theta)\, d\theta$$

where

$$\frac{D}{q}(\theta) = -\frac{1}{2\pi}\int_{l_1}^{l_2}\int_{l_1}^{l_2} S''(x;\theta)\, S''(x_1;\theta)\, \ln|x-x_1|\, dx\, dx_1$$

the limits of the integration $l_1$ $l_2$ defining the extent of the elemental area distribution .

On comparison with our slender body results we see that the wave drag may be regarded as the average drag of a series of equivalent bodies of revolution defined by the cut area distributions $S(x;\theta)$.

This technique is known as the supersonic area rule.

Transferred Area Rule

We have already indicated that the calculation of the wave drag of a wing-body combination by the supersonic area rule requires the body to be slender. If the body is slender enough for each of its cut area distributions to be considered the same as its normal cross-sectional area distribution then we can make a further simplification by writing the elemental area distribution as

$$\begin{aligned} S(x,\theta) &= S_f(x,\theta) + S_w(x,\theta) \\ &\approx S_f(x) + S_w(x,\theta) \end{aligned}$$

Placing this in the drag formula there obtains, after some manipulation, the result

$$\frac{D}{q} = \frac{D}{q}\{S_F + A\} - \frac{D}{q}\{A\} + \frac{D}{q}\{S_w\}$$

where $\frac{D}{q}\{S_F + A\}$ is the drag of a body with the area distribution equal to the sum of the fuselage plus the 'transferred' wing

$\frac{D}{q}\{A\}$ is the drag of the transferred wing

$\frac{D}{q}\{S_W\}$ is the wave drag of the exposed wing

and $A(x) = \frac{1}{2\pi}\int_0^{2\pi} S_W(x,\theta)\, d\theta$ is the transferred wing area defined as the average of the cut area distributions.

It should be noted that we may replace the supersonic area rule calculation for the exposed wing alone (the last term above) by any other suitable method.

The beauty of the transferred area rule is that the wing-body interference is contained in the first term and involves only the drag of a single equivalent body.

This means that for a given wing we can determine the optimum body area distribution for a minimum drag combination in the same manner as that used for slender bodies, subject, of course, to the slenderness restrictions noted above. The latter will become more important at the higher supersonic Mach numbers.

While we are discussing the drag of bodies we consider one other development for bodies of revolution. This method is capable of dealing with non-slender (i.e. nonsmooth) bodies that have discontinuous surface slopes.

Warren and Fraenkel's Combined Quasi-Cylinder Slender Body Theory

The quasi-cylinder theory was devised to deal with bodies whose surface lies close to a circular cylinder with its generators parallel to the freestream. Specifically it was aimed at the problem of calculating the supersonic flow over open nosed bodies such as engine nacelles and bodies with discontinuities in the surface slope.

The theory (ref. 7) relies on the development of some special quasi-cylinder functions with rather complex definitions. Specifically, the particular function of interest for axi-symmetric bodies is

$$U_1(x) = \mathcal{L}^{-1}\left\{ \frac{K_0(p)}{pK_1(p)} \right\}$$

where $\mathcal{L}^{-1}$ denotes the inverse Laplace transform and $K_0(z)$ , $K_1(z)$ are modified Bessel functions of the second kind.

Now, for large $x$

$$U_1(x) \sim \ln 2x$$

and by comparison of the equation for the potential on a quasi-cylinder of mean radius $\bar{R}$

$$\phi(x, \bar{R}) = -\bar{R}\int_0^x U_1\left(\frac{x-\xi}{\beta\bar{R}}\right) d\,R(\xi)$$

with the slender body result

$$\phi(x, r) = -\frac{1}{2\pi}\int_0^x \ln\left[\frac{2(x-\xi)}{\beta r}\right] d\,S'(\xi)$$

Warren and Fraenkel arrived at the combined result for the perturbation velocity

$$\phi_x(x) = \frac{1}{2\pi\beta r}\int_0^x U\left(\frac{x-\xi}{\beta r}\right) d\,S'(\xi)$$

where

$$U(x) = \frac{d}{dx}U_1(x)$$

The integrals are expressed in Stieltjes form to allow for discontinuities in $S'(x)$. The pressure coefficient is given by the same non-linear formula as that of slender body theory, namely,

$$C_p = -2\phi_x - [R']^2$$

and the drag may be obtained by direct integration, that is

$$\frac{D}{q} = \int_0^l C_p\, S'(x)\, dx = -\int_0^l (2\phi_x + [R']^2)\, S'(x)\, dx$$

By way of example we show the results for the pressure distribution over an afterbody compared with those according to slender body theory and the method of characteristics in Figure 2.6.

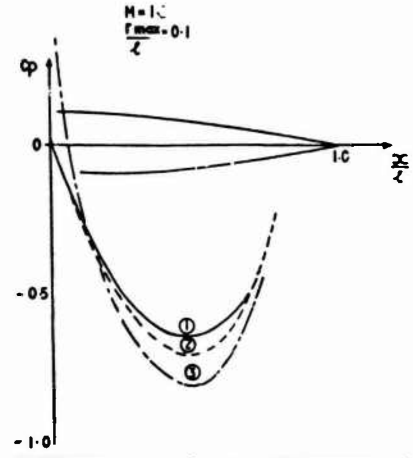

COMPARISON OF TWO LINEARISED THEORIES WITH THE METHOD OF CHARACTERISTICS FOR A PARABOLIC AFTERBODY

FIG 2.6

## Application of Methods - Accuracy

Here we are not concerned with the accuracy of numerical techniques, but of the basic theories themselves. In order to investigate this an extensive set of test cases were set up to which the slender body and supersonic area rule methods were applied (Ref. 8).

The bodies used were all bodies of revolution enabling the results to be checked against the method of characteristics.

The results are summarised in Figures 2.7, 2.8 for smooth bodies.

Of these methods slender body theory shows no dependence of the drag upon Mach number as all the bodies had $S'(l)$ zero.

Supersonic area rule has Mach number dependence as this effects the angle of the oblique cutting planes. Warren and Fraenkel's method incorporates the Mach number effects explicitly. Of the three only the Warren and Fraenkel method is expressly designed to cater for open nosed bodies and bodies with discontinuous surface slope, although the supersonic area rule does appear capable of handling these with reasonable accuracy (fig. 2.9). Slender body theory implies that the bodies must be smooth, i.e. $S'$ continuous.

The results of this exercise indicate that if slender body theory is to be used then the body must indeed be very slender for it to be valid. This in turn implies that the transfer rule may only be used on configurations with very slender bodies. The improvement in the estimates afforded by the supersonic area rule is considerable, although the errors might still be regarded as too high when dealing with fighter aircraft.

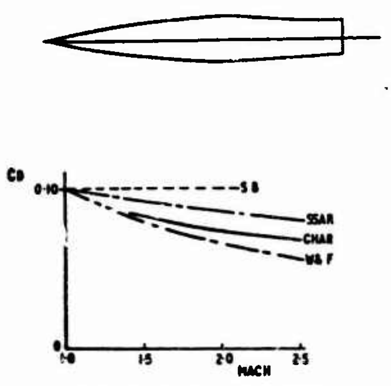

DRAG OF A BODY OF REVOLUTION BY VARIOUS THEORIES

SB–SLENDER BODY
SSAR–SUPERSONIC AREA RULE
W & F–WARREN & FRAENKELS COMBINED THEORY
CHAR–METHOD OF CHARACTERISTICS

FIG 2.7

For general bodies of revolution it is the combined theory of Warren and Fraenkel that on the whole gives the best results.

## Evaluation of the Double Integral

So far we have not considered by what process we shall numerically evaluate the basic double integral that pervades our analysis, namely,

$$\frac{D}{q} = -\frac{1}{2\pi}\int_0^l\int_0^l S''(x)\,S''(x_1)\,\ln|x-x_1|\,dx\,dx_1$$

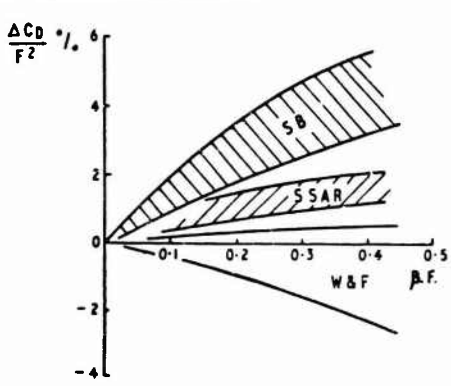

FINENESS RATIO DEFINED AS:-

$$F = \frac{d_{MAX}}{l}\sqrt{1 - 1/2\left(\frac{S_N + S_B}{S_{MAX.}}\right)}$$

$$\Delta C_D = C_{D_{LIN.}} - C_{D_{CHAR.}}$$

ACCURACY OF LINEAR THEORIES - SMOOTH BODIES

FIG. 2.8

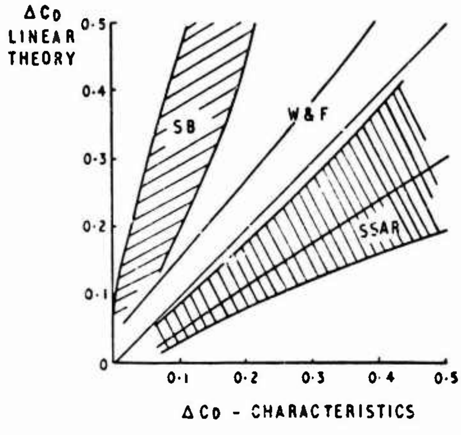

$$\Delta C_D = \frac{(D/q)\ \text{WITH BULGE} - (D/q)\ \text{WITHOUT}}{\text{MAX. X-SECTION AREA OF BULGE}}$$

ACCURACY OF LINEAR THEORIES FOR BODIES WITH BULGES

FIG. 2.9

There are two methods commonly used in the evaluation of this integral, that due to Cahn and Olstad and that due to Eminton.

Before examining the results obtained by these two methods, we will outline briefly the basic formulae involved.

Cahn and Olstad

The first step is to re-write the double integral in the alternative form

$$\frac{D}{q} = -\frac{1}{\pi}\int_0^\ell S''(x)\int_0^x S''(x_1)\,\ln(x-x_1)\,dx_1\,dx$$

which, on changing the order of integration, becomes

$$\frac{D}{q} = -\frac{1}{\pi}\int_0^\ell \ln(x)\int_x^\ell S''(x_1)\,S''(x_1-x)\,dx_1\,dx$$

This integral is then approximated by the summation

$$\frac{D}{q} = -\frac{\ell^2}{\pi N^2}\sum_{j=0}^{N-1} L_j \sum_{i=j}^{N-1} S''_i\, S''_{i-j}$$

where

$$S''_i = S''\left[\frac{\ell}{N}\left(i+\frac{1}{2}\right)\right]$$

and

$$L_j = \left[j+\tfrac{1}{2}\right]\ln\left[j+\tfrac{1}{2}\right]-\left[j-\tfrac{1}{2}\right]\ln\left[j-\tfrac{1}{2}\right] \;;\; j \neq 0$$

$$L_0 = -\frac{1}{2}\ln 2$$

They also suggest that $S''$ be calculated using the finite difference formula

$$S''_i = \frac{S_{i+1} - 2S_i + S_{i-1}}{\left[\ell/N\right]^2}$$

where

$$S_i = S\left[\frac{\ell}{N}\left(i+\tfrac{1}{2}\right)\right]$$

Minimal Drag Bodies and Emintons Method

Noting the similarity between the wave drag integral and the vortex drag integral suggests that we use a 'classical' Fourier series approach.

Introducing the variable $\theta$ (not to be confused with earlier usage) defined by

$$x = \frac{1}{2}\ell\,(1-\cos\theta)$$

the nose is represented by $\theta = 0$ and the base by $\theta = \pi$. Assuming that $S'(0) = S'(\ell) = 0$, we express $S'(x)$ by the Fourier sine series

$$S'(x) = \ell\sum_{n=1}^{\infty} a_n \sin n\theta$$

the drag integral reduces to

$$\frac{D}{q} = \frac{\pi}{4}\ell^2\sum_{n=1}^{\infty} n\,a_n^2$$

The corresponding area distribution is found by integrating the Fourier series over $x$ :

$$S(x) = \frac{\ell^2}{4}\left\{a_1\left(\theta - \tfrac{1}{2}\sin 2\theta\right) + \sum_{n=2}^{\infty} a_n\left(\frac{\sin(n-1)\theta}{n-1} - \frac{\sin(n+1)\theta}{n+1}\right)\right\}$$

$$= \frac{\ell^2}{4}\left\{a_1\theta + \sum_{n=1}^{\infty}\frac{1}{n}\left(a_{n+1} - a_{n-1}\right)\sin n\theta\right\}$$

where $a_0$ is defined to be zero in the last expression.

A further integration gives the total volume

$$V = \frac{\pi \ell^3}{8}\left(a_1 + \frac{a_2}{2}\right)$$

and from the expression for $S(x)$ with $\theta = \pi$ we have the base area

$$S_B = S(\ell) = \ell^2 \frac{\pi}{4} a_1$$

Consider the problem of finding the area distribution with minimum drag and given base area. Since all the Fourier components contribute to the drag the solution is given by setting $a_n = 0$, $n \neq 1$, and the drag is

$$\frac{D}{q} = \frac{4}{\pi \ell^2} S_B^{\,2}$$

The area distribution is

$$S = \frac{S_B}{\pi}\left(\theta - \tfrac{1}{2}\sin 2\theta\right) = \frac{S_B}{\pi}\left\{\cos^{-1}\left(1 - \frac{2x}{\ell}\right) + \left(1 - \frac{2x}{\ell}\right)^{\frac{1}{2}}\right\}$$

which is the von Karman ogive.

For a body which is pointed at both ends ( $S_B = 0$) and has a given volume we obtain the Sears-Haack distribution

$$S(x) = \frac{4V}{\pi \ell}\left(\sin\theta - \tfrac{1}{3}\sin 3\theta\right) = \frac{128}{3\pi}\frac{V}{\ell}\left(\frac{x}{\ell} - \frac{x^2}{\ell^2}\right)^{3/2}$$

with the drag

$$\frac{D}{q} = \frac{128 V^2}{\pi \ell^4}$$

By considering more general mimima, constrained to have given areas $S_i$ at N points $\frac{x}{\ell} = \xi_i$ Eminton has derived the formula

$$\frac{D}{q} = \frac{4}{\pi \ell^2} S_B^{\,2} + \pi \ell^2 \sum_{i=1}^{N}\sum_{j=1}^{N} \lambda_i \lambda_j \phi(\xi_i, \xi_j)$$

where the equations $$\sum_{i=1}^{N} \lambda_i \phi(\xi_i, \xi_j) = \frac{S_i}{\ell^2} - \frac{S_B}{\ell^2} u(\xi_j) \quad ; \quad j = 1, 2 \cdots N$$

give the $\lambda_i$. The functions $u(\xi_i)$ and $\phi(\xi_i, \xi_j)$ are defined by

$$u(\xi_i) = \frac{1}{\pi}\left\{\cos^{-1}(1 - 2\xi_i) - 2(1 - 2\xi_i)\sqrt{\xi_i(1 - \xi_i)}\right\}$$

and

$$\phi(\xi_i, \xi_j) = \tfrac{1}{2}(\xi_i - \xi_j)^2 \ln\left\{\frac{\xi_i + \xi_j - 2\xi_i\xi_j - 2\sqrt{\xi_i\xi_j(1-\xi_i)(1-\xi_j)}}{\xi_i + \xi_j - 2\xi_i\xi_j + 2\sqrt{\xi_i\xi_j(1-\xi_i)(1-\xi_j)}}\right. + 2(\xi_i + \xi_j - 2\xi_i\xi_j)\sqrt{\xi_i\xi_j(1-\xi_i)(1-\xi_j)}$$

The area distribution is then

$$S(x) = \frac{1}{\pi} S_B\, u\left(\frac{x}{\ell}\right) + \sum_{i=1}^{N} \lambda_i \phi\left(\frac{x}{\ell}, \xi_i\right)$$

This approach is useful in that minimum drag bodies may be designed to satisfy certain area constraints (and with a slight modification a volume constraint) as required. Alternatively, by specifying the area distribution of a given body at a suitably large number of points the above formulae gives a technique for the numerical evaluation of the integral. Since the method is based on a minimisation process the drag values obtained for increasing numbers of points will approach the true value from below.

## Comparison of the two Methods

Both of the above methods have been used to estimate the value of the wave drag integral for both smooth and bumpy bodies. The bodies were defined analytically and the numerical results have been compared with the exact analytic result in figure 2.10.

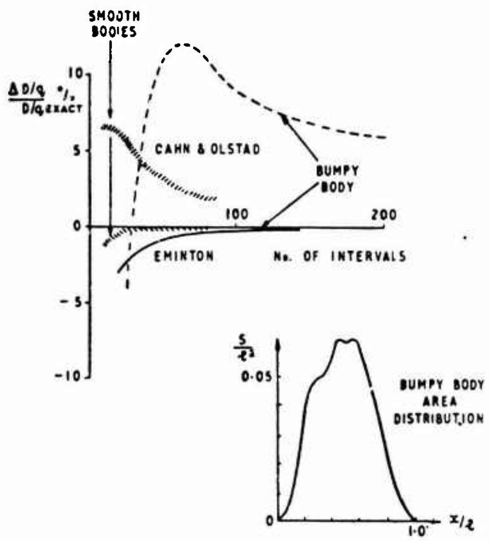

COMPARISON OF TWO METHODS TO COMPUTE THE DRAG INTEGRAL NUMERICALLY

FIG. 2.10

Emintons method stands out as being the more reliable of the two methods converging more rapidly and consistently with increasing number of points used. However, it should be said that much depends on the positioning of the points especially with regard to the rounded noses of wing-like surfaces.

When computing the drag of a general configuration using the supersonic area rule there is the additional problem of what interval $\Delta\theta$ one should use to determine the elemental drags. Figure 2.11 shows a plot of $D/q$ versus $\theta$ for a wing body combination at $M = 1.4$. The value of $\theta$ at which the Mach plane lies along the wing leading edge is marked; linear theory would suggest an infinite value and the calculation results in a peak value. When the Mach plane cuts through the wing so that the wing cross sectional area is found there is another peak ( $\theta = 90^\circ$ ).

The second plot in figure 2.11 shows how the drag value varies with the choice of $\Delta\theta$. The percentage error bears little relation to $\Delta\theta$ (these results were obtained by simply averaging the drags of the equivalent bodies). In this particular example $\Delta\theta$ must be less than $5^\circ$ to achieve less than 1% error.

## Geometric Considerations

The practical application of the foregoing methods to general aircraft configurations presents us with the formidable task of determining the area distributions. While the numerical determination of the drag of a given area distribution is readily programmed for the computer, the development of numerical techniques to evaluate the cut areas is not so obvious. Draughting techniques whereby plane sections of a general body may be produced are well known. However, attempts to reproduce these methods in a digital computer program rapidly lead to difficulties which may be attributed to the use of the cartesian coordinate system as a basis. It ie necessary therefore to find a system which is both simple and yet flexible and which is amenable to digital computation.

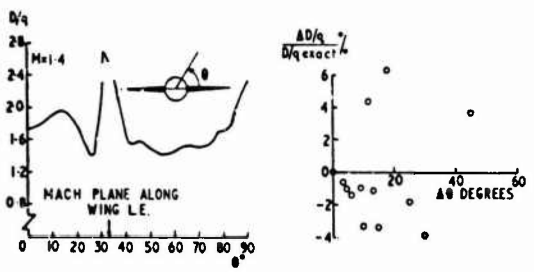

SENSITIVITY OF NUMERICAL INTEGRATION PROCESS TO ANGULAR INTERVAL

FIG. 2.11

The representation chosen is completely compatible with the Numerical Master Geometry systems used in our organisation. This means that surfaces designed using this representation will remain unchanged through to model or even full size aircraft manufacture.

The method is bi-parametric; that is the surface is described in the surface coordinates (parameters) $u$ and $v$ :

$$x = x(u,v)$$

$$y = y(u,v)$$

$$z = z(u,v)$$

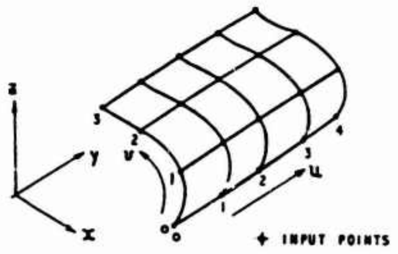

A PARAMETRIC SURFACE

FIG. 2.12

Such a surface is illustrated in fig. 2.12.

Just as a point on the earths surface is uniquely defined by the two quantities latitude and longitude, so the position of a point on a general surface may be defined through the values $u$ and $v$. The use of a parametric representation also enables us to deal easily with regions of steep slope. For example consider a case where y is independent of $u$

i.e. $y = y(v)$

If the surface is that of a wing then the curves $v$ = constant represent chordwise sections. We then have the streamwise slope

$$\left.\frac{dz}{dx}\right|_{v = \text{CONSTANT}} = \frac{\partial z/\partial u}{\partial x/\partial u}$$

and $\frac{dz}{dx} = \infty$ corresponds to $\frac{dz}{du}$ finite with $\frac{dx}{du} = 0$. We can therefore handle rounded leading edges (for example) without special consideration.

The fitting process assumes that the input control points, at which values of $x, y, z$ are supplied, correspond to integer values of $u$ and $v$ (see fig. 2.12). Fitting is performed first in the $u$ direction, then in the $v$ direction. For example take $v = j$. Then the curve $v = j$ is specified by the points

$$\left.\begin{array}{l} x(i,j) \\ y(i,j) \\ z(i,j) \end{array}\right\} i = 1, 2, 3 \cdots m.$$

Each of these sets of points is used to define a mathematical spline. That is each arc from $x(i,j)$ to $x(i+1,j)$ is represented by a cubic polynomial in $u$, matching its neighbours in ordinate and first and second derivatives.

Since the cubic is completely determined by its end point ordinates and slopes the fitting process is used to deduce these slopes rather than the coefficients of the polynomial.

By repeating the process in the $v$ direction we now have a scheme whereby set of input points

$$\{ x_{ij}, y_{ij}, z_{ij} : i = 1, 2, 3, \cdots m, j = 1, 2, 3, \cdots n \}$$

is used to define a complete surface. It should be mentioned at this point that some care is necessary in the choice of distribution of the input control points.

The advantages of the system may be summarised :

(i) The coefficients of the surface fit are physically meaningful as they are the surface ordinates and slopes at the control points.

(ii) The surfaces are invariant under all linear transformations of the coordinate system. These transformations are applied directly to the coefficients and are easily executed using matrix operations.

The resulting geometry syste [illegible] markably simple involving, as it does, only one type of surface representation, and yet capable of representing very general surface geometries accurately.

Add to this a routine capable of tracing a plane section

$$x(u,v) = \text{constant, say}$$

then we can determine any plane section $a_1 x(u,v) + a_2 y(u,v) + a_3 z(u,v) = \text{CONSTANT}$

by first applying the transformation $x' = a_1 x + a_2 y + a_3 z$

and determining the points $(u, v)$ such that

$$x'(u,v) = \text{constant}$$

Once the section has been traced in terms of $(u, v)$ then it is a simple matter to determine the coordinates $x$, $y$, $z$ and the area, centroid etc.

As an example of the application of the method figure 2.13 illustrates a parabolic body of revolution together with the numerical results for the area distributions at M = 1 and M = 1.414.

Obviously such a system is of more general use than that of determining the cut area distributions for supersonic area rule calculations. For example the ability to produce oblique plane sections will help in wind tunnel model manufacture as well as providing surface slopes for use in wing theories etc.

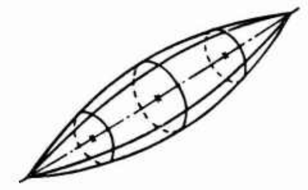

(a) VIEW OF THE BODY

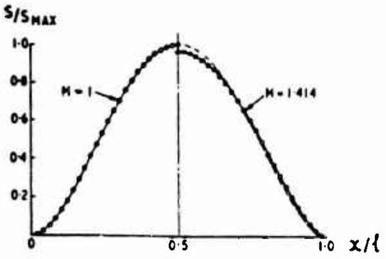

(b) AREA DISTRIBUTIONS AT M = 1, M = 1·414

PARABOLIC BODY OF REVOLUTION - GEOMETRY

FIG. 2.13

## 2.3 PRESSURE DRAG DUE TO LIFT-WINGS

Although simplified theories exist for slender and not-so-slender wings (ref. 9) and have supplied general results of use in configuration selection studies, practical wings cannot be regarded as slender in general. We therefore consider the full linearised equation for potential flow.

$$-\beta^2 \phi_{xx} + \phi_{yy} + \phi_{zz} = 0$$

where $\beta = \sqrt{M^2-1}$. The associated boundary condition for tangential flow at the wing surface is, within the linearised theory

$$\phi_z = \begin{cases} \dfrac{\partial z_u}{\partial x} & \text{on } z = 0^+ \\ \dfrac{\partial z_l}{\partial x} & \text{on } z = 0^- \end{cases} \quad \text{for } (x,y) \text{ on } S$$

where $S$ is the wing surface. In addition the flow perturbations must vanish forward of the most upstream point of the wing. The Kutta condition need not be specified in supersonic flow unless the trailing edge has a sweep greater than that of the Mach lines. In this case the flow velocity component normal to the edge is subsonic. Such an edge is termed subsonic. A wing with all edges supersonic (i.e. with sweep less than the Mach lines) is said to have a 'simple' planform. An example is shown in figure 2.14.

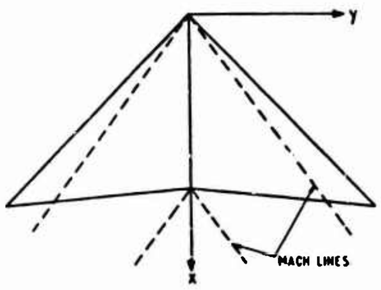

A SIMPLE PLANFORM

FIG. 2.14

A solution of the potential equation suitable for use in thin wing problems is the source superposition integral

$$\phi(x,y,z) = -\frac{1}{\pi}\iint_{\tau} \frac{\omega(\xi,\eta)\,d\xi\,d\eta}{\sqrt{(x-\xi)^2-\beta^2[(y-\eta)^2+z^2]}}$$

where $\omega(\xi,\eta) = \frac{\partial z_u}{\partial x}$ on $z = 0^+$

and the pressure coefficient is given by $C_p = -2\phi_x$

The region of integration, $\tau$, is that portion of the $z = 0$ plane intercepted by the upstream Mach cone from the point $(x, y, z)$ : see figure 2.15.

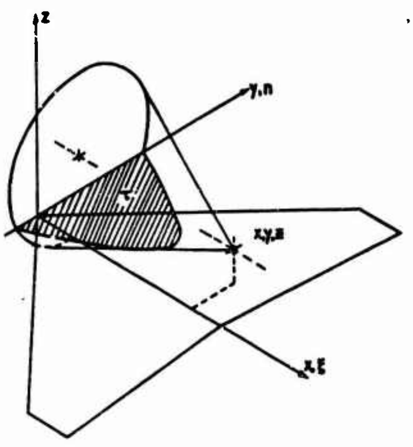

REGION OF SOURCE DISTRIBUTION INFLUENCING THE POINT (x,y,z)

FIG. 2.15

While the source superposition integral is strictly only to be applied to the symmetric flows due to thickness, we shall see that in supersonic flow how this simple formula may be used to calculate lifting flows.

### Simple Planforms

For wings with only supersonic edges there is no interaction between the flows over the upper and lower surfaces of the wing. Hence the flow above the wing, will be the same as that for a symmetric wing with the same upper surface shape. In this case the source superposition integral may be applied directly to obtain the flow for $z > 0$. The flow for $z < 0$ is obtained from the basic antisymmetry of the lifting flow with respect to $z = 0$.

### General Planforms

Whenever the wing has an edge, or a part of one, that is subsonic, the problem becomes more complicated. This is because the source integral requires that $\omega$ be known throughout the whole upstream region of influence from the field point. In the non-lifting case the symmetry of the flow about $z = 0$ leads to $\omega = 0$ outside the wing planform. In the case of a simple planform no disturbance can propagate ahead of the wing leading edge and thus $\omega$ is zero ahead of the leading edge; that is $\omega$ is known within the region of influence regardless of whether the wing is lifting or not. In the case of a wing with a subsonic leading edge however $\omega$ is not zero ahead of the edge; on the contrary it is, in general, singular just ahead of the edge.

Fortunately, in supersonic flow, the region of the $z = 0$ plane that may be influenced by or that may influence the wing is finite in extent. We may utilise this fact by extending the wing forward from its leading edge into the undisturbed flow by a flexible diaphragm that is to carry zero load (see figure 2.16).

Due to antisymmetry the load acting on the plane $z = 0$ is

$$\Delta C_p(x,y) = C_p(x,y,0^-) - C_p(x,y,0^+)$$
$$= -4\phi_x(x,y,0^+)$$

thus the zero load condition becomes

$$\phi_x = 0$$

which may be integrated to give

$\phi = 0 \quad (x,y)$ forward of the leading edge
$\phi = \phi_{T.E.}(x,y)$ in the wake

The problem is now

$$\phi(x,y,0) = -\frac{1}{\pi}\iint_{\tau} \frac{\omega(\xi,\eta)\,d\xi\,d\eta}{\sqrt{(x-\xi)^2-\beta^2(y-\eta)^2}}$$

where $\omega$ is known on the wing but has to be determined from the conditions

$\phi = 0$ on the diaphragm
$\phi = \phi_{TE}$ on the wake

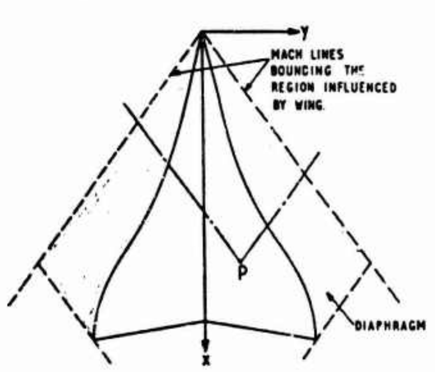

PLANAR WING IN SUPERSONIC FLOW ILLUSTRATING THE DIAPHRAGM CONCEPT

FIG. 2.16

**Numerical Procedures**

While analytic results exist for a restricted class of planforms and upwash distributions practical wings have to be treated by a suitable numerical method. The usual procedure is to subdivide the area of integration into suitable elements assuming $w$ to be constant within each elementary area. Two main types of element have been used extensively (fig. 2.17).

(a) the "Mach box" where the elements are rectangles having their diagonals parallel to the Mach lines

and (b) the "Mach diamond" or "Characteristic box" where the element is a rhombus with sides parallel to the Mach lines.

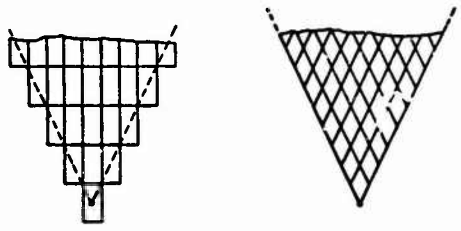

(a) MACH BOX (b) MACH DIAMOND

SUBDIVISION OF INTEGRATION AREA IN NUMERICAL SCHEMES

FIG 2.17

Since the elements are of constant size the integration can be carried out in advance for unit $w$ and tabulated as a function of the position of the box relative to the pivotal point $(x, y)$ on the wing or diaphragm.

Assume that $w$ is known or has been calculated for all the boxes influencing the pivotal point, $P$. Then if $P$ is on the wing $w$ is known and $\phi$ can be calculated from the double summation

$$\phi_{ij} = \sum_{i'=1}^{i}\sum_{j'=1}^{j} \Phi_{i-i',j-j'} \cdot w_{i'j'}$$

where $\Phi_{i-i',j-j'}$ is the influence of the element $(i', j')$ on the pivot point in the element $(i, j)$ for unit $w$.

If, however, $P$ is off the wing then $\phi$ is known from the diaphragm or wake condition. The summation is now written

$$\phi_{ij} = \Phi_{00} w_{ij} + \sum_{i'=1}^{i}\sum_{j'=1}^{j} \delta^{ij}_{i'j'} \Phi_{i-i',j-j'} w_{i'j'}$$

where

$$\delta^{ij}_{i'j'} = \begin{cases} 0 & \text{if } i'=i \text{ and } j'=j \\ 1 & \text{otherwise} \end{cases}$$

The double sum now excludes the effect of the element on itself and we have the solution for

$$w_{ij} = \frac{1}{\Phi_{00}}\left\{\phi_{ij} - \sum_{i'=1}^{i}\sum_{j'=1}^{j} \delta^{ij}_{i'j'} \Phi_{i-i',j-j'} w_{i'j'}\right\}$$

By starting at the foremost element it is always possible to perform the calculations in such an order as to ensure that the $w_{ij}$ are known for every element influencing the pivot excepting, possibly, the pivot element itself. The solution is therefore easily obtained using the simple formulae above.

The above procedure is crude as the decision as to whether an element lies on the wing or not is determined by whether the pivot point itself lies on the wing or not. Boxes lying partially on the wing may therefore be treated as being wholly on or wholly off the wing.

A simple refinement is firstly to treat the box as wholly off the wing thus giving a value for the upwash, $w'$, say. The upwash on that part of the element covered by the wing is known, however, so we combine this with $w'$ according to

$$\bar{w}_{ij} = a\, w_{ij} + (1-a)\, w'$$

where $\bar{w}_{ij}$ is a 'mean value' for the upwash acting on the element and $a$ is the ratio of the area of element covered by the wing to the area of the element.

Finally $\phi_{ij}$ is recomputed using $\bar{w}_{ij}$ in place of $w_{ij}$.

This procedure, known as 'area weighting', results in a significant improvement in the computed load distribution and overall forces, although it still leaves much to be desired near the wing leading edges.

There has been much argument about the relative merits of the two grid systems defined by the Mach-box and Characteristic-box methods described above. Briefly, we may say that the Mach box is better for treating supersonic edges while the Characteristic box gives better results for wings with subsonic edges.

However, as we shall now explain, there are considerable reductions in computing time to be had if we re-examine the problem in terms of characteristic coordinates.

## A Fast Method

We cannot hope to explain the details of this technique, due to Roberts (ref. 10), in full. However we shall endeavour to indicate the more important features. The method is based on the transformation of the coordinates

$$\tau = \tfrac{1}{2}\left\{\frac{x}{\beta} - y\right\}$$
$$s = \tfrac{1}{2}\left\{\frac{x}{\beta} + y\right\}$$

so that $\tau$ and $s$ are parallel to the freestream Mach lines. The source superposition integral now becomes

$$\phi(\tau, s, 0^+) = -\frac{1}{\pi}\int_0^{\tau}\int_0^{s}\frac{\omega(\rho,\sigma)\,d\rho\,d\sigma}{\sqrt{(\tau-\rho)(s-\sigma)}}$$

where the wing is assumed to be wholly contained in the positive quadrant of the $\tau$-$s$ plane. The relationship between the coordinates and the wing is illustrated in figure 2.18. The integral can now be factored into two line integrals

$$\phi(\tau,s) = \frac{1}{\sqrt{\pi}}\int_0^{\tau} g(\rho,s)\,\frac{d\rho}{\sqrt{\tau-\rho}}$$

where $$g(\tau, s) = -\frac{1}{\sqrt{\pi}}\int_0^{s}\omega(\tau,\sigma)\,\frac{d\sigma}{\sqrt{s-\sigma}}$$

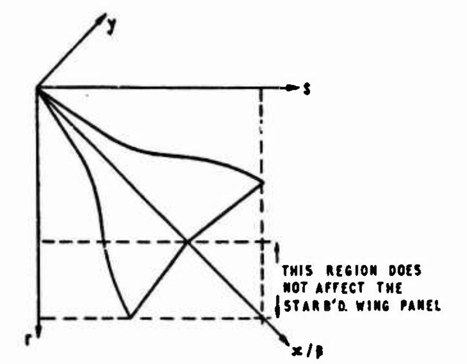

THE WING IN (r, s) CO-ORDINATES

FIG. 2.18

Herein lies the 'secret' of the method, for by retaining the intermediate function, $g$, and the line integral format in our numerical technique we can organise the calculation so that the conventional double summation required for each pivotal point is replaced by two line sums.

Before describing the method consider the line integral

$$f(\tau) = \frac{1}{\sqrt{\pi}}\int_0^{\tau}\frac{d\rho}{\sqrt{\tau-\rho}}\,h(\rho)$$

which is known as Abel's integral. It is not difficult to show that the inverse is given by

$$h(\tau) = \frac{1}{\sqrt{\pi}}\frac{\partial}{\partial\tau}\int_0^{\tau}\frac{d\rho}{\sqrt{\tau-\rho}}\,f(\rho)$$

This means that the condition $\phi = 0$ on the diaphragm implies

$$g(\tau, s) = 0$$

providing that the characteristic line $s =$ const does not cross the planform for $0 < \tau < \tau_{LE}(s)$

Providing the leading edge is not swept forward, figure 2.18 indicates that this holds on the starboard diaphragm. (From this we can determine Evvards well known reflection principle since $g(\tau, s) = 0$ on the diaphragm leads to

$$\phi(\tau, s) = \frac{1}{\sqrt{\pi}}\int_{\tau_{LE}(s)}^{\tau} g(\rho, s)\,\frac{d\rho}{\sqrt{\tau-\rho}}$$

with $g$ defined as before).

We can also determine the behaviour of the $g$ function along lines $s =$ const. as we cross the leading edge. For a subsonic edge $g$ is a step function with a jump from zero to some finite value at the edge. For a supersonic edge $g$ behaves locally like $\sqrt{\tau - \tau_{LE}}$.

Now assume that we have a discrete form for the integral with $\tau = mh$

$$f(\tau) = f(mh) = f[m] = \frac{1}{\sqrt{\pi}}\int_0^{mh}\frac{d\rho}{\sqrt{\tau-\rho}}\,h(\rho)$$
$$= \sum_{\mu=1}^{m} A_{m-\mu}\,h[\mu]$$

where $h[\mu] = h(\{\mu - \tfrac{1}{2} + \varepsilon\})$ and $\varepsilon$ is a constant between 0 and 1.

We can re-write this as

$$f[m] = A_0 h[m] + \sum_{\mu=1}^{m-1} A_{m-\mu} h[\mu]$$

whence

$$h[m] = \frac{1}{A_0}\left\{f[m] - \sum_{\mu=1}^{m-1} A_{m-\mu} h[\mu]\right]$$

By applying this last relation recursively for $m = 1, 2, \ldots$ we arrive at a discrete inverse form :

$$h[m] = \sum_{\mu=1}^{m} B_{m-\mu} f[\mu]$$

where

$$B_0 = \frac{1}{A_0}$$

$$B_m = -B_0 \sum_{\mu=1}^{m-1} B_\mu A_{m-\mu}, \quad m = 1, 2 \ldots .$$

In Roberts' method the A and B coefficients take the particularly simple forms

$$A_m = (-1)^m C_m^{-\varepsilon} \qquad B_m = (-1)^m C_m^{+\varepsilon}$$

where $C_m^a$ is the binomial coefficient. In this case the constant $\varepsilon = \frac{1}{4}$ is used. However our argument still holds whatever form the discretisation takes providing it is based on equally spaced samples as indicated above.

We are now in a position to describe the basic computing sequence. Assume that the flow is symmetric about the vertical plane $y = 0$. Only that portion of the port wing that influences the starboard wing panel need then be considered (fig. 2.18).

Referring to figure 2.19 we assume that $g$ is known for $r < n$ and that $\phi$ is known within the Mach forecone from $r = s = n-1$. The calculation for $r = n$ is then

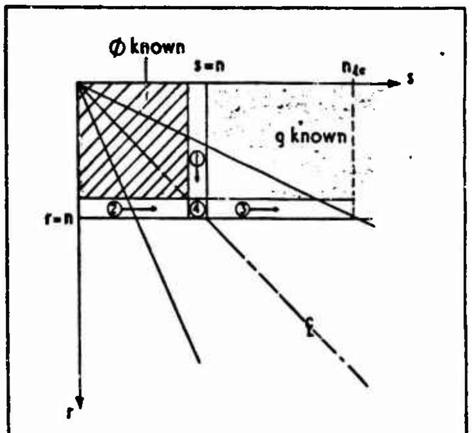

BASIC COMPUTING SEQUENCE FOR FAST SUPERSONIC WING METHOD

FIG. 2.19

(1) Calculate $\phi$ from $g$ along $s = n$ using

$$\phi[m,n] = \sum_{\mu=1}^{m} A_{m-\mu} g[\mu], \quad m = 1 \text{ to } n-1$$

(i.e. up to but not including the point on the wing centre line)

(2) Copy $\phi$ from the starboard to the port side

$$\phi[n,m] = \phi[m,n]$$

and calculate $g$ using

$$g[n,m] = \sum_{\mu=1}^{n} B_{n-\mu} \phi[\mu,m]$$

for $m = 1$ to $n-1$.

(3) Calculate $g$ from $w$ using

$$g[n,m] = -B_0 w[n,m] - \sum_{\nu=1}^{m-1} B_{m-\nu} g(n,\nu)$$

for $m = n$ to $n_{LE}$

(4) Calculate $\phi$ on the centre line

$$\phi[n,n] = \sum_{\mu=1}^{n} A_{n-\mu} g[\mu,n]$$

This process is used for $n = 1$ to nmax such that the whole grid is covered. Some variations of the above sequence are necessary to cater for trailing edge and wake effects and certain types of leading edge.

It should be noted that the order of calculation can be arranged such that $w$, $g$ and $\phi$ may be stored in the same array in computer core, the values of $g$ overwriting those of $w$ and being overwritten in turn by those of $\phi$.

Given a knowledge of the type of singularity to be found near the leading edge together with the line integral format it is not difficult to devise suitable techniques to refine the calculation in this region. However as the form of this refinement will depend on the nature of the discretisation used we do not discuss it in detail. Suffice it to state that Roberts has achieved a very high degree of accuracy by fitting a function exhibiting the correct singularity to the $\xi$ values close to the leading edge. The values of $\phi$ in this region are then obtained analytically. For calculations away from the edge the fitted $\xi$ values are modified by a smoothing process before applying his discrete formula.

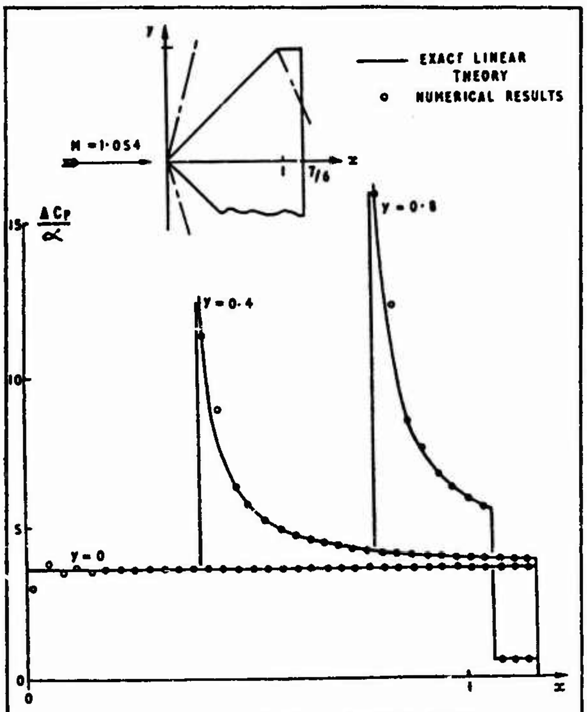

LOAD DISTRIBUTION ON A CROPPED DELTA

FIG.2.20

Figure 2.20 presents a comparison of a numerical calculation using a slightly less refined method than that of Roberts with exact linear theory for a cropped delta wing at incidence. Had the full leading edge refinement been employed the load distribution near the leading edge would have been even closer to the exact linear theory.

In order to indicate the time savings made we note that in the conventional method the double summation at the $(m, n)$ th grid point (box) involves $mn$ terms, the calculation of each term involving one multiplication with one addition to add the term into the sum. Taking our unit as the time to complete one addition and one multiplication, the total time for the conventional method applied to an $M \times N$ grid is

$$T_c = \sum_{m=1}^{M}\sum_{n=1}^{N} mn$$

$$= \tfrac{1}{4} MN(M+1)(N+1) \text{ units.}$$

For the fast method however each grid point involves only the calculation of two line integrals. The time is then given approximately by

$$T_F = \sum_{m=1}^{M}\sum_{n=1}^{N}(m+n)$$

$$= \tfrac{1}{2} MN\,(M+N+2)$$

The ratio of the two times is then

$$\frac{T_c}{T_F} = \frac{(M+1)(N+1)}{2(M+N+2)} \doteqdot \frac{MN}{2(M+N)}$$

For a typical grid size of, say, $M = N = 80$

then $\quad \frac{T_c}{T_F} \doteqdot 20$

That is computing times of the order of 1 minute using the conventional method are reduced to a few seconds using the fast method.

This reduction in computing time - and hence cost - means that wing calculations of this type can be performed at an early stage in the project design cycle.

### Overall forces and Optimum Camber Design

The lift, pitching moment and pressure drag due to lift acting on the wing are given by

$$C_L = \frac{1}{S_{REF}} \iint_S \Delta C_p \, dx\, dy$$

$$C_M = \frac{1}{S_{REF}\, c_{REF}} \iint_S \Delta C_p(x,y)(x_0 - x)\, dx\, dy$$

$$C_D = -\frac{1}{S_{REF}} \iint_S \Delta C_p(x,y) \,.\, w(x,y)\, dx\, dy.$$

where $S_{REF}$, $c_{REF}$ and $x_0$ are the wing reference area, reference chord and pitching moment reference point respectively.

Note that the definition given for $C_D$ does not include the leading edge suction forces that arise from the theoretical infinities in $\Delta C_p$ along subsonic leading edges. The reason is that they are not often realised in practise. It is further found that cambers designed without these suction terms are more likely to maintain attached flow near the design incidence than those designed by including the full theoretical suction.

In order to derive a suitable camber surface giving low drag due to lift at a design lift and, possibly, pitching moment we assume that the camber slope, $\omega$, may be expressed as a linear combination of a set of $N$ camber modes

$$\omega(x,y) = \sum_{i=1}^{N} q_i \, \omega_i(x,y)$$

where $\omega_i(x,y)$ is the ith camber mode shape and $q_i$ is the ith generalised coordinate or 'weighting coefficient'.

The load distribution may then be written as

$$\Delta C_p(x,y) = \sum_{i=1}^{N} q_i P_i(x,y)$$

where $P_i(x,y)$ is the load distribution due to the ith camber mode.

The overall forces are then given by

$$C_L = \sum_i q_i \frac{1}{S_{REF}} \iint P_i \, dx\,dy = \sum_i q_i \ell_i \quad \text{say.}$$

$$C_M = \sum_i q_i \frac{1}{S_{REF} c_{REF}} \iint P_i (x_0 - x) \, dx\,dy = \sum_i q_i m_i$$

$$C_D = \sum_i \sum_j q_i q_j \left\{ -\frac{1}{S_{REF}} \iint P_i \, \omega_j \, dx\,dy \right\} = \sum_i \sum_j q_i q_j d_{ij}$$

In matrix form we have

$$C_L = \underset{\sim}{q}^T \underset{\sim}{\ell}$$

$$C_M = \underset{\sim}{q}^T \underset{\sim}{m}$$

$$C_D = \underset{\sim}{q}^T [d_{ij}] \underset{\sim}{q}$$

where $\underset{\sim}{q} = \{q_i\}, \; \underset{\sim}{\ell} = \{\ell_i\}, \; \underset{\sim}{m} = \{m_i\}$

We write $\underset{\sim}{c} = \begin{Bmatrix} C_L \\ C_M \end{Bmatrix} = M^T \underset{\sim}{q} \; ; \; M = [\underset{\sim}{\ell}, \underset{\sim}{m}]$

and $C_D = \frac{1}{2} \underset{\sim}{q}^T [d_{ij} + d_{ji}] \underset{\sim}{q} = \frac{1}{2} \underset{\sim}{q}^T D \underset{\sim}{q}$

We wish to minimise $C_D$ with respect to $\{q_i\}$ subject to the conditions on $C_L$ and $C_M$. This is achieved through an application of Lagranges method of undetermined multipliers giving the system of linear simultaneous equations

$$D \underset{\sim}{q} - M \underset{\sim}{\lambda} = 0$$

$$M^T \underset{\sim}{q} = \underset{\sim}{c}$$

where $\underset{\sim}{\lambda}$ is the vector containing the Lagrange multipliers.

The solution of this system may be written as

$$\underset{\sim}{q} = D^{-1} M \underset{\sim}{\lambda}$$

where $\underset{\sim}{\lambda} = A^{-1} \underset{\sim}{c}$

and $A = M^T . D^{-1} . M$

From this solution we obtain a result for the drag in terms of the design $C_L$ and $C_M$

$$\begin{aligned}C_D &= \tfrac{1}{2}\,\underset{\sim}{q}^T D\,\underset{\sim}{q}\\ &= \tfrac{1}{2}\,\underset{\sim}{c}^T \underset{\sim}{\lambda}\\ &= \tfrac{1}{2}\,\underset{\sim}{c}^T A^{-1}\,\underset{\sim}{c}\\ &= \tfrac{1}{2}\{C_L, C_M\}\,A^{-1}\begin{Bmatrix}C_L\\ C_M\end{Bmatrix}\end{aligned}$$

This result constitutes a 'design carpet' in that it relates the change in drag to changes in the design point for a given set of camber modes. Combined with speed of the numerical method outlined previously for the calculation of the load distributions we have a useful tool for project work.

To demonstrate the application of the method we give an example of some early designs for the Concorde pre-production aircraft tip.

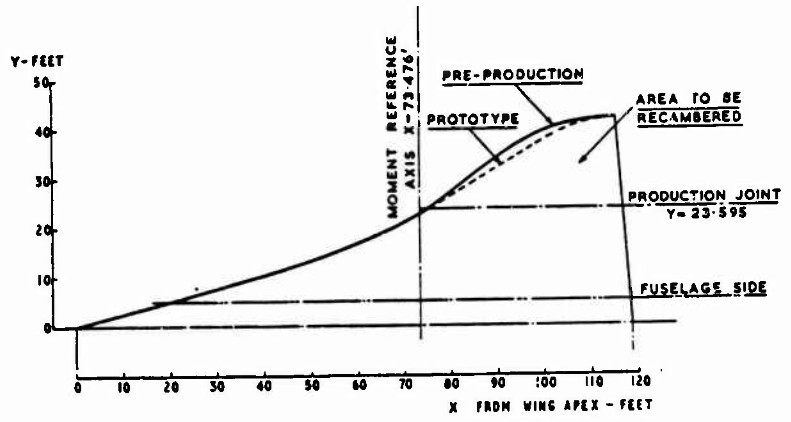

WING PLANFORM SHOWING TIP PLANFORM MODIFICATION

FIG. 2.21

In order to improve the aircraft's low speed lifting capability the pre-production aircraft incorporated an increase in the area of the outboard wing panels (fig. 2.21) relative to the prototype. The design requirement was then to define a camber surface for this region with a minimum drag penalty in cruise. To provide a basis for the work a 'first attempt' was made by stretching the prototype camber to match the new planform.

To design for a low drag this camber surface was treated as a 'fixed' mode (i.e. its coefficient was held constant at 1). Eight additional free modes were defined to have zero slope over the inboard section. Optimisation was then carried out at the design cruise $C_L$ and Mach number using combinations of 4, 6 and 8 free modes. Figure 2.22 shows the resulting drag values relative to prototype corrected for skin friction and volume effects at the cruise altitude. The curves shown give the drags obtained by designing for different centre of pressure positions. An interesting point is that the drag is a minimum for the c.p. ½% of the reference chord forward of the prototype position for all combinations of modes.

Also shown in the figure are the theoretical and experimental results obtained for the 'first attempt' indicating the accuracy of the basic wing method. (The height of the symbol for the experimental point indicates the accuracy of the tunnel result.)

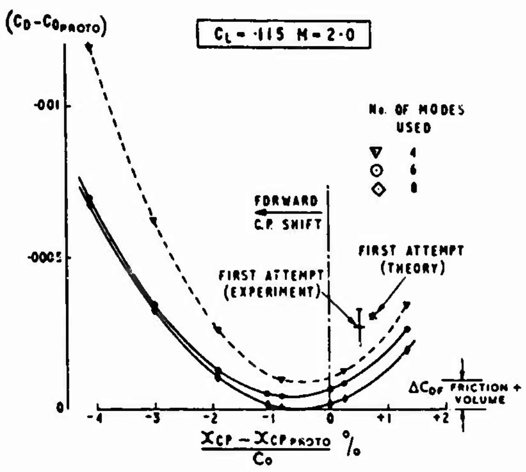

DRAG OF CAMBERS OPTIMISED AT CRUISE $C_L$

FIG. 2.22

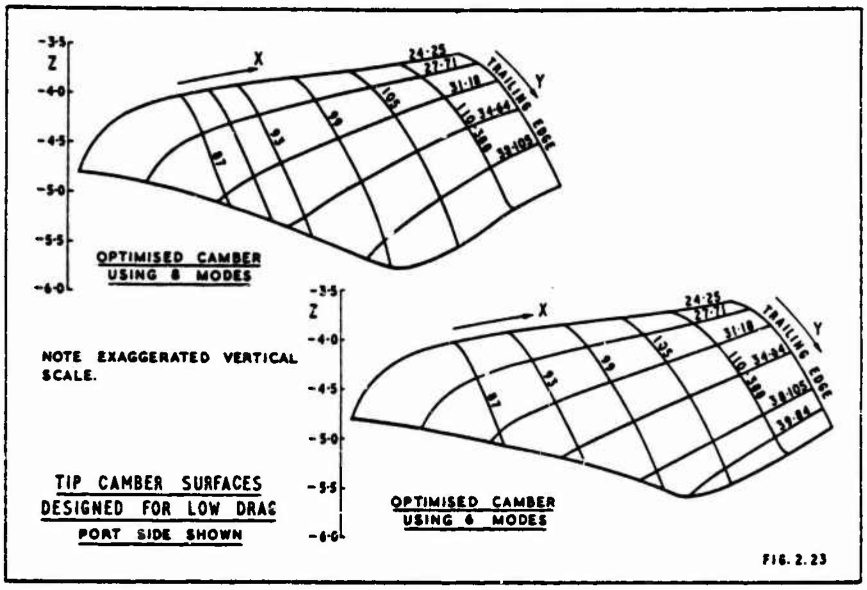
-3·5
Z
-4·0
-4·5
-5·0
-5·5
-6·0
X
Y
TRAILING EDGE
24·25
27·71
31·18
34·64
38·105
39·84
87
93
99
105
135
110·388
OPTIMISED CAMBER USING 8 MODES
OPTIMISED CAMBER USING 6 MODES
NOTE EXAGGERATED VERTICAL SCALE.

TIP CAMBER SURFACES DESIGNED FOR LOW DRAG

PORT SIDE SHOWN

FIG. 2.23

Figure 2.23 gives two examples of the camber surfaces obtained. Both were designed for the prototype centre of pressure position. The slightly distorted shape obtained by using 8 modes indicates that some care is needed, not only in the choice of camber shapes used but also to avoid specifying too large a number of degrees of freedom.

However, restricting ourselves to 6 modes we obtain a quite reasonable camber surface with very little theoretical increase in drag.

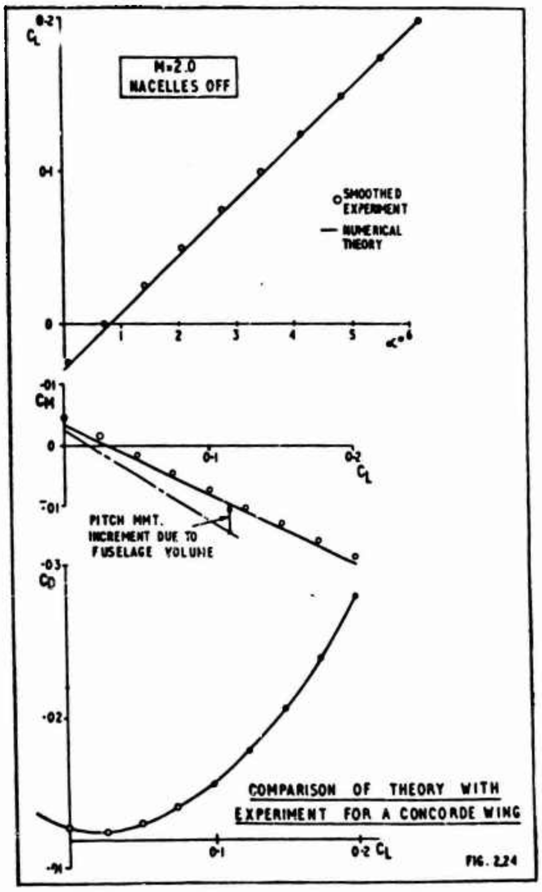

COMPARISON OF THEORY WITH EXPERIMENT FOR A CONCORDE WING

FIG. 2.24

It should be mentioned that these results were obtained using a conventional Characteristic box method rather than the fast method we have outlined here, and that neither of the designs shown have actually been tested.

As a final example, therefore, figure 2.24 shows a comparison of results using the fast method for the lift, drag and pitching moment of the Concorde pre-production wing with experiment. Here we have employed a crude but apparently effective method to deal with the wing-fuselage interference. Slender body theory is used to calculate the upwash field due to the fuselage at incidence and this in turn is cancelled by applying a suitable twist distribution to the wing (for the calculation of the load distribution only).

The region of the wing covered by the fuselage is set to zero incidence.

As the fuselage is assumed to be pointed at each end the only direct contribution it makes to the overall forces is the pitching moment increment due to volume shown in the figure. It is obviously a very important term.

The lift and pitching moment curves are shown in direct comparison with the experiment whereas the drag polar has been shifted vertically to coincide with the experiment at $C_L = 0$. This then demonstrates the accuracy achieved in estimating $C_L$ for minimum drag and the induced drag factor, but not of $C_{D_{min}}$.

## SECTION 3 ESTIMATION OF PARASITIC DRAG

### General Remarks

Obviously there are many ways of estimating the parasitic drag of aircraft, and each Company has its own preferred method.

The methods described below are those used by B.A.C. (C.A.D) and are based both on theory and on empirical data. Because the parasitic drag is perhaps of the order of 2% of total aircraft drag it is not necessary that all of the formulae and working methods should be rigorously justified although care is taken to use best available data.

The supersonic cruise case being dominant for transport aircraft, the data sheets and most of the calculations have been made for this case. However, based upon an assessment of the proportions of surface imperfections such as steps, gaps, bumps, fairings holes and the typical sizes of each, factors to give the overall parasitic drag at other altitudes and speeds may be derived. The work of Winter and Gaudet for gaps, steps, holes etc. covers the full Mach number range but for fairings shapes etc. the data of Refs. 12 and 13 can be used.

## 3.1 Basic Calculation Methods

### Skin Friction Drag

The skin friction drag in compressible turbulent flow can be estimated using Michel's method (see Section 2.1). For parasitic drag accounting the method is excellent and is easy to estimate and apply.

The method of Michel is strictly applicable to two-dimensional flow and in applications to the fuselage a false leading edge point should be taken some 3 ft. behind the true leading tip.

### Wave Drag

#### Two-Dimensional surface deformations

Where the wave length of a surface distortion is long compared with the boundary layer thickness (and this is usual for many types of distortion); in particular if the surface slope deviation does not exceed about 1-2 degrees; then theory and experiment agree quite well (see Ref. 14).

For such surface distortions linear theory predicts $C_P = 2\delta/\beta$ and hence drag values for certain distortion profiles may be estimated. For example $C_D = 9.85\,(t/c)^2/\beta$ for sinusoidal distortions, to which a factor may be applied (typically x 1.5) to account for the departure of an actual profile from sinusoidal.

The exact two-dimensional flow characterisitics may be derived from flow tables such as those in Ref. 15. which are based upon Prandtl-Meyer inviscid flows.

#### Three-dimensional surface deformations

As for two-dimensional distortions, slender shapes of small surface slope can be assumed (typically those associated with wing panels deforming due to fuel tank pressurisation.). The method used for such a distortion is that given in Ref. 14 by K.G. Smith, which is in turn based on the linearised theory elaborated by J.W. Nielsen in Ref. 16 for a particular type of three-dimensional bump and for a finite number of bumps on a cylinder.

For axially symmetric fairing shapes having profile discontinuities (actually discontinuous variation of cross-sectional area with distance) the quasi-cylinder theory of Lighthill as developed by L. Ohman in Ref. 17 can be used. Simpler shapes (e.g. cones) can be handled using the method given by L.E. Fraenkel in Ref. 18.

Although in practice half-bodies on plane surfaces are encountered, the calculations can be made using actual areas assuming complete bodies. It can also be assumed further, that reflection effects double the drag so derived.

Where the evolution of the cross-sectional area of a body meets the criterion of Lord and Eminton (see Journal of R.Ae.Soc. Jan. 1956) the wave drag of slender bodies (or half-body fairings) can be calculated. In actual design the profile of such a fairing can be optimised using their method. However, taking account of skin-friction and fairing weight usually gives best fairing lengths somewhat shorter than the "optimum".

When a fairing such as that over the ADF and radio compass aerials is considered one has a thin fairing of relatively large span. For such a fairing the linear theory method due to Evvard has been used to derive the wave drag (see "Aerodynamic components of aircraft at high speeds" by A. Donovan and H. Lawrence, Princeton Press).

This method or the method described in section 2.3 may be used to derive the forces on quite complex shapes. These tools also give an alternative method for deriving the parasitic drag due to panel deformations on the wing arising from tank pressures.

### Interference accounting

When long fairings are considered, or fairings near leading or trailing edges of fuselage, wing, or fin, the buoyancy effects due to the basic pressure gradient are included. For fairings with pointed ends (actually zero cross-sectional areas at front and back) immersed in a constant pressure gradient the drag due to buoyancy is $\frac{D}{q} = -\frac{dC_p}{dx}$ x Volume of fairing.

The interference of the fairing on the parent surface should also be accounted where it is appreciable. Usually an approximation to the fairing pressure distribution is good enough to estimate this effect.

## 3.2 Calculation of Parasitic Drag for Individual Items

### Forward and Aft Facing Steps

Such steps may be formed by machining tolerances on rebated lap points or due to the mal-fit or doors, hatches, etc.

One useful method of estimation is based on an analysis of the work of Gaudet and Winter reported in Ref. 11. Figure 3.1 gives a data sheet prepared for forward facing steps at a datum flight condition; that for aft facing steps is similar.

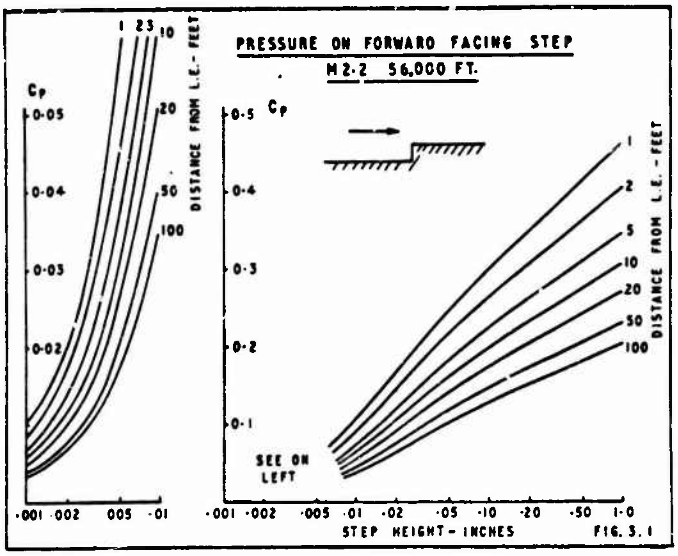

FIG. 3.1

### Chamfered Steps

It is a desirable design requirement that all skin-joint steps be chamfered as much as possible. Fig. 3.2 gives an estimate of the effect as a factor on the drag of steps as derived above.

### Streamwise and Swept Steps

The drag of a streamwise step can be taken as being due to the extra wetted area at the local skin friction coefficient.

Swept step values are derived by resolution into spanwise and streamwise components.

A data sheet, Fig. 3.3, for the special cases of steps with elliptical and parabolic planforms has been prepared on the same basis.

Optimum sweep angles for steps can be evaluated taking account the weight penalty of additional surface material required to produce the configuration.

### Spanwise Grooves

The data produced by Gaudet and Winter has been analysed and the data sheet shown as Fig. 3.4 prepared for a standard flight case. It should be noted that the two cases of relatively deep, narrow grooves and relatively shallow wide grooves are covered on the same data sheet by using either the width or the depth in the effective area on which $C_D$ is based.

## Inlets and Outlets at Zero Flow

Flush holes, such as are used for ventilating unpressurised compartments and for drainage, have drag contents which are not well correlated with hole geometry, boundary layer depth and etc. Source data are contained in Refs. 12, 19, 20 and 21.

These suggest that the drag coefficients are a minimum for ducted exits inclined at about 30 degrees and take values of .0004; .012 and .025 based upon exit area for circular, square and high aspect ratio (above 4) exit shapes.

The available information for inlets is inadequate but suggests that drag coefficients are around 0.2 - 0.7 for NACA inlets at subsonic speeds and 0.1 - 0.4 for aspect ratio = 4 rectangular inlets at up to 1.3M.

## Ventilating Airflows

In general small ventilating air flows do not have special inlets or outlets, the flow being induced by siting in suitable pressure areas. Larger flows such as the cabin discharge have carefully designed variable geometry exits.

The drag due to the airflow is taken to be equal to the freestream momentum of the mass flow. No exit momentum is credited for small flows but the larger discharge nozzles have calibrated thrusts which are credited.

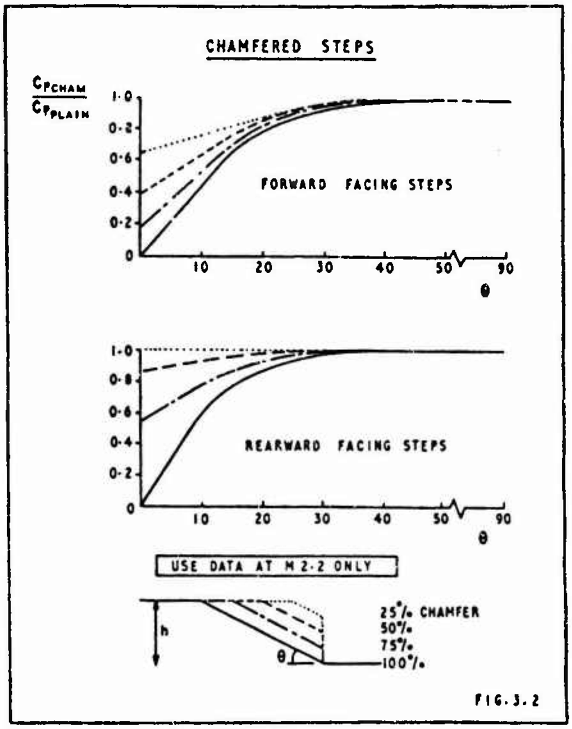

FIG. 3.2

## 3.3 Leakage Drag

Bitter experience has taught us that leakage of air from the aircraft, and in particular from the powerplant can be a significant source of loss of performance.

Such leakages can only be eliminated by meticulous attention to detail design in the region of hinges, access panels, fuel drains etc.

Not all of the momentum is lost of course. In general some of the air at least will be exhausted in a more or less aft direction although it will be found very difficult to quantify the reliefs. As a guide based on flight test experience a momentum recovery factor of 50% should be assumed.

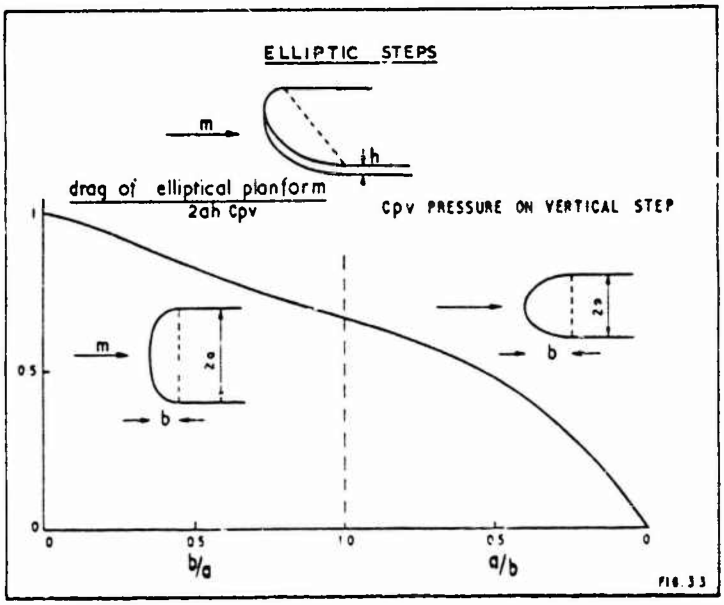

FIG. 3.3

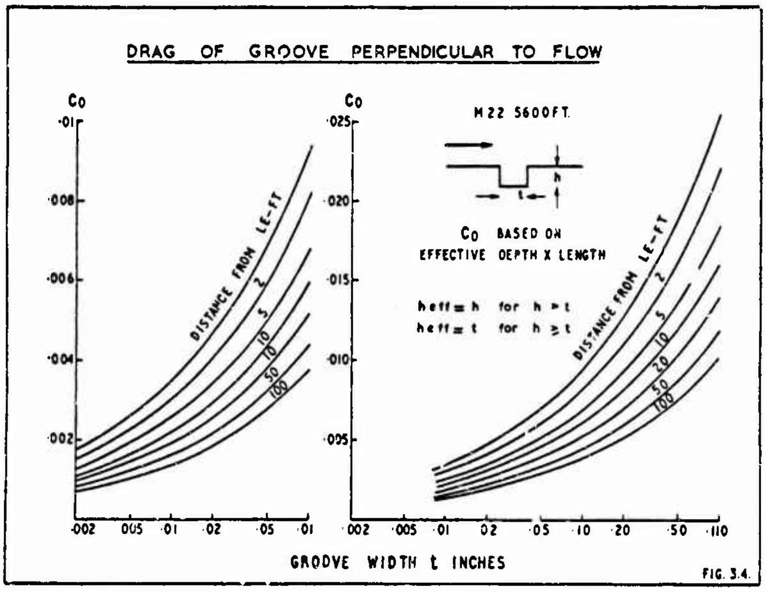
DRAG OF GROOVE PERPENDICULAR TO FLOW

FIG. 3.4.

## SECTION 4 ESTIMATION OF INSTALLED POWERPLANT PERFORMANCE

This section discusses some aspects of supersonic powerplant design which have an influence on aircraft performance calculations.

### Design Features of Supersonic Powerplants

### 4.1 Intakes

A glance through publications such as Janes All the World's Aircraft, will reveal that designers of supersonic aircraft are by no means agreed on the best way to install an engine into an airframe, Fig. 4.1.

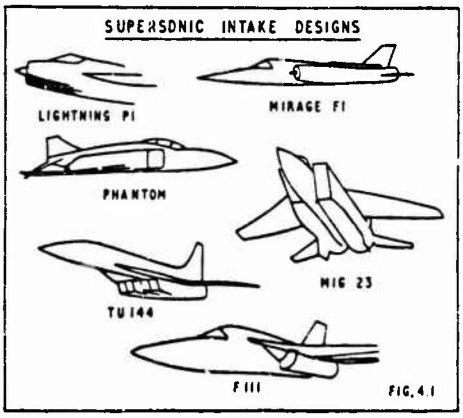
SUPERSONIC INTAKE DESIGNS

FIG. 4.1

Fuselage intakes can be semi-circular, circular (pitot), two-dimensional with vertical compression surfaces or two-dimensional with horizontal compression surfaces. Underwing intakes have been podded, axisymmetric or two-dimensional mounted directly under the wing.

What then determines the choice of intake location and type? Predominantly of course the design specification. Fighters, with a requirement for high manoeuvrability at subsonic speeds with supersonic dash capability have very different constraints from the bomber or transport which needs to fly economically for long periods in well defined supersonic conditions.

The former, will normally have fuselage mounted engines to reduce the roll inertia, and the intake location almost inevitably becomes a fuselage side mounting. The intake itself may, depending on the mission, be either a very simple fixed geometry design or at the most a scheduled or simple closed loop intake control system. Maximum intake recovery at top speed will be subordinated to the provision of adequate flow qualities at the extremes of attitude encountered during manoeuvres : -3g to +3g, perhaps in combination with significant sideslip.

Transport aircraft on the other hand will have a more restricted flight envelope - typically 0 to 2 g; and the installation must be designed to maximise intake recovery and minimise drag whilst providing adequate capability to deal with atmospheric disturbances etc. In this case the designer can invoke the aid of sophisticated control systems if necessary.

## Underwing versus Fuselage Mounting

Mounting the intakes under the wing has several advantages :-

i) The underwing Mach number is less than freestream, so that problems of intake design are lessened and the potential intake recovery increased.

ii) Incident flow angles due to aircraft incidence changes are greatly reduced, although care must be taken to ensure that changes in the local wing flow field with incidence do not provoke a growth wing boundary layer which may be ingested by the intake. This may be accomplished by a suitable designed boundary layer bleed (diverter).

iii) The forces associated with pre-entry spillage and flow turning in the compression process (discussed below) may be used to give lift components which materially improve the overall lift/drag balance of the installation.

iv) Access to the powerplant for maintenance is straight forward.

Against these must be set the fact that the intake is more prone to ingestion of water and debris from the runway, and that there is no possibility of shielding of noise emanating from the intake. The intake design case will probably be sideslip at the highest expected Mach number.

With a fuselage mounting, the intake operates at close to freestream Mach number. It will be necessary for the intake to accept a wide range of flow angles corresponding to the required aircraft manoeuvrability limits. Although it might be thought that there was at least protection from sideslip variations, it has been found that the build up of fuselage boundary layer due to crossflow effects can produce flow conditions which adversely affect the intake operation. For this reason one often sees very wide boundary layer diverters on aircraft with fuselage side intakes.

Water ingestion will be less likely than is the case with underwing installations, although the chances of debris pick-up will be very similar.

## Characteristics of Supersonic Intakes

Supersonic intakes can be subdivided into two basic categories; those in which all the supersonic compression is carried out externally and those in which some of the supersonic compression is carried out inside the intake.

Supersonic compression is achieved by reducing the speed of the air through a shock wave, or system of shock waves, until the airstream is subsonic. Having reduced the Mach number to less than unity the air is then further compressed in a subsonic diffuser, to a speed acceptable to the engine or ram-jet.

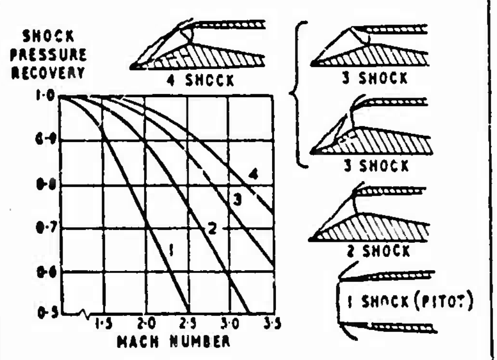

FIG. 4.2

The simplest example is a pitot-type intake with the supersonic compression being achieved through a single normal shock, and further compression carried out in a simple subsonic diffuser (see Fig. 4.2). There is, of course, some loss in total pressure at the shock and further skin friction losses in the diffuser; typically, 2% total pressure.

By introducing a sloping surface in front of the shock, a second, oblique shock is produced which reduces the strength of the normal shock. The overall losses of the system are thereby reduced.

Further improvements can be achieved by making use of more sloping surfaces, but in so doing certain disadvantages are introduced, which will be discussed later. Fig. 4.2 shows the maximum shock pressure recoveries which can be achieved using various geometries, assuming the optimum geometry at each speed.

The following examples relate to two-dimensional intakes, being simpler to calculate and understand, but the general conclusions apply to both rectangular and axi-symmetric cases.

Before considering the effect of intakes on performance calculations we must understand the behaviour of an intake under various mass flow conditions.

The efficiency of an intake is given by the ratio of the mean total head at the engine compressor face to the free-stream total head. The loss in total head is comprised of losses through the shock wave system, which can be calculated, and losses due to viscous effects, which include skin friction and shock wave - boundary layer interference effects.

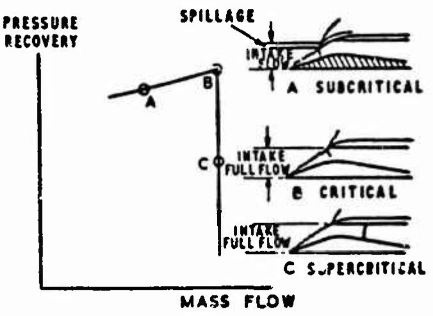

FIG.4.3

Fig. 4.3 shows the characteristic curve of the simplest type of multi-shock intake, a single-wedge, two shock system. The variation of pressure recovery with intake mass flow is shown with the intake running at the design condition, that is, with the oblique shock crossing the lip of the intake at the design mass flow. In the section on test techniques 'first wedge spill' is mentioned. This is simply a variation in which the oblique shock wave from the first wedge passes in front of the cowl lip, thus permitting some air deflected by the wedge to escape from the intake. At the optimum pressure recovery condition the normal shock is at the throat of the diffuser where the mass flow has just reached the maximum value. At low mass flow, such as point 'A', the normal shock is expelled forward to enable the excess air to be spilled over the outside of the lip. Some of the air entering the intake in this condition passes thorugh the single shock formed by the fusion of the normal oblique shocks and, therefore, enters the diffuser at a lower total pressure than that nearer the wedge, which has passed through the two shocks. There is, therefore, a lower pressure recovery at this point. In such conditions of flow 'spillage' the intake is said to be "subcritical".

As the mass flow is increased the recovery increases lightly and reaches a maximum as the normal shock passes into the throat (point B). At this point the mass flow has also reached a maximum and the intake is said to be running "full" or "critical". Any further increase in engine speed would only decrease the back pressure in the diffuser causing the normal shock to move into the diffuser, gaining strength as the Mach Number in front of it increases. There is no increase in mass flow as the stream tube, now at the lip, is not influenced by further changes in intake condition. The net result is a decrease in total pressure recovery at a constant mass flow. The intake is now said to be "supercritical".

Performance Aspects

Having explained the operation of an intake over the mass flow range it is possible to examine the main performance characteristics of the intake, the first of which is to supply the correct mass flow at all aircraft speeds with high efficiency and low drag.

The drag of the intake includes the pressure drag on the incidence streamline to the lip (ab, Fig. 4.4), also the external pressure drag on the cowl lip (bc), both of which are governed by the strength of the oblique shock.

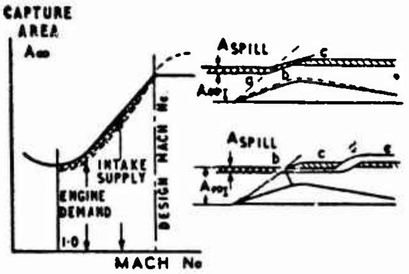

FIG. 4.4

There is, therefore, a wedge angle which will give a maximum value of thrust minus drag at each Mach number and a corresponding mass flow for this position. This mass flow characteristic can be seen in Fig. 4.4, on which the capture area, i.e. the area of the stream tube entering the intake reduced to freestream conditions, for the optimum thrust minus drag is plotted against Mach number. A typical engine requirement is also shown, to which the intake has been matched at the design condition. It is usual to match near the design condition if the aircraft has a prolonged supersonic cruise since the volume of air to be spilled, hence the drag, is a minimum. With aircraft having a short supersonic duration e.g. fighters, the maximum speed performance is not so critical and the emphasis is on the maximum acceleration in the transonic phase. In this case the intake is usually matched at sonic speeds with due accounting for the performance requirement during sustained manoeuvres.

As the engine will accept only a given amount of air the excess during the transonic phase or as the result of engine throttling must be diverted back to the freestream as efficiently as possible. To do this it is necessary to vary the geometry of the intake still further.

If the ramp angle is increased, pushing the oblique shock forward and diverting the excess over the top of the intake, the overall thrust minus drag of the system is reduced because the chosen position is already at the optimum.

If the excess air is accepted into the intake, spill vents can be provided in the diffuser which must allow the correct mass flow to be expelled efficiently into the freestream. This system will produce some pressure drag on the spill vents and exit streamline (de, fig. 4.4) and drag due to the loss of momentum between the intake fact (b) and the spill vent exit (d).

On aircraft like the Concorde facilities are provided for both methods of spillage allowing a choice of compromise settings which result in a minimum of drag at each Mach number.

Variable mass flow will, of course, need intake control, and a study of the aircraft's performance requirements will indicate what type of control system is necessary.

For short-duration aircraft it is sufficient to move either the wedge or the spill vents and to suffer some increase in spillage drag. In longer range aircraft it is necessary to adopt a full control system in which the positions of the wedge and the spill vents are varied in order to reduce the excess drag to a minimum. Changes in intake mass flow due to changes in speed can usually be set against a Mach number programme. The resulting motions required by these changes can be relatively slow. Adjustments in mass flow, due to variations in engine airflow or ambient conditions, on the other hand, must be rapid.

So far only a simple two-shock system has been considered, with all the supersonic compression carried out upstream of the lip. This system is perfectly adequate for speeds below a Mach number of 2, but at higher speeds the shock losses become too great and a more advanced design is necessary.

Fig. 4.2 shows the maximum shock pressure recovery to be expected from various geometries, assuming the optimum geometry at each speed. The simplest system is, of course, the pitot-type intake, which can be used efficiently up to Mach numbers of 1.6. Above this speed the normal shock losses become too great, and a second oblique shock produced by a wedge is introduced to reduce the Mach number in front of the normal shock and increase the overall efficiency.

By introducing further wedges the shock losses can be further reduced, the optimum configuration being, of course, the isentropic intake, a curved wedge giving an infinite number of infinitely small shocks, terminating in a single normal shock.

On the basis of Fig. 4.2 it would be apparent that the choice would automatically go to the isentropic intake. However, three points must be considered.

(i) Cowl lip drag

(ii) Off-design performance

(iii) Shock/boundary layer interactions

An increase in the number of wedges results in the flow being turned through a large angle, relative to the freestrean, at the entry and, consequently, the lip angles, and hence the cowl drag, are high. This factor and the poor off-design performance eliminates the isentropic intake for aircraft such as a supersonic transport.

Furthermore, as the number of wedges increases, so the extra-to-shock losses increase. These losses are in part due to the interaction of the shocks on the boundary layer of the wedge and the side of the intake and (on a two-dimensional intake) can quickly become of such an order as to overcome the benefit of the increased compression efficiency.

To a limited extent the boundary layers before the shocks can be led away by discrete bleeds or perforations. If a moderate amount of bleed is found to improve the performance it should be incorporated; nevertheless it is somewhat of an embarrassment as it must be disposed of in an efficient manner, otherwise the drag losses may be greater than the improvement of thrust obtained from an increased pressure recovery.

With the multi-shock systems it is possible to reduce the lip drag of the intake by introducing some internal compression before the throat of the diffuser.

Fig. 4.2 shows two three-shock intakes which have the same theoretical performance. The first is an all-external compression type which has a high lip drag. By removing the second wedge from the lower surface and putting the same compression on the upper surface, as shown in the second illustration, the cowl lip angle can be reduced to zero. This implies no external drag in the cruise condition but, although there is an improvement in the overall performance, it has to be gained at the expense of more complication.

With sufficient internal compression to make the venture worthwhile the shock system will not establish itself unless the contraction is reduced to a small enough value to enable this to happen. Once the shock system is established, i.e. the intake is 'started' the geometry of the intake is adjusted until the required optimum compression is achieved. Should some disturbance, such as gust or engine malfunction push the normal shock forward of the throat it will immediately move to a position forward of the intake lip and remain there until the geometry is altered in the manner just described. This is known as intake unstart. To provide the necessary adjustment, devices must be incorporated to override the sensing mechanisms controlling the mass flow. The control must be rapid, but must not result in sudden surges in mass flow which may upset the normal operation of the engine.

## 4.2 Engines

A proper treatment of the characteristics of engine design for supersonic aircraft is really beyond the scope of this paper. Excellent résumés of the problem can be found elsewhere, e.g. Refs. 22, 23, 24.

There are nevertheless certain features of the engine which have a bearing on aircraft design and on the test techniques to be described in the next section and which should be briefly discussed beforehand.

There are two notable differences in the supersonic operation of air breathing engines in comparison with the subsonic case :-

(i) At high Mach numbers a dominant portion of the cycle pressure ratio is generated in the intake.

(ii) The high total temperatures reduce the cycle temperature ratio since the maximum cycle temperature is limited by availability of materials.

The former dictates that much attention must be devoted to the measurement (and improvement) of intake recovery.

For an un-reheated turbo jet, at a given level of intake total temperature and T.E.T., an increase in pressure ratio will reduce the amount of fuel which can be used which reduces the specific thrust but improves the specific fuel consumption see Fig. 4.5. For aircraft where supersonic economy is unimportant, the thrust loss can be made up by the use of reheat, but for transport aircraft this is uneconomical.

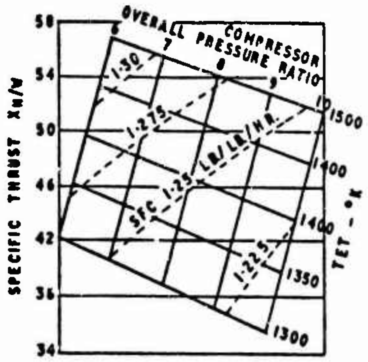

M 2·2 TROPOPAUSE

OPTIMUM CON-DI NOZZLE

(HOOKER AND GARNIER 1964)

FIG. 4.5

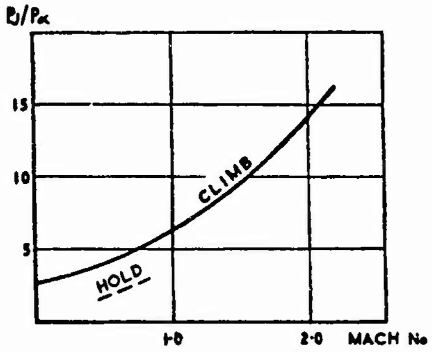

(HOOKER AND GARNIER 1964)

FIG. 4. 6.

As with most aspects of aircraft design, the final choice will be a compromise depending on the existing circumstances.

Whatever the choice of engine pressure ratio, it is inevitable that the jet pipe pressure ratio $P_J/P_\alpha$ will vary greatly throughout the flight (Fig. 4.6). At around 2.0M $P_J/P_\alpha$ will be about 15 whereas in hold or subsonic cruise conditions it will be as low as 2 or 3.

In addition it must be borne in mind that the engine thrust, or the nett thrust $X_N$ is the difference between the gross thrust of the jet $X_G$ and the air momentum drag $X_D$.

$$X_N = X_G - X_D$$

At M 2.0, $X_G/X_N = 2.5$, under hold conditions it is also about 3. At subsonic climb conditions $X_G/X_N$ reduces to about 1·2 , this is because of the higher TET than in hold. This means that in cruise, for example, a 1% loss in gross thrust is a 2½% loss in nett thrust.

It can therefore be seen that the combination of engine characteristics and flight dynamics makes the net thrust highly sensitive to the nozzle gross thrust efficiency so that great care is needed to obtain the best possible estimate of nozzle performance.

## 4.3 Nozzles

As outlined above, the conditions to which the exhaust system has to adapt itself vary so greatly that it is virtually impossible to avoid variable geometry - at least for transport aircraft.

Cruise thrust could be maximised by expanding the gasses isentropically in a Laval nozzle i.e. a convergent-divergent nozzle with the exit area chosen such that the static pressure at the outlet equals the external back pressure.

It is however well known that a nozzle of convergent/divergent form exhibits poor thrust characteristics at pressure ratios well below design. This arises from a defect peculiar to supersonic flow and commonly referred to as over-expansion. Despite the benefit which shock induced separation confers on performance in this region there remains a substantial loss. For example at an applied pressure ratio of 3, a nozzle of design pressure ratio 20 would suffer a 10% fall-off in efficiency under static conditions.

On the other hand the simple convergent nozzle which gives good subsonic performance may lose about 10% gross thrust i.e. 25% nett thrust relative to the optimum Convergent-Divergent nozzle at a pressure ratio of say 15 Fig. 4.7.

Solutions which have been put forward from time to time range from, on the one hand, nozzles of continuously variable geometry which can be modulated to provide the correct area ratio in accordance with the prevailing exhaust pressure ratio to, on the other hand, nozzles of fixed outlet area incorporating various aerodynamic techniques intended to prevent the jet over-expanding at selected conditions of operation.

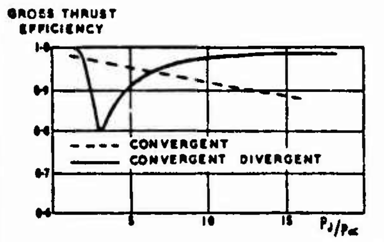

FIG. 4.7

It is not intended to enter into this controversy in this paper. For now, it is sufficient to note that a commonly seen solution is that shown diagrammatically on Fig. 4.8.

This consists of a convergent primary nozzle which may be variable in area either as an engine control or to provide for reheat operation; surrounded by a divergent section with variable exit area obtained by aerodynamically balanced flaps or, as on the production Concorde directly powered buckets.

Ventilating air is supplied to the annular gap between primary and secondary nozzles, this air coming either from the engine bay cooling air, or from external sources with a suitable intake.

The required nozzle exit area will rarely be either the same size or shape as the maximum nacelle (or fuselage) cross section, so that some degree of 'boat-tailing' or base area will be present.

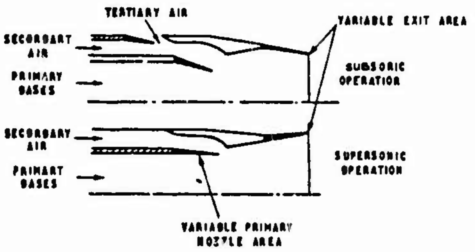

FIG. 4.8

The amount of base or boat-tail required will vary with the flight condition. At supersonic speeds the required nozzle exit area is at a maximum (because of the high overall pressure ratio and, for fighter aircraft, the use of reheat). In subsonic conditions the required exit area is much lower, and, for optimum performance, the afterbody must be closely cowled down to this area fairing over the maximum possible length.

The pressures on the base (or boat-tail) will be affected both by airframe flows and by the nozzle exit conditions. This leads to complications in the necessary testing techniques as described below.

## SECTION 5 - DERIVATION OF THRUST AND DRAG FROM WIND TUNNEL TESTS

As stated in the Introduction, the techniques now to be described are not the only ones possible. They do however form a consistent well documented set which is common to several parties and which has been proved to give excellent results.

These methods rely heavily upon component aerodynamic characteristics measured on small scale models in wind tunnels.

The outline below first gives the definition of thrust and drag which is used and this is followed by descriptions of the methods used to obtain each component.

### 5.1 Drag and Thrust Definitions

The drag and thrust definitions are

(1) Aircraft Drag

$$D = D_D + D_E + D_{FL} + D_{NO} + D_{u/c} + D_R + (D_S + D_{AI} + D_{DD}) + D_P + (D_{EXT})_N + (D_{EXT})_{NP} + D_B$$

(2) Nozzle Thrust

$$X_G = (X_G)_{GL} + (D_{EXT})_N + (D_{EXT})_D + D_B - (D_{INT})_{NP} + X_{TD} + X_{GOB}$$

(3) Momentum Drag

$$X = (W_1 + W_{RB} + W_{HE} + W_{GR}) \frac{V}{g}$$

where :-

D - drag

X - thrust

W - mass flow

V - true air speed

g - acceleration due to gravity

Suffices

D - datum configuration (see Section 3) below

E - elevators

FL - flexibility effects

No - nose

u/c - undercarriage

R - rudders

S - spillage (additional to free flow nacelle mass flow ratio at subsonic speeds and extra to first wedge spill at supersonic speeds)

AI - Auxiliary inlet

DD - Dump door

P - parasitic items not represented on models

EXT - external to nozzle

N - fully representative nozzle configuration, tertiary doors closed

NP - nozzle parasitic items not included on models

B - central base between twin nozzles

G - gauge gross force

GL - global (in context of nozzle testing the force measured on the model is equivalent to $X_G - [(D_{EXT})_D + (D_{EXT})_N + D_B]$

TD - tertiary doors

Suffices (Cont'd)

INT - internal to nozzle

1 - compressor face

RB - ramp bleed

HE - heat exchanger

OB - overboard bleed

L - leakage

- freestream conditions

## 5.2 Datum Configurations

Since it is not possible to test completely representative aircraft models with nacelle internal characteristics varied over the full range of mass flow and pressure ratio through which the powerplant operates, the derivation of thrust and drag is based on characteristics obtained from four sources :-

(1) Aircraft models with representative external geometry but non-representative internal flow.

(2) Intake/aircraft models with representative intake entry flow and external geometry representation sufficient to give the effects of wing flow field on internal intake performance.

(3) Engine bay models to measure the internal pressure loss characteristics of the secondary system.

(4) Isolated nozzle models with representative internal flow but non-representative external flow.

In combining the characteristics measured on the models, (1) and (4) above, use is made of common datum configurations to provide a link between the separate measurements. The drag and thrust definitions given above are formulated on this basis.

Datum configurations are also used to minimise the amount of testing necessary to cover the aerodynamic characteristics of components incorporating geometric variability. To test aircraft models throughout the full operational range (Mach number, attitude) with all possible geometric configurations would lead to an enormous wind tunnel programme at prohibitive cost.

The datum configurations are defined below.

### Aircraft Model

The datum aircraft model incorporates the following components :-

(1) Wing and Fin

One 'g' mid-cruise shape, elevons neutral, jack fairings represented, undercarriage retracted, undercarriage fairings represented.

(2) Fuselage

Nose in cruise configuration, all fully defined features represented.

(3) Nacelles

(a) External

Direct scale of aircraft nacelle including diverter system, first wedge, intake splitter plate and nozzle afterbody. The external lines of the nozzle afterbody are different for subsonic and supersonic models, the representation of the setting of the final petals on the divergence of the nozzle being :-

Subsonic - fully closed (minimum exit)

Supersonic - fully open (maximum exit)

Note that (i) items such as thrust reverser grills and base between the two nozzles are not represented on aircraft models for supersonic tests. The base is represented on subsonic models. (ii) intake spill doors and auxiliary intakes are closed on the datum model.

(b) Internal

For subsonic and transonic testing (intake control system inactive regime), free flow nacelles are used giving mass flow ratio close to maximum continuous power requirements at the high Mach numbers. For supersonic testing (intake control system operative regime) the datum configuration is such that first wedge spill is represented on the model. The nacelle exit geometry on supersonic models is not representative of the actual nozzle exit, a single near rectangular duct being used to exhaust the flow from the nacelle (see (2) below). The supersonic models therefore have a large unrepresentative base surrounding the jet.

Nozzle Models

The nozzle models consist of a representation of a single nozzle with a reflection plate to simulate the plane of symmetry. No attempt is made to generate a representation of the wing flow field. The wing/nacelle representation is limited to :-

(1) Wing (Datum and actual models)

Upper surface representative aft of elevon hinge line and within the confines of the nacelle sidewall/wing lower surface junction.

(2) Datum Nacelle

Representative aft of engine face. External shape is consistent with the subsonic and supersonic definitions given in (3) (a) above. Internal geometry definition is consistent with (3) (b) above. Exit mass flow and pressure ratio are defined to be the same as those measured on the aircraft models. Thrust reverser grills are not represented.

(3) Actual Nacelle

External lines and internal geometry are representative of the aircraft configuration. Thrust reverser grills are represented. This model is tested through a range of primary nozzle area, pressure ratio and secondary mass flow ratio.

## 5.3 Derivation of Drag and Thrust from Wind Tunnel Models

The drag and thrust characteristics, used in Concorde performance assessment, are based on measurements made in various facilities.

These facilities operate at Reynolds numbers substantially lower than those encountered in flight. It is therefore necessary to correct the model measurements for Reynolds number effects. Particular attention is directed to achieving a high degree of accuracy in assessing the corrections for application to supersonic testing, since the effect of supersonic drag level (cruise flight) has a profound effect on aircraft mission performance. On the other hand, for subsonic and transonic drag derivation, some corrections are not considered since the effect on mission performance of errors at these conditions is considerably smaller. The basic corrections are :-

(1) Nacelle Internal Drag

Nacelle internal drag and non-representative base drag is deducted from basic model measurements. Internal drag derivation depends on the facility being used. Tests in the RAE facility use exit flow survey and pressure integration to determine momentum loss in the nacelle flow. Tests in the NLR facility use mass flow and momentum calibration of the nacelle.

(2) Skin Friction Drag

Flat plate skin friction theory is used to calculate skin friction drag as a function of Mach number, Altitude and ambient temperature as discussed in Section 2 . Application at wind tunnel conditions permits the pressure drag to be obtained.

(3) Heat Transfer

Calculated as an increment relative to the zero heat transfer calculations in (2) above (see Section 2 ).

(4) Diverter Drag

Pressure drag of the diverter varies with boundary layer depth. Linearly scaled models at wind tunnel Reynolds numbers are operating in a boundary layer thicker than will be encountered in flight. Isolated diverter models are used to assess this correction which is applied only at Supersonic Mach Numbers.

(5) First Wedge Spill Drag

Mass flow spilled through the first wedge shock increases as boundary layer depth increases. Linearly scaled models at wind tunnel Reynolds numbers operate in thicker boundary layers than encountered in flight and hence the spillage (and its associated drag) are greater. This correction is applied to supersonic tests only.

Aircraft Drag - Component Contributions

Examination of the drag equation, Section 5.1, shows that a number of component drags are required to assess the total drag of the aircraft. Some of these will be measured by component tests on the same models and in the same facilities as the datum configuration discussed above. Other components will require special tests or analytical treatment. The derivation of the component drag contributions is discussed below.

$D_E$ - This term is the drag change due to elevator movement required to trim the aeroplane. The basic aerodynamic data used for the trim calculation is obtained from the models and facilities discussed above. It should be noted that rigid aircraft data (including elevator effectiveness) are used in estimating this term. All flexible effects are combined in the component $D_{FL}$ as below.

$D_{FL}$ - This term represents the total change in drag due to the various effects on flexibility including

(a) derivation of the basic camber distribution from the one g mid cruise shape datum and its effects on lift, pitching moment and drag polar.

(b) flexibility influence on elevator effectiveness

$D_{Ho}, D_{y/c}, D_R$ - Component tests on the models discussed above are used to establish these items.

$D_S$ - Spillage drag is derived by testing the datum models discussed above with a range of nacelle flow varied by

(a) nacelle blockage at subsonic and transonic speeds, the fixed geometry range of intake operation

(b) representative second ramp geometries together with nacelle blockage at supersonic speeds. The interference lift effect of spillage is of course determined by the same tests.

$D_{AI}$ - Tests on a 1/6th scale model were used to assess auxiliary inlet drag.

$D_{DD}$ - Dump door drag was assessed using external drag measurements on a 1/60th scale model together with calculations of the thrust recovery of the dump door exhaust flow. This term is non-critical for all missions of interest, the dump door will be closed.

$D_P$ - Parasitic drag of all items not included in wind tunnel models is calculated using experimental data where available (steps, gaps, etc.). (See Section 3 ).

$(D_{EXT})_N$ - Item measured on nozzle tests, see below

$(D_{EXT})_{NP}$ - Nozzle parasitic drag derived by same technique as $D_P$.

Intake Performance

The definitive intake performance is measured using intakes mounted under partial wing representation.

The measured results need correction for

(1) Reynolds number - affects capture flow and intake recovery, corrections assessed from isolated intake models.

(2) Diverter System - the diverter height/boundary layer depth ratio pertaining to full scale Reynolds numbers cannot be achieved at wind tunnel conditions using a directly scaled model. The wing profile in the immediate vicinity of the intake is distorted to ensure that the correct proportion of the boundary layer is swallowed by the intake.

## 5.4 Secondary System Pressure Losses

The pressure losses experienced by the engine bay flow are measured on a representative half scale model. Characteristics are measured for all sources of flow into the engine bay (e.g. ramp bleed, ground running door). These results are used directly in performance estimates and assumed to apply to all engine bays.

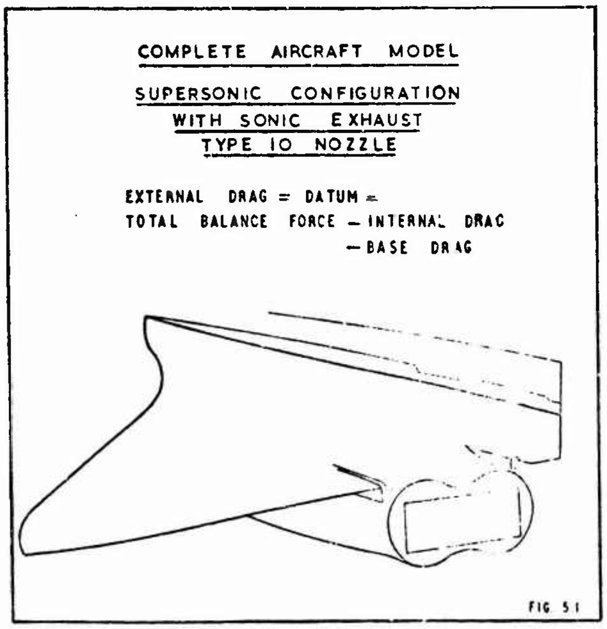

COMPLETE AIRCRAFT MODEL

SUPERSONIC CONFIGURATION
WITH SONIC EXHAUST
TYPE 10 NOZZLE

EXTERNAL DRAG = DATUM =
TOTAL BALANCE FORCE − INTERNAL DRAG
− BASE DRAG

FIG. 5.1

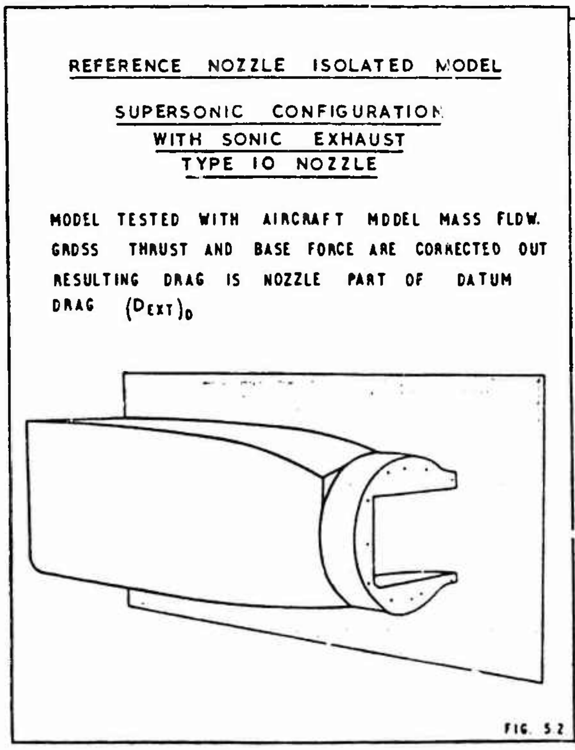

REFERENCE NOZZLE ISOLATED MODEL

SUPERSONIC CONFIGURATION
WITH SONIC EXHAUST
TYPE 10 NOZZLE

MODEL TESTED WITH AIRCRAFT MODEL MASS FLOW. GROSS THRUST AND BASE FORCE ARE CORRECTED OUT RESULTING DRAG IS NOZZLE PART OF DATUM DRAG $(D_{EXT})_D$

FIG. 5.2

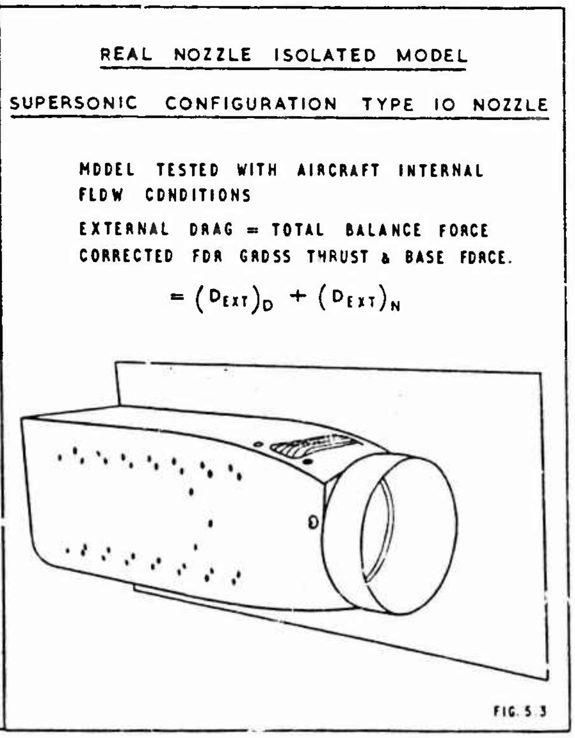

REAL NOZZLE ISOLATED MODEL

SUPERSONIC CONFIGURATION TYPE 10 NOZZLE

MODEL TESTED WITH AIRCRAFT INTERNAL FLOW CONDITIONS

EXTERNAL DRAG = TOTAL BALANCE FORCE CORRECTED FOR GROSS THRUST & BASE FORCE.

$$= (D_{EXT})_D + (D_{EXT})_N$$

FIG. 5.3

## 5.5 Nozzle Performance

Nozzle performance is measured on small scale models (approximately 1/20th scale). These models are tested through the full Mach number range from 0 to 2.0M. Datum models are tested with internal flows representative of the flow in the datum nacelle used on aircraft models. Internal thrust and base drag are corrected out of the measurements. Mass flow measurements and exit pressure surveys are used to determine these corrections. The actual nozzle model is tested through a range of internal flow conditions representative of the full range of possible engine settings at each Mach number. In addition static testing at internal conditions representative of supersonic cruise is carried out on 1/10th scale models to determine internal performance to a high degree of accuracy. These measurements are used to facilitate the derivation of the thrust components. The model measurements are corrected for the non-representative primary flow temperatures used in the wind tunnel tests (hot gas or $\gamma$ effect). This correction is applied at supersonic conditions only, and is derived by calculation of internal nozzle pressure distributions for cold and hot flows using the method of characteristics.

Two important terms in the drag equation (section 5·1 equation (2)), associated with the nozzle, are

$(D_{EXT})_N$ - this term includes reverser cascade drag with leakage and any effect of internal nozzle flow on external boat-tail surface

$D_B$ - drag of central base between twin nozzles in presence of nozzle flow

Both items will be functions of engine setting and secondary flow and are determined from the 1/20th scale tests.

## SECTION 6 EFFECT OF DESIGN MISSION ON DESIGN PHILOSOPHY

This section gives an outline of the sort of decision processes that lead to a definition of an aircraft which will perform a given mixed subsonic/supersonic mission.

### (a) Supersonic Transport

### Design Mission

As a typical design mission consider the design mission which was used as a basis for Concorde

| | | |
|---|---|---|
| (i) | Pre Take-off | 2650 lb Fuel<br>(Engine start + about 10 minutes idle) |
| (ii) | Take-off | Brake release to 1,000 ft. 12,000 ft field ISA+10°C Sea Level |
| (iii) | Climb Cruise descend to 1,000 ft | 3203 n.m., ISA +5°C, 13 kt headwind, Cruise at about 2.0M |
| (iv) | Destination Terminal Manoeuvre | 7 minutes at 200 kt, 1,000 ft. |
| (v) | En-route Reserves | 5% BLOCK FUEL (i) + (ii) + (iii) + (iv) |
| (vi) | Destination Hold | 15 minutes at 250 kt, 10,000 ft |
| (vii) | Divert to Alternate | 270 n.m., zero wind, 0.93M, 36,090 ft cruise |
| (viii) | Alternate Hold | 20 minutes at 250 kt, 10,000 ft |
| (ix) | Alternate Terminal Manoeuvre | 7 minutes at 200 kt, 1,000 ft |
| (x) | Final Reserve | 0.75% Tankage |
| (xi) | PAYLOAD | NOT LESS THAN 20,000 LB (100 PAX) |

In the first place it may be noted that although the specification is for a Supersonic Transport, by far the greater part of the requirements concern the subsonic operation. It will be seen later that this is no accident - about 25% of the total fuel load will eventually be designated for subsonic conditions and fuel reserves.

Next it will be noted that the mission calls for a prolonged supersonic cruise at around 2.0M. This choice of cruise Mach number has important repercussions on the design of the wing, the powerplant and the structure which will be discussed below. Finally, the specification contains no specific requirements for airfield noise. The exclusion of such a requirement has had an important effect on the definition of wing and powerplant - the effect of including such an item is also briefly discussed later.

There is no specific requirement for Direct Operating Costs (DOC). In effect the requirement is to reduce these to an absolute minimum, and as a first order criterion, this may be taken as minimising the required take-off weight.

General Configuration

The actual configuration is of course arrived at by successive iterations over a long period of time - Concorde took about eight years from the back of an envelope to freezing the definition of the production aircraft, the Boeing 2707 at the time of cancellation had been under study for twelve years.

The design process must start with a consideration of the cruise requirements. The need to cruise at 2.0M immediately specifies that the aircraft will need a wing leading edge sweep of the order of 60 - 65° in order to maintain subsonic leading edge conditions which past experience shows to be a desirable condition for low drag.

It is well known that wings with this sort of sweep have a low lift curve slope, which in turn implies that to obtain the desirable low speeds for take-off and landing with a fixed geometry either the wing loading must be low and/or the incidence must be much larger than that of todays aircraft.

The classical method of reducing take-off and landing speeds is to use trailing edge flaps. To do this however there must be an auxiliary lifting surface - either a tail or a canard which can be used to trim the associated pitching moments. The alternative method; that of using variable wing sweep, also requires the use of another lifting surface. All of these proposals must be examined, but before this can be done it is necessary to examine the cruise requirements in more detail.

In Section 2, the supersonic drag was given as

$$D_{TOTAL} = D_{0\,FRICTION} + D_{0\,WAVE} + D_{i\,VORTEX} + D_{i\,WAVE}$$

where

$$D_{0\,FRICTION} = \frac{1}{2}\rho V^2 S_{WETTED}\, C_F$$

where $C_F$ is obtained from charts such as Fig. 2.3

$$D_{0\,WAVE} = \frac{1}{2}\rho V^2 k_0 \frac{128}{\pi} \frac{\text{VOLUME}^2}{\text{LENGTH}^4}$$

where $k_0 = 1$ for an ideal body of revolution but can be $< 1$ for a wing body configuration

$$D_{i\,VORTEX} = \frac{1}{2}\rho V^2 k_v \frac{1}{4\pi} \frac{\left(L/\frac{1}{2}\rho V^2\right)^2}{b^2}$$

which is identical to the subsonic lift induced vortex drag and

L = lift
b = semispan
$k_v$ = 1 for planar elliptic span loading

$$D_{i\,WAVE} = \frac{1}{2}\rho V^2 k_w \frac{\beta^2 \left(L/\frac{1}{2}\rho V^2\right)^2}{2\pi\,(\text{LIFTING LENGTH})^2}$$

for a slender wing

$k_w = 1$ for an elliptical chordwise loading but in general can be less than unity.

For non-slender configurations and for more sophisticated estimates of slender aircraft it will be necessary to evaluate $D_{i\,WAVE} + D_{i\,VORTEX}$ using a suitable computer calculation method as described in Section 2.

It can be seen at once that whereas in subsonic conditions the maximum L/D (in the simplest terms) comes from associating minimum wetted area with maximum span i.e. high aspect ratio; the supersonic case is more complicated.

To maximise the supersonic L/D the following features are necessary

| | |
|---|---|
| Low wing area | $D_{0\,FRICTION}$ |
| Low total volume ) | $D_{0\,WAVE}$ |
| Large length ) | |
| Large span | $D_{i\,VORTEX}$ |
| Long lifting length | $D_{i\,WAVE}$ (and sonic boom overpressure) |

It is obvious that these requirements conflict to a much greater extent than in purely subsonic design :-

1. Considerations of low volume lead to a configuration with discrete wing and body components rather than an 'integrated' configuration. However these components must at least be integrated sufficiently to give the smooth area distribution required to minimise $k_0$ and a smooth lift distribution to give low $k_v$ and $k_w$ .

2. The requirement for a long lifting length leads to a fuselage designed for 'narrow' rather than 'wide body' seating.

3. High span for reduced vortex drag and a long lifting length are associated by the wing leading edge sweep requirements and taken together are in direct conflict with the need to minimise the wetted area.

4. The need for low wetted area is in conflict with the low wing loading required to keep take-off and landing speeds to a minimum.

General considerations of this sort lead to a configuration of the sort shown in fig. 6.1.

Putting 'good' values of the various coefficients into the equations and making a parametric study gives the results shown in Fig. 6.2.

The optimum $\beta b/\ell$ is seen to be about 0.35 leading to an optimum span/length ratio of 0.4 at 2.0M

The subsonic aerodynamics of the design must now be examined using whatever theories/data sheets/empirical correlations that the designer has at his disposal. For slender wings it is reasonable to use standard methods e.g. E.S.D.U. data sheets for 'form' drag, but for the induced drag, it will be necessary to make some approximation based on past experience, with due allowance being made for the effects of wing camber on the incidence for attached leading edge flow, and with varying 'K' factors depending on whether or not the flow can be considered to be attached at the leading edge. Fig. 6.3 shows typical variations of K for plane wings i.e. flow detached. Wings with high LE droops can obtain reductions in induced drag of up to 20% but at the expense of increased supersonic drag.

It is assumed that for simplicity that one unique polar applies to all subsonic conditions and that the available thrust always allows $(L/D)_{MAX}$ to be used, except where speed conditions are specified.

For a first iteration it is assumed that the profile drag is related by a simple factor to the skin friction drag, and that the induced drag is 10% less than the plane wing value given in Fig. 6.3.

Fig. 6.4 shows the variation of $L/D_{MAX}$ and L/D at 250 kts (with a weight which will be defined later) with Aspect Ratio.

While this simplified approach can be used to choose the initial, datum, configuration more work will be needed to make a fine optimisation between subsonic and supersonic requirements. This inevitably will rely heavily on wind tunnel tests.

The aerodynamic drag information is now available, and it is necessary to study the powerplant philosophy.

An outline of the elements of supersonic powerplant design has been given in Section 4. For the cruise Mach number being considered it will be a matter of fine judgement for the designer to decide if he will opt for the relative simplicity of the predominantly external compression intake and accept the drag penalty, or for the drag gains of a mixed compression intake and accept the complexity. For higher Mach numbers, say 2.5 plus, there is little doubt that he will choose a mixed or internal compression intake.

For the case discussed here it will be assumed that the choice is a three shock intake with external compression giving a recovery of 94% at 2.0M and 98% subsonic (Fig. 4.2 with 2% diffuser losses).

The choice of engine cycle is again a fine drawn compromise. The pure jet engine, as shown in Fig. 4.5 can produce the good values of specific thrust which are required to minimise the powerplant frontal area (and hence volume and wave drag). However the basic s.f.c. will be inferior to that of an engine with a modest bypass ratio, and the take-off noise for a given thrust will also be higher.

With the mission definition given above, the choice goes to the pure turbojet. If present day noise regulations were added to the mission definition the balance would probably be in favour of some form of bypass engine, although there would be great pressure on the engine designer to achieve high mass flow for minimum frontal area.

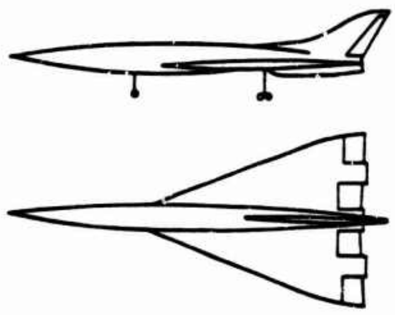

SLENDER SUPERSONIC TRANSPORT LAYOUT

FIG. 6.1

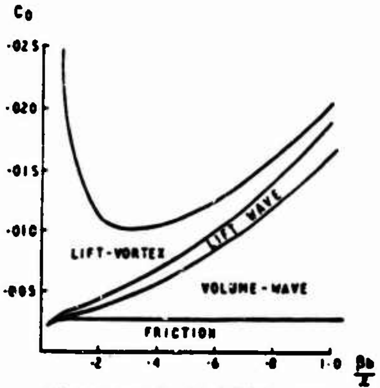

CONTRIBUTION TO CRUISE DRAG

FIG. 6.2

SUBSONIC LIFT INDUCED DRAG

STREAMWISE TIPS — ZERO CAMBER

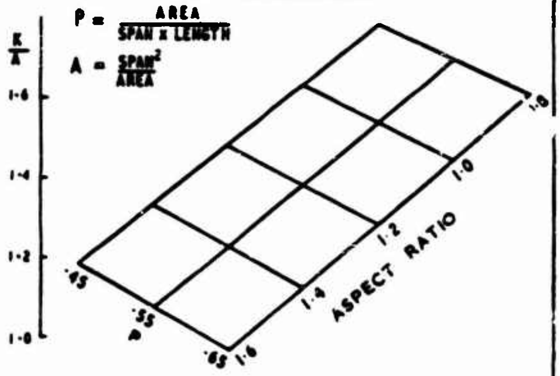

FIG. 6.3

SUBSONIC L/D

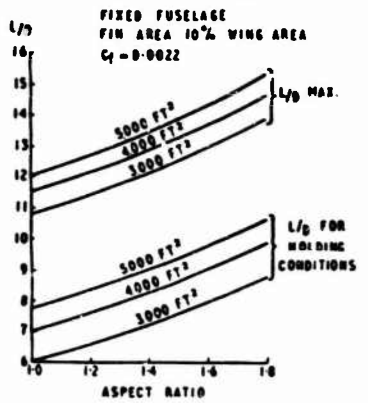

FIG. 6.4

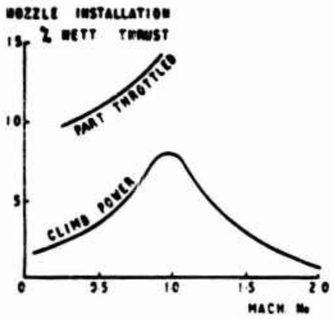

NOZZLE INSTALLATION LOSS

FIG. 6.5

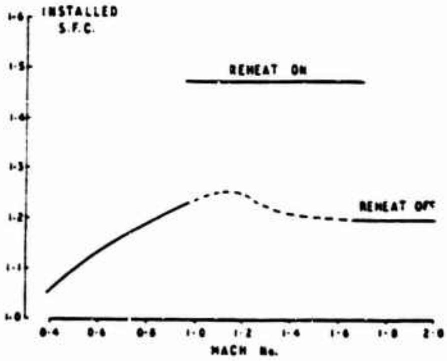

SPECIFIC FUEL CONSUMPTION

FIG. 6.6

SUPERSONIC OPTIMISATION

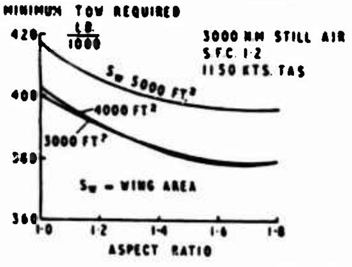

FIG. 6.7

SUBSONIC/SUPERSONIC OPTIMISATION

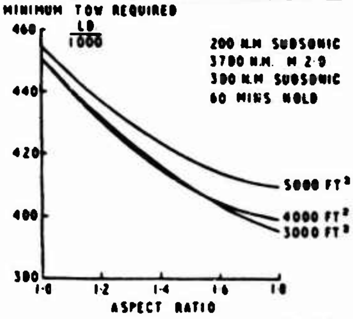

FIG. 6.8

Despite the arguments which have been bandied about over several years, it would seem today that there is little to choose between the performance of various nozzle designs. The cruise efficiency can be raised to very high levels (circa 99.5%) if the expansion angles are kept relatively low i.e. a long nozzle. The subsonic losses primarily depend on the area of the engine jet pipe relative to the area of the secondary nozzle in its subsonic position and the mixing length between primary and final nozzle stations i.e. a short nozzle. A nozzle design which permits the secondary nozzle closure to be spread over a long length of afterbody while still maintaining a short mixing length will be best, but the weight/performance balance must be carefully watched. A typical variation of nozzle loss through a mixed subsonic/supersonic flight plan is given in Fig. 6.5.

Typical installed s.f.c's for a pure jet engine are shown in Fig. 6.6. These installation losses are relative to a datum configuration as defined in Section 5. It will therefore be necessary to allow for the basic nacelle drag in computing the drag polar. If it is assumed that for a given state of the art the nacelle cross-section per unit thrust will be roughly constant then the nacelle drag, which is proportional to nacelle cross-section, can be taken as proportional to the thrust required i.e. the nacelle drag can be represented by a percentage increase in the bare airframe drag. For an initial assessment a value of 6% will be assumed.

### Structures and Weights

Strictly, the analysis of aircraft structure is no part of this presentation. However in order to examine the influence of the design mission it is necessary to at least give a cursory discussion of the problem.

In the first place, the choice of 2.0M as a cruise Mach number limits the stagnation temperature (ISA+5°C deg) to 400°K (127°C). This allows the use of aluminium alloy construction which has the advantage of cashing many years experience.

Secondly, and most important, it is a fact that the payload fraction of a supersonic transport (which is operating on the fringes of what is possible) will be much smaller than that of todays airliners. Consequently the premium paid for structural inefficiency is much greater.

At the same time, several desirable aerodynamic design features of an SST are acting against the designer. For example structure weight will tend to be increased by :-

Reduced wing thickness/chord ratio

Increased nose overhang

Increased take-off/landing attitude (undercarriage weight)

These effects are to some extent offset by the low aspect ratio of the wing.

On the systems side, the increased avionics complexity, air conditioning and hydraulic requirements will also contribute to the weight growth spiral.

For the powerplant, the much more complex intake and nozzle arrangements will subtract their quota from the available payload fraction.

In order to get a first appreciation of the design problems, let us assume that the weight can be represented by the following grossly over-simplified breakdown

| | |
|---|---|
| Wing weight | 8 lb/ft$^2$ |
| Fuselage weight (including systems and furnishing) | 350 lb/ft run |
| Fin weight | 6 lb/ft$^2$ |
| Undercarriage weight | 4% TOW |
| Powerplant (including intake and nozzle)* | 750 lb per sq.ft. cruise drag |
| Payload | 25,000 lb |

* It is assumed that the powerplant weight is proportional to cruise thrust i.e. to drag and a convenient parameter in the analysis (see below) is drag/$\frac{1}{2}\rho U^2$ which has the dimensions of ft$^2$.

### Design Assessment

With the elements assembled, it is now possible to examine the effect of various parameters on the design.

We shall study a family of aircraft with a given fuselage length and diameter associated with wings of 3,000, 4,000 and 5,000 ft$^2$ permuted with aspect ratios of 1.0, 1.4 and 1.8 to get a first idea of the problem.

Using some very simple ideas of target L/D and s.f.c. together with an equivalent still air range at 2.0M, we find that a wing volume of 4,500 - 5,000 ft$^3$ will be required for fuel, and that with a 200 ft long 11ft diameter fuselage with 100 ft parallel centre section and a fin 10% of the wing area, the total volume will be of the order 23,500 - 24,500 ft$^3$.

The expressions of Section 2 are then used to evaluate L/D for each member of the family, and taken an installed s.f.c. of 1.2 (Fig. 6.6), with an equivalent still air range of 5,000 n.mls. the ratio of start of cruise/end of cruise weight is obtained using the Breguet range formula. The end of cruise weight can be calculated from the weight expressions given above, leading to a variation of required TOW for the 'supersonic' mission as shown on Fig. 6.7.

This suggests that an aircraft optimised solely on the supersonic cruise condition would have about 3,000 ft$^2$ wing area and an aspect ratio of about 1.6. It should be noted that implicit in this optimum is the effect of varying wing and powerplant weights.

The optimum aircraft does not in general cruise at L/D$_{MAX}$ but at some lower value which reduces the required powerplant weight and gives a lower overall TOW than that obtained by flight at L/D$_{MAX}$.

If one now includes the effect of subsonic conditions, the picture changes slightly.

To simplify things a bit, we will assume that the original mission can be represented by the following

| | |
|---|---|
| 200 n.mls. at 450 kts TAS at L/D$_{MAX}$ | (subsonic climb) |
| 3780 n.mls. at 1150 kts TAS at L/D defined above | (includes effect of headwind and 5% block fuel reserves) |
| 300 n.mls. at 450 kts TAS at L/D$_{MAX}$ | (diversion cruise) |
| 1 hr at 250 kts at ZFW + 12,000 lb | (amalgamatum of three holding cases - 12,000 lb is first guess at mean holding fuel load) |

Using the subsonic characteristics given previously, the required TOW is as shown on Fig. 6.8.

It is now seen that the optimum wing area is still about 3,000 ft$^2$ but the optimum Aspect Ratio has increased to over 1.8. In practice the take-off requirements will demand a wing area in excess of 3,000 ft$^2$ and, as may be seen, the penalty for this need not be large.

From this point on, the design process is one of continual refinement of the iterative procedure. For example, the assumption of constant wing weight per unit area would certainly be challenged, since weight would be expected to vary with span and t/c at a given area. This would probably reduce the optimum aspect ratio.

Equally, the assumption that systems weights can be lumped together in an effective fuselage weight per ft is a gross over-simplification. In practice the fuselage length would be optimised for length on a drag/weight basis, and for this a more sophisticated model of the weight would be required.

With the cruise thrust requirement specified, the powerplant can be sized and the design optimised etc. etc.

Enough has been said to show that the problem of supersonic transport design is, in essence, one of compromise between conflicting subsonic and supersonic requirements. As will be seen in the next section, this problem is not confined to supersonic transports.

(b) Combat aircraft - Contribution by W.D. Horsfield and B.R.A. Burns, British Aircraft Corporation, Military Aircraft Division

Design Specification

A typical design specification might be as follows :-

Take-off to 50 ft and landing within 2,000 metre field
300 n.mls. range including 100 n.mls at 0.9M with 5 mins. at maximum power at 0.9M carrying specified weapon load
Supersonic capability with Maximum Mach number greater than say 2.0.
Specific excess power greater than :- 700 ft/sec at S.L. 1g
200 ft/sec at 10,000 ft, 0.9M, 6g
150 ft/sec at 1.5M, 36,000 ft, 1g
Time to 40,000 ft/1.8M less than 1.5 mins.
Design I.A.S. at least 750 kts
Design Normal 'g' 8.5
Attainable normal 'g' at 400 kts at least 4

In addition the specification may define tyre size and/or pressure, the number of guns and rounds of ammunition to be carried, the missile load (usually exceeded later) the fatigue life and radar/navigation equipment to be carried.

It will be seen from this that the design considerations for a supersonic fighter differ from those of the previous example in that :-

i) The fighter has no single supersonic design point at which maximum aerodynamic efficiency is required. It must perform efficiently over a wide range of Mach number - typically 1.2 to 2.0, and incidence - up to 20°.

ii) The fighter's structure and its stabilising and control surfaces are designed by manoeuvre requirements e.g. +6 -3g and 180°/sec roll rate; rather than by gust and system malfunction considerations.

It is evident from what has been stated earlier, that for efficient supersonic flight low frontal area is required. Consequently for this role, the weapon load will be kept to a minimum. In addition a thin low aspect ratio highly swept wing is desirable, but as will be seen later, this may conflict with the needs of airfield performance.

By its very nature, the fighter requires a very high thrust/weight ratio - typically 0.7 to 1.0 and this gives rise to major difficulties in integrating the intake, engine and nozzle into the design. The powerplant size is very large compared with the general size of the aircraft and dominates the layout.

There is generally a critical section around the C.G. where the requirements of fuel and undercarriage stowage, wing, air intake duct and installation of essential services all conflict with the need to minimise frontal area.

At the rear of the fuselage the need for an all moving tail (necessary for supersonic manoeuvre), a stiff fin with a substantial rudder plus the thrust reverser/parachute installation, reheat and arrester hook all add their quota of volume. At the same time, as mentioned in the powerplant section, there can be very large subsonic drag if the afterbody is not closely faired down to the cold nozzle area.

At the other end of the aircraft, the intake, pilot, radar, guns/weapons, aerials and pitot systems all require forward looking area as bluff as possible while the supersonic requirements demand fine angles and long fairings.

All this adds up to a design which must concentrate on the supersonic performance and then be optimised as far as possible to get reasonable subsonic performance using flaps/slats/variable geometry/parachute to meet airfield requirements, and, as in the supersonic transport, subsonic and supersonic requirements are in basic conflict.

## Some Performance Considerations

A typical weight breakdown and fuel breakdown of a supersonic fighter and its interception mission are shown in figure 6.9. The small fixed weight fraction (Armament, Crew and Support Systems, Avionics), totalling 12% means that the design is very sensitive in the project stage to changes in the performance requirements. It is noted also that although only 12% of the mission time is spent supersonically, 40% of the fuel is used in this time.

Figure 6.10 illustrates the primary interactions. Design wing loading is dictated by either combat or airfield performance requirements and largely controls the airframe weight fraction. Powerplant weight is dependent primarily on the thrust/weight ratio required to satisfy Maximum M, SEP (Specific excess power T-D/W x V) and sustained 'g' requirements. It is influenced also by the choice of design by-pass ratio and reheat boost. Their effects on engine weight and fuel weight are opposite, as shown in figure 6.10. Increasing by-pass ratio gives a more efficient but heavier engine; increasing reheat boost gives a lighter but thirstier engine. These features must therefore be carefully chosen to give the minimum total powerplant + fuel weight in the design mission.

Finally (figure 6.10) the fuel fraction is influenced largely by the radius of action and maximum Mach number requirements and is dependent also on the wing design parameters.

The small fixed weight fraction means also that aircraft size is sensitive to variations in drag and weight. This is expressed by a growth factor, illustrated in figure 6.12 as a function of fixed weight fraction. For the example quoted the growth factor is about 8; in other words for every kilogram of weight added locally or of fuel added to overcome drag without detriment to performance, the take-off weight increases by 8 kg. This demands very close attention to weight and drag control to achieve an efficient and cost-effective design. It requires also the correct balance between subsonic and supersonic design optimisation, particularly where the trends are conflicting. For example figure 6.13 shows how wing design parameter variations affect the relationship between supersonic and subsonic combat performance, indicating that increasing sweep is the way to go. However, figure 6.14 shows that increasing sweep is strongly detrimental to take-off distance would demand increased wing area to restore performance, negating the benefit of increased sweep in combat performance.

Figure 6.15 illustrates the breakdown of profile drag for a typical supersonic fighter and figure 6.16 the sensitivity of climb and acceleration performance to profile drag (amongst other things). To cite one example, halving excrescence drag (scoops, aerials, etc.) results in a drag saving of 4%, yielding 6% reduction in time to climb and accelerate.

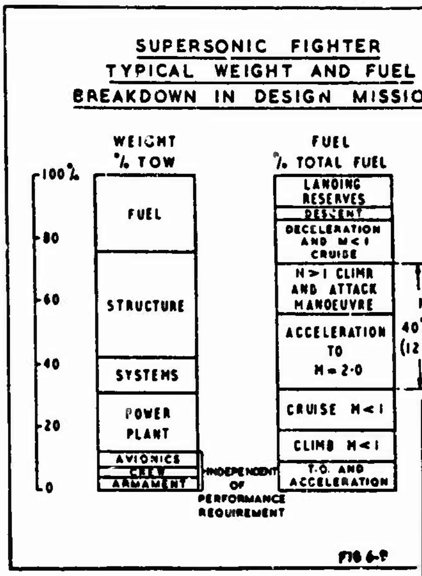
SUPERSONIC FIGHTER TYPICAL WEIGHT AND FUEL BREAKDOWN IN DESIGN MISSION

FIG 6-9

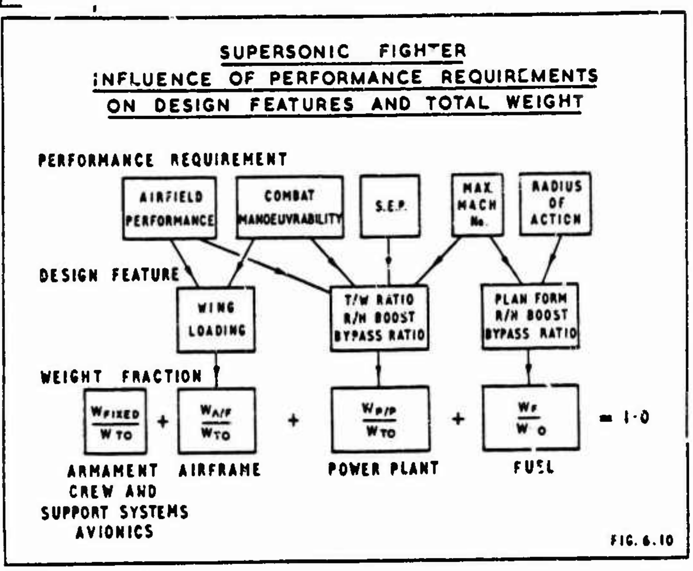
SUPERSONIC FIGHTER INFLUENCE OF PERFORMANCE REQUIREMENTS ON DESIGN FEATURES AND TOTAL WEIGHT

PERFORMANCE REQUIREMENT
AIRFIELD PERFORMANCE
COMBAT MANOEUVRABILITY
S.E.P.
MAX MACH No.
RADIUS OF ACTION
DESIGN FEATURE
WING LOADING
T/W RATIO R/H BOOST BYPASS RATIO
PLAN FORM R/H BOOST BYPASS RATIO
WEIGHT FRACTION
$\frac{W_{FIXED}}{W_{TO}} + \frac{W_{A/F}}{W_{TO}} + \frac{W_{P/P}}{W_{TO}} + \frac{W_F}{W_O} = 1\cdot0$
ARMAMENT CREW AND SUPPORT SYSTEMS AVIONICS
AIRFRAME
POWER PLANT
FUEL

FIG. 6.10

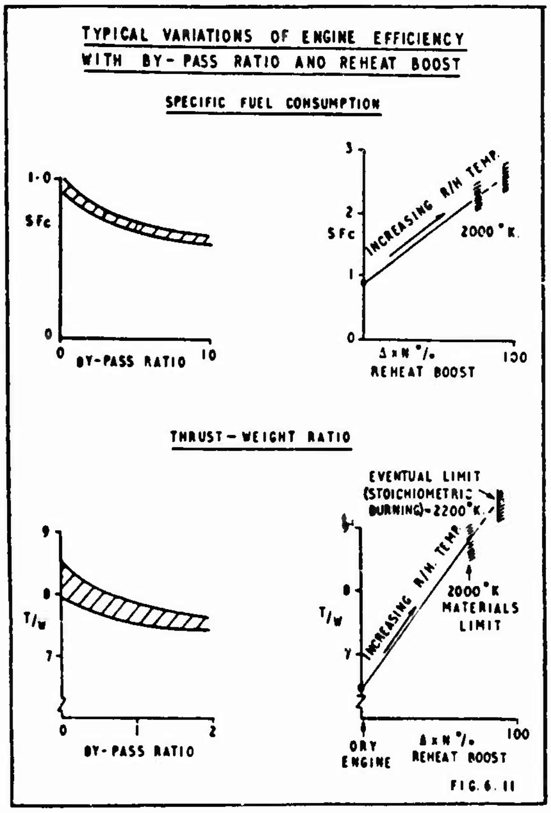
TYPICAL VARIATIONS OF ENGINE EFFICIENCY WITH BY-PASS RATIO AND REHEAT BOOST

SPECIFIC FUEL CONSUMPTION

THRUST – WEIGHT RATIO

FIG. 6. 11

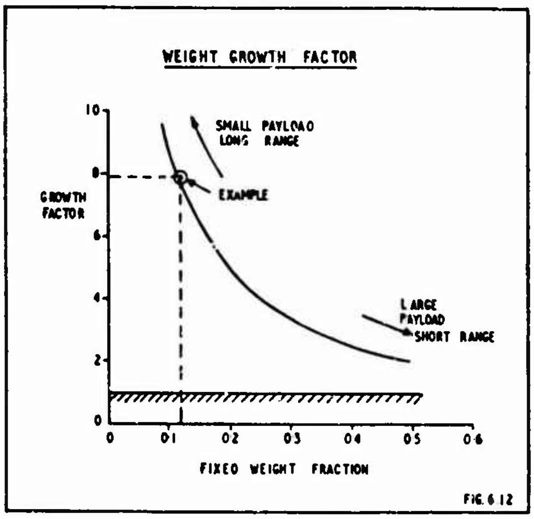
WEIGHT GROWTH FACTOR

FIG. 6 12

## Manoeuvrability Considerations

It is rare for wing lift limits to dictate supersonic manoeuvrability; except at low supersonic speed. More often it is the excessive longitudinal stability combined with diminishing tailplane effectiveness at high supersonic speed which defines the maximum trimmable incidence, or tailplane size to achieve a required limit. A typical picture is shown by the shaded area in figure 6.17.

In addition to longitudinal control, lateral/directional stability can constitute a limit to usable incidence. At increasing supersonic speed the effectiveness of the fin as a stabiliser reduces steeply, due to its diminishing lift slope and due to aeroelastic distortion, with increasing incidence its effectiveness is further reduced, due to body and wing vortex interference. The design case for sizing the fin is therefore likely to be at high supersonic speed, high C.A.S., high g/incidence, as illustrated in Figure 6.18. Shown also are typical relative sizes of fin required to satisfactory rapid rolling characteristics at high 'g', compared with the fin size required for adequate handling qualities in 1g flight.

## REFERENCES

1. Michel. ONERA Note Technique No. 8/2259 A.

2. Spalding D.B. and Chi S.W.
The drag of a compressible turbulent boundary layer on a smooth flat plate with and without heat transfer
J. Fl. Mech. 1964.

3. Winter K.G. and Gaudet L.
Turbulent Boundary Layer - Studies at High Reynolds Numbers and Mach Numbers between 0.2 and 2.8
R.A.E. Technical Report 2629, 1959.

4. Sommer S.C. and Short B.J.
Free Flight Measurements of Turbulent Boundary Layer Skin Friction in the presence of severe aerodynamic heating at Mach Numbers from 2.8 to 7.
NACA Tech. Note 3391 (1955).

5. Lighthill M.J.
"Mathematics and Aeronautics" Fourty-Eigth Wilbur Wright Memorial Lecture
JRAeS July 1960.

6. Lomax H.
The Wave Drag of Arbitrary Configurations in Linearised Flow as Determined by Areas and Forces in Oblique Plans
NACA/TIB/4620

7. Warren, C.H.E, Fraenkel, L.E.
A Combination of the Quasi-Cylinder and Slender Body Theories.
JRAeS April 1955

8. Farmer, Stoddart, Roberts
A Computer Study of Wave Drag Calculation
BAC (Warton) Report Ae 307 July 1970

9. Adams, Sears
Review and Extension of Slender Body Theory

10. Roberts, A
B.A.C. (Weybridge) Report MA 26 (Unpublished)

11. Gaudet and Winter RAE TR 90190

12. Hoerner AERODYNAMIC DRAG

13. R.Ae.SOC. Data Sheets

14. K.G. Smith RAE TR 65173

15. - NACA TR 1135

16. J.W. Nielsen NACA TN 3873

17. L. Ohman SAAB TN 45

18. L.E. Fraenkel R and M 2842

19. NASA TN D 1478

20. NASA TIL 6469

21. NASA TIB 1563

pages 5-49, and 5-50 are blank

22. S.G. Hooker and M. Garnier
Power for Supersonic Flight - Seventeenth Louis Bleriot Lecture

23. R.R. Jamison and R.J. Love
Engines for Supersonic Airliners
Jour R.AeS Sept. 1960

24. J.S. Alford
Powerplants for Supersonic Transports
Jour R.AeS Oct. 1960

## Acknowledgements

The authors wish to thank the British Aircraft Corporation for permission to publish this paper and to acknowledge the contributions made by Mr. R.H. Doe, Mr. E.N. Brailsford, Mr. B. Furness and Mr. J.E. Talbot of B.A.C.

N74-26451

# Appraisal of Wing Aerodynamic Design Methods for subsonic flight speed.

By W. Loeve, Head Scientific Services
National Aerospace Laboratory
Anthony Fokkerweg 2
Amsterdam
The Netherlands.

## SUMMARY

For a number of direct calculation methods for the prediction of flows around wings at subsonic speed, the basic assumptions are discussed. This forms the basis of the demonstration of the applicability of the methods. Comparison of calculated pressure distributions with results from windtunnel tests serve to illustrate this for three-dimensional wings and for the limiting case of plane flows around aerofoils.
Attention is paid to the use of inverse methods. In this context the use of hodograph methods for the design of aerofoils with transonic shockfree flow is discussed.

## 1. INTRODUCTION

In principle aerodynamic design methods consist of iterative processes in which alternately simulation of flows around bodies by means of (mostly digital) computers and experiments with models in windtunnels are used. Finally a verification in free flight takes place from which it can become clear that it is necessary to improve on the design by means of the original process again. The design process in general is complicated because the aircraft has to be operated safely and economically under a number of quite different conditions. Besides an interaction takes place of structural and aerodynamic considerations. Very often the expression "design method" is used for only the simulation of the flow by means of a digital computer. In the following the expression "calculation method" will be used to indicate this.

For stationary flow important aerodynamic characteristics of the wing are lift, drag and pitching moment as functions of angle of attack and flight speed. For the iterative design process of the wing it is essential to have detailed knowledge of the relation of the results of calculation methods, model experiments in windtunnels and free flight tests. In the present paper attention will be paid to the relation of results of calculation methods and tunnel experiments. Differences between calculated and measured results are caused by simplifications in the flow models underlying the calculation methods. The differences strongly depend on the geometry and flow conditions. As a consequence any appraisal of calculation methods depends on parameters that determine these quantities.

The discussions in the present paper will be restricted to subsonic compressible flows around swept wings. Much attention will be paid to the limiting case of plane flow around aerofoil shapes because this can give insight in many characteristics of calculation methods for three-dimensional wings. The model of the flow that underlies the methods that will be discussed is such that viscosity is neglected. Further the flow is assumed to be irrotational. This leads to potential flow with a potential $\phi$ from which velocity components in any coordinate direction can be obtained by differentiation with respect to the coordinate. The assumption of potential flow makes that flow separation and strong shock waves cannot be simulated by the models. One well known exception is formed by separation at sharp trailing edges of wings that is represented by a layer behind the wing across which a jump in potential exists.

Most of the calculation methods that will be discussed are such that for a given geometry the flow is calculated. The method for such cases is called a direct method. When the geometry is a result of the computation the method will be called an inverse method.

An important reason to make use of direct calculation methods in the design process is that when the computer programme is available the flexibility of the calculation with respect to change of wing geometry is much larger than the flexibility of model manufacture for tests in windtunnels. Moreover computers are much more generally available than windtunnels.

In addition to this the direct calculation methods in principle can be regarded as sets of rules that describe fluid flow. As such the methods are very useful as guides for finding a shape with appropriate aerodynamic characteristics. Part of this process often is the analysis of experimental results by comparison with results of calculations. This comparison for example can serve to distinguish between potential flow effects and viscous effects. It will be clear that experiments are essential tools to determine the characteristics of the configuration to be designed in flows that are outside the range of applicability of the calculation methods. It has been tried to illustrate the combined use of calculation methods and experiments in the diagram below (fig. 1). It can be seen in this figure that the design process in principle is a trial and error process.

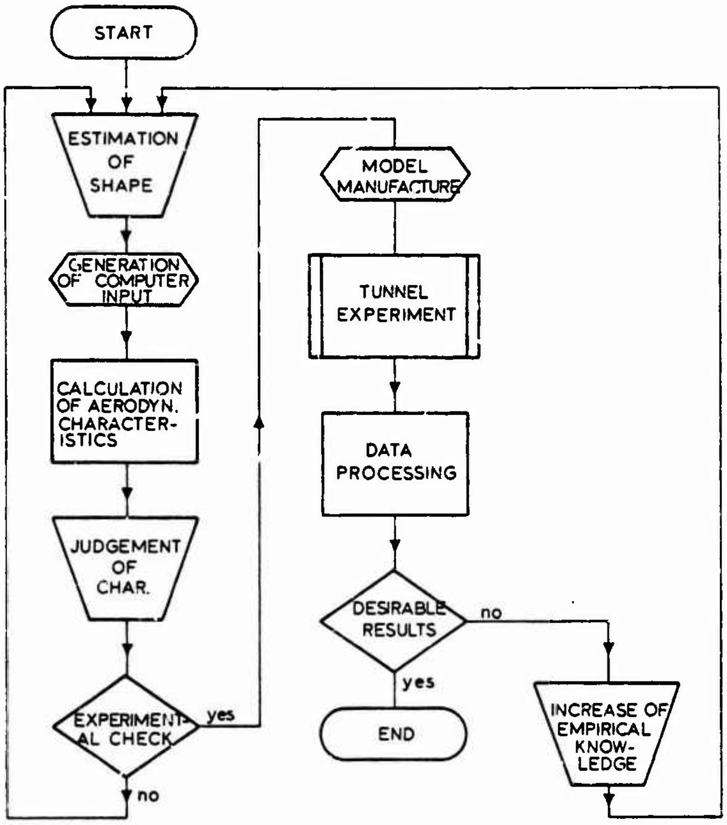

fig. 1

Simplified representation of the aerodynamic design process with direct calculation methods.

The shape by which the design process of fig. 1 is started, often is obtained partly or in total by means of inverse methods. In that case the designer has specific ideas about the required pressure distribution or load distribution at the design condition. Also under these circumstances the design process is a trial and error process because a desirable flow not always appears to be related to a feasible shape and because a check at the off-design conditions may show that the design has to be improved. One of the most important applications of an inverse method nowadays is the technique by which aerofoils with shock free transonic flow are obtained via the choice of flow characteristics in the hodograph plane and transformation of the flow and the related shape to the physical plane.

The characteristics of calculation methods are defined by the basic assumption with regard to the mathematical representation of the behaviour of the flow, the boundary conditions that are fulfilled on the wing-surface and at infinity and the numerical treatment of the partial differential equations that form part of the mathematical flow model. For the details of the numerical procedures in the various methods that will be discussed reference will be made to the papers in which the methods are described. Further it can be mentioned that of most methods numerical details have been presented earlier in the course on numerical fluid dynamics presented at the Von Karman Institute.

## 2. DISCUSSION OF SIMPLIFICATIONS OF POTENTIAL THEORY IN THE VARIOUS EXISTING CALCULATION METHODS.

Inviscid compressible flow is described by the conservation of mass, momentum and energy. Furthermore there holds the equation of state of the flow medium. When the flow is assumed irrotational it is possible to define a potential $\phi$ The derivative of the potential in any direction is equal to the component of the velocity in that direction. The flow around a wing that moves in air with a constant speed $U_\infty$ can be considered as an undisturbed flow with velocity $U_\infty$ at infinity upstream with a perturbation, induced by the wing, that is defined by a perturbation potential $\varphi$. When the x-axis of an orthogonal axis system (x,y,z) is chosen in the direction of $U_\infty$ and when gravity forces are neglected, the exact equation for the perturbation potential is (ref. 1):

$$(1-M_\infty^2)\frac{\partial^2\varphi}{\partial x^2}+\frac{\partial^2\varphi}{\partial y^2}+\frac{\partial^2\varphi}{\partial z^2}=M_\infty^2\left[(\gamma+1)\frac{\frac{\partial\varphi}{\partial x}}{U_\infty}+\frac{(\gamma+1)}{2}\left(\frac{\frac{\partial\varphi}{\partial x}}{U_\infty}\right)^2+\frac{(\gamma-1)}{2}\frac{\left(\frac{\partial\varphi}{\partial y}\right)^2+\left(\frac{\partial\varphi}{\partial z}\right)^2}{U_\infty^2}\right]\frac{\partial^2\varphi}{\partial x^2}+$$

$$+ M_\infty^2 \left[ (\gamma-1) \frac{\frac{\partial\varphi}{\partial x}}{U_\infty} + \frac{(\gamma+1)}{2} \left( \frac{\frac{\partial\varphi}{\partial y}}{U_\infty} \right)^2 + \frac{(\gamma-1)}{2} \, \frac{\left(\frac{\partial\varphi}{\partial z}\right)^2 + \left(\frac{\partial\varphi}{\partial x}\right)^2}{U_\infty^{\,2}} \right] \frac{\partial^2\varphi}{y^2}$$

$$+ M_\infty^2 \left[ (\gamma-1) \frac{\frac{\partial\varphi}{\partial x}}{U_\infty} + \frac{(\gamma+1)}{2} \, \frac{\frac{\partial\varphi}{\partial z}}{U_\infty^2}^{\,2} + \frac{(\gamma-1)}{2} \, \frac{\left(\frac{\partial\varphi}{\partial x}\right)^2 + \left(\frac{\partial\varphi}{\partial y}\right)^2}{U_\infty^{\,2}} \right] \frac{\partial^2\varphi}{\partial z^2}$$

$$+ M_\infty^2 \left[ 2 \frac{\frac{\partial\varphi}{\partial y}}{U_\infty} \left( 1 + \frac{\frac{\partial\varphi}{\partial x}}{U_\infty} \right) \frac{\partial^2\varphi}{\partial x \partial y} + 2 \frac{\frac{\partial\varphi}{\partial z}}{U_\infty} \left( 1 + \frac{\frac{\partial\varphi}{\partial x}}{U_\infty} \right) \frac{\partial^2\varphi}{\partial x \partial z} \right.$$

$$\left. + 2 \frac{\frac{\partial\varphi}{\partial y} \frac{\partial\varphi}{\partial z}}{U_\infty^{\,2}} \frac{\partial^2\varphi}{\partial y \partial z} \right] \tag{1}$$

In this equation $M_\infty$ is the Machnumber of the undisturbed flow.

The condition that the wing forms a streamline body in the flow is:

$$\frac{\partial\varphi}{\partial n} = - \vec{n} \cdot \vec{U}_\infty \tag{2}$$

where n is the local unit outward normal to the surface of the wing.

For all applications of potential theory to calculate the flow around wings with sharp trailing edge it is necessary to introduce the Kutta condition that guarantees that the flow leaves the trailing edge smoothly. In real flow this is the result of viscosity effects that prevent that a discontinuity in the velocity field arises at sharp edges. The circulation around the wing is determined by the Kutta condition. The result of the circulation is that a surface exists behind the wing across which there is a jump $\Delta\varphi$ in the potential. Because no forces can act on this wake surface it is aligned with the local velocity.

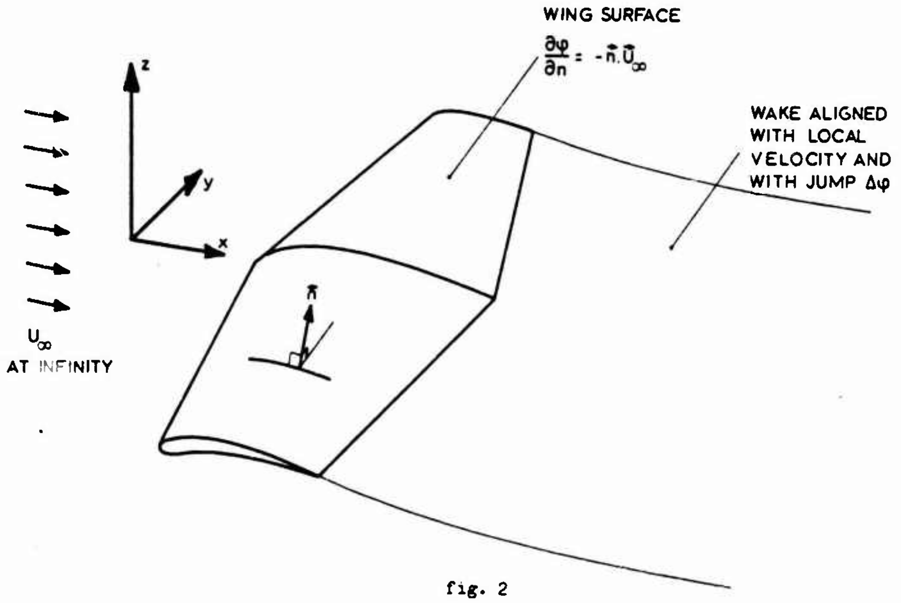
WING SURFACE
$\frac{\partial\varphi}{\partial n} = -\vec{n}.\vec{U}_\infty$
WAKE ALIGNED WITH LOCAL VELOCITY AND WITH JUMP $\Delta\varphi$
z
y
x
$\vec{n}$
$U_\infty$ AT INFINITY

fig. 2

The model for the flow around a wing.

The equation for the perturbation potential is non-linear. As a consequence it is not possible to find a general analytical method of solution of this flow problem. In most calculations use is made of simplifications of the potential equation and/or the boundary condition. The simplifications are based on assumptions with regard to the magnitude of the perturbation velocity components in comparison with $U_\infty$ and with regard to the Machnumber $M_\infty$. In the following sections some simplifications will be discussed.

## 2.1 Simplifications of the potential equation.

When all terms at the right hand side of eq. (1) may be neglected in comparison with those at the left hand side, that contain no perturbation velocities, eq. (1) reduces to the linear equation

$$(1 - M_\infty^2)\frac{\partial^2\varphi}{\partial x^2} + \frac{\partial^2\varphi}{\partial y^2} + \frac{\partial^2\varphi}{\partial z^2} = 0 \qquad (3)$$

In the following attention will be paid to the solutions of eq. (3) for plane flow that fulfil the boundary condition eq. (2) on the surface of the wing exactly. From the results conclusions can be drawn with respect to the desirability to extend the approach to three-dimensional flows. The judgement will be based on comparison of results with exact solutions of the full potential equation.

In most methods to solve eq. (3) use is made of similarity rules by which solutions of eq. (3) and boundary condition eq. (2) are related to solutions of the equation for incompressible flow ($M_\infty = 0$ in eq. (1) ):

$$\frac{\partial^2\varphi'}{\partial x'^2} + \frac{\partial^2\varphi'}{\partial y'^2} + \frac{\partial^2\varphi'}{\partial z'^2} = 0 \qquad (4)$$

with boundary condition

$$\frac{\partial\varphi'}{\partial n'} = -\vec{n}' \cdot U_\infty \qquad (2a)$$

Here n' is the local unit outward normal to the wing in the $\varphi'(x',y',z')$ flow. The advantage is that the solution of eq. (4) and eq. (2a) can be determined slightly easier. However it is not possible to find a simple set of similarity rules that result in a solution of the flow described by eq. (3) that fulfils the boundary condition eq. (2) exactly.

Eq. (4) can be obtained from eq. (3) by introduction of:

$$\begin{aligned} x' &= x \\ y' &= \sqrt{1 - M_\infty^2}\; y \\ z' &= \sqrt{1 - M_\infty^2}\; z \end{aligned} \qquad (5a)$$

According to the boundary condition eq. (2) the wing has to be a streamline surface in the compressible flow $\varphi(x,y,z)$. It is not possible to realise that also in the incompressible analogous flow the wing, that is transformed according to eq. (5a) is a streamline surface. The best approximation is obtained by making sure that the perturbation velocities in y and z direction are transformed in the same way as the y and z coordinate. This is the case when

$$\varphi' = (1 - M_\infty^2)\, \varphi \qquad (5b)$$

The streamline analogy then is obtained when $\frac{\partial\varphi}{\partial x}$ can be neglected on the surface in comparison with $U_\infty$. This in principle already was assumed when eq. (3) was introduced. The assumption is violated near blunt leading edges. This leads to errors, especially when $M_\infty$ is not small compared to unity, when the compressible $\varphi(x,y,z)$ flow is related according to eq. (5a,b) to an incompressible $\varphi'(x',y',z')$ flow that fulfils eq. (2a) at the surface of the analogous wing. However, errors due to this effect are surpassed by other errors due to neglecting the right hand side of eq. (1). In this equation e.g. the $\frac{\partial^2\varphi}{\partial x^2}$ term becomes of the same order of magnitude as the $(1-M_\infty^2)\frac{\partial^2\varphi}{\partial x^2}$ term at the left side when $M_\infty$ approaches unity.

The transformation via eq. (5a,b) is called the Göthert rule. According to these equations perturbation velocities in compressible flow can be obtained from perturbation velocities on an analogous configuration in the incompressible flow $\varphi'(x',y',z')$ according to:

$$\begin{aligned} \frac{\partial\varphi}{\partial x} &= \frac{1}{1-M_\infty^2}\frac{\partial\varphi'}{\partial x'} \\ \frac{\partial\varphi}{\partial y} &= \frac{1}{\sqrt{1-M_\infty^2}}\frac{\partial\varphi'}{\partial y'} \\ \frac{\partial\varphi}{\partial z} &= \frac{1}{\sqrt{1-M_\infty^2}}\frac{\partial\varphi'}{\partial z'} \end{aligned} \qquad (6)$$

With the velocity V from

$$V^2 = (U_\infty + \frac{\partial\varphi}{\partial x})^2 + (\frac{\partial\varphi}{\partial y})^2 + (\frac{\partial\varphi}{\partial z})^2$$

the pressure coefficient $C_p$ is

$$C_p = \frac{2}{\gamma M_\infty^2}\left[\left\{1 + \frac{\gamma-1}{2} M_\infty^2 (1-V^2)\right\}^{\frac{1}{\gamma-1}} - 1\right] \qquad (7)$$

$\gamma$=1.4, the ratio of specific heats of air.

Especially when the local Machnumber in the compressible flow approaches unity large discrepancies occur between results that fulfill eq. (1) and results of the linearized eq. (3). In view of this in section 3.4 attention will be paid to methods in which eq. (6) is supplemented with semi-empirical corrections for the differences between the actual potential equation and the approximation eq. (3).

It is not necessary in principle to determine the $\varphi'(x',y',z')$ flow in such a way that the boundary condition eq. (2a) is fulfilled exactly. In section 2.2 various simplifications of the boundary condition will be discussed.

In view of the shortcomings of linearized theory and the undesirable arbitrariness of semi-empirical corrections, attention will be paid in section 3.3 to a second order theory of Gretler for plane flow that leads to simple formulas. In this theory all terms in eq. (1) that contain squares of perturbation velocities are neglected whereas all terms containing first powers are taken into account. The concerning potential equation is the two-dimensional limiting case of:

$$(1-M_\infty^2)\frac{\partial^2\varphi}{\partial x^2} + \frac{\partial^2\varphi}{\partial y^2} + \frac{\partial^2\varphi}{\partial z^2} = M_\infty^2\,(\gamma+1)\,\frac{\frac{\partial\varphi}{\partial x}\,\frac{\partial^2\varphi}{\partial x^2}}{U_\infty} +$$

$$+ M_\infty^2\,(\gamma-1)\,\frac{\frac{\partial\varphi}{\partial x}}{U_\infty}\,(\frac{\partial^2\varphi}{\partial y^2} + \frac{\partial^2\varphi}{\partial z^2}) + \qquad (8)$$

$$+ 2\,M_\infty^2\,\frac{\frac{\partial\varphi}{\partial y}}{U_\infty}\frac{\partial^2\varphi}{\partial x\partial y} + 2\,M_\infty^2\,\frac{\frac{\partial\varphi}{\partial z}}{U_\infty}\frac{\partial^2\varphi}{\partial x\partial z}$$

Also in the concerning theory the boundary condition is taken into account up to second order accuracy in the perturbation velocities and aerofoil coordinates in thickness direction. When this would appear to lead to useful results it might be considered desirable to extend the approach to three-dimensional flow. This would be far more attractive then the use of semi-empirical corrections for compressibility effects that has been mentioned above.

There also exist methods in which choices are made of terms in the right hand side of eq. (1) in such a way that optimum results can be expected for certain cases. These lead to small perturbation equations in which all terms are taken into account that for the cases under consideration can be expected to be of the same order of magnitude. For three-dimensional wings with sweep angles larger than about 15° and local supersonic flow regions it however appears that in principle all terms in eq. (1) have to be taken into account. Methods to solve eq. (1) do not exist yet for three-dimensional wings.
General methods to determine these solutions up to now only exist for plane flows.

One way to obtain full solutions of eq. (1) for plane flows is that via the hodograph transformation that can be applied as an inverse method to determine aerofoil shapes with shock free transonic flow at the design condition. Another way is application of finite difference techniques. It has appeared that it is possible then to calculate details of flows with shocks.

## 2.2 Simplifications of the boundary condition.

When the potential equation is linearized for $M_\infty \neq 0$ it is consistent also to linearize the boundary condition. This can lead to less analytical work in the development of the calculation methods and less computational work for the applications. When the surface of the wing is described by an equation of the form $g(x,y,z)=0$, the boundary condition eq. (2) can be written:

$$(U_\infty + \frac{\partial\varphi}{\partial x})\frac{\partial g}{\partial x} + \frac{\partial\varphi}{\partial y}\frac{\partial g}{\partial y} + \frac{\partial\varphi}{\partial z}\frac{\partial g}{\partial z} = 0 \qquad (9)$$

This equation has to be satisfied on the surface. Now the wing dimensions are such that $\frac{\partial g}{\partial y}=0$. Further it is possible to neglect $\frac{\partial\varphi}{\partial x}$ in comparison with $U_\infty$ as has been done already in the derivation of the Göthert rule in section 2.1.
When $\frac{\partial\varphi}{\partial z}$ is developed in powers of z and when all terms after the first are neglected, the boundary condition eq. (9) reduces to:

$$\frac{\partial\varphi}{\partial z}(x,y,0) = -U_\infty\frac{\frac{\partial g}{\partial x}}{\frac{\partial g}{\partial z}} = U_\infty \left.\frac{dz}{dx}\right|_{\text{wing}} \qquad (10)$$

It can be said that in eq. (10) the boundary condition is applied in the plane of the wing (upper and lower side). It will be clear that eq. (10) cannot be applied to fuselages. For those shapes $\frac{\partial g}{\partial y}$ cannot be neglected and near the axis the development of $\frac{\partial g}{\partial z}$ in power series is not possible.

Apart from eq. (10) a number of other simplifications of the boundary condition eq. (9) are used in various calculation methods. One of these is the application of the correct condition in the chordal plane. This for instance simplifies the construction of the network in finite difference methods. Further a second order boundary condition with respect to wing coordinates and perturbation velocities is used in the second order theory of Gretler of which some results will be discussed in the following.

## 3. THE APPLICABILITY OF VARIOUS METHODS FOR SUBCRITICAL FLOW.

### 3.1 Linearized lifting surface theory.

Linearization of the potential equation and the boundary condition leads to linearized lifting surface theory when also thickness effects are neglected. This theory is still being treated by a large number of people. Application of fast computers has stimulated recent developments that have increased the flexibility of the linearized lifting surface methods with regard to the shape of the wing planform. In some cases it has been made possible also to treat combinations of lifting surfaces as wing and tail. Most methods by which the load distribution on wings according to linearized lifting surface theory can be determined lead to an integral equation for the load distribution $\Delta C_p(x,y)$:

$$\frac{dz_{warp}}{dx} = \iint\limits_{\substack{\text{wing}\\ \text{planform } S}} \Delta C_p(x',y')\ K\,(x,y;x',y')\ dS \qquad (11)$$

Mathematically one of the main problems is that the kernel function K is highly singular. Two numerical approaches to solve eq. (11) can be distinguished roughly: the loading function method (LoFuMe) and the loading element method (LoElMe).

In the LoFuMe the load distribution is represented by series appropriate functions of which the coefficients are determined by fulfilling eq. (11) in a number of selected collocation points. The distribution of these points on the wing plan form is optimized mathematically in relation to the character of the functions chosen. The Kutta condition is introduced by choosing the loading functions in such a way that $\Delta C_p = 0$ at the trailing edge of the wing.

The LoElMe is based on the assumption that a wing plan form can be devided into a number of panels at each of which the loading is a prescribed simple function of the x and y coordinates. The magnitude of the function is determined by fulfilling eq. (11) in a collocation point in each element. This can be done in such a way that it appears that the flow automatically fulfills the Kutta condition at the trailing edge.

In fig. 3 below the principles of both methods are illustrated. In ref. 2 numerical details of examples of both methods are described by Labrujère (NLR). The LoFuMe in ref. 2 is that of Zandbergen (NLR ref. 3) for which it is required that the wing plan form has edges with a continuous radius of curvature. For wings with kinks in the leading edge or trailing edge a procedure for rounding off the kinks is presented in ref. 3. Increase of accuracy of the solution requires increase of the number of terms in the series of loading functions and consequently increase of the system of linear equations that must be solved.

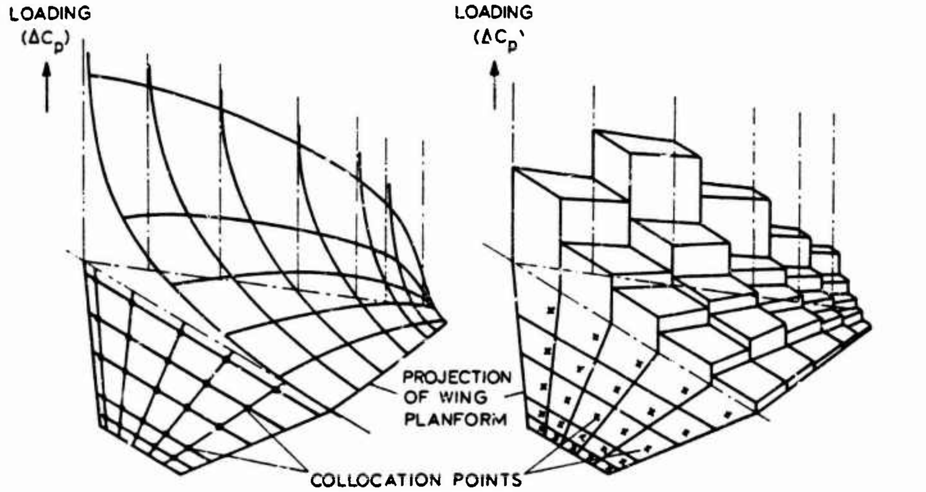

a. representation of load distribution
by means of loading functions
(LoFuMe)

b. representation of load distribution
by piece-wise constant functions
(LoElMe)

fig. 3

Solution of the integral equation of linearized lifting surface theory by prescribing the flow direction parallel to the wing surface in a limited number of collocation points.

Because the functions used for the series representation of $\Delta C_p$ form a complete system, any solution of the integral equation can be approximated as accurately as desired in this way. The accuracy of the method has been demonstrated amongst others by application to a circular wing for which exact results of linearized lifting surface theory have been determined by Van Spiegel (NLR ref. 4). A demonstration of this type however does not lead to an appraisal of the method in view of the use in the design process indicated in fig. 1. For this at least comparison with experimental results is required also. Some interesting information concerning this can be found in ref. 5 (Garner, RAE) as part of an analysis of the applicability of a lifting surface theory that is the result of combining the linearized lifting surface theory of ref. 3 with results of second order theory for plane flows around aerofoils. In fig. 4 below for spanwise station $\eta$=0.383 of two wings the chordwise loading, in terms of the local lift coefficient $C_{LL}$, according to linearized lifting surface theory is compared with experimental results. At the left hand side of fig. 4 results are presented for a wing with a 9 % thick RAE 101 section in the direction of the undisturbed flow. At the right hand side results for a similar wing with a 5 % thick RAE 101 section are presented.

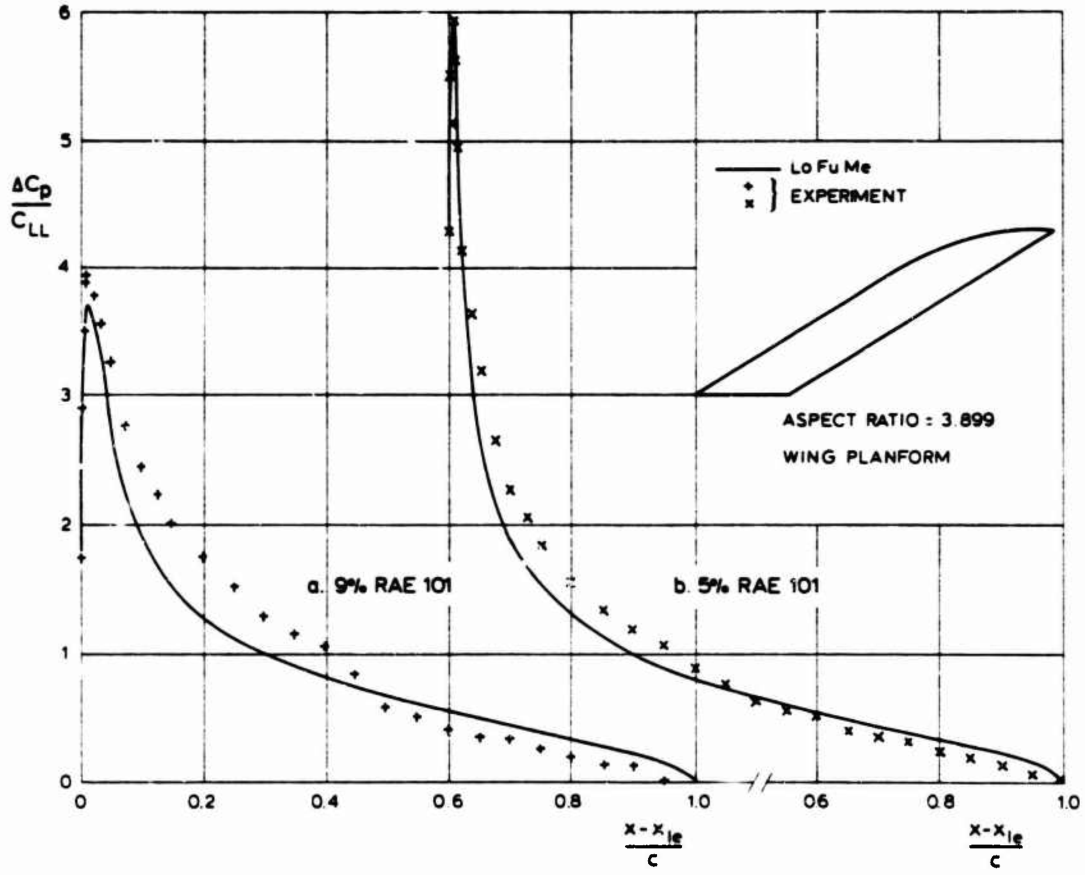

fig. 4

Chordwise loading at $\eta$ = 0.383 as fractions of local lift (Garner ref. 5).

The results in fig. 4 illustrate the type of discrepancies between results of linearized lifting surface theory and experimental results for wings with finite thickness and blunt leading edge. In the theory the first of the loading functions is such that near the leading edge $\Delta C_p = \frac{1}{\sqrt{x-x_{l.e.}}}$ where $x_{l.e.}$ is the local x-coordinate of the leading edge. This singularity represents correctly the behaviour of plane potential flow around a sharp leading edge. In the experiments use is made of a wing with a blunt leading edge on which the loading remains finite. Further thickness-lift interaction effects are present in the experiment because the wing has finite thickness. As a result the loading in the experiment is larger upstream of the point of maximum thickness of the aerofoil and is smaller downstream of this point in comparison with linearized theory.

In total, the lift is underestimated by linearized theory in comparison with full potential theory. In comparison with experimental results differences are smaller as a result of the fact that in the experiments the boundary layer effects cause a loss in lift.

The thickness-lift interaction varies in spanwise direction for a wing as shown in fig. 4. This only can be studied by comparison of results of linearized theory with results from theories that take into account the boundary conditions better. The variation of boundary layer effects in spanwise direction in the experiments obscure the variation of thickness-lift interaction effects in the comparison of experimental results with results of linearized lifting surface theory. In ref. 5 some information is presented with regard to an estimation of thickness-lift interaction as a function of spanwise position for the wing of fig. 4.

It should be mentioned that especially for wings as shown in fig. 4 in the experiment, for angles of attack larger than about 5°, non-linear effects are introduced in the tip region by a leading edge vortex. In the present paper no methods will be discussed that contain a mechanism that represents these vortices. Nevertheless it is useful to look at the predicted and measured local lift coefficients for different spanwise locations and the variation of the position of the aerodynamic centre in spanwise direction. The main reason to do this for this wing is that very accurate experimental results are available that are obtained with a large number of pressure measuring points on the wing model. This causes errors in the integrated values of local pitching moment and local lift coefficient to be smaller than in most cases where experimental results are taken from models that have been used in an actual design process. In fig. 5 the results are presented for the spanwise lift distribution and position of the aerodynamic centre.

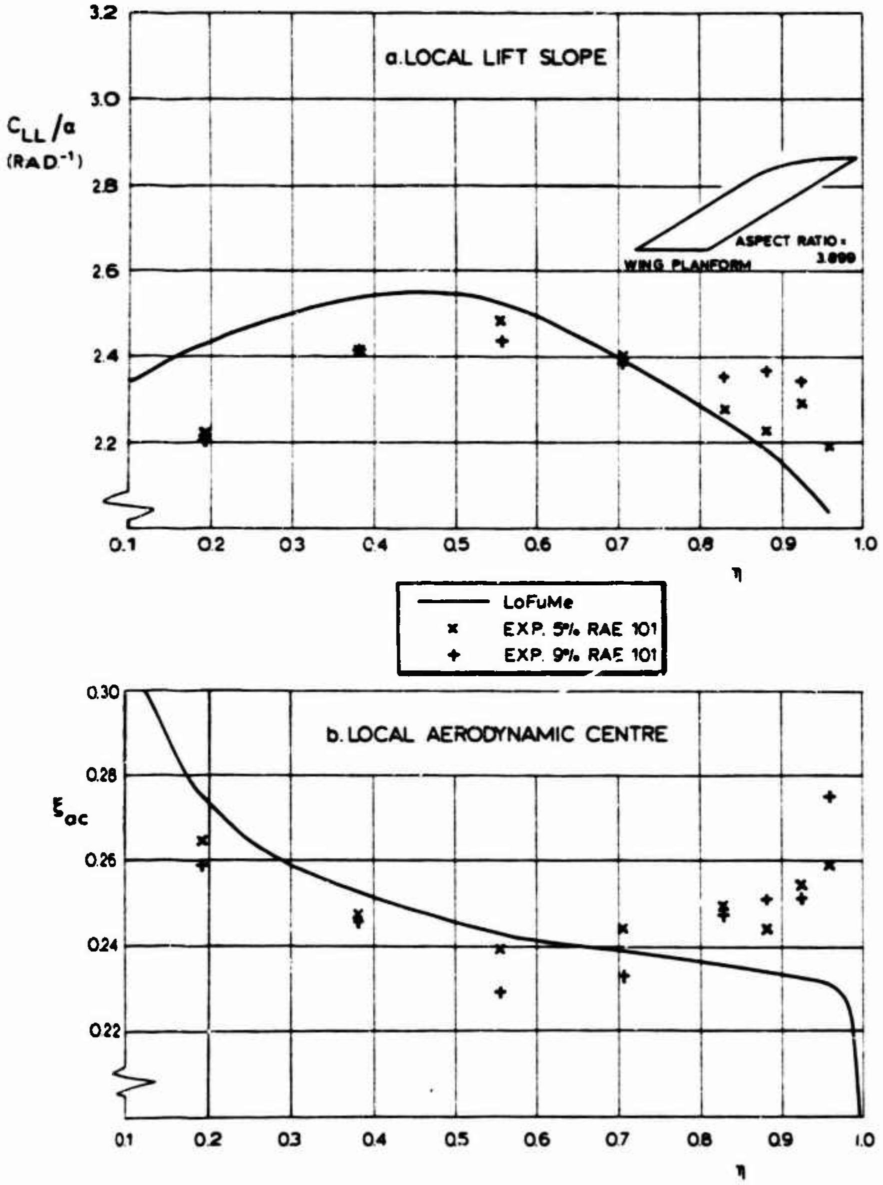

fig. 5

Calculated and measured spanwise distributions of lift slope and aerodynamic centre. (ref. 5)

In fig. 6 some results are presented that were obtained many years ago at NLR. It concerns the comparison of calculated load distributions from the LoFuMe with experimental distributions for a wing of a wing-body combination with and without nacelles mounted at the fuselage downstream of the wing. In the calculation the bodyside was treated as a reflection plane. To represent the effect of the nacelles in a simple way use was made of the possibility to add solutions of the linearized potential equation. One of these solutions is that of the source flow. In the calculation the nacelle was represented by a single source above and downstream of the wing. This generates a streamline body that extends in downstream direction to infinity. In view of this the source can be regarded to represent the displacement effect of the nacelle together with its wake in the experiment. The source generates perturbation velocities in vertical direction at the projection plane of the wing, equal to $\frac{\partial \varphi_{source}}{\partial z}$ .

Now for the determination of the load distribution $\Delta C_p$ with eq. (11) the value $\frac{\partial \varphi_{source}}{\partial z}$ is added to the angle of attack and camber effect in the left hand side of this equation.
Results for the configuration with and without nacelles are presented in fig. 6. For the sake of completeness in fig. 6b also the effect of the nacelles on the lift distribution is given as it follows from the calculation.

It will be clear that the applicability of the assumption that the fuselage side acts as a reflection plane strongly depends on the angle of attack of the configuration and the vertical position of the wing with respect to the fuselage. For the low wing configuration of fig. 6 the angle of attack induced by the fuselage near the wing root is small so that the effect of the fuselage is represented rather good by the reflection plane, also when the angle of attack of the fuselage differs from zero.

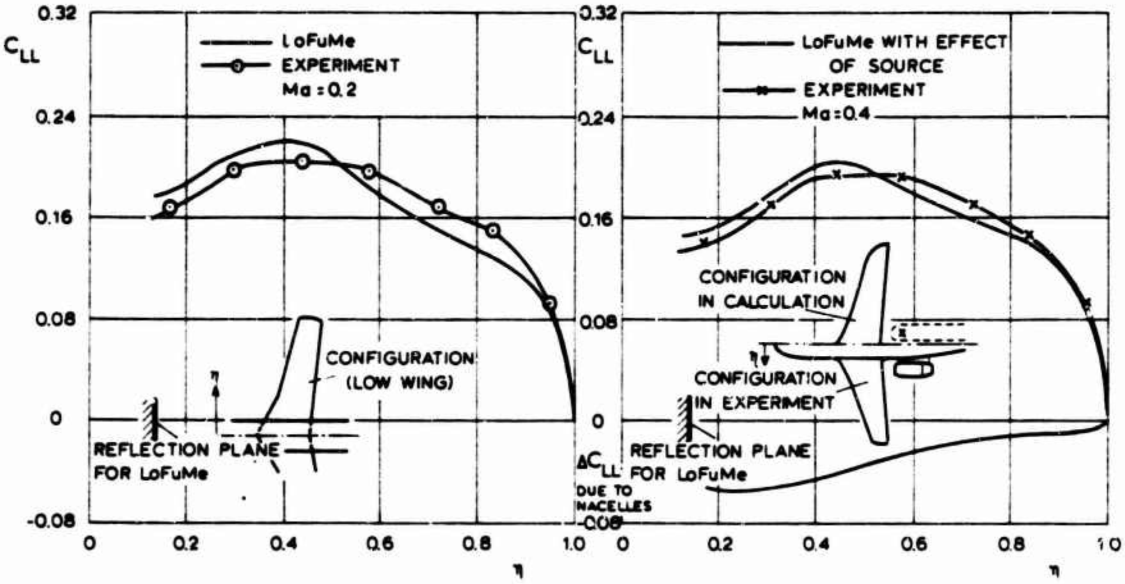

fig. 6

Calculated and measured lift distribution on wing-body combination with and without nacelle.

To introduce the loading element method (LoElMe) it can be mentioned that it is possible to obtain solutions of potential flows that are determined by the linear eq. (4), by adding elementary solutions of this equation. An elementary solution is a source layer that introduces a jump in normal derivative of the potential across the layer that is proportional to the source strength. Other elementary solutions are a doublet layer that introduces a jump in potential that is proportional to the doublet strength and a vortex layer that introduces a jump in the tangential derivative of the potential across the layer that is proportional to the vortex strength. Instead of continuous distributions also discrete sources, doublets and vortex lines can be used in approximate discretisations of the continuous distributions. It is attractive to look at the LoElMe and the panel methods to be discussed later as being based on the application of distributions of singularities in continuous or discrete form.

In linearized lifting surface theory the lift is induced by a pressure jump $\Delta C_p$ across the projection S of the wing on a plane tangential to $U_\infty$. This pressure jump is due to a discontinuity in the tangential velocity across the plane. This discontinuity can be represented by a doublet distribution with their axis normal to the plane. However, in a velocity potential solution the pressure jump is related to the first derivative of the doublet strength. In view of this it is convenient to represent the pressure jump by means of a vortex distribution of which the strength is directly related to the pressure jump.

Quite different from the LoFuMe the LoElMe leaves a large number of freedoms to the user. He can choose vorticity distribution and collocation points in an easy way. In view of this a more detailed discussion of the LoElMe seems to be useful within the scope of the present paper.

The loading element method that will be described is based on the idea of Falkner (1943) to use discrete vortex lines (instead of continuous vortex layers) for the representation of the effect of a wing according to linearized theory. This method is formulated in view of automatic computation by Hedman (FFA, ref. 6). It is assumed that the main behaviour of the load distribution in chordwise direction over the main part of the wing is similar to that in plane flow around an infinitely thin aerofoil.

The vorticity vector $\gamma$ in the vortex sheet on the projection of the wing planform in the (x,y)-plane is defined as the vector product of the unit vector normal to the (x,y)-plane and the difference vector of the velocities just above and below the sheet. The components of this vector can be expressed as:

$$\gamma_x = -\left\{ \left(\frac{\partial\varphi}{\partial y}\right)^+ - \left(\frac{\partial\varphi}{\partial y}\right)^- \right\}$$

$$\gamma_y = \left(\frac{\partial\varphi}{\partial x}\right)^+ - \left(\frac{\partial\varphi}{\partial x}\right)^- \qquad (12)$$

$$\gamma_z = C$$

Here the + sign refers to the side of the (x,y)-plane with positive values of the z-coordinate. The - sign refers to the other side of the (x,y)-plane. Helmholtz' law says that lines of constant vorticity in potential flow form closed contours. When the vortex system is such that at the wing trailing edge the Kutta condition is fulfilled, a sheet of vortices leaves the trailing edge in downstream direction as a consequence of this law. Because the pressure jump across the wake sheet has to be zero the vortex lines in principle have to be aligned with streamlines. To simplify the mathematical model in first instance straight lines are taken such that $\gamma_z = 0$ at the sheet and consequently $\gamma_x$ only varies with y at the sheet. To avoid also that both $\gamma_x$ and $\gamma_y$ have to be determined in the plane of the wing the direction of the vortices in the plane of the wing also is chosen a priori. A vortex system that has proved to be highly successful is presented in fig. 7 below. It is based on a division of the wing plan form in chordwise strips, each divided in quadrilateral panels that in the limit can become triangularly shaped.

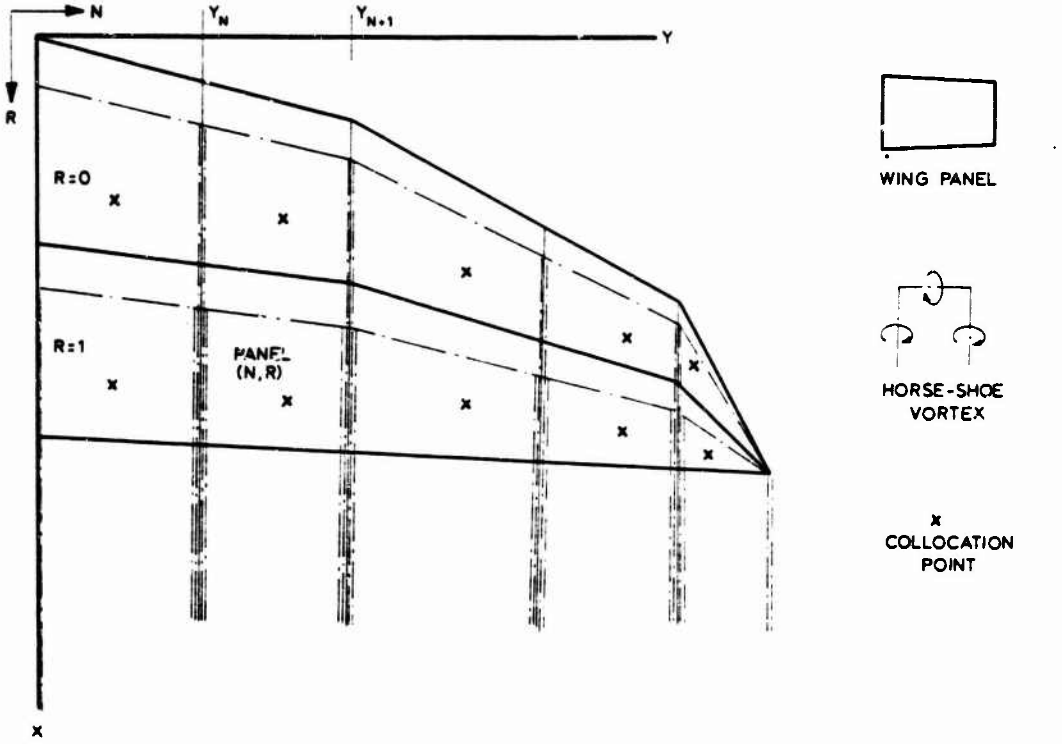

fig. 7

The horse shoe vortex, panel and collocation point arrangement in the LoElMe.

The influence of each vortex element on the $\frac{\partial\varphi}{\partial z}$ can be determined in each point of the wing plan form at some distance from the vortex elements by the Biot-Savart law. In the LoElMe the unknown vorticity strenghts are determined by application of the boundary condition eq. (10) in a collocation point in each panel. From an analysis of James (Douglas, ref. 7) and of ref. 2 it can be concluded that probably an optimum descretisation is obtained with panels of equal chord for each spanwise position and in each panel a vortex line at $\frac{1}{4}$ of the panel chord and a collocation point at $\frac{3}{4}$ of this chord in the middle in spanwise direction.

From the description of the method it will be clear that the quality of the LoElMe Solution of linearized lifting surface theory strongly depends on the choice of the panel distribution. This has to be done in such a way that the vortex direction that is connected with this choice deviates as less as possible from the direction that would be the result of a proper solution of the problem without an a priori choice of that direction. In relation to this in ref. 2 it has been shown that for the circular wing with the LoElMe that is described, the proper solution for lift and pitching moment cannot be obtained. The LoElMe can be regarded to be less suited for application to planforms with strongly curved edges. Because results of linearized lifting surface theory already have been compared with experimental results in this section an appraisal of the LoElMe is possible by a comparison with the LoFuMe with regard to the possibility to reach the correct solution of linearized theory with increasing number of collocation points. A result of this comparison is presented in fig. 8 together with an indication of relative computing time needed. It can be mentioned that the CDC 3300 by which the results have been obtained is a batch processing computer. The wall clock time needed for the calculations on this computer is about 10 times longer than the amount of system seconds needed on a CDC 6600 multiprocessing computer.

The term $C_{L\text{correct}}$ in fig. 8 needs some clarification. For the various planforms that are indicated in the figure the definition is different: For the circular wing $C_{L\text{correct}}$ refers to the results of Van Spiegel (ref. 4); for the rectangular wing it is the result of the LoFuMe with a number of collocation points for which a full solution can be expected. For the swept wing the results of the LoFuMe are influenced by the rounding off of the centre line kink. This rounding off becomes smaller with increasing number of spanwise collocation points. It cannot be expected in principle that with the LoFuMe "exact" results can be obtained for this case. On the other hand it cannot be predicted for what panel distribution an exact solution of the theory is obtained with the LoElMe for a swept wing. For the swept wing $C_{L\text{correct}}$ in

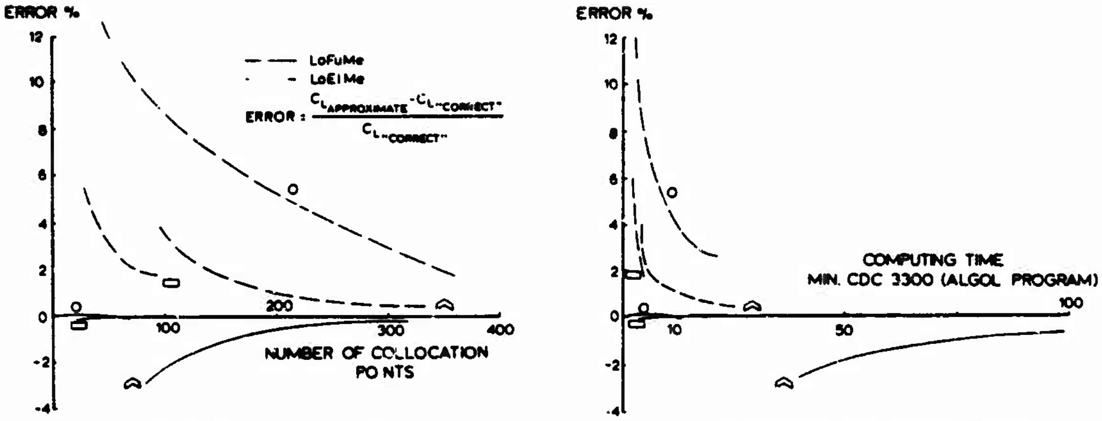

a. The effectiveness of the LoFuMe and the LoElMe expressed in terms of error percentage as a function of the number of collocation points.

b. The effectiveness of the LoFuMe and the LoElMe expressed in terms of error percentage as function of the computing time.

fig. 8

The influence of the number of collocation points in the LoElMe and the IoFuMe on the accuracy of the solution and the computing time (Labrujère ref. 2).

fig. 8 refers to the value that results from extrapolation of the results of both methods.

It is relatively easy to organise the computer programme for application of the LoElMe in such a way that the flexibility of the method can be used to determine the load on a combination of wings such as wing and horizontal tail plane. The value of these solutions however is limited because no fuselage effect can be taken into account and in the method as such no allowance is made for the displacement of the wake of the wing that for many configurations influences the load on the tail downstream. At several places calculation methods are being developed by which it is possible to determine the deformation of the vortex sheet such that the vorticity vector is aligned with the local velocity vector. Mostly the methods are based on an iterative procedure in which in each step a new shape of the discrete vortices is determined. Although in some cases it appears to be possible to obtain satisfactory agreement between experimental and numerical results as in ref. 8 (Labrujère and De Vries, NLR) the methods cannot be considered as standard design tools yet. For wings at moderate angle of attack and without deflected flaps the effect of the wake displacement on the wing loading is small.

One other aspect of the applicability of the LoElMe is worthwile to be mentioned. This concerns cases in which the slope of the thin-wing surface contains a discontinuity such as occurs at the hinge line of deflected central surfaces. Because limitations of the number of elements to describe the surface is desirable in view of computation time, it seems attractive to use for this problem a non-equidistant element distribution. A large density of panels then is applied near the hinge line where maximum gradients in $\Delta C_p$ may be expected. These thoughts have been the basis of the results of the LoElMe that are presented in fig. 9a for a flat plate at angle of attack $\alpha = 1$ rad. in plane flow. For this case the results of the LoElMe can be compared with an exact loading distribution that is for this case

$$\Delta C_p = 4\alpha \left( \frac{1 - \frac{x-x_{le}}{c}}{\frac{x-x_{le}}{c}} \right)^{\frac{1}{2}} .$$

The LoElMe has been applied with a non-equidistant element distribution that is indicated in fig. 9a. The results that have been obtained from unpublished work at NLR (Bennekers and Roos) show a peculiar oscillation near $\frac{x-x_{le}}{c} = 0.625$ where the minimum panel width is chosen. From this it can be concluded that it is better to avoid non-equidistant elements. For a flat plate the loading element method gives exact results with 32 equidistant elements.

It is possible to obtain exact results for a flat plate with deflected flap in incompressible flow by means of the steady limiting case of the method presented by Zwaan (NLR, ref. 9). In this method a version of the LoFuMe is described that is based on expansion techniques to represent the behaviour of the flow near the hinge axis. In fig. 9b results of the LoElMe are compared with exact results of the LoFuMe for this case. It appears that by means of the LoElMe in a simple way results can be obtained that are comparable with results of the LoFuMe that is based on much more analytical work. This is also the case for three-dimensional flow.

The importance of the linearized lifting surface theory at the moment is larger for the study of unsteady flow phenomena generated by deformation of structures and oscillating control surfaces, than for steady flows. An exception is formed by the inverse version of the LoElMe that is being used frequently to generate part of the input of the design process in fig. 1. This concerns the camber surface when the designer has specific ideas about the required load distribution on a configuration or on a part of it. In those cases however mostly also a version of a direct method is applied by which it is possible to calculate details of the pressure distribution on thick wings. In those cases the inverse LoElMe and the direct method are used alternately to generate the camber surface in an iterative way.
The semi-empirical direct method that is described in section 3.4 is adequate for this type of design procedure. For a better understanding of the need to make use of such a semi-empirical method first two methods with a more rigorous mathematical basis will be described.

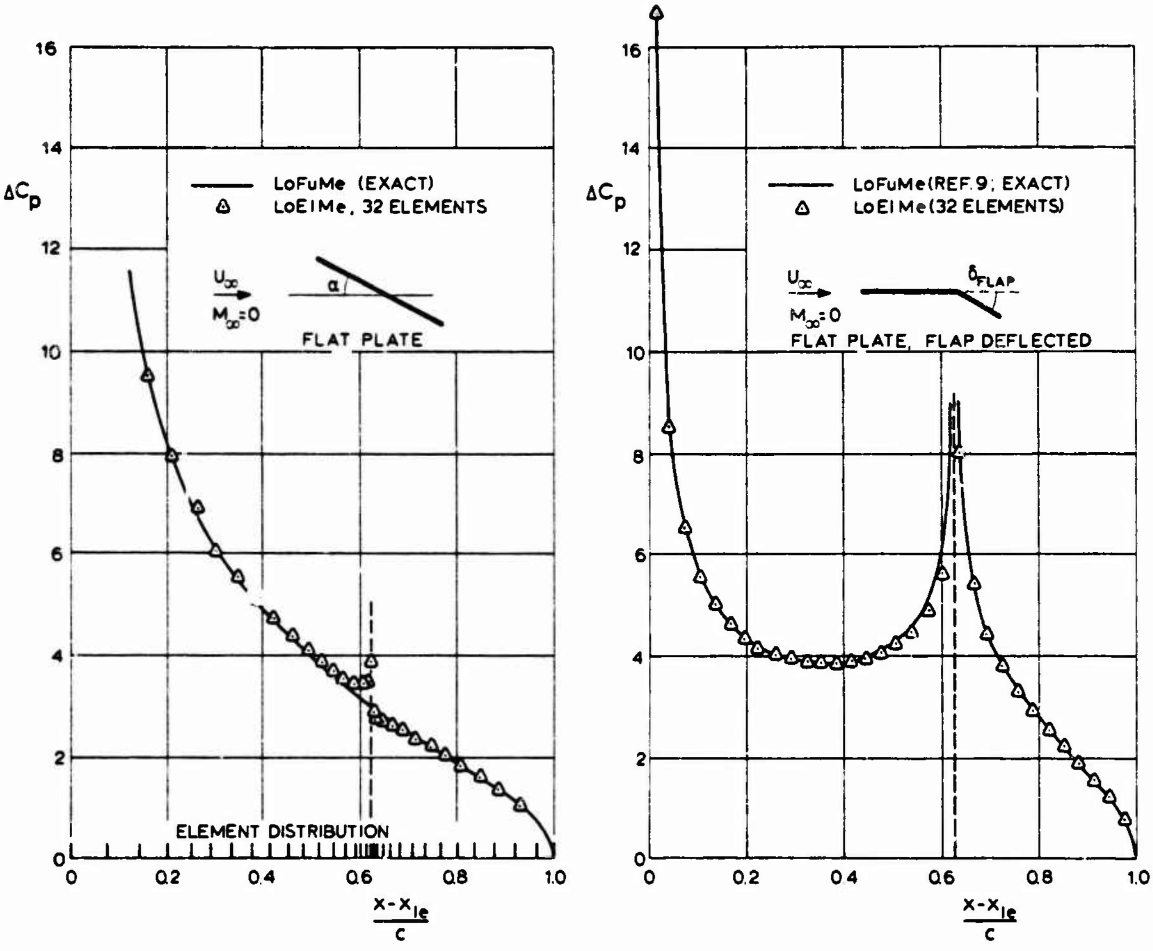

a. non-equidistant element distribution
flap angle = 0

b. equidistant element distribution
flap angle ≠ 0

fig. 9

Comparison of loading distribution obtained with the LoElMe and the LoFuMe for plane flow.

### 3.2 Linearized potential equation and exact boundary conditions.

It has been shown by Zandbergen (unpublished NLR work, 1968) that solutions of the linear eq. (3) can be obtained for the exact boundary condition eq. (2) making use of distributions of singularities. The computer programme for this solution is presented in ref. 10 (Labrujère and Schipholt, NLR) for plane flow. This work formed part of orientative investigations within the scheme of the development of a semi-empirical method at NLR. The approach is based on the transformation of eq. (3) into eq. (4). Different from what has been described in section 2.1 however now also the boundary condition is transformed correctly to give:

$$\left.\frac{dz'}{dx'}\right|_{surface} = (1 - M_\infty^2)\frac{\frac{\partial\varphi}{\partial z'}}{\frac{\partial\varphi}{\partial x'}} \qquad (13)$$

with the total potential

$$\phi = U_\infty x + \varphi \qquad (14)$$

When this is written as a relation between the tangential and normal derivative of $\phi$ along the contour of the transformed aerofoil:

$$\frac{\partial\varphi}{\partial n} = - \frac{M_\infty^2 \frac{dz}{dx}}{(1-M_\infty^2)+\left(\frac{\partial z'}{\partial x'}\right)^2} \frac{\partial\phi}{\partial t} \qquad (15)$$

The sign convention is given in scetch a, below.

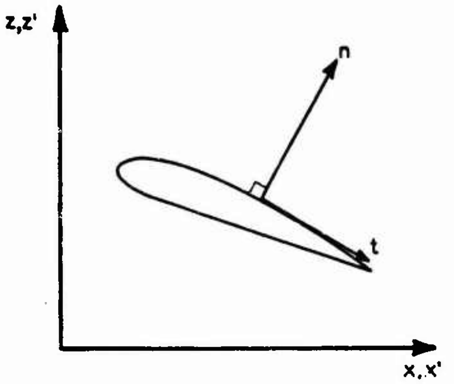

It can be seen that in the transformed flow the aerofoil is not a streamline curve. Now a distribution of vortices and sources is applied along the contour.

sketch a

Sign convention.

The vortices cause a jump in $\frac{\partial\varphi}{\partial t}$ across the contour and the sources cause a jump in $\frac{\partial\varphi}{\partial n}$ across the contour, both proportional to the local singularity strength.
Now for the singularity distribution no unique solution can be found without an additional requirement. When it is chosen that on the inner side of the contour $\left.\frac{\partial\varphi}{\partial n}\right|_{\substack{\text{inner}\\\text{side}}} = 0$
then according to Green's theorem also $\left.\frac{\partial\varphi}{\partial t}\right|_{\substack{\text{inner}\\\text{side}}} = 0$ (ref.11)
As a consequence the normal and tangential derivative of $\phi$ at the outer side of the contour are directly related to the local source and vorticity strength respectively. Substitution in the boundary condition eq. (15) gives the relation between vorticity and source strength. When this is substituted in the integral equation that represents $\left.\frac{\partial\varphi}{\partial n}\right|_{\substack{\text{inner}\\\text{side}}} = 0$ as a function of the undisturbed flow, the vorticity distribution and the source distribution, then an integral equation is obtained from which the vorticity distribution can be calculated. To evaluate the integral equation for the vorticity numerically, the contour is represented by a number of straight line segments. On each a vorticity is assumed that varies linearly along the segment. By satisfying the integral equation at the mid points of the segments and requiring that the vorticity at the upper side of the trailing edge point is equal and opposite to that at the lower side (Kutta condition), just as many equations are obtained as unknown vorticity strengths are introduced. The form in which the Kutta condition is applied guarantees a system of linear equations that can be solved by standard techniques. Full details of the method can be found in ref. 10. The pressure coefficient is obtained by the two-dimensional limiting case of eq. (8).

A comparison of the exact solution of the linearized potential equation with exact solutions of the full potential equations gives some insight in the applicability of the linearized equation. It will be clear that for this comparison enough segments must be chosen to represent the contour, to make sure that the numerical approximation of the solution does not cause discrepancies from the ideal result. The possibility to do this has been demonstrated in ref. 10. The exact solutions of the full potential equation have been obtained by means of a hodograph method of Nieuwland (ref. 31). Attention to this method will be paid in section 4.1 of the present paper. In fig. 10 the result for the linearized potential equation has been compared with an exact result for a relatively simple aerofoil. To give much information about the comparison in the nose region the result has been plotted as a function of $\sqrt{\frac{x-x_{l.e.}}{c}}$

From fig. 10 it can become clear that in the nose region the results for the linearized potential equation differ from exact results for eq. (1). Also the minimum pressure is not represented well by eq. (3) for this case that is just subcritical. This makes that the linearized potential equation as such is not suitable as a basis for calculation methods for flows where the local speed approaches the speed of sound.

The aerofoil section of fig. 10 generates a smooth acceleration of the flow from the stagnation point. Even in that case relative large errors are caused by linearization of the potential equation near the nose. When rapid changes in the pressure distribution are present, the results obtained for the linearized equation are much worse. From the type of result that is presented in fig. 10 the conclusion has been drawn at NLR that to calculate high subsonic flows around wings it is not useful to try to obtain exact results of the linearized potential equation.

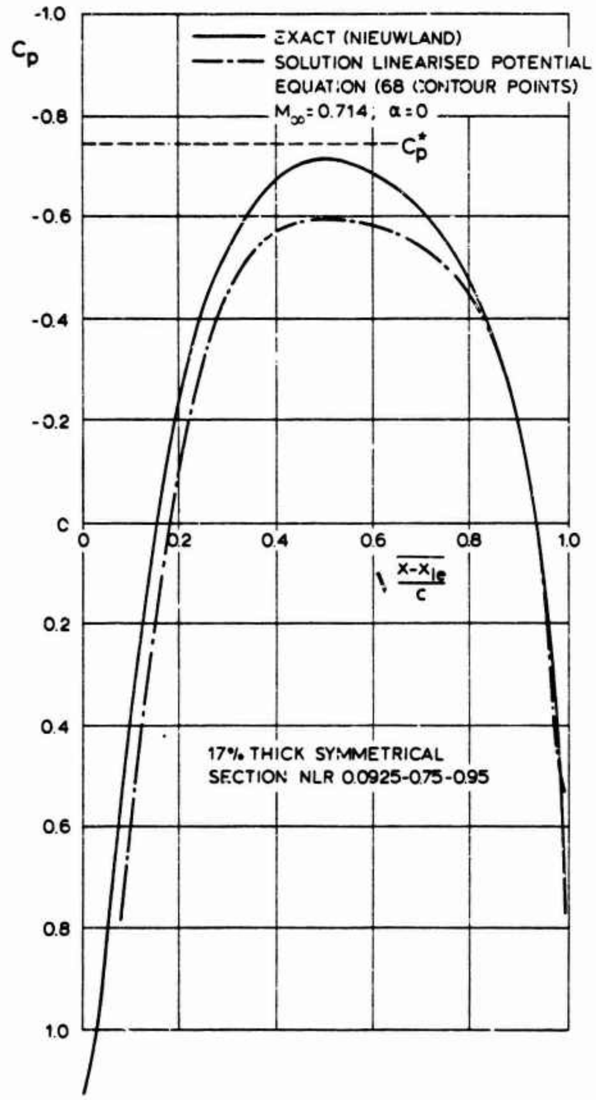

fig. 10

Exact results for the linearized potential equation (eq.(3) ) in comparison with exact results for the full potential equation (eq.(1) ).

### 3.3 Second order approximation of the potential equation and the boundary condition.

In ref. 13 Gretler has presented an interesting solution of the problem to calculate for plane flow the compressible pressure distribution on the surface of an aerofoil up to second order accuracy with respect to the boundary condition as well as the potential equation. He has reduced the problem to the calculation of simple integrals that only depend on the aerofoil coordinates. Moreover he has given a simple correction that renders the solution "uniformly valid" up to second order near a blunt leading edge. An appraisal of the result is considered useful because it might show that it is worthwhile to develop second order theories for three-dimensional wings to obtain methods for the calculation of compressible pressure distributions.

Gretler has introduced camber $z_c$ and thickness $z_t$ of an aerofoil with z-coordinate $z_p$ according to $z_p = z_c \pm z_t$, all in parts of the aerofoil chord. His formula for the velocity V along the contour is:

$$\frac{V}{U_\infty} = \frac{1}{\sqrt{1+\left(\frac{dz_p}{dx}\right)^2}}\left[1+\frac{1}{\sqrt{1-M_\infty^2}}u_1^{(o)}+\left\{1+\frac{M_\infty^2}{1-M_\infty^2}\left(1+\frac{\gamma+1}{4}\frac{M_\infty^2}{1-M_\infty^2}\right)\right\}\Delta w^{(o)}+\right.$$

$$+\frac{M_\infty^2}{2(1-M_\infty^2)}\left(1+\frac{\gamma+1}{4}\frac{M_\infty^2}{1-M_\infty^2}\right)u_1^{(o)2}+$$

$$\left.+\frac{\left(\frac{dz_p}{dx}\right)^2}{2}\left\{1-(1-M_\infty^2)\frac{M_\infty^2}{1-M_\infty^2}\left(1+\frac{\gamma+1}{4}\frac{M_\infty^2}{1-M_\infty^2}\right)\frac{\left(u_1^{(o)2}-\left(\frac{dz_p}{dx}\right)^2\right)}{1+(1-M_\infty^2)\left(\frac{dz_p}{dx}\right)^2}\right\}\right] \tag{16}$$

where

$$u_1^{(o)} = u_{11}^{(o)} \pm u_{12}^{(o)}$$

$$\Delta w^{(0)} = \Delta u_1^{(0)} \pm \Delta u_2^{(0)} + (z_t \pm z_o)\left(\frac{d^2z_t}{dx^2} \pm \frac{d^2z_c}{dx^2}\right) + \frac{1}{2}\left(\frac{dz_t}{dx} \pm \frac{dz_c}{dx}\right)^2$$

$$u_{11}^{(o)} = \frac{1}{\pi}\int_{x_{le}}^{x_{tre}} \frac{\frac{dz_o}{dx}}{x-\xi}\,d\xi$$

$$u_{12}^{(o)} = \sqrt{\frac{x_{tre}-x}{x-x_{le}}}\left[\alpha+\frac{1}{\pi}\int_{x_{le}}^{x_{tre}}\frac{\frac{dz_t}{dx}}{x-\xi}\sqrt{\frac{\xi-x_{le}}{x_{tre}-\xi}}\,d\xi\right]$$

$$\Delta u_1^{(o)} = -\frac{1}{2}\alpha^2+\frac{1}{\pi}\int_{x_{le}}^{x_{tre}}\left(\frac{u_{11}^{(o)}z_c+u_{12}^{(o)}z_t}{x-\xi}\right)d\xi$$

$$\Delta u_2^{(o)} = \sqrt{\frac{x_{tre}-x}{x-x_{le}}}\,\frac{1}{\pi}\int_{x_{le}}^{x_{tre}}\left(\frac{u_{12}^{(o)}z_c+u_{11}^{(o)}z_t}{x-\xi}\right)\sqrt{\frac{\xi-x_{le}}{x_{tre}-\xi}}\,d\xi$$

The pressure coefficient again is obtained by eq. (8).

At some distance from the leading edge where $\frac{dz_p}{dx}$ is very small eq. (16) reduces to:

$$\frac{V}{U_\infty} = 1+\frac{1}{\sqrt{1-M_\infty^2}}u_1^{(0)}+\left\{1+\frac{M_\infty^2}{1-M_\infty^2}\left(1+\frac{\gamma+1}{4}\frac{M_\infty^2}{1-M_\infty^2}\right)\right\}\Delta w^{(0)}+\frac{M_\infty^2}{2(1-M_\infty^2)}\left\{1+\frac{\gamma+1}{4}\frac{M_\infty^2}{1-M_\infty^2}\right\}u_1^{(0)2}$$

For the nose region of blunt aerofoils where $\frac{dz_p}{dx}$ differs much from zero the multiplicative correction

$$\frac{1}{\sqrt{1+\left(\frac{dz_p}{dx}\right)^2}}$$

and the additive correction

$$\frac{1}{2}\left(\frac{dz_p}{dx}\right)^2 \left\{1-(1-M_\infty^2)\frac{M_\infty^2}{1-M_\infty^2}\left(1+\frac{\gamma+1}{4}\frac{M_\infty^2}{1-M_\infty^2}\right) \approx -\frac{u_1(0)^2+\left(\frac{dz_p}{dx}\right)^2}{1+(1-M_\infty^2)\left(\frac{dz_p}{dx}\right)^2}\right.$$

are the simple corrections by which the second order theory is rendered uniformly valid.

For a number of symmetrical aerofoils results of eq. (16) have been compared with exact results from hodograph theory (section 4.1) for compressible flow and for incompressible flow with exact results from the panel method that will be described in section 3.4. The numerical evaluation of eq. (16) that has been used is described in ref. 14 (Baurdoux and Schipholt, NLR).
For comparison also results of the uniformly valid first order theory are presented in the figures below. The aerofoil of fig. 11 is the same as that of fig. 10.

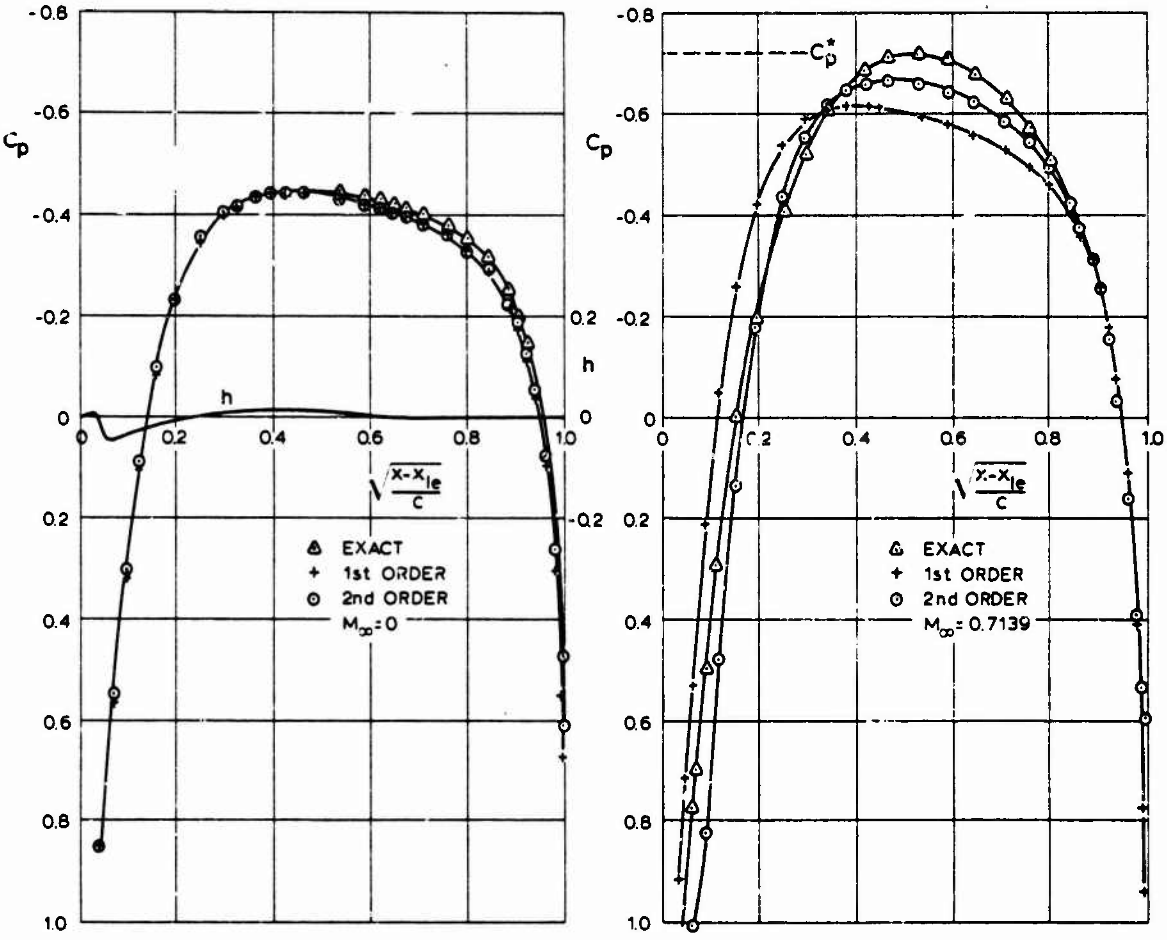

fig. 11

Pressure distribution for a symmetrical aerofoil with nearly elliptical nose shape.
(17 % thick section NLR 0.0925 - 0.75 - 0.95)

By comparison of the results in fig. 10 and the right hand side of fig. 11 it can be seen that for the concerning aerofoil errors in the minimum pressure are about the same for the first order theory and for the full solution of the linearized potential equation. In the area where the surface slope is small both solutions also should be about equal. Near the nose the errors of both approximations have opposite sign. Especially for the compressible flow second order theory gives much better results than first order theory for this aerofoil with nearly elliptical nose shape. The discrepancy of the aerofoil shape from an elliptical shape is represented by the parameter h in the figure that is equal to the difference between the slope of the aerofoil contour and the slope of the contour of an ellips with the same nose radius and the same distance between the leading edge and the maximum thickness as the aerofoil.

In fig. 12 and fig. 13 similar results are presented for aerofoils with non-elliptical nose shapes.

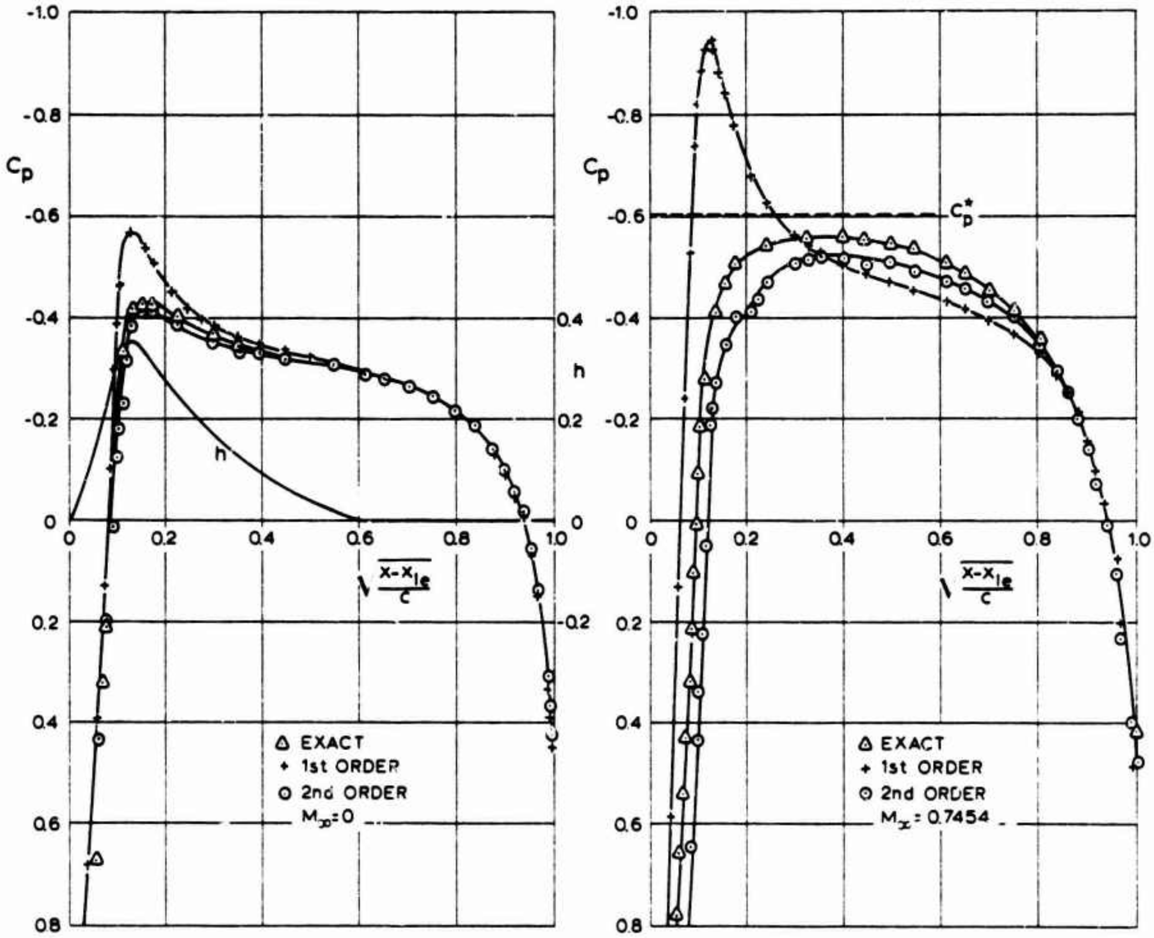

fig. 12

Pressure distribution for a symmetrical aerofoil with non-elliptical nose shape.
(12.5 % thick section NLR 0.10 - 0.75 - 1.25)

From fig. 12 and fig. 13 it becomes clear that when large discrepancies between the exact pressure distribution and the uniformly valid first order results exist that also second order theory does not give good results. It appears that many aerofoils on which supersonic flow regions can be present without shocks have nose shapes that strongly differ from elliptic shapes. The advantages of application of those aerofoils are illustrated in fig. 14.

When local supersonic flow regions can occur without an increase of drag due to shockwaves, then either the flight Mach number or the lift or the aerofoil thickness can be larger before the transonic dragrise diminishes the efficiency, then for aerofoils where shockwaves appear together with supersonic regions. This makes it desirable to find calculation methods that also for this class of aerofoils give good results at high subsonic speeds. None of the methods discussed above meets the needs of the designer in this respect.

From the results presented the conclusion can be drawn that the only way seems to be to solve the non-linear potential equation eq. (1). However a disadvantage of this non-linear equation is that no use can be made of the superposition principle that forms the basis of the application of singularity distributions. By means of this the dimension of the problem can be reduced by one because the solution can be formulated in such a way that only unknowns at the surface of the wing play a role. This is the reason that in the next section attention is paid to a semi-empirical method that is based on a solution of the linear potential equation again but in which non-linear compressibility effects are introduced afterwards in the form of a Göthert-type transformation with factors that depend on the local flow conditions.

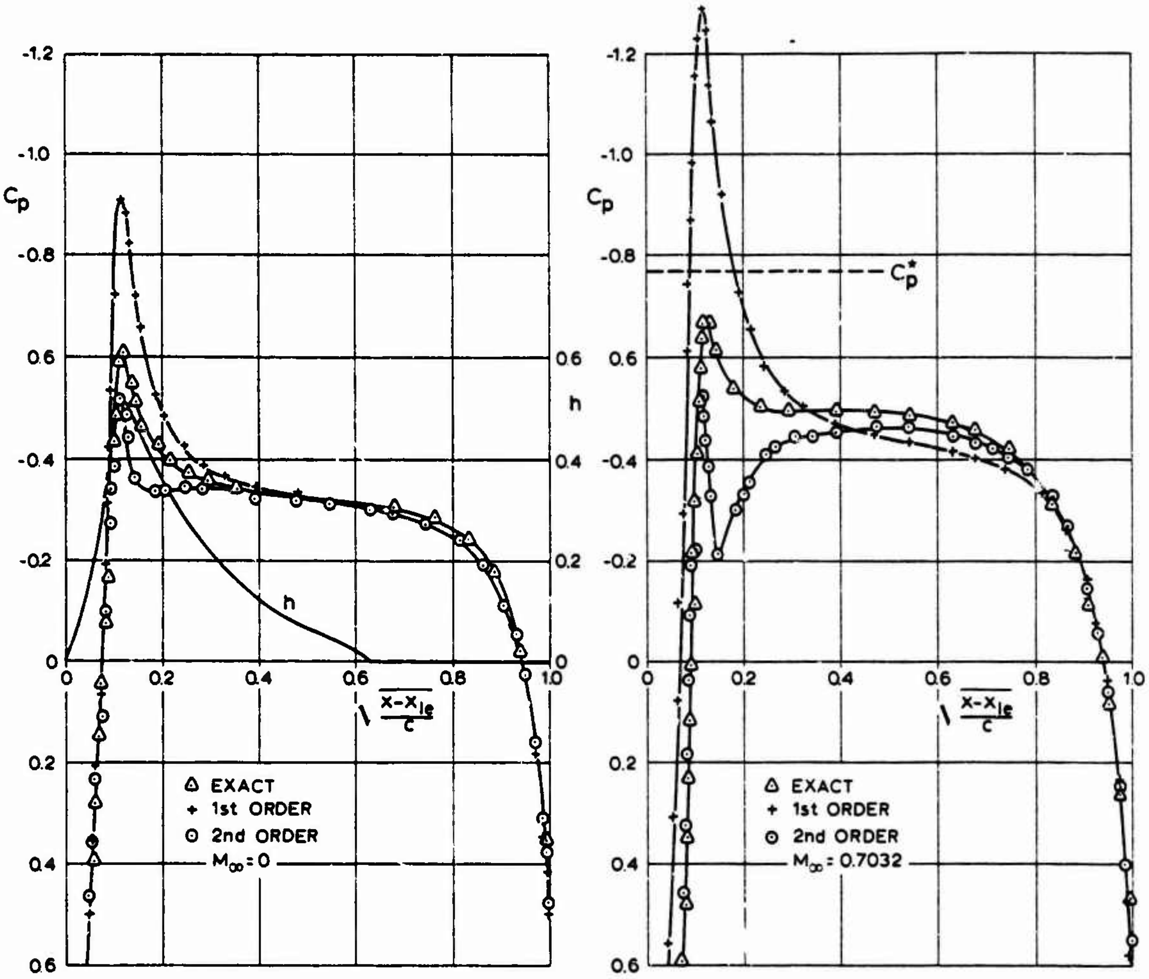

fig. 13

Pressure distribution for a symmetrical aerofoil with non-elliptical nose shape.
(13 % thick NLR 0.09 - 0.75 - 1.4)

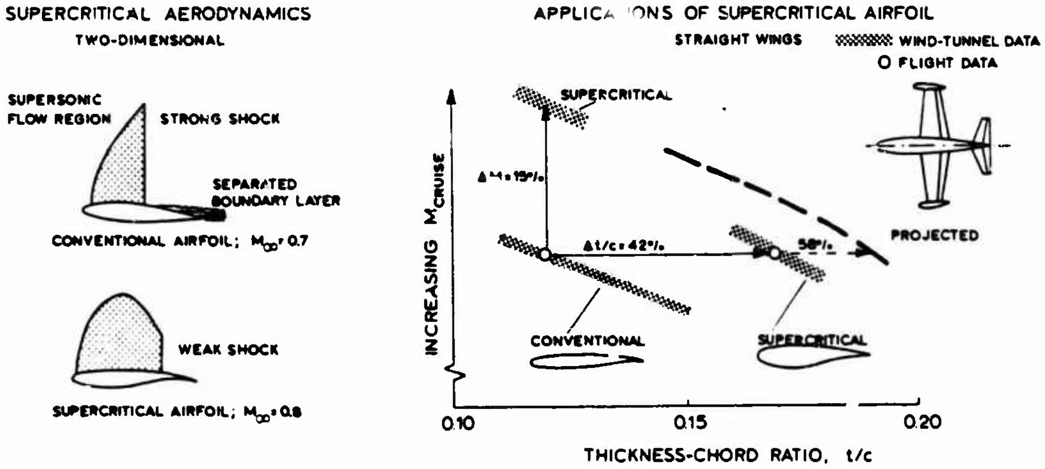
SUPERCRITICAL AERODYNAMICS
TWO-DIMENSIONAL
SUPERSONIC FLOW REGION
STRONG SHOCK
SEPARATED BOUNDARY LAYER
CONVENTIONAL AIRFOIL; $M_\infty = 0.7$
WEAK SHOCK
SUPERCRITICAL AIRFOIL; $M_\infty = 0.8$
APPLICATIONS OF SUPERCRITICAL AIRFOIL
STRAIGHT WINGS
▨ WIND-TUNNEL DATA
○ FLIGHT DATA
SUPERCRITICAL
ΔM = 15%
Δt/c = 42%
58%
PROJECTED
CONVENTIONAL
SUPERCRITICAL
INCREASING $M_{CRUISE}$
0.10
0.15
0.20
THICKNESS-CHORD RATIO, t/c

POLHAMUS, NASA SP-292

fig. 14

Advantages of application of supercritical aerofoil.

### 3.4 Exact representation of the boundary condition in incompressible flow and semi-empirical compressibility corrections.

Eq. (16), the second order result of Gretler, can be interpreted as a result for incompressible flow with compressibility corrections (the terms that depend on $M_\infty$). Also from a comparison of the results in the figures 12 and 13 it appears that errors in the second order theory increase with Mach number. From these observations may be concluded that perhaps a simple calculation method for high subsonic Mach numbers can be based on a combination of accurate results for incompressible flow with the proper compressibility corrections.

When a sufficient large and fast computer is available it is relatively easy to make use of singularity distributions to construct solutions of the linear potential equation for incompressible flow eq. (4) that fulfil the boundary condition eq. (2) at the surface of the wing and that induce a potential jump $\Delta\varphi$ across the wake sheet in the lifting case. This has been shown first by A.M.O. Smith (ref. 15, Douglas) and later by the authors of ref. 16 (Boeing) who extended the approach to lifting configurations. With the help of fundamental features of potential theory (e.g. ref. 11) it can be shown that a solution can be constructed by a source distribution on the surface and a doublet distribution on the wake surface. The strength of the distribution is determined by the requirement that at the trailing edge the velocity is finite and that everywhere the flow is tangential to the surface of the wing. To find these solutions a discretization is used in ref. 15 and ref. 16.

It is assumed that the surface of the wing is described by a set of discrete points. The surface then is approximated by quadrilateral panels obtained by connecting the points by straight line segments. It is assumed that the surface of the wing is described by the points in such a way that the panels form chord wise strips bounded by curves y = constant. On each panel a source distribution with constant density is chosen. The wake is represented by strips extending to infinity downstream. The edges of the strips are chosen on curves y = constant and for these y values the same are chosen as that are used for the panelling of the wing surface. At each strip on the wake surface the doublet strength is constant. The effect of the doublet strips can be represented by a vortex of constant strength at the edges. At the edges the induced velocity is infinite. Because the upstream edge coincides with the wing trailing edge, this makes it not possible numerically to apply the Kutta condition. For this reason the doublet strips in ref. 16 are extended inside the wing on the camber surface. This is being done in such a way that the distribution of the doublet strength, that is specified a priori, can be represented by a set of discrete vortices in spanwise direction in each strip. The strength of the singularity distributions is determined by solving the set of linear equations that is found when for each surface panel it is required that at the centroid of the panel the normal component of the velocity that is induced by all singularities (horse shoe vortices and source distributions) is equal and opposite to the normal component of the undisturbed velocity. Further it is required that on each strip of the wake in a point midway between the edges and at a small distance downstream of the trailing edge, the flow is tangential to the bisector of the local trailing edge angle. The vertical position of the wake is chosen a priori (see sketch b below).

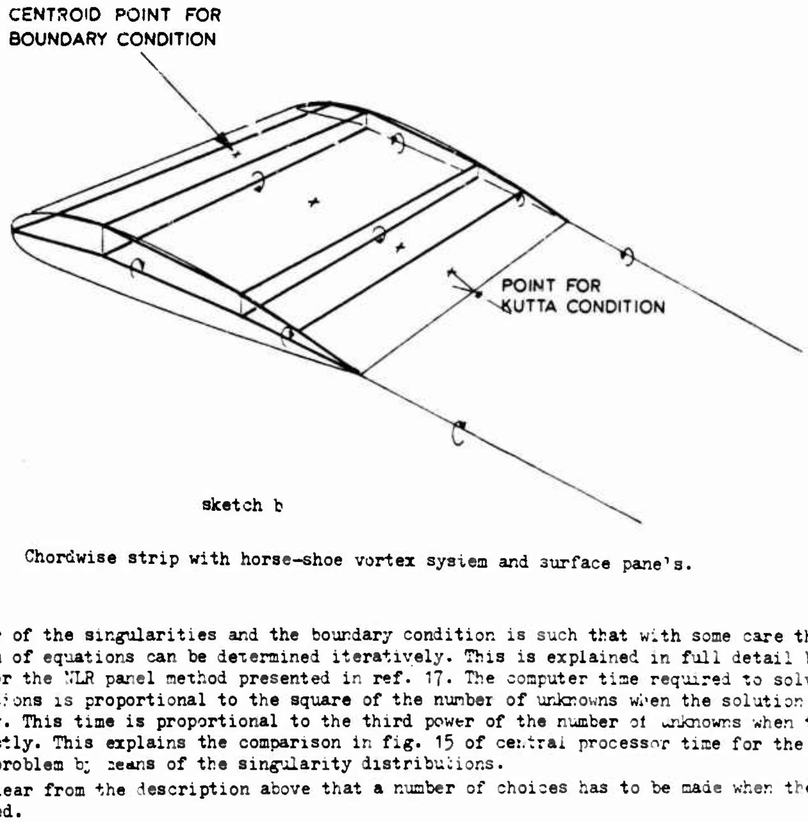

sketch b

Chordwise strip with horse-shoe vortex system and surface panels.

The character of the singularities and the boundary condition is such that with some care the solution of the system of equations can be determined iteratively. This is explained in full detail by Bleekrode in ref. 2 for the NLR panel method presented in ref. 17. The computer time required to solve a system of linear equations is proportional to the square of the number of unknowns when the solution is determined iteratively. This time is proportional to the third power of the number of unknowns when the system is solved directly. This explains the comparison in fig. 15 of central processor time for the solution of the flow problem by means of the singularity distributions.

It will be clear from the description above that a number of choices has to be made when the panel method is applied.

These concern:

- the panel distribution on the wing surface
- the vortex distribution on the camber surface, as well the position as the variation of strength
- the Kutta point

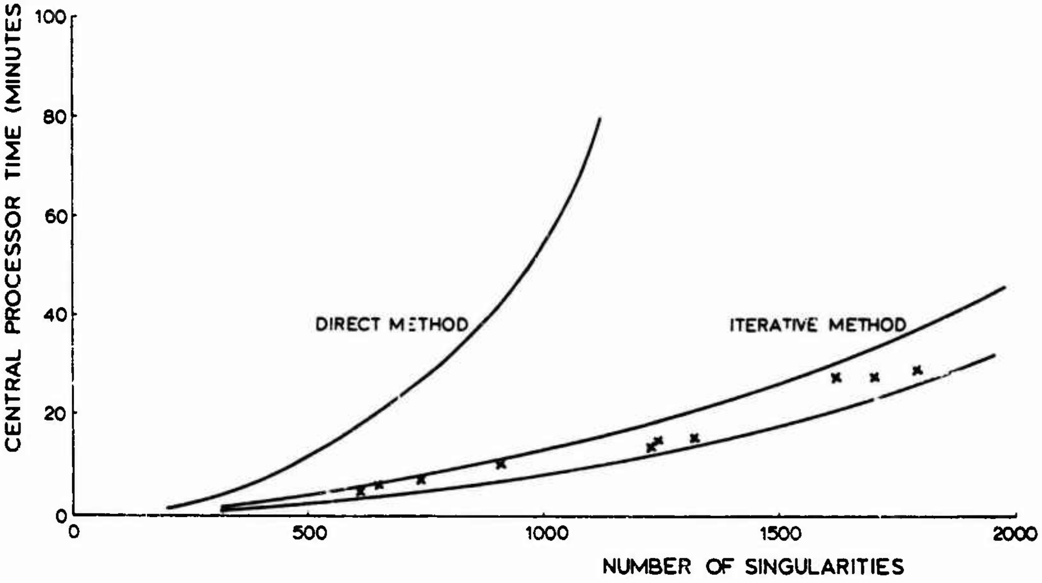

fig. 15

Comparison of the central processor times on a CDC 6600 computer of the vortex-source method for a direct and iterative method of solution.

Up to now no theoretical background is formulated on which these choices can be based.
In practice numerical experiments and comparison of solutions with results from other methods for specific cases are used to obtain some insight in the behaviour of the solution as a function of the choices.

Because in the method no restrictions are present with regard to the relative dimensions of the surface on which the boundary condition is applied, the method is very well suited for wing-body combinations. Only in that case one of the shortcomings of potential theory becomes apparent, namely the assumption of non-viscous flow. As a result circulation cannot be predicted without an additional condition. For bodies with sharp edges such as wings the Kutta condition serves to take into account the main effect of viscosity. At the Reynolds number of tunnel experiments and in free flight however also vorticity is shed from fuselages. In the calculation method an arbitrary choice has to be made with respect to the circulation around the fuselage.

In ref. 18 (Kramer, NLR) some results are presented from an analysis of the behaviour of the solution of the Neumannproblem by means of the panel method. In the analysis results of the panel method are compared with analytical results for a vortex-cylinder combination. The axis of the cylinder is parallel to the undisturbed flow direction. The vortex is perpendicular to this direction. Vortex length and cylinder length are infinite. In the numerical calculations the length of vortex and cylinder has been chosen very large in comparison with the diameter of the cylinder. Just as in the LoElMe irregularities in the panel distribution cause disturbances in the solution according to ref. 18. This means that when the panel method is applied a compromise must be found between accuracy and number of panels also with regard to local refinement of panel distribution in regions with large gradients in flow quantities. When panel densities change it is essential to choose panels in the right direction instead of "sealing" gaps in the description of the body by means of the panels.

For the two-dimensional limiting case it is possible to compare results of the panel method with results of analytical methods such as based on transformation techniques. From these comparisons the user has to develop a "feeling" with regard to panel distributions, number of panels depending on aerofoil characteristics and the relation of the position of panel edges on the surface and the location of the vortex lines on the camber. In general best results are obtained when the vortex lines on the camber surface and the panel edges on upper and lower side of the wing for comparable chordwise positions are chosen in one plane that is more or less vertical. Also the distribution of the vortex strength in chordwise direction is a parameter that has to be chosen carefully as a function of the aerofoil characteristics such as camber and thickness distribution. The vortex distribution must be such that near the wing leading edge and trailing edge, vortices do not come to close to the wing surface. For wings about 50 to 60 panels in chordwise direction and 10 to 15 strips on the half span is mostly sufficient to obtain accurate pressure distributions. Making use of the symmetry of the wing flow this means that 500 to 1000 equations must be solved.

For application of panel methods on a routine basis it is essential to make use of computer programs for panel generation. In general these must contain surface fitting routines to interpolate available coordinates of the surface. The ideal situation of course is that the designer makes use of analytical surfaces from which the input for the calculation as well as for the workshop that has to manufacture windtunnel models can be derived directly.

In ref. 19 (Mangler and Smith, RAE) the theoretical background can be found with regard to the direction in which the vortex sheet leaves the trailing edge. From this it appears that the wake leaves the trailing edge either in the direction of the tangent of the upper surface or of the tangent of the lower surface. This depends on the sign of the shed vorticity and on whether the mean flow is directed inboard or outboard. An intermediate direction of the wake at the trailing edge is possible exceptionally. For the numerical calculation this result does not mean very much, because it is not possible to apply the

Kutta condition just at the trailing edge point for numerical reasons. But at least the boundaries can be used in practice. In ref. 2 some results, obtained at NLR, are presented by Labrujère with regard to the variation of sectional lift as a function of the position of the point where the Kutta condition is applied and the direction that is required. The main conclusion is that it is very likely that the prescription of the velocity parallel to the trailing edge bisector will give a result that is only 0,5 % in error if the distance of the Kutta point downstream of the trailing is $10^{-7}$ in parts of the local wing chord.

Based on a solution for incompressible flow it is possible to find solutions for compressible flow. In the first place this can be done along the lines of the Göthert rule described in section 2.1. This gives an approximation of a solution of the linearized potential equation. It has been demonstrated however above that when the local Mach number approaches unity even the exact solution of the linearized potential equation is not very good in comparison with exact results of potential theory. Because also second order solutions as those of Gretler do not give useful results for aerofoils with non-elliptic nose shapes, at NLR semi-empirical compressibility corrections were developed. These have proved to make it possible to obtain useful predictions of high subsonic flow only at the cost of solving the Neumann problem for incompressible flow by means of the panel method. A description of the compressibility corrections can be found in ref. 17.

In principle the semi-empirical method of ref. 17 is based on an analysis of plane flow Based on the result of second order theory it is assumed that for plane incompressible flow the velocity $\Omega_i$ along the surface of an aerofoil can be written as

$$\Omega_i = \frac{1+u_i}{\sqrt{1+\left(\frac{dz_p}{dx}\right)^2}} \tag{17}$$

In this expression the factor $\sqrt{1+\left(\frac{dz_p}{dx}\right)^2}$ is the socalled Riegels factor that also can be found back in the result of Gretler in eq. (16) and that is the principal correction to render the second order theory uniformly valid for blunt leading edges. $u_i$ is the perturbation velocity in incompressible flow. When the third order solution of Imai in ref. 20 is written in the appropriate form for the velocity at the crest of an ellips in compressible flow (where $\frac{dz_p}{dx} = 0$) then

$$\Omega_{crest} = 1 + \frac{u_{a,c}}{B_{2D}^{\ 2}} \tag{18}$$

with

$$B_{2D}^{\ 2} = 1 - M_\infty^2 \left\{ 1 + \lambda_1 u_{a,c} (1 + \lambda_2 u_{a,o}) \right\}$$

$u_{a,c}$ in eq. (18) is the perturbation velocity at the crest on the analogous ellips in incompressible flow. As in the Göthert rule the analogous ellips is obtained from the original one by shrinking the thickness coordinate by the factor $\sqrt{1-M_\infty^2}$ . $\lambda_1$ and $\lambda_2$ are functions of $M_\infty$ only (see ref. 17).
When $B_{2D}$ is used as a general compressibility correction by which the perturbation velocity in analogous incompressible flow can be corrected, then for an aerofoil can be written in first instance

$$\Omega = \frac{1}{\sqrt{1+\left(\frac{dz_p}{dx}\right)^2}} \left(1 + \frac{u_a}{B_{2D}^{\ 2}}\right) \tag{20}$$

It is known from experiences with the semi-empirical RAE standard method based on second order approximations for $u_a$ (ref. 21), that better results are obtained when also in the Riegels factor a compressibility correction is introduced in such a way that:

$$\Omega = \frac{1}{\sqrt{1+\frac{1}{B_{2D}^{\ 4}}\left(\frac{dz_{p,a}}{dx}\right)^2}} \left(1 + \frac{u_a}{B_{2D}^{\ 2}}\right) \tag{21}$$

When first or second order theory give appropriate results for incompressible flow it is possible to obtain a good approximation for the concerning aerofoil shape for compressible flow by substitution of the first or second order result for $u_a$ in eq. (21). In other cases $u_a$ can be obtained easily from eq. (17) by substitution of the exact velocity $\Omega_a$ along the surface of the analogous shape in incompressible flow. The exact velocity along the surface is obtained by the panel method that is described above.
From eq. (17):

$$u_a = \Omega_a \sqrt{1+\left(\frac{dz_{p,a}}{dx}\right)^2} - 1 \tag{22}$$

This can be substituted in eq. (21) to give the relation of the velocity $\Omega$ on the surface in compressible flow and the velocity $\Omega_a$ on the surface of the analogous wing in incompressible flow.

The semi-empirical approach has been generalized to three-dimensional wings on the basis of a separate analysis of an infinite sheared wing and the centre section of an infinite swept wing. The result of these are interpolated, based on the local flow direction, to give for a three-dimensional wing the basic formula for the NLR panel method (ref. 17):

$$\Omega^2 = \frac{\cos^2\Lambda^* (1 + \frac{\omega_a}{q^2}\sec^2\Lambda^*}{1 + \frac{1}{B^4}\frac{\beta^2}{\beta^2_n}(\frac{dz_a}{dx})^2 \sec^2\Lambda} + \sin^2\Lambda^* \qquad (23)$$

with $\omega_a$ defined as the perturbation velocity on the analogous wing that is obtained by shrinking the dimensions in y and z direction by a factor $\sqrt{1-M_\infty^2}$. $\omega_a$ is calculated by means of eq. (24):

$$\Omega_a^2 = \frac{\cos^2\Lambda_a^* (1 + \omega_a \sec^2\Lambda_a^*)}{1 + (\frac{dz_a}{dx})^2 \sec^2\Lambda_a} + \sin^2\Lambda_a^* \qquad (24)$$

In this equation $\Omega_a$ is the total velocity along the surface of the analogous wing in compressible flow.

The effective local sweep angles $\Lambda^*$ and $\Lambda_c^*$ are defined by

$$\tan\Lambda^* = \beta\tan\Lambda_a^* = -\beta\frac{v_a}{u_a} \qquad (25)$$

where $u_a$ and $v_a$ are the perturbation velocity components in the incompressible flow in x and y direction respectively.

$$B^2 = 1 - M_\infty^2 \left\{ 1 + (\cos^2\Lambda + \sin^2\Lambda^*)\, \lambda_{1n}\omega_a\, (1 + \lambda_{2a}\frac{\omega_a}{\cos^2\Lambda_a}) \right\} \qquad (26)$$

$\Lambda$ is the local geometrical sweep angle and $\lambda_{1n}$ and $\lambda_{2n}$ are functions of $M_\infty$.

It can be seen that for the limiting case $M_\infty=0$ the result of eq. (23) reduces to the result that is obtained by the panel method for incompressible flow around the configuration. The pressure coefficient in all cases again is obtained by eq. (8) by substitution of $\Omega$ for the velocity V.

Application of eq. (23) for the limiting case of plane flow gives for the aerofoil of fig. 13 where the first and second order theory appeared to fail, the results that are presented in fig. 16. For comparison in this figure also the result is given for the Göthert rule applied to exact results for the incompressible flow around the analogous aerofoil. Further also is presented the result that is obtained by application of the wellknown Karman-Tsien pressure rule. This rule is based on the assumption that density and pressure in the flow are related according to the simplified formula, representing the so-called Karman-Tsien gas. By means of a hodograph transformation of the flow a relation is found between the pressure coefficients in compressible flow and in incompressible flow around a perturbed aerofoil. When the contour perturbations are neglected the relation between the pressure coefficient Cp and the pressure coefficient $C_{p_i}$ in incompressible flow about the aerofoil becomes:

$$C_p = \frac{C_{p_i}}{(1-M_\infty^2) + \frac{1}{2}\frac{M_\infty^2 C_{p_i}}{1 + (1-M_\infty^2)^{\frac{1}{2}}}} \qquad (27)$$

The relation eq. (27) is being used frequently. The results for the aerofoil in fig. 16 do not differ very much near the nose from the results of the Göthert rule. The pressure near the maximum thickness is predicted better by the Karman-Tsien rule than by the Göthert rule. The results of the NLR panel method are the best for this aerofoil. It can be mentioned that when the Von Karman-Tsien gas theory is applied in its complete form, the results are about as accurate as those from the NLR method (ref. 22, Boerstoel,NLR). However this theory cannot be extended to three-dimensional flow.

In fig. 17 comparable results are given for a lifting aerofoil with non-elliptical nose shape. Results of the type that are presented in fig. 16 and fig. 17 have been found to be representative for the applicability of the NLR panel method. An example for an aerofoil with elliptic nose shape is given in fig. 18. In that case the exact result is from Sells (ref. 23, RAE). His method is based on a transformation technique that is applicable to plane subcritical flow. It can be expected that for the roof-top type pressure distribution of the aerofoil in fig. 18, the result of Sells' computation is very close to the exact result for potential flow.

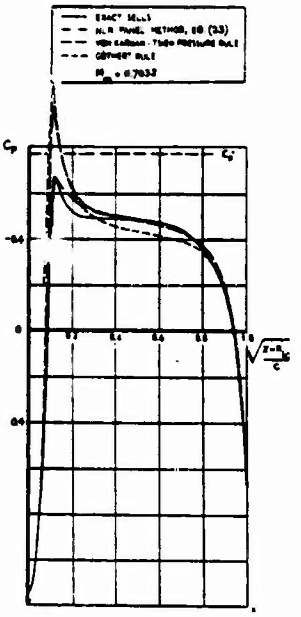

fig. 16

Pressure distributions on symmetrical aerofoil (13 % thick section NLR 0.09 - 0.75 - 1.4)

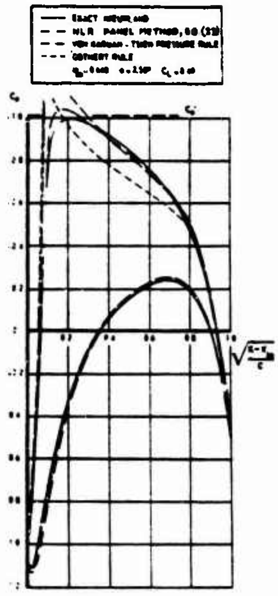

fig. 17

Pressure distributions on non-symmetrical aerofoil (NLR quasi-elliptical section)

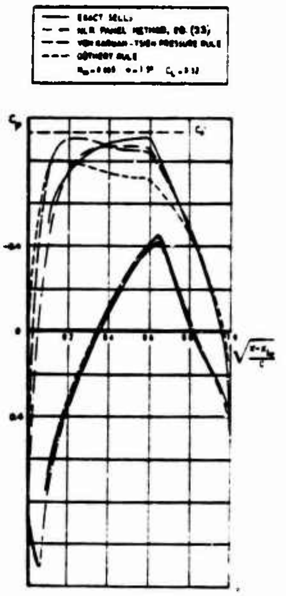

fig. 18

Pressure distributions on non-symmetrical aerofoil (section NPL 3111)

In fig. 19 results are presented that have been obtained with the panel method for a non-lifting wing-body combination.

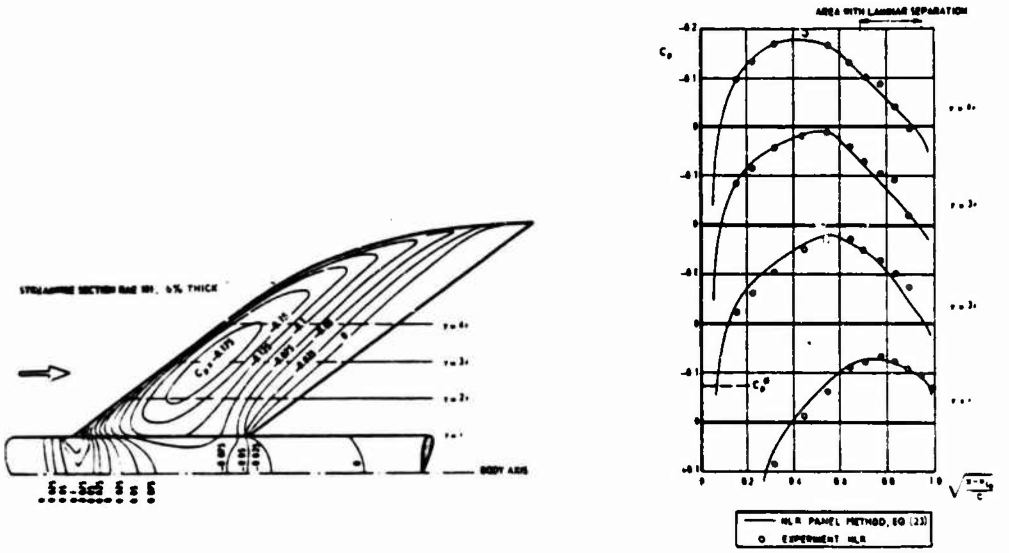

fig. 19

Isobar pattern and chordwise pressure distribution for a non-lifting wing-body combination at $M_\infty = 0.96$.

In fig. 20 and fig. 21 results are presented that have been obtained with the panel method for a lifting wing-body of a transport aeroplane combination.

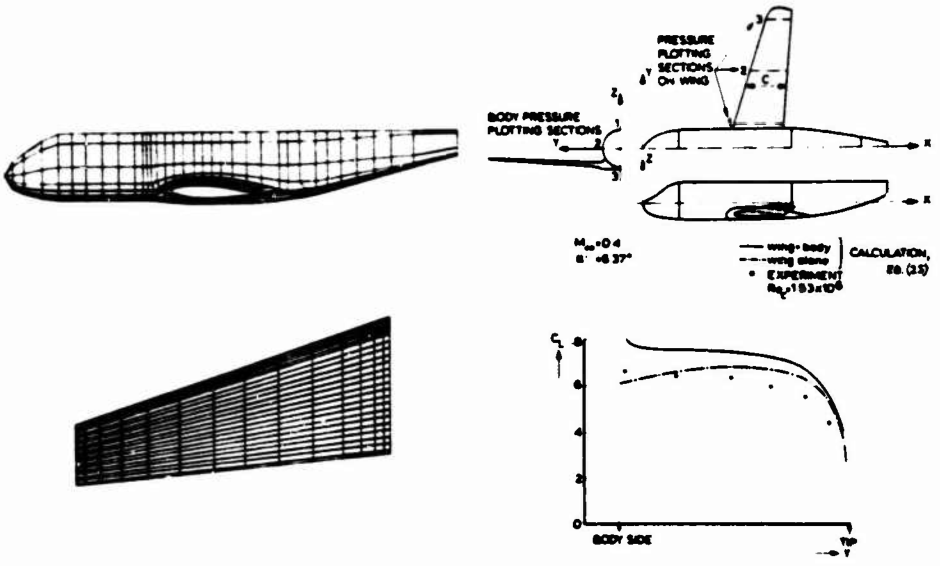

a. panel arrangement

b. spanwise lift distribution

fig. 20

Panel arrangement and spanwise lift distribution for a wing-body combination.

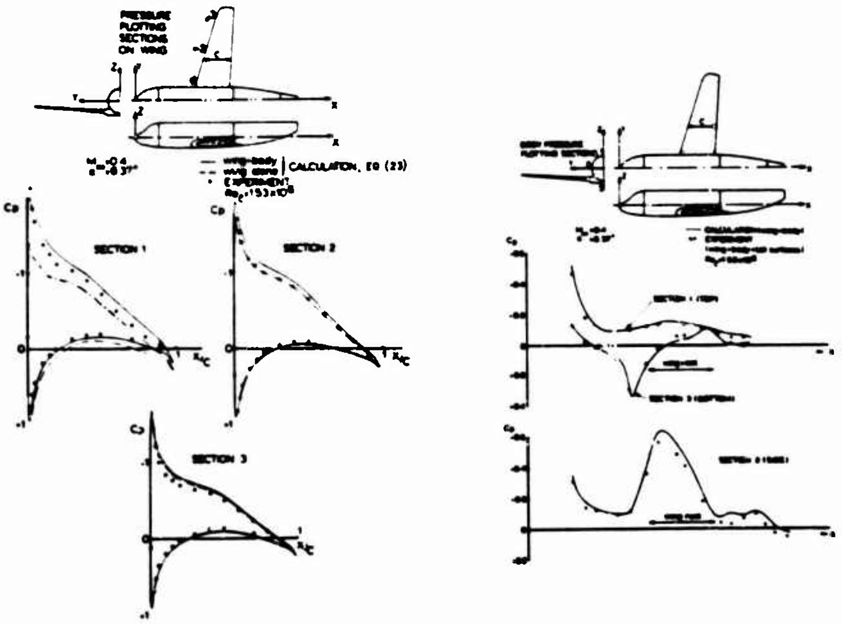

a. wing pressure distributions

b. body pressures

fig. 21

Pressure distribution on wing and body of a lifting wing-body combination.

In both fig. 20 and fig. 21 the calculated results are presented for wing alone and wing-body combination to demonstrate the influence of the body.

Finally in fig. 22 and fig. 23 results are presented for a research wing-body combination.

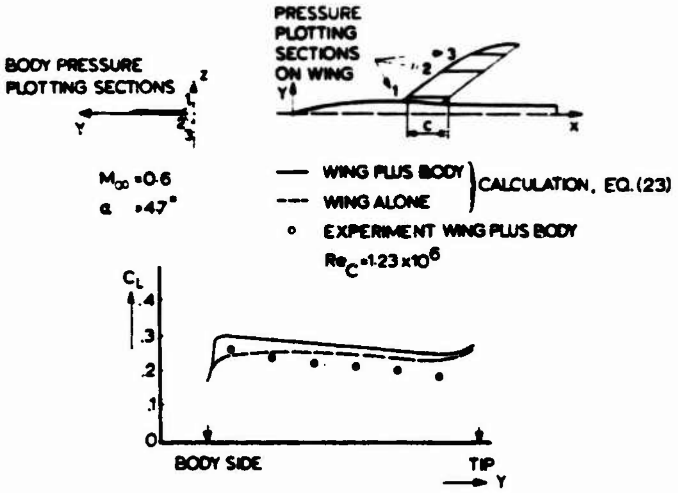

fig. 22

Spanwise lift distribution on a slender wing-body combination.

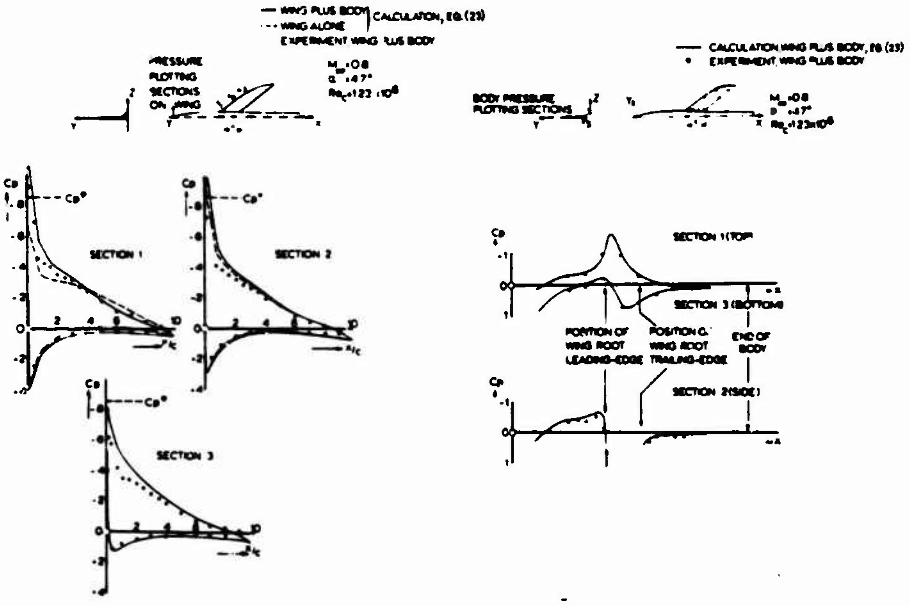

a. wing pressure distribution

b. body pressures

fig. 23

Pressure distribution on wing and body of a wing-body combination.

It can be seen that for lifting configurations the calculated lift is larger than the experimental lift. This mainly is the result of the effect of the boundary layer in the experiments. From results presented in ref. 25 by Labrujère and Sytsma (NLR), it is clear that the position of the wake behind the wing that is chosen a priori in the calculations hardly influences the pressure distribution on the wing. In the calculations the straight trailing vortices leave the trailing edge in the direction of the bisector of the trailing edge angle. In ref. 25 the results obtained in this way are compared for the wing of fig. 21 with results that are obtained for a trailing vortex sheet that has rolled up.

With regard to the effect of the boundary layer, Preston and Spence already nearly 20 years ago (ref. 26 and ref. 27) tried to correct potential flow calculations for the effect of the boundary layer that is present in experiments. Up to now no satisfactory engineering method for the calculation of viscous flow around lifting aerofoils is available. For three-dimensional swept wings the situation is even worse. Most methods are based on the concept that the displacement thickness of the boundary layer must be added to the aerofoil contour to form the boundary on which the normal velocity in the potential flow calculation is zero.

For computer applications a more efficient method results when this is modified by local expansion in such a way that on the original aerofoil

$$\frac{d\phi}{dn} = \frac{d}{ds}\left(U_e \delta^*\right) \tag{28}$$

where $U_e$ is the velocity at the edge of the boundary layer and $\delta^*$ is the displacement thickness. This is called the "leak flow" form of the displacement concept.

At NLR the displacement concept boundary condition in its leak flow form has been applied by Piers and Slooff (ref. 28) by incorporating it in the potential flow calculation according to the NLR panel method that is described above. To avoid errors due to shortcomings of boundary layer calculation methods and due to problems with the iterative procedure in which alternately potential flow calculations and boundary layer calculations must be performed, in ref. 28 the calculations have been based on measured boundary layer displacement thickness distributions. For the conditions under which the boundary layers were measured, calculated and measured pressure distributions were compared. The results are presented in fig. 24 for two aerofoils.

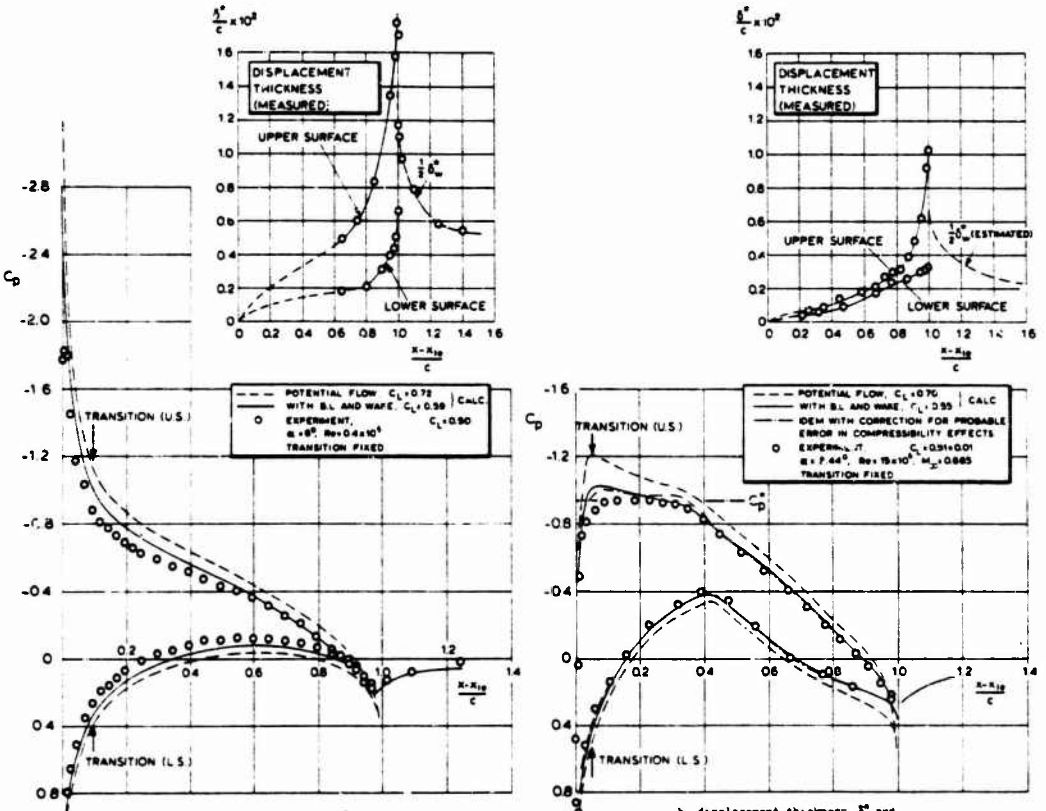

a. displacement thickness $\delta^*$ and pressure distribution for the Piercy 12/40 aerofoil at $\alpha = 6^o$ and low speed.

b. displacement thickness $\delta^*$ and pressure distribution for the NPL 3111 aerofoil at $\alpha = 2.44^o$ and $M_\infty = 0.665$.

fig. 24

Application of the displacement concept in leak flow form to correct potential flow for boundary layer effect.

From fig. 24 it is clear that the viscous lift loss is underestimated in the calculation for these rather extreme cases for as well the low speed as the high speed conditions. In ref. 28 the conclusion is drawn that especially with regard to the behaviour of the flow near the trailing edge, the calculation method must be improved when the boundary layer is present. This improvement very likely also has to concern the representation of the wake that is based on empirical considerations. When the boundary layer corrections are based on calculated boundary layer characteristics, even larger discrepancies between calculated and measured pressure distributions will occur than in fig. 24.

## 4. THE APPLICABILITY OF METHODS FOR SUPERCRITICAL FLOW.

In view of the possible advantages of application of flows with local supersonic regions (fig. 14) much attention has been paid in recent years to the development of calculation methods for that type of flow. The height of the suction peak near the leading edge, the position of this peak in chordwise direction and the relative position of any shockwaves at the upper and the lower surface are very important parameters in view of the transonic characteristics of wings and aerofoils. Therefore the calculation methods that must be used as design tools must be able to predict these parameters correctly. It has appeared that this by no means is possible with calculation methods that are based on linearizations of the potential equation of the type discussed in the preceding sections.

In principle network methods are natural means to solve the partial differential equations that represent potential flow. In these methods the derivatives of flow quantities are approximated by differences of the quantities at various control points. With decreasing spacing between these points it can be expected that the accuracy of the result increases. For compressible flow the approach results in a set of non-linear algebraic equations relating the values of the flow quantities at the control points, that usually are chosen on a rectangular grit in the flow field. In general the computational effort for application of a finite difference method is larger and increases more rapidly with the accuracy of the solution than the effort to apply a panel method. In view of this, only when the amount of non-linearity of the basic equations to be solved does not make it possible to make use of panel methods, finite difference methods are an acceptable alternative. This is the case for transonic flow around given shapes.

At several places finite difference methods with numerical viscosity are in use that are based on simplified non-linear forms of the potential equation. Applications are mostly combined with linearized boundary conditions that amongst others simplifies the generation of the finite difference network. In ref. 29 (Lomax, Baily and Ballhaus, NASA) application is presented of the small disturbance equation:

$$(1-M_\infty^2)\frac{\partial^2\varphi}{\partial x^2}+\frac{\partial^2\varphi}{\partial y^2}+\frac{\partial^2\varphi}{\partial z^2}=(\gamma+1)\,M_\infty^2\frac{\partial^2\varphi}{\partial x^2} \tag{29}$$

for the wing of the C141 that has a relatively small angle of sweep. The Kutta condition is applied by requiring a continuous pressure across the wake. The boundary condition is applied in the (x,y) plane by specifying $\frac{\partial\varphi}{\partial z}$ at the lower and upper surface to be equal to the local slope of the wing surface.

The comparison of the results with experimental results is impressive for that case. Also the computing time is very modest. For three-dimensional flow up to now only finite difference methods are available that are based on simplified potential equations and simplified boundary conditions. However just as in the case of subcritical flow for a large number of aerofoils with attractive characteristics the simplifications in the potential equation and in the boundary conditions do not lead to results that can be used for design purposes. This is illustrated in the interesting survey of computational methods for 2D and 3D transonic flows with shocks by Yoshihara (ref. 30).

In the following only attention will be paid to methods by which the full equations for potential flow are solved. These methods up to now only exist for plane flows although attention is paid to extensions to three-dimensional flows by amongst others Jameson (Grumman).

Two classes of methods will be introduced. The first concerns the application of finite difference techniques to the equations of the flow around given shapes. The second concerns the solution of the hodograph equations that are the result of interchanging dependent and independent variables. The hodograph equations for plane flow are linear. Making use of this linearity smooth transonic flow can be specified in the hodograph plane that can be transformed to solutions in the physical plane around shapes that also are a result of the transformation. The importance of the technique is that it can be used as an inverse method for the design of aerofoils with shockfree transonic flow at the design condition (the so called supercritical aerofoils of fig. 14). Because results of the hodograph methods will be used as a reference in the discussion of the applicability of the finite difference techniques, in the following first the hodograph methods will be introduced.

### 4.1 Hodograph methods for the full potential flow equations.

The hodograph transformation of the equations for compressible potential flow is based on a interchange of dependent and independent variables. By this transformation a linear equation is found for the streamfunction $\psi$ from which with the stagnation density $\rho_0$ the velocity components in x and z direction are obtained according to:

$$\frac{\partial\psi}{\partial z}=-\frac{\rho}{\rho_0}u \tag{30}$$

$$\frac{\partial\psi}{\partial x}=\frac{\rho}{\rho_0}\,v$$

The linear equation for $\psi$ is:

$$\tau(1-\tau)\frac{\partial^2\psi}{\partial\tau^2}+\left(1+\frac{2-\gamma}{\gamma+1}\tau\right)\frac{\partial\psi}{\partial\tau}+\frac{1-\frac{\gamma+1}{\gamma-1}\tau}{4}\frac{\partial^2\psi}{\partial\theta^2}=0 \tag{31}$$

where $\tau$ is the velocity parameter that is related to the Mach number according to:

$$M_\infty^2=\frac{2\tau}{(\gamma-1)(1-\tau)} \tag{32}$$

and $\vartheta$ is the flow angle.

Nieuwland (NLR, ref. 31) used the possibility to obtain solutions of the linear equation for $\psi$ to construct a class of compressible flows. He derived a Mellin integral transform for the analytic stream function describing the incompressible flow around an ellips in hodograph variables, and then substituted particular solutions of the hodograph equation for compressible flow (the Chaplygin particular solutions) into this. In this way he related a compressible flow to a given incompressible one. A general feature of this function theoretic method is that the aerofoil shape in the compressible flowfield is found as a result of the transformation. For vanishing compressibility the original incompressible flow around the ellips is recovered, but with increasing Mach number the shape becomes rather strongly distorted. As a result of this, special measures must be taken to guarantee the regularity of the transformed ellips that have been called "quasi-elliptical aerofoils". It has appeared that a family of considerable geometrical variety can be obtained on a routine basis (refs. 32 and 33) that contains also shapes with supersonic flow regions that decelerate smoothly to subsonic flow. It has been shown by Spee (NLR, ref. 34) that the local supersonic flow also can be realised experimentally for the non-lifting case and that the shockfree flow is stable with respect to unsteady disturbances. He also demonstrated experimentally that the shockfree design condition is embedded in an interval of free stream Mach numbers and angles of attack where wave drag is negligable. Later Boerstoel and Uylenhoet (ref. 32) presented comparable results for a lifting quasi-elliptical aerofoil. The results for the non-lifting and lifting aerofoil are presented in fig. 25a and fig. 25b respectively.

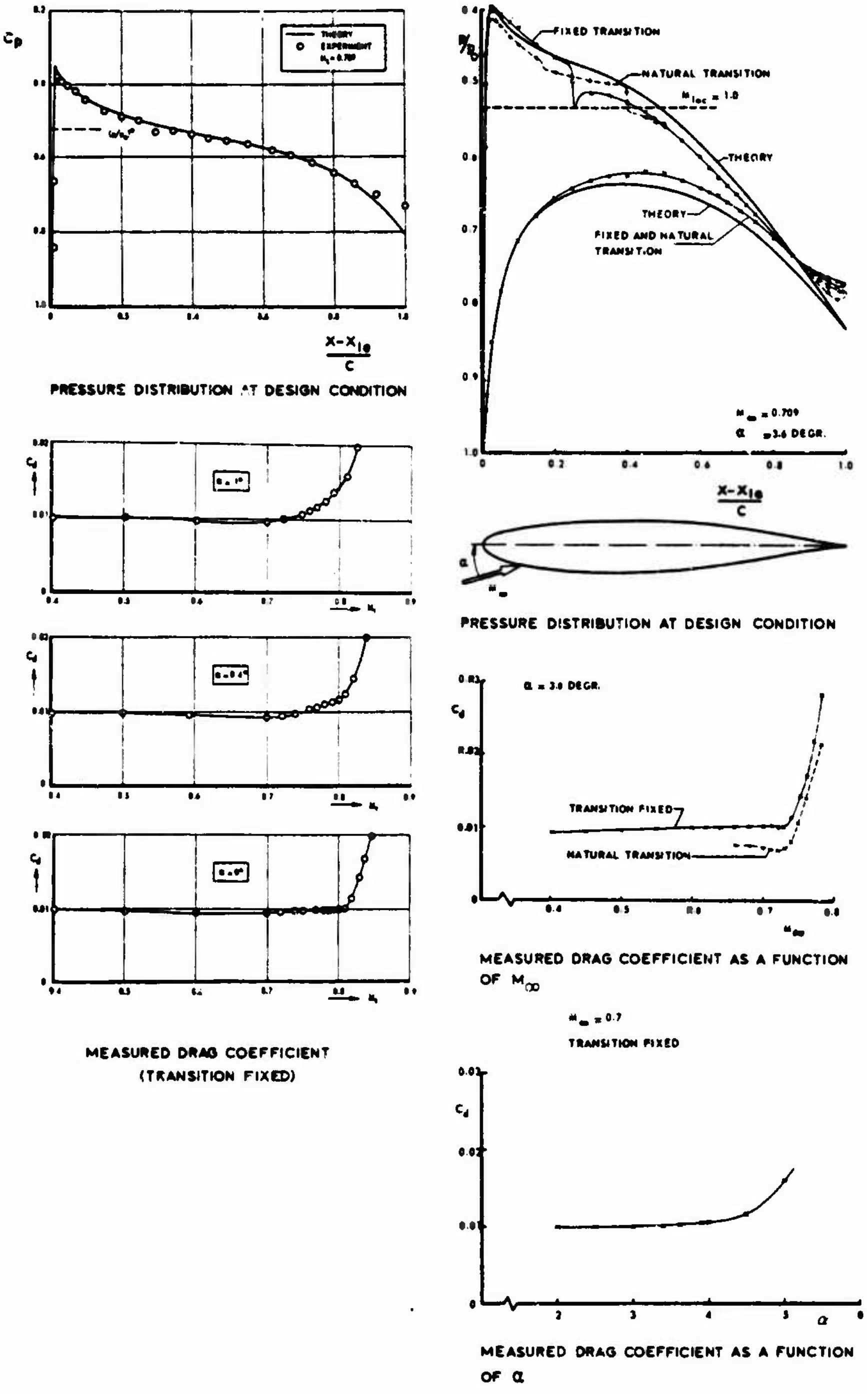

a. non-lifting aerofoil

b. lifting aerofoil

fig. 25

Experimental and theoretical results for quasi-elliptical aerofoils with shockfree transonic flow.

It has been found that parts of the analytical shape of the quasi-elliptical aerofoils can be changed without destroying the low-drag properties of the basic shockfree flow. The modifications must be restricted to parts of the aerofoil where the local speed is smaller than the speed of sound at the design condition. This additional degree of freedom has been used to satisfy multiple design requirements. In ref. 24 (Loeve and Slooff, NLR) an example is presented where the additional freedom has been used to increase the lift coefficient at "shockfree" conditions at the design Mach numbers. The design process was based on the assumption that the difference between the exact pressure distribution according to full potential theory and the pressure distribution according to the NLR panel method on the front part of the aerofoil is not influenced by modifications at the rear. The result that was found by trial and error is presented in fig. 26. Some more details on aerodynamic characteristics of the section NLR 7101 will be presented in section 4.2 as part of the demonstration of the applicability of finite difference methods.

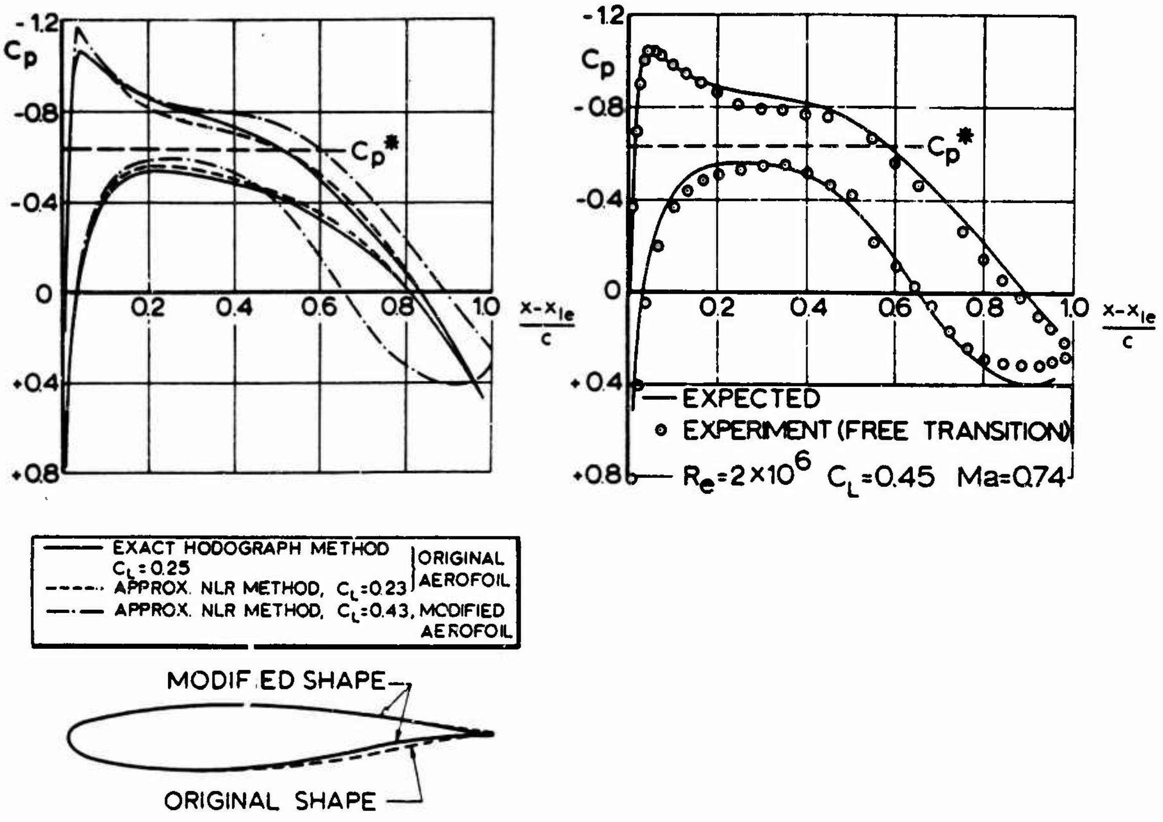

a. design process

b. comparison of measured and expected pressure distribution on modified quasi-elliptical aerofoil.

fig. 26

Example of the design of a rear loaded shockfree aerofoil by means of a combination of a hodograph theory and a panel method (NLR section 7101, thickness 14 %, $M_\infty = 0.74$).

After the results presented so far had proved the usefulness of hodograph techniques to generate aerofoils with shockfree transonic flow, at NLR a new method was developed by Boerstoel to design shockfree transonic aerofoils by hodograph techniques. The main reason was that the class of quasi-elliptical aerofoils was to restricted. The new method is described in ref. 35. Most of the following is taken from this reference and from unpublished work of Boerstoel.

In fig. 27 the structure of the hodograph of shockfree transonic flow is illustrated in relation to the flow in the physical plane. At the left hand side of fig. 27 the two-sheeded $(\tau, \vartheta)$-surface is presented with the point $(\tau^*, \vartheta^*)$ as a branch point.

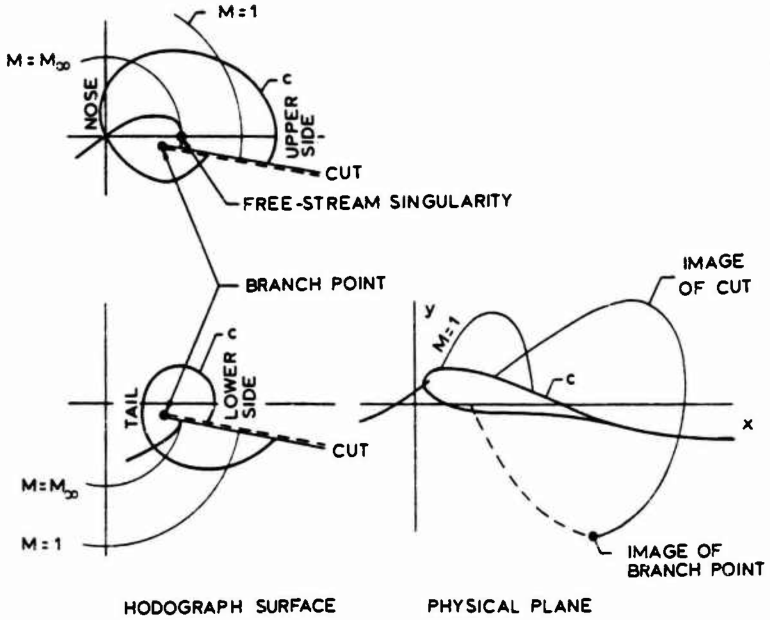

fig. 27

The structure of the hodograph of shockfree transonic flow.

a. $(\tau,\vartheta)$ are polar variables on the hodograph surface, with $\vartheta$ as radial variable.
b. The hodograph surface may be devided into two sheets by a cut that begins at the branch point $(\tau^*,\vartheta^*)$ and that extends outward along the radius $\vartheta=\vartheta^*$. The sheets are called upper and lower sheet respectively.
c. The image of the aerofoil on the hodograph surface is a closed curve C where the stream function $\psi=0$ and that encircles the branch point. The exterior of the aerofoil in the physical plane maps onto the interior of the aerofoil image C on the hodograph surface.
d. The stream function of the flow has a free-stream singularity of known type at infinity in the physical plane, and thus at a point $(\tau_\infty,0)$ on one of the sheets of the hodograph plane. ($\tau_\infty$ and $M_\infty$ are related according to eq. (32):
$$M_\infty^2=\frac{2\tau}{(\gamma-1)(1-\tau_\infty)}$$
The sheet that contains the free-stream point $(\tau_\infty,0)$ is called the upper sheet.
e. The free-streamline $\psi=0$ that extends in the physical plane from the front stagnation point to infinity upstream corresponds to a curve on the upper sheet from the origin to $(\tau_\infty,0)$ where $\psi$ has its free-stream singularity. Similarly, the free-streamline $\psi=0$ from the tail point downstream to infinity maps onto a curve connecting the tail point image on the lower sheet with $(\tau_\infty,0)$ on the upper sheet.
f. The linear hodograph equation eq. (31) can be represented by

$$L\,\psi(\tau,\theta)=0 \tag{33}$$

g. The mapping of the hodograph surface $(\tau,\vartheta)$ to the physical plane $z=x+iy$ can be represented by

$$z\,(\tau,\theta)=M\psi(\tau,\theta) \tag{34}$$

where M is a known linear operator.

h. The stream function $\psi$ may be splitted in a basic stream function $\psi_b$ that satisfies $L\psi_b=0$ and that contains the desired free-stream singularity, and an additional stream function $\psi_a$ that is regular everywhere inside the aerofoil image C and satisfies $L\psi_a=0$:

$$\psi=\psi_b+\psi_a \tag{35}$$

For given $\psi_b$ and aerofoil image C we may then formulate a Tricomi boundary value problem for $\psi_a$ and solve this under the boundary condition $\psi_a=-\psi_b$ on C.

Now in the design process C is chosen and the boundary valve problem is approximately solved by representing $\psi_a$ by a finite sum of linearly independent solutions $\psi_{an}$ as follows: $\psi_a=\sum c_n\psi_{an}$ with

$L\psi_{an}=0 \quad n=1(1)N.$

By the proper determination of $c_n$ the boundary condition is satisfied approximately.
By application of the transformation eq. (34) the aerofoil shape is found finally. Three examples of results obtained by the method of Boerstoel are presented in fig. 28.

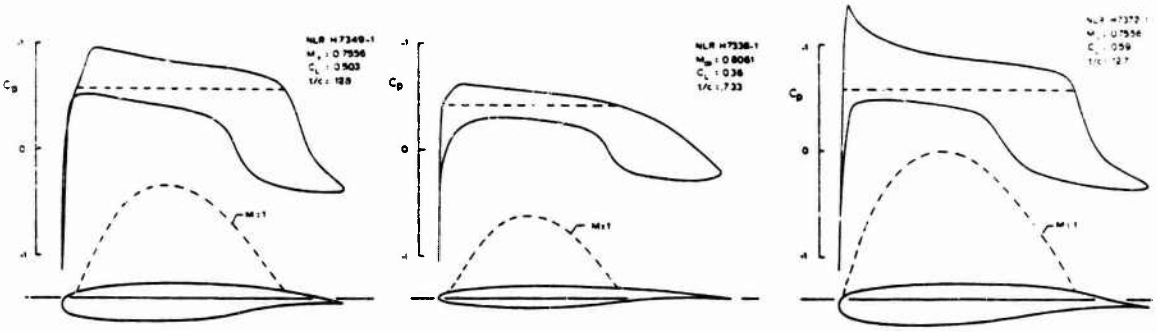

a b c

fig. 28

Examples of full solutions of the inverse potential flow calculation by Boerstoel(ref.35).

Solutions of this type can form input data of the aerodynamic design process.

Another design method based on the hodograph transformation is that presented by Bauer, Garabedian and Korn in ref. 36. In this method the equations for incompressible flow are written in complex characteristic form. The complex hodograph potential of an incompressible flow is used to define an initial-value problem for these equations. The result is translated into a solution of the compressible hodograph equations. For vanishing compressibility the original solution is found back. The problem is solved by finite difference techniques. The method is suitable to obtain a much larger family of shapes than with the analytic method of Nieuwland. In comparison with the method of Boerstoel the family of shapes seems to be of the same magnitude. However the numerical process of Garabedian and Korn is controlled by about 70 parameters that must be chosen by the user of the method. In the method of Boerstoel that is based on computing series, less than 10 parameters control the process. Experience influences much the computer time needed to generate useful aerofoils by means of the approach of Garabedian and Korn whereas in the case of Boerstoel's method experience plays a smaller role in the design process. Garabedian and Korn according to ref. 36 are able to generate aerofoils in 1 to 2 hrs computing time on a CDC-6600. The time required to generate aerofoils by means of Boerstoel's method is about 1 hr on the same computer. Examples of aerofoils designed by the method of Garabedian and Korn are presented in fig. 29.

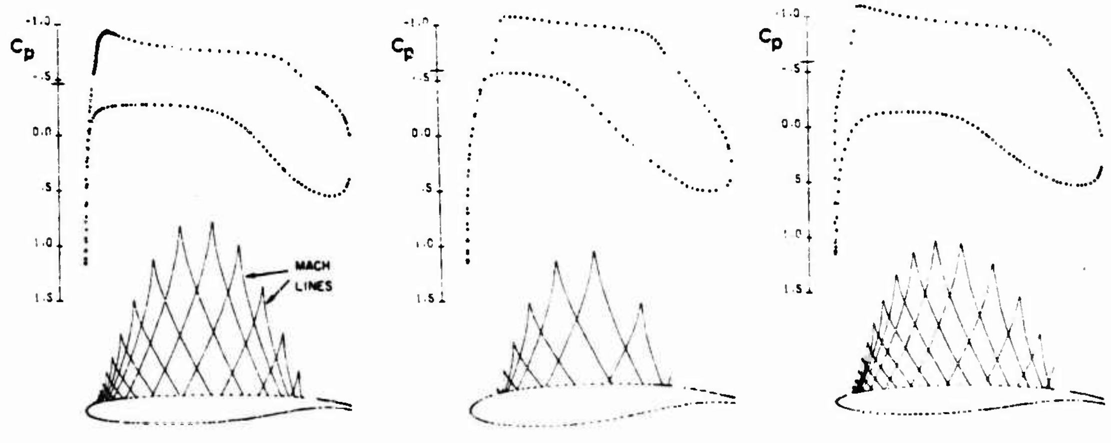

$M_\infty = 0.790$
$C_L = 0.677$
$t/c = 0.105$

$M_\infty = 0.750$
$C_L = 0.667$
$t/c = 0.151$

$M_\infty = 0.75$
$C_L = 0.963$
$t/c = 0.106$

fig. 29

Examples of full solution of the inverse potential flow calculation by Bauer, Garabedian and Korn (ref. 36).

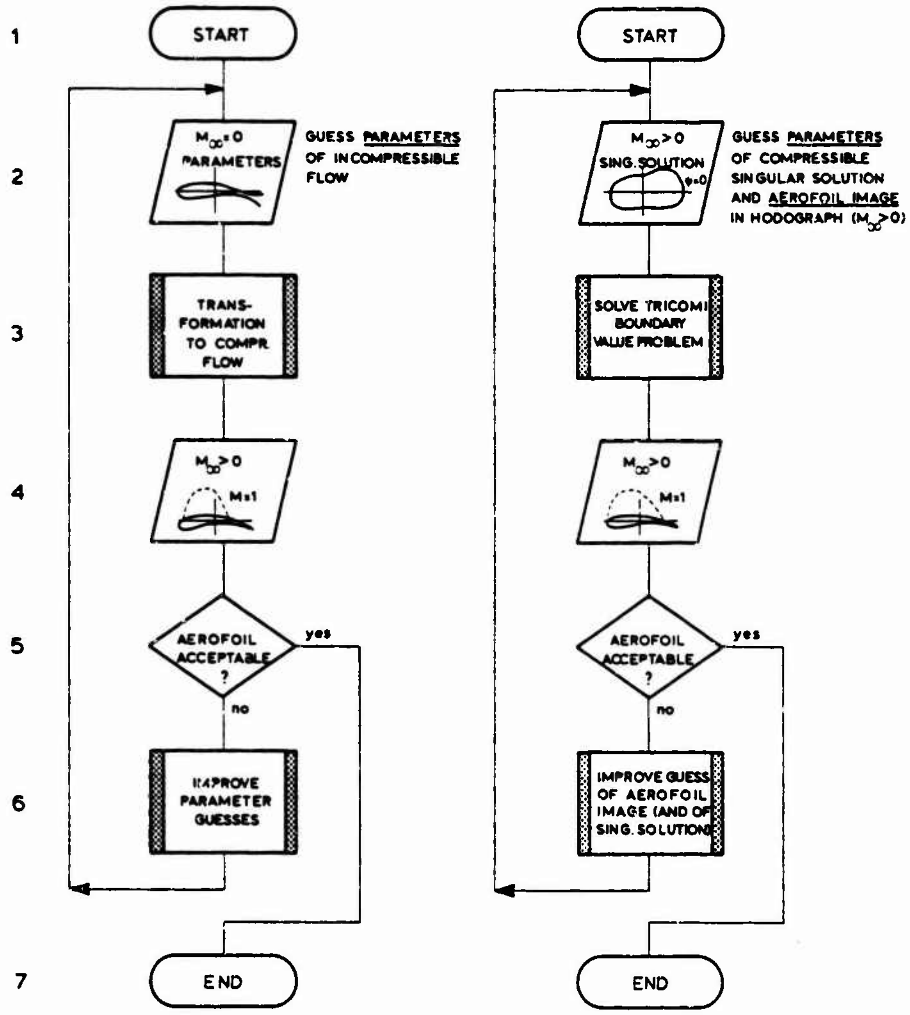
1
2
3
4
5
6
7
START
$M_\infty = 0$
PARAMETERS
GUESS PARAMETERS OF INCOMPRESSIBLE FLOW
TRANS-FORMATION TO COMPR. FLOW
$M_\infty > 0$
M=1
AEROFOIL ACCEPTABLE ?
yes
no
IMPROVE PARAMETER GUESSES
END
START
$M_\infty > 0$
SING. SOLUTION
φ=0
GUESS PARAMETERS OF COMPRESSIBLE SINGULAR SOLUTION AND AEROFOIL IMAGE IN HODOGRAPH ($M_\infty > 0$)
SOLVE TRICOMI BOUNDARY VALUE PROBLEM
$M_\infty > 0$
M=1
AEROFOIL ACCEPTABLE ?
yes
no
IMPROVE GUESS OF AEROFOIL IMAGE (AND OF SING. SOLUTION)
END

a. TRANSFORMATION METHOD
(GARABEDIAN - KORN)

INCOMPR. FLOW = INCOMPR. HODOGRAPH ⇒ COMPR. FLOW

b. BOUNDARY VALUE PROBLEM SOLUTION
(BOERSTOEL)

COMPR. HODOGRAPH ⇒ COMPR. FLOW

fig. 30

Flow diagrams of two hodograph methods for the design of aerofoils with shockfree transonic flow.

In fig. 30 simplified flow diagrams of both hodograph methods are presented.

When the inverse calculation method for the determination of a shape with shockfree transonic flow is used as input in the design process indicated in fig. 1, the aerodynamic characteristics have to be determined in off-design conditions. Also other design conditions may be subject of study. For an aerofoil for a wing e.g. apart from high speed characteristics also low speed characteristics play a role. For aerofoils for helicopter rotor blades as well manoeuver as hover conditions must be met. In general $C_l$, $C_d$ and $C_m$ curves of the final aerofoil must be estimated. For this, use is made of potential flow methods as the panel method and boundary layer calculation methods. Further empirical knowledge is used to extrapolate from the conditio [illegible] at are covered by these methods to conditions outside the range of applicability of these metho [illegible] ards the boundaries in the $C_l - M_\infty$ plane that determine the occurrence of buffet or rapid variatio [illegible] rodynamic characteristics of the aerofoil. At high subsonic Mach numbers direct solutions of the ful [illegible] tial flow equation are used to predict aerofoil characteristics as close as possible to the boundaries [illegible] ne $C_l - M_\infty$ plane where shock induced boundary layer separation occurs. In the next section attention will be paid to some limits of applicability and shortcomings of some finite difference methods that are being used successfully for this.

### 4.2 Finite difference methods for the full potential equation of plane flow.

In the paper presented by Yoshihara last year at the Von Karman Institute (ref. 30) a complete description is given of recent developments in the calculation of steady transonic flow with shocks using finite difference procedures. In view of this in the present paper only a few remarks will be made on this subject and some results will be presented that have been obtained at NLR.

As far as the methods for the solution of the full potential flow problem in plane flow are concerned two approaches exist: the time dependent procedure of Magnus and Yoshihara (ref. 37) and the steady relaxation procedures of Steger and Lomax (ref. 38), Garabedian and Korn (ref. 36) and of Jameson (ref. 39).

In the time-dependent procedure the desired steady flow is obtained asymptotically for large times by a finite difference marching procedure. Embedded shockwaves can develop automatically. The flow model that is used describes conservation of mass and momentum whereas the isotropic pressure/density relation $\frac{p}{\rho^{\gamma}}$ = constant is used to eleminate the pressure. The flow model can be written as vector partial differential equation:

$$\begin{Bmatrix}\rho\\ \rho u\\ \rho w\end{Bmatrix}_t + \begin{Bmatrix}\rho u\\ \rho u^2+p\\ \rho uw\end{Bmatrix}_x + \begin{Bmatrix}\rho w\\ \rho uw\\ \rho w^2+p\end{Bmatrix}_z = 0 \qquad (36)$$

u and w are velocity components in x and z direction. Much attention is paid in the method to the correct representation of the boundary condition at the aerofoil surface.

The computational effort to apply the time-dependent method is large in comparison to that of the steady relaxation methods because it requires representation of the time history of details of the flow that is irrelevant for the asymptotic solution which is the steady flow. It may be expected that transient flow problems in future can be solved along these lines. Comparison of the results of the time-dependent method with exact results for shockfree flow from hodograph theory generally show very good agreement. The computing time is in the order of 40 minutes on the CDC 6600 computer whereas 4-10 minutes are required for application of the steady relaxation method of Garabedian and Korn.

The steady relaxation methods of Garebadian and Korn and of Jameson are based on the equations that describe conservation of mass and irrotationality and the conservation of energy, together with the isentropic pressure/density relation. As vector partial differential equation the first two relations are:

$$\begin{Bmatrix}\rho u\\ -w\end{Bmatrix}_x + \begin{Bmatrix}\rho w\\ u\end{Bmatrix}_z = 0 \qquad (37)$$

The energy equation reads:

$$\frac{u^2+w^2}{2} + \frac{\gamma}{\gamma-1}\,\frac{p}{\rho} = \text{constant} \qquad (38)$$

for the entire flow field.
In the actual calculations not the conservation form of the equations is used but:

$$(a^2-u^2)\frac{\partial^2\varphi}{\partial x^2} - 2uw\frac{\partial^2\varphi}{\partial x\partial z} + (a^2-w^2)\frac{\partial^2\varphi}{\partial z^2} = 0 \qquad (39)$$

with for the velocity of sound:

$$a^2 = a_\infty^2 + \frac{\gamma-1}{2}(U_\infty^2-U^2-w^2) \qquad (40)$$

In these methods the fulfillment of the boundary condition is simplified by mapping the exterior of the aerofoil onto the interior of a circle.

The appearance of shocks in the solutions is an interesting feature. Some attention will be paid to this, based on ref. 40 (NLR, Van der Vooren and Slooff) and on unpublished work of Van der Vooren.

As has been explained also in ref. 30, cases with shocks are mathematically a weak solution of the differential equations that define the flow model. In conservation form these equations are represented by:

$$\operatorname{div}\,\vec{v} = 0 \qquad (41)$$

where e.g. $\operatorname{div} = \frac{\partial}{\partial t} + \frac{\partial}{\partial x} + \frac{\partial}{\partial z}$ in the plane time dependent flow.

A weak solution of eq. (41) is a solution that fulfills eq. (41) almost everywhere; there may be lines (shocks) across which eq. (41) does not hold. The jump conditions across these lines follow from the theory of weak solution (ref. 41) of differential equations and read

$$(\vec{v}.\vec{n})^+ + (\vec{v}.\vec{n})^- = 0 \qquad (42)$$

Here + and - denote opposite sides of the lines of discontinuity.

From the theory of weak solutions the shock relations for the time-dependent approach read according to eq. (36) and the isentropic pressure/density relation (ref. 39 and fig. 31):

$$\rho_1 u_{n1} = \rho_2 u_{n2}$$

$$\rho_1 u_{n1}^2 + p_1 = \rho_2 u_{n2}^2 + p_2 \qquad (43)$$

$$\rho_1 u_{n1}\ u{+1} = \rho_2 u_{n2} u_{t2}$$

$$\frac{p_1}{\rho_1^{\gamma}} = \frac{p_2}{\rho_2^{\gamma}}$$

expressing conservation of mass, momentum and entropy across the shock. It is shown in ref. 39 that in this version of the time-dependent method an energy loss across the shock is predicted dependent on the flow conditions upstream of it. To first order this loss is

$$H_1 - H_2 \sim (M_{n1}^2 - 1)^2 \qquad (44)$$

The related rotation in the wake is stronger than that which occurs behind the shock in the exact inviscid, non isentropic compressible Rankine Hugoniot flow in which conservation of mass, normal and tangential components of momentum flux and energy exists (ref. 1). In this flow the rotation is related to the increase in entropy across the shock, which to first order is only

$$S_2 - S_1 \sim (M_{n1}^2 - 1)^3 \qquad (45)$$

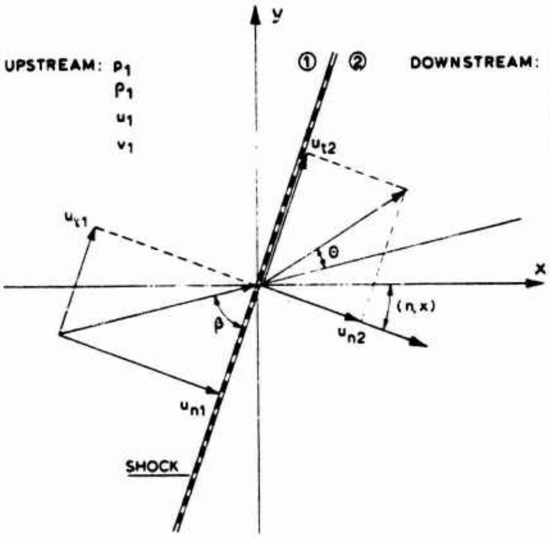

fig. 31

Definition of shock parameters.

Later in their time-dependent method Magnus and Yoshihara applied a procedure in which the total pressure is upgraded after every few time steps by changing the density $\rho$ in such a way that the algebraic energy equation eq. (38) is valid again along streamlines. It appears that in the limiting steady case the calculations then represent a model that is both isentropic and isoenergetic at the expense of relaxing on the requirements for the conservation of mass and momentum. Still later on procedures were used that differ from the description of the method in the literature in other ways. It is not always clear from the description of results with which procedures they were obtained.

For the steady relaxation methods the theory of weak solutions for eq. (37) and eq. (38) and the isentropic pressure/density relation leads to the shock relations (ref. 39):

$$\rho_1 u_{n1} = \rho_2 u_{n2}$$

$$u_{t1} = u_{t2} \qquad (46)$$

$$\frac{\gamma}{\gamma-1}\,\frac{p_1}{\rho_1} + \frac{u_{n1}^2 + u_{t1}^2}{2} = \frac{\gamma}{\gamma-1}\,\frac{p_2}{\rho_2} + \frac{u_{n2}^2 + u_{t2}^2}{2}$$

$$\frac{p_1}{\rho_1^{\gamma}} = \frac{p_2}{\rho_2^{\gamma}}$$

These express the conservation of mass, energy and entropy as well as the continuity of tangential velocities across the shock. The first two relations in eq. (46) imply the continuity of the tangential component of momentum flux. The normal component of momentum flux is not conserved across the shock in this model. In fact there is a momentum gain across the shock.

The shock relations according to the time-dependent and the steady relaxation methods are compared in fig. 32 with the Rankine-Hugoniot shock relations. The impression from this figure that the results of the time-dependent method will come closest to that of Rankine Hugoniot flow is confirmed in fig. 33a. In this figure the calculated pressure distributions are given for a NACA 64A-410 aerofoil. It can be seen in this figure that the pressure jumps that are determined numerically in both methods differ from the jumps that can be determined from the shock relations of the flow models. In comparison with experimental results, where the shock is weakened due to boundary layer effects, it happens very often that the result of the steady relaxation method corresponds well with the experiments. This is also the case in fig. 33b that has been obtained from Kacprzynski (NAE, ref. 42). This should be regarded as a coincidence.

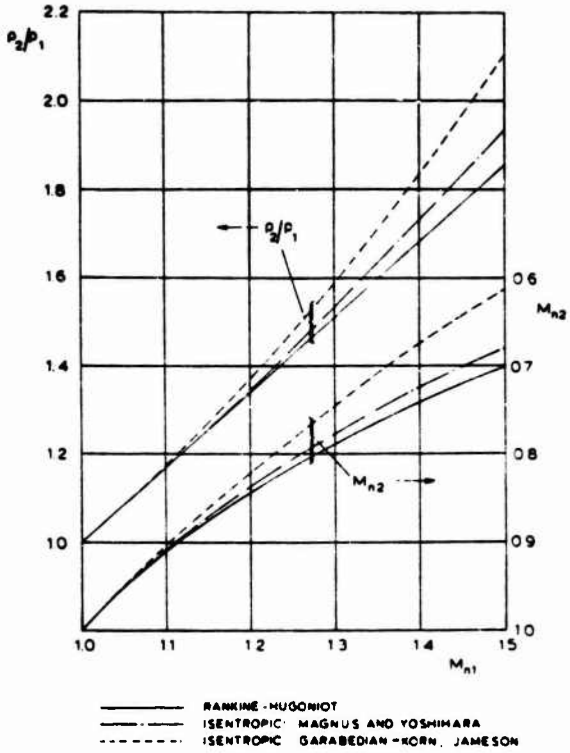

fig. 32

Density ratio $\rho_2/\rho_1$ and downstream Mach number $Mn_2$ as a function of upstream Mach number $Mn_1$ at a shock.

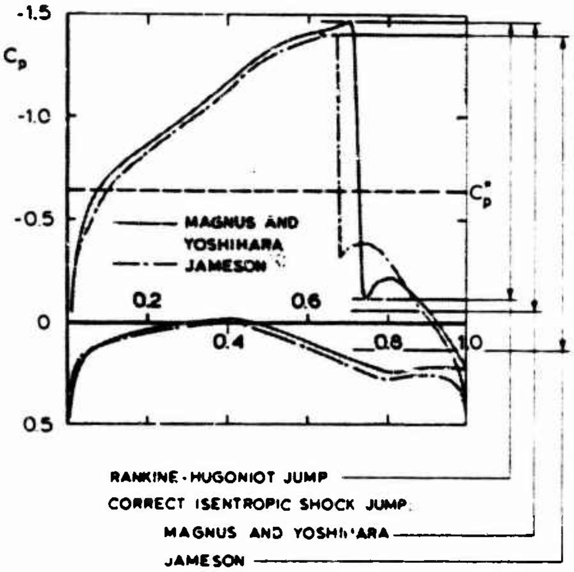

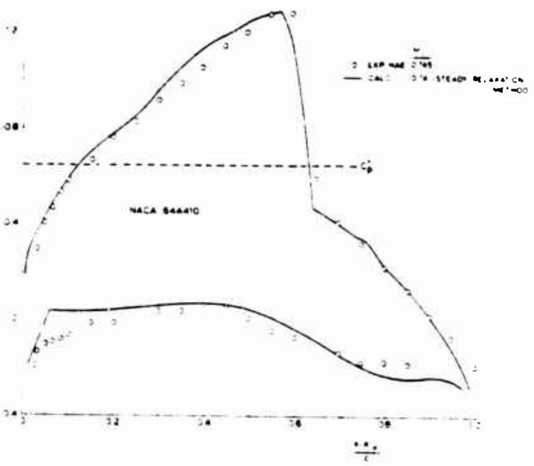

fig. 33

Pressure distribution on the NACA 64A-410.

Finally, some other examples will be presented of the steady relaxation method of Garabedian and Korn. In fig. 34 results are presented from unpublished work of Smith (NLR) for the shockfree rear-loaded aerofoil NLR7101 of which the experimental pressure distribution is given for the design conditions in fig. 26. As can be seen in fig. 34 the Garabedian-Korn method produces a pressure distribution that shows a shock which is not present in the experiment. It is important to know that this can happen when the method is used as a design tool. For the same aerofoil the $C_L$-$M_\infty$ relations for various values of the angle of attack according to the Garabedian-Korn method are presented in fig. 35.

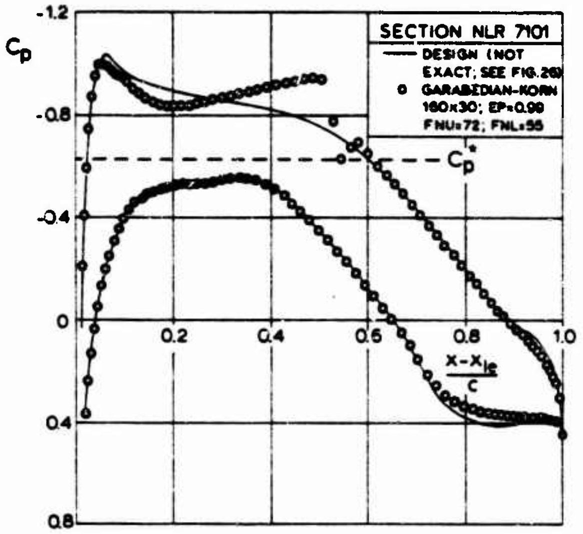

fig. 34

Pressure distribution on section NLR 7101.

In this figure which is obtained from unpublished work of Zwaaneveld (NLR) the drag divergence Mach numbers $M_{DD}$ are indicated from calculated and measured results. $M_{DD}$ is defined for each angle of attack as the Mach number for which the variation of the drag coefficient as a function of Mach number

$$\left.\frac{dC_d}{dM_\infty}\right|_{\alpha\,=\,\text{constant}} = 0.1$$

The drag in the experiments of NLR has been determined by means of a rake. The drag from calculated results has been obtained by means of integration of the pressure distribution on the aerofoil. The result for the drag divergence of the calculation method corresponds rather well with experimental results. This can be explained by the fact that in the absence of shocks the calculation method is equivalent and identical to Rankine-Hugoniot flow so that the prediction of the drag rise Mach number in the calculation method is correct although the drag value itself is in error.

It has been shown in ref. 30 and ref. 42 that it can be very difficult to explain differences between experimental and calculated pressure distributions when strong shocks are present. Tunnel wall interference, shockwave-boundary layer interactions and errors in the representation of pressure jumps due to shocks in the calculation methods, are difficult to separate.

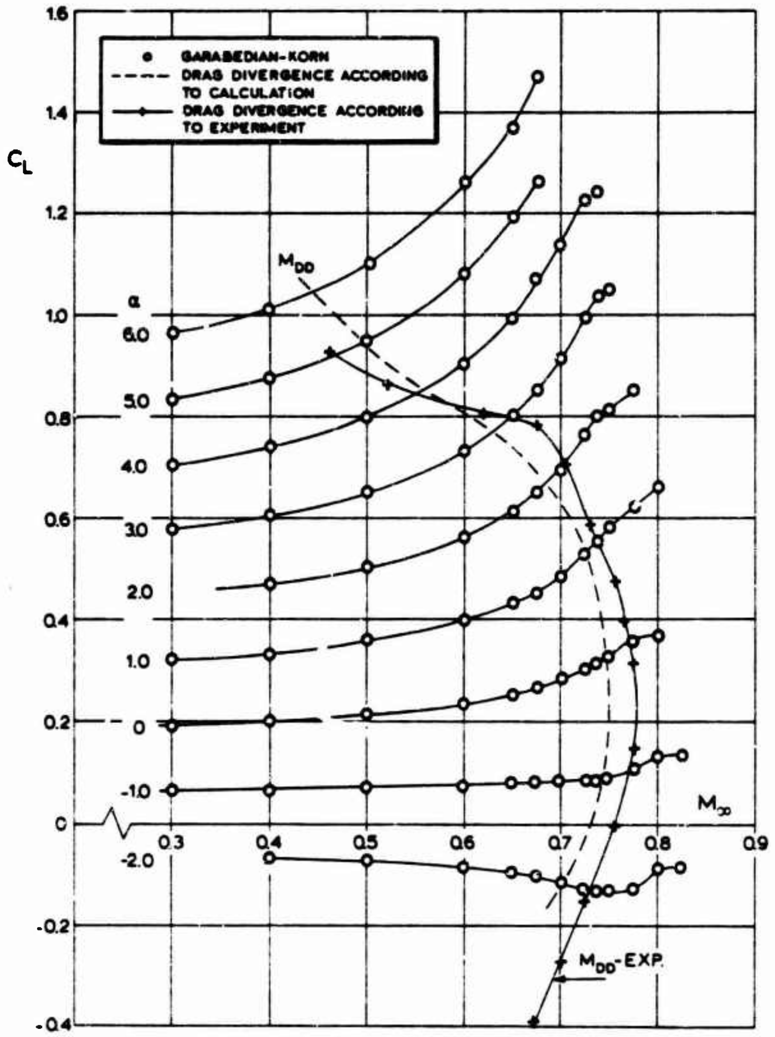

fig. 35

Calculated lift as a function of $M_\infty$ and α with points where drag-divergence occurs for section NLR 7101.

## 5. CONCLUDING REMARKS

During the past years large progress is made in the development of potential flow methods for calculation of flows around aerofoils and wings. For subcritical flows around wing-body combinations direct panel methods are available that, partly as a result of introduction of semi-empirical compressibility corrections, are very suitable design tools. For plane transonic flows inverse hodograph techniques and direct finite difference methods, both solving the full potential flow equations for exact boundary conditions at the aerofoil surface, form a useful combination for the design of aerofoils for wings and helicopter rotors. For attached flow and relatively smooth pressure distributions, in principle boundary layer effects can partly be taken into account.

For three-dimensional wings in transonic flow only finite difference methods are available that are based on small-perturbation flow equations and simplified boundary conditions. Results of these techniques can differ much from results of the full potential equation for exact boundary conditions. When strong shocks are present even in attached flow the shockwave-boundary layer interaction effects cannot be predicted yet in plane flow or in three-dimensional flow. Also separation of the flow that causes lift divergence and buffet is outside the region of applicability of existing standard calculation methods. Semi-empirical techniques that are used by many designers, seem the only design aids for the time being with respect to these effects.

The last points that are mentioned make clear that for the design of aerofoils and wings, experiments are indispensable. Wall interference in tunnels however may cause troubles especially in cases with strong shocks and high lift with and without boundary layer separation effects.

It is desirable to combine calculations and experiments in the design process in an optimum way. No general rules can be given for this because the empirical knowledge of the designer plays an essential role in the process. Apart from considerations concerning the applicability of the results also cost- and time aspects play an important role when a choice is made between calculations and experiments.

For an experiment in a windtunnel to determine aerofoil characteristics,a model is required. In most cases it is necessary to determine details of the flow so that it must be possible to measure the pressure distribution on the model. Accurate aluminium alloy models for 2D tests in a small transonic tunnel cost \$ 15.000 to \$ 20.000. The costs of a complete test of the aerofoil including data processing in such a tunnel is about \$ 10.000 for about 200 $M_\infty-\alpha$ combinations. This means that for each $M_\infty-\alpha$ combination a test costs about \$ 50 without model costs or \$ 150 including model costs. This can be "compared" with the costs of application of the steady relaxation method of Garabedian and Korn that takes 4-10 minutes on a CDC 6600 for one case. Making use of special features in the programme the computation of more than one case takes less time for the second and each succeeding case. Experiences at NLR are that 100 $M_\infty-\alpha$ combinations cost about \$ 5000 on a CDC 6600 in a commercial centre. That is \$ 50 for each case. For the calculation the price for each $M_\infty-\alpha$ combination is about equal when input generation for the computer is neglected and when the computer programme is available. The price of a complete windtunnel test is little influenced by the number of test points. The time required to make a tunnel model is much larger than the time required to generate computer input.

A similar "comparison" can be made for 3D cases. A steel model for pressure measurements on a wing that is mounted on a body costs \$ 50.000 to \$ 70.000. A short test that is relatively expensive and that only concerns symmetrical flow conditions for one configuration costs about \$ 25.000 including data processing. It is assumed that a suitable tunnel is being used with a test section of say 2 x 1.6 $m^2$. With again about 200 $M_\infty-\alpha$ combinations the experiment costs about \$ 125 without model costs or including model costs about \$ 400 for each $M_\infty-\alpha$ combination. Application of the NLR panel method costs for a given configuration for the second and each succeeding $M_\infty-\alpha$ combination \$ 350 to \$ 1400 dependent on panelling.

The choice between experiment and calculation strongly depends on the phase in the design process as can be seen also in fig. 1. When e.g. the effect of a large number of geometrical variations has to be determined, time and costs considerations very often will lead to the use of the computer. In some cases computational methods provide possibilities that differ from the possibilities of tests. E.g. to design aerofoils with transonic shockfree flow existing theoretical inverse methods directly give results that in general cannot be obtained by a trial and error procedure that is entirely based on experiments. It has been shown that in some cases this type of flow can be found by experimental means but in those cases only at the cost of a large number of experiments with different models.

To be able to apply a computer programme a mathematical model must be developed first and the computer programme must be written (and debugged). It is not possible to produce numbers about the costs that are involved. As an order of magnitude it can be assumed that complicated computer programmes of the types that have been used to generate the examples presented in the present paper, at least cost the same as the windtunnel models mentioned above. Also in this case a large difference exists between costs related to plane flow and to three-dimensional flow. In principle it is possible to improve programming techniques in comparison with normal practice in scientific programming. Further the price/performance ratio of computers will be influenced considerably by amongst others new computer memory technology. Both circumstances have to lead to a more competitive price of computations in comparison with experiments.

## 6. REFERENCES

1. Liepmann, H.W. and Roshko, A. — Elements of gasdynamics. John Wiley and Sons. Inc., London.

2. Bleekrode, A.L. and Labrujère, Th.E. — A survey of current collocation methods in inviscid subsonic lifting surface theory. NLR MP 72005. Lecture presented at the V.K.I. during the short course on Numerical methods in Fluid Dynamics. February 1972.

3. Zandbergen, P.J., Labrujère, Th.E. and Wouters, J.G. — A new approach to the numerical solution of the equation of subsonic lifting surface theory. NLR TR G49 (1967).

4. Spiegel, E. van — Boundary value problems in lifting surface theory. NLR TR W1 (1959).

5. Garner, H.C. — Low speed theoretical and experimental aerodynamic loading on highly swept curved-tipped wings of two thicknesses. RAE TR 72177 (1972).

6. Hedman, S.G. — Vortex lattice method for calculation of quasi-steady state loadings on thin elastic wings in subsonic flow. FFA Report 105 (1966).

7. James, R.M. — On the remarkable accuracy of the vortex lattice discretization in thin wing theory. Mc Donnell Douglas Rept DAC 67211 (1969).

8. Labrujère, Th.E. and de Vries, O. — The deformation of a vortex sheet behind a swept wing; comparison of measurements and calculations. NLR (1974, to be published).

9. Zwaan R.J. — On a kernel function method for the calculation of the pressure distribution on a two-dimensional wing with harmonically oscillating control surface in subsonic flow. NLR F 261 (1968).

10. Labrujère, Th.E. and Schipholt, G.J. — An ALGOL programme for the approximate calculation of pressure distributions on aerofoils in two-dimensional subsonic flow using a surface vorticity distribution method. NLR TR 72084 (1972).

11. Kellogg, O.D. — Foundations of potential theory. Dover Publications, Inc., New-York.

12. Lamb, H. — Hydrodynamics.

13. Gretler, W. — Neuere Methode zur Berechnung der ebene Unterschallströmung an dünnen Profilen bei kleinen Anstellwinkeln. Acta Mechanica Vol. 1 (1965).

14. Baurdoux, H.I. and Schipholt, G.I. — The applicability of first and second order theory for the determination of subcritical pressure distributions on non-lifting aerofoils. NLR TR 69028 (1969).

15. Smith, A.M.O. and Pierce, J. — Exact Solution of the Neumann Problem. Calculation of non-circulatory plane and axially symmetric flows about or within arbitrary boundaries. Douglas Aircraft Company Rep. 26988 (1958).

16. Rubbert, P.E.; Saaris, G.R.; Scholey, M.B.; Standen, N.M. and Wallace, R.E. — General method for determining the aerodynamic characteristics of fan-in-wing configurations. Boeing Company, USAAVLABS TR 67-61A (1967).

17. Labrujère, Th.E., Loeve, W. and Slooff, J.W. — An approximate method for the calculation of the pressure distribution on wing-body combination at subcritical speeds. NLR MP 70014 (1970) AGARD CP No. 71 Paper presented at the AGARD Specialist Meeting "Aerodynamic Interference", Silver Spring Maryland, 1970.

18. Kramer, H. — Some analytical and numerical calculations for a cylinder vortex combination in incompressible flow. NLR TR 69057 (1969).

19. Mangler, K.W. and Smith, J.H.B.
Behaviour of the vortex sheet at the trailing edge of a lifting wing.
RAE TR 69049 (1969).

20. Imai, J.
Approximate methods in compressible fluid dynamics.
Univ. of Maryland, TN BN 95 (1957).

21.
Method for predicting the pressure distribution on swept wings with subsonic attached flow.
RAe Soc. TDM 6312 (1964).

22. Boerstoel, J.W.
Application of the Karman-Tsisn gas theory to high subsonic and transonic non-circulatory flows over quasi-elliptical aerofoil sections. Results of an iterative computation method.
NLR TR 68037 (1968).

23. Sells, C.C.L.
Plane subcritical flow past a lifting aerofoil.
RAE Rep. TR 67146 (1967).

24. Loeve, W. and Slooff, J.W.
On the use of "panel methods" for predicting subsonic flow about aerofoils and aircraft configurations.
NLR MP 71018 (1971).
Paper presented at the 4. Jahrestagung
DGLR, Baden-Baden October 1971.

25. Labrujère, Th.E. and Sijtsma, A.
Aerodynamic interference between aircraft components: illustration of the possibility for prediction.
NLR MP 72020 (1972)
Paper presented at the 8th ICAS congress, 1972.

26. Preston, J.H.
The calculation of lift taking account of the boundary layer.
R&M 2725 (1949).

27. Spence, D.A.
Prediction of the characteristics of two-dimensional aerofoils.
J. Aero Sci. 21 p. 577 (1954).

28. Piers, W.J. and Slooff, J.W.
Calculation of the displacement effect in two-dimensional subsonic attached flow around aerofoils; examples of calculation using measured displacement thicknesses.
NLR TR 72116 (1972).

29. Lomax, H., Bailey, F.R. and Ballhaus, W.F.
On the numerical simulation of three-dimensional transonic flow with application to the C 141 wing.
NASA TN D 6933 (1973).

30. Yoshihara, H.
A survey of computational methods for 2D and 3D transonic flow.
Paper 6 of the 55 Lecture series: "Advances in numerical fluid dynamics", presented at the Von Karman Institute in 1973.

31. Nieuwland, G.Y.
Transonic potential flow around a family of quasi-elliptical airfoil sections.
NLR TR T 172 (1967).

32. Boerstoel, J.W. and Uylenhoet, R.
Lifting aerofoils with supercritical shockless flow.
NLR MP 70015 (1970).
Paper presented at the 7th ICAS Congress Roma 1970.

33. Boeretoel, J.W. and Huizing, J.H.
ALGOL programs for the computation of quasi-elliptical shockfree transonic aerofoils.
NLR TR 72128 (1972).

34. Spee, B.M.
Investigations on the transonic flow around aerofoils.
NLR TR 69122 (1969).

35. Boerstoel, J.W. and Huizing, G.H.
Transonic shockfree aerofoil design by analytic hodograph methods.
NLR MP 73023 (1973)
Paper presented at the Euromech 40 Colloquium Stockholm 1973.

36. Bauer, F., Garabedian, P. and Korn, D.
Supercritical wing sections. Lecture notes in economics and mathematical systems 66.
Springer Verlag.

37. Magnus, R. and Yoshihara, H.
Steady inviscid transonic flows over planar airfoils - A search for a simplified procedure.
NASA CR No. 2186 (1972).

38. Steger, J.L. and Lomax, H.
Numerical calculation of transonic flow about two-dimensional airfoils by relaxation procedures.
AIAA Paper No. 71-569 (1971).

39. Jamsson, A.
Transonic flow calculations for airfoils and bodies of revolution.
Grumman Report 390-71-1 (1971).

40. Van derVoorsn, J. and Slooff, J.W. — On inviscid isentropic flow models used for finite difference calculations of two-dimensional transonic flows with embedded shocks about airfoils.
NLR MP 73024 (1973).
Paper presented at Euromech 40: "Transonic Aerodynamics", Sweden.

41. Lax, P. — Weak solution of non-linear hyperbolic equations and their numerical calculation.
Communications on Pure and Applied Mathematics, Vol. III (1954).

42. Kacprzyneki, J.J. — Drag of supercritical aerofoils in transonic flow.
NAE Canada
Paper presented at AGARD specialists' meeting on aerodynamic drag, Izmir (1973).

N74-26452

# BOUNDARY LAYER CALCULATION METHODS AND APPLICATION TO AERODYNAMIC PROBLEMS

J. Steinheuer *

## 1. INTRODUCTION

### 1.1 General Remarks

The aerodynamic design of aircraft may be characterized generally as the ability to develop such forms and shapes of aircraft which will ensure a stable and controllable type of flow at a maximum efficiency. The basic flow to be achieved, for the Mach number range up to low-supersonic speeds, would ideally be the classical attached Kutta-Joukowsky flow. The type of aircraft under consideration then is one having wings of large to moderate aspect ratio where the lifting surfaces are physically distinct from the propulsion units and from the fuselage. In the high subsonic speed range compressibility effects can be delayed to a certain extent by using swept wings, but still retaining the essential features of an attached flow. The aerodynamic design should be based on a full understanding of the fluid mechanics of the flow from which, either by theoretical considerations or by experimental research, design criteria and calculation methods are derived for the prediction of the aerodynamic properties of an aircraft.

Historically, the outstanding event by which our understanding of the physics of the flow around an obstacle such as an airplane was given its foundations has been the introduction of the boundary-layer concept by Prandtl in 1904 [1]. In this year of the 70th anniversary of that event it seems quite appropriate to recall that without the recognition that viscous forces, though small, play a crucial part in any flow, the experimentally observed finite drag in attached flows and the occurence of separation could not be understood with the then existing and already highly developed perfect fluid theory on one hand or the Stokes viscous theory on the other. Prandtl's theory explained how viscosity exerts its influence on the flow in a thin boundary layer adjacent to the body surface. Drag is readily recognized as the sum of the shear forces in the thin boundary layer, and separation is the consequence of the retardation of fluid by viscous forces causing it to break away from the surface and thereby disturbing large areas of the flow field. Since its foundation boundary-layer theory has developed into a discipline of fluid dynamics of its own standing comprizing a broad variety of theoretical problems and practical applications. The analytic and numerical treatment of the boundary-layer equations has been greatly advanced especially by the use of computers. Calculation methods have been devised in great number by which many problems of practical significance in aircraft aerodynamics could be solved, and of which this paper is trying to give a few examples.

Since the emphasis of this lecture course is on aerodynamic characteristics and their prediction, it seems appropriate first to point out in more detail the role of boundary-layer behavior and its influence on the aerodynamic characteristics. In view of the envisaged type of flow around an aircraft with wings of large to moderate aspect ratio it is justified to do this by considering the two-dimensional flow-over an airfoil section where most of the basic boundary layer phenomena are present.

### 1.2 The Influence of Boundary-Layer Behavior on the Aerodynamic Characteristics of Wing Sections

The low speed flow characteristics about a single airfoil i.e. an airfoil without flaps and slats are well-known from wind-tunnel investigations as summarized in Refs. [2], [3] and [4] giving data on lift vs. incidence, $c_{L\,max}$ and drag coefficients for Reynolds numbers up to about $10^7$. From these experiments one arrives at the following qualitative picture of the boundary-layer behavior and its influence on the aerodynamic coefficients. At small to moderate incidences the flow along the contour of the airfoil is completely attached, and an almost ideally potential flow pattern is established. The boundary layer starts on both sides of the stagnation point at the nose as a laminar boundary layer, undergoes transition beginning at some downstream position and extending usually over a relatively short distance, and continues as a turbulent boundary layer to the trailing edge where the boundary layers from the upper and lower sides merge to form a wake which is a turbulent thin shear flow. The location of the transition region depends on the pressure distribution, normally beginning at a small distance downstream of the point of minimum pressure, and on the Reynolds number. In general, increasing Reynolds number at a constant incidence decreases the boundary-layer thickness at any point including the trailing edge which leads to an increase in circulation of the inviscid flow thus increasing the lift coefficient $c_L$ and the slope $dc_L/d\alpha$ while the pitching moment $c_M$ becomes more positive. The profile drag $c_D$ being composed of friction drag and pressure drag is generally reduced with Reynolds number by virtue of a decreasing pressure drag and also a reduction in friction drag. An indirect influence of the Reynolds number is brought about by a change in the transition location which is very sensitive to changes in pressure distribution. As the angle of incidence is increased at constant Reynolds number the transition region moves forward on the upper side and rearwards on the lower side. On the other hand transition moves upstream on both sides with increasing Reynolds number at constant incidence. Thus the role of transition location as a Reynolds number dependent parameter is seen to have a prominent significance when it comes to extrapolating wind-tunnel measurements to the desired full scale data known as the scale effect to which some remarks will be made later on.

As the angle of incidence of an airfoil is further increased eventually the boundary layer will separate from the surface at some point on the upper side. Depending on the section shape, the separation location, and the Reynolds number significant differences occur as to the subsequent disturbance of the inviscid flow field. Two major characteristic types of separation can be distinguished (see Fig. 1), i.e. (1) separation of the turbulent boundary layer at the trailing edge and (2) separation of the laminar boundary layer near the leading edge. Rear separation of the turbulent boundary layer results from the increased positive or adverse pressure gradient as the lift increases with incidence. This type of separation occurs on thick airfoil sections with a well-rounded minimum pressure peak and transition lies at about the location of minimum pressure. The maximum lift is reached steadily with incidence as shown by the lift curve of Fig. 1 for the NACA $63_3$-018 airfoil profile indicating that the separation flow pattern is preserved even beyond the maximum lift. Raising the Reynolds number at constant incidence tends to push the separation point back again resulting in a gain of lift and thus allowing to achieve a higher $c_{L\,max}$-value at a larger angle of incidence. However, lowering the Reynolds number eventually results in the

---

* Dr.-Ing., Research Scientist, Institut für Aerodynamik der DFVLR, Braunschweig, Germany.

separation of the laminar boundary layer on the forward part i.e. before transition could take place. The once separated laminar boundary layer being unstable will very quickly turn turbulent and may then reattach again to the surface creating a closed separation region or bubble as shown for the cases ⓒ and ⓓ in Fig. 1. This type of separation usually occurs with thinner airfoils where the suction pressure peak is more pointed even at low angles of incidence. The bubble may behave in two distinct ways when after its establishment the incidence is raised or the Reynolds number is increased: it may shorten or it may enlarge forming either a "short" or a "long" bubble. The contracting short bubble moves closer to the front and suddenly bursts when some critical incidence is reached causing complete separation of the flow over the entire upper side of the airfoil. Consequently the lift-curve (curve for the NACA $63_1$-012 profile in Fig.1) has a sharp maximum with a drastic reduction of lift beyond this maximum and a corresponding drastic increase in drag. In contrast, the long bubble occuring at very thin airfoils extends rearwards with increasing incidence until it reaches the trailing edge. The lift slope decreases steadily during this process and the lift curve itself is rather flat around its maximum (curve for the NACA 64A006 profile in Fig. 1). On profiles of moderate thickness the type of separation can change from the leading edge short bubble type to the trailing edge turbulent separation type. Also a range of Reynolds number may exist for which the two types are present simultaneously, e.g. a short bubble and turbulent rear separation the latter being enhanced by the existence of the short bubble causing the adverse pressure gradient to be larger.

The main conclusion to be drawn is that the lift characteristics of an airfoil are determined to a large extent by the boundary layer behavior being primarily dependent on Reynolds number. Transition location has a very important influence on the type of separation to be expected. No generally valid criteria exist by which the two types of bubble separation can be predicted. Only by a very detailed knowledge of the boundary layer development at every stage can one hope to predict quantitatively the aerodynamic characteristics of lift, moment and drag of airfoil profiles at least up to the point where separation first occurs. However, the calculation of the boundary layer development depends on the given pressure distribution which in turn is influenced by the boundary layer displacement effect. So, when trying to determine e.g. the lift by purely computational means, an iterative procedure is necessary in order to account for this interaction between inviscid outer flow and the boundary layer.

A much fuller account of the airfoil section characteristics and also of the following topics in connection with the general aspects of aircraft behavior at high angles of attack has been given in a recent review by G.J. Hancock [5]. The remarks made here are meant only to point out the role and significance of the boundary layer effects without attempting to be exhaustive.

The classical means of ensuring satisfactory landing and take-off performance of an aircraft is the addition of trailing edge flaps and leading edge slats to the basic wing. The development of the boundary layers around an airfoil with a flap and a slat is depicted in Fig. 2 together with measured pressure distributions reproduced from [6]. In addition to the phenomena connected with single airfoil flow which may occur on each part of the multiple profile separately there are essentially two more features to be considered. The first is the appearance of a separation bubble on the lower sides of the main airfoil and the slat where the approaching turbulent boundary layer passes a contour discontinuity like that of the slat or highly curved parts of the profile contour like that at the flaps housing. The location of the reattachment point of these bubbles depends on the flap setting and the shape of the slat. Secondly there exists an interaction between the wake of the slat and of the main profile and the boundary layer over the back of the main profile and the flap which will certainly influence the boundary layer characteristics and hence the overall profile behavior.

The typical boundary-layer development over the back of a profile with slat and flap can be deduced from the total pressure head distributions given in Fig. 3 as measured by Ljungström [7]. Note that the only difference for the two cases shown is the different slat setting with a wider slat gap $h_S$ in the upper diagram, resulting in a marked change in the boundary-layer development as influenced by the slat wake, and also in noticeable changes of the pressure distributions and the overall lift coefficient $c_L$. A very important practical problem with such configurations is the problem of finding the optimum positions of the slat and the flap with regard to maximum lift. Fig. 4 shows the results of wind-tunnel measurements for a drooped-nose profile with a slat for three different slat angles and two Reynolds numbers according to E. Bartelt [8]. The pattern for positions of equal $c_{L\,max}$ is quite irregular with the optimum locations being displaced considerably by small changes of the flap angle and a Reynolds number variation. These diagrams strikingly show that although flap and slat locations can be found in extensive and costly wind-tunnel experiments the extrapolation of the experimental results to the full scale wing i.e. to a higher Reynolds number is very doubtful. On the other hand, the prediction of the aerodynamic characteristics in such cases by purely computational means seems to be an almost insolvable task in view of the complexity of the problem. An attempted approach for the prediction of the optimum flap setting to attain maximum lift will be presented later. Very useful papers on the subject have been given by A.M.O. Smith [9] and D.N. Foster [10].

If the Mach number is raised in the flow around an airfoil a supersonic flow region is established on the upper surface which is terminated by a normal shock. Since a shock wave is a sudden flow compression it is expected that there is a considerable influence on the boundary-layer development underneath. Although the flow upstream of the shock is supersonic the inner regions of the boundary layer must be subsonic so that the compression is being spread out to some extent over the surface as shown in Fig. 5. It depends very much on the shock strength and on the state of the approaching boundary layer whether or not it will separate in this region. If separation occurs this will drastically influence the inviscid flow and consequently also the aerodynamic properties of the profile. It is generally agreed that the approaching boundary layer should by all means be a turbulent one since a laminar boundary layer would almost invariably separate due to its very limited capability to withstand an adverse pressure gradient. This is the main reason why in wind-tunnel experiments the boundary layer is tripped to forced transition well ahead of the expected shock location.

The different types of separation phenomena as a consequence of the interaction of the shock with a turbulent boundary layer including various other aspects of the transonic flow over profiles and wings have been pointed out in several papers by H.H. Pearcey, e.g. in [11]. Recent reviews on the subject are also due to J.E. Greene [12], [13]. The two main models are depicted schematically in sketches ⓐ and ⓑ of Fig. 5. Flow model A postulates the existence of a separation bubble underneath the shock which is growing in extent towards the rear with increasing incidence i.e. with growing shock strength. The adverse pressure gradient over the rear part is not strong enough in this case to induce rear separation which is to be expected for relatively thin and lightly loaded airfoils. However, for the thicker and more highly loaded sections used in modern designs the pressure gradients in the rear subsonic flow are steeper so that flow model B with separation from the trailing edge is expected to exist. Mixed types of flows may exist according to Pearcey, Osborne and Haines [11] with a bubble at the shock location and rear separation. Model B type separation being essentially the analogue to the classical low speed turbulent trailing edge separation is very sensitive to the local pressure gradient, the boundary-layer thickness, and the upstream history of the boundary layer. Even without separation the interactions at the foot of the shock and at the trailing edge are locally strong as pointed out by J.E. Greene [13] and influence the overall flow behavior and hence the aerodynamic characteristics of the profile. Incipient rear separation also marks the onset of the very severe phenomenon of buffeting and it is of utmost practical importance to be able to predict the buffet boundaries as a function of Mach numbar and Reynolds number.

The above short description of examples of flows over single and multiple airfoils in the low speed range and the flow on an airfoil at high subsonic speeds may suffice to point out the eminent importance of the boundary layer in any flow situation. The extension of profile flow to the actual flow over wings with finite span, of course, must be taken into consideration in an actual design. However, the essential features of the boundary-layer development will not be changed radically by the inclusion of three-dimensionality as long as the aspect ratio of the wing remains large and the sweep angle in case of a swept wing is not too large, say less than 40°. The problem of assessing the aerodynamic characteristics of a finite wing from the knowledge of its sectional behavior has been treated by Küchemann [14] and reviewed by Hancock [5] and by Williams and Ross [15] with many pertinent references. Sine the aerodynamic characteristics of an aircraft are dominated by the properties of its lifting surfaces it seems justified to leave aside the problems associated with fuselage interference. The boundary-layer aspect of the attached flow over the fuselage and other aircraft components such as engine nacelles is primarily concerned with the reduction of drag at low lift cruise speeds assuming attached flow conditions. Therefore, in the following survey on boundary layer calculation methods essentially two-dimensional boundary layer flow is presupposed.

The purpose of boundary-layer calculations within the framework of the general objective of predicting the aerodynamic characteristics of a projected aircraft may be characterized as the ability (1) to positively define the state of flow i.e. to decide if attached flow exists or if regions of separated flow must be expected, and (2) to provide a quantitative measure of the effect that the boundary layer has on the aerodynamic characteristics i.e. to be able to calculate the friction drag, the reduction of lift and the change of moment as compared to the non-viscous flow condition.

The difficulties encountered in achieving the first task are concerned not so much with the calculation of the attached boundary layer in the laminar or turbulent state but with the reliability of criteria for predicting the onset and extent of transition and hence turbulent separation. It may easily be visualized that an inaccurate location of transition leads to wrong initial conditions for the calculation of the fully turbulent boundary layer and its characteristics including the location of possible turbulent separation even if the method applied is quite satisfactory otherwise. This is especially true in the case where transition takes place over a laminar-turbulent separation bubble. The second task above implies the use of advanced criteria exceeding the well-known Kutta-Joukowsky condition for the behavior of the external flow in the vicinity of the trailing edge. The treatment of the confluent boundary layers forming the wake in this region enters decisively into the subsequent recalculation of the entire inviscid flow field and is consequently responsible for the success in predicting the frictional drag and the reduction of lift due to the presence of the boundary layer. Thus, it must be realized that it is the combination of boundary layer calculation methods on the one hand and the utilization of adequate criteria of various types and at different stages in the computational process on the other hand which will determine the applicability and accuracy of a proposed overall prediction method.

In what follows an attempt is made to give a survey on existing boundary layer calculation methods while the various criteria needed to complete the overall prediction method will not be treated in any greater detail.

## 2. THE BOUNDARY-LAYER CONCEPT

The concept of the boundary layer as introduced by L. Prandtl [1] in 1904 consists in the realization, that the flow around a (more or less streamlined) obstacle such as an airfoil can be subdivided into two distinct regions: (1) the main flow in which velocity gradients are so small that the influence of the viscosity of the fluid may be disregarded completely, and (2) the thin layer in the immediate vicinity of the surface of the body in which the gradient of the velocity in main direction of the flow is so large that a viscous shear force according to Newton's friction law $\tau = \mu(\partial u/\partial y)$ is produced and must be taken into account. While in the main region of the flow (which for simplicity may be viewed to be two-dimensional steady and incompressible) the Navier-Stokes equation reduce to the frictionless Euler equations characterized by the absence of vorticity and therefore convertible to the Laplace potential equation. In the frictional region close to the wall, i.e. the boundary layer, the Navier-Stokes equations are reduced to Prandtl's boundary-layer equations.

Written in the simplest form, i.e. for a steady two-dimensional incompressible boundary layer the equations are:

(1) $$\frac{\partial u}{\partial x} + \frac{\partial v}{\partial y} = 0 \quad \text{(continuity equation)}$$

(2) $$u\,\frac{\partial u}{\partial x} + v\,\frac{\partial u}{\partial y} = -\frac{1}{\rho}\frac{dp}{dx} + \frac{1}{\rho}\frac{\partial \tau}{\partial y} \quad \text{(momentum equation).}$$

Equations (1) and (2) apply equally for laminar and turbulent boundary layers, if in the turbulent case the velocities u and v are understood as being time averaged mean quantities of the respective fluctuating velocities $u = \bar{u} + u'$ and $v = \bar{v} + v'$. The pressure-gradient term in Eq. (2) may be expressed by Bernoulli's equation as

(3) $$\frac{1}{\rho}\frac{dp}{dx} = -\,U(x)\,\frac{dU(x)}{dx} \quad ,$$

where $U = U(x)$ is the velocity-distribution of the main stream assumed as given just outside the boundary layer of thickness $\delta(x)$, as depicted in Fig. 6. The appropriate boundary conditions then are:

$$(4) \qquad y = 0:\ u = v = 0;\ \lim y \to \delta:\ u = U(x) \quad .$$

The shear stress $\tau = \tau(x,y)$ appearing in Eq. (2) formally as a third independent variable is expressed as

$$(5) \qquad \tau = \frac{\partial u}{\partial y}$$

in the laminar case, and by

$$(6) \qquad \tau = -\rho \cdot \overline{u'v'}$$

in the turbulent case, which in the boundary layer approximation is the so-called Reynolds shear stress or apparent turbulent stress as distinct from the Newton stress expressed by Eq. (5). For large Reynolds numbers, a necessary assumption when using boundary-layer theory, the Reynolds stress in fully developed turbulent flow exceeds the Newton stress generally by orders of magnitude. It is also usually assumed that the Reynolds stress is much larger than the turbulent normal stress which is an implication for Eqs. (1) and (2) above to be valid in this simple form.

For laminar boundary layers the known relation Eq. (5) for the shear stress with the constant molecular viscosity $\mu$ completes the set of partial differential equations (1) and (2). Therefore, together with the boundary condition, in principle, exact solutions of this system of equations are possible. The boundary-layer equations are of parabolic nature implying that the solution for the unknown variables $u$ and $v$ which are to be determined within the striplike domain between the body surface and the external flow region can be found by a stepwise marching procedure in the downstream direction. This means that the solution at a location $x$ is not influenced by conditions at a location downstream of $x$, the upstream conditions, however, affecting it very much generally. This property is often referred to as the boundary layer's memory capability for its upstream "history".

Exact solutions for the laminar boundary-layer equations have been obtained for a wide range of external pressure (or velocity) distributions of which the similarity solutions are especially important. In these cases the external velocity distribution

$$(7) \qquad U(x) \sim x^m$$

allows the system of partial differential equations (1) and (2) to be reduced to one ordinary differential equation by removing the x-dependence from the equations which results in "similar" velocity profiles for all x-stations (Falkner-Skan equation). These and other exact solutions of the laminar boundary-layer equations are fully described for example in the books of H. Schlichting [16] and L. Rosenhead [17]. The usefulness of exact solutions for the outer velocity distribution $U(x)$ according to Eq. (7) with continuously accelerated ($m > 0$) or continuously decelerated ($m < 0$) flows lies in the fact that they provide a good physical insight into the character of boundary-layer flows in general. Furthermore, approximate solution methods designed to be valid for the general case of a laminar layer with an arbitrary free-stream pressure distribution can be checked against these exact solutions. In fact, some of the approximate integral methods for the laminar case make direct use of the similarity velocity profile family gained by solution of the Falkner-Skan equation.

In order to formally complete the set of the partial differential equations (1) and (2) also for turbulent boundary layers, the Reynolds stress term in Eqs. (2) and (6) is often replaced by the semi-empirical relations known as the eddy-viscosity concept or the mixing-length concept of Prandtl. In the former case the Reynolds stress is required to assume the form

$$(8) \qquad -\rho\ \overline{u'v'} = \varepsilon \cdot \frac{\partial u}{\partial y} \quad ,$$

where $\varepsilon = \varepsilon(x,y)$, the turbulent exchange coefficient or eddy-viscosity, is not a constant but varies from point to point. With the mixing-length theorem the Reynolds stress is expressed by

$$(9) \qquad -\rho\ \overline{u'v'} = \rho \ell^2 \left|\frac{\partial u}{\partial y}\right| \cdot \frac{\partial u}{\partial y}$$

where the mixing length $\ell = \ell(x,y)$ is also an unknown function. The mixing length is interpreted as that distance which a turbulent fluid lump moves on the average in the y-direction before it is dissolved through a mixing process with other lumps and thus looses its identity. In a more modern interpretation the mixing length is assumed to be a characteristic length scale for the transport of turbulent energy. Usually it is tried to further break down the eddy-viscosity $\varepsilon$ or the mixing length $\ell$ and relate them by suitable empirical functional relationships to the lateral distance $y$ and the mean velocity and its derivatives. One such special assumption is von Kármán's similarity hypothesis

$$(10) \qquad \ell = K \cdot \left| \left(\frac{\partial u}{\partial y}\right) \Big/ \left(\frac{\partial^2 u}{\partial y^2}\right) \right|$$

where $K$ denotes an empirical constant. There has been much argument on the validity of the mixing-length and eddy-viscosity concepts from physical reasons (Bradshaw [18] and Rotta [19]). The most serious objection is that the Reynolds shear stress is related to local mean flow quantities only whereas it is actually influenced also by the turbulence transport mechanisme, i.e. it should be more closely connected to turbulent properties of the boundary-layer flow including upstream - or "history" - effects of this turbulent process. Mathematically, however, the shear stress term must be related ultimately to the local independent space variables $x$ and $y$ whatever the degree of sophistication of the physical model may be to achieve this.

## 3. ON THE STRUCTURE OF BOUNDARY LAYERS

Before going further in the description of the main features of the various boundary-layer calculation methods it seems appropriate to make some remarks on the structure of boundary layers. This is done again for two-dimensional incompressible boundary-layer flows giving the opportunity to recapitulate on the terminology used in boundary-layer theory.

### 3.1 Laminar Boundary Layers

As its denomination suggests a laminar boundary layer consists of a well-behaved flow of stratified laminae of fluid moving along the solid surface of a body, Fig. 7. Although there is a considerable momentum exchange between neighbouring streamlines through the action of viscosity which produces the shear forces the structure of the laminar boundary layer remains unaltered as long as it adheres to the wall. The thickness $\delta$ of the boundary layer is determined by the x-wise distribution of the external velocity U(x) just outside the boundary layer. In general the thickness $\delta$ increases with x ($\delta \sim \sqrt{Re_x}$ ; $Re_x = U \cdot x/\nu$ in laminar flat plate boundary layer where $U(x) = U_\infty$ = const.). Physically this is explained by the decelerating effect of the shearing forces on a lamina of fluid causing the adjacent lamina of higher velocity to be pushed outwards in the y-direction. As a net result of this action the outer flow is displaced somewhat away from the well. The displacement is quantitatively expressed as the defect of mass flow in the boundary layer as compared to the ideal mass flow in the absence of the boundary layer by

$$U\delta_1 = \int_0^\delta (U - u)\,dy \tag{11}$$

where here, for the incompressible case, the constant density $\rho$ could be dropped. $\delta_1$ then is the familar displacement thickness.

If the prescribed free stream velocity U(x) is increasing i.e. the pressure p(x) decreases in the streamwise direction x ($dp/dx < 0$) the boundary-layer thickness $\delta$ (and $\delta_1$) grows only very slowly. Much more interesting is the case of increasing pressure or adverse pressure gradient ($dp/dx > 0$) i.e. decreasing external velocity U(x). In this case the deceleration of the boundary-layer fluid becomes more pronounced. The boundary layer now quickly grows thicker and the velocity profile will soon show an inflexion point. The gradient $(\partial u/\partial y)_y$ at the wall, which is a measure for the local friction force exerted to the wall diminishes rapidly with persisting adverse pressure gradient. The eventual loss of all kinetic energy of a fluid particle adjacent to the wall under the combined influence of an increasing pressure and the shear forces leads to the stagnation of this particle. As a consequence the particles on a neighbouring streamline are forced to leave the surface and follow some path just above a dividing streamline which separates fluid coming from the upstream region from fluid that is, of necessity, being pushed in from downstream in a reversed flow. This is the phenomenon of boundary-layer separation. At the point of separation the dividing streamline intersects the wall at a finite small angle $\sigma$ determined by the relation

$$\mathrm{tg}\,\sigma = -3\,\frac{\left(\frac{d\tau_w}{dx}\right)_{x_S}}{\left(\frac{dp}{dx}\right)_{x_S}} \tag{12}$$

and the point of separation itself is determined by the condition that the velocity gradient normal to the wall vanishes there

$$\left(\frac{\partial u}{\partial y}\right)_{\substack{y=0\\x=x_S}} = 0 \quad \text{or} \quad \tau_w(x_S) = 0 \quad . \tag{13}$$

The appearance of an inflaxion point in the laminar boundary-layer velocity profile usually signalizes the inclinition of the boundary layer to be unstable against small disturbances, i.e. at a sustained adverse pressure gradient, $dp/dx > 0$, the boundary layer will turn into its transitional state. Transition of this boundary layer from a pure laminar state into the fully developed turbulent state takes place over some distance in the streamwise direction, this transition length being mainly dependent on the outer pressure variation, on the roughness of the surface, and on the turbulence level of the outer stream. The onset of transition is marked physically by the appearance of an irregular and intermittent sequence of laminar and turbulent regions (turbulent spots). The theoretical prediction of transition onset is the subject of boundary layor stability theory, the first remarkable success of which are connected with the names of W. Tollmien and H. Schlichting [20] who were able to calculate the critical local Reynolds number $Re = U\delta_1/\nu$ for neutral stability on a flat plate boundary layer. The streamwise location $x_i$ of this theoretical point of instability lies ahead of the actual region or point of transition. The transition point may be characterized to be that point in the streamwise direction at which the regular oscillations appearing downstream of the instability point suddenly break down and are transformed into irregular patterns of high frequency which are characteristic of the fully turbulent motion.

It is not intended to go any further into the details of boundary-layer transition. Critical reviews of the subject of boundary-layer stability and transition were given by Betchov and Criminale [21], and Obremski et al. [22]. However, some remarks in view of an actual prediction method seem to be appropriate. There still is no rational method in existence to accurately predict transition from laminar to turbulent boundary-layer flow. Most of the earlier boundary-layer calculation methods make use of the concept that transition takes plsce instantaneously at a transition point the location of which is taken as the point of minimum pressure or the point of instability which is determined roughly from correlation curves connecting the critical local Reynolds number based on the boundary-layer thickness with the local pressure gradient. In more refined methods the actual transition point is taken as being downstream of the instability point by an amount taken from an experimental correlation curve such as those of Granville [23] or Smith and Gamberoni [24], and the most advanced methods realise the fact that the transition from laminar to turbulent flow takes place over some finite surface distence. This is accomplished by slowly activating the turbulent eddy-viscosity $\varepsilon$ over a finite surface length as based on an intermittency factor proposed by Chen and Thyson [25] which accounts for the intermittent appearance of turbulent regions in the transition region.

The transition mechanism dealt with above was concerned with boundary layers which remain atteched during the transition process. As has been mentioned earlier transition may alternatively take place through the mechanism of a laminar separation bubble followed by turbulent reattachment. A basic review on this type of transition has been given by Teni [26]. Again the incorporation of criteria for a quantitative prediction of this type of transition relies heavily on experimentally observed correlation curves between bubble length, a suitable chosen pressure gradient coefficient, and the boundary-layer thickness at the point of laminar separation such as those given by Crabtree [27], Owen and Klanfer [28] and Gaster [29].

### 3.2 The Turbulent Boundary Layer

Let us now turn to a description of the main features of the fully developed turbulent boundary layer. It is characterized by the very vigorous mixing of fluid contained in it, where the velocity vector and other quantities like pressure, density and temperature (in the compressible case) fluctuate randomly with respect to space and time. Thus in a nominally two-dimensional turbulent boundary layer there is random motion also in the lateral direction. In contrast to the laminar boundary layer a single momentary observation in a turbulent boundary layer would never give a repeatable result. Consequently the turbulent boundary-layer flow can only be described in terms of statistical quantities. Therefore the quantities $u, v, \rho$ and $p$ in Eq. (1), as already mentioned are statistical mean quantities.

Despite the radically different internal structure of turbulent boundary layers their general behavior and development under the influence of the free stream velocity or pressure variation resembles much to that of a laminar boundary layer. With pressure decreasing in the x-direction the turbulent boundary layer grows slowly in thickness, although at a faster rate ($\delta \sim X^{4/5}$ as compared to $\delta \sim X^{1/2}$ in the laminar case for flat plate boundary layer) while in a persisting adverse pressure gradient flow it eventually will separate from the wall. However, with the very vigorous mixing action present in the turbulent boundary layer transfer of kinetic energy from the external flow is much greater than for laminar boundary layers resulting (1) in the fuller velocity profile u(y), (2) in the capability to endure much larger pressure gradients, and (3) in higher frictional drag forces on the wall.

Returning to the structure of the turbulent boundary layer, I do not intend to review the complicated theory of turbulence but I shall rather limit myself to the description of a generally accepted model of the turbulent boundary layer. For a full account of turbulence theory I may refer you to the recent publications by Bradshaw [18] and Rotta [19]. Figure 8 shows a sketch of the turbulent boundary layer which may be regarded as a momentary picture of the vortex-like or eddying motion, the mean velocity profile being also indicated. From this at first sight it would seem to be impossible to deduce any principle of order. However, as we know, the mean boundary-layer thickness grows in the streamwise direction which means that a permanent entrainment of originally non-turbulent high-energy fluid takes place. This capture of fluid from the free stream is achieved by tangential viscous shear forces acting along the distorted and "wiggling" but distinct boundary layer edge which has been named therefore the "viscous superlayer". The high energy is then transported to the inner parts of the boundary layer by the largest turbulent eddies of a size in the order of the mean thickness $\delta$ of the boundary layer which enables them to be in contact with the irrotational outer flow in the first place. The turbulent energy is then exchanged among the eddies of smaller size which are forming and disappearing constantly. It is assumed that eddies of all sizes are present but that eddies of widely different sizes have no direct influence on each other. An eddy of given size exchanges energy at an appreciable rate only with another eddy of nearly the same size. The energy exchange thus is comparable with a cascade process in which the biggest eddies lose energy to eddies one order of magnitude smaller, which lose energy to smaller eddies in their turn, and so on until the eddies are so small that they lose so much energy by direct action of viscous stress that no smaller ones can be formed so that at last all energy is converted into heat by direct viscous dissipation. The physical mechanism invoked for this cascade process is that of stretching of the eddies, which may be envisaged as line vortex elements, by the gradient of the mean velocity. Therefore the largest eddies can best interact with the mean flow as compared to small-sized eddies. Thus the large eddies whose lifetime is also large carry most of the turbulent energy and Reynolds stresses while the scale of the smallest eddies is determined by the magnitude of the molecular viscosity.

### 3.3 The Reynolds Stress Equation

It is now clear that the turbulent shear stress needed in the momentum equation, Eq. (2), is not likely to be determinable from consideration of mean flow properties only, such as the mean local velocity gradient as suggested by the eddy viscosity concept or the mixing length concept. For this reason turbulence research workers as Bradshaw and Rotta demand the use of transport equations which can be derived from the Navier-Stokes equations and by which the transport of any turbulent quantity such as the Reynolds stress $-\rho\overline{u'v'}$ or the turbulent kinetic energy $1/2\ \overline{q'^2} = 1/2\ (\overline{u'^2} + \overline{v'^2} + \overline{w'^2})$ can, in principle, be described. Since the Reynolds stress enters the boundary layer momentum equation directly, let us consider the appropriate transport equation. For a two-dimensional turbulent incompressible boundary $\rho = \text{const}$ we have:

$$\underbrace{u\frac{\partial \overline{u'v'}}{\partial x} + v\frac{\partial \overline{u'v'}}{\partial y}}_{\text{advection by mean flow}} + \underbrace{\overline{v'^2}\frac{\partial u}{\partial y}}_{\substack{\text{generation}\\ \text{by interac-}\\ \text{tion with}\\ \text{mean flow}}} - \underbrace{\overline{\frac{p'}{\rho}\left(\frac{\partial u'}{\partial y} + \frac{\partial v'}{\partial x}\right)}}_{\substack{\text{redistribution by}\\ \text{pressure fluctuations}}} + \tag{14}$$

$$+ \underbrace{\frac{1}{\rho}\frac{\partial \overline{p'u'}}{\partial y}}_{\substack{\text{transport by}\\ \text{velocity}\\ \text{fluctuations}}} - \underbrace{\nu\,\overline{(u'\nabla^2 v' + v'\nabla^2 u')}}_{\substack{\text{destruction by}\\ \text{viscous forces}}} = 0 \quad .$$

The physical meaning of the different terms is indicated.

Similary, the transport equation for the turbulent kinetic energy $\overline{q'^2/2}$ reads:

$$\underbrace{\frac{1}{2}u\frac{\partial \overline{q'^2}}{\partial x} - + \frac{1}{2}v\frac{\partial \overline{q'^2}}{\partial y}}_{\text{advection}} + \underbrace{\overline{u'v'}\frac{\partial u}{\partial y}}_{\text{production}} + \underbrace{\frac{\partial}{\partial y}(\overline{p'v'} + \frac{1}{2}\overline{q'^2v'})}_{\substack{\text{transport by}\\ \text{diffusion}}} + \underbrace{\varepsilon_d}_{\substack{\text{viscous}\\ \text{dissipation}}} = 0 \quad . \tag{15}$$

Also transport equations for other turbulent fluctuating quantities such as $\overline{u'^2}$, $\overline{v'^2}$ and $\overline{w'^2}$ can be derived which all have the same structure as the above equations (14) and (15). To make these equations soluble one must represent the individual terms by empirical functions of the Reynolds stress. This is what is often referred to as "modelling" or "closure" of the transport equations.

It is not my intention to go any further into the details of modelling the turbulent transport equations. I just wanted to indicate the general feature of this approach to complete the momentum equation, Eq. (2), by introducing additional partial differential equations pertaining to the Reynolds stresses instead of purely empirical formulae. However, I would like to draw your attention to one point. For high Reynolds number boundary layers the assumption can be made that in the transport equation for the turbulent energy, Eq. (15), the production of energy is equal to the dissipation, with all other terms negligibly small. This means that whatever amount of turbulent energy is produced by the large size eddies and transferred from big to small eddies will be dissipated by viscous action eventually. The controlling parameter then is the production term, and energy dissipation is independent of viscosity. Then $\varepsilon_d$ in Eq. (15) can be expressed by the relation

$$(16) \qquad \varepsilon_d = c \cdot \left(\frac{\overline{q'^2}}{2}\right)^{3/2} \cdot \frac{1}{L} \quad ,$$

where L is a length scale of the big eddies and c is a dimensionless proportionality factor. With the additional assumption made by P. Bradshaw [30] that the ratio of the Reynolds shear stress to the turbulent energy is constant, i.e.

$$(17) \qquad -\overline{u'v'} = a \cdot \overline{q'^2} \qquad (a = \text{const.}) \quad ,$$

and equating $\varepsilon_d$ from Eq. (16) with the production term from Eq. (15) one arrives at the expression

$$(18) \qquad -\overline{u'v'} = c_1^2 \cdot L^2 \cdot \left(\frac{\partial u}{\partial y}\right)^2$$

with $c_1^2 = (2a)^3/c^2$. This relation is identical with Eq. (9) for the mixing length concept, if $\ell = c_1 \cdot L$. The derivation of the mixing length formula from the transport equation for the turbulent kinetic energy, Eq. (15), seems somewhat artifical, it shows however that the required information on the Reynolds stress can be obtained from these equations which relate one turbulent quantity to another turbulent quantity, as in Eq. (17), and that under special assumptions the same relation is retrieved which originally has been an hypothesis. In the case of high Reynolds number boundary layers the mixing length formula turns out, indeed, to be a good approximation. For other cases of thin shear layers as the turbulent wake or jet flow it might not be so adequate (see [18], [18a] and [19]). Calculation methods which are based on the system of partial differential equations embracing both, those for the mean flow velocities, Eqs. (1) and (2), and those for the transport of turbulent quantities such as the Reynolds stress, Eq. (14), and the turbulent kinetic, Eq. (15) are called turbulence field methods. Some of these methods will be listed later.

### 3.4 The Two-Layer Model

Having recognized the usefulness of the mixing length concept it is appropriate to recapitulate its consequences on the boundary layer velocity profile. In the case of incompressible two-dimensional flow over a smooth surface and in the absence of strong x-wise pressure gradients, the shear stress is almost independent of distance from the surface and equal to the wall shear stress $\tau_w$. For the mixing length $\ell$, being a measure for the size of the eddies in the vicinity of the wall, the reasonable assumption is made that it is proportional to the distance y from the wall,

$$(19) \qquad \ell = K\,y \quad .$$

Introducing this into the mixing length formula, Eq. (9), one has

$$(20) \qquad \sqrt{\frac{\tau_w}{\rho}} = K\,y\,\frac{\partial u}{\partial y} = u_\tau \quad ,$$

which integrates to the familiar logarithmic velocity profile

$$(21) \qquad \frac{u}{u_\tau} = \frac{1}{K}\ln\left(\frac{y \cdot u_\tau}{\nu}\right) + C \quad ,$$

where K = 0.4 is the v. Kármán constant, and C = 5.0 is an integration constant determined from experiment. In Eq. (20) $u_\tau$ is the so-called shear stress velocity, being introduced as a convenient measure of the constant wall shear stress $\tau_w$. The range of validity of the law-of-the-wall, Eq. (21), extends from about 1 to 2 % of the mean total thickness $\delta$ (see Fig. 8). The usual representation of the law-of-the-wall velocity distribution is that in a semi-logarithmic plot as in Fig. 9a, which shows the velocity distribution $u/u_\tau$ according to Eq. (21) together with experimental results according to Coles [31].

The narrow region from y = 0 at the wall to about 0.2 % of $\delta$ is not included in the velocity distribution of the law-of-the-wall. In this region the turbulent eddy motion is more or less damped out as a consequence of the adherence condition u(0) = 0. This very thin layer is essentially laminar and it must carry the constant shear stress $\tau_w$ as a laminar shear stress to the wall very much like a Couette flow between a stationary and a moving parallel wall. The distribution of velocity in this viscous sublayer is accordingly a linear one

$$(22) \qquad \frac{u}{u_\tau} = \frac{u_\tau y}{\nu} \quad ,$$

which is shown also in Fig. 9a. A continuous single function for the velocity distribution $u/u_\tau$ extending right from the wall y = 0 which comprizes the linear relation, Eq. (22), as well as the logarithmic part according to Eq. (21), can be achieved by modifying the linear relation for the mixing length, Eq. (19), as suggested by van Driest [32]

$$(23)\qquad \ell = K\, y \left[1 - \exp\left(-\frac{y u_\tau}{A \nu}\right)\right] \quad ,$$

where the empirical value A = 26 gives good agreement with experiment.

The outer portion of the boundary layer, which extends from about $y = 0.2\cdot\delta$ up to the outer edge $y = \delta$ (see Fig. 8) does not obey the law of the wall. This is best seen by replotting in Fig. 9b the curves of Fig. 9a to show the velocity defect $(U - u)/u_\tau$ as a function of the wall distance $y/\delta$, where $\delta$ is taken to be that point for which $u/U = 0.995$. Also shown is the law-of-the-wall curve as the straight line in this semi-logarithmic graph. Comparing the experimental data with the logarithmic law one observes first that they deviate from it appreciably in the region $0.2 < y/\delta < 1$, and second that the experimental curves for the two different Reynolds numbers fall together into one single curve. For this behavior of the outer portion of the turbulent boundary layer D. Coles [33] has developed his wake model also called the law-of-the-wake. Under this concept the whole boundary layer is visualized essentially as a turbulent half-wake flow which is constrained by a wall. The wake-like behavior is apparent from the intermittent character of the outer boundary layer where, at a fixed distance $y/\delta \le 1$, turbulent flow is alternating with rotation-free flow. Furthermore the outer velocity profiles are quite sensitive to external pressure gradients dp/dx. On the other hand, the logarithmic inner part of the boundary layer is almost completely defined by the magnitude of the wall shear stress $\tau_w$ appearing as the shear stress velocity $u_\tau = \sqrt{\tau_w/\rho}$ in the velocity distribution, Eq. (21).

From this idea of two distinct scales determining the turbulent boundary layer flow Coles developed a two-parametric standard representation of the velocity distribution by extending the logarithmic part to include an additional wake part.

$$(24)\qquad \frac{u}{u_\tau} = \frac{1}{K} \ln\left(\frac{y\cdot u_\tau}{\nu}\right) + C + \frac{\Pi}{K}\cdot w\left(\frac{y}{\delta}\right) \quad ,$$

where $w(y/\delta)$ is Coles' wake function which may be approximated by either of the two following equations

$$(25)\qquad w\left(\frac{y}{\delta}\right) = w(\eta) = 1 + \sin\left[\frac{\pi}{2}(2\eta - 1)\right]$$

or

$$(26)\qquad w(\eta) = 2 \sin^2\left(\frac{\pi}{2}\,\eta\right) \quad .$$

In Eq. (24) $\Pi$ is a new parameter which will determine the magnitude of the wake-part and which is dependent strongly on the streamwise pressure gradient. In Fig. 10 the composition of a complete boundary-layer profile is illustrated.

The standard two-layer velocity-profile representation in the form of Eq. (24) plays an important role in the boundary layer calculation methods which are based on the integrated form of the boundary layer equations. Thus e.g., on putting u = U, the free-stream velocity, and $y = \delta$ the local friction law is obtained in the form

$$(27)\qquad \frac{U}{u_\tau} = \frac{1}{K} \ln\left(\frac{\delta u_\tau}{\nu}\right) + C + \frac{2}{K}\,\Pi \quad .$$

Given the constants $K = 0.4$, $C = 5.0$ (for a smooth wall), and the kinematic viscosity $\nu$ as well as the local free stream velocity $U = U(x)$ the last equation determines any one of the three parameters $u_\tau$, $\delta$, and $\Pi$ if the other two are known. For instance, the local skin friction parameter

$$(28)\qquad c_f = \frac{\tau_w}{\frac{\rho}{2} U^2} = 2\left(\frac{u_\tau}{U}\right)^2$$

is expressible by Eq. (27) as a two-parametric function

$$(29)\qquad c_f = c_f\left(\delta, \Pi\right) = c_f\left(H_{12}, Re_{\delta 2}\right) \quad .$$

Just as we replaced here the wall shear velocity $u_\tau$ by the local skin friction parameter one may replace also $\delta$ and $\Pi$ by suitable other form parameters, as indicated in Eq. (29). The most commonly used form parameters are the thickness ratio $H_{12} = \delta_1/\delta_2$ and the local Reynolds number $Re_{\delta 2} = \delta_2 \cdot U/\nu$ based on the momentum thickness $\delta_2$.

Since we have derived the law-of-the-wall, Eq. (21), for the inner boundary-layer region from the mixing-length concept one might expect that also the outer region can be adequately described by it. This is indeed possible if one assumes the mixing length to be constant, i.e.

$$(30)\qquad \ell = \lambda \cdot \delta$$

where $\lambda = 0.09$ is a constant. This constant mixing layer assumption was applied to the case of plane turbulent mixing layer of a uniform flow over a region of quiescent fluid by W. Tollmien [34] and by Spalding and Patankar [35]. Properly scaled the solution for velocity distribution is almost identical with Coles wake function giving strong support to the applicability of using the constant mixing layer concept to the outer part of the turbulent boundary layer.

Equally it has been shown by application in boundary layer calculation methods (e.g. by Cebeci-Smith [36]) that also the use of the eddy-viscosity concept according to Eq. (8) results in an adequate representation of turbulent boundary layers. Noting from Eqs. (8) and (9) that $\varepsilon$ can be expressed in terms of mixing length as

(31) $$\varepsilon = \rho \ell^2 \left|\frac{\partial u}{\partial y}\right| \quad ,$$

this is not surprising from the discussion above on mixing length. Again the algebraic expressions for the eddy viscosity will differ in two regions of the boundary layer. For the inner wall layer the eddy viscosity is usually taken to be that resulting from Eq. (31) with the mixing layer $\ell$ varying linearly with distance from the wall as given in Eq. (19) or with the van Driest extension as given in Eq. (20). Thus the eddy viscosity formulation for the inner region of an incompressible boundary layer is

(32) $$\varepsilon = \rho\, K^2\, y^2 \left[1 - \exp\left(-\frac{y\, u_\tau}{A\, \nu}\right)\right]^2 \frac{\partial u}{\partial y} \quad .$$

For the outer region the eddy viscosity is taken to be a local constant of the form

(33) $$\varepsilon = k \cdot \rho\, U(x) \cdot \delta_1(x)$$

where the constant $k = 0.0168$, $U$ and $\delta_1$ are the local values of the free-stream velocity and the displacement thickness.

## 4. BOUNDARY LAYER INTEGRAL EQUATIONS

In the foregoing paragraph some aspects of the structure and general behavior of boundary layers in two-dimensional incompressible flow have been discussed. The starting point has been the system of partial differential equations, Eqs. (1) and (2), which form the basis for the so-called direct calculation methods using some finite difference computational procedure. These methods have become feasible only through the use of high-speed computers with appreciable memory capacity. Because of the difficulty of solving partial differential equations without a computer the methods developed earlier, especially those for airfoil boundary-layer calculations are based on the integral relationships that can be obtained from the basic equations (1) and (2). Since these so-called integral methods are, and will persist to be in use, it is proposed to briefly outline their main features.

A general way of obtaining integral relations (see e.g. Thompson [37]) is to multiply the boundary layer momentum equation, Eq. (2), by the product $u^m y^n$ ($m,n = 0,1,2,3\ldots$) and to integrate over the distance $y$ from the wall to the boundary layer edge. The velocity component $v$ is eliminated by means of the continuity equation, Eq. (1), beforehand. A doubly infinite family of ordinary differential equations (depending on the integer values for $m$ and $n$) are formally obtained called the moment-of-momentum equations. In general only the first two members of this family are used in calculation methods. Omitting all the mathematical manipulations of their derivation, these are

(34) $$\frac{d\delta_2}{dx} + (H_{12} + 2)\,\frac{\delta_2}{U(x)}\,\frac{dU(x)}{dx} = c_f$$

the momentum integral equation ($m = 0, n = 0$) and

(35) $$\frac{d\delta_3}{dx} + 3\,\frac{\delta_3}{U(x)}\,\frac{dU(x)}{dx} = c_D$$

the kinetic energy integral equation ($m = 1$, $n = 0$), with the following definitions (including $\delta_1$ from Eq. (11))

(36a) $$\delta_1 = \int_0^\infty (1 - u/U)\, dy;$$ (displacement thickness)

(36b) $$\delta_2 = \int_0^\infty (u/U)\,(1 - u/U)\, dy;$$ (momentum thickness)

(36c) $$\delta_3 = \int_0^\infty (u/U)\left[1 - (u/U)^2\right] dy;$$ (energy thickness)

(37a) $$H_{12} = \delta_1/\delta_2 \quad (= H)$$

(37b) $$H_{32} = \delta_3/\delta_2 \quad (= H^+)$$

(37a), (37b): (shape factors or form parameters)

(38a) $$c_f = \frac{\tau_w}{\frac{1}{2}\rho U^2}$$ (skin friction coefficient)

(38b) $$c_D = \frac{2}{U^3}\int_0^\infty \left(\frac{\tau}{\rho}\,\frac{\partial u}{\partial y}\right) dy$$ (energy dissipation coefficient) .

With the definition of the local Reynolds number based on momentum thickness

(39) $$Re_{\delta 2} = \frac{\delta_2 \cdot U}{\nu}$$

the momentum integral equation (34) can also be written as

(40) $$\frac{d\,Re_{\delta 2}}{dx} + (H_{12} + 1)\,\frac{Re_{\delta 2}}{U}\,\frac{dU}{dx} = \frac{U}{\nu}\,\frac{c_f}{2}$$

In the laminar case the velocity distribution in the boundary layer can be represented by a polynomial of the form

(41) $$\frac{u}{U} = a\eta + b\eta^2 + c\eta^3 + d\eta^4 \quad (0 \leq \eta = \frac{y}{\delta} \leq 1) \quad ,$$

as used in the Kármán-Pohlhausen method, which when introduced into the definitions (36a), (36b), (37a) and (38a) and into the momentum integral equation (34) finally results in the single ordinary differential equation

(42) $$\frac{d(\delta_2^2/\nu)}{dx} = \frac{1}{U(x)} \cdot F(\kappa) \quad ,$$

which can be solved for a given free-stream velocity distribution $U(x)$. In Eq. (42) $F(\kappa)$ is an algebraic function sometimes called the auxiliary function. A linear approximation for this function is

(43) $$F(\kappa) = a - b \cdot \kappa \; (a = 0.47, \;\; b = 6) \quad ,$$

which, when inserted into Eq. (42), allows a simple quadrature giving the well-known formula

(44) $$\delta_2^2(x) = \frac{0.47 \cdot \nu}{U^6} \int\limits_{x=0}^{x} U^5\, dx$$

applicable for the approximate calculation of laminar boundary layers.

The reason for reviewing this Kármán-Pohlhausen laminar method (for details see H. Schlichting [16]) is to point out that the momentum integral equation (34) can be solved with the help of one additional auxiliary function $F(\kappa)$, the argument $\kappa$ of which can easily be represented as a function of $H_{12}$ and $c_f$. This pattern for a solution procedure is seen to be followed in almost all integral methods, also in the turbulent case. However, the auxiliary relation needed usually is not an algebraic function but an ordinary differential equation of the form

(45) $$\delta_2\,\frac{dH_{12}}{dx} = f_1\left(H_{12},\, Re_{\delta 2},\, \frac{\delta_2}{U}\,\frac{dU}{dx}\right) \quad .$$

An equation of this kind will account for the second term in Eq. (34). The only unknown left then is the local skin friction coefficient $c_f$. Fortunately this can be related to the local velocity profile quite accurately by means of a relationship of the general form

(46) $$f_2\left(c_f,\, Re_{\delta 2}\right) = 0 \quad ,$$

of which Eq. (27) in connection with the standard turbulent two-layer model would be an example. Other well-known examples are the empirical skin-friction formulae by Ludwieg and Tillmann 38

(47) $$c_f - 0.246 \cdot 10^{-0.678 \cdot H_{12}} \cdot (Re_{\delta 2})^{-0.268} = 0$$

and by Squire and Young [39]

(48) $$c_f - 0.0576 \cdot \left[\log\,(4.075 \cdot Re_{\delta 2})\right]^{-2} = 0 \quad .$$

Note that in the last formula any dependence of $c_f$ on $H_{12}$ is neglected, which will lead to too large values of $c_f$ near separation of the boundary layer.

The auxiliary equation of the type of Eq. (45) need not have $H_{12}$ as the main dependent variable. There are other shape factors in use such as the energy thickness ratio $H_{32}$ defined by (37b). If $H_{32}$ is to be used, then the auxiliary equation is derived from equation (35) for the integral mean kinetic energy. This approach seems to have been particularly favoured by German research workers such as Truckenbrodt [40], Walz [41], and Rotta [42]. By combining Eq. (35) with Eq. (34) the appropriate auxiliary equation is obtained in the form

(49) $$\delta_2\,\frac{dH_{32}}{dx} = (H_{12} - 1)\, H_{32}\,\frac{\delta_2}{U}\,\frac{dU}{dx} + c_D - \frac{1}{2}\, H_{32} \cdot c_f \quad ,$$

where for the dissipation coefficient $c_D$, defined in (38b), different empirically established relations can be used. An early suggestion by Truckenbrodt [40] is

(50) $$c_D = 0.0112 \cdot (Re_2)^{\frac{1}{6}} \quad .$$

It is based on the evaluation of a number of non-equilibrium boundary layers. A more refined relation is one which can be derived from Eqs. (34) and (35) assuming the magnitude of $H_{32}$ to be independent of x (see Rotta [43])

$$c_D = \frac{1}{2}\, c_f \cdot H_{32} \left(1 + \frac{H_{12}-1}{H_{12}} \cdot \beta\right) \quad . \tag{51}$$

Here $\beta$ is the so-called equilibrium parameter and is implicitly related to $H_{12}$ by a formula suggested by Nash [44]

$$\frac{H_{12}-1}{H_{12}\sqrt{c_f/2}} = 6.1 \cdot \sqrt{\beta + 1.81} - 1.7 \quad . \tag{52}$$

Using Eq. (47) for $c_f$, $c_D$ can be calculated as a function of $H_{12}$ and $Re_{\delta 2}$ thus completing the system of the two ordinary differential equations, Eq. (34) and Eq. (49), which then can be solved simultaneously by a Runge-Kutta procedure delivering as output all interesting boundary layer parameters such as $c_f$ and $\delta_1$.

Another relatively modern approach is that introduced by Head [45] in his famous entrainment method. Head departs from the continuity equation (1) which on integration over y from $y = 0$ to $y = \delta$ and using the definition for displacement thickness, Eq. (36a), gives

$$\frac{d}{dx}\left[U\,(\delta - \delta_1)\right] = v_e = U \cdot c_E\,(H_1) \tag{53}$$

where $v_e$ is the normal velocity (in y-direction) at the nominal outer edge of the boundary layer, also called the entrainment rate, and $H_1$ is a new form parameter defined as

$$H_1 = \frac{\delta - \delta_1}{\delta_2} \quad . \tag{54}$$

The physical interpretation of Eq. (53) is that the mass flow in the turbulent boundary layer is a function of the large scale eddies, characterized by the length scale $\delta - \delta_1$ referenced to the momentum thickness $\delta_2$. The form parameter $H_1$ is correlated to the usual form parameter $H_{12}$ by the empirical relationship

$$H_1 = 1.535\,(H_{12} - 0.7)^{-2.715} + 3.3 \quad , \tag{55a}$$

while the funtional form of the entrainment rate coefficient $c_E$ is taken to be

$$c_E = 0.0306\,(H_1 - 3)^{-0.653} \quad . \tag{55b}$$

Both, Eq.(55a) and Eq.(55b) are curve fits of Head's original charts for $c_E$ and $H_1$ as gained from experiments. It is interesting to note that the entrainment equation (53) can be brought into the general form of the auxiliary equation (45) giving, with the help of Eq. (34),

$$\delta_2 \frac{dH_{12}}{dx} = U \frac{dH_{12}}{dH_1} \quad c_E - H_1 \frac{1}{U} \frac{d}{dx}\,(U\,\delta_2) \quad . \tag{56}$$

With Head's method very good results are obtained for airfoil-type boundary-layer flows predicting also separation quite well. The method was improved more recently by Head and Patel [46] whereby the development of $H_{12}$ with x conforms better to flows with high shear stress, i.e. high entrainment rates and to decelerating flows in strong adverse pressure gradients.

The integral methods mentioned so far are all based on empirical relationship between local quantities at one given station x, taking account of the upstream history only through the auxiliary equation which physically provides a measure for the deformation of the velocity profile as it develops with x. Turbulence properties enter the equation only through empirical information on the skin friction, for example Eqs. (47) and (48), and the dissipation coefficient, Eqs. (51) and (52), and these are connected to local mean flow properties. From what has been discussed in the previous chapter on the need for using the turbulence transport equations in order to adequately describe the history effects, when using complete (differential) methods, it appears necessary to also incorporate turbulence transport equations in integral methods.

This has been attempted by several authors, e.g. McDonald and Camarata [47], Hirst and Reynolds [48] with the most recent development, I know of, by J.E. Green et al. [49]. All these methods start out by considering the transport equation for turbulent kinetic energy, Eq. (15), to gain an additional ordinary differential equation that will describe the streamwise change of the turbulent shear stress. The approach to achieve this, however, is quite different for the references just quoted. In [47] the turbulent kinetic energy transport equation is used in an integrated form yielding an equation which governs the variation of the mixing-length distribution in the x-wise direction. The two other integral equations used are the momentum integral equation, Eq. (34) and a y-moment-of-momentum integral equation ($m = 0$, $n = 1$).

Hirst and Reynolds [48] also use the integral turbulent kinetic energy equation as a starting point and, by an assessment of the relative importance of the terms contained in it, arrive at a relatively simple equation for the turbulent energy balance in the outer region of the boundary layer, i.e. balance between the net downstream convection of turbulent energy and the turbulent energy locally supplied to the outer layer form the inner region near the wall,

$$\frac{d}{dx}\left(\frac{1}{2}\,Q^2 \cdot I\right) = \text{const} \cdot u_\tau \cdot Q^2 \tag{57}$$

where the integral quantities Q and I are defined as

$$Q^2 = \frac{1}{I} \int_0^\delta u\,\overline{q'^2}\,dy \quad , \tag{58}$$

and

$$I = \int_0^\delta u\,dy = U\,(\delta - \delta_1) \tag{59}$$

By postulating that the entrainment rate $v_e = dI/dx$ according to Eq. (53) is linearly related to the square root of the turbulent kinetic energy an ordinary differential equation for the entrainment rate is obtained from Eq. (57)

$$\frac{d}{dx}\left(\frac{v_e^2}{2}\cdot I\right) = K_1 \cdot u_\tau\, v_e^2 \tag{60}$$

where $K_1 = 0.14$ is an empirical constant. Thus this "turbulence model equation", Eq. (60), the entrainment equation, Eq. (53), and the momentum integral equation (34) together with Eq. (27) as a matching condition, form the system of ordinary differential equations to be solved.

In the new method of Green et al. [49] consideration of the turbulent kinetic energy equation starts out from its differential form as used originally by Bradshaw, Farris and Atwell [50] in their famous finite difference method. By again assessing all terms an ordinary differential equation for the maximum shear stress occuring within the boundary layer is derived. By invoking also a universal relationship between the $c_f$-value of this maximum shear stress and $c_E$, an ordinary differential equation is obtained

$$\delta_2\,(H_1 - H_{12})\,\frac{dc_E}{dx} = F\quad c_E,\ c_f,\ \frac{\delta_2}{U}\,\frac{dU}{dx} \tag{61}$$

called the "lag equation" which is a rate equation for the entrainment coefficient $c_E$. The use of Eq. (61) requires some additional empirical relations for $H_1$ as a function of $H_{12}$ and $c_f$ as function of the friction coefficient $c_{fo}$ for the flat plate boundary layer as well as some empirical formulae for the equilibrium values of $c_E$ and $(\delta_2/U)\,dU/dx$. The joint solution then of the momentum integral equation (34), the entrainment equation in the form of Eq. (56) and the above lag equation (61) completely determines the development of the boundary layer. This method was extended to wakes which seems to make the method especially attractive for the aircraft aerodynamicist. Green's report [49] also contains the complete scheme of the calculation procedure for the compressible case.

Another assumption to include the history affect is due Rotta [43]. The reasoning is that the dissipation coefficient $c_D$, needed in the energy integral equation (35) when this is used as the auxiliary equation, does not immediately react to changes of the turbulent velocity profile and of the pressure gradient. To account for this relaxation effect $c_D$ as calculated at station $x$ is considered to be the effective value for the downstream station $x + \Delta x$. The lag length $\Delta x$ is assumed to be four times the local boundary-layer thickness $\delta$. This assumption is plausible in as far as this distance corresponds roughly to the decay length of a turbulent eddy. Substantial improvement could be achieved by this simple principle.

## 5. CLASSIFICATION OF CALCULATION METHODS

From the discussion in the preceding section a classification on the existing boundary layer calculation methods can be inferred. Table 1 summarizes schematically the procedure for a boundary layer calculation. The problem at hand must be properly defined: (1) by the general flow characteristics, i.e. the undisturbed free-stream velocity and the Reynolds number based on a characteristic length scale, (2) by the initial conditions for a wall surface point from which the calculation is to be started, and (3) by the boundary conditions, the most important of which is the given velocity or pressure distribution at the outer edge of the boundary layer as obtained by potential theory. The desired result is the determination of all boundary layer parameters, as indicated, of which, from the engineering point of view, the skin friction coefficient $c_f(x)$ and the displacement thickness $\delta_1(x)$ are the most important ones. Equally important is the prediction of the locations of the transition point $x_t$ and the separation point $x_S$ which may be laminar or turbulent.

| | | | |
|---|---|---|---|
| Problem definition: (Input) | General flow characteristics<br>$U_\infty$, $L$, $\nu$, Re | Initial conditions:<br>at $x = x_o$<br>$u = u(y)$; $\delta$, $\delta_1$, $\delta_2$, $H_{12}$ | Boundary conditions<br>at $y = 0 : u = v = 0$<br>at $y = \delta : U(x)$ or $p(x)$ |
| Result (Output) | 1.) Solution at all $x > x_o$ for:<br>Velocity profile $u(x,y)$<br>Boundary layer thickness: $\delta, \delta_1, \delta_2, \delta_3$<br>Skin friction: $c_f$<br>Form parameters: $H_{12}$, $H_{32}$ | 2.) Prediction of<br>Transition point $x_t$ or transition-zone<br>laminar separation point: $x_{lS}$<br>turbulent separation-point: $x_{tS}$ | if existent |
| Solution procedure | Complete Field Methods: | Integral Methods: | |
| Mathematics | Numerical solution of the partial differential equations for continuity and momentum | Numerical solution of coupled ordinary differential equations for momentum integral and appropriate form-parameters | |
| Physics on | Reynolds stress $-\rho\,\overline{u'v'}$ | Skin friction $c_f$<br>energy dissipation integral $c_D$<br>entrainment $c_E$ | |

Table 1: Boundary layer calculation scheme

| | | | | |
|---|---|---|---|---|
| Mathematics | Numerical solution of the partial differentiel equations of continuity and momentum by finite difference procedures | | | |
| Physics | Derivetion of the Reynolds shear stress $-\rho\ \overline{u'v'}$ coupled to characteristics of the | | | |
| | Mean flow field. Reynolds stress determined by empirical algebraic reletions for | | Turbulence field. Reynolds stress determined from differential transport equations for | |
| | Eddy viscosity | Mixing length | Eddy viscosity | turbulent kinetic energy |
| Assumptions | $-\rho\ \overline{u'v'} = \underline{\varepsilon} \cdot \frac{\partial u}{\partial y}$<br>$\varepsilon = \varepsilon(y)$ et $x$=const | $-\rho\ \overline{u'v'} = \rho \underline{\ell}^2 \left(\frac{\partial u}{\partial y}\right)^2$ | $\underline{\varepsilon} = \varepsilon\ (x,y)$ | $-\rho\ \overline{u'v'} = k \cdot \overline{\underline{q}'^2}$ or<br>$-\rho\ u'v' = k \cdot \sqrt{\overline{\underline{q}'^2}}\,\ell\ \frac{\partial u}{\partial y}$ |
| Authors (representative) | Mellor-Herring [51]<br>Cebeci-Smith [36] | Spalding-Patankar [35] | Nee-Kovasznay [52] | Bredshaw-Ferris 50<br>Beckwith-Bushnell 53 |

Table 2: Complete Field Methods

In order to perform a boundary layer calculation one must decide on the calculetion method to be used. A gross criterion for distinction between the calculation methods is given by the mathematical solution procedure, i.e. wether one uses a so-called Complete Field Method or an Integral Method. The former involves the numerical solution of the partial differential equation for continuity and momentum directly while the latter embraces the numerical solution of ordinary differential equations for the momentum integral and some suitable form parameter. In laminar boundary-layer calculations the direct methods need no further input since the stress term $\partial\tau/\partial y$ is uniquely defined by Newtons law $\tau = \mu(\partial u/\partial y)$. In integral methods, however, some empirical information on the velocity profiles to be inserted and the laminar wall shear stress $\tau_w$ is needed usually being supplied from local similarity conditions as obtained from exact laminar solutions. For turbulent boundary layers both methods need empirical input concerning the turbulent or Reynolds shear stress in the direct methods and concerning the skin friction coefficient, the energy dissipation integral, and the entrainment coefficient in the integral methods.

As has been pointed out previously a second distinction between methods may be made by asking wether this empirical information is obtained from consideration of mean field quantities or from consideretion of the turbulence quantities. This criterion will then again divide each type of methods (complete or integral) into two branches. For the complete methods table 2 indicates this distinction. Eddy viscosity and mixing length methods normally are based on empirical expressions for $\varepsilon$ and $\ell$ in which mean field quantities such as the derivatives of the mean velocity are appearing (see Eqs. (23) and (32), (33)). The second group of complete methods utilizes turbulence transport equations for the determination of the Reynolds stress. Transport equations may be formulated for eddy viscosity $\varepsilon$ as for example in the Nee-Kovasznay method or, more usually for the turbulent kinetic energy $q'^2$ which then necessitates a postulated relation connecting this quantity to the Reynolds stress. Two such relations are stated in table 2. The last row of the table lists the origin of some methods representative for the different treatment.

In table 3 a tentative survey on the integral methods is made. The empirical input concerning the physics of turbulence consists of correlation function for the skin friction coefficient $c_f$, the integral

| | | | | |
|---|---|---|---|---|
| Mathematics | Numerical solution of coupled ordinary differential equations for the momentum integral and one or more form parameters | | | |
| Physics | 1.) Correlations between integral properties:<br>$c_f = c_f\left(H_{12}, Re_{\delta 2}\right)$; $c_D = c_D\left(c_f, H_{32}\right)$; $c_E = c_E\left(c_f, H_1\right)$<br>2.) Auxiliary differential equations for form parameter H:<br>$\delta_2 \frac{dH}{dx} = F\left(\frac{\delta_2}{U}\frac{dU}{dx}, H, Re_{\delta 2}, c_X\right)$<br>where: $H = H_{12}, H_{32}, H_1$ and $c_X = c_f, c_D, c_E$ | | | |
| Auxiliary equation developed from | mean flow integral equation for<br>energy | entrainment | moment of momentum | turbulent property equations for kinetic energy |
| Assumptions concerning | $c_D$ | $c_E$ | $c_f$ ($\varepsilon$ or $\ell$)<br>$c_D$ ($\varepsilon$ or $\ell$) | $\overline{q'^2}$, $\varepsilon_d$, $c_D$, $c_E$ |
| Authors (representative) | Truckenbrodt [40]<br>Rotta [43]<br>Walz-Geropp-Felsch [54]<br>Alber [55]<br>Zwarts [56] | Head-Patel [46]<br>Michel-Quémard [57] | McDonald [47]<br>Nash-Hicks [58]<br>Herring-Mellor [51] | Hirst-Reynolds [48]<br>Green et al. [49]<br>(history effects from the turbulence field) |

Table 3: Integral Methods

energy dissipation coefficient $c_D$, and for the entrainment coefficient $c_E$. Furthermore, an auxiliary ordinary differential equation for the development of a typical form parameter H is needed, the functional form of which depends on the empirically based correlations between the pressure gradient parameter $(\delta_2/U)(dU/dx)$, the form parameter H being considered, the local Reynolds number $Re_{\delta 2}$ and one at the coefficients $c_f$, $c_D$ or $c_E$. One may now make a distinction between methods in which all correlation functions used in the auxiliary equation are developed from mean flow integral equations or from equations for a turbulent property. Thus, if the integral energy equation is used this involves assumptions on the functional relationship of the dissipation coefficient $c_D$ with the form parameter $H_{32}$ while with integrated continuity equation an assumption for the functional relationship between the entrainment rate $c_E$ and the form parameter $H_1$ is needed. In this category of methods are also included those methods which utilize integrated forms of higher moments-of-momentum where it is possible to incorporate algebraic formulae for eddy viscosity or mixing length into the functional form of the integral coefficient under consideration, e.g. the shear stress integral and the energy dissipation integral. The second group of integral methods relies on true turbulence property equations i.e. mostly the transport equation for turbulent kinetic energy. From it a third ordinary differential equation is developed which will provide for the dissipation coefficient or entrainment coefficient needed in the auxiliary equation and the basic momentum integral equation.

The distinction between integral methods based on mean flow integral equations and on turbulent property relations is not so clearcut as for the direct methods. Thus, some of the moment-of-momentum methods, e.g. McDonald and Camarata [47], employ a differential equation of the turbulence as a basis to account for history effects in a similar way as for the methods of Hirst-Reynolds 48 and Green et al.[49]. This is indicated by the dotted line around the two last columns of table 3. Much more information on the classification of boundary layer calculation methods are given in the papers by W.C. Reynolds [59], P. Bradshaw [18], [60], and Launder and Spalding [61].

## 6. EXAMPLES OF BOUNDARY-LAYER CALCULATIONS

When looking for comparative calculations in the literature it is not easy to find examples where the computations were performed with several different methods for the same flow configuration except for the extensive comparisons made at the Stanford conference [62] for incompressible turbulent boundary layers. Therefore it is proposed to show two examples from this source for two cases where the experimental pressure distributions resemble those for the suction side of an airfoil.

The first example is that for the flow around an elliptical airfoil-like section of Schubauer and Klebanoff [63] where the pressure gradient first is negative, then strongly positive with eventual separation as seen in Fig. 11. This figure shows the result of computations by the competitive methods. The first column gives the development of the form parameter $H_{12}$, the second contains the local skin-friction curve $c_f$, and the third is for the local momentum thickness Reynolds number $Re_{\delta 2}$. The dots represent the corresponding measurement. It is seen that virtually all methods predict these boundary-layer characteristics very well up to the point of maximum velocity (at about x = 18 ft) but that deviations begin to show quite distinctly in the strong adverse pressure gradient region up to the separation point which lies at about $x_S$ = 26 ft. On the left I have marked the different methods according to the category which they belong to, with the additional marking of those methods that were rated first-class at Stanford. From this comparison no general superiority of any of the three types of methods can be deduced. Note, however, the consistently good prediction of all three parameters as computed by the complete field method of Bradshaw and Ferris [50]. This is attributable to the fact that they have accounted for three-dimensional effects, i.e. the convergence of the flow as it approaches separation. Also allowance has been made in the Bradshaw-Ferris calculations of longitudinal curvature effects. It is therefore not surprising that most of the other methods which were applied to this case without these corrections could not predict the boundary-layer development in the adverse pressure gradient region as well. In order to show that also an integral method is capable of taking account of convergence and curvature effects let us look on the results of test calculations from Green's new lag entrainment method [49] for the same example. Fig. 12 reflects the predictions assuming two-dimensionality by the solid line. The dotted line shows the effect of allowing for flow convergence in such a way that the $Re_{\delta 2}$-curve is forced to match the experimental data. The effect on $H_{12}$ and $c_f$ then is to halve the discrepancy between the previously calculated and measured values. The further allowance for longitudinal curvature then will again improve the calculations considerably so that even the separation point is predicted satisfactorily. The conclusions are (1) that an integral method such as Green's is not inferior to a complete field method if it is capable of handling secondary effects, (2) that on the other hand a good method should possess the built-in capability to allow for such secondary effects in order to be able to judge from the results of comparative calculations on the possible deviations from a nominally two-dimensional experiment.

The second example is on the experiment of Schubauer and Spangenberg [64] the velocity-distribution of which is shown at the top of Fig. 13. This is a case of a severely retarded flow in which the slope of the adverse pressure gradient increases with x as occurs typically on the upper side of a lifting airfoil. Fig. 13 again gives the result from Stanford, where not all competitors have run this case which was not mandatory. Most of the methods again performed very well with the integral methods of Rotta (RO) and Walz (FG) not being in any way inferior to the complete methods like that of Herring and Mellor (HM2) or Spalding-Patankar (NP). These methods predict the incipient separation equally well and in accordance with experiment. The representation of Green's lag entrainment results in Fig. 14 reveals that the history effect on the development of turbulence structure does have an influence when comparison is made to the results of Head's method without the lag equation used by Green.

In the light of the conclusions drawn in the introduction concerning the importance of being able to predict the separation point accurately it is appropriate to show some comparisons gained from different methods. I have found this comparison in the paper by Cebeci et al. [65] from which Fig. 15 is taken. It shows the predicted separation points for the experimental pressure distribution on a NACA 66.2-420 airfoil at various angles of attack. The experimental separation points are to be inferred as the point where the velocity levels off to the horizontal constant value after the step descent. The best prediction quality then are to be attributed to those methods which come closest to this point. Of the new methods those of Head and Cebeci-Smith are the most satisfactory ones under this criterion while the older methods of Stratford [66] and Goldschmied [67] predict separation too early. Here again the competition between a complete method (Cebeci-Smith) and an integral method (Head) is undecided. This example together with the foregoing examples where also separation was present show that with the best methods available at present turbulent separation can be predicted with confident accuracy.

As to the prediction of transition the situation is not as encouraging. Although the qualitative nature of the transition process for low-speed boundary layers remaining attached is known no sure criteria have yet been developed for the onset and the streamwise extent of the transition region. However, with some of the presently available boundary layer methods remarkable success is achieved for the development of boundary-layer characteristics especially the skin friction coefficient if the point of onset and length of transition region are assumed known. Fig. 16 gives an example of calculations through the transition region by McDonald and Fish [68] performed with a complete finite difference method. The method uses the turbulent kinetic energy transport equation which essentially provides the development and change of an effective viscosity to be used in the simultaneous solution of the differential boundary-layer equations. By inserting a small but nonzero value of the free-stream turbulence level (which is the parameter to the curves in Fig. 15) into the energy-transport equation the increasing production of turbulent shear stress is triggered and followed up to the point of fully turbulent flow. In Fig. 17 the comparison between measurement and calculated prediction of the development of the shape parameter $H_{12}$ and the momentum thickness $\delta_2$ is made for a transitional boundary layer. The agreement is very good. This is an encouraging example of how the modern boundary-layer methods are able to tackle the difficult problem of transition provided that there is some additional information for its onset and extent. A similar method was proposed by Harris [69].

## 7. COMPRESSIBLE BOUNDARY LAYERS

Modern aircraft are operating in a Mach number range extending up to Ma = 3, if we disregard the designs for space craft such as the space shuttle. Special importance is directed to the high subsonic Mach number range representing the cruising speed of modern transport aircraft. Consequently also the boundary layer under these conditions including boundary layer shock-wave interaction must be taken into account. Not attempting to be complete at all, I propose to describe in this paragraph some of the phenomena and effects which will influence or change the behavior of boundary layers in compressible flow as distinct from the incompressible case and to indicate in which way boundary layer calculation methods are extended to incorporate these compressibility effects.

In laminar compressible boundary layers the main sources for deviation from the incompressible behavior are the generation of heat by viscous shear stresses (i.e. dissipation) as the velocity gradients increase with Mach number leading to temperature gradients. Also the temperatures in the free stream at the boundary-layer edge and at the wall surface with or without heat transfer differ in general giving rise to heat transport across the boundary layer in addition to the convection heat transport. Furthermore, the density of the fluid will vary appreciably across the boundary layer according to the thermodynamic state. Density and temperature variations will lead to a variation also of the molecular viscosity. So, besides the velocity boundary layer, there will be a thermal boundary layer if either the main stream temperature differs from the temperature of the wall or/and if there is a significant amount of dissipation in the velocity boundary layer. Compared with incompressible flow at least four additional quantities must be taken into account in the calculation of compressible boundary layers: the Mach number as a measure of compressibility and frictional heat, the Prandtl number as a measure of the diffusion (or transport) of heat, viscosity change with temperature, and heat transfer across the wall determining the temperature distribution along the wall. Accordingly all phenomena known from the behavior of the incompressible boundary layer will be affected in one or the other way, the main effects being: 1.) The temperature increase towards the wall, as occurs with adiabatic surfaces (no heat transfer), thickens the boundary layer leading to a decrease of skin friction coefficients with Mach number. 2.) In flows with heat transfer to the wall the heat transfer coefficient is also reduced with Mach number. 3.) The reduction of skin friction enhances separation. 4.) Laminar compressible boundary layers are less stable, i.e. transition Reynolds number from laminar to turbulent decreases with Mach number up to Ma = 3.5. Wall cooling on the other hand stabilizes the boundary layer again and delays transition.

As to calculation procedures for the laminar compressible boundary layer there are powerful methods in existence of the complete field type by which the full nonlinear partial differential equations can be solved by finite difference techniques. These methods are devised to include foreign gas injection and chemical reaction of several gas species present in a high-temperature laminar boundary layer. A review on these methods was given by Blottner [70]. But also the integral method have been developed to a satisfactory degree of accuracy for engineering purpose, e.g. by Geropp (see Walz [41]).

A third type of method which has proven to be very powerful for incompressible and compressible laminar boundary layer calculations is the so-called GKD method (Galerkin-Kantorovich-Dorotnitzyn) also known as the multimoment method or the method of integral relations. This method is a generalisation of the Kármán-Pohlhausen method but instead of using only the one integral equation for momentum, Eq. (34), many moment-of-momentum equations are solved simultaneously. Representative for this type of boundary-layer method is the work of Abbott and Bethel [71] for incompressible laminar boundary layers and of Nielsen et al. [72] for compressible laminar boundary layers. A specially useful feature of the GKD-methods for laminar boundary layers is the fact that they are able to compute formally past the laminar separation point, while with finite difference methods this, in general, cannot be achieved. In summarizing then, it may be safely stated that for the calculation of laminar compressible boundary layers a number of sufficiently accurate methods are at our disposal. In view of the application to two-dimensional boundary layers over airfoil sections the calculation of the laminar portion does not seem to become a critical problem except for the prediction of transition from laminar to turbulent.

For turbulent compressible boundary layers the effect of Mach number on the general behavior qualitatively follows that of laminar boundary layer at least in the high subsonic to moderately supersonic Mach number range considered here. Regarding external turbulent boundary layer on typical aerodynamic shapes both skin friction and heat transfer coefficients decrease with Mach number. The effort on the various empirical techniques to account for compressibility effects in turbulent boundary layers were directed to give quantitative predictions of skin friction and heat transfer by introducing suitable parameters such as the wall-to-free stream temperature ratio. Quite good correlation formulae for skin friction due to Wilson [73] and van Driest [74] and for heat transfer due to Spalding and Chi [75] were developed in this way. In the light of the modern methods for turbulent boundary-layer methods, however, this parametric approach must be valued as an attempt to circumvent the actual solution of the turbulent boundary-layer equations and the consideration of the turbulence characteristics.

The main effect of Mach number and the accompanying heating on the turbulence structure is the additional appearance of temperature and pressure fluctuations which produce density fluctuations so that there is a strong interaction between the velocity and temperature distribution. Consequently the fluctuating part of pressure, temperature and density enter the boundary layer equations which of course must be augmented by the energy equation usually written as an equation for temperature or total enthalpy. Without going into any details of the derivation of these equations let me point out the most important results regarding the incorporation of compressibility effects into them. For Mach numbers below about Ma = 5 Morkovin's hypothesis [76] holds which says that the density fluctuations to the mean density are small and that therefore the turbulence structure is not influenced being the same as in incompressible boundary layer. This means that compressibility does not affect the functional form of the usual incompressible models of the turbulent eddy viscosity and mixing length as shown also by Maise and McDonald [77]. Consequently these concepts are extensively used in calculation methods of complete field type the model of eddy viscosity $\varepsilon$ for the momentum transport ($-\rho\,\overline{u'v'} = \varepsilon\,\partial u/\partial y$) being analogously applied to define a thermal eddy conductivity $\lambda_T$, in order to treat the term $-\rho\,\overline{v'H'} = (\lambda_T/c_p)\cdot(\partial H/\partial y)$, and an effective turbulent Prandtl number $Pr_T = c_p\cdot\varepsilon/\lambda_T$, usually assumed to be constant and equal to unity. Also the integral methods are extended to compressible boundary layers in which however even more empiricisme concerning the relationships between the various form parameters, the skin friction coefficient and the energy dissipation coefficient are needed. - Recent reviews of compressible methods were given by Beckwith [78] and by Peake et al. [79].

As an example of the capability of calculation methods for the prediction of a boundary layer in compressible flow the results of the experiment of Winter et al. [80] for high speed flow over a waisted body of revolution are compared first with the results of the field method of Herring and Mellor [81] and second with those found by the compressible version of the integral lag entrainment method of Green et al. [49]. Fig. 18 shows the flow situation and the measured pressure distributions for two different free-stream Mach numbers. In Fig. 19 the skin friction and momentum thickness distributions as calculated by the field method of Herring and Mellor are compared with the measured data obtained by surface pitot tubes is shown. Fig. 20 presents the result of Green's calculations in a plot with different scales. Shown here are also the results as obtained with Head's method and the curves for which corrections for curvature, lateral strain and dilatation were made. Such secondary effects are provided for in Green's lag entrainment method. These comparisons show that both field and integral methods will produce good to fairly good agreement with measurements. None of the two methods can be said to be supperior to the other except may be for the shorter computer time in Green's integral method.

In connexion with high subsonic Mach number flows, of course, the appearance of shocks brings about a new situation for boundary layer calculation capabilities. In aircraft aerodynamics the most important example of shock and boundary-layer interaction occurs on transonic airfoils or wings. It will be shown in section 9.4 in which way boundary layer calculations through the interaction region below a normal shock on an airfoil serves as a means of predicting buffet onset on a wing. A deeper insight into the general problem of interaction between shock waves and boundary layers may be gained from the review article of Green [13].

## 8. THREE-DIMENSIONAL BOUNDARY LAYERS

From the aircraft aerodynamicist's point of view the interest for calculating three-dimensional boundary layers is prompted by the need for more accurate predictions of skin friction drag than are possible by the conventional application of the flat plate estimate. For instance the drag of a swept wing may be in serious error because of the neglect of three-dimensional flow effects on the development of the boundary layer. In the mid semispan of a swept wing the actual boundary layer "run" is longer than the geometric chord because the inviscid flow above the surface follows a curved path. In addition, as the boundary layer looses energy the spanwise pressure gradient causes it to drift outboard thus further increasing the "run". Therefore the boundary layer near the trailing edge of swept wings is significantly thicker than on a two-dimensional section, in general, thereby increasing also the pressure drag by interaction with the inviscid flow. Also the three-dimensional separation characteristics on a swept wing are totally different from their two-dimensional counterpart. Of course, also the flow over the fuselage is three-dimensional and the determination of its drag should strictly be based on calculations of the three-dimensional boundary layer instead of by the method for equivalent bodies of revolution.

When speaking of three-dimensional boundary layers, it is again assumed that they are defined as being the thin layer next to the surface of the body to which the viscous effects of the flow are confined. The inviscid main-stream flow in a three-dimensional case will depend on all three space coordinates one of which may be envisaged to be the normal to the surface at every surface point, so that within the boundary layer approximation the pressure variation along these normals can be ignored. Two effects are immediately apparent which were absent in the two-dimensional case. The first is due to lateral convergence or divergence of the three-dimensional main flow stramlines parallel to the surface and the second is introduced by the curvature of these streamlines. While streamline convergence (or divergence) results in a change in boundary-layer thickness different from the two-dimensional development, the lateral curvature of the outer streamlines gives rise to a secondary flow in the boundary layer also called the cross-flow, which is defined as the component of velocity parallel to the surface but perpendicular to the inviscid outer streamline. This effect is qualitatively well understood in being the consequence of the full lateral pressure gradient acting on the fluid of reduced velocity within the boundary layer causing the boundary layer fluid to evade towards the concave side of the potential streamlines. The full complexity of three-dimensional boundary layer flow reveals itself when it comes to separation, two typical examples of which are depicted in Fig. 21. Sketch ⓐ represents the case where a "bubble" is formed inside of which fluid is carried along with the body. Only at the singular point S the behavior of two-dimensional separation zero-wall-shear stress is seen to exist while the confluent wall shear stress lines (or wall "stream lines") forming the curved line of separation suggest that the wall shear stress along this line is nonzero. Sketch ⓑ shows the formation of a free shear layer due to confluent wall stream lines. The extent of the viscous region, attached or free, is indicated by the shaded projected areas. In sketch ⓒ the situation of case ⓑ is illustrated for the flow over a yawed or swept wing with three-dimensional separation. These examples show that the concepts of boundary-layer theory may be applicable upstream of and away from separation lines but that in the vicinity of separation they may not be adequate.

At present the calculation methods for three-dimensional boundary layers is in a state of vigorous development. Recent reviews have been given by Eichelbrenner [82], Nash and Patel [83] and Wheeler and Johnston [84], Horlock et al. [85] and Fernholz [86]. A paper on the numerical treatment of three-dimensional boundary-layer problems was presented at an AGARD-VKI short course by Krause [87], which includes a large bibliography. For the laminar case, methods of the finite-difference type have been successfully applied to a number of flows including the laminar three-dimensional boundary layer at the forward stagnation point of an ellipsoid and the flow along the leading edge of an infinite swept wing. It may be noted that these numerical methods are not restricted to boundary layers with small cross-flow or small spanwise pressure gradients. Also the problem of transition in three-dimensional boundary layers has been considered by Hirschel [88].

As to methods for calculating three-dimensional turbulent boundary layers these may again be divided into complete or integrel methods. The complete methods developed so far are extensions either of finite difference methods for laminar boundary layers with the inclusion of a suitable expression for the Reynolds shear stress or of established two-dimensional turbulent methods. With a leterel velocity component present, the Reynolds shear stress must now be considered as a vectoriel quantity. The eddy-viscosity or mixing-length concept are again utilized, e.g. in [89],[90],[91], with special essumptions regarding their functional form for the two components of the local flow direction. Other methods [92],[93],[94] use the turbulent energy equation in the vector form as proposed by Bradshaw [94]. However, the predictive quality of these complete field methods depends critically on the assumptions on the lateral shear stress component especially close to the wall by which the local flow angle will be determined.

The situation seems to be a little better for the integral methods developed so far, Refs. [95],[96], [97],[98]. The basic assumption in all of these methods is that the streamwise component of the boundary-layer velocity is analogous to that in the two-dimensional case. As shown by Cumpsty and Head [95] the entrainment concept seems to be suited best for three-dimensional methods. Of course, the two integral-equations for the streamwise direction (the momentum integral equation and entrainment shape parameter equation) are completed by the addition of the momentum integral equation for the cross flow. The three equations then contain more than three unknowns, however, and to make the problem determinate a coupling between the crosswise and the streamwise velocity profiles is introduced. The assumption made on the representation of the two profile types and their interconnection form the essential difference between the various methods. For the cross-flow profile the simplest formula is that due to Mager [99]

$$\frac{w}{u} = \left(1 - \frac{y}{\delta}\right)^2 \cdot \tan\beta \tag{62}$$

where w, u are the crosswise and streamwise velocity components respectively, y is the wall distance along a normal to the surface, and $\beta$ is the angle between the wall streamline and the local external streamline. The famous triangle representation according to Johnston [100] may be written as

$$\frac{w}{u} = \begin{cases} \tan\beta & \text{for } \frac{u}{U} \leq 1 - \frac{\tan\beta}{A} \\ A\left(1 - \frac{u}{U}\right) & \text{for } \frac{u}{U} \geq 1 - \frac{\tan\beta}{A} \end{cases} \tag{63}$$

with

$$A = \tan\beta \Bigg/ \left(\frac{0.1}{\cos\beta \cdot \sqrt{c_f}} - 1\right) \quad ,$$

where U is the external velocity and $c_f$ is the streamwise component of the skin friction. Still another formula has been proposed by Eichelbrenner [96]

$$\frac{w}{U} = \tan\beta + B \cdot \frac{u}{U} - (\tan\beta + B) \cdot \left(\frac{u}{U}\right)^2 \tag{64}$$

where B is a known function of $\beta$ and $c_f$. The limiting angle $\beta$ then is essentially the form parameter to be determined from the solution of the crosswise momentum integral equation. Michel et al. [101] use a cross-profile representation of the general form:

$$\frac{w}{U} = k \cdot \delta \cdot f(y/\delta) \tag{65}$$

where k is the geodesic curvature to the outer free stream, and the function $f(y/\delta)$ is determined from a differential equation of similarity type. Note that the Mager and Johnston representations do not allow for crossover profiles while Eichelbrenner's and Michel's expressions do.

As to the predictive qualities of the above methods an assessment is difficult to make since adequate experiments are scarce. For instance comparisons with measurements of Cumpsty and Head [102] on a swept wing model showed serious descrepancies especially in the growth of the streamwise momentum thickness, while the wall crossflow angle $\beta$ was predicted quite well by their calculation method. Similar results were obtained from a comparison between the method of P.D. Smith [97] and an experiment with curved duct flow by Vermeulen [103], where, expect for the streamwise momentum thickness, the prediction was generally satisfectory. Good overell agreement is cleimed by Michel et al. [101] of the results of their method with the measured boundary layers on swept wings and in front of a blunt body.

In closing these remarks on three-dimensional boundary layer celculation methods, allow me to cite part of the conclusions drawn in Eichelbrenner's recent review article [82]: "In laminar flow, several fairly reliable methods for the calculation of ..... three-dimensional boundary layers have been developed. Far less satisfactory is the stete of the art in three-dimensional turbulent flow, where, to date, only integrel methods are available; even these methods depend still on too many simplifying assumptions to be trusted in the general case."

## 9. PREDICTION OF AERODYNAMIC CHARACTERISTICS USING BOUNDARY LAYER CALCULATION METHODS

As mentioned in the introduction the inviscid free stream over a lifting body is influenced by the presence of the boundary layer. Even in the case of the two-dimensional flow over an airfoil we have seen that the interection may become very strong especially when separation (bubble or rear separation) occurs. But also when the boundary layer remains atteched the pressure distribution is affected. From the aircraft aerodynamicist's point of view not the boundary layer es such but these interaction effects constitute the problems that one wishes to solve with the help of boundary layer calculation methods. It is therefore proposed to review some of the problems for which boundary layer methods have been successfully applied. These are: (1) attached flow over a single airfoil, (2) attached flow over an airfoil with a slotted flap, (3) flow over single end flapped airfoil with rear separation, and (4) shock induced rear separation on straight and swept wings determining buffet-onset limits.

### 9.1 Attached Flow over a Single Airfoil

The general principles of the way in which the pressure distribution and hence the lift are changed as compared to the potential theory are well-known and have been described by Thwaites[4]. The main influence is the displacement effect of the boundary layer and the wake. The procedure then is to recalculate the potential flow around the airfoil with the boundary layer displacement thickness added to the airfoil geometric coordinates. At this stage, however, this seemingly straight-forward procedure already shows its drawbacks. The first inviscid potential flow calculation uses the Kutta condition at the trailing edge, having generally a nonzero trailing edge angle, to determine the overall circulation (i.e. the lift) of the airfoil. But what condition is to be applied in the second potential flow calculation? It is known that the prediction for the overall lift depends critically on exactly the condition specified at the trailing edge region with the boundary layers from the upper and lower surfaces having different thickness. If one applies the criterion that the vorticity contained in the two merging turbulent boundary layers must be equal and opposite at the trailing edge this, together with the boundary layer approximation that $\partial p/\partial y = 0$ leads to the conclusion that the velocities at the upper and lower edges of the beginning wake are equal. Experiment shows that this condition is wrong; also the lift coefficient at a given angle of attack of the airfoil obtained by applying this condition is much too low. It was therefore argued that a pressure difference across the two boundary layers is induced at the trailing edge by the curvature of the ensuing wake. Fig. 22 depicts this situation at the trailing edge. The formula

$$\frac{\Delta c_L}{c_L} = \frac{c_D}{\pi} \tag{66}$$

for the relative lift reduction was given by Spence [104] in which, however, the unknown drag coefficient must be estimated from approximate formulas like that of Squire and Young. The above formula is only a crude approximation which underestimates the lift reduction especially with increasing angles of incidence. Later Spence and Beasley [105] developed another formula arguing that the nonzero vorticity in the wake will induce a circulation about the whole airfoil as is the case with a jet flap. By interpreting the effect of the wake to be analogous to the jet effect they arrived at the nonlinear expression

$$\frac{\Delta c_L}{c_L} = k \cdot \sqrt{c_D} \quad , \tag{67}$$

with k = -0.214. In this formula again the profile drag coefficient $c_D$ would have to be calculated approximately again from the Squire-Young formula. Steinheuer 106 found that quite good agreement with experiment is achieved by leaving the form of Eq. (67) unchanged but replacing $c_D$ by the overall skin friction coefficient $c_F$ as defined by

$$c_F = \oint \frac{\tau_w(s)}{\rho U_\infty^2} \, ds \quad , \tag{68}$$

where the integral is taken around the profile contour, leading to

$$\frac{\Delta c_L}{c_{Lo}} = k \cdot \sqrt{c_F} \quad . \tag{69}$$

Here $c_{Lo}$ is the value of the lift coefficient of the potential flow calculation using the original Kutta condition, and k was found to have the empirical value k = 2. This formula is very convenient insofar as it does not necessitate the calculation of the wake, and $c_F$ is easily obtained from the skin friction distribution of a boundary-layer calculation. Another advantage is that the formula, Eq.(69), can be applied to multiple airfoils as well. Fig. 23 shows a comparison of the calculated lift curve with the experiments of Brebner and Bagley [107] for two different Reynolds numbers.

A different line of approach to the problem is that employing the concept of reduced camber a measure of which is the added total displacement thickness of the boundary layer at the trailing edge. This method has been perfected by Powell [108]. For the ratio of the displacement thickness to chord length the assumption is made that it assumes half of the value of the drag coefficient at a specified distance downstream of the trailing edge. The drag coefficient again has to be known in advance and is calculated by a method due to Nash and Macdonald [109] based on the momentum thickness at the trailing edge. The special feature of Powell's method is that potential source and vorticity distributions placed along an effective camber line are sought for, which is determined from the calculated displacement thickness added to the original airfoil contour. This results effectively in a change of angle of incidence. The usual Kutta condition is applied and the source and vorticity distributions are found by fullfilling the boundary condition at the displacement surface of the camber-modified airfoil. An iterative procedure is then set up where the pressure distribution from a potential flow calculation is up-dated according to the change in effective camber, and boundary-layer calculations are performed with this new pressure distribution. Convergence is reached after about 10 iterations.

The method of Powell described above has been found to give good general agreement with measured pressure distributions if the comparison is made at the same value of the lift coefficient. However, when the solution is sought for a given angle of incidence the method overestimates the lift coefficient by up to 10 %, i.e. it underestimates the reduction of lift due to the boundary-layer effect. This is the case with all methods that have been proposed so far like that of Bhateley and Bradley [110] and of Giesing [111]. The discrepancies are attributed to the uncertainty of the older nominally two-dimensional wind-tunnel experiments, as evidenced by the more recent investigations of Firmin and Cooke [112].

An interesting discussion on the subject of the interaction of the outer flow with the confluent boundary layers and the wake in the trailing edge region of an airfoil has recently been given by Green [13]. A theoretical model for the immediate vicinity of the trailing edge is developed envisaging the confluent boundary layers to be effectively inviscid but rotational shear layers with slip velocity at the surface. The main result of Green's discussion is that a correlation between the shape parameter $H_{12}$ of the upper surface turbulent boundary layer approaching the ideally sharp trailing edge and accompanying pressure rise could be established resulting in a lower pressure (higher velocity) at the edge of the upper surface boundary layer than at a corresponding point at the edge of the lower surface boundary layer. This is in qualitative accord with the formula developed by Giesing [111]. It is not known whether Green's trailing edge flow model has been incorporated into a prediction method.

## 9.2 Attached Flow over an Airfoil with a Slotted Flap

The need for still more efficient high-lift devices for use in RTOL and STOL aircraft has led to extensive research activities mostly on the experimental side as far as full three-dimensional configurations are concerned. The basis for theoretical studies, however, still is the simplest case of a high lift device i.e. the airfoil with one trailing edge flap. With the modern methods for the calculation of the potential flow around multiple airfoils, such as those developed by Riegels and Jacob [113], Giesing [111] and Bhateley and Bradley [110] the prospect of developing a prediction method including viscous effects has come within reach.

The typical development of the viscous layers around an airfoil with a slotted flap has already been shown in Fig. 2. This case has been extensively studied at RAE [114],[115] and at NLR [116],[117] experimentally and theoretically. The difficulties imposed on the theoretical analysis lie mainly in the appearance of two features: (1) the mixing of the wake from the main airfoil and the boundary layer of the upper surface of the flap, and (2) the presence of a closed zone of separation (or bubble) on the lower surface of the main airfoil near to the trailing edge. The interaction of the wake and boundary layer at optimum lift at a given incidence and flap deflection has been found to be relatively weak, meaning, that the two shear layers retain their separate identities almost to the flap trailing edge. However, this is only true as long as the relative translatory position of the flap (characterized e.g. by the gap width and the trailing edge overlap) is such that the flow at the slot exit contains an essentially inviscid core. Fig. 24 shows schematically the flow situation, where sketch ⓐ applies to the favorable situation just described. Sketch ⓑ below shows the effect on the slotflow when the gap has become too narrow. The limiting streamline, by which the recirculation bubble is bounded in the situation of sketch ⓐ, no longer reattaches to the lower side of the main airfoil ahead of its trailing edge but is swept down below the lower side of the flap. This then gives rise to separation over the back of the flap or even the back of the main profile resulting in a substantial loss in the overall-lift of the flapped airfoil.

A more detailed picture of the mechanism of flow in the slot region is gained from the results of a recent investigation made by W. Schröder [118], here at the VKI, on a thin airfoil with flap. Fig. 25 shows some measured pressure distributions over the upper and lower sides of the main wing and the flap for a decreasing gap width of the flap nose location at constant overlap these parameters being determined by the coordinates d and s. Beginning with the case of the largest gap width, s/c = 1.8 %, it is seen that the pressure coefficient reaches its full potential value of unity at the flap's stagnation point, while the pressure within the bubble forms a relatively low plateau, rather sharply bounded towards the trailing edge by a pressure peak which marks the reattachment point. This peak lies just ahead of the overlap location marked by the arrow. When the gap is diminished the stagnation pressure at the flap nose becomes less than unity indicating that low-energy fluid is shed over the flap nose. Correspondingly the overall-lift is reduced. Also the pressure level at the bubble location is reduced and the region of separated flow extends upstream beyond the discontinuous corner of the contour. Surprisingly, however, with still non-separated flow over the main-airfoil's trailing edge and over an appreciable part of the flap back, the flow through the slot still is maintained as evidenced by the sharp pressure fall just ahead of the trailing edge. The still noticeable pressure peak here suggests that the bubble structure continues to be maintained, its bounding streamline, however, being formed of fluid of reduced kinetic energy. Three distinct regions of flow are tentatively indicated in the accompanying sketch of the slot flow: region I is the region of irrotational potential flow with full total pressure energy, region II is composed of rotational fluid forming a free shear layer originates from the separated boundary layer of the lower side of the main airfoil and region III is the closed recirculating bubble region. The described mechanism of the slot flow is strongly supported by the smoke visualization pictures made by Schröder of which the obtained smoke contours are presented in Fig. 26. These smoke contour lines roughly correspond to the line of division between the regions II and III of the previous figure.

The prediction method devised by the author [106] for the calculation of the optimum lift as dependent on the flap-setting especially with respect to gap width and overlap at given flap angle, incidence, and Reynolds number assumes that the bubble region can be replaced by a solid fairing contour for the calculation of the potential flow and hence the pressure distribution and the lift coefficient. This approach has been used previously by Labrujere et al. [117] and Werlé [119] for the analogous situation of the flow around the lower side of a slat to successfully calculate the pressure distribution. However, as the replacement contour is not known a priori it was chosen to coincide with the fairing contour used in the experiments of Foster et al. [114] in the particular example for which the first comparative calculations were made. The potential flow was calculated by means of the method of Giesing [111] for multiple airfoils, and a boundary-layer calculation was performed using Walz's integral method [41]. With the values of gap width and overlap as parameters a series of potential flow and boundary-layer calculations werde made in which the lift reduction due to the boundary layer displacement effect was computed from Eq. (69) applied to the main airfoil and the flap individually. It turned out that, by varying the flap position, the boundary-layer calculation predicted either completely attached flow along the fairing contour right down to the trailing edge or the occurrence of separation at a point well upstream of the trailing edge. In Fig. 27 a comparison of calculated and measured values of the total lift is made for a case where the gap width is varied at a constant overlap distance. It is seen that the experimentally found optimum gap width very well coincides with the point of flap position for which the calculations predict the occurrence of separation. Note further the relatively small error of the absolute values of the lift coefficient as compared to the experimental values in the range of predicted attached flow.

The weak point of the proposed prediction method, of course, is the a-priori assumption to be made for the replacement contour in the bubble region. However, this difficulty should be overcome by exploiting the results of Schröder's experiment which showed that the point of bubble reattachement always lies just ahead of the flap nose position (see Fig. 25) and that the bubble contour line for the case of optimum lift forms a well-behaved curve which can probably be approximated by a cubic (see Fig. 26).

The potentialities of a prediction method as that described above are immediately apparent. Not only the extensive (and expensive) wind-tunnel measurements to determine an optimum slot configuration would be greatly reduced by a preceding computational survey but also the transfer of the low Reynolds number wind tunnel results to the actually intended high Reynolds number configuration could be made with much more confidence.

### 9.3 Airfoil Flow with Separation

The prediction of incipient trailing edge separation for a given airfoil section is of extreme importance in the design of aircraft wings of moderate sweep angle especially for the low speed range at take-off and landing. The purely theoretical determination of the maximum lift of wings with mechanical high lift devices such as single or multiple trailing edge flaps and slats or other fore-flaps is rendered especially difficult not only because of the mutual influence of the inviscid flow around the different parts of the wing but also by the fact that the maximum lift of the configuration is almost always associated with moderate rear separation already established on one of the elements forming the complete section. While a prediction method for the general three-dimensional compressible case seems remote for a long time to come the incompressible two-dimensional problem such as the one depicted in Fig. 28 has been attacked with some success by Jacob [120] and Bhately and Bradley [110].

Following Jacob, I wish to outline briefly his line of approach and show some recent examples of his method, [121]. The concept of simulating the flow over an airfoil with a separated region ahead of the trailing edge is to add to the otherwise classically determined potential flow (i.e. with Kutta-condition fullfilled at the trailing edge) a source distribution along that part of the contour where separation is present. From the development of a preceding boundary-layer calculation the separation point has been determined. The added source distribution will then alter the original pressure distribution over the upper side of the airfoil and a new boundary-layer calculation (using Rotta's method [42]) will predict the separation point to lie at some other location, as in the preceding run. The area of simulating source flow is altered accordingly and a new pressure distribution is calculated. This process of alternatingly calculating the potential flow and boundary-layer development is continued until the assumed location of the separation point coincides with the predicted one. In order to avoid a stagnation point to occur in front of the outflow region the source distribution is modelled in such a way that the streamline forming the surface ahead of separation leaves the surface smoothly i.e. with zero-slope. Further the problem is made determinate by requiring an equal pressure (or velocity) to prevail at a point L shortly upstream of the trailing edge on the lower side, at a point 0 above the trailing edge through which the separation streamline passes, and at the separation point S itself. As soon as convergence of the iteration process is achieved all section characteristics can be determined for the particular case considered, i.e. for a given angle of incidence and given flap settings. By repeating the calculation for a range of angles of incidence, of flap deflection angles, and of flap positions the dependence of the lift coefficient on any of these parameters can be predicted for attached flow and flow with trailing edge separation. Also Reynolds number dependence is included through the use of boundary-layer calculations. Note, however, that up to the present the boundary-layer calculations have been used solely for the purpose of determining the separation point while boundary layer displacement effect is not included.

To show the potentialities of Jacob's method I propose to show two examples from his recent report [121]. The first example is on the flow over a hypothetical flapped airfoil with a NACA 23012 main section (see Fig. 29) and a flap the section shape of which is a 20 % replica of the main airfoil. Graph ⓐ shows the $c_L(\alpha)$-curve for three different flap defection angles $\delta_F$ and two different Reynolds numbers. With the smaller Reynolds number (solid line curves) separation occurs first on the main wing causing immediate separation on the flap as well. For $\delta_F = 20^\circ$, in contrast, the flap flow is separated already at zero angle of incidence and separation over the main wing occurs at about $\alpha = 8.5^\circ$. A very interesting behavior is exhibited for the higher Reynolds number $Re = 10^7$ (broken line curves). Again with the flap angles $\delta_F = 0^\circ$ and $10^\circ$ separation is predicted to first occur over the main profile while the flow remains attached up to considerable higher angles of incidence. At the high flap defection angle $\delta_F = 20$ now the flow separates first over the flap while it continues to remain attached on the main airfoil causing the $c_L(\alpha)$-curve to again rise to a second peak value where then separation takes over also to the main airfoil. In the graph ⓑ the boundaries for the different types of separation behaviors are shown, i.e. no separation, separation on flap only, separation on main airfoil only, and separation on both main airfoil and flap depending on the angle of incidence and on the flap defection angle. Note that at the lower Reynolds number $Re = 10^6$ the domain, where there is separation on the main airfoil only, is degenerated to a very narrow range of possible angles of incidence.

The second example treats the case of a main airfoil with drooped nose and an additional slat (as seen in Fig. 30). The main profile here is a modified NACA 64-210 section. The reference chord c is therefore taken to be that of the unmodified profile. The figure shows the calculated pressure distribution at a given slat position and an effective angle of incidence of $\alpha = 20^\circ$ corresponding to equal values of lift coefficient of the calculation and of the measurements by Baumert [122]. The transition point was taken as the point of laminar separation. Considering that the displacement effect of boundary layer is not accounted for, the agreement between the theoretical and the measured pressure distribution is most satisfactory, although the measured separation point seems to lie slightly downstream of the predicted location. The flexibility of the method may be demonstrated by Fig. 31 where for the same profile at a given flap position the measured $c_L(\alpha)$-curve (dotted line) is seen to have two maxima, the first of which corresponds to slat separation at about $\alpha = 33^\circ$, followed by the second peak at $\alpha = 40^\circ$ for main wing stall. The solid line curve represents the result of the calculations and the broken line curve corresponds to the experimental curve corrected for an effective angle of attack at an infinite aspect ratio. First of all, it is noted that the computed curve exhibits correctly the existence of the two maxima. The deviations from the corrected experimental curve may be attributed to the inexplicable difference of about two degrees in incidence at zero lift and to the boundary layer displacement effect not accounted for in the calculations. - In closing this paragraph then, it can be stated without exaggeration that Jacob's prediction method has now matured to a degree that it may be applied with confidence to explore numerically the low speed aerodynamic characteristics of an airfoil with slats and even multiple flaps in the design state with only a very reduced number of wind-tunnel runs necessary for assurance.

### 9.4 Prediction of Buffet Boundaries for a Wing in Transonic Flow

One of the important problems in modern aircraft design is constituted by the appearance of a normal shock on the upper surface of a wing or airfoil involving an interaction between shock and boundary-layer development. Specifically shock-induced boundary-layer separation marks the phenomenon of buffeting loosely defined as the state of very severe random oscillations of the aerodynamic forces on a wing. Buffeting thus poses structural limits to the range of flight conditions attainable. The influence of buffet onset on the flight envelope (curve $c_{L\max}$ versus Mach number) for a transport aircraft with wings of large aspect ratio and moderate sweep angle is depicted in Fig. 32 schematically. In incompressible flow (range I) the maximum lift is determined by separation phenomena induced by adverse pressure gradients involving either rear separation or bubble bursting as discussed previously. Range II beginning at a Mach number of about $Ma_\infty = 0.3$ is characterized by the appearance of a small supersonic zone around the airfoil nose at high angles of incidence with $c_{Lmax}$ decreasing with increasing Mach number. An extended supersonic flow region terminated by a normal shock is encountered in range III beginning at about $Ma_\infty > 0.6$. Here, now, the maximum lift is rapidly falling off with Mach number. It is in this range that buffeting is the constraining factor. The diagram includes the curve for drag rise close to which the operating point for cruise of an aircraft is usually chosen so as to keep some margins $\Delta Ma$ and $\Delta c_L$ with respect to the $c_{Lmax}$ or buffet-onset curve.

Adopting flow model B according to the classification of transonic separation types (see Fig. 5) after Pearcey et al. [11], F. Thomas [123] has been the first to develop a purely computational method to predict the onset of buffeting which hitherto could only be obtained by wind tunnel and flight tests. The method relies on the argument that if buffet-onset is the consequence of boundary-layer separation behind a normal shock on a transonic wing it was to be expected that the problem could be solved by employing boundary-layer methods. The analytical steps in the method of Thomas as applied to two-dimensional airfoils are as follows:

1.) Using available semi-empirical [124] or theoretical [125] methods, the pressure distribution including the position of the shock is calculated assuming the flow to be attached and inviscid.

2.) With the above pressure distribution a boundary-layer calculation along the upper surface of the airfoil and through the shock region is performed to determine the separation point by one of the available boundary layer calculation methods for compressible turbulent flow.

3.) Steps 1.) and 2.) are repeated for a series of flight conditions (Mach number) and the movements of the obtained separation points and the shock position are determined as shown schematically in Fig. 33.

4.) In Ref. [123] buffet-onset was taken as being the condition where the boundary layer separation point and the shock position coincide (point A in Fig. 33). Later, with some revisions in the analysis components, it was assumed [126] that buffeting occured at the condition where the separation has moved forward from the trailing edge to 90 % of the chord (point B in Fig. 33).

The above criterion for buffet-onset has been discussed by Thomas and Redeker [126] and by Gentry and Oliver [127] who made comparative calculations using different method in the computational steps 1 and 2 above.

Some of the results of Thomas' method as compared to wind tunnel and flight test results are shown in Fig. 34 where $c_{LB}$ denotes lift coefficient for buffet-onset. For these two-dimensional examples the agreement between predicted and measured buffet limits is very satisfactory.

The first attempts of Thomas [123] to extend his method also to swept wings by applying the independence principle for an infinite swept wing and by correcting the results obtained for the section airfoil normal to the leading edge by the cosine law were successful only for wings of moderate sweep. For large angles of sweep the neglect of the truly three-dimensional boundary-layer development produced too optimistic limits of buffet-onset. Therefore Redeker [128] (see also [126]) extended the incompressible boundary layer entrainment method of Cumpsty and Head [95] for the three-dimensional boundary layer flow over swept wings to include compressibility. A weak-shock concept is adopted which does not lead to separation of the boundary layer ahead of the shock, and again it is assumed that three-dimensional separation marked by confluent wall streamlines sets in first at the trailing edge and moving up towards the shock position. Also the 90%-chord criterion for buffet-onset is adopted.

In Fig. 35 the results of the example calculations taken from [128] are shown. In case ⓐ the buffet boundaries for the fighter aircraft F-86A as determined in flight test [129] are compared with the results of Redeker's method and with the quasi-two-dimensional method of Thomas. It is seen that accounting for three-dimensionality results in much better agreement with experiment. In case ⓑ the comparison extends to two wings of different thickness ratios and sweep angles at equal aspect ratio and drag-rise Mach number. The wind-tunnel experiments made in the Göttingen-transonic-tunnel [130] revealed that in spite of the equal drag-rise Mach number the thinner wing with less sweep is more favorable with respect to the buffet boundaries. This is also reflected in the theoretical prediction which is in very satisfactory agreement with experiment.

The foregoing examples show convincingly that again with the help of boundary-layer methods a complex problem in aircraft design is made amenable to analytical prediction.

## 10. SOME REMARKS ON THE SCALE EFFECT

By scale effect generally the differences are understood which exist between the results obtained from model testing in a wind tunnel and the result of the full scale flight test with respect to any aerodynamic characteristic being investigated. The principle cause for these differences is the dependence of various flow phenomena on Reynolds number which is, in general, not the same in the flow at model scale and at full scale. This Reynolds number dependence gives rise to serious problems in the extrapolation of model test results to the conditions of full scale or vice-versa in the ability to simulate properly full scale conditions in a model test e.g. by artificially fixing of boundary-layer transition.

In actual wind tunnel-testing besides the Reynolds number simulation, although of prime importance, other aspects must be considered some of which are: tunnel wall constraints, model support interferences, elastic model strength, model surface conditions, the representation of components such as the engines. Also, the free stream turbulence level may become very important as it influences the onset of transition from laminar to turbulent boundary-layer flow. In the discussion to follow all these effects will not be considered, the major attention being given to the pure Reynolds number effect. Recent reviews of various influences on the scale effect have been given by Hall [131], Green [13], Little [132], and Paterson [133].

The study of the Reynolds number scale effect consists of essentially the study of the complex interactions between boundary-layer development and the external inviscid flow. Thus, again, the basic boundary-layer phenomena will determine the sensitivity of the flow over a given model-configuration to scale effects. In the two-dimensional airfoil flow these are: (1) attached boundary-layer flow, either laminar or turbulent, (2) transition from laminar to turbulent flow, (3) complete laminar separation, (4) laminar separation with subsequent turbulent reattachment over short and long separation bubbles, (5) turbulent separation, (6) turbulent reattachment e.g. downstream of the shock-boundary layer interaction zone in the flow over a transonic airfoil, and (7) the wake development. Although in most occasions the real flow is three-dimensional it is expected that the study of the basic two-dimensional boundary-layer phenomena will provide the criteria for assessing scale effects, as for instance the effects on a swept wing being discussed by considering a sheared wing of infinite span. The above mentioned boundary-layer phenomena may be subdivided into two categories according to their effect on the flow field as a whole. Strong interaction is provoked usually by the phenomena (3) and (5) involving complete detachment of the outer flow over an appreciable portion of the surface. Phenomena (1), (2) and (7) belong to the weak interaction category while the items (4) and (6) involving closed separation regions play an intermediate role. However, it must be born in mind that phenomena which only weakly affect the outer flow locally are responsibly in many cases for the appearance of strong interaction. Thus e.g. transition from laminar to turbulent being highly Reynolds number dependent influences by its location and streamwise extent the subsequent development of the turbulent boundary layer and hence the possible turbulent separation at a location relatively far downstream of the transition zone. Another example is the change of a separation bubble from the short to the long type depending on the Reynolds number. Typical pressure distributions obtained at ONERA as referenced in [5] are shown in Fig. 36. At the higher Reynolds number (higher velocity $V_o$) a short bubble exists up to a 14° angle of incidence causing the kinks in the $c_p$-curves but otherwise not affecting the pressure distribution. At the lower Reynolds number the short bubble apparently bursts into the formation of a long bubble at about 8° incidence resulting in the deterioration of the suction peak pressure close to the leading edge. This example exhibits the inherent dangers in extrapolating low Reynolds number data to full scale Reynolds number if, as in this case, a fundamentally different type of boundary layer free-stream interaction phenomenon comes into existence within the range of Reynolds numbers over which the extrapolation is desired. An example of this kind has actually occured with the C-141 airplane as reported on by Loving [134] and demonstrated in Fig. 37. Turbulent boundary-layer separation in flight test was much more downstream on the wing than had been predicted by wind-tunnel tests. The downstream shift of the shock and the increased circulation around the wing changed considerably the pressure distribution and hence the location of the lift-center causing in turn different trim requirements and greater loads on the fuselage structure than were anticipated in the design.

The above examples lead to the following conclusions:

(1.) Reynolds number scale effects may arise from a change in any part of the boundary-layer flow, the most significant sources of deviation being associated with boundary-layer transition and boundary-layer separation.

(2.) Extrapolation of results from one Reynolds number to another may lead to significant errors in the prediction of the aerodynamic characteristics st the desired full-scale Reynolds number.

One solution for remedy in this situation is to enlarge the capability of the experimental facilities in such s way as to always make full-scale experiments. In fact, the need for larger wind tunnels especially in the regime of transonic speeds has been established by the AGARD HIRT Group [135](High Reynolds Number Wind Tunnel Study Group). The second possibility, not as an alternative but rather as a complementary means, is to develop new, and refine existing calculation methods comprizing methods for the calculation of inviscid flow fields and boundary layers. The latter must be supplemented by increasingly reliable method or criteria to determine transition and separation in detail. Furthermore methods are needed by which the interactions between the inviscid and viscous flow regimes are predictable realistically so as to allow for a feedback of the influences of one flow type on the other. A composite prediction method may then be conceived, built up by way of evolution, in which only the best component methods available are utilized. Although the evolution of such an ideal method seems to be remote at the present, the progress made in the last decade in developing numerical procedures, both for the calculation of external flow fields and of the boundary layer provides an optimistic outlook into the future. As encouraging first steps into the right direction I would consider the examples of sections 9.1 to 9.4 where composite methods have been devised to attack Reynolds number dependent problems (calculation of maximum lift coefficient of a multiple airfoil, determination of buffet-onset boundaries) which hitherto were not thought to be solvable.

## REFERENCES

[1] Prandtl, L. Über Flüssigkeitsbewegung bei sehr kleiner Reibung. Proceedings 3rd Intern. Math.Congr. Heidelberg 1904, 484-491; translated as NACA TM 452 (1928); see also: Gesammelte Abhandlungen (Collected Works), Vol. II, Springer, Berlin, 1961, 575-584.

[2] Abbott, I.H., v. Doenhoff, A.E. Theory of Aerofoil Sections. Dover Publ., 1960.

[3] Riegels, F.W. Aerodynamische Profile. Oldenbourg Verl. München, 1958; also: Aerofoil Sections. Butterworth, London, 1961.

[4] Thwaites, B. (ed.) Incompressible Aerodynamics, Fluid Motion Memoirs, Clarendon, Oxford, 1960.

[5] Hancock, G.J. Problems of Aircraft Behaviour at High Angles of Attack. AGARDograph 136, 1969.

[6] Foster, D.N. The Low-Speed Stalling of Wings with High-Lift Devices. AGARD-CP-102, 1972.

[7] Ljungström, B.L.G. Boundary Layer Studies on a Two-dimensional High-lift Wing. FFA Rapport AU-862 of the Aeron. Res. Inst. of Sweden, 1972.

[8] Bartelt, E. Klärung realisierbarer Möglic [illegible] des Hochsuftriebs. MBB-Bericht UH8/1-70 of Messerschmitt-Bölkow-Blohm, [illegible]

[9] Smith, A.M.O. Aerodynamics of High-lift Airfoil Systems. AGARD-CP-102, 1972.

[10] Foster, D.N. The Flow around Wing Sections with High-Lift Devices. AIAA Paper No. 71-96, 1971.

[11] Pearcey, H.H., Osborne, J., Haines, A.B. The Interaction between Local Effects at the Shock and Resr Separation - a Source of Significant Scale Effects in Wind Tunnel Tests on Airofoils and Wings. AGARD-CP-35, 1968.

[12] Green, J.E. Interactions between Shockwsves and Turbulent Boundary Layers. Prog. Aerospace Sci., Vol. 11 (ed. D. Küchemann et al.), 235-340, Pergamon, 1970.

| | | |
|---|---|---|
| [13] | Green, J.E. | Some Aspects of Viscous-Inviscid Interactions at Transonic Speeds, and their Dependence on Reynolds Number. AGARD-CP-83-71, 1971; also as RAE TR 72050, 1972. |
| [14] | Küchemann, D. | Types of flow on swept wings with special reference to free boundaries and vortex sheets. J.Roy.Aero.Soc., Vol. 57, 683-699, 1953. |
| [15] | Williams, J.<br>Ross, A.J. | Some airframe aerodynamic problems at low speeds. Annals New York Acad.Sci., Vol. 154, Art. 2, Int.Congr.on Subsonic Aeronautics, 264-305, 1968. |
| [16] | Schlichting, H. | Boundary-Layer Theory. McGraw-Hill, New York, 1968. |
| [17] | Rosenhead, L. (ed.) | Laminar Boundary Layers, Fluid Motion Memoirs, Clarendon, Oxford, 1963. |
| [18] | Bradshaw, P. | The understanding and prediction of turbulent flow. Aeronautical J., Vol. 76, 403-418, 1972. |
| [18a] | Bradshaw, P. | Effects of streamline curvature on turbulent flow. AGARDograph No. 169, 1973. |
| [19] | Rotta, J.C. | Turbulente Strömungen. Teubner, Stuttgart, 1972. |
| [20] | | Chapter XVI of 16 : "Origin of turbulence". |
| [21] | Betchov, R.<br>Criminale, W.O. | Stability of parallel flows. Acad.Press, New York, 1969. |
| [22] | Obremski, H.J. | A portfolio of stability characteristics of incompressible boundary layers. AGARDograph 134, 1969. |
| [23] | Granville, P.S. | The calculation of the viscous drag of bodies of revolution. D.Taylor Model Basin Rep. 849, 1953. |
| [24] | Smith, A.M.O.<br>Gamberoni, N. | Transition, pressure gradient and stability theory. Douglas Rep. ES 26388, 1956. |
| [25] | Chen, K.K.<br>Thyson, N.A. | Extension of Emmons' spot theory to flows on blunt bodies. AIAA J., Vol. 9,1971. |
| [26] | Tani, I. | Low-speed flows involving bubble separations. Progr. in Aeron.Sci., Vol 5, 70-103, Pergamon, New York, 1964. |
| [27] | Crabtree, L.F. | The formation of regions of separated flows on wing surfaces. ARC R&M 3122,1959. |
| [28] | Owen, P.R.<br>Klanfer, L. | On the laminar boundary layer separation from the leading edge of a thin airofoil. ARC CP 220, 1953. |
| [29] | Gaster, M. | The structure and behaviour of laminar separation bubbles. NPL Aero. Rep. 1181, 1966; see also AGARD-CP-4, 813-854, 1966. |
| [30] | Bradshaw, P. | Calculation of boundary layer development using the turbulent energy equation. VKI Lecture Series 5, Part 2, 1968. |
| [31] | Coles, D. | Measurements in the boundary layer on a smooth flat plate in supersonic flow. Jet Prop.Lab.Rep. No. 20-69, 1953. |
| [32] | van Driest, E.R. | On turbulent flow near a wall. J.Aeron.Sci., Vol. 23, 1007-1011, 1956. |
| [33] | Coles, D. | The law of the wake in the turbulent boundary layer. J.Fluid Mech., Vol. I, 191-226, 1956. |
| [34] | Tollmien, W. | Berechnung turbulenter Ausbreitungsvorgänge. ZAMM, Vol. 6, 468-478; also translated in NACA TM 1085, 1945. |
| [35] | Patankar, S.V.<br>Spalding, D.B. | Heat and mass transfer in boundary layers. 2nd. ed. Intertext Books, London, 1970. |
| [36] | Smith, A.M.O.<br>Cebeci, T. | Numerical solution of the turbulent boundary-layer equations. Rep. DAC 33735 of Douglas Aircraft Co., 1967. |
| [37] | Thompson, B.G.J. | A critical review of existing methods of calculating the turbulent boundary layer. ARC R&M No. 3447, 1964. |
| [38] | Ludwieg, H.<br>Tillmann, W. | Untersuchungen über die Wandschubspannung in turbulenten Reibungsschichten. Ing. Archiv, Vol. 17, 288-299, 1949; translated in NACA TM 1285, 1950. |
| [39] | Squire, H.B.<br>Young, A.D. | The calculation of profile drag of airflow. ARC R&M 1838, 1937. |
| [40] | Truckenbrodt, E. | Ein Quadraturverfahren zur Berechnung der laminaren und turbulenten Reibungsschicht bei ebener und rotationssymmetrischer Strömung. Ing.Archiv, Vol. 20, 211-228, 1952; translated in NACA TM 1379, 1955. |
| [41] | Walz, A. | Strömungs- und Temperaturgrenzschichten. Braun, Karlsruhe, 1966; translated as: Boundary layers of flow and temperature. MIT.Press, 1969. |
| [42] | Rotta, J.C. | FORTRAN IV - Rechenprogramm für Grenzschichten bei kompressiblen, ebenen und achsensymmetrischen Strömungen. AVA-Bericht 68-R-03, 1968; also DLR-FB 71-51, 1971. |
| [43] | Rotta, J.C. | Turbulent boundary layer calculations with the integral dissipation method. Contribution in [62], Vol. 1, 177-181, 1968. |
| [44] | Nash, J.F. | Turbulent-boundary-layer behaviour and the auxiliary equation. NPL Aero. Rep. 1137, 1965. |
| [45] | Head, M.R. | Entrainment in the turbulent boundary layer. ARC R&M 3152, 1958. |
| [46] | Head, M.R.<br>Patel, V.C. | Improved entrainment method for calculating turbulent boundary layer development. ARC R&M 3643, 1968. |

[47] McDonald, H.; Camarata, F.J. — An extended mixing length approach for computing the turbulent boundary layer development. Contribution in [62], Vol. 1, 83-98, 1968.

[48] Hirst, E.A.; Reynolds, W.C. — An integral prediction method for turbulent boundary layers using the turbulent kinetic energy equation. Contribution in [62], Vol. 1, 213-234, 1968.

[49] Green, J.E.; Weeks, D.J.; Brooman, J.W.F. — Prediction of boundary layers and wakes in compressible flow by a lag-entrainment method. RAE Tech. Rep. 72231, 1973.

[50] Bradshaw, P.; Ferris, D.H.; Atwell, N.P. — Calculation of turbulent boundary layer development using the turbulent energy equation. J.Fluid Mech., Vol. 28, 593-616, 1967.

[51] Mellor, G.L.; Herring, H.J. — Two methods of calculating turbulent boundary layer behavior based on numerical solutions of the equations of motion. Contribution in [62], Vol. 1, 331-345, 1968.

[52] Nee, V.W.; Kovasznay, L.S.G. — The calculation of the incompressible turbulent boundary layers by a simple theory. Contribution in [62], Vol. 1, 300-319, 1968.

[53] Beckwith, I.E.; Bushnell, D.M. — Calculation of mean and fluctuating properties of the incompressible turbulent boundary layer. Contribution in [62], Vol. 1, 275-299, 1968.

[54] Felsch, K.O.; Geropp, D.; Walz, A. — Method for turbulent boundary layer prediction. Contribution in [62], Vol. 1, 170-176, 1968.

[55] Alber, I.E. — Application of an exact expression for the equilibrium dissipation integral to the calculation of turbulent nonequilibrium flows. Contribution in [62], Vol. 1, 126-135, 1968.

[56] Zwarts, F.J. — Turbulent boundary layer predictions using a dissipation integral method. Contribution in [62], Vol. 1, 154-169, 1968.

[57] Michel, R.; Quémard, C.; Durant, R. — Hypotheses on the mixing length and application to the calculation of the turbulent boundary layers. Contribution in [62], Vol. 1, 195-212, 1968.

[58] Nash, J.F.; Hicks, J.G. — An integral method including the effect of upstream history on the turbulent shear stress. Contribution in [62], Vol. 1, 37-45.

[59] Reynolds, W.C. — A morphology of the prediction methods. Contribution in [62], Vol. 1, 1-15, 1968.

[60] Bradshaw, P. — Advances in turbulent shear flows. VKI-Lecture Series 56, 1973.

[61] Launder, B.E.; Spalding, D.B. — Mathematical models of turbulence. Academic Press, London, 1972.

[62a] Kline, S.J.; Morkovin, M.V.; Sovran, G.; Cockrell, D.G. (eds.) — Computation of turbulent boundary layers - 1968 AFOSR-IFP-Stanford Conference.Vol I - Methods, predictions, evaluation and flow structure. Stanford Univ., 1969.

[62b] Coles, D.E.; Hirst, E.A. (eds.) — Computation of turbulent boundary layers - 1968 AFOSR-IFP-Stanford Conference. Vol. II - Compiled data. Stanford Univ., 1969.

[63] Schubauer, G.B.; Klebanoff, P. — Investigation of separation of the turbulent boundary layer. NACA TN 2133, 1950; NACA TR 1030, 1951.

[64] Schubauer, G.B.; Spangenberg, W.G. — Forced mixing in boundary layers. J.Fluid Mech., Vol. 8, 10-32, 1960.

[65] Cebeci, T.; Mosinskis, G.J.; Smith, A.M.O. — Calculation of separation points in incompressible turbulent flows. J.Aircraft, Vol. 9, 618-624, 1972.

[66] Statford, B.S. — The prediction of separation of the turbulent boundary layer. J.Fluid Mech., Vol. 5, 1-16, 1959.

[67] Goldschmied, F.R. — An approach to turbulent incompressible separation under adverse pressure gradients. J.Aircraft, Vol. 2, 108-115, 1965.

[68] McDonald, H.; Fish, R.W. — Practical calculations of transitional boundary layers. AGARDograph 164, 1972.

[69] Harris, J.E. — Numerical solution of the equations for compressible laminar, transitional and turbulent boundary layers and comparisons with experimental data. NASA TR R - 368, 1971.

[70] Blottner, F.G. — Finite difference methods of solution of the boundary-layer equations. AIAA J., Vol. 8, 193-205, 1970.

[71] Abbott, D.E.; Bethel, H.E. — Application of the Galerkin-Kantorovich-Dorotnitsyn method of integral relations to the solutions of steady laminar boundary layers. Ingenieur-Archiv, Vol. 37, 110-124, 1968.

[72] Nielson, J.N.; Lynes, L.L.; Goodwin, F.K. — Inhibition of flow-separation at high speed. Air Force Flight Dyn. Lab. Rep. AFFDL-TR-68-119, 1969.

[73] Wilson, R.E. — Turbulent boundary layer characteristics at supersonic speeds. J.Aeron. Sci., Vol. 17, 585-594, 1950.

[74] van Driest, E.R. — Turbulent boundary layer in compressible fluids. J.Aeron.Sci., Vol. 18, 145-160, 1951.

[75] Spalding, D.B.; Chi, S.W. — The drag of a compressible turbulent boundary layer on a smooth flat plate with and without heat transfer. J.Fluid Mech., Vol. 18, 117-143, 1964.

| | | |
|---|---|---|
| [76] | Morkovin, M.V. | Effects of compressibility on turbulent flows; in: The Mechanics of Turbulence, Gordon & Breach Sci. Pub., 367-380, 1964. |
| [77] | Maise, G.<br>McDonald, H. | Mixing length and eddy viscosity in a compressible boundary layer. AIAA J., Vol. 6, 73-80, 1968. |
| [78] | Beckwith, I.E. | Recent advances in research on compressible turbulent boundary layers. in: Analytic methods in aircraft aerodynamics. NASA SP-228, 355-416, 1970. |
| [79] | Peake, D.J.<br>Brakman, G.<br>Romeskie, J.M. | Comparisons between some high Reynolds number turbulent boundary layer experiments at Mach 4 and various recent calculation procedures. AGARD CP-93, 1971. |
| [80] | Winter, K.G.<br>Rotta, J.C.<br>Smith, K.G. | Studies of the turbulent boundary layer on a waisted body of revolution in subsonic and supersonic flow. ARC R&M 3633, 1968. |
| [81] | Herring, H.J.<br>Mellor, G.L. | A method of calculating compressible turbulent boundary layers. in: Compressible turbulent boundary layers, NASA SP-216, 27-132, 1969; also: NASA CR-1144, 1968. |
| [82] | Eichelbrenner, E.A. | Three-dimensional boundary layers. Annual Review of Fluid Mechanics, Vol. 5, 339-360, 1973. |
| [83] | Nash, J.F.<br>Patel, V.C. | Three-dimensional turbulent boundary layers. SBC Technical Books, Atlanta, 1972. |
| [84] | Wheeler, A.J.<br>Johnston, J.P. | Three-dimensional turbulent boundary layers - an assessment of prediction methods, data sets for two-space coordinate flows. Reports MD-30 (1971) and MD-32 (1972) of Thermosciences Div. Dep. Mech. Eng., Stanford University. |
| [85] | Horlock, J.H.<br>Norburg, J.F.<br>Cooke, J.C. | Three-dimensional boundary layers: a report on EUROMECH 2. J.Fluid Mech., Vol. 27, 369-380, 1967. |
| [86] | Fernholz, H. | Three-dimensional turbulent boundary layers - a report on EUROMECH 33. J.Fluid Mech., Vol. 58, 177-186, 1973. |
| [87] | Krause, E. | Numerical treatment of boundary layer problems. AGARD-LS-64, 1973. |
| [88] | Hirschel, E.H. | Theoretische Untersuchung von Transitionsphänomenen in der Grenzschicht eines unendlich gestreckten gepfeilten Flügels. Interner Bericht der DFVLR, Inst.f. Angew. Gasdynamik, Porz-Wahn, 1972; also in AGARD Rep. No. 602, 1973. |
| [89] | East, J.L.<br>Pierce, F.J. | Explicit numerical solution of the three-dimensional incompressible turbulent boundary layer equations. AIAA J., Vol. 10, 1216-1223, 1972. |
| [90] | Krause, E.<br>Hirschel, E.H.<br>Kordulla, E.H. | Finite difference solutions for three-dimensional turbulent boundary layers. Paper EUROMECH 33, Berlin 1972. |
| [91] | Fannelop, T.K. | A simple finite difference procedure for solving the three-dimensional laminar and turbulent boundary layer equations. Paper EUROMECH 33, Berlin 1972. |
| [92] | Wesseling, P.<br>Lindhout, J.P.E. | Three-dimensional incompressible turbulent boundary layers: comparison between calculations and experiments. Paper EUROMECH 33, Berlin 1972; also in AGARD-CP-93-71, 1971. |
| [93] | Nash, J.F. | The calculation of three-dimensional turbulent boundary layers in incompressible flow. J.Fluid Mech., Vol. 37, 625-642, 1969. |
| [94] | Bradshaw, P. | Calculation of three-dimensional turbulent boundary layers. J.Fluid Mech., Vol. 46, 417-445, 1971. |
| [95] | Cumpsty, N.A.<br>Head, M.R. | The calculation of three-dimensional turbulent boundary layers. Part 1: Flow over the rear of an infinite swept wing. Aero-Quart., Vol. 18, 55-84, 1969. |
| [96] | Eichelbrenner, E.A. | Three-dimensional turbulent boundary layers with heat transfer at the wall. Phys.Fluids (Suppl.) S157-S160, 1967. |
| [97] | Smith, P.D. | Calculation method for three-dimensional turbulent boundary layers. ARC R&M 3523, 1968. |
| [98] | Myring, D.F. | An integral prediction method for three-dimensional turbulent boundary layers in incompressible flow. RAE TR 70147, 1970. |
| [99] | Mager, A. | Generalization of boundary layer momentum integral equations to three-dimensional flow including those of rotating systems. NACA Rep. 1067, 1952. |
| [100] | Johnston, J.P. | On the three-dimensional turbulent boundary layer generated by secondary flow. J.Basic Eng. (ASME), Vol 82, 233-248, 1960. |
| [101] | Michel, R.<br>Quémard, C.<br>Consteix, J. | Méthode pratique de prévision des couches limites turbulentes bi- et tri-dimensionnelles. Réch.Aérospatiale (ONERA) No. 1972-1, 1-14, 1972. |
| [102] | Cumpsty, N.A<br>Head, M.R. | see [95] Part 4: Comparison with measurements on the rear of a swept wing. Aero.Quart., Vol. 21, 121-132, 1970. |
| [103] | Vermeulen, A.J. | Measurements of three-dimensional turbulent boundary layers. Ph.D.thesis, Univ. of Cambridge, 1971. |
| [104] | Spence, D.A. | Prediction of the characteristics of two-dimensional airfoils. J.Aero.Sci., Vol. 21, 577-588, 1954. |
| [105] | Spence, D.A.<br>Beasley, J.A. | The calculation of lift slopes, allowing for boundary layer, with application to the RAE 101 and 104 aerofoils. ARC R&M 3137, 1958. |

[106] Steinheuer, J. Berechnung des Reibungseinflusses auf den Auftrieb eines Spaltklappenprofils. DLR-FB 73-04, 1973; translated as RAE Lib. Transl. No. 1717, 1973.

[107] Brebner, G.G., Bagley, J.A. Pressure and boundary layer measurements on a two-dimensional wing at low speed. ARC R&M 2886, 1952.

[108] Powell, B.J. The calculation of the pressure distribution of a thick cambered aerofoil at subsonic speeds including the effect of the boundary layer. NPL Aero.Rep. 1238, 1967; also as: ARC CP 1005, 1967.

[109] Nash, J.F., Macdonald, A.G.J. The calculation of momentum thickness in a turbulent boundary layer at Mach numbers up to unity. NPL Aero.Rep. 1207, 1966; also as: ARC CP 963, 1966.

[110] Bhateley, I.C., Bradley, R.G. A simplified methematical model for the analysis of multi-element airfoils near stall. Paper 11 in AGARD-CP-102, 1972.

[111] Giesing, J.P. Potential flow about two-dimensional airfoils. Douglas Aircraft Co. Rep. LB 31946, 1965.

[112] Firmin, M.C.P., Cook, T.A. Detailed exploration of the compressible viscous flow over two-dimensional aerofoils at high Reynolds numbers. ICAS Paper No. 68-09, 1968.

[113] Riegels, F.W., Jacob, K. Berechnung der Druckverteilung endlich dicker Profile ohne und mit Klappen und Vorflügeln. Z.Flugwiss., Vol. 11, 1963; also as RAE Libr.Transl. No. 11, 1965.

[114] Foster, D.N., Irwin, H.P.A.H., Williams, B.R. The two-dimensional flow around a slotted flap. RAE Tech.Rep. 70164, 1970.

[115] Foster, D.N. The flow around wing sections with high-lift devices. AIAA Paper 71-96, 1971.

[116] de Vries, O. Comments on the methods developed at NLR for conducting two-dimensional research on high-lift devices. AGARD-CP-102, 1972.

[117] Labrujere, T.E., Schipholt, G.J., de Vries, O. Potential flow calculations to support two-dimensional wind tunnel tests on high-lift devices. ICAS Paper No. 72-13, 1972.

[118] Schröder, W. Investigation of the flow field in the slot region of a two-dimensional slotted trailing edge flap on a NACA-0006 aerofoil. VKI Project Report 73-12, 1973.

[119] Werlé, H. Sur l'écoulement au bord d'attaque d'un profil portant. La Récherche Aérospatiale (ONERA), 197-218, 1973.

[120] Jacob, K. Berechnung der abgelösten inkompressiblen Strömung um Tragflügelprofile und Bestimmung des maximalen Auftriebs. Z.Flugwiss., Vol. 17, 221-230, 1969.

[121] Jacob, K. Berechnung der inkompressiblen Strömung mit Ablösung für Profilsysteme. DFVLR-AVA Bericht IB 065-72A34, 1972.

[122] Baumert, W. Messungen an Druckverteilungen und Geschwindigkeitsprofilen an einem Rechteckflügel mit Vorflügel und abgesenkter Nase. AVA Bericht 71C31, 1971, and AVA Bericht 71C29, 1971.

[123] Thomas, F. Die Ermittlung der Schüttelgrenzen von Tragflügeln im transsonischen Geschwindigkeitsbereich. in: Jahrbuch WGLR 1966, 126-144, Vieweg Braunschweig; also as: ARA Libr.Transl. No. 19, 1969.

[124] Sinnott, C.S. On the prediction of mixed subsonic/supersonic pressure distributions. J.Aerospace Sci., Vol. 27, 767-778, 1960.

[125] Murman, E.M., Cole, J.D. Calculation of plane steady transonic flows. AIAA Paper 70-188, 1970.

[126] Thomas, F., Redeker, G. A method for calculating the transonic buffet boundary including the influence of Reynolds number. AGARD-CP-83-71, 1971.

[127] Gentry, A.E., Oliver, W.R. Investigation of aerodynamic analysis problems in transonic maneuvering. McDonnell-Douglas Rep. MDC-J5264-01, 1971.

[128] Redeker, G. Die Berechnung der Schüttelgrenzen von Pfeilflügeln. Z.Flugwiss., Vol. 21, 345-359, 1973.

[129] Gadeberg, B.L., Ziff, H.L. Flight-determined buffet boundaries on ten airplanes and comparisons with five buffeting criteria. NACA RM A50J27, 1951.

[130] Vanino, R., Wedemeyer, E. Wind tunnel investigations of buffet loads on four airplane models. AGARD-CP-83-71, 1971.

[131] Hall, M.G. Scale effects in flows over swept wings. AGARD-CP-83-71, 1971, also as RAE TR 71043, 1971.

[132] Little, B.H. Scaling effects on shock induced separation. AGARD-LS-37-70, 1970.

[133] Paterson, J.H. Scaling effects on drag prediction. AGARD-LS-37-70, 1970.

[134] Loving, D.L. Wind-tunnel-flight correlations of shock-induced separated flow. NASA TND-3580, 1966.

[135] Report of the High Reynolds Number Wind Tunnel Study Group of the Fluid Dynamics Panel. AGARD Adv.Rep. 35-71, 1971.

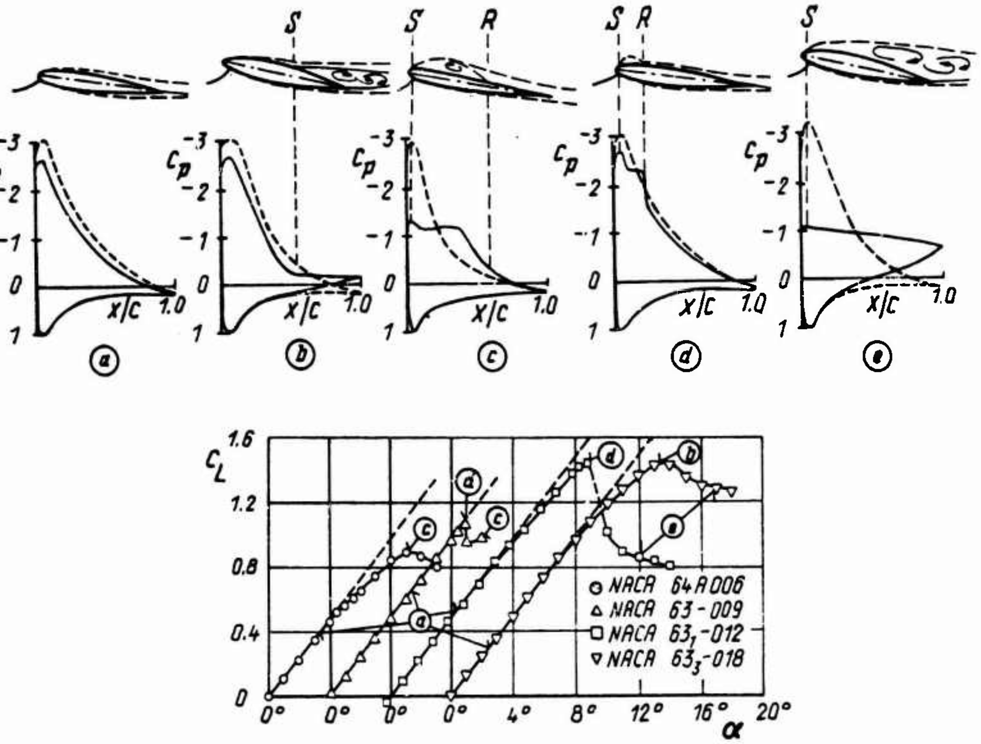

**Fig. 1:** Effects of the boundary layer on the pressure distribution and the lift characteristics of single airfoils (schematical)

| | | | |
|---|---|---|---|
| ⓐ | with attached boundary-layer flow, | ----- | inviscid flow |
| ⓑ | with trailing edge separation, | ——— | viscous flow |
| ⓒ | with leading edge separation and long bubble, | S | separation point |
| ⓓ | with leading edge separation and short bubble, | R | reattachment point |
| ⓔ | with leading edge separation | | |

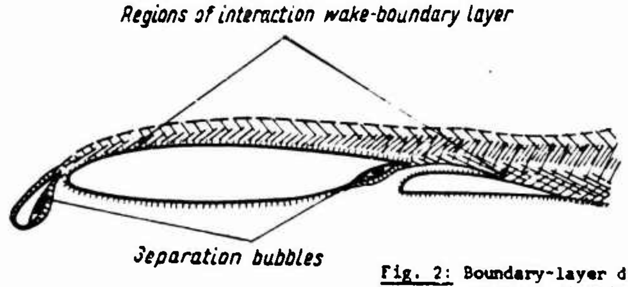
Regions of interaction wake-boundary layer
Separation bubbles

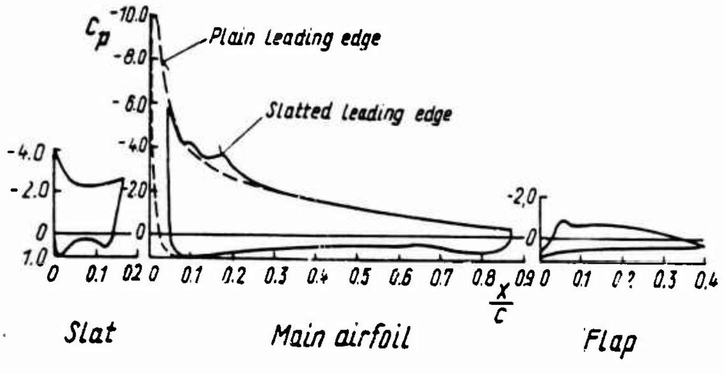

**Fig. 2:** Boundary-layer development and typical pressure distribution for the flow over an airfoil with leading edge slat and trailing edge flap; from [6].

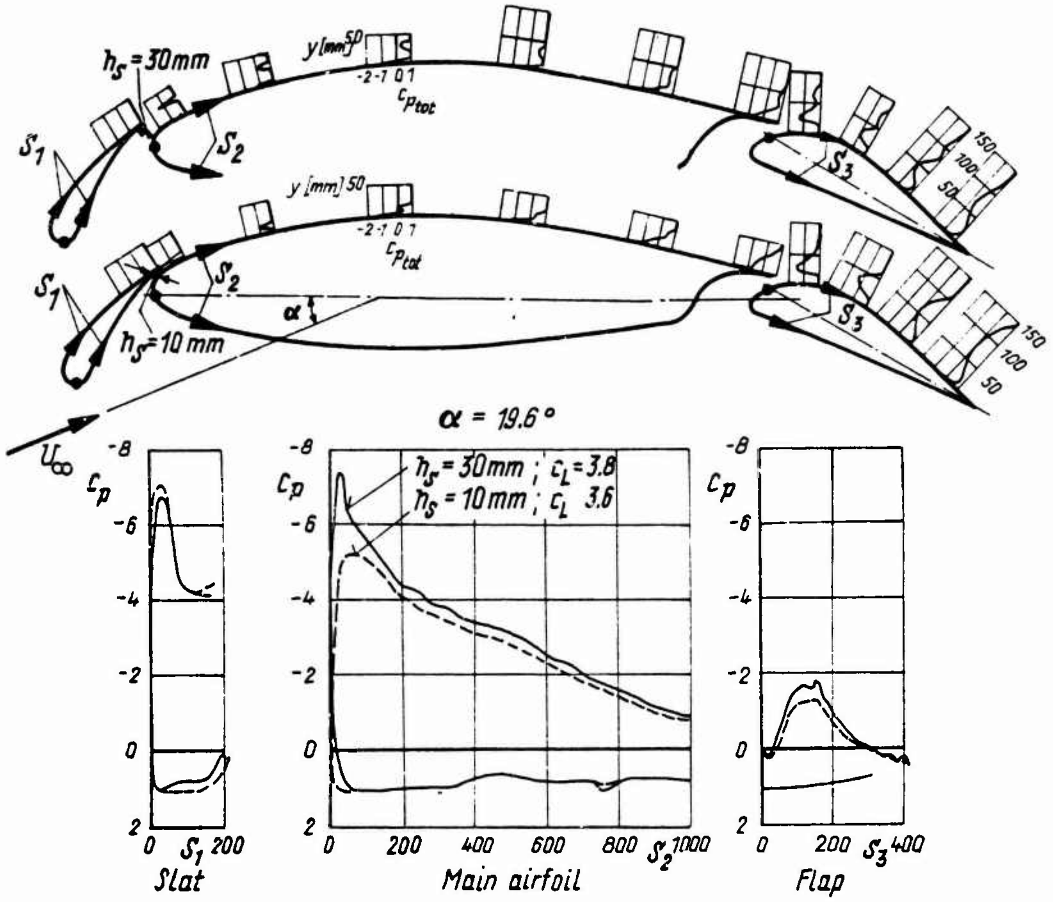

Fig. 3: Development of the total head pressure in the boundary-layer flow over an airfoil with slat and flap; comparison of measured static pressure distributions for two different flap settings; from [7].

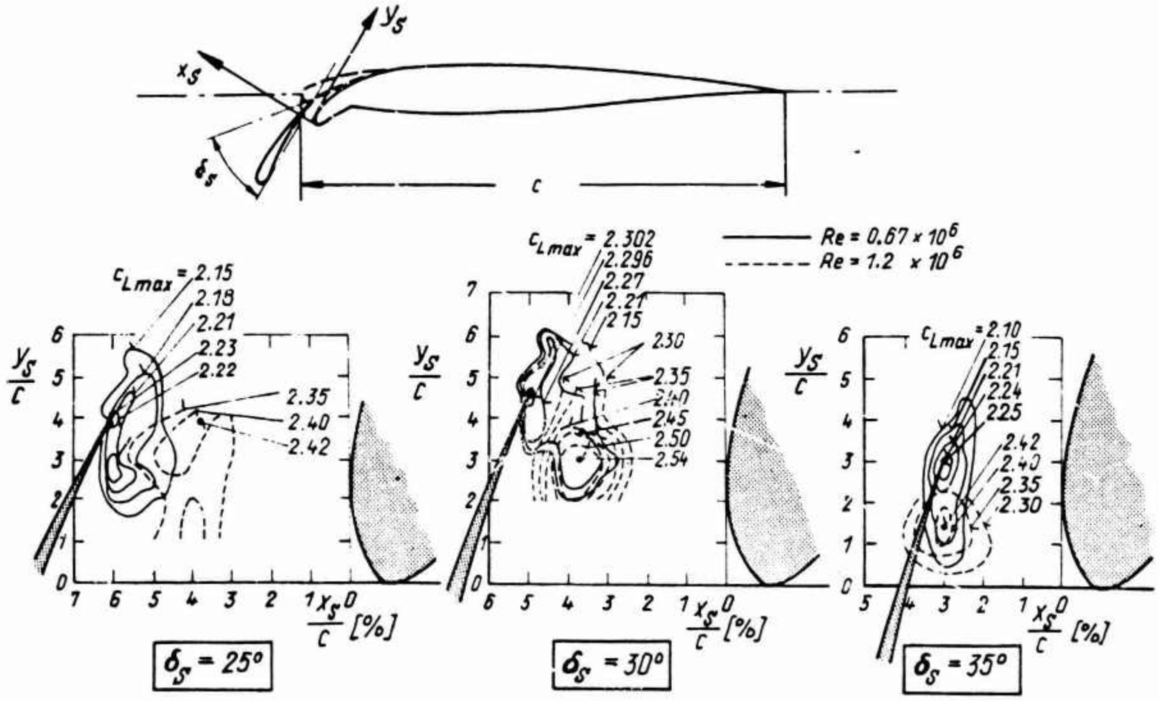

Fig. 4: Effect of Reynolds number on the optimal slat position for maximum lift at three different slat angles for flow over a slatted airfoil with drooped nose, after [8].

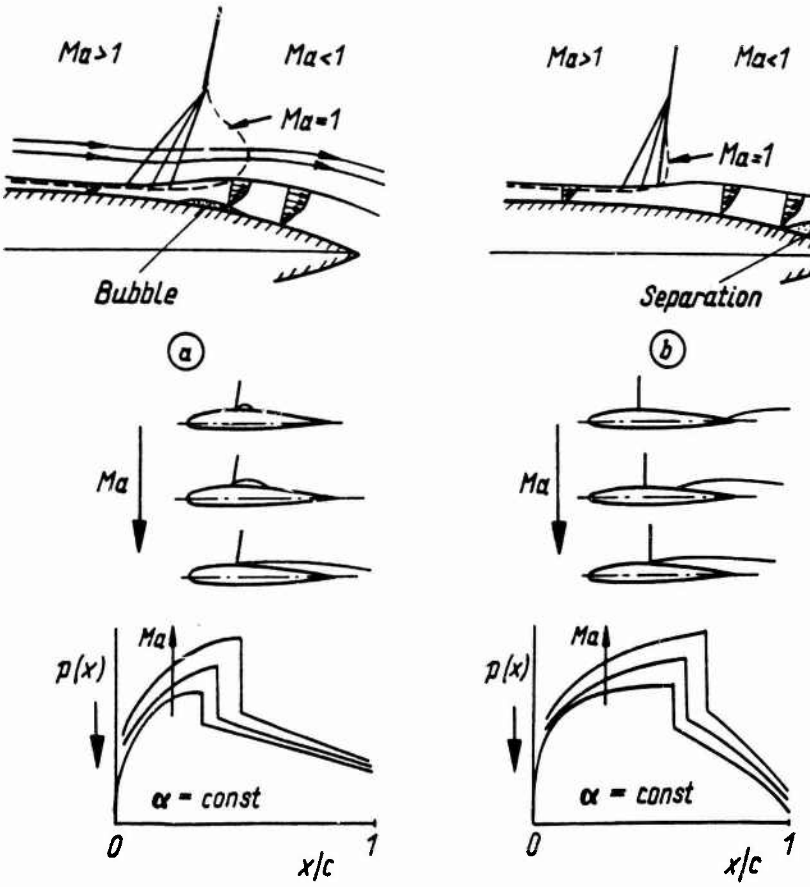
Ma>1
Ma<1
Ma=1
Bubble
Ma>1
Ma<1
Ma=1
Separation
a
b
Ma
Ma
p(x)
Ma
α = const
0
1
x/c
p(x)
Ma
α = const
0
1
x/c

*Model A: Bubble type separation* *Model B: Rear separation*

**Fig. 5:** Flow models explaining shock induced separation effects on transonic airfoils.

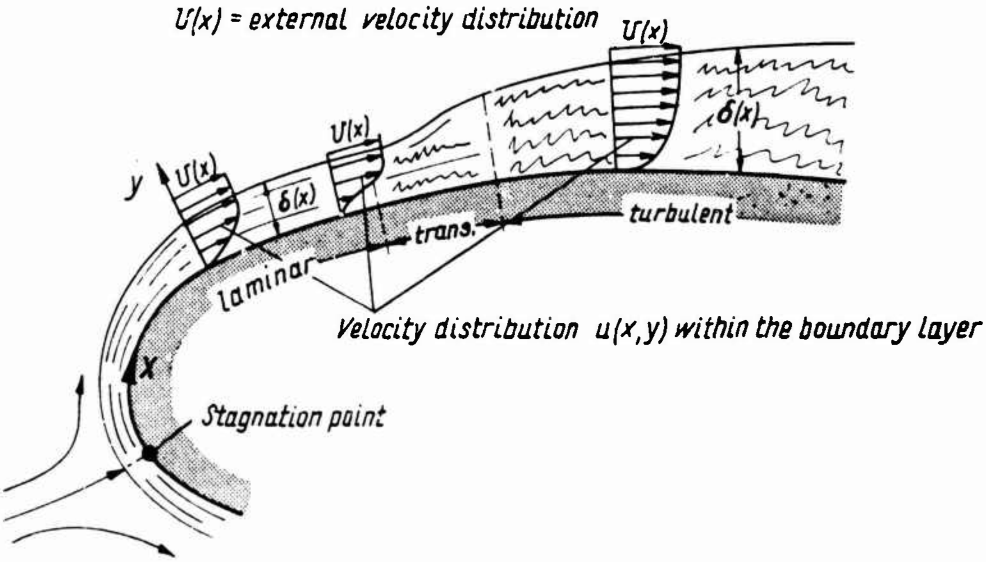
U(x) = external velocity distribution
U(x)
U(x)
U(x)
δ(x)
δ(x)
y
laminar
trans.
turbulent
Velocity distribution u(x,y) within the boundary layer
x
Stagnation point

**Fig. 6:** Development of an attached boundary on an airfoil like body (schematical).

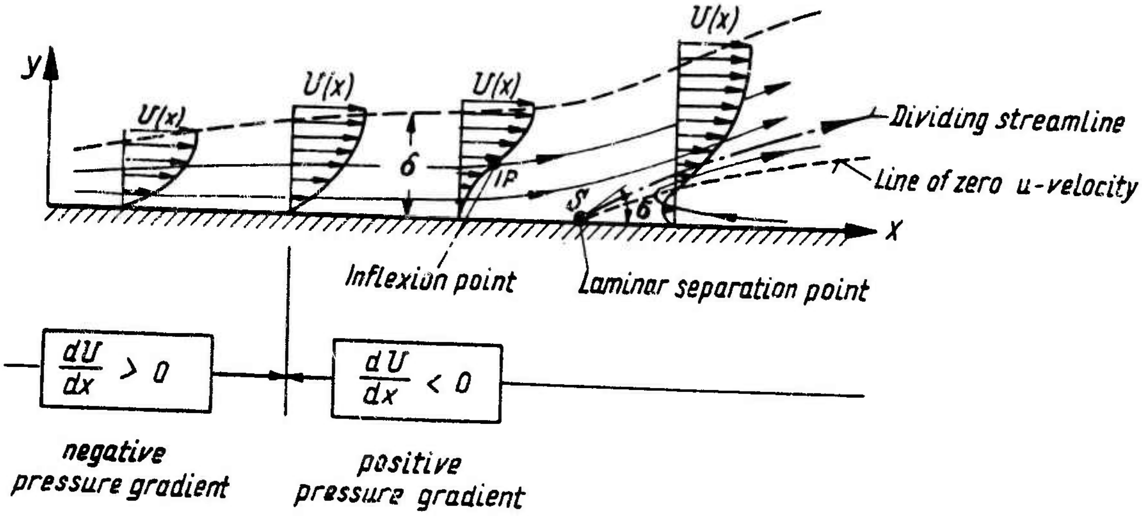
y
U(x)
U(x)
U(x)
U(x)
δ
IP
S
δ
Dividing streamline
Line of zero u-velocity
x
Inflexion point
Laminar separation point
$\frac{dU}{dx} > 0$
$\frac{dU}{dx} < 0$
negative pressure gradient
positive pressure gradient

Fig. 7: Laminar boundary-layer development including separation (schematical)

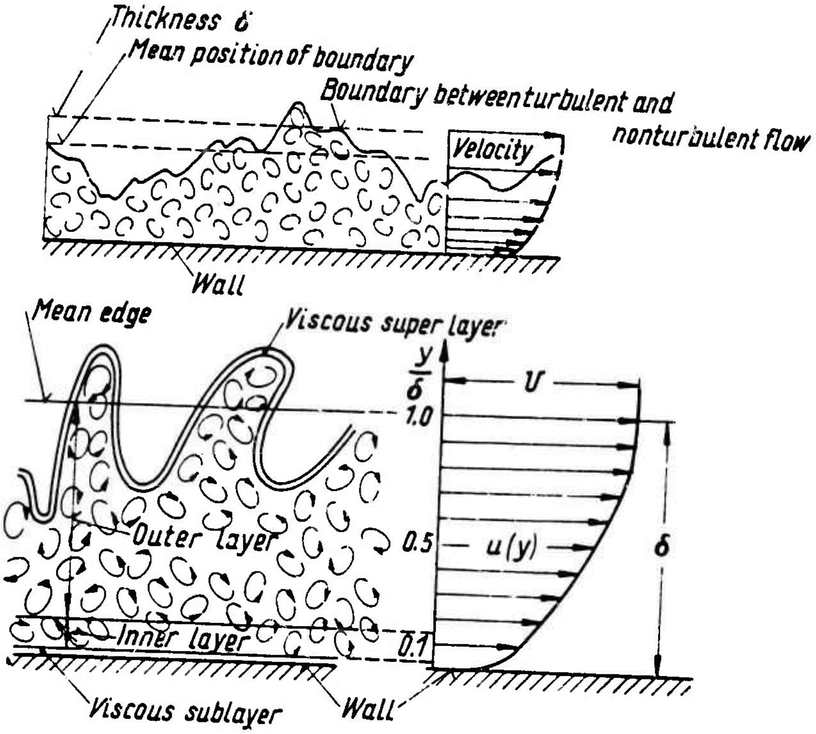
Thickness δ
Mean position of boundary
Boundary between turbulent and nonturbulent flow
Velocity
Wall
Mean edge
Viscous super layer
y/δ
U
1.0
0.5
u(y)
δ
0.1
Outer layer
Inner layer
Viscous sublayer
Wall

Fig. 8: Schematical sectional view of a turbulent boundary layer and mean velocity profile.

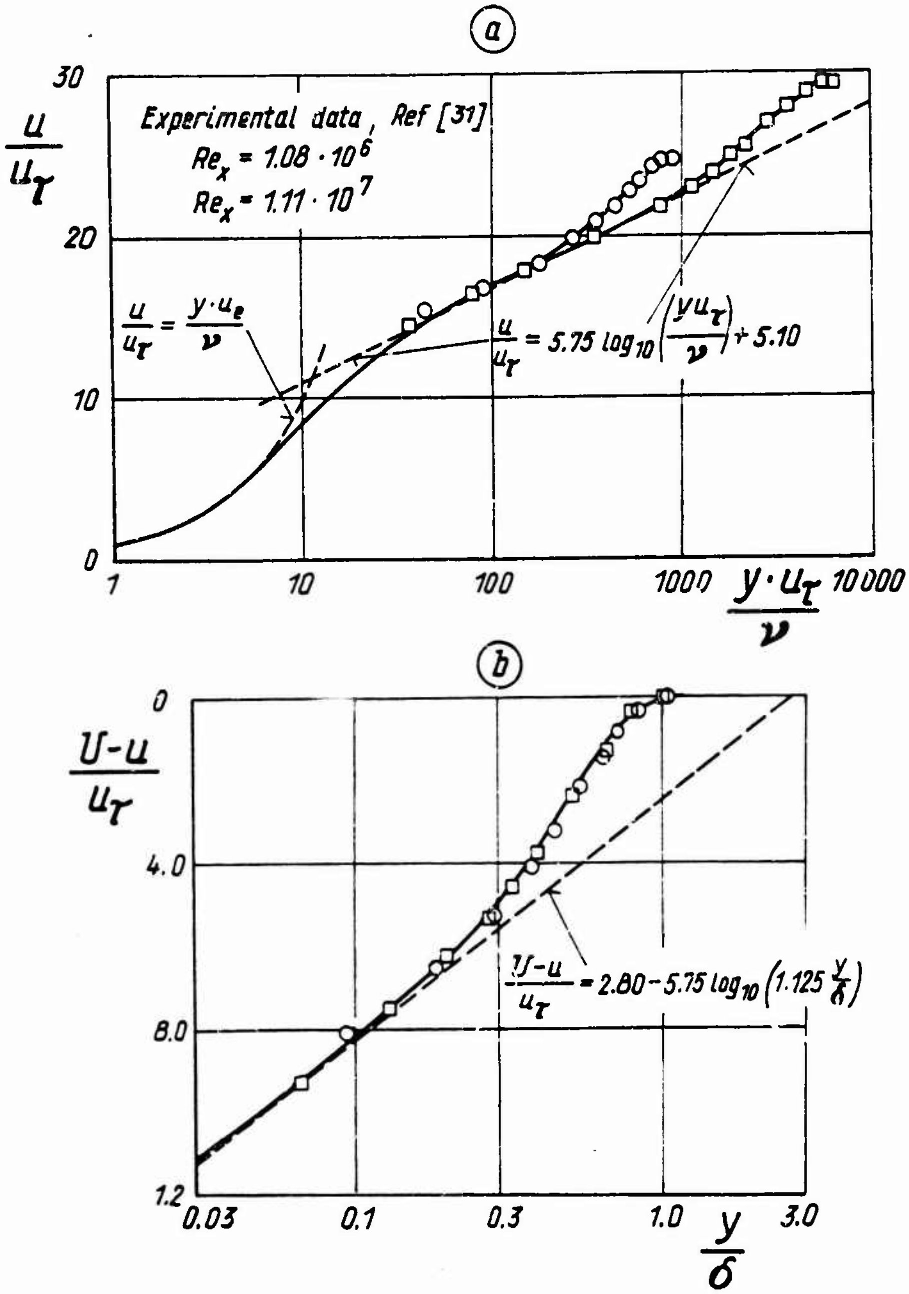

Fig. 9: Logarithmic representation of the velocity distribution of a turbulent boundary layer:

ⓐ in wall-orientated coordinates (law-of-the-wall),

ⓑ in edge-orientated coordinates (velocity-defect-law or law-of-the-wake).

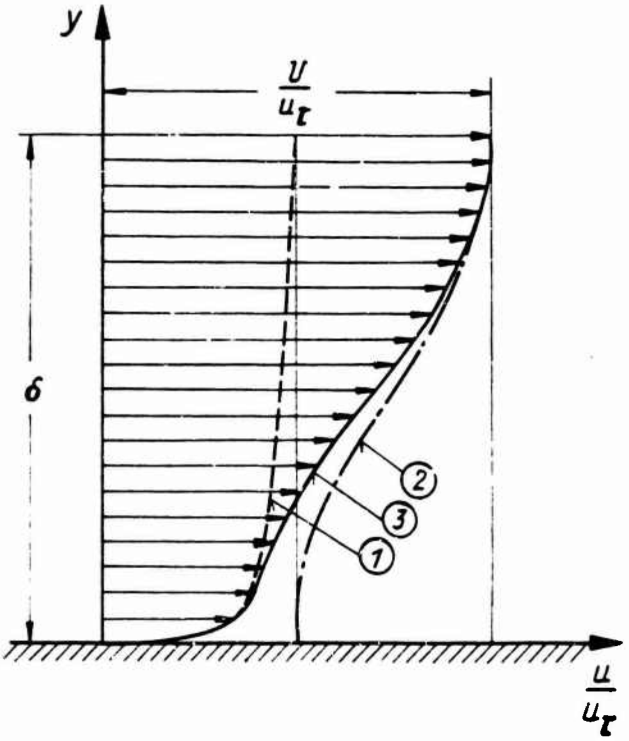

Fig. 10: Composite velocity profile of a turbulent boundary layer

$$\underbrace{\frac{u}{u_\tau}}_{\textcircled{3}} = \underbrace{\frac{1}{\kappa}\ln\left(\frac{y\cdot u_\tau}{\nu}\right)+C}_{\textcircled{1}} + \underbrace{\frac{\Pi}{\kappa}\cdot\omega\left(\frac{y}{\delta}\right)}_{\textcircled{2}}$$

① Law-of-the-wall component
② Wake component
③ Composite velocity profile

| Method | Field | Integral | Moment-of-momentum | 1st. grade (Stanford) |
|---|---|---|---|---|
| AL | | X | | X |
| EN | | X | | |
| LM$_1$ | | X | | |
| RO | | X | | |
| FG | | X | | X |
| ZW | | X | | |
| ME | | X | | |
| MR | | X | | |
| LM$_2$ | | X | | |
| MO | | X | | |
| RC | | | X | |
| MC | | | X | |
| MO | | | X | X |
| MR | | | X | |
| NA | | | X | |
| NH | | | X | X |
| FN | | | X | |
| MH | | X | | |
| DT&TR | | X | | |
| BB | X | | | |
| BF | X | | | X |
| CS | X | | | X |
| KR | X | | | |
| MH | X | | | X |
| NR | X | | | |
| NP | X | | | |
| RE | X | | | |

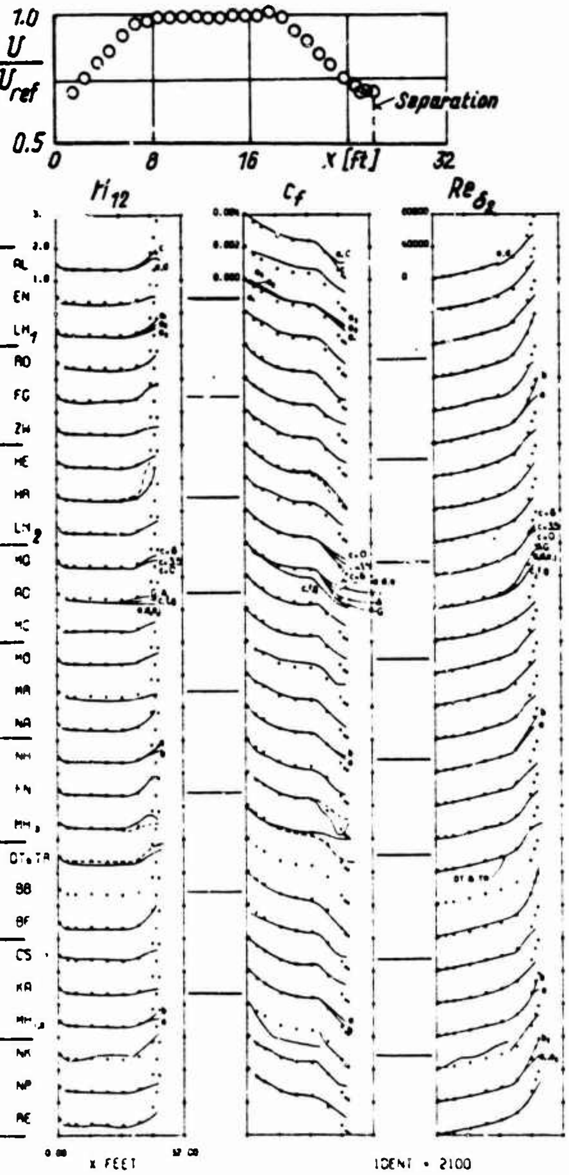

Fig. 11: Results of different boundary layer calculation methods applied to the experimental case of Schubauer and Klebanoff [63] as presented at the Stanford Conference [62].

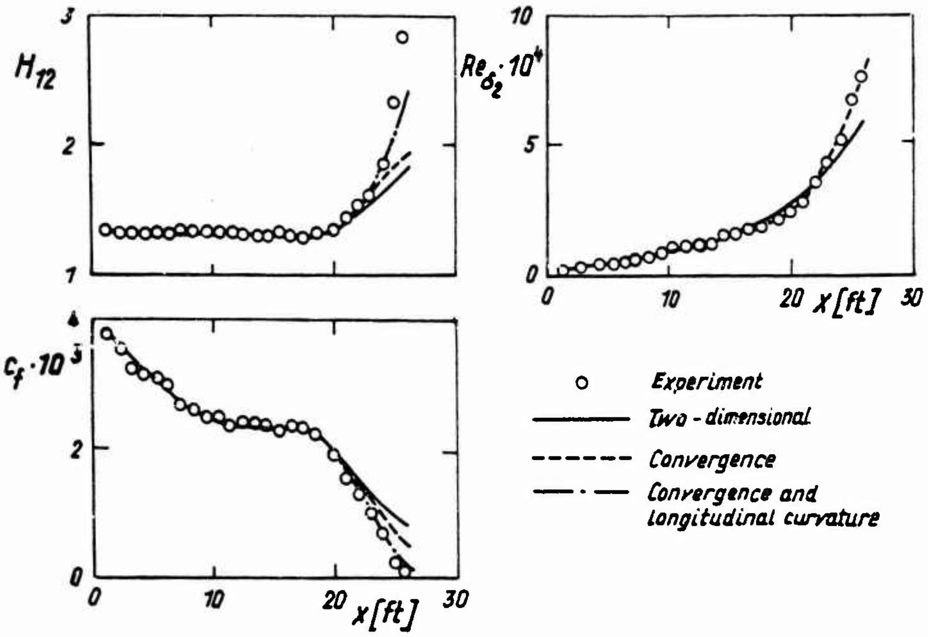

Fig. 12: Results of the calculation method of Green et al. [49]applied to the experimental case of Schubauer and Klebanoff [63] including the effects of convergence and longitudinal curvature.

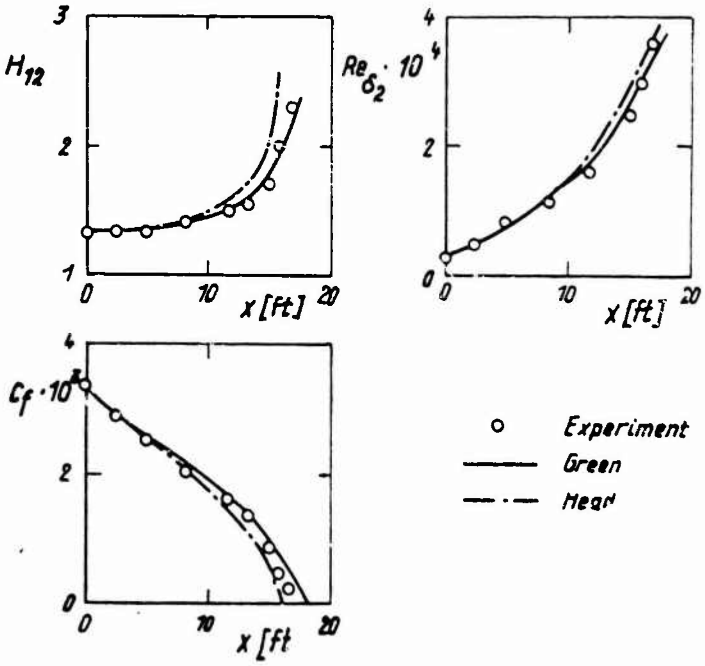

Fig. 14: Results of the calculation methods of Green et al. [49] and Head [45] applied to the experimental case of Schubauer and Spangenberg [64].

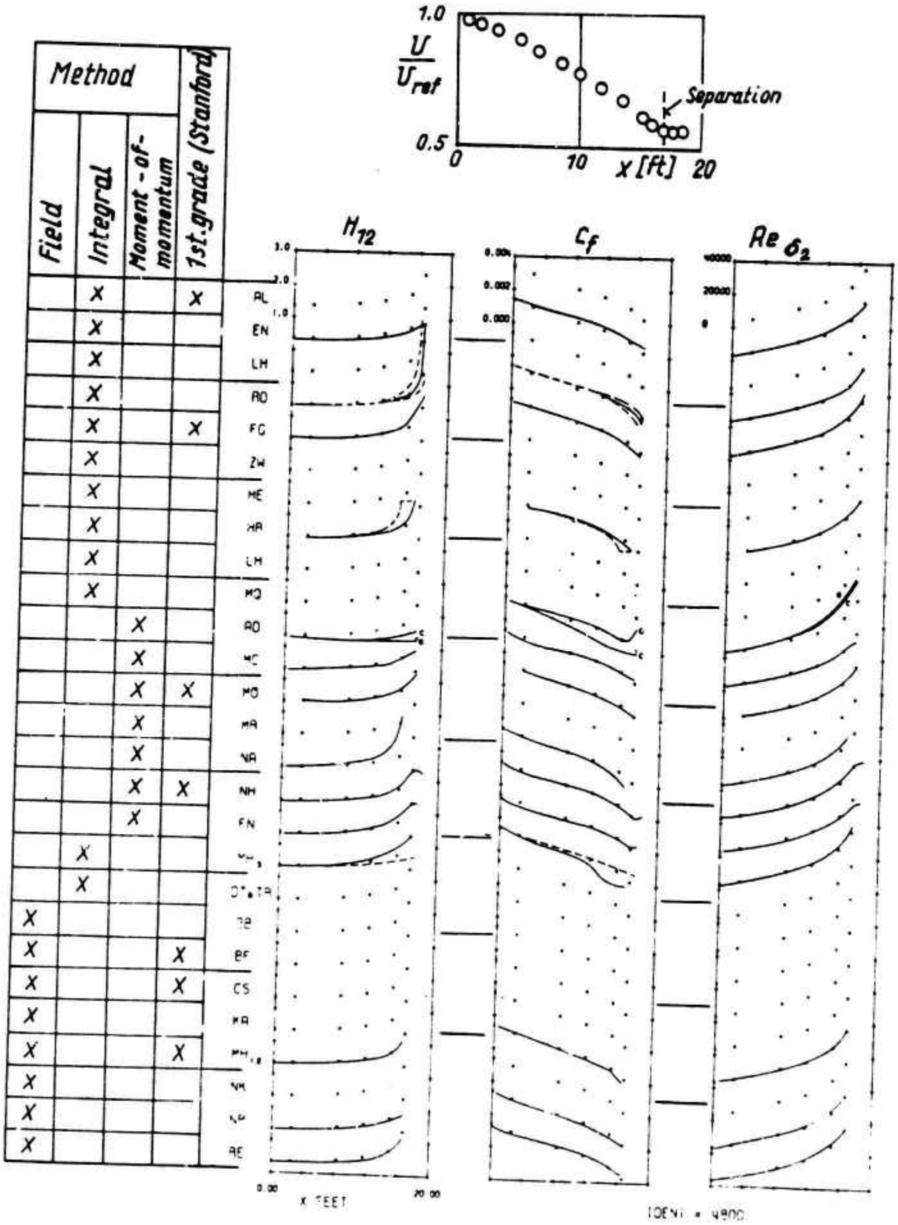

| Method: Field | Integral | Moment-of-momentum | 1st.grade (Stanford) | |
|---|---|---|---|---|
| | X | | X | AL |
| | X | | | EN |
| | X | | | LH |
| | X | | | RO |
| | X | | X | FG |
| | X | | | ZW |
| | X | | | HE |
| | X | | | HA |
| | X | | | LH |
| | X | | | MO |
| | | X | | AO |
| | | X | | MC |
| | | X | X | MO |
| | | X | | MA |
| | | X | | NA |
| | | X | X | NH |
| | | X | | FN |
| | X | | | $MH_3$ |
| | X | | | D*, TA |
| X | | | | [illegible] |
| X | | | X | BF |
| X | | | X | CS |
| X | | | | KA |
| X | | | X | $MH_{1,2}$ |
| X | | | | NK |
| X | | | | NP |
| X | | | | RE |

Fig. 13: Results of different boundary layer calculation methods applied to the experimental case of Schubauer and Spangenberg [64] as presented at the Stanford Conference [62].

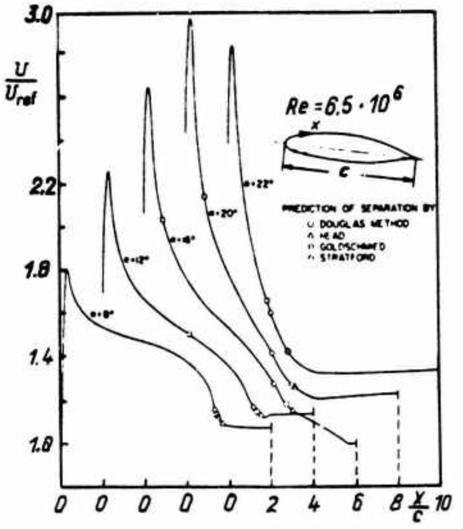

**Fig. 15:** Predicted separation points for the experimental pressure distribution on the NACA $66_2$-420 airfoil; from [65].

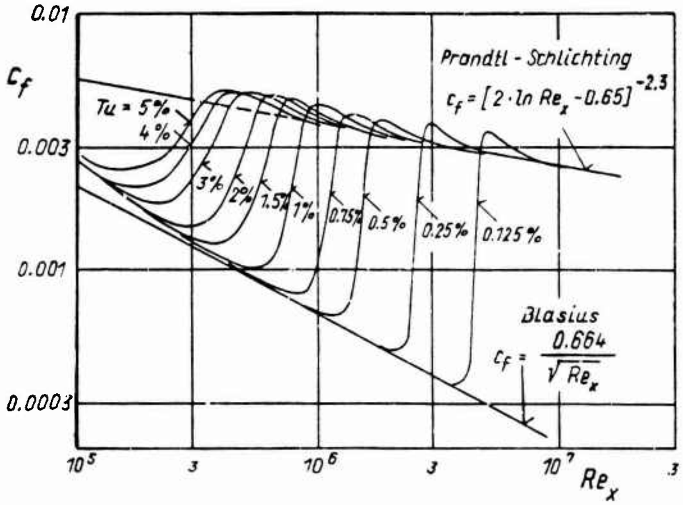

**Fig. 16:** Calculated skin-friction coefficient of the transitional flat plate boundary layer for different levels of free-stream turbulence; from [68].

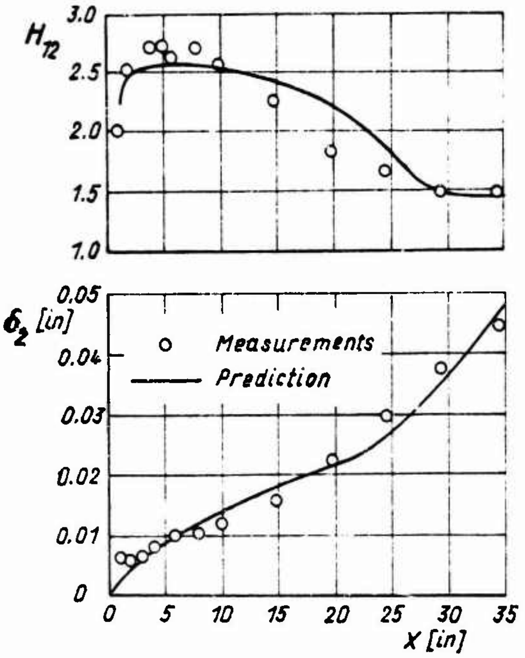

Fig. 17: Calculated shape parameter and momentum thickness of a transitional boundary layer in comparison with measurements; from [68].

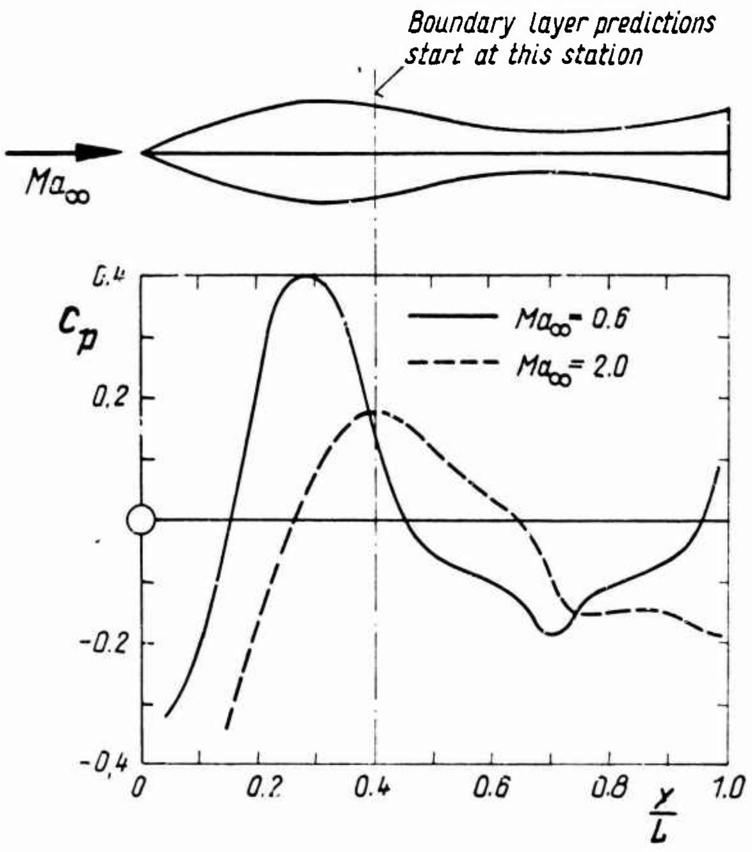

Fig. 18: Geometry and measured pressure distribution for waisted body of revolution, after Winter et al. [80].

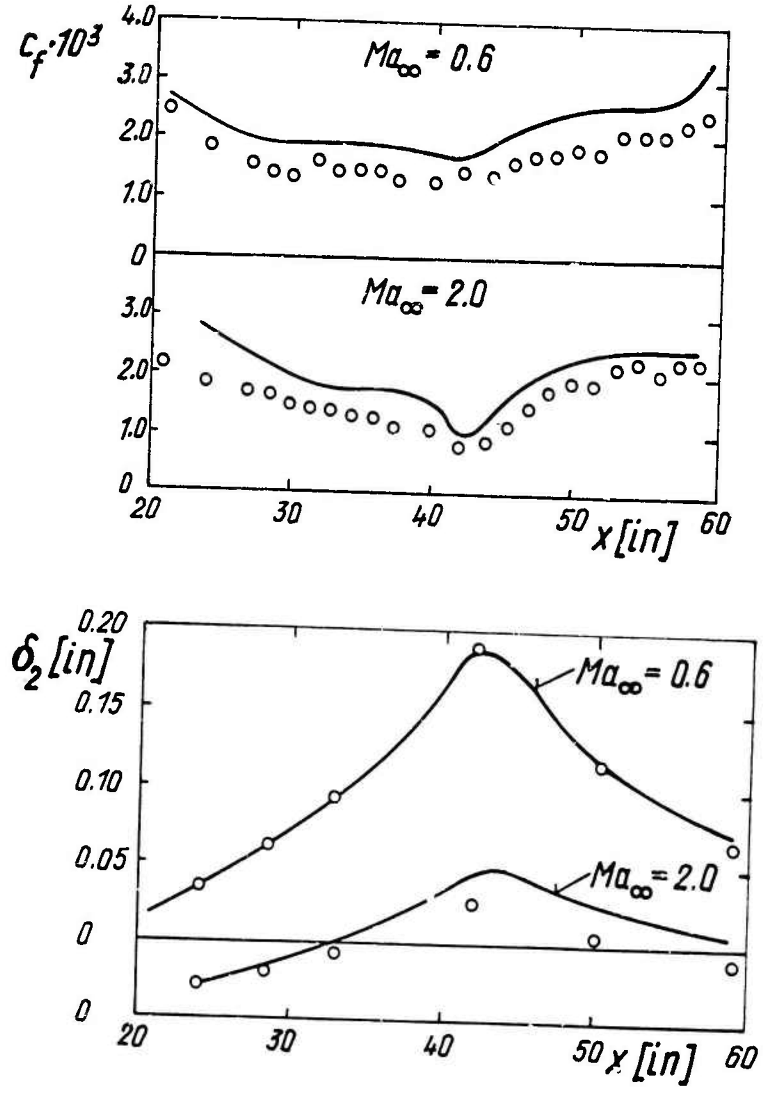

Fig.: 19: Comparison between the distributions of skin friction and momentum thickness as measured by Winter et al. [80] and the predicted distributions as calculated by the complete field method of Herring and Mellor [81].

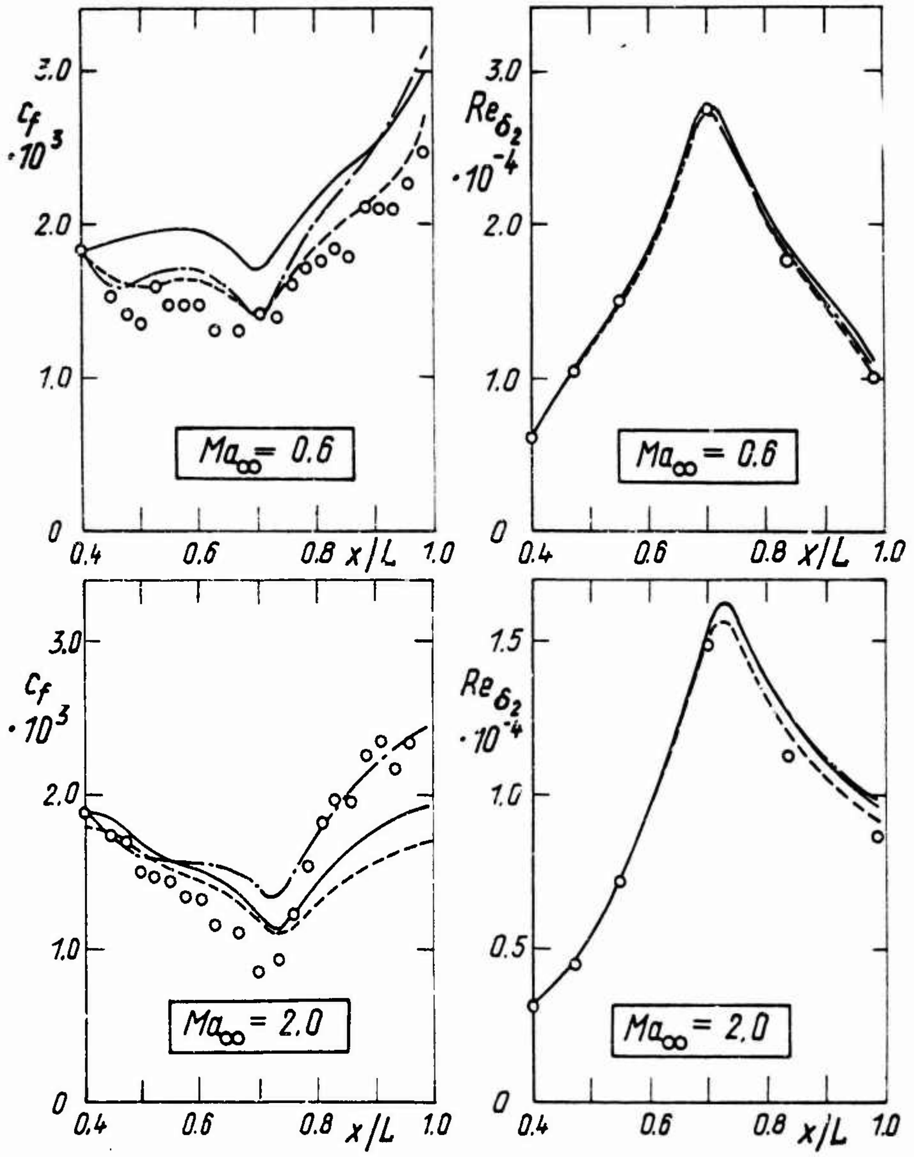

Fig. 20. Comparison between the distributions of skin friction and momentum thickness Reynolds number as measured by Winter et al. [80] and the predicted distributions as calculated by the methods of Head [45] and Green et al. [49] including secondary effects;

– – – – – – Head, ———————— Green: quasi two-dimensional

— · — · — Green: corrected for longitudinal curvature, lateral strain, and dilatation

○ experimental

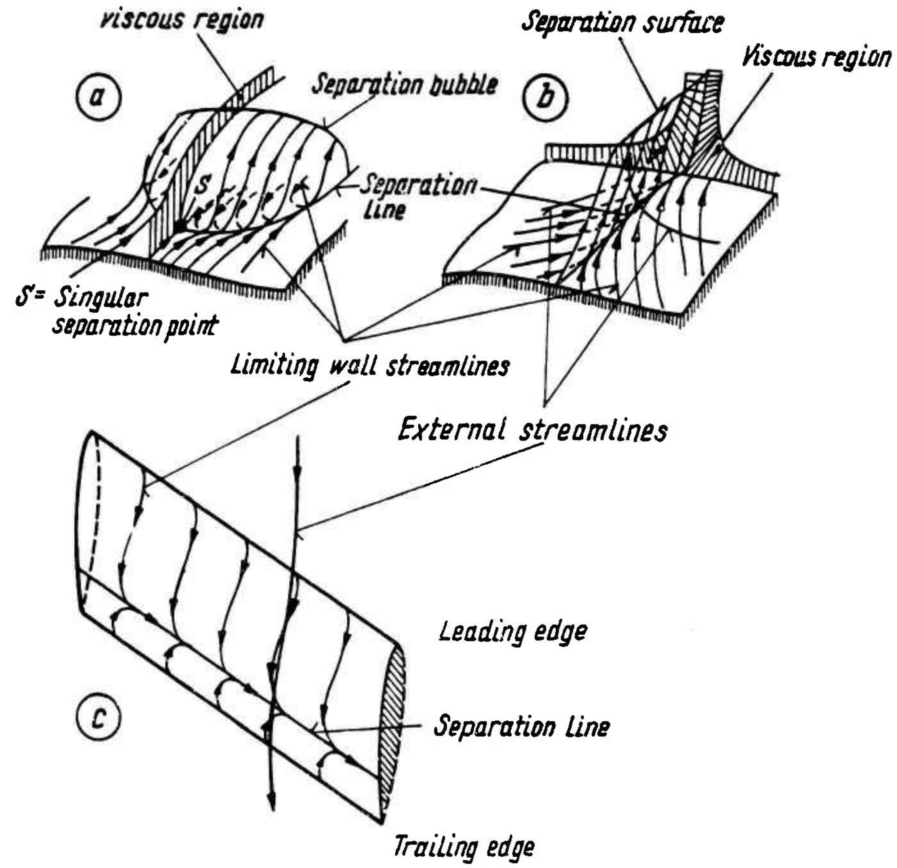
viscous region
Separation bubble
Separation surface
Viscous region
a
b
S
Separation line
S = Singular separation point
Limiting wall streamlines
External streamlines
Leading edge
c
Separation line
Trailing edge

Fig. 21: Patterns of three-dimensional boundary-layer separation: ⓐ separation with a singular point S; ⓑ separation from a line of confluent limiting wall streamlines; ⓒ separation on a yawed infinite wing.

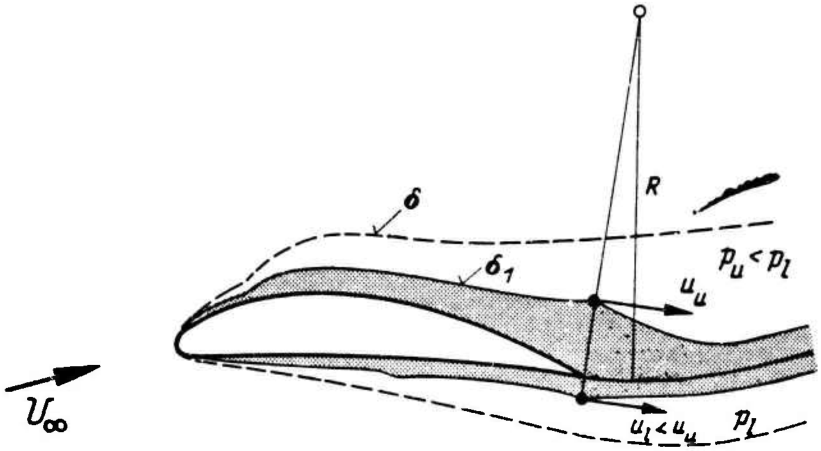
R
δ
δ₁
$u_u$
$p_u < p_l$
$U_\infty$
$u_l < u_u$
$p_l$

Fig. 22: Sketch illustrating curvature effect of trailing edge wake on the external velocities and pressures.

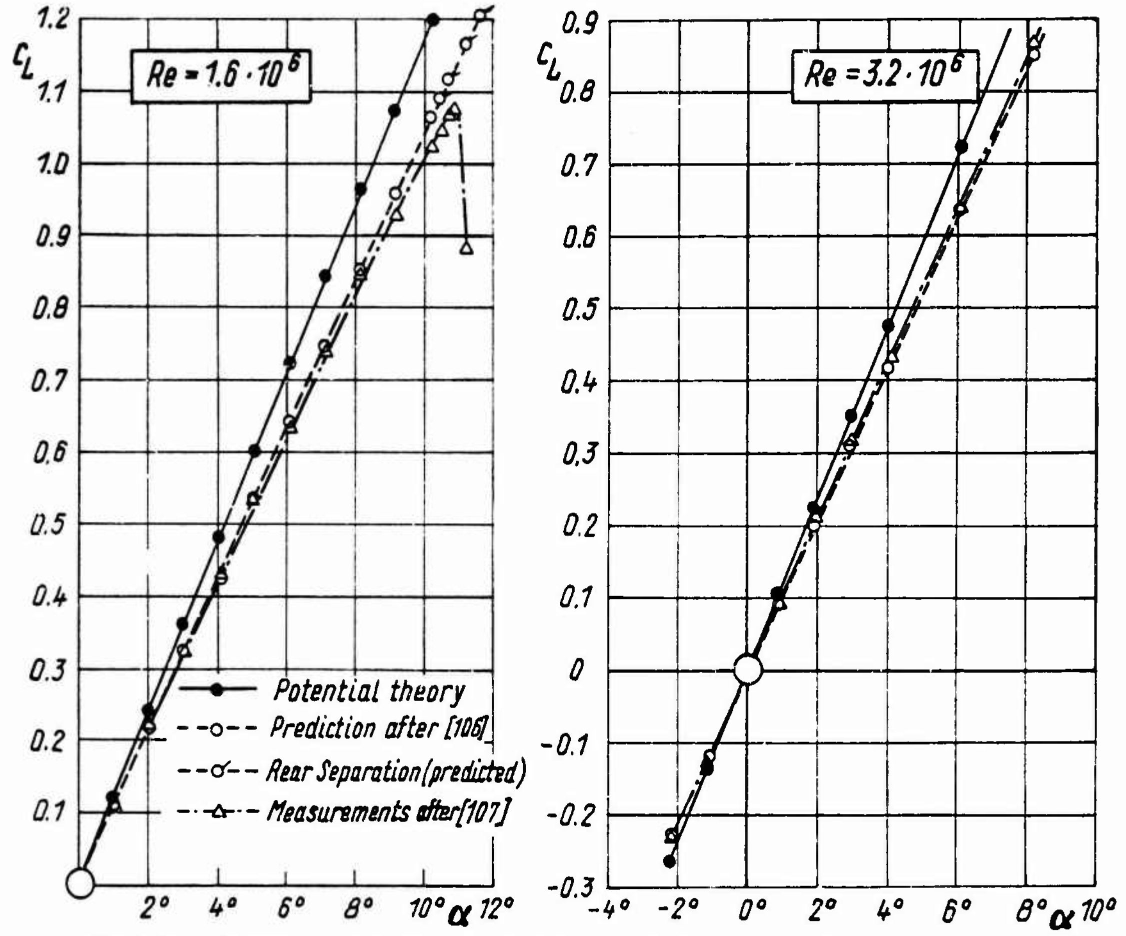

Fig. 23: Lift coefficient of the RAE 101-airfoil vs. incidence; comparison between calculations after [106] and experiments after [107].

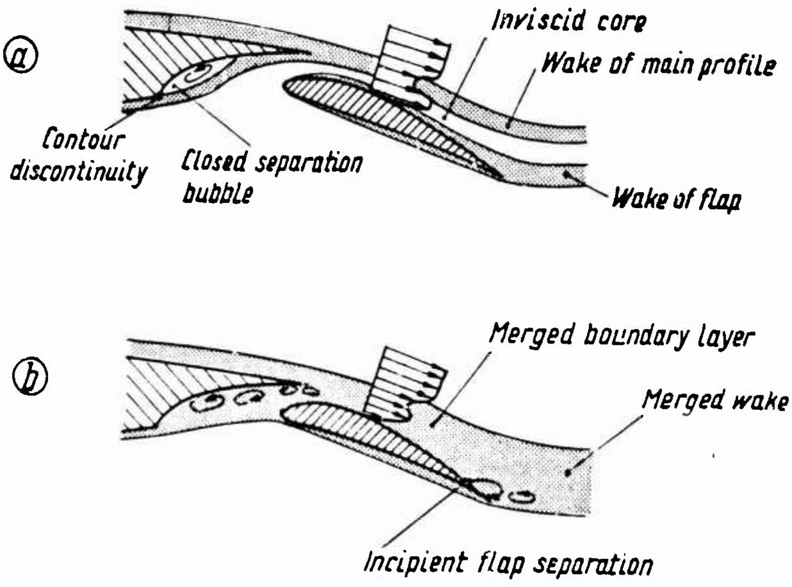
ⓐ
Inviscid core
Wake of main profile
Contour discontinuity
Closed separation bubble
Wake of flap
ⓑ
Merged boundary layer
Merged wake
Incipient flap separation

Fig. 24: Illustration of the qualitative behavior of the viscous flow through the flap slot of a flapped airfoil: ⓐ favorable, ⓑ unfavorable flow situation.

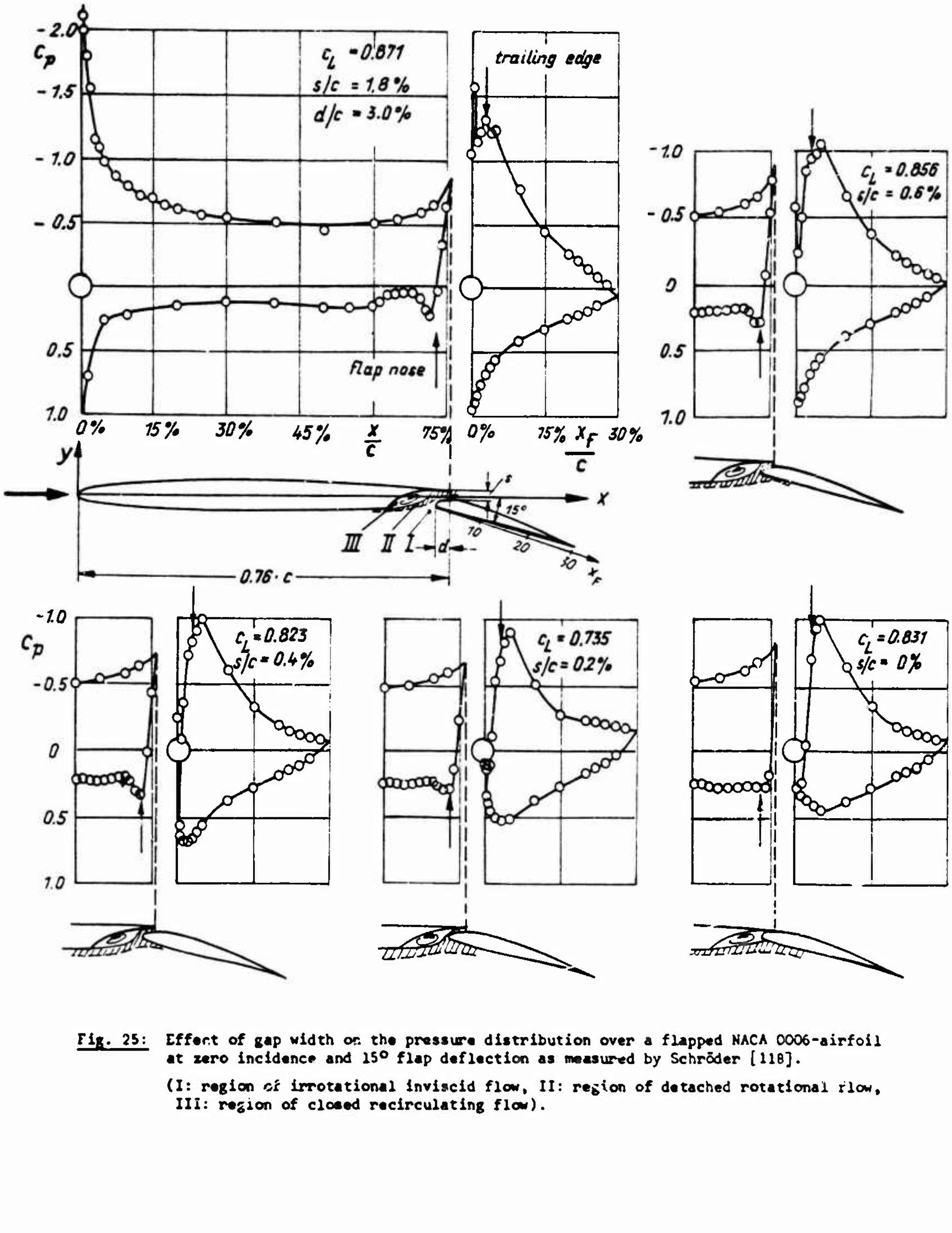

Fig. 25: Effect of gap width on the pressure distribution over a flapped NACA 0006-airfoil at zero incidence and 15° flap deflection as measured by Schröder [118].

(I: region of irrotational inviscid flow, II: region of detached rotational flow, III: region of closed recirculating flow).

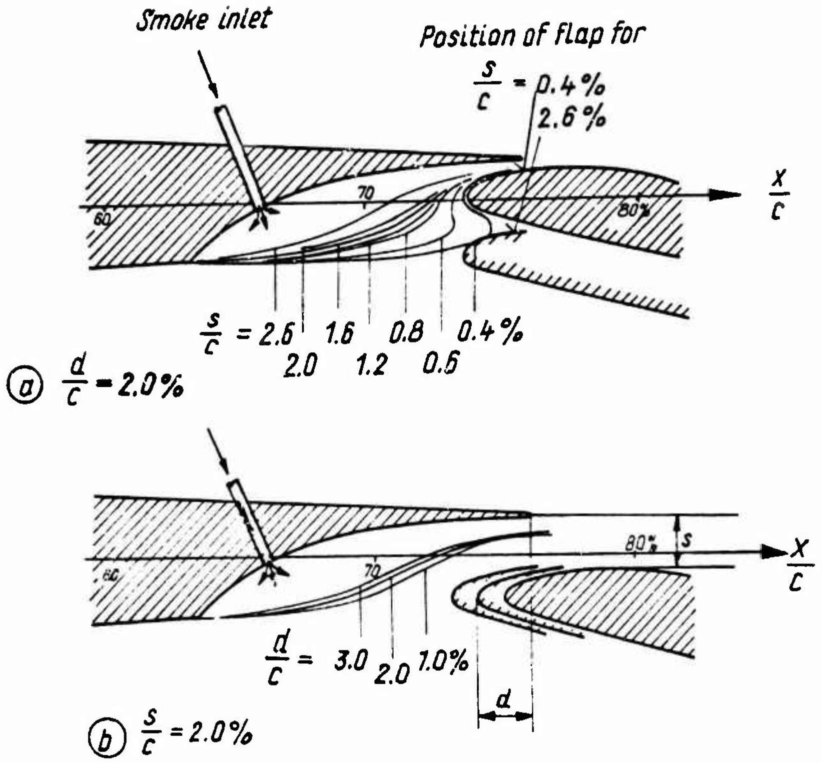
Smoke inlet
Position of flap for
$\frac{s}{c}$ = 0.4%
2.6%
70
60
80%
$\frac{x}{c}$
$\frac{s}{c}$ = 2.6 1.6 0.8 0.4%
2.0 1.2 0.6
ⓐ $\frac{d}{c}$ = 2.0%
70
80%
s
$\frac{d}{c}$ = 3.0 2.0 1.0%
d
ⓑ $\frac{s}{c}$ = 2.0%

Fig. 26: Smoke contour lines derived from flow visualization pictures in the slot region of a flapped NACA 0006-airfoil; from [118]: ⓐ for varying gap width s at constant overlap d, ⓑ for varying overlap d at constant gap width s.

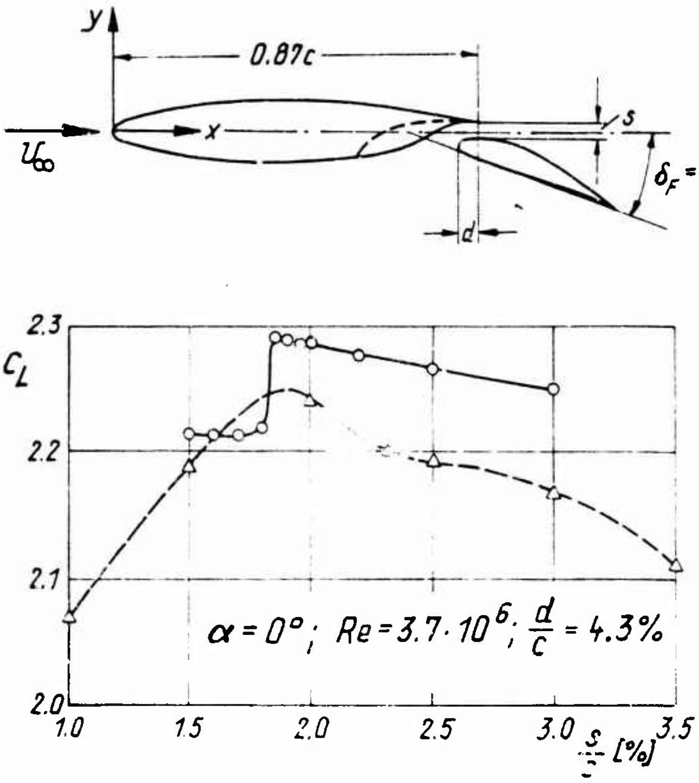

Fig. 27:

Comparison of measured [114] and calculated [106] lift coefficients showing the effect of varying gap width s at constant overlap d for a flapped NPL 3111-airfoil.

---Δ--- experimental

——○—— calculation

(Note that the experiments were carried out with the broken line contour while in the calculations the solid line contour was used).

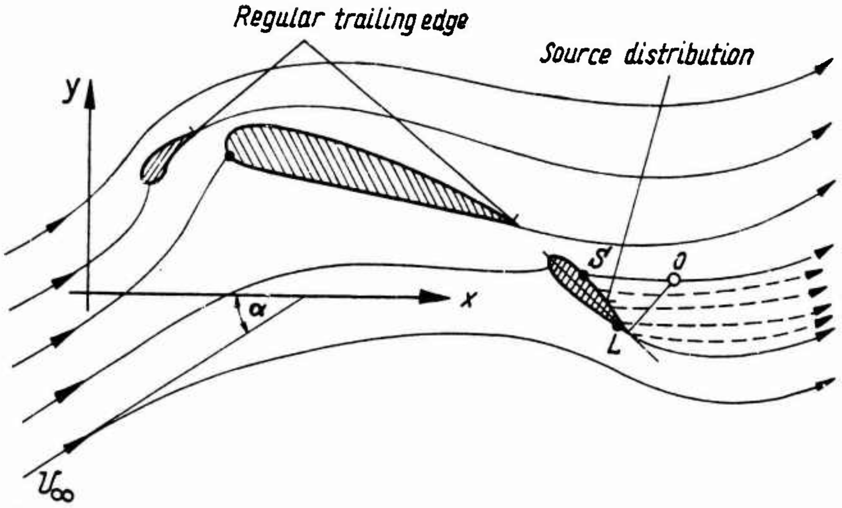
Regular trailing edge
Source distribution
y
x
α
S
0
L
$U_\infty$

Fig. 28: Theoretical model of the two-dimensional flow over an airfoil with slat and flap simulated by an additional source flow over the separated region according to Jacob [121]

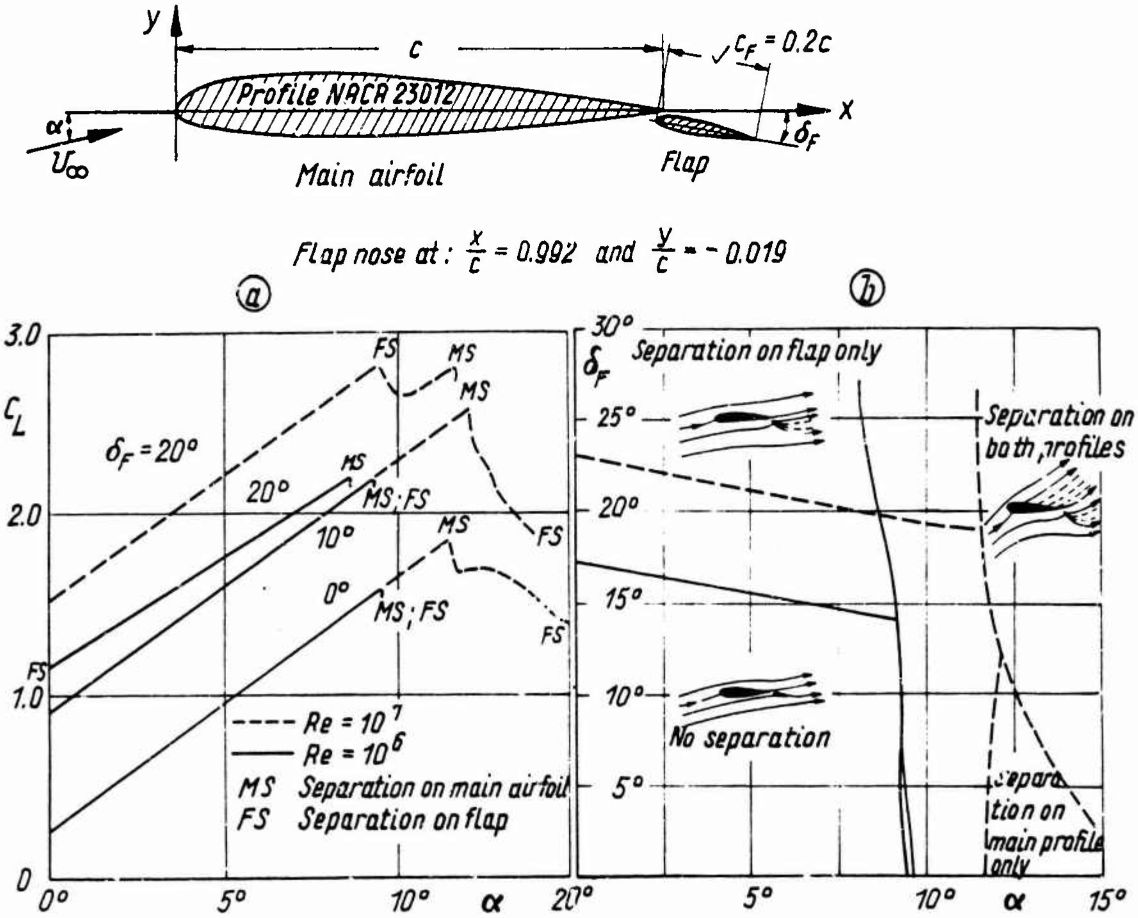

Fig. 29: Calculated separation characteristics of a NACA 23012-airfoil with flap at two different Reynolds numbers: ⓐ lift coefficient vs. incidence for constant flap deflection, ⓑ limits of flow types dependent on incidence and flap deflection; from [121]

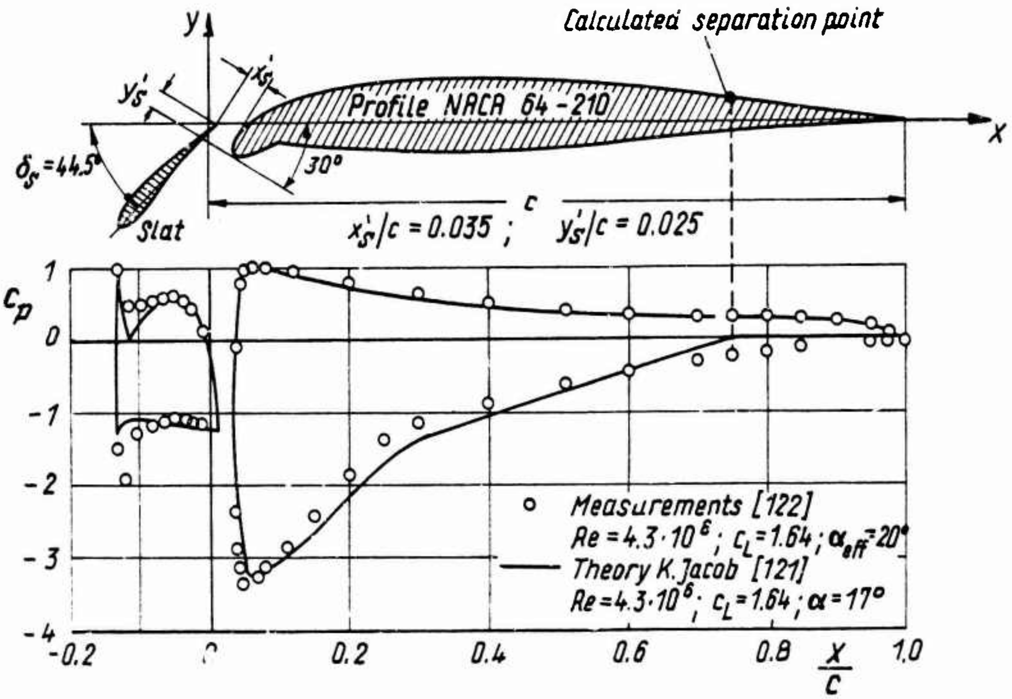

Fig. 30: Calculated and measured pressure distribution on a slatted NACA 64-210-airfoil with drooped nose; from [121].

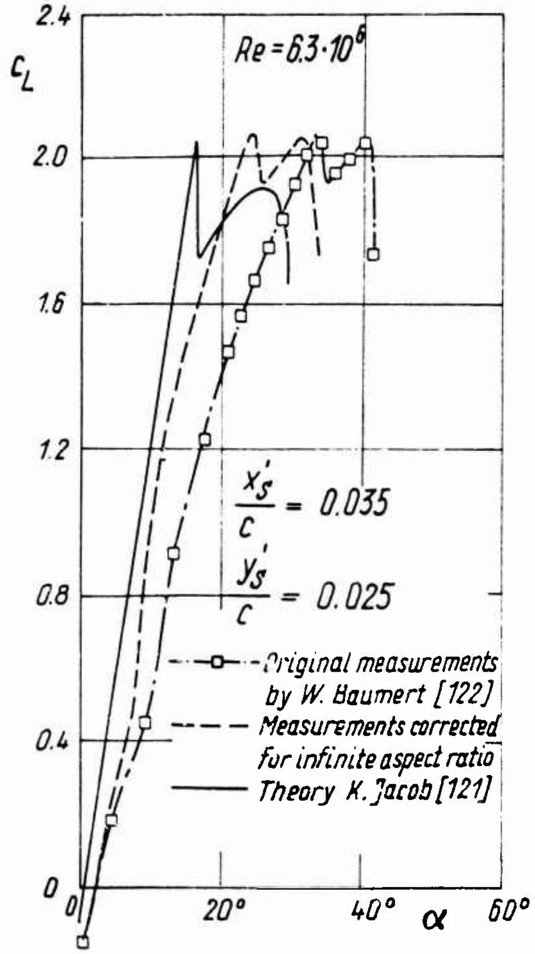

Fig. 31:
Comparison between measured and calculated lift-vs.-incidence curves of a slatted NACA 64-210-airfoil with drooped nose; from [121]

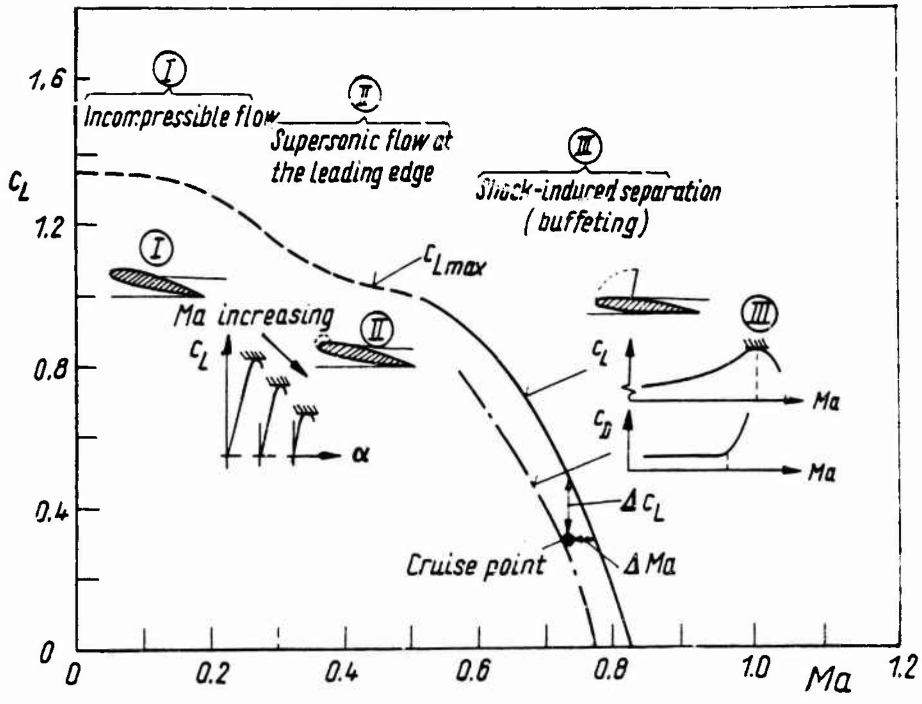

Fig. 32: Dependence of maximum lift on Mach number and associated separation phenomena.

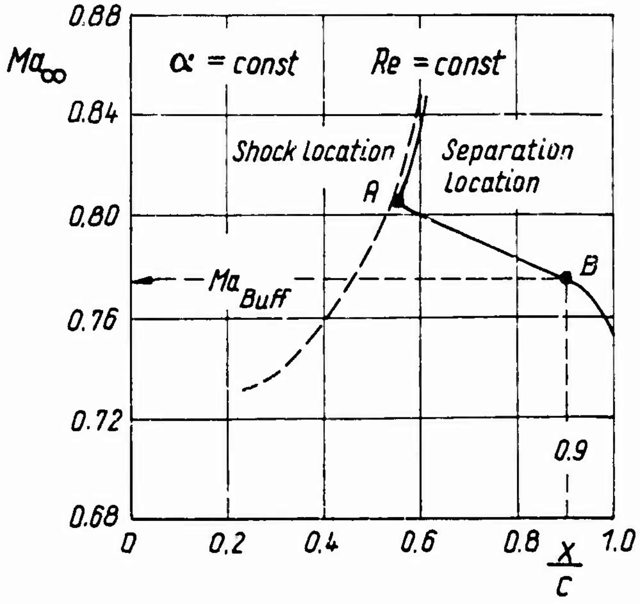

Fig. 33: Chordwise location of normal shock and separation point depending on Mach number on a transonic wing section (schematical); point A indicates separation immediately behind shock, point B explains 90 %-chord criterion of Thomas [126] for buffet-onset.

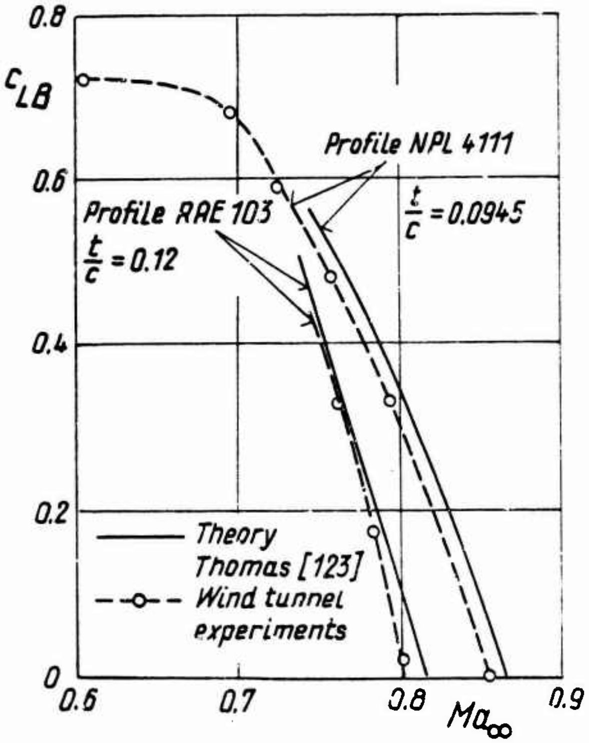

**Fig. 34:**

Comparison of experimentally determined buffet boundaries with the theoretical predictions after the method of Thomas [123] for two different wing sections.

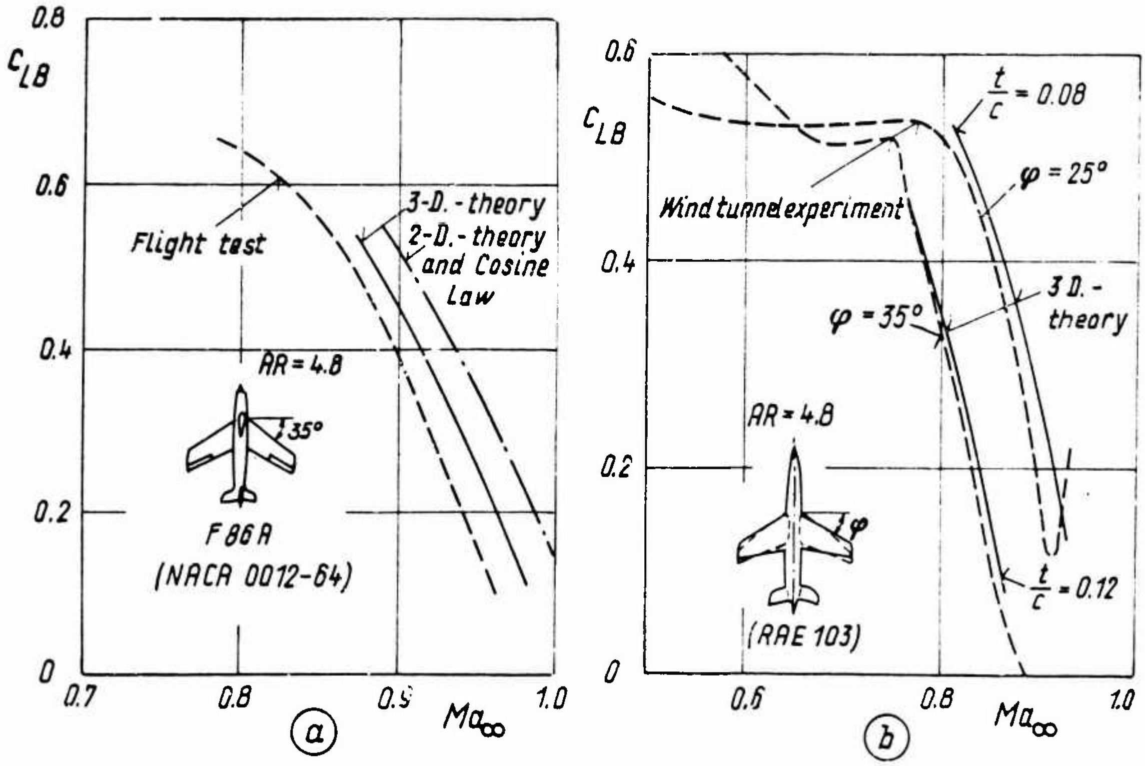

**Fig. 35:** Comparison of experimentally determined buffet boundaries with theoretical predictions
ⓐ for the fighter aircraft F-86A in flight test [129] at Re = $10^7$,
ⓑ for a variable sweep wind tunnel model [130] at Re = $1.3 \cdot 10^6$; from [128].

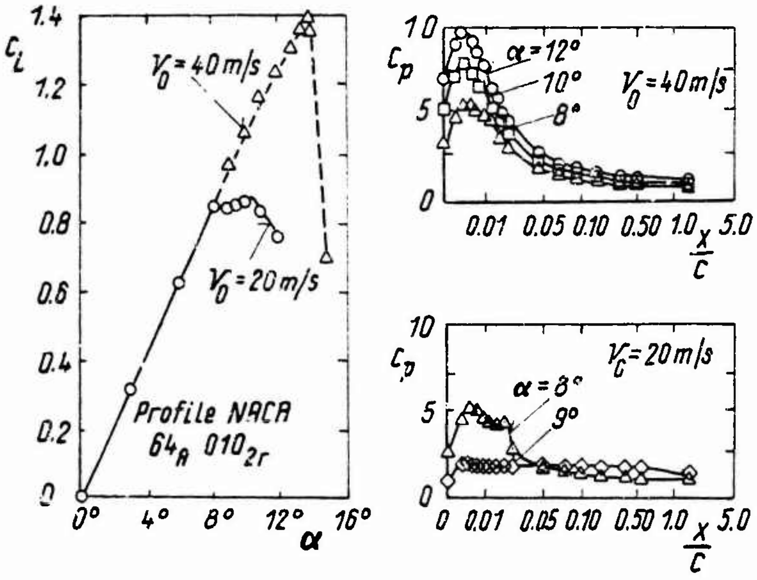

**Fig. 36:** Experimental lift-vs.-incidence curve and pressure distributions in the presence of short and long bubbles; from [5].

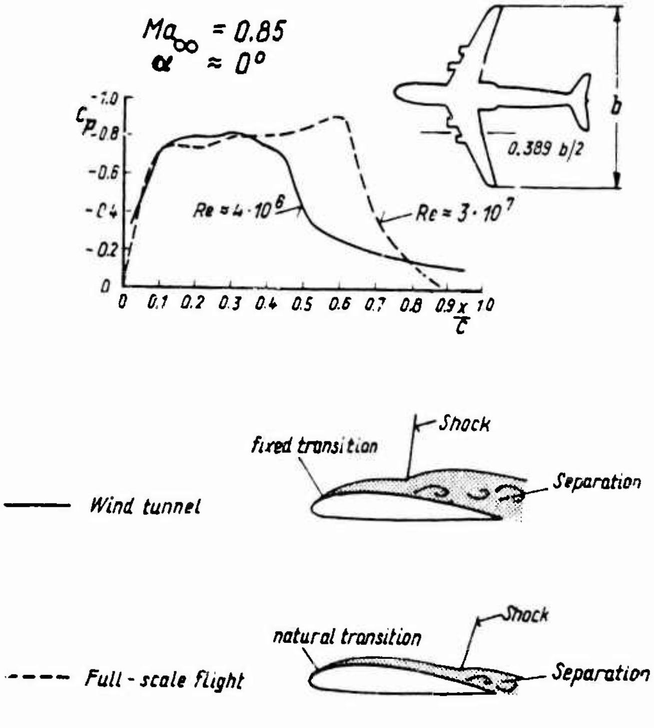

**Fig. 37:** Scale effect on a transport aircraft; from [134].

N74-26453

# ENGINE INSTALLATION AERODYNAMICS

J. LEYNAERT
Head, Applied Aerodynamics Division
Office National d'Etudes et de Recherches Aérospatiales (ONERA)
92320 Châtillon (France)

## SUMMARY

Two aspects of engine installation aerodynamics are considered : theoretical design and optimization of the engine installation, and experimental study.

Air intake, afterbody, and engine/aircraft integration problems are analysed for high subsonic and supersonic aircraft.

High speed and low speed performance are discussed, and variable geometry devices are commented on.

Special attention is given to the signification of the various propulsion and drag balance terms.

## CONTENTS

1. INTRODUCTION
2. GENERAL
  2.1. Thrust and drag components
  2.2. Intake pressure recovery definition
  2.3. Distorsion problem
3. ENGINE INSTALLATION FOR SUBSONIC AIRCRAFT
  3.1. Intake profile
  3.2. Variable geometry
  3.3. Ground effect
  3.4. Intake noise
  3.5. Afterbody shape
  3.6. Nacelle installation aerodynamics
  3.7. Wind tunnel tests
    3.7.1. Intake tests
    3.7.2. Afterbody tests
    3.7.3. Complete nacelle and interaction tests
4. ENGINE INSTALLATION FOR SUPERSONIC AIRCRAFT
  4.1. Supersonic inlets
    4.1.1. Computation problems
    4.1.2. External supersonic compression intakes
    4.1.3. Mixed supersonic compression intakes
    4.1.4. Manoeuverability margin
    4.1.5. Intake/airframe interference and integration
    4.1.6. Variable geometry intake adjustement at reduced Mach number
    4.1.7. Auxiliary intake for take-off and low speed
    4.1.8. Windtunnel intake tests
  4.2. Complete nacelle/aircraft model tests
  4.3. Supersonic aircraft nozzle and afterbody
    4.3.1. "Laval" nozzle and "plug nozzle"
    4.3.2. Variable geometry concept for subsonic adaptation
    4.3.3. Afterbody tests

## 1. INTRODUCTION

The purpose of this lecture is to present some elements that have to be considered while evaluating the engine installation aerodynamics.

The subject will be focussed on air intake and afterbody studies for high subsonic or supersonic aircraft. In some measure, definitions, computation methods and test processes can be extended to V.T.O.L. or hypersonic engine installation.

The subject will be only partially covered, and other general information could be obtained from recent review papers or basic courses [1] to [9]. References reported in this paper are only illustrative, and are very incomplete.

## 2. GENERAL

### 2.1. Thrust and drag components

Engine bench test results, complemented by some computations, give the possibility to predict the flow at the rear throat of the engine, or at the two exhaust stations in the case of a by-pass engine, when we know the characteristics of the flow delivered by the air intake, or these characteristics and the local static pressure field at each exit station if the flow is not choked by a sonic throat at the exit.

Wind tunnel tests or computations give the possibility to define the intake flow and the exhaust flow conditions (taking into account the preceding engine characteristics) and then to estimate the net forces applied to the aircraft.

The engine nominal thrust has to characterize the engine performance, and can be defined as the increase of momentum between :

i - the free-stream (upstream infinity) mass flow that would feed the engine if the compression was isentropic, or was governed by a given standard air intake pressure recovery, and

ii - the corresponding exhaust flow(s) that is(are) supposed expanded, parallel to the free stream and isentropically, down to the free stream static pressure, -or the same exhaust flow minus a standard thrust reduction defined by a standard exhaust nozzle,- or with a given friction drag on a rear plug or annular centerbody.

Standard air intake pressure recovery and standard afterbody thrust reduction coefficient are still to be defined and adopted, if we are to obtain a standard presentation of the engine data. There exists only an USA normalized intake pressure recovery law for military aircraft (see fig. 20 and [10]).

### "glider" and engine installation (fig. 1)

To discuss the aerodynamic performance of an engine installation, at a given altitude and constant flight Mach number, it is necessary to define a "glider" that represents the aircraft without engine installation, although this is always more or less arbitrary.

This glider is characterized by a "polar", curve of the lift coefficient $C_L$ versus the drag coefficient $C_D$.

The optimum engine installation is the one that gives the maximum net propulsive force, when the weight of the aircraft is balanced by the lift. That means, as can be easily verified, that the jet is deviated downwards, the net thrust angle being given by $\operatorname{tg}\varepsilon = dC_D/dC_L$ at the functioning point on the polar (assuming no external interaction).

To analyse the thrust and drag elements of the engine installation, we have in the same way to take into account their contribution to the lift, a lift effect $\Delta L$ being equivalent to a thrust increase or a drag reduction $\Delta D$

$$\Delta D = \frac{-\Delta L}{dC_L/dC_D}$$

It would be also necessary to consider the effect of the engine installation aerodynamics on the equilibrium drag : that would be easy if the longitudinal trim was associated with a given law of drag.

To simplify, we will not mention any more this effect, that can be rendered negligible in some cases, for instance by an adequate camber of the wing.

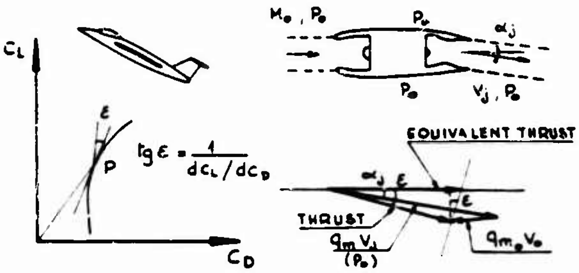

GLIDER POLAR OPTIMUM ENGINE INSTALLATION

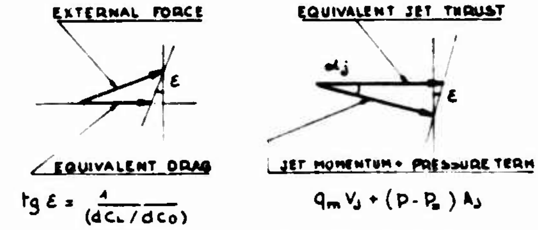
EXTERNAL FORCE
ε
EQUIVALENT DRAG
$\operatorname{tg}\varepsilon = \frac{1}{(dC_L/dC_D)}$
EQUIVALENT JET THRUST
$\alpha_j$
ε
JET MOMENTUM + PRESSURE TERM
$q_m V_j + (P - P_0) A_j$

EQUIVALENT DRAG EQUIVALENT JET THRUST

*FIG. 1 - THRUST AND DRAG EQUIVALENCE*

The effect of the engine on the weight and the center of gravity position is not involved here, since only the aerodynamic forces are examined, for gives total weight and center of gravity.

The preceding equivalence are well adapted to configurations with the main component of the thrust aligned with the speed. For V/S.T.O.L. aircraft in horizontal low speed flight, the horizontal forces would be no more convenient to appreciate the effect of the engine installation : a vertical projection would be more appropriate.

### The engine nominal equivalent thrust

The engine nominal thrust $T_n$ deflected of $\mathcal{E}$ gives an horizontal thrust of $(1-\mathcal{E}^2/2)T_n$, and a lift force equal to $\mathcal{E}T_n$, what is equivalent to an horizontal supplementary thrust of $\mathcal{E}^2T_n$. Then, the engine nominal equivalent thrust is equal to $(1+\mathcal{E}^2/2)T_n$

### The engine installation (or nacelle) net equivalent thrust

If $C_D$ and $C_L$ are the drag and the lift coefficients of the "glider", in horizontal flight, and if $C_{LW}$ is the lift coefficient that equilibrates the weight, $C_{LW} - C_L$ represents the lift effect of the engine installation. The equivalent thrust is then equal to $C_D + (C_{LW} - C_L)\, dC_D/dC_L$. As $(C_{LW} - C_L)$ is small enough to be linearized on the polar, the sum represents the drag coefficient of the polar at a $C_L = C_{LW}$ that equilibrates the weight : this will be taken as a definition of the "net equivalent thrust" of the engine installation.

The engine installation aerodynamics can be judged by the thrust reduction between the nominal equivalent thrust and the net equivalent thrust.

This loss can be introduced into internal and external aerodynamics of the engine installation, by the definitions given below.

The installed engine equivalent internal thrust has to reflect the internal performance of the engine installation.

It can be defined as the increase of momentum, from the free stream total mass flow that is captured by the air intake, to the exhaust sections of the same flow (that can have fluid frontiers, for instance in the case of an auxiliary flow captured by a door downstream of the air intake, and limiting the nozzle flow), plus pressure terms in these sections (with respect to the free stream pressure), plus forces (with respect to the free stream pressure) on some parts of external surfaces that are considered as internal, like centerbody annular boattail of a by-pass engine.

If the exhaust system is not parallel to the free stream, and presents a lift component $\Delta L$, a thrust increment $\Delta T = \dfrac{\Delta L}{dC_L/dC_D}$ has to be added.

The engine installation (or nacelle) equivalent external drag is then the difference between the "installed engine equivalent internal thrust" and the "engine installation net equivalent thrust" and reflects the external drag of the engine installation. This drag includes not only the interference drag between the nacelle and the glider, but also between the jet and the glider.

The installed engine equivalent internal thrust reduction, that is the difference between the "nominal" and the "installed" engine equivalent internal thrust, may include the following elements :

- The intake/engine equivalent internal thrust reduction, that is the difference between the "nominal" and the "maximum intake/engine" equivalent internal thrust , and characterizes the effect of the pressure recovery of the intake : the "maximum intake/engine equivalent internal thrust" is the increase of momentum, from the free-stream tube that feeds the engine with the actual pressure recovery of the intake, to the corresponding exhaust flow that is supposed expanded down to the free stream static pressure with the same assumptions than for the nominal equivalent thrust.
- The internal boundary layer bleed and by-pass flow equivalent drag, that is the resulting inner drag force on the stream tube, from the free-stream to the exhaust, of the bleed or by-pass flow, minus possibly the drag correction due to a lift effect. If a part of the mass flow is ejected by the nozzle, it can be considerer that the flow is exhausted by an isentropic expansion from its maximum stagnation pressure, the supplementary drag effect being accounted in the "nozzle equivalent thrust reduction".
- The nozzle equivalent internal thrust reduction, that is the difference between the "nominal engine eq. thrust", less the "intake/engine eq. internal thrust reduction", less the "internal bleed and by pass flow eq. drag", and the "installed engine eq. internal thrust".

This term characterizes the fact that the internal flows delivered to the nozzle are not used with their maximum efficiency.

The engine installation (or nacelle) equivalent external drag may include the following elements :

- the boundary-layer diverter eq. drag,
- the strut eq. drag,
- the addive eq. drag, that is the equivalent drag of the pressure forces applied to the intake flow stream tube going from the upstream infinity to the capture section,
- The intake cowl eq. drag (from the intake capture section to the maximum section of the engine installation),
- The spillage eq. drag : if the additive and cowl drag are evaluated for the maximum mass flow of the intake, the supplementary parts of the additive and cowl drag (and possibly other drag terms) that appear when the mass flow is smaller than the maximum, is called the spillage drag .

- The afterbody external eq. drag, that may include :

. the auxiliary flow eq. drag : drag of the auxiliary stream tube from its section at the maximum diameter of the engine installation to its exhaust section, that may have a common fluid frontier with the internal flow,

. the boattail eq. drag : from the maximum diameter plus possibly an auxiliary stream tube, to the final external section of the engine installation,

. the base eq. drag : from the final external section of the engine installation to the exhaust sections of the afterbody total mass flow ;

- The interference eq. drag that is the complement to the engine installation eq. external drag ; the interference effect can be distributed between some of the preceding elements.

"Friction drag" and "pressure drag" can be distinguished as parts of some drag elements.

The sum of the "nozzle eq. thrust reduction" and of the "afterbody external eq. drag" constitutes the afterbody net equivalent thrust reduction.

The list of the thrust and drag components is summatized fig. 2. The definitions may have to be more specified, adapted or completed for each particular case, but, when they are, they give a good view of the propulsion balance and of the engine installation characteristics and performance, keeping in mind, however, that the various terms are not independent of each other.

## Weight, drag and pressure recovery exchange coefficients

At a given Mach number, a drag modification can be expressed as a lift, or a weight modification, by the relation $\Delta W = \Delta D \times dC_L / dC_D$ plus possibly the longitudinal trim drag term.

An increase of the intake pressure recovery implicates a higher mass flow and a revised nacelle (mainly larger entry and exhaust section areas), and provides an increased internal thrust and a decreased external drag, or an increased net thrust, that can also be expressed as an equivalent weight decrement.

However, as the Specific Fuel Consomption is also a function of the intake pressure recovery, and as the weight involves all the stages of the flight, it is necessary to calculate some exchange coefficients between the weight, the thrust (or drag), and the SFC, at various given flight conditions, based on some aircraft global performance like payload, range, or Direct Operating Cost.

This problem of optimization of the global performance is discussed for instance ref. [11].

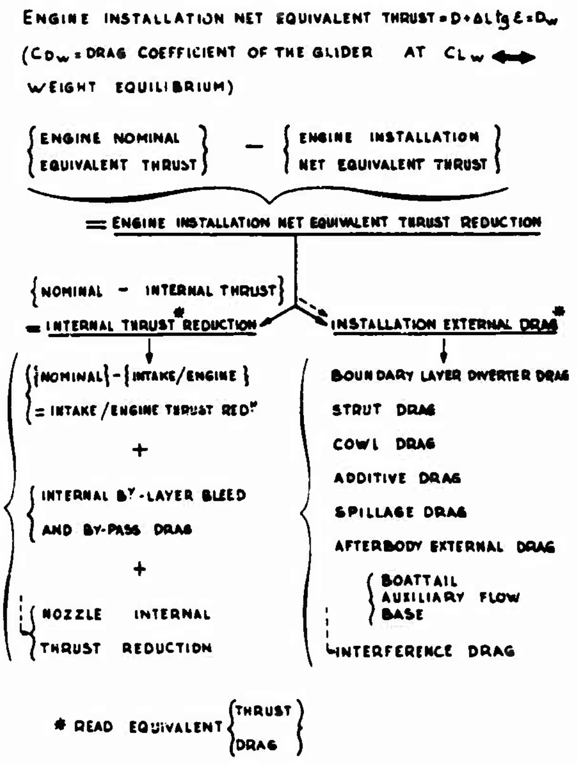
ENGINE INSTALLATION NET EQUIVALENT THRUST = D + ΔL tg ε = D_W
(C_DW = DRAG COEFFICIENT OF THE GLIDER AT C_LW ⟷ WEIGHT EQUILIBRIUM)
ENGINE NOMINAL EQUIVALENT THRUST
–
ENGINE INSTALLATION NET EQUIVALENT THRUST
= ENGINE INSTALLATION NET EQUIVALENT THRUST REDUCTION
NOMINAL – INTERNAL THRUST
= INTERNAL THRUST* REDUCTION
INSTALLATION EXTERNAL DRAG*
{NOMINAL} – {INTAKE/ENGINE}
= INTAKE/ENGINE THRUST REDn
+
INTERNAL By-LAYER BLEED AND BY-PASS DRAG
+
NOZZLE INTERNAL THRUST REDUCTION
BOUNDARY LAYER DIVERTER DRAG
STRUT DRAG
COWL DRAG
ADDITIVE DRAG
SPILLAGE DRAG
AFTERBODY EXTERNAL DRAG
BOATTAIL
AUXILIARY FLOW
BASE
INTERFERENCE DRAG
* READ EQUIVALENT THRUST DRAG

FIG. 2 - THRUST - DRAG BALANCE

## Thrust and drag terms evaluation

Wind tunnel model tests are mainly used to verify the global aerodynamic characteristics ; the various terms of the thrust and drag balance are rather discussed in the preliminary theoretical evaluations of a project. However, fundamental test results on isolated parts of the engine installation are used to assess the computations.

Theoretical evaluations and experiments will be commented on further for the cases of high subsonic and supersonic aircraft.

## 2.2. intake pressure recovery definition

One of the main parameters of the propulsion performance is the intake pressure recovery, ratio of the mean stagnation pressure of the flow at the compressor face, to the isentropic stagnation pressure of the free stream.

As the flow is not uniform at the compressor face, a mean flow has to be defined. Due to the function of the air intake, it is convenient to do that by replacing the actual flow by an uniform flow that has the same mass flow, enthalp, and "dynalp" (sum of the momentum and of the pressure force).

Almost equivalent definitions [9], easier to apply to the air intake tests, are obtained either by taking an uniform flow of the same mass flow, enthalp and static pressure (when the static pressure is constant), or by computing the mean stagnation pressure by an area-weighted integration of the measured stagnation pressure distribution.

The definition used has to be specified, although the differences of results are usually smaller than the precision of the knowledge of the engine thrust.

On the other hand, the definition by a mass-flow-weighted pressure recovery has to be condemned, because it eliminates the effect of low stagnation pressure (and mass flow) regions, and gives too optimistic values, leading to an overestimation of the thrust and the surge margin.

### 2.3. Distorsion problem

A number of publications ([12] to [18]) show that the working of an engine in a non-uniform, stationary or non-stationary flow can be pretty well predicted when the distorsion of the flow delivered by the intake is known.

Stationary flow survey is easely obtained in air intake tests by "pitot" pressure measurements at the compressor face station.

When the flow is unstable, the distorsion has to be measured by dynamic fast response stagnation pressure instrumentation. A cut-off frequency $1/T$ of the measure should be chosen in such a way that the well length $\lambda = V_n . T$, product of the axial velocity $V_n$ at the first blade stage by the cut-off period T, be of the order of two or three times the blade chord [15].

Each engine manufacturer has its own distorsion index, and it is still not possible to know the most representative. These various indices are, in fact, similar, in that sense that they take into account the amplitude and the extension of the reduced speed regions (low stagnation pressure regions) that give higher incidence on the blades and give rise to a stall risk.

The following distorsion indices can be mentioned :

- $DC\ 60 = \dfrac{\overline{P}_{60\,min} - \overline{P}}{\overline{q}}$ [13, 14],
    - ▲ $P_{60\,min}$ : area-weighted stagnation pressure of the 60° section where the mean stagnation pressure is minimum,
    - ▲ $\overline{P}$ : area-weighted stagnation pressure of the whole section,
    - ▲ $\overline{q}$ : mean dynamic pressure, $1/2\, \gamma\, \overline{p}\, \overline{M}^2$
- $KD_1 = 100 \sum_{n=1}^{n=5} \left( \dfrac{\overline{P} - \overline{P}_{min}}{\overline{P}} \, \theta^- \right)$ [12],
    - ▲ $n$ : index of a ring, the whole section being divided into 5 rings of equal area,
    - ▲ $\overline{P}$ : mean stagnation pressure of the ring,
    - ▲ $\overline{P}_{min}$ : minimum stagnation pressure of the ring,
    - ▲ $\theta^-$ : angular extent, in degrees of the largest depression under $\overline{P}_{min}$, on the ring
- $KD = \dfrac{\sum_{n=1}^{n=8} \left( \dfrac{\overline{P} - \overline{P}_{min}}{\overline{P}} \, \theta^- \, \dfrac{r_{max}}{r_n} \right)}{\sum_{n=1}^{n=8} \dfrac{r_{max}}{r_n}}$ [14 à 17].

This last index gives more weight to the flow near the hub than the preceding one ; the surge correlation has been improved this way, for a particular engine.

The influence of the distorsion index on the engine performance and on the surge margin depends of the engine characteristics.

Some examples can be found in the given references, or others.

## 3. ENGINE INSTALLATION FOR SUBSONIC AIRCRAFT

### 3.1. Intake profile

The Mach number distribution reported figure 3 illustrates the problem of the intake profile that is a compromise between high and low speed performance.

At high speed (M = 0.85) the external flow is supercritical, and, in order to avoid the drag that would result of too high an overspeed, it is necessary to limit the deviation of the flow around the lip. That means a small external radius of the lip at the stagnation point of the capture streamline, and also a pretty thin lip to avoid an internal sonic throat.

At static and low speed, it is necessary to avoid a separation of the boundary layer inside the leading edge due to the flow turning around the lip to gather the intake. That means a large entry area (that is limited by the high speed drag) and a large internal radius (that is limited by an internal sonic throat).

The result of an optimization process gives to the lip the characteristic shape drawn in the figure.

A small drag nacelle at high Mach number has also to have a very small curvature at the maximum diameter, what corresponds to a long intake duct, but a compromise has then to be found with the weight.

It is interesting to note the use of a "peaky" type supercritical profile. When the mass flow is reduced, this effect is more pronounced, and drag appears. A large margin may be necessary when the nacelle drag, with one engine out, is critical (two-engine aircraft).

At low speed, the worst (and determining) condition is at static with cross wind. The internal overspeed on the lip facing the cross wind is increased, as shown figure 3, and an internal separation of the boundary layer may result that gives an high internal flow distorsion.

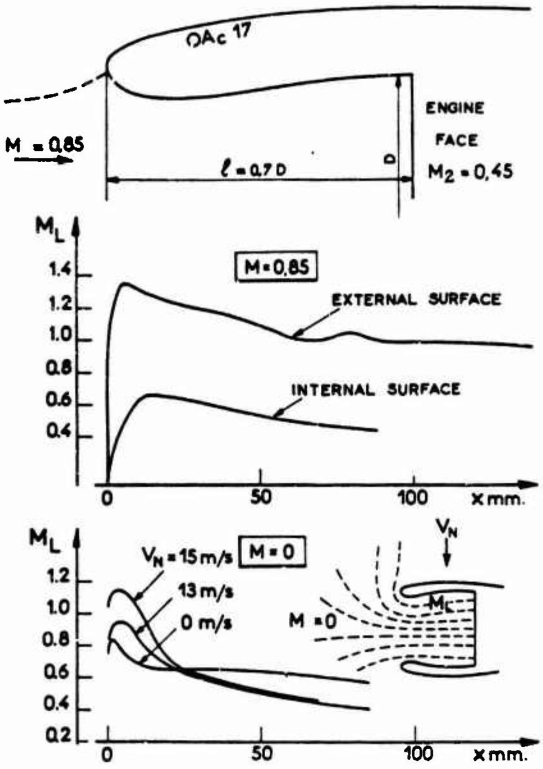

FIG. 3 - INTAKE PROFILE DEFINITION

Figure 4 shows a typical effect of the cross wind at various forward speed $V_0$, and mass flow (identified by the internal Mach number $M_2$).

For a given forward speed $V_0$, and a given cross-wind (for instance the maximum normalized cross-wind, 15 m/s), at low mass flow, we observe an internal separation due to a too low Reynolds number, and that disappears at higher mass-flow. At a still higher mass flow, separation reappears, due to a too high overspeed on the lip.

For a given cross wind, the forward speed reduces the well-effect of the intake and improves the lip flow, widening the mass flow range without separation.

If an improvement of the lip shape (thicker internal radius) cannot be accepted due to the other conditions, a solution has already been used what is to apply the maximum power of the engine only when the speed of the aircraft on the runway is sufficient to be above the separation area.

Variable geometry can help to solve this problem (parag. 3.2).

Calculation methods of subcritical potential flow and boundary-layer are currently used in the design offices ; they are applied to a configuration of the same mass flow coefficient (ratio of the upstream captured streamtube to a reference intake section), but to a reduced Mach number, to remain subcritical. The results are generally satisfying, although development of a supercritical method will permit one to improve the precision of the performance prediction. Several published experimental analyses allow one to start a preliminary design [19] to [26].

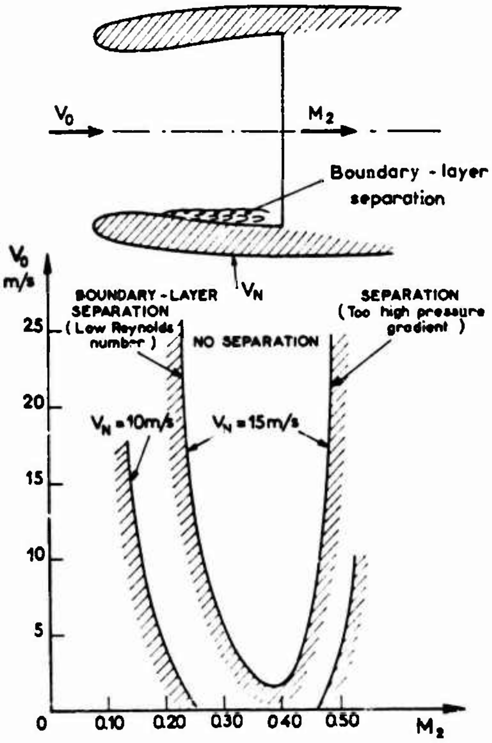

FIG. 4 CROSS WIND EFFECT

Definition of a high performance fixed geometry intake can be achieved this way when the cruise Mach number is lower than 0.85 or 0.90, according to the engine mass flow characteristic. For higher Mach number, drag penalties have to be accepted, or variable geometry to be required.

### 3.2. Variable geometry

When a high cruise Mach number imposes a thin leading edge, variable geometry can be used to reduce the overspeed on the inner profile of the lip at low speed, either by enlarging and rounding the lip, or by opening auxiliary intakes, which reduces the mass flow passing through the front entry.

Some of these devices are presented on figure 5. The best solution is still to be defined in terms of efficiency, weight, and noise effect. Leading edge flaps, for instance, could be a competitive solution for large engines compared with the other devices already used.

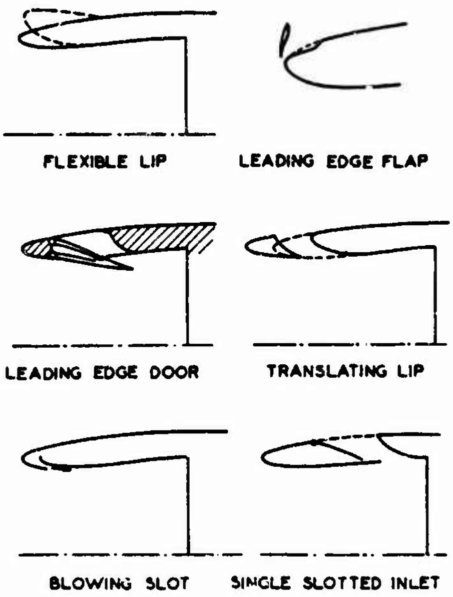

FIG. 5 - AUXILIARY TAKE-OFF DEVICES

### 3.3. Ground effect

Figure 6 is only presented to emphasize the effect of the ground proximity.

At static, the boundary layer on the ground, due to the velocity induced by the intake suction, gives rise to a vortex that may be swallowed by the intake, giving an internal flow distorsion.

If the ground boundary layer is amplified by the wind, or is generated by the wind-tunnel speed (intake test at take off speed without "moving belt"), the vortex may be increased as shown on the figure. Of course, it is blown at higher speed.

The comparison of the flow visualizations and of the stagnation pressure distribution without and with «moving belt» proves that the study of the ground effect without moving belt is not representative, the strong vortex that may exist in the wind tunnel test being a parasitic effect.

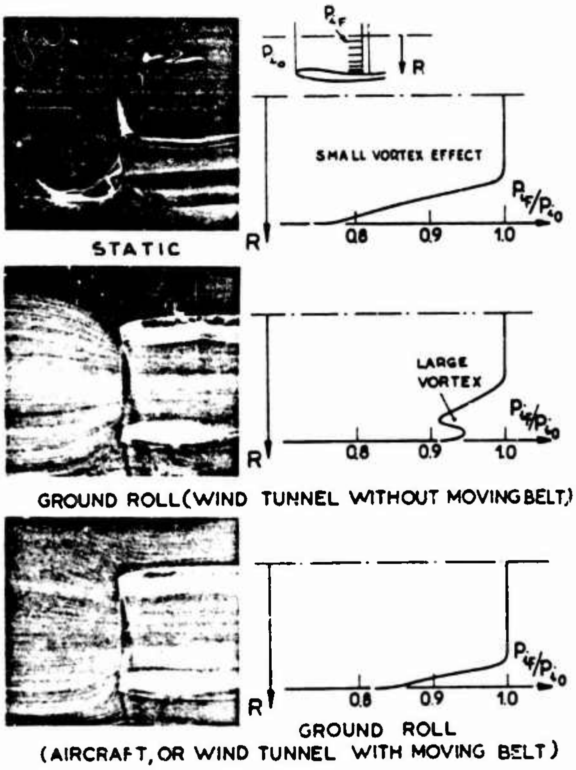

FIG. 6 - GROUND EFFECT

### 3.4. Intake noise

Some devices to reduce the noise from the intake are presented on figure 7. [24], [27], [28].

The first type of device consists in forming a near sonic throat ahead of the compressor face. As the noise has also to be reduced at reduced R.P.M. (approach flight), the throat section has to be ajustable. This can be realized by a contracting cowl wall or a translating centerbody.

A second type consists in reducing or suppressing the "line of sight" to the rotating blades through the inlet ; parts of the walls are of absorbing materials. Intake is then longer, but with a fixed geometry.

Discussion of the various possibilities are still progressing, one of the problems being to know the effect of the change of distorsion and turbulence level of the intake flow on the exhaust noise, at static and in fly-over situation, and to take into account the effect on the noise of a readjusted engine power to compensate a reduced intake pressure recovery.

### 3.5. After body shape

Two types of afterbodies seem competitive for a by-pass engine : the mixed flow and the separated flow, with or without a terminal plug (fig. 8) [24] [25].

The experimental result reported figure 9 shows that the fan exhaust flow presents a succession of transonic waves that are still not accessible to computation.

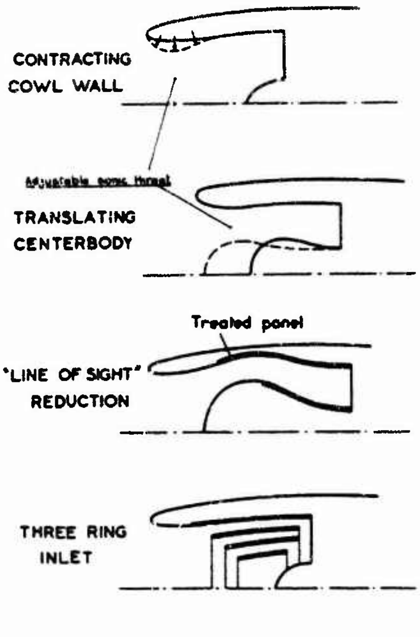

*FIG. 7 - INTAKE NOISE ATTENUATION DEVICES*

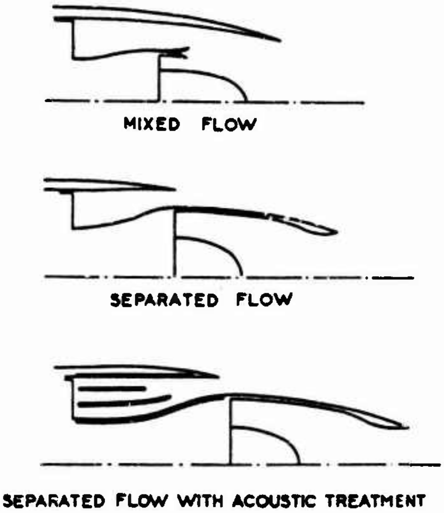

*FIG. 8 - AFTERBODY CONFIGURATION*

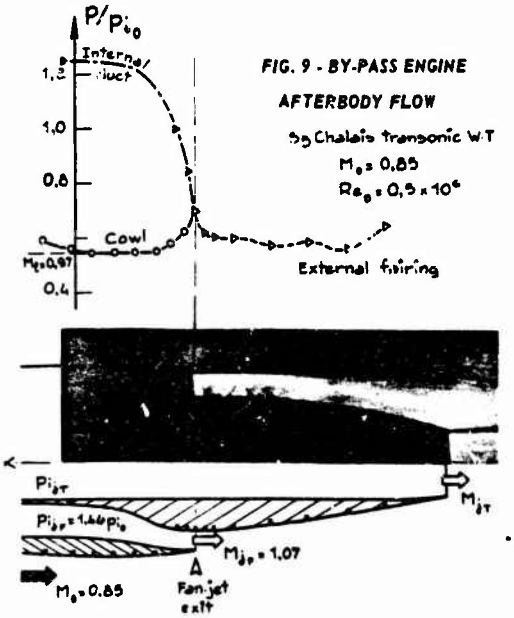

*FIG. 9 - BY-PASS ENGINE AFTERBODY FLOW*

The compressible transonic method can only be applied to calculate the flow on the boattail by giving a approximated shape to the jet frontier. It is very profitable to optimize the boattail length and curvature.

A discussion of comparative performance requires also to calculate the friction drag, including the drag (thrust reduction) of the internal flow, the thrust improvement due to an internal mixing of the hot jet with the cold jet [29], and the respective weights.

Rules for preliminary design based on experimental results are proposed ref. [30, 31, 32].

Slightly convergent-divergent nozzles are usually desirable to adjust the jet to the ambient pressure, but the nozzle expansion has to be a compromise between cruise and take-off, due to higher jet pressure ratio in cruise [24].

Studies of acoustic treatments of various afterbodies on the performance characteristics are reported ref. [24] (internal wall equipped with absorbing materials, and installation of acoustically treated rings into the fan exhaust channel).

It is shown that the "terminal plug" is not attractive, and that the choice between the separated or the mixed flow is not decisive, and can be a function of the reverse performances (that are not evaluated) : a higher reverse thrust indeed permits a reduced length of landing roll, and consequently a higher altitude of fly over at approach, which means a reduced noise...

### 3.6. Nacelle installation aerodynamics

The choice of the nacelle position is guided by the area rule applied to the complete aircraft [33] to [35].

For large capacity aircraft, the variation of the center of gravity with the passengers number is more important when the engines are near the tail than when they are under the wing : the trim drag is higher for the first solution, and has to be taken into account in the aircraft performance comparisons [35].

On the other hand, the engine installation near the rear fuselage, which permits the capture of the fuselage boundary-layer, may be considered, as it may improve the propulsion efficiency [36].

A complete discussion of the engine position is beyond the scope of this paper, but it must be emphasized that it is important to study the engine nacelle in its environment.

Three-dimensional flow theories give useful indications on the pressure distribution around the wing, body, strut and nacelle arrangement [37] to [39].

Wind tunnel tests complete the flow analysis, and permits detailed investigation of some jet interference effects (on the control surface), and other complex phenomena [40].

### 3.7. Wind tunnel tests

#### 3.7.1. Intake tests

Wind tunnel test arrangements are presented figure 10.

Intake drag (additive + cowl drag) can be obtained by internal flow survey giving the momentum and pressure force increase from the upstream section of the captured mass flow to the internal measuring section, and by measurement of the longitudinal force acting on the cowl (pressure integration + external boundary layer survey giving the friction drag, or force measurement by a balance) [41] to [43].

Measurements of the pressures on the external nacelle profile permits one to appreciate in which limits the measured drag has an absolute value (if the pressures on the rear part of the nacelle are practically identical to those created by a mass flow, the external flow being entirely isentropic), or has only a comparative value (if the pressures on the rear part are the same for the compared configurations). This is discussed ref. [42]. The conclusion of this discussion is that, at high subsonic Mach number, the inlet drag indicated by the intake test is not perfectly representative of an absolute drag term, and cannot be dissociated from the afterbody drag.

#### 3.7.2. Afterbody tests

Usual arrangements of afterbody tests are presented figure 11 from [44].

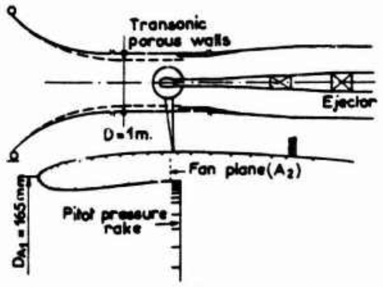

Intake drag by pressure and boundary-layer measurement [41-42]

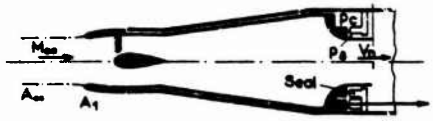

Isolated fan inlet tests with metric cowl [43]

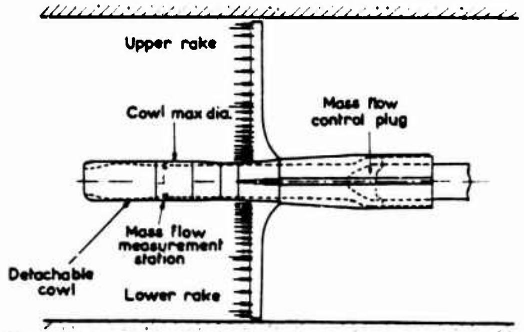

Measurement of spillage drag by the wake traverse method [43]

*FIG. 10 - EXPERIMENTAL INTAKE STUDY*

These arrangements are not perfectly representative. because the flow curvature around the leading edge of the intake is not reproduced, and the boundary layer is not at the proper scale. Boundary layer bleed on the upstream sting has already been used to reduce the boundary layer thickness. An example is shown figure 11, from ref. [45] (nacelle/wing profile interference test).

An arrangement permitting one to reproduce the flow from the leading edge, and to eliminate the sting boundary layer upstream of the leading edge, is suggested at the bottom of the figure [42].

#### 3.7.3. Complete nacelle and interaction tests

Simulation of the engine on a wind tunnel model, at a given Mach number, would mean :

- same intake mass flow coefficient,
- same external geometry (intake and nacelle cowl, exhaust section and afterbody profile),
- same jet static pressure and Mach number,

– same jet temperature and ratio of specific heats.

A good approximation is obtained by restraining the simulation to the three first item.

No possibility exists today to obtain such a simulation.

The best approach (and the most difficult and expensive) is the "powered nacelle" [32] (fig. 12). It permits one to reproduce the exhaust condition (even the jet temperature) with only a small difference on the captured mass flow.

More simple is ejector system (fig. 12), that necessitates a more important reduction of the captured mass flow to obtain the correct simulation of the exhaust flow [46]. In that case, the intake entry section and cowl profile may be reajusted, to keep the external flow as isentropic as the real flow, if possible. An emerging bulled in the center of the inlet can be used to this purpose; the supplementary drag introduced by this solution can be measured on an air intake test ring . (fig. 12, at the bottom), [47], [48].

At low speed, it has been proved for a long time that is was sufficient to reproduce the thrust coefficient $C\mu$ of the jet to obtain a good simulation of the global effect of the jet on the airplane aerodynamic characteristic, even with a modified nacelle (afterbody geometry, captured mass flow...). Faired over-inlet are often acceptable ("blown nacelle").

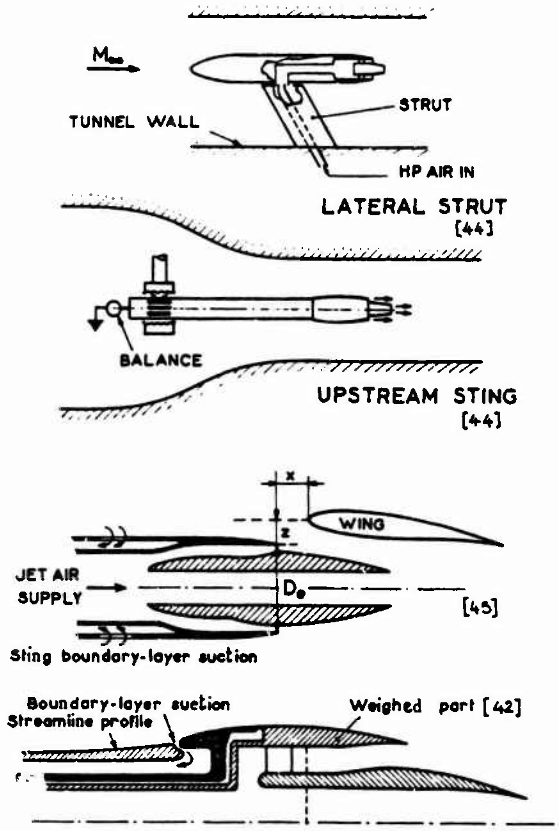
M∞
STRUT
TUNNEL WALL
HP AIR IN
LATERAL STRUT
[44]
BALANCE
UPSTREAM STING
[44]
x
z
WING
JET AIR SUPPLY
D_e
[45]
Sting boundary-layer suction
Boundary-layer suction
Streamline profile
Weighed part [42]

FIG. 11 - AFTERBODY STUDY

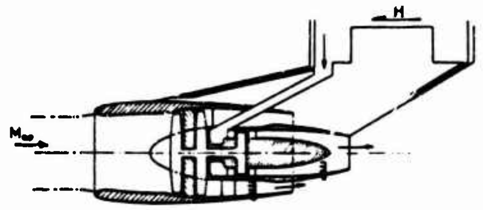

POWERED NACELLE MODEL [32]

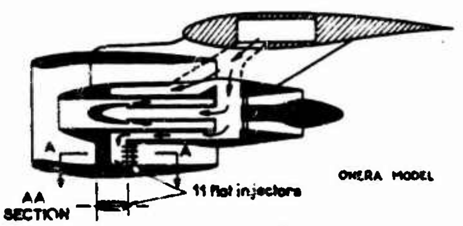
A
A
AA SECTION
11 flat injectors
ONERA MODEL

EJECTOR SYSTEM

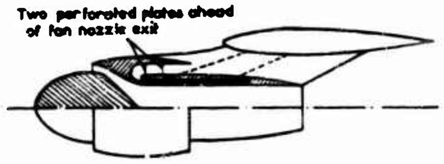
Two perforated plates ahead of fan nozzle exit

BLOWN NACELLE [47]

FIG. 12 - ENGINE/AIRPLANE INTERACTION STUDY

Coefficient $C\mu$ is the (non dimensional) product of the exhaust mass flow by the speed of the jet flow expanded to the stream static pressure, divided by the reference of the forces. Since the speed of the wind tunnel in incompressible flow is an independent parameter (neglecting the Reynolds number effect),it is possible to adjust it to obtain a simultaneous simulation of the intake mass-flow and the $C\mu$ in the "ejector nacelle". But it is often more useful to test the model at the maximum Reynolds number.

Repeatability and precision of the ejector and blown-nacelle technique are discussed ref. [49].

## 4. ENGINE INSTALLATION FOR SUPERSONIC AIRCRAFT

### 4.1. Supersonic inlets

Two types of inlets are used on supersonic aircraft : the external supersonic compression inlet, and the "mixed" (external/internal) supersonic compression.

For cruise Mach number equal or lower than about 2.2, external supersonic compression gives the highest pressure recovery with an acceptable cowl drag penalty, and with a short total length and weight.

For higher Mach number, mixed compression becomes more attractive, in spite of the starting problem that complicates the control system, thanks to a lower drag and an equivalent or better pressure recovery.

Common computation problems, and particular characteristics of each type of intakes will be successively presented.

#### 4.1.1. Computation problems

The supersonic compression is calculated by the well known method of characteristics (fig. 13) [50] to [52] ; the example of fig. 13 is taken from ref. [53].

The wall is corrected by the displacement thickness of the boundary layer.

Boundary layer theories have been developed to take into account oblique shock/boundary layer interactions, and boundary layer suction that may be applied in the high pressure gradient or shock region of the supersonic compression [54] to [56].

The "normal" shock/boundary layer interaction is a complex problem of coupling a strong shock transonic flow with a boundary layer, and is still not solved. As the compression capability of the subsonic diffusor is function of the entry flow and its boundary-layer, the design of the transonic region and the subsonic diffusor of the intake is still based on experimental results.

The internal bleed system of the Boeing SST intake is reported fig. 13 [57] When the flight Mach number decreases, the centerbody is translated forward, but the normal shock always takes place at about the same position ; then the bleed has to be successively applied at various location of the centerbody, which is obtained by the complete perforated wall of the subsonic part of the centerbody combined with the partitioning of the internal structure and a fixed bleed exhaust position, as shown by the figure.

Furthermore, vortex generators are often fixed on the subsonic diffusor wall so that the boundary layer can accept high pressure gradients without separation.

In these particular conditions, the boundary layer computation, that is essential to a theoretical study of the subsonic diffusor, is still not achievable.

The fluid-wall bleed of figure 14, compared to the perforated-wall bleed system, offers the advantage of more flexibility and higher bleed pressure recovery. A computation method described ref. [59] gives very good results by predicting the evolution of the intake flow pressure

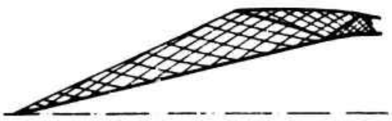

[53]

INVISCID FLOW CALCULATION (Method of characteristics)

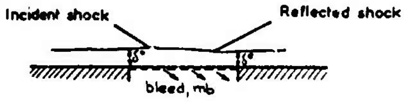

BOUNDARY LAYER CALCULATION [54]

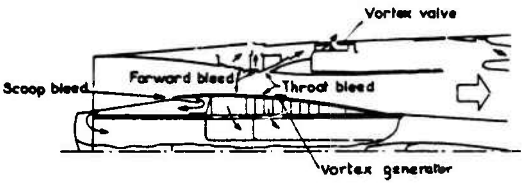

BLEED SYSTEM (BOEING SST) [57]

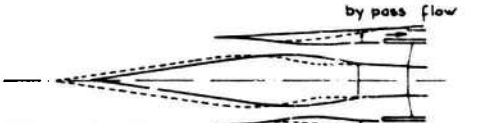

STARTING PROCESS AND M.N. ADJUSTMENT (Boeing SST)

*FIG. 13 - MIXED SUPERSONIC COMPRESSION INTAKE*

recovery with the bleed flow, and the stability limit of the system.

Some experimental results of normal shock (boundary layer interaction in a duct with "educated" holes and other particular bleed devices) are given ref. [59] and [60].

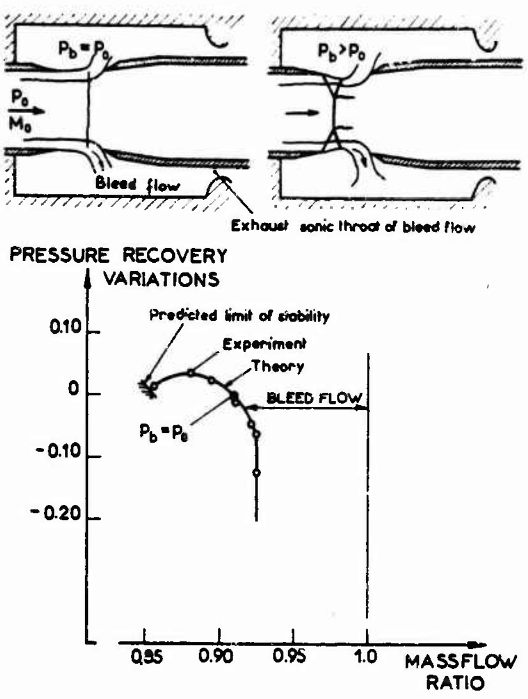
$P_b = P_o$
$P_b > P_o$
$P_o$
$M_o$
Bleed flow
Exhaust sonic throat of bleed flow
PRESSURE RECOVERY VARIATIONS
Predicted limit of stability
Experiment
Theory
BLEED FLOW
$P_b = P_o$
0.10
0
-0.10
-0.20
0.85
0.90
0.95
1.0
MASSFLOW RATIO

FIG. 14 - FLUID WALL THROAT BLEED

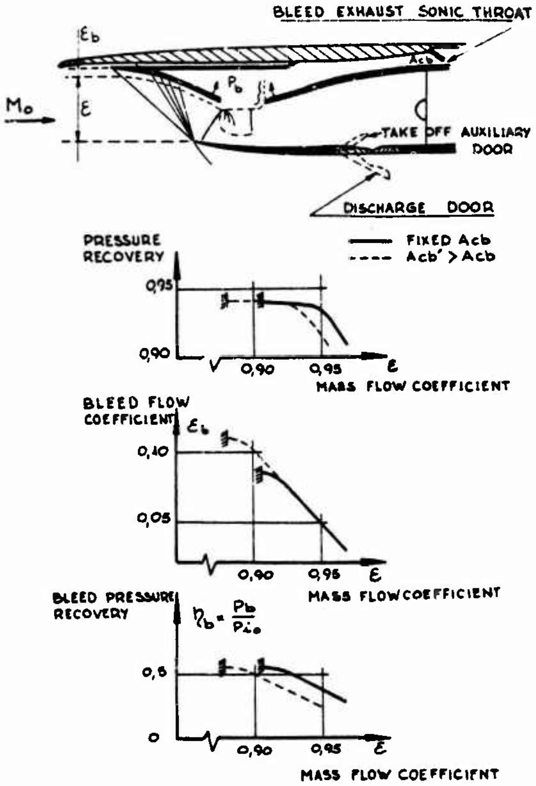
BLEED EXHAUST SONIC THROAT
$\varepsilon_b$
Acb
$M_o$
$\varepsilon$
$P_b$
TAKE OFF AUXILIARY DOOR
DISCHARGE DOOR
PRESSURE RECOVERY
FIXED Acb
Acb' > Acb
0,95
0,90
0,90
0,95
$\varepsilon$
MASS FLOW COEFFICIENT
BLEED FLOW COEFFICIENT
$\varepsilon_b$
0,10
0,05
0,90
0,95
$\varepsilon$
MASS FLOW COEFFICIENT
BLEED PRESSURE RECOVERY
$\eta_b = \frac{P_b}{P_{io}}$
0,5
0
0,90
0,95
$\varepsilon$
MASS FLOW COEFFICIENT

FIG. 15 - CONCORDE-TYPE AIR INTAKE

### 4.1.2. External supersonic compression intakes

A large number of experimental results have been published on this type of inlet. Many of them are collected ref. [3].

When a fluid-wall bleed system is installed at the entry normal shock impingement on the wall, at the end of the supersonic compression, the usual normal shock is replaced by a two-shock system like that of figure 15 (Concorde-type intake [61]). The entry shock is incurved from the intake lip, where it is a strong oblique shock, to the bleed cavity where it is a weaker oblique shock. Along the fluid wall of the dead-water cavity, a supersonic internal expansion takes place at the same pressure as the cavity pressure. This expansion is limited towards the cowl by a sonic line, and is closed downstream by a limited normal shock. The bleed flow is injected into the cavity by a small jet originated between the terminal shock and the leading edge of the diffusor flap.

Due to a compensation effect between the two shocks, the pressure recovery is almost constant in the whole compressor entry flow, and is not very sensitive to the cavity pressure.

The internal sidewall boundary layer is drained along the wall towards the bleed gap, due to the transverse pressure gradient. This three-dimensional effect does not simplify the boundary layer computation, but reduces the lateral boundary layer sensitivity to the subsonic diffusor pressure gradient.

This advantage can contribute to the choice of a large gap cavity, in parallel with the possibility of a quicker turning of the internal flow and a reduced cowl drag.

Experimental pressure recovery at Mach 2.0 is drawn on the figure, with the corresponding bleed mass flow and bleed pressure recovery, for a given exhaust section of the bleed flow. By enlarging this section, more bleed flow can be by-passed by the bleed gap.

The cavity pressure is used to control the intake : when the pressure rises, the entry shock becomes detached, and buzz appears. To avoid that, the rotating part of the supersonic compression ramp is lowered, then a by-pass door is open, in order to spill some mass flow out of the intake and to keep the pressure cavity at the required level.

Some features of the F-14 intake are presented figure 16, taken from ref. [62]. The inlet geometry and the bleed exhaust sonic throat adjustements are computed from the flight Mach number, the aircraft incidence and the engine corrected R.P.M., which is another control possibility.

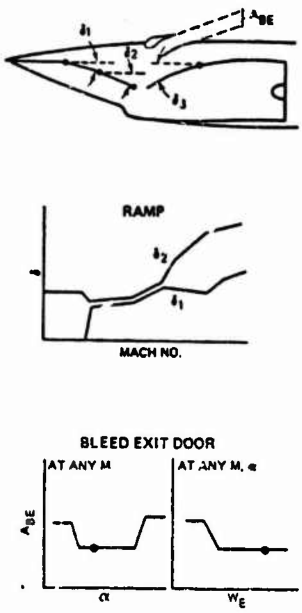

*FIG. 16 - F-14 INTAKE [62]*

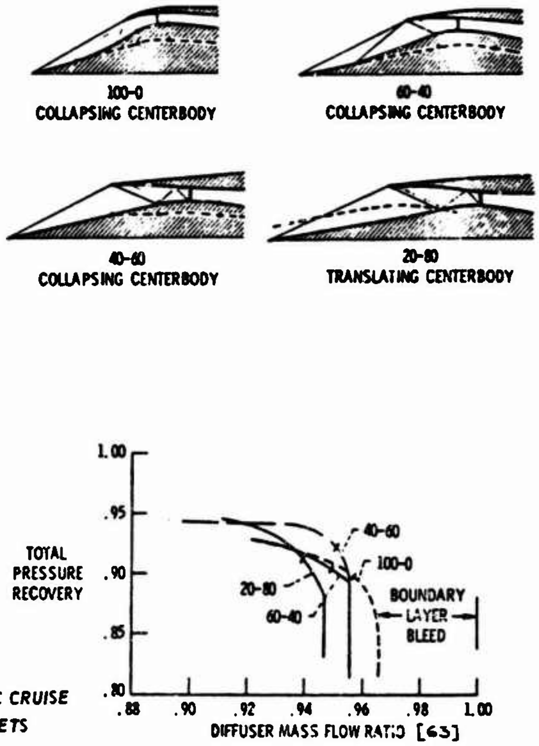

*FIG. 17 - SUPERSONIC CRUISE AXISYMMETRIC INLETS*

### 4.1.3. Mixed compression intake

Mixed (external/internal) supersonic compression intakes are penalized by the complexity of the starting process. The variable geometry devices that are used for it are the same as for the adaptation of the intake at various engine rating and flight Mach number, but complex monitoring laws and sensors have then to be adjusted.

Figure 17, reproduced from ref. [63], gives comparative results of axisymmetric inlets at about Mach 2.6, designed respectively with external supersonic compression (100 - 0), 60 % of external supersonic compression and 40 % of internal supersonic compression (60 - 40), "40 % and 60 %" (40 - 60), and "20% and 30%" (20 - 80).

Variable geometry devices for intake adjustement at lower Mach number are indicated for each type of intake.

Total pressure recovery comparisons give an advantage to the third solution, but structural point of view may incite to choose another one.

Starting the inlet is obtained by the same manoeuver as for M.N. adjustement but, for configurations (2) and (3), it is necessary at the same time to spill some flow by a discharge door or by an internal by-pass.

A collapsing ramp was the solution adopted for the two-dimensional intake of the B-70 aircraft. Sliding centerbody is the solution of the YF-12-A. The solution defined for the Boeing SST is drawn figure 13. Its control system is described ref. [64].

On less isentropic inlets, the starting problem may be avoided thanks to an internal supersonic compression surface formed by a fluid-wall bleed system like that represented figure 18.

When the inlet is started, there exists a margin for varying the mass flow without choking the flow, while keeping a high pressure recovery. Unstarting and starting the intake without any action on the geometry nor on the bleed exhaust section are observed at reduced values of the mass flow, with only a small hysteresis margin between the two phenomena.

Prediction of the starting limit is still hazardous. Starting is facilitated by the shock/boundary-layer interaction [65], and this effect may be very strong, as shown figure 19. A correlation of the test results, based on a boundary layer separation criterium, is discussed ref. [66].

Numerous test reports have been published on this type of inlet, for instance ref. [67] (two-dimensional), or [53], [63], [68], [69] (axisymmetric).

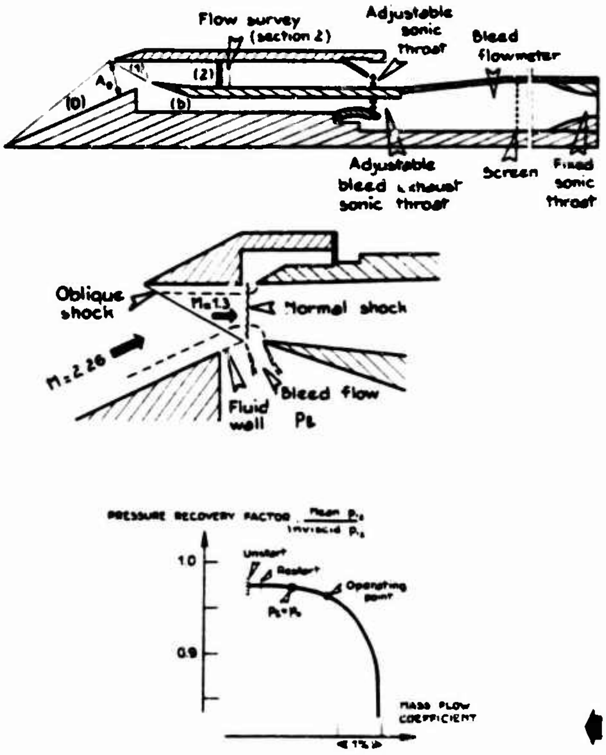
Flow survey (section 2)
Adjustable sonic throat
Bleed flowmeter
(0)
(1)
(2)
(b)
$A_e$
Adjustable bleed exhaust sonic throat
Screen
Fixed sonic throat
Oblique shock
M=1.3
Normal shock
M=2.26
Fluid wall
Bleed flow
$P_b$
PRESSURE RECOVERY FACTOR Mean $P_{t2}$ / Inviscid $P_{t2}$
1.0
0.9
Unstart
Restart
Operating point
$P_b=P_c$
MASS FLOW COEFFICIENT
1%

**FIG. 18 - FLUID WALL BLEED GAP**

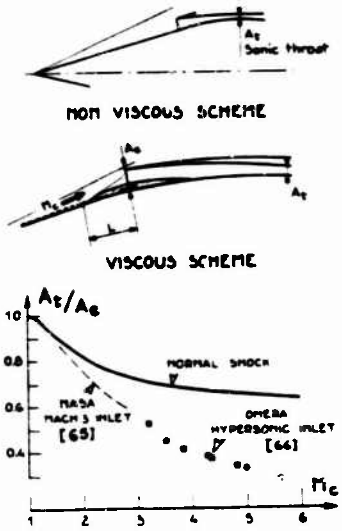

**FIG. 19 - STARTING PROCESS**

Typical pressure recoveries are compared figure 20 to the USA military specification for supersonic aircraft [10]. Improved inlets with mixed compression, internal bleed and geometry control system achieve a higher pressure recovery. External supersonic compression inlet with fixed geometry, no bleed, low drag cowl, are below the specifications.

### 4.1.4. Manoeuverability margin

Pressure recovery, drag, weight and also incidence and yaw capabilities have to be considered while evaluating an intake.

The two last points are connected with the intake control response time. For instance, if an intake is sensitive to yaw, it is possible to put the inlet in supercritical regime ("normal" shock more downstream than at the limit of detachment from the entry or unstarting). when the aircraft is going in sideslip, by acting on a ramp position or a by-pass door, and to avoid this way the detachment of the shock and the buzz, or the unstart, that the yaw would produce.

When a partial margin exists without any special device, as on figure 16 for the incidence, or ref. [14] (Concorde yaw capability analysis) and ref. [64] (Boeing SST intake control), the control system has enough time to adjust the intake.

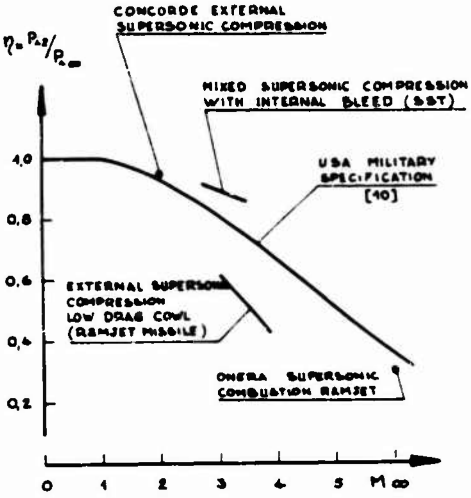

**FIG. 20 - PRESSURE RECOVERY**

If it is not the case, a pressure recovery loss has to be accepted in cruise flight to keep a sufficient manoeuverability margin.

Improvement in yaw capability may sometimes be obtained by very limited geometry modifications. Figure 21 shows the effect of a small swept cut of the sidewall leading edge of a two-dimensional intake at Mach 2. Without cut, the sidewall is like a delta wing, and in yaw, an upper surface leading edge vortex appears that enters the intake, spoils the pressure recovery and may initiate buzz. Cutting the leading edge gives a deviation of the approaching flow in the opposite to the yaw and suppresses the vortex, which provides a large performance improvement. The characteristic curves of figure 21 represent what happens at constant $q_m\sqrt{T}/p$

(reduced mass flow at given reduced engine R.P.M.). Without cut, no stable operating point exists at $\beta = 4°$ if the cavity pressure $p_b$ is maintained constant ; a control law reducing $p_b$ with $\beta$ would permit to operate at the point (a'), with a poor pressure recovery and a high level of distorsion. With the cut-back cowl, the normal control law adjusts the intake at the new point (a'), lowering automatically the ramp to keep constant the bleed cavity pressure $p_b$. At this point the distorsion level is still very acceptable.

### 4.1.5. Intake/airframe interference and integration

The choice of an intake/airframe configuration implies aerodynamics' and structural studies and global evaluation of the aircraft.

Supersonic three-dimensional linearized flow theories, and boundary-layer theories, help to evaluate the external forces applied to a given integrated configuration [70].

Interference effect on the intake performance results mainly from the flow field ahead of the entry, and from the incident boundary layer.

A large experimental program, designed by "Project Tailor Mate", has been devoted to this subject by the U.S.A.F., for a fighter aircraft up to about Mach 2.5.

Results giving the influence of the forebody shape, the wing/intake interference, the effect of the type of the intake and its position are collected ref. [71].

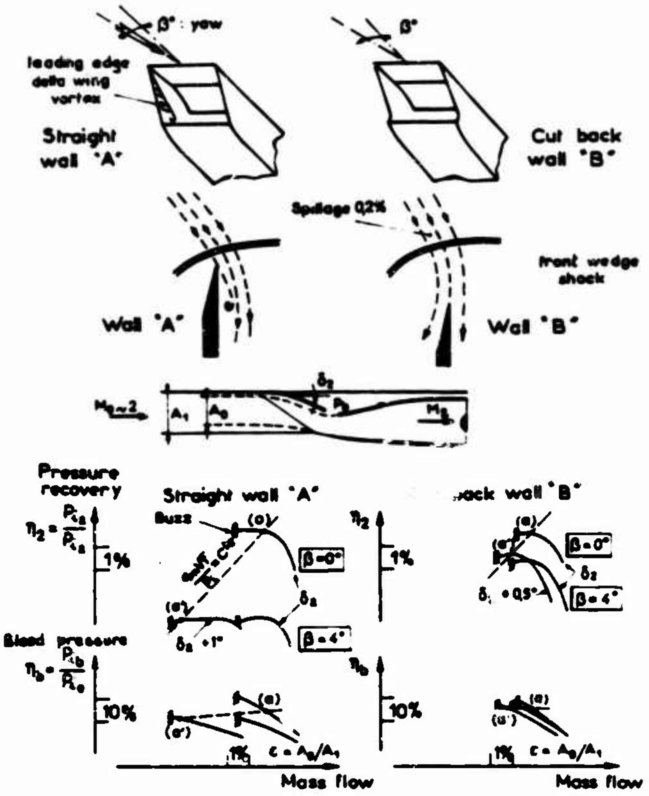

FIG. 21 - YAW EFFECT ON TWO-DIMENSIONAL INTAKE

Comparisons of lateral intakes dispositions are also given ref. [72].

The effect of the body boundary layer on a lateral two-dimensional or half conical spike intake has been the object of many experimental studies (see ref. [3]). Half-conical shock boundary layer intersction has been analysed, for instance ref. [73].

Fuselage flow field analysis can be found ref. [74].

Comparisons between two-dimensional and axisymmetric engine nacelle installation for an SST are presented ref. [75].

### 4.1.6. Variable geometry intake adjustment at reduced Mach number

A large amount of flow has to be spilled at Mach number lower than the cruise one : about 25% (or 50%) of the upstream flow corresponding to the frontal intake area, in transonic, for intake designed for a cruise Mach number of 2 (or 3). At the same time, the intake throat has to be enlarged.

Spillage can be obtained by deviating the flow ahead of the entry. In this case, additive drag may be important, and, to reduce it by smoothing the flow deviation, it is possible to position a long small slope ramp ahead of the entry, or to let a small angle spike emerge. For instance, a double cone intake with a multi flap second cone will be translated forward, with the second cone being collapsed to the same angle as the first one.

The other solution consists in by-passing the mass flow by an internal duct to feed the nozzle with the excess air. In that case, additive drag will be replaced by a by-pass installation drag, but adaptation of the nozzle may be easier.

Additive and cowl drag are easy to compute by the method of characteristics if the flow is entirely supersonic. At transonic speed, or if the spill results from a detached shock, experimental measurements are necessary. Some results can be found in many particular test reports, for instance ref. [76] to [78].

### 4.1.7.-Auxiliary intake for take-off and low speed

Pressure recovery reduction due to the thin lip flow turning around, at take off or low subsonic speed, can be predicted by a simple application of the momentum theorem [1], [79]. Auxiliary intakes are designed to reduce the main intake mass flow, and the resulting flow turning.

Inviscid subsonic flow computation method can be used to choose the dimension and the shape of auxiliary doors. An example of the streamline obtained by such a computation is reproduced figure 22.

It may be interesting to emphasize the device used to represent a boundary layer separation bubble of known pressure and extent, by successive adjustment of the stream potential value of partial elements of the cowl profile in the separated region, till a given value of the normal derivative of the stream function is obtained, that corresponds to the known pressure.

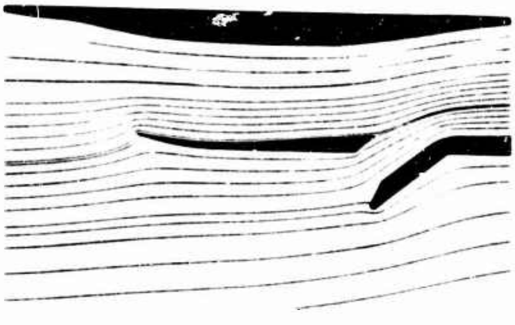

INVISCID THEORY

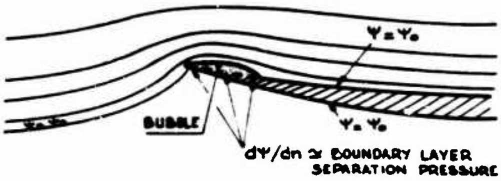
Ψ = Ψ₀
BUBBLE
Ψ = Ψ₀
dΨ/dn ≃ BOUNDARY LAYER SEPARATION PRESSURE

VISCOUS BUBBLE REPRESENTATION

FIG. 22 - AUXILIARY AIR INTAKE DESIGN

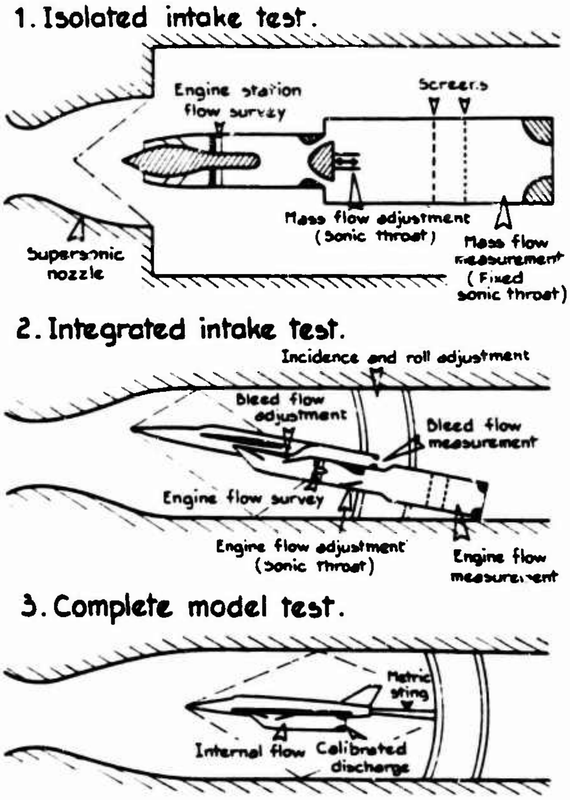
1. Isolated intake test.
Engine station flow survey
Screens
Mass flow adjustment (Sonic throat)
Mass flow measurement (Fixed sonic throat)
Supersonic nozzle
2. Integrated intake test.
Incidence and roll adjustment
Bleed flow adjustment
Bleed flow measurement
Engine flow survey
Engine flow adjustment (Sonic throat)
Engine flow measurement
3. Complete model test.
Metric sting
Internal flow
Calibrated discharge

FIG. 23 - SUPERSONIC INTAKE TEST

### 4.1.8. Wind tunnel intake tests (fig. 23)

A large scale isolated intake test in uniform flow is usually the only way to achieve a representative Reynolds number, which is necessary to obtain a precise evaluation of the intake pressure recovery. The results are used to correct the tests on an integrated intake model at a smaller scale. This latter scale is limited by the Mach Rhomb giving a correct entry flow field.

Test arrangements are shown on figure 23.

Intake/engine compatibility can be also studied in a large wind tunnel on isolated intake or partially integrated intake with the real engine internal installation.

### 4.2. Complete nacelle/aircraft model test (fig. 23)

As the aim of the complete nacelle/aircraft model test is to obtain the net forces applied to the aircraft, the nacelle is reproduced on the model as closely to the real one as possible.

Internal forces applied to the model have to be deduced from the measured forces, and replaced by the propulsive forces.

The internal forces evaluation is based on a very accurate measurement of the model exhaust flow. The best way of achieving that is to choke the internal flow by a calibrated sonic throat at the exit. Calibration is obtained by a preliminary test with a mass flow-meter (plenum chamber and second sonic throat) fixed behind the nacelle exhaust sonic throat, as represented figure 23, for the integrated intake test. A fine survey of the stagnation pressure at the sonic nacelle exhaust is then to be achieved in order to obtain a momentum coefficient that is applied to the calibrated exhausting mass flow.

The results have to be corrected for the Reynolds number effect, the sting support effect, and the afterbody real flow. Reynolds number corrections involve boundary layer calculations, and comparative tests on partial elements (intake, boundary-layer diverter...) at various Reynolds numbers. The two other corrections are connected with the afterbody tests raised up later.

Some test techniques are discussed ref. [41] and [43].

### 4.3. Supersonic aircraft nozzle and afterbody

#### 4.3.1. "Laval nozzle" and "Plug nozzle"

Afterbody design has to optimise the aircraft from a given external section of the engine installation (maximum diameter, for instance) and from the exit of the engine to which a given sonic throat has to be installed; secondary air passages complete the given elements.

Two types of nozzles can be considered : the converging-diverging "Laval" nozzle, and the "plug" nozzle (fig. 24).

Method of characteristics and boundary layer theories enable one to calculate the external and the internal supersonic flow, and to design a configuration of minimum drag for a given length. When a secondary flow is present, one-dimensional assumption for the corresponding stream tube gives the possibility of coupling the computation of the main flow with the secondary flow. A correction is applied to take into account the mixing effect at the boundary of the two flows. If the secondary flow is null or very small, a calculation is also possible by the theory of boundary layer reattachment of the main flow to the nozzle wall. The two solutions can be linked by continuity [1], [7], [80] to [84].

The example given figure 24 is taken from ref. [83].

Throat sonic line shape and initial conditions of the characteristic computation are examined in detail in ref. [85].

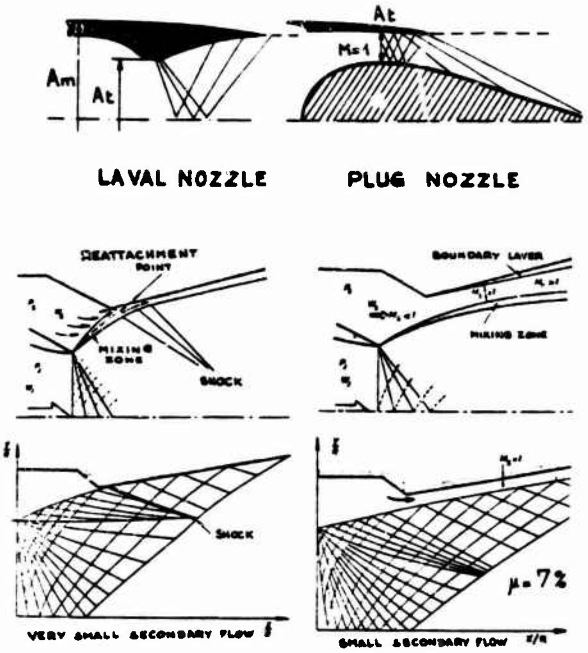

LAVAL NOZZLE PLUG NOZZLE

VERY SMALL SECONDARY FLOW SMALL SECONDARY FLOW

*FIG. 24 - AFTERBODY COMPUTATION METHOD [83]*

A secondary passage can also be designed to let a by-pass or an auxiliary flow be admitted into the nozzle at reduced Mach number, or to let a reverse flow be ejected by cascades installed in the surrounding structure.

Combination of intake performance as a function of the bleed flow, and afterbody performance as a function of the secondary flow, in terms of aircraft performance, is necessary to optimize the configuration (see, for instance, ref. [86]).

In supersonic cruise, the two types of nozzles seem equivalent from on aerodynamic point of view, but the necessity of cooling the plug nozzle is a disavantageous for this solution [84].

In fact, the afterbody performance at Mach number lower than supersonic cruise, and mainly in high subsonic flight, are the most critical problem for the aircraft performance, and the afterbody design.

#### 4.3.2. Variable geometry concept for subsonic adaptation

Adaptation problem is characterized by the pressure ratio of the jet stagnation pressure to the ambient static pressure, that corresponds to a high rate of supersonic jet nozzle expansion in supersonic cruise, and to a low rate of expansion at reduced Mach number, in subsonic flight. This is shown figure 25 from ref. [97].

Ideal solutions for "Plug" and "Laval" nozzle are compared to actual solutions of afterbody, on figure 26.

The performance of these two types of afterbody at high subsonic speed are very similar, and relatively good [84]. The translation of the cowl of the plug nozzle, as the only mean of adjusting the external profile, limits the performance of the plug nozzle ; the long internal nozzle of the "fully variable afterbody", and the quick slope increase at the hinge of the external profile are responsible for a loss of thrust, for this configuration.

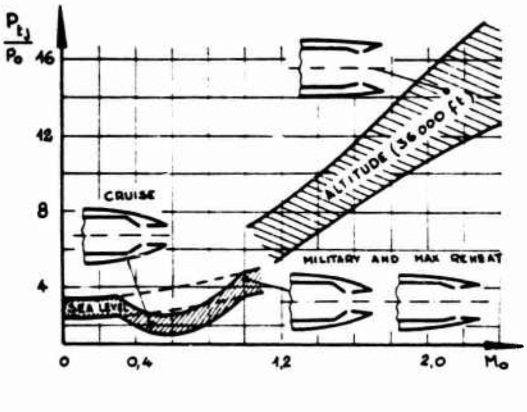

*FIG. 25 - REQUIRED VARIATION OF NOZZLE GEOMETRY [87]*

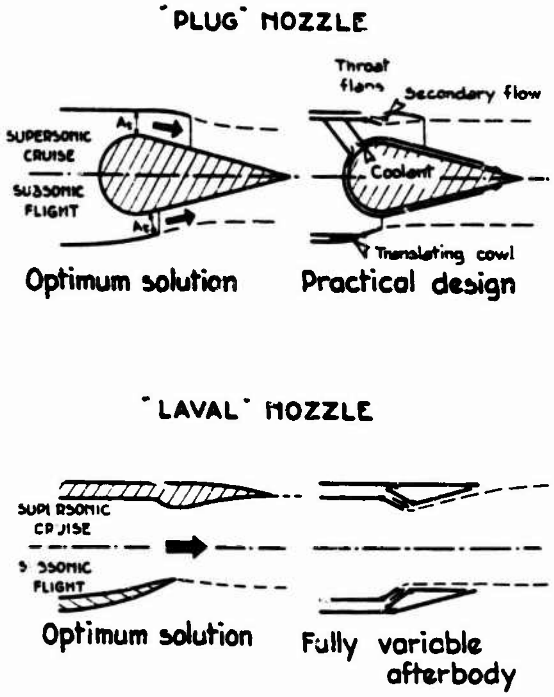
"PLUG" NOZZLE
Throat flaps
Secondary flow
SUPERSONIC CRUISE
SUBSONIC FLIGHT
Coolant
Translating cowl
Optimum solution
Practical design
"LAVAL" NOZZLE
SUPERSONIC CRUISE
SUBSONIC FLIGHT
Optimum solution
Fully variable afterbody

FIG. 26 - AFTERBODY ADAPTATION CONCEPT

More simple is the simple ejector nozzle (fig. 27), but the constant-pressure supersonic expansion of the jet in the supersonic cruise configuration implicates a shock at the reattachment of the jet on the flap, that causes a loss of thrust. This solution is used on strike fighters for which simplicity and subsonic performance are relatively more paying than supersonic cruise performance.

Convergent-divergent iris ("con-di-iris") may be another compromise between supersonic penalised by a very short supersonic nozzle, and subsonic performances. In a proposed version, the nozzle throat is formed by the iris throat. In this case, however, the fact that the throat section is not independent from the nozzle divergence penalises some flight stages (for instance, subsonic with reheat on).

The "blow-in-door" ejector is simpler than the fully variable ejector, but the gap provided between the throat and the divergent nozzle to let pass the auxiliary flow has to be pretty large, and causes a slight reduction of the cruise thrust. The auxiliary flow blowing into this gap at high subsonic speed entails also some losses, but the performances are still acceptable.

The "rear buckets" version of the blow-in-door nozzle is lighter than the preceding one, but when the buckets are in subsonic position, the internal configuration is no more axisymmetric, and some losses have to be accepted.

The "fixed ring" nozzle, where a well shaped auxiliary duct is formed, may be also attractive.

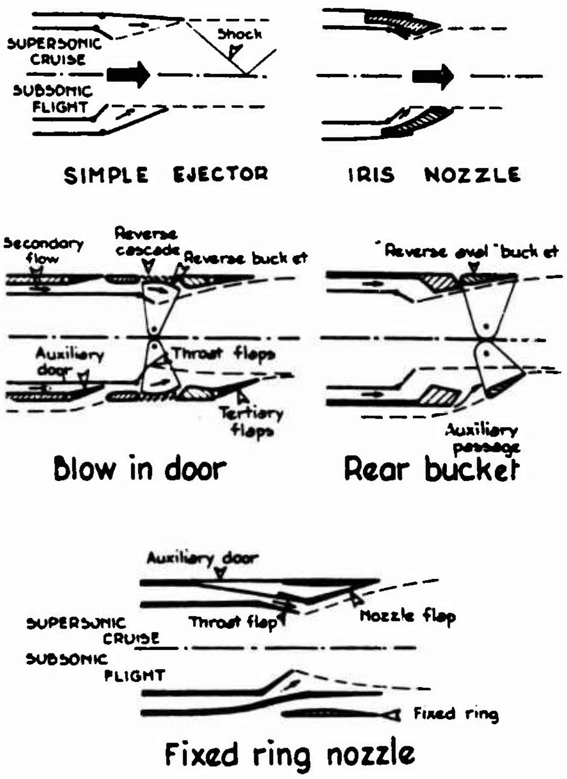
SUPERSONIC CRUISE
SUBSONIC FLIGHT
Shock
SIMPLE EJECTOR
IRIS NOZZLE
Secondary flow
Reverse cascade
Reverse bucket
Auxiliary door
Throat flaps
Tertiary flaps
"Reverse oval" bucket
Auxiliary passage
Blow in door
Rear bucket
Auxiliary door
SUPERSONIC CRUISE
Throat flap
Nozzle flap
SUBSONIC FLIGHT
Fixed ring
Fixed ring nozzle

FIG. 27 - AFTERBODY ADAPTATION CONCEPT

### 2.3.3. Afterbody tests

The aim of the afterbody tests is to correct the measurements made on complete nacelle/aircraft model tests mentionned section 4.2.

It consists in reproducing on a upstream mounting the rear part of the engine installation, and to compare the forces by reproducing successively the exhaust flow of the complete nacelle/aircraft model test and the real jet and exhaust flow.

This is usually done by feeding the nozzle with compressed air through a balance, as for subsonic afterbody studies.

One of the problems is to reproduce exactly, on the afterbody model, the correct external flow field ; a symmetry panel, for instance (fig. 28), is necessary to simulate a two-engine nacelle on a isolated afterbody wind tunnel rig, though the boundary layer of the panel may disturbe the rear flow.

Tests of a calibrated nozzle may be useful to assess the measurement accuracy. Calibration of mass flow measurement by a sonic throat, and of thrust measurement by a calculated nozzle, is discussed in detail in ref. [88].

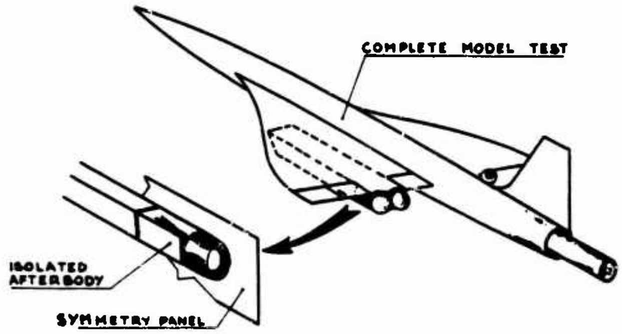

*FIG. 28 - ISOLATED AFTERBODY TEST [88]*

Most often, only the axial component of the thrust is measured, due to the flow-through balance complexity. Separated measurements of the drag of the external wall of the afterbody and of the thrust of the nozzle may be provided to give more detailed results. The book-keeping procedure of the corresponding tests is presented on figure 29, from [89]. The complete nacelle/aircraft model afterbody reproduced on the mounting gives the reference afterbody drag, $D_{AB\ REF}$; the actual afterbody test gives the installed afterbody drag, $D_{AB\ INST}$ ; the corrective term $\Delta D_{AB}$ is the difference $D_{AB\ INST} - D_{AB\ REF}$.

The nozzle thrust measurement gives the external forces on the nozzle, $- D_N$, plus the installed thrust, $F_{INST}$; that can be compared to a reference thrust, $F_{REF}$.

Attempts are done to achieve a six components balance on half model (fig. 29), which is necessary to reach a complete evaluation of the afterbody performance.

Corrections have to be applied to the afterbody test results, mainly due to hot gas effect and incipient-boundary layer differences between the complete nacelle/aircraft test, the afterbody test, and the flight conditions. Hot gas correction can be obtained by computation (for instance, ref. [83]). Upstream boundary layer control could be installed on the mounting, as for subsonic aircraft afterbody studies, to evaluate the effect of boundary layer discrepancies.

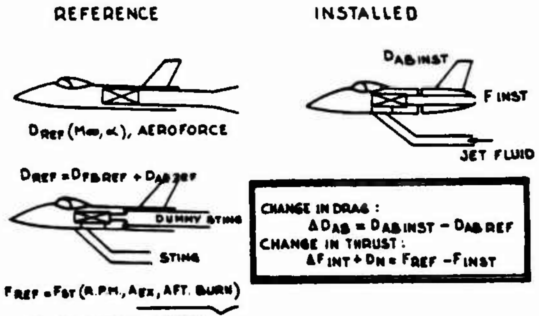

BOOKKEEPING PROCEDURE FOR INTEGRATED NOZZLE-AIRFRAME SYSTEMS [89]

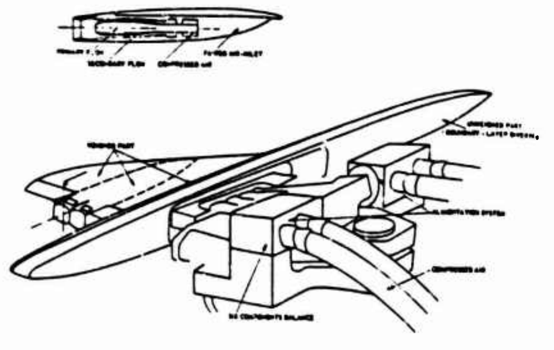

HALF MODEL BALANCE

*FIG. 29 - AFTERBODY EXPERIMENTAL STUDY*

## REFERENCES

### A. BASIC PAPERS

[1] P. CARRIERE - Aerodynamique interne des réacteurs. a) Prises d'air b) Tuyères et jets. Cours de l'Ecole Nationale Supérieure de l'Aéronautique et de l'Espace (Complexe aérospatial, Toulouse) (1972).

[2] P. CARRIERE - Aperçu de quelques problèmes actuels posés par les prises d'air supersoniques. $1^{er}$ Symposium International sur les Progrès des Réacteurs d'Aviation. Marseille (1972).

[3] AGARD : Supersonic inlets (I. FARO) - Agardograph 102 (1965).

[4] AGARD : Aerodynamics of power plant installation - Agardograph 103 (1965).

[5] AGARD : Airframe/engine integration. AGARD Lecture Series LS 53 (1972).

[6] AGARD : Inlets and nozzles for aerospace engines - AGARD CP 91 (1971).

[7] AGARD : Supersonic ejectors - Agardograph 163 (1972).

[8] NASA : Aircraft propulsion - NASA SP 259 (1970).

[9] J. LEYNAERT - Entrées d'air supersoniques dans «Chocs et ondes de choc» (A. Jammotte), tome II, Masson et Cie éditeurs (1973).

### B. INTAKE PRESSURE RECOVERY AND DISTORSION

[10] USA Military Specification (1959) - Specification for engines, aircraft, turbojet, models MIL.E.5008 E.

[11] AGARD : Aircraft performance - Prediction methods and optimization. AGARD Lecture Series LS 56 (1972).

[12] J. ALFORD - Inlet flow distorsion index - I.C.A.S., Paris (1956).

[13] L. DAWSON - Engine designer's point of view. Agardograph 103 (1965).

[14] C. LEYMAN, D. MORRIS - Concorde power plant development - AGARD CP 91 (1971).

[15] S. ELLIS - Inlet engine compatibility analysis - AGARD CP 91 (and discussion on the paper at the end of the report) (1971).

[16] F. BURCHAM, D. BELLMAN - A flight investigation of steady state and dynamic pressure phenomena in the air inlet of supersonic aircraft. AGARD CP 91 (1971).

[17] J. POVOLNY, F. BURCHAM, J. CALOGERAS, C. MEYER, R. RUDEY - Effects of engine inlet disturbances on engine stall performance. NASA SP 259 (1971).

[18] D. ZONARS - Dynamic characteristics of engine inlets. AGARD LS 53 (1972).

### C. SUBSDNIC NACELLE

[19] W. VIALL - Aerodynamic considerations for engine inlet design for subsonic high by-pass fan engines SAE paper 660 734 (1966).

[20] W.S. VIALL - The engine inlet on the 747. ASME 69 GT 41.

[21] W. BAUERMEISTER, C. ROSEBURG - 727 airplane engine inlet development. AIAA paper 68-595.

[22] J. SAYLOR, J. HANCOCK - C5 engine inlet development. ASME 69 GT 52.

[23] C. YDUNG - An analysis of the drag of two annular aerofoils. RAE TR 71-126.

[24] M. SUSSMAN, D. GUNNARDSON, P. EDWARDS - Nacelle design studies for advanced transport aircraft. AIAA paper 72-1204.

[25] W. DOUGLASS - Aerodynamic installation of high-by pass ratio fan engines. SAE paper 660 732 (1966).

[26] J. LEYNAERT, G. MEAUZE - Quelques problèmes transsoniques du fuseau moteur d'un avion de type Airbus. AGARD CP 35 (1968).

[27] F. KLUJBER - Results of an experimental program for the development of sonic inlets for turbofan engines. AIAA paper 73 222 (1973).

[28] A. MARSH, I. ELIAS, J. HOEHNE, R. FRASCA - A study of turbofan-engine compressor-noise-suppression techniques. NASA CR 1056 (1968).

[29] A. HARTMANN - Theoretical and experimental investigation of fan engines with mixing. AIAA paper 67-416.

[30] G.T. FRAZIER - Aerodynamic considerations for engine exhaust design for subsonic high by pass flow engines. SAL paper 660-734 (1966).

[31] D. BERGMAN - An aerodynamic drag study of jet engine nozzles. AGARD CP 91 (1971).

[32] J. KUTNEY - Airframe/propulsion system integration analysis using the propulsion simulation technique. AGARD CP 71 (1971).

[33] S. ALDRIDGE, J. NYE - Experimental results of high by-pass ratio turbo fan and wing aerodynamic interference. AGARD CP 71 (1971).

[34] B. WILLIAMS - Advanced technology transport configuration development. AIAA paper 72-756.

[35] P. WILLIAMS, D. STEWART - The complex aerodynamic interference pattern due to rear fuselage mounted powerplants. AGARD CP 71 (1971).

[36] P. WILLIAMS, D. STEWART - An aircraft designer's review of some aircraft and engine integration concept. 1st International Symposium on Airbreathing Engines - 1972.

[37] W. SWANN, A. SIGALLA - The problem of installing a modern high by-pass engine on a twin jet transport aircraft. AGARD CP 124 (1972).

[38] S. SPANGLER, M. MENNDENHALL, M. DILLENIUS - Theoretical investigation of ducted fan interference for transport-type aircraft. NASA SP 228 (1969).

[39] J. HESS, S. FAULKNER - Determination of low speed interference effects by superposition. AGARD CP 71 (1971).

[40] W. GEISSLER, R. WULF - Jet simulation and jet interference effects on tailplane - AGARD CP 71 (1971).

[41] J. JAARSMA - Inlets-airplane testing in transonic wind tunnel. AGARD CP 91 (1971).

[42] J. LEYNAERT - Entrée d'air et arrière-corps de fuseau-moteur en transsonique. AGARD CP 83 (1971).

[43] E. CARTER - Experimental determination of inlet characteristics and inlet and airframe interference. AGARD LS 53 (1972).

[44] A. FUHS - Nozzle and exhaust testing in transonic flight regime. AGARD CP 91 (1971).

[45] J. BAGLEY - Wind tunnel experiments on the interference between a jet and wing at subsonic speeds. AGARD CP 35 (1968).

[46] G. NICOLOFF, H. WEBER - Characteristics of an ejector type engine simulator for STOL model testing. AIAA paper 72-1028.

[47] F. JAARSMA - Expérimental determination of nozzle characteristics and nozzle airframe interference - AGARD LS 53 (1972).

[48] G. PAULEY - Interim note on tests with a wing-mounted fan nacelle with the fan jet simulated by cold air blowing and alternatively by a gaz generator shroud. ARC-CP 1111 (1970).

[49] C. HODGE, V. SALEMAN - Aerodynamic performance testing using wind tunnel models and blown nacelle engine simulators. AIAA paper 68-396.

### D. SUPERSONIC INTAKE

[50] V. SORENSEN - Computer program for calculating flow field in supersonic inlet. NASA TN D 2897 (1965).

[51] B. ANDERSON - Design of supersonic inlets by a computer program incorporating the method of characteristics. NASA TN D 4960 (1969).

[52] P. DIRINGER - Reflexions régulières et singulières d'ondes de choc. Applications aux entrées d'air et au problème du disque de Mach. ONERA N.T. 183 (1971).

[53] N. SORENSEN, D. SMELTZER - Investigation of a large-scale mixed compression axisymmetric inlet system capable of high performance at Mach number 0.6 to 3.0 - NASA TMX 1507 (1968).

[54] T. REYHNER, T. HICKCOX - Combined viscous inviscid analysis of supersonic inlet flow fields. Journal of Aircraft, vol. n° 8, Aug. 1972.

[55] W. SEEBAUGH, M. CHILDS, G. PAYNTER - Calculation of turbulent boundary layer characteristics across an oblique shock reflexion including the effects of mass bleed. AIAA paper 68-110.

[56] N. SORENSEN, D. SMELTZER - Performance estimates for a supersonic axisymmetric inlet system. AIAA paper 72.45.

[57] E. TJONNELAND-The design, development and testing of a supersonic transport intake systems. AGARD CP 91 (1971).

[58] G. MEAUZE - Etude de la recompression par chocs en présence d'un piège à couche limite. 2nd International Symposium on Air Breathing Engines. (Sheffield, England, March 74). Note Technique ONERA, to be published.

[59] G. Mc LAFFERTY, E. KRASNOFF, E. RANARD, W. ROSE, R. VERGARA - Investigation of turbojet inlet design parameters. UAC Report 0790-13 (1955).

[60] A. KARANIAN - Characteristics of normal shock waves in the throat of precompression inlets. UAC Report 0955-20 (1955).

[61] J. LEYNAERT - Fonctionnement du piège à couche limite interne d'une prise d'air à compression supersonique externe. Agardograph 103 (1965).

[62] W. HINZ, H. HUTTENLOCHER, P. STIGLIC - The F14A air inlet control system. AIAA paper 70-697.

[63] D. BOWDITCH, R. COLTRIN, B. SANDERS, N. SORENSEN, J. WASSERBAUER - Supersonic cruise inlets. NASA SP 259 (1970)

[64] H. LARSEN, R. SCHWEIKHARDT - Control concept and wind tunnel testing of a supersonic intake control system. AGARD CP 91 (1971).

[65] G. MITCHELL, R. CUBBISON - An experimental investigation of the restart area ratio of a Mach 3.0 axisymmetric mixed compression inlet. NASA TMX 1547 (1968).

[66] G. LARUELLE et J. LEYNAERT - *Amorçage d'une prise d'air de révolution à compression supersonique mixte.* AGARD CP 91 (1971).

[67] W. ANDERSON, N. WONG - *Experimental investigation of a large scale two-dimensional mixed compression inlet system. M = 3.0,* NASA TMX 2016 (1970).

[68] D. SMELTZER, N. SORENSEN - *Investigation of a nearly isentropic mixed compression axisymmetric inlet system at Mach numbers 0.6 to 3.2* - NASA TN D 4557 (1968).

[69] J. KONCSEK, J. SYBERG - *Transonic and supersonic test of a Mach 2.65 mixed-compression axisymmetric intake* - NASA CR 1977 (1972).

[70] H. CARLSON, R. HARRIS - *A unified system of supersonic aerodynamic analysis* - NASA SP 228 (1969).

[71] P. ANTONATOS, L. SUBER, J. STAVA - *Inlet/airframe interference and integration* - AGARD LS 53 (1972).

[72] C. BROWN, E. GOLDSMITH *Measurement of the internal performance of a rectangular air intake (mounted on a fuselage at Mach numbers from 1.6 to 2.5).* - RAE TR 71-159 - 71-236 - 72-236.

[73] D. PEAKE, D. JONES, W. RAINBUD - *The half cone pressure field and its significance to side mounted intakes.* AGARD CP 71 (1971).

[74] L. KING, T. SCHMIDT - *Studies of aircraft flow fields at inlet locations* - AGARD CP 71 (1971).

[75] A. VAN DUINE, W. RHOADES, W. SWAN - *Configuration aspects of propulsion installation on supersonic transports* - AGARD CP 71 (1971).

[76] J. MOUNT - *Additive drag of inlet cowls and its effects on aircraft performance.* Agardograph 103 (1965).

[77] M. DOBSON, E. GOLDSMITH - *The external drag at subsonic and supersonic speeds of fuselage-side intakes for strike-flighter aircraft.* ICAS paper 70-49.

[78] G. MULLER, W. GASKO - *Subsonic/transonic drag of supersonic inlets.* J. of Aircraft, vol. 4, n° 3 - (May 1967).

[79] J. LEYNAERT - *Etude par analogie rhéoélectrique de prises d'air auxiliaires pour le décollage des avions supersoniques.* La Recherche Aérospatiale n° 119 (juillet-août 1967).

## E. SUPERSONIC AFTERBODY AND NOZZLE

[80] P. CARRIERE, M. SIRIEIX, J.M. HARDY - *Problème d'adaptation de tuyères* - AGARD CP 34 (1968).

[81] J.L. SOLIGNAC, J. DELERY - *Contribution à l'étude aérodynamique des systèmes propulsifs à double flux.* Israël J. of Technology, vol. 10, 1-2 (1972).

[82] J.M. HARDY - *Influence de quelques paramètres caractéristiques sur les performances des éjecteurs* - AGARD CP 91 (1971).

[83] J.M. HARDY - *Etude théorique d'une tuyère convergente-divergente biflux.* L'Aéronautique et l'Astronautique, n° 37 (1972).

[84] M. BEHEIM, B. ANDERSON, J. CLARK, B. CORSON, L. STITT, F. WILCOX - *Supersonic exhaust nozzle* - NASA SP 259 (1970).

[85] J. SOLIGNAC, M. FENAIN, DUTOUQUET - *Calcul des performances d'une tuyère propulsive convergente ; comparaisons avec l'expérience.* IXth ICAS Congress, Haifa, 26-30 Aug. 1974 (to be published).

[86] J. TALBOT, B. FURNESS - *A fully integrated propulsion system for a supersonic transport aircraft.* Agardograph 103 (1965).

[87] F. AULEHLA, K. LOTTER - *Nozzle/airframe interference and integration* - AGARD LS 53 (1972).

[88] B. MASURE - *Problèmes de mesure sur maquette de la poussée d'un arrière-corps supersonique - Tuyères de référence* - AGARD CP 91 (1971).

[89] F. JAARSMA - *Experimental determination of nozzle characteristics and nozzle airframe interference* - AGARD LS 53 (1972)

N74-26454

# EXTERNAL STORE AERODYNAMICS FOR AIRCRAFT PERFORMANCE PREDICTION

BY

J.B.BERRY
AIRCRAFT RESEARCH ASSOCIATION LTD.BEDFORD,ENGLAND

## SUMMARY

Some effects of external stores on the aerodynamic characteristics of aircraft and in particular the incremental drag due to various types of store installation are described. Examples of drag increments for single and multiple store assemblies installed underwing and underfuselage and the effects of $C_L$ and Mach number up to high subsonic speeds, illustrate some of the interference features in the aircraft-store flow field which contribute to high or low drag. The prospects for incremental drag prediction, the possible use of calculated or measured flow field data, empirical methods and flight-tunnel comparisons are discussed. Approximate empirical estimation procedures for simple underwing and underfuselage store installations are described. It is suggested that for multiple store assemblies, opportunities for drag reduction offer considerably more promise than attempts to predict the drag increment. Significant drag savings are demonstrated not only for new types of installation but also by relatively simple modifications to existing designs.

## NOTATION

| | |
|---|---|
| $C_A$ | Axial force coefficient |
| $C_B$ | Unsteady wing root bending moment coefficient |
| $C_D$ | Drag coefficient |
| $C_L$ | Lift coefficient |
| $C_m$ | Pitching moment coefficient |
| $C_n$ | Yawing moment coefficient |
| $C_p$ | Pressure coefficient |
| M | Mach number |
| S | Area |
| d | Diameter |
| q | Dynamic pressure |
| $n_v$ | $\partial C_n/\partial \beta$ |
| $\alpha$ | Incidence angle |
| $\beta$ | Sideslip angle |

All other symbols and suffices used in this paper are defined in the text.

## 1. INTRODUCTION

The title 'external store aerodynamics for aircraft performance prediction' may seem distasteful to the aerodynamicist, since external stores almost always degrade some aspects of the 'aerodynamic' performance of the aircraft carrying them. It is necessary however to distinguish between performance involving aerodynamic considerations - range, rate of climb, stability, manoeuvrability, etc. - and the overall performance of the aircraft-stores combination as an efficient weapons delivery system. Desirable aerodynamic features may sometimes have to be compromised to achieve the optimum overall solution. However, having acknowledged this distinction, this paper will be concerned with the effects of external stores on the 'aerodynamic' characteristics of aircraft and in particular the incremental drag due to external stores. The large drag contribution of external stores is a significant and often limiting factor in the performance of strike and combat aircraft. The importance of both the reliable prediction and the reduction of the incremental drag is now widely recognised[1] and considerable research effort has recently been expended on this topic in the U.K.

To provide a background for the main part of the paper, some examples of more general characteristics of aircraft carrying external stores are briefly described in section 2. Section 3 presents examples of incremental drag due to various types of store assemblies installed underwing or underfuselage and attempts to identify some of the interference features involved and also particular sources of high or low drag. In section 4 the prospects for predicting the store drag increment and the value of flow field data and flight-tunnel comparisons are discussed and tentative empirical methods for simple underfuselage and underwing installations are proposed. Finally some examples of and possibilities for the reduction of the drag of stores, assemblies and installations are described in section 5. Except for some flight results quoted in section 4, all the experimental data used to illustrate the discussion have been obtained from wind tunnel models, most of which were tested in the A.R.A. 9ft x 8ft transonic wind tunnel.

## 2. GENERAL EFFECTS OF EXTERNAL STORES

Figure 1 shows the effects of a multiple underwing store installation - 3 stores on the inboard pylon and a single store outboard under each wing - on the total lift, pitching moment and unsteady root bending moment at $M = 0.8$. Also shown is the effect of a large underfuselage store on directional stability. The lift curve slope $\partial C_L/\partial\alpha$ is considerably reduced even at low incidence, in the 'stores on' case and the $C_L$ 'break', although at roughly the same incidence as for the clean wing, occurs at a much lower $C_L$. The $C_m - C_L$ curve also breaks at a correspondingly lower $C_L$, with a significant reduction in static stability before the break, compared with the clean wing. The unsteady wing root bending moment coefficient is a useful indication of the onset and severity of wing buffet associated with unsteady pressures in regions of boundary layer separation. $C_B$, 'stores on' increases more rapidly with $C_L$ and the peak value of $C_B$ occurs at a lower $C_L$ and is considerably greater than that for the clean wing, indicating a significant reduction in buffet penetration ability. $C_B$ 'stores on' is also higher than for the clean wing at low $C_L$ with a tendency for $C_B$ to increase with reductions in $C_L$ to $C_L = 0$. This may be due to boundary layer separations caused by the stores on the wing lower surface at negative and low positive $C_L$. The lower graph on figure 1 shows that the clean aircraft value for $n_v$ is reduced by about half at low $\alpha$ and to zero at high $\alpha$, when the underfuselage store is installed. These results indicate that external stores can impose very severe penalties on the manoeuvre capability and handling qualities of an aircraft, quite apart from any structural limitations involved in store carriage. These are admittedly extreme examples, but they represent practical configurations at a Mach number well within the normal envelope of the aircraft considered.

## 3. INCREMENTAL DRAG CHARACTERISTICS OF EXTERNAL STORES

In this section some typical incremental drag characteristics of various types of external store installations in common use on current aircraft will be described. The examples discussed are mainly restricted to results obtained at $M < 1.0$ and at low to moderate $C_L$ - i.e. conditions for relatively well behaved flow with no large scale flow separations on the parent aircraft wing. The framework used in the analysis of the experimental data is based on the comparison of the installed drag increments with the freestream drag of the components of the store assembly.

It will be helpful to start by defining some particular terms and symbols to be used in the following discussion :-

$\Delta C_D$ = $(C_D)$ aircraft + store(s) - $(C_D)$ aircraft measured either at constant $C_L$ or at constant incidence

$\sum C_{D_{COMP}}$ or $\sum \left(D/q\right)_{COMP}$ = the sum of the estimated low speed freestream drags of the components of the store assembly, including drag due to bluff forebodies, bases and excrescences, but no allowance for mutual interference between components. (See Appendix A).

$$K_A = \frac{\left(D/q\right)\text{ store assembly in isolation}}{\sum\left(D/q\right)_{COMP}}$$

$$K_S = \frac{\Delta C_D}{\sum C_{D_{COMP}}}$$

$M_D$ = M at which $\partial C_D/\partial M = 0.01$

The use of estimated drag values in the denominators of the interference factors, $K_A$ and $K_S$ perhaps requires some explanation. Obviously when assessing or predicting the incremental drag due to a particular store installation, any reliable measured freestream drag data for individual components should be used.

However when comparing, as in this paper, the relative merits or penalties of several different installations, possibly on different aircraft, it is unlikely that measured drag data for comparable components or assemblies would be available for all the configurations. In order to compare the various installations and to analyse the contributions of the many components in a consistent manner, it is necessary to start with information which is readily available and commonly applicable - 'a lowest common denominator'. At present this is probably best provided by a simple low speed freestream drag estimate. The method used at A.R.A. to estimate $\sum\left(^{D}/_{q}\right)_{COMP}$ is outlined in an appendix to this paper.

A simpler form of interference factor is sometimes used in which the freestream drag of either a single store or all the stores carried forms the denominator, implying that the drag of the carriage equipment is part of the interference penalty. This may be justified for operational comparisons on particular aircraft e.g. of alternative store carriers, but it tends to evade the responsibility of the aerodynamicist in examining in detail the reasons why a particular installation has high or low drag. The task of estimating $\sum\left(^{D}/_{q}\right)_{COMP}$ often provides a valuable insight into some of the sources of high drag, before any assembly or installation factors are applied. Also the incremental drag of the empty pylons and carriers must be known for the homeward flight.

### 3.1. Underwing installations

#### 3.1.1. Simple single stores

In the simple case of an aerodynamically clean pylon mounted single store at low speed and low $C_L$, with thin attached boundary layers and no shock waves, interference effects in the flow about the wing, pylon and store would arise due to[2] :-

(i) interaction of the wing, pylon and store pressure fields - buoyancy effects,

(ii) changes in skin friction drag due to local changes in dynamic pressure,

(iii) induced drag on the store or pylon and changes in induced drag on the wing due to changes in local flow direction.

In most cases (ii) and (iii) (for stores without significant lifting surfaces) are probably small, leaving (i) as the major contribution to the interference. Figure 2 shows a streamlined store located in the low speed, zero incidence pressure field beneath a symmetrical section swept wing. The pressure field measurements are taken from ref.3, and are not modified for the presence of the store and pylon. These measured pressures have been used to calculate the buoyancy forces on a streamlined store similar to the one shown and on a flat based store with cruciform wings, each mounted at various chordwise locations below the wing. The axial buoyancy forces have been added to the estimated freestream drag of the stores to obtain estimates of the total axial force on the installed stores[4]. Comparison with the measured axial forces on the two stores beneath a similar wing to that for which the pressure field data were obtained (figure 2) shows very close agreement both in the absolute values of $C_A$ and the variation of $C_A$ with store chordwise position. To obtain $\Delta C_D$ (or $\Delta D/_q$) the interference drag on the wing would also have to be calculated. In potential flow these buoyancy forces between the wing and the store would cancel. In real flow, complete cancellation of the interference might not be expected. However, the quite close agreement shown on figure 2 between the overall drag increment due to the stores, $\Delta D/_q$ and $\sum\left(^{D}/_{q}\right)_{COMP}$ and the relative insensitivity of $\Delta D/_q$ to the store chordwise position do indicate effective cancellation of the interference for these examples. In fact the analysis of a large amount of data, including some for bluff and 'dirty' stores, indicates that for single stores pylon mounted close to the wing lower surface the installation factor, $K_S$, generally has a minimum value near 1.0 at low M and $C_L$.

These encouraging results unfortunately no longer apply when significant viscous and compressibility effects appear. Figure 3 compares the variation of $K_S$ with $C_L$ for fairly slender stores mounted beneath four different wings. The results are shown for both a moderate subsonic Mach number, at which no significant increase in $\Delta C_D$ with M has occurred, and at approximately $M_D$ for the respective clean wings. Except for the minimum values of $K_S$ at the lower M, excess interference drag appears even over this low to moderate $C_L$ range, with values of $K_S$ as high as 1.8 at moderate M and 2.5 at $M_D$ (clean wing). In all cases except wing D (with an almost symmetrical thin section unlike the other wings) at moderate M, for which $K_S$ increases with $C_L$ from $C_L = 0$, $K_S$ has a minimum value or level $(K_S)_{MIN}$, at some positive $C_L$. There is a considerable variation between wings in the value of $C_L$ at which $(K_S)_{MIN}$ occurs and in the rate of change of $K_S$ with $C_L$. This suggests that the "excess" interference at values of $C_L$ other than that for $(K_S)_{MIN}$ is mainly dependent on the aerodynamics of the parent wing and pylon, since the drag force on these streamlined stores would be comparatively insensitive to incidence.

The variation of $\Delta C_D$ with M for two different stores on the same wing - fuel tank and missile - is shown on figure 4. Considering the $C_L = 0$ curves first; at $M = 0.5$, $\Delta C_D$ for the missile is nearly 3.5 x $\Delta C_D$ for the tank. At $M = 0.8$, $M_D$ approximately, for the clean wing, $\Delta C_D$ has increased more rapidly for the missile than for the tank. By $M = 0.9$, however, the increase in $\Delta C_D$ is slightly greater for the tank than for the missile. The high proportion of excrescence and base drag on the missile installation $\left(52\% \text{ of } \sum C_{D_{COMP}}\right)$ and associated flow separations are probably responsible for the early drag rise for this store. The more rapid increase in $\Delta C_D$ for the tank between $M = 0.8$ and $0.9$ is probably a genuine interference wave drag increase due to the chordwise variation in cross section area of the tank beneath the wing compared with the essentially constant cross section of the missile body. The $\Delta C_{D_{MIN}}$ comparison for the two stores is generally similar to that at $C_L = 0$. The reduction in $\Delta C_D$, between $C_L = 0$ and $C_{D_{MIN}}$, is of the same order for both stores rather than in proportion to $\Delta C_D$

(or $\Delta C_{D_{MIN}}$), which again suggests that the extra $C_L$ dependent interference drag originates on the wing, or possibly the pylon. At M = 0.5 and 0.6, $(K_S)_{MIN}$ for both stores is close to 1.0, illustrating that at low M local flow separations due to the bluff base and excrescences on the missile do not significantly affect the "buoyancy" nature of the wing-pylon-store interference. However, at M = 0.9, the larger increase in $\Delta C_D$ due to the clean fuel tank, compared with the "dirty" missile is even more striking in terms of $(K_S)_{MIN}$ = 6.3 for the tank, 2.3 for the missile.

Figure 4 also compares the variation of $\Delta C_{D_{MIN}}$ with M for similar streamlined stores mounted beneath wings of low and high sweep. The increase in $\Delta C_{D_{MIN}}$ is delayed to a higher Mach number for the store installed on the more highly swept wing, but in both cases the increase in drag starts at Mach numbers well below $M_D$ for either the clean wing or the isolated store.

Summarising the main interference effects contributing to $\Delta C_D$ for single underwing store installations :-

(i) At low M, for a small range of $C_L$ about a low to moderate value, the combined pressure field about the wing-store-pylon is essentially of the potential flow type, with negligible resultant interference drag,

(ii) The variation of $\Delta C_D$ with $C_L$ is strongly dependent on the aerodynamic characteristics of the parent wing.

(iii) The increase in $\Delta C_D$ with M results from the appearance of wave drag, both locally on the store (a function of store shape) and in the combined wing-pylon-store pressure field.

### 3.1.2. Multiple Installations

The term multiple installation used here for underwing stores refers to two or more stores carried on one pylon. On figure 5 the variation of $\Delta C_D$ with M and $C_L$ for an installation with 3 bombs on a triple carrier is compared with that for a single pylon mounted bomb of the same type carried on the same aircraft model[5]. Even at low M, $\Delta C_D$ for the triple installation is much more than 3 x $\Delta C_D$ for the single pylon mounted bomb. The extra drag of the triple carrier itself is unlikely to account for this. The slope of $\Delta C_D$ - M for the 3 bomb case suggests that compressibility effects are present even at the lowest Mach number shown, M = 0.5. It should be noted that for M ≥ 0.7 at $C_L = 0$, $\Delta C_D$ for the triple case is greater than the clean aircraft drag. As for single underwing stores this multiple installation, in common with others, shows the characteristic reduction in $\Delta C_D$ with increasing $C_L$, particularly at the higher Mach numbers. $(K_S)_{MIN}$ at M = 0.5 is about 1.6, but this is probably not a true low speed value, as noted above. Above about M = 0.85 $(K_S)_{MIN}$ is in fact less for 3 bombs than for the single bomb case. It is worth noting that this apparently extreme example is a practical installation carried by a number of current strike aircraft.

It is readily suspected that a significant part of the extra interference drag for such multiple installations occurs in the flow within and around the store assembly itself. Figure 6 presents some results for similar store assemblies to those discussed above tested in simulated isolated conditions[6]. The pylon and store assembly were mounted beneath a long parallel tube. The slender nose and the base of the tube were sufficiently far upstream and downstream respectively of the stores to achieve effectively freestream conditions around the stores, carrier and most of the pylon. The drag of the carrier and stores only was measured, the pylon being "earthed" to the support tube. Hence the measured drag does include pylon interference. In the absence of the parent aircraft model, it was possible to use larger (1/4) scale stores than would normally be used for installed tests. Besides increased local Reynolds numbers, improved representation of the many excrescences present in multiple installations (such as crutch arms) is achieved at larger scale. Figure 6 compares the extra measured drag due to adding one bomb to an empty carrier and to the carrier with one or two bombs already in position with the drag of a single pylon mounted bomb. The excessive drag penalties involved in this type of assembly are striking. To take the most extreme case, adding the third bomb to the assembly causes a drag increase approximately 4 times the drag of the single pylon mounted bomb, throughout the Mach number range shown. As noted previously for the installed case, the slope $\Delta C_D$ - M, when adding the second and third bombs, indicates a significant compressibility contribution to $\Delta C_D$ even at M = 0.5. These tests also showed that the drag of the isolated assemblies were relatively insensitive to incidence and sideslip up to about ±4°. For the fully loaded triple carrier $K_A$ is about 1.5 at M = 0.5 (cf. $(K_S)_{MIN}$ = 1.6 for the installed case).

A photograph of oil flow on the bombs at M = 0.75 (figure 7) illustrates the complex flows which contribute to the high drag of the triple assembly. The bottom bomb has been removed from the carrier after the test in order to photograph the oil flow (or absence of flow) in the channel formed by the carrier and the bombs. Particular features of the oil flow are :-

(i) Marked outflow, away from the central channel, on the carrier and bomb noses.

(ii) Evidence of a shock induced separation on the shoulder of each bomb in the region on the circumference nearest to the adjacent bomb.

(iii) Extensive regions of separated flow on the inner surfaces or the afterbodies of the bombs and carrier and the bomb fins.

Considering now the additional interference effects when the store assembly is installed beneath the aircraft wing, figure 8 compares the "isolated" drag of the fully loaded triple carrier with the corresponding installed drag increments. For this purpose the "isolated" assembly drag has been reduced using the appropriate parent aircraft reference dimensions. The installed $\Delta C_D$ values have been obtained by taking half the total $\Delta C_D$ for two assemblies - one beneath each wing - and subtracting an estimated $\Delta C_D$ for the pylon. At $M = 0.5$, the isolated $\Delta C_D$ is in good agreement with the installed value at $C_L = 0.4$, indicating $K_S = K_A$ at this condition. At lower $C_L$ values, at $M = 0.5$, the installed $\Delta C_D$ is progressively higher than the isolated value. This extra wing-store assembly interference amounts to about a 50% increase in $\Delta C_D$ above the isolated value at $C_L = 0$. Above about $M = 0.75$ there is apparently additional wing-store interference at all values of $C_L$, with the installed $\Delta C_D$ (at $M = 0.9$, $C_L = 0.4$) approaching twice the isolated value. The example discussed here illustrates both the complex nature of the interference flows typical of underwing multiple installations and the cost in terms of drag and hence the performance of loaded strike aircraft.

### 3.2. Underfuselage Installations

It would be expected that the flow environment for stores beneath relatively flat underfuselage surfaces, typical of aircraft designed for underfuselage store carriage, is less complex than that for underwing stores, with consequently smaller residual interference effects. In contrast to underwing stores, for which the resultant interference almost invariably increases $\Delta C_D$, some favourable viscous effects might reasonably be hoped for in certain cases, e.g. small diameter stores or store arrays partially immersed in the underfuselage boundary layer.

Some low M, low $C_L$ drag increments for various single and multiple underfuselage store installations are shown on figure 9, in the form: measured $\Delta D/_q$ plotted against $D/_{q_{(COMP)}}$[4]. The majority of the points are scattered within ±10% of the line representing $K_S = 1$, indicating negligible resultant interference drag for these cases. They include not only single stores but streamlined stores carried singly or in tandem on well spaced separate side by side pylons. The one point significantly above $K_S = 1.0$ is for two closely spaced side by side stores on a single pylon with a larger than usual separation between the stores and the fuselage. Several cases are significantly below the $K_S = 1$ boundary with values as low as 0.4. The mechanisms of these apparently favourable interference effects may be only speculatively discussed, but it is interesting to consider two possible explanations. The points numbered 3, 4 and 10 are all for combinations of blunt nosed and/or flat based stores in close coupled tandem arrangements (cf. $K_S = 1.0$ for streamlined stores in tandem). These low values of $K_S$ possibly result from a reduction in base drag on the forward stores due to the proximity of the noses of the rear stores and/or reduced drag of the rear stores when immersed in the wakes of the bluff forward stores - an example of favourable viscous interstore interference. Point 2 is for two long thin stores with bluff bases mounted side by side very close to the fuselage. In this case the reduced drag may be due both to the partial immersion of the stores in the underfuselage boundary layer and a reduction in store base drag due to the proximity of the fuselage - an example of favourable viscous store-fuselage interference.

The effects of $C_L$ and M on $\Delta C_D$ for some typical underfuselage installations are shown on figure 10 presented in the form $K_S - C_L$, M. $C_L$ has an almost negligible influence on $K_S$ for 4 stores (2 lateral rows of 2 stores in tandem). The total variation of $K_S$ is only 0.9 to 1.2. Also shown are $K_S$ values for a similar arrangement of 4 stores on a model with a very different wing planform. These points also fall within the $K_S$ variation noted above. The Mach number effects on $K_S$ for these underfuselage stores are quite small when compared with the variation of $K_S$ with M for even simple underwing installations ($K_S$ typically varying from 1 to 5 or more over a similar Mach number range). The increase in $K_S$ with M for these underfuselage installations probably reflects the freestream $C_D$ - M characteristics of the store assemblies themselves rather than increased store-fuselage interference. This is indicated in the increased values of $K_S$ at high M ($K_S = 2$ at $M = 0.95$) shown for 8 similar stores (2 lateral rows of 4 stores) with considerably reduced lateral spacing between the stores.

The examples in figure 10 are all for relatively small diameter stores. In the case of a store or group of stores which considerably enlarge the effective local fuselage cross section area, more severe Mach number effects, with the early appearance of wave drag on the combined fuselage-store assembly, may be expected. This is seen on figure 11[4]. For a single row of 5 closely spaced streamlined stores of relatively large diameter, $K_S = 2.5$ at the moderately low $M = 0.7$. In this case compressibility effects probably increase both interstore and store-fuselage adverse interference. Figure 11 also shows the effect of adding further lateral rows of 5 stores in tandem close behind the first row. At $M = 0.7$, $K_S$ is reduced from 2.5 for one row (5 stores) to 1.5 for two rows (10 stores) with a further reduction to $K_S = 1.3$ for either 3 or 4 rows (15 or 20 stores). This apparently favourable interference effect, relative to the high drag single row, may possibly arise because little additional wave drag on the fuselage-store combination is caused by adding the rear stores. (If the extra $\Delta C_D$ due to the second row was merely $\Sigma \Delta C_{D_{COMP}}$ for 5 stores, $K_S$ for 2 rows would be about 1.75). Also the interstore interference within the aft rows may be reduced in the wake of the closely spaced forward stores. However, even for the 4 row (20 store) case, $K_S = 1.3$ at $M = 0.7$, which is high compared with the examples of relatively small diameter stores described earlier (figure 10).

The very low $K_S$ values obtained at low M for some close coupled tandem arrangements of small diameter flat based stores have already been mentioned. Figure 12 illustrates this favourable effect in more detail for a multiple arrangement with lateral rows of 5 closely spaced stores and includes the effects of Mach number. The comparison with the numerically similar arrangement of larger diameter streamlined stores discussed above is striking. Adding extra rows of stores at $M = 0.6$ gives a reduction in $K_S$ from 1.05 for 1 row (5 stores) to 0.45 for 4 rows (20 stores). The fact that $K_S$ is as low as 1.05 for a single row with small lateral spacing is probably because the adverse interstore interference is, in this case, offset by the reduced drag of the stores when partially immersed in the fuselage boundary layer. The large reductions in $K_S$, as extra rows of stores are added, are a further example of favourable fore and aft interstore interference. At transonic Mach numbers this favourable effect in adding extra rows of stores is even more striking. Above $M = 0.92$ the total $\Delta C_D$ for 4 rows is less than that for a single row.

The foregoing examples show that, although the flow field beneath an aircraft fuselage is usually simpler than that beneath the wing, there are still considerable variations in interference drag, in terms of $K_S$, between different underfuselage store installations. The contrast is that whereas for underwing stores $K_S$ typically varies between 1 and 10 according to type of installation, $C_L$ and M, the possibilities of favourable interference for underfuselage stores lead to a range of $K_S$ between 0.5 and 4.

## 4. POSSIBILITIES FOR INCREMENTAL DRAG PREDICTION

The problem of predicting the drag increment for various types of external store installations at a range of conditions of $C_L$ and Mach number embraces many aspects of current research in aerodynamics. First a detailed description and understanding of the complex flows involved, both within the store assemblies and around the aircraft-store combination is required. Secondly, powerful calculation methods are required in order to quantify the resulting drag quickly and accurately. To achieve either of these objectives for the general case of external stores is not feasible within the present state of the art. It is debatable whether they are proper objectives, since even given adequate theoretical methods, the lengthy computing times and expense likely to be involved for the many configurations considered in project studies would almost certainly be prohibitive. A more profitable long term aim is the possibility, with recent advances in the calculation of aircraft and aircraft-store flow fields, of identifying both suitable store locations and the conditions likely to cause significant flow separations or local supersonic flow - i.e. a more integrated approach to the aerodynamic design of the complete aircraft-stores combination at the initial project stage. At present simple empirical prediction methods have an important role, but these are severely limited in range of application both to relatively simple store assemblies with well spaced stores and to conditions not far removed from potential flow involving only local separations and shock waves. For an aircraft designed to carry a large range of stores in various locations and operating over a large $C_L$, M envelope, wind tunnel tests remain the most reliable method of obtaining the incremental drag and even then the results have to be extrapolated to full scale flight conditions.

Having noted the difficulties and limitations encountered in the prediction of store drag increments, some procedures which may be helpful for initial project studies are now suggested.

### 4.1. The Aircraft-Store Flow Field

It was noted in section 3 that for essentially potential flow situations the interference effects between the aircraft and the stores tend to cancel, giving installation factors, $K_S$, near unity. Local departures from potential flow such as flow separations on individual components - e.g bluff excrescences and bases - not situated in high velocity regions and not interacting with other store components or the parent aircraft, can be tolerated and, when included in $\sum C_{D_{COMP}}$ also yield $K_S = 1.0$.

Recently methods capable of calculating the combined aircraft-store flow field have been developed. Reference 7 describes a technique in which the flow fields for individual components are superposed. This does not, however, satisfy the boundary conditions on all the individual components simultaneously and care is required in the way in which the superposition is performed. This has been confirmed by experience at A.R.A., where recent attempts to superpose the far field pressures due to a simple axisymmetric body on the measured chordwise pressure distributions on the clean parent wing failed to predict the peak suctions measured experimentally on the wing lower surface with the store installed. These calculations, however, did not include the effect of the pylon. A method for calculating the complete resultant flow field for a wing-pylon-store combination has been proposed by Loeve and Sloof[8]. An example, taken from reference 8 which compares measured and calculated pressure distributions both on the wing, with and without the store-pylon and on the installed store is shown on figure 13. The configuration also included a wing tip store. The agreement between calculation and experiment is most encouraging, particularly for the axial pressure distribution on the store itself and in the effect of the store on the wing spanwise lift distribution. The measured increases in suction on the wing lower surface just inboard and outboard of the store location are apparently slightly underestimated.

The use of calculated aircraft flow fields to predict the normal and side forces and centres of pressure on stores and pylons, for stressing purposes and release trajectory calculations is now quite common and relatively successful. Calculating the drag or axial forces on the stores and aircraft components as a possible stage in the prediction of $\Delta C_D$, is however unlikely to be so successful. This is because of both the limitations of currently available boundary layer calculation procedures and the inadequate definition of the store axial and wing chordwise pressure distributions provided by the panel methods usually used to calculate the flow fields. The value of such flow field information is in helping to avoid excessive drag penalties due to stores rather than in predicting the drag increment. When just the clean aircraft flow field is known at low $C_L$ and Mach number, it may be possible to avoid regions of high local velocities and take advantage of low velocity regions in choosing locations for stores. Where programmes for calculating the combined aircraft-store flow field including some lift and compressibility effects are available, it may also be possible for given stores and locations, to identify the conditions likely to cause the onset of flow separations and local supersonic flow.

### 4.2. Empirical Prediction Methods

In the two examples of empirical techniques described here, the aim has been to produce first approximations of $\Delta C_D$ for relatively simple underfuselage and underwing store installations at Mach numbers up to about $M_D$ for the clean aircraft, and to provide acceptable accuracy for project calculations. They should also prove helpful in establishing target values for the drag penalties due to external stores. Both examples are based almost entirely on the low speed drag characteristics of the store assemblies, with little input from the parent aircraft aerodynamic characteristics. It should be stressed that, at present, the correlations used are somewhat tentative, but it is hoped that these are sufficiently flexible to provide scope for modification by the addition of further experimental data, where these are available to the project designer.

#### 4.2.1. Underfuselage Stores

A method for predicting the incremental drag for a range of underfuselage stores is described in reference 4. As noted in section 2, $\Delta C_D$ for underfuselage stores is usually relatively insensitive to $C_L$, at least at low to moderate $C_L$. A framework describing the variation of $\Delta C_D$ with M is shown on figure 14(a). It requires the derivation of :-

(i) $\Delta C_{D_A}$ for $M \leq M_A$ - the low speed drag increment,

(ii) $M_A$ - the initial drag rise Mach number for $\Delta C_D$,

(iii) $M_c$ - the Mach number at the start of the steep drag rise,

(iv) $\Delta C_{D_c}$ at $M = M_c$,

(v) A fairing between points A and C - the variation of $\Delta C_D$ between $M_A$ and $M_c$,

(vi) $\Delta C_D$ at $M = 1.0$ - the "aiming point" for the curve for $M \geq M_c$.

Taking these parameters in turn,

(i) $\Delta C_{D_A} = K_S$ (at low M) x $\sum C_{D_{COMP}}$

The discussion in section 3.2 and figure 9 showed that for many underfuselage store arrangements $K_S$ is about 1.0 at low speed. Figure 9 may be used as a guide in obtaining a low speed value for $K_S$. A value of $K_S$ far removed from 1.0 might indicate that the method would not be adequate for predicting the variation of $\Delta C_D$ with M.

(ii) The initial rise or "creep" in $\Delta C_D$ is often very gradual, which makes the correlation of $M_A$ rather difficult. Figure 14(b) presents approximate correlations for single and side-by-side stores using an aerodynamic fineness parameter for the store assembly defined as

$$\lambda_{SI} = \frac{\sum C_{D_{COMP}} - \text{bluffness, base and excrescence drag}}{\sum C_f S_{WET}}$$

where $\sum C_f S_{WET}$ = Total estimated flat plate skin friction drag of the store-pylon assembly.

(iii) $M_c$ has been found to be within the range $0.90 < M < 0.95$ for a large number of configurations with no evidence of any consistent correlation with the type of assembly or e.g. $M_A$. For prediction purposes it is suggested that we take $M_c = 0.92$.

(iv) A correlation of $\Delta C_{D_c}$ in terms of $M_A$, $\Delta C_{D_A}$ and $\left(\Delta C_{D_A}\right)_{S_{WET}}$ is presented on figure 14(c), where

$\left(\Delta C_{D_A}\right)_{S_{WET}}$ is $\Delta C_{D_A}$ based on the wetted area of the store assembly rather than the parent aircraft reference area. This coefficient effectively combines a "dirtiness parameter" with the low speed installation factor $K_S$. It is interesting to note that, as for underwing stores at high subsonic Mach numbers (cf. section 3.1) where $K_S$ for a 'dirty' store was less than that for a clean store, figure 14(c) shows a reduction in $\Delta C_{D_c}/\Delta C_{D_A}$ with increasing $\left(\Delta C_{D_A}\right)_{S_{WET}}$.

(v) Figure 14(d) presents a normalised fairing for the variation of $\Delta C_D$ between $M_A$ and $M_c$. This is a mean curve obtained from a large amount of data for underfuselage stores. For high drag cases with low values of $M_A$, a high degree of accuracy should not be expected, but for most simple configurations when $\left(\Delta C_{D_c} - \Delta C_{D_A}\right)$ and $(M_c - M_A)$ are small the fairing is probably acceptable.

(vi) Very few drag data are available for underfuselage stores at $M = 1$. However, for some simple underwing store installations, fair agreement has been obtained between wave drag calculations by the Eminton method[9], with some judicious fairing of discontinuities in the area distributions, and experimental data. The wave drag was calculated for complete wing-body and wing-body-pylon-store combinations. This should also be possible for underfuselage store installations and it is suggested that the resulting wave drag increment added to $\Delta C_{D_A}$ should be sufficiently accurate as an 'aiming point' for the $\Delta C_D$ - M curve for $M \geq M_c$.

Figure 15 illustrates the use of this method up to stage (v) for an installation of 4 stores underfuselage and compares the prediction with experimental values of $\Delta C_D$. The prediction overestimates $\Delta C_D$ by about 6% at low Mach number and by about 10% above $M = 0.9$. These errors are within 3% of the total aircraft plus store drag.

### 4.2.2. Single Pylon Mounted Underwing Stores

The empirical approach to the estimation of $\Delta C_D$ and its variation with $C_L$ and Mach number for underwing stores has proved much less successful, as would be expected in the more complex flow situation of the store beneath a wing. As shown in section 3.1 the effect of $C_L$ on $\Delta C_D$ for similar stores varies considerably for different wings. However the variation of $\Delta C_{D_{MIN}}$ or $(K_S)_{MIN}$ with Mach number, at least up to $M_D$ for the clean aircraft, does appear to be strongly dependent on the freestream store drag and in particular the "dirtiness" of the store installation, $\Delta C_{D_{(M)}} / \Delta C_{D_{(M=0)}}$ typically being greater for clean than for "dirty" stores at high subsonic Mach numbers.

Figure 16 presents a carpet graph for predicting approximate values of $(K_S)_{MIN}$, given values of $\Delta M$ and a "dirtiness" factor, E[10], where

$$\Delta M = M - M_D \text{ (CLEAN WING)}$$

and

$$E = \frac{\sum (D/q)_{COMP}}{\sum C_f S_{WET}} \quad \dots\dots\dots\dots \text{ cf } \left(\Delta C_{D_A}\right)_{S_{WET}} \quad \text{section 4.2.1.}$$

This is based on a correlation of ad hoc incremental drag data from wind tunnel tests of a variety of types of single pylon mounted stores under several different wings. It should be noted that, although $(K_S)_{MIN}$ at a given $\Delta M$ decreases with increasing E, $(K_S)_{MIN} \cdot E$ (and hence, for a given size of store, $\Delta C_{D_{MIN}}$) in fact increases with E. An example in which the $(K_S)_{MIN}$, M, E, carpet has been used to predict $\Delta C_{D_{MIN}} - M$ for the fuel tank and missile installations previously referred to in section 3.1.1. (figure 4) is shown on figure 17. Except for an underestimate of about 10% in $\Delta C_{D_{MIN}}$ for the missile at low M, there is good agreement between prediction and experiment for both stores up to $M = 0.85$ ($M_D + 0.05$ approximately).

### 4.3. Prediction for Full Scale Flight Conditions

The empirical correlations mentioned in the previous section 4.2 are derived from wind tunnel data generally obtained at test Reynolds numbers $< 5 \times 10^6$ based on store length or local wing chord. For attached boundary layers with a specified position for transition to turbulent flow, the extrapolation of skin friction drag from typical model to full scale Reynolds numbers is fairly well established, but the corresponding variation of the drag due to features involving flow separations, such as bluff noses, bases and excrescences is less certain. Also the interference between the store components and between the aircraft and the store-pylon assembly may be subject to scale effects. Both the empirical procedures mentioned in section 4.2. would require modification if there were significant changes in the relative proportions of bluffness, base and excrescence drag between model and full scale conditions. Some improvements in drag prediction for excrescences at typical flight Reynolds numbers may be hoped for, following the recent R.A.E. research programme on this topic[11,12,13].

Unfortunately there are hardly any published "in flight" incremental store drag data suitable for direct comparison with model results. Considerable care is necessary when comparing store drag increments measured in the wind tunnel with those in flight, particularly in allowing for possible changes in tailplane drag due to the store installation e.g. any direct interference between the store installation and tailplane flow fields should be present in the wind tunnel data, but thrust increases in flight, due to the stores, may modify the downwash distribution at the tailplane and hence the tailplane lift dependent drag. It is also important, particularly for underwing stores where $\Delta C_D$ may vary rapidly with $C_L$, that comparisons are made at the equivalent values of wing $C_L$. A tentative example illustrating the uncertainties in the flight - tunnel comparison of some underwing store drag increments is shown on figure 18. The comparisons are at moderate $C_L$ and are all for the same aircraft. Two are for single stores and the third is for a multiple installation. The flight and tunnel results have been corrected to wing chord Reynolds numbers of $30 \times 10^6$ and $4 \times 10^6$ respectively. The agreement in the variation of $\Delta C_D$ with M is encouraging, but quite varied conclusions regarding possible scale effects on the absolute values of $\Delta C_D$ might be drawn from the three cases individually. The results for store A suggest that no significant extrapolation would be required in this case. For store B, however, an increase of about 25% in $\Delta C_D$ between tunnel and flight is indicated, while for the multiple installation $\Delta C_D$ is approximately 15% lower in flight than at model scale.

## 5. POSSIBILITIES FOR REDUCED INCREMENTAL DRAG

The discussion in section 3 included examples of store installations incurring excessive interference drag penalties and others in which favourable interference effects had led to very low drag increments. These extreme results illustrate the considerable scope for designing either good or bad installations in terms of incremental drag and one suspects that this aspect has received insufficient attention in the design of many existing store installations. It is recognised that drag is one of many factors to be considered when assessing the overall operational performance of the aircraft-store combination as an effective weapons system. Other important considerations include structural, weight and C.G. requirements, satisfactory stability and handling characteristics, safe store jettison and initial trajectories and accurate weapon delivery. Nonetheless it is necessary to be fully aware of the possible drag penalties or benefits involved in the choice of particular engineering solutions and the reduction of the installed store drag increment is a proper and important aerodynamic objective. Drag reductions may be obtained both from improvements of current installations and by the design of new types of installation. It is directly beneficial to reduce the freestream drag of the components of the store $\left(\sum C_{D_{COMP}}\right)$. Reductions in E and $\lambda_{SI}$ also yield corresponding improvements in the installed drag -

reduced $(K_S)_{MIN}$ E and increased $M_A$ respectively (cf. section 4.2.). It should also be possible in some cases to exploit favourable interference effects or at least to reduce the adverse interference within store assemblies and between the aircraft and the stores - i.e. improvements in $K_A$ and $K_S$. Examples of both approaches for store assemblies and installations are described in this section.

### 5.1. Removal of Excrescences (Reduction of $\sum C_{D_{COMP}}$, $E, \lambda_{SI}$)

A high proportion of $\sum C_{D_{COMP}}$ for many stores and assemblies is the contribution from excrescences. The crutch arms or sway braces incorporated in the ejector release unit (E.R.U.) housed in store pylons and carriers is a notable excrescence. Recently a new E.R.U. (MACE) has been developed in the U.K., in which these crutch arms have been eliminated. The results of an investigation of the effects of crutch arms on the freestream drag of a simple pylon-store assembly[14] are shown on figure 19. The total drag of this simple assembly is reduced by approximately 30% at low M, when the crutch arms are removed. This reduction is approximately equal to the estimated drag of the crutch arms alone. Also shown on figure 19 is a comparison of the drag increment for a relatively simple underfuselage store installation with and without crutch arms. In this installed case removal of the crutch arms reduces $\Delta C_D$ by about 40%. There is also a small reduction in $K_S$ from 1.0 to 0.94. Both the configurations discussed here are good examples of localised excrescence effects which have not interacted with other components to create more general increases in interference drag. They also illustrate the benefits to be obtained from modifications of existing store-pylon assemblies and do not require any fundamental redesign of the installations.

### 5.2. Reduced Interference between Stores (Reduction of $K_A$)

In reference 1 the possibility of reducing the wave drag of pairs of stores in close proximity by the application of 'area rule' principles was discussed. Some results showing the effect of relative axial position on the total drag of pairs of parabolic bodies[15] indicated that if one body was moved forward or backward by ½ x body length from the line abreast position, the wave drag at $M = 1$ of the resulting combination was close to that of a single body - 1/3 of the wave drag of the line abreast combination. As would be expected for parabolic bodies, the benefits of this axial stagger decreased rapidly as Mach number was reduced from 1.0 and there was no significant reduction in drag at $M \leq 0.9$. However most practical store shapes have freestream drag rise Mach numbers considerably lower than that for simple parabolic bodies e.g. for typical bomb shapes $M_D = 0.85$. For closely spaced combinations of such stores, it may well be possible to achieve worthwhile drag reductions at high subsonic Mach numbers, by staggering the stores axially to obtain a more gradual axial variation of cross section area of the combination. Figure 20 shows a result from an experimental investigation of the effect of axial stagger on the drag of a pair of sting mounted stores with cylindrical mid-bodies[16]. The average drags of the two stores for the line abreast case ($x_S = 0$) and with an axial stagger of 0.75 x store maximum diameter ($x_S = \pm 0.75D$) are compared with the drag of a single store. Below about $M = 0.8$ the three results agree closely, indicating no significant resultant interstore interference and hence no benefit from the stagger. Above $M = 0.8$, however, there is considerable interference drag at $x_S = 0$ - at $M = 0.9$, the average drag of 2 stores is about 70% higher than the single store drag. With $x_S = \pm 0.75D$, the increase in drag relative to the single store at $M = 0.9$ is reduced to about 25%. This suggests that significant reductions in interference drag could be obtained by very modest amounts of axial stagger within groups of stores. It is probable that the optimum stagger will vary with Mach number - figure 20 shows that for $M \geq 0.95$ the average $C_D$ for $x_S = \pm 0.75D$ is about equal to that for $x_S = 0$.

The interference between 'line abreast' stores can of course be reduced by increasing their lateral spacing. Figure 21 shows the variation of the ratio

$$\frac{\Delta C_D \text{ (measured for two stores)}}{\sum C_{D_{COMP}} \text{ (for two stores)}}$$

with lateral spacing between a pair of stores[6]. For this purpose the estimated drag of the carriers has been subtracted from the measured results. At low Mach number there is a 25% penalty, compared with the isolated estimate, for the stores at minimum spacing ($y/D = 1$). This penalty is almost eliminated when the lateral separation is increased to ½ x store diameter ($y/D = 1.5$). At $M = 0.9$ the drag of 2 stores at $y/D = 1$ is nearly $4 \times \sum C_{D_{COMP}}$. This factor is reduced to about 3.2 and 3.0 with increases in y/D to 1.5 and 2.0 respectively. Thus by spacing the stores just half a store diameter apart a worthwhile reduction in $K_A$ is achieved. It should be mentioned that the estimated increase in drag due to the larger carrier required to increase the spacing from $y/D = 1.0$ to 1.5 is about 7% of $\sum C_{D_{COMP}}$ for a single isolated store.

The introduction of stagger and/or increased lateral spacing between stores in multiple installations are measures which would require the design of new types of store carrier. However some current installations involve a tandem arrangement and, as noted previously, (section 3.2), a pair of stores can usually be carried in this way with little adverse interstore interference and hence no significant increase in $K_S$ compared with a single store assembly. For bluff or flat based stores, tandem carriage can give $K_S$ for two stores less than that for a single store of the same type, due to favourable fore and aft interference between the stores. Certainly, where practicable, tandem carriage is to be preferred to line abreast arrangements.

### 5.3. Application to An Underwing Multiple Store Installation

Recent experiments at A.R.A.[5,6] have explored the application of the methods described in 5.1 and 5.2 to the triple carrier loaded with 3 bombs, which was discussed in 3.1.2., both as a simulated isolated assembly and when installed underwing. Figure 22 shows the variation of $C_D$ with M for the loaded carrier in simulated freestream conditions,

(i) in standard form,

(ii) with all crutch arms removed (8 pairs including those on the pylon E.R.U.),

(iii) with the remaining excrescences on the carrier removed or faired in,

(iv) with the two shoulder bombs staggered by approximately 0.9 x bomb diameter fore and aft relative to the lower store.

At $M = 0.4$, $C_D$ for the assembly without crutch arms is about 0.65 $C_D$ for the standard configuration. The important feature of this result is that $K_A$ is also reduced from 1.75 to 1.50 i.e. the total drag has been reduced by much more than the freestream drag of the crutch arms. This is therefore a case where the excrescences have caused significant interference drag within the assembly. A possible explanation for this interference is that the local disturbances in the bomb and carrier body boundary layers due to the crutch arms have increased the tendency for widespread flow separation on the bomb and carrier afterbodies. With increases in Mach number above about $M = 0.7$, the magnitude of the reduction in $C_D$ due to removing the crutch arms is progressively reduced. This does not mean that the interference at the higher Mach numbers is any less severe, but more probably that compressibility effects in the store-store and store-carrier interference are then the major factor influencing the drag of the assembly, e.g. the evidence of shock induced separation on the shoulders of the stores noted in the oil flow photograph at $M = 0.75$ (figure 7). The further stage (iii) in the "cleaning up" process on the carrier reduces $C_D$ at $M = 0.4$ to about half that of the standard configuration. $K_A$ remains at 1.5 which shows that these relatively small excrescences were also contributing 1.5 times their freestream drag when installed on the loaded carrier. The reduction in $C_D$ again falls off rapidly at higher Mach numbers. Staggering the shoulder bomb has no further significant effect on $C_D$ or $K_A$ at low Mach numbers compared with the stage (iii) cleaned up carrier, but at the higher Mach numbers, as had been hoped, there is a considerable further reduction in $C_D$. At $M = 0.9$, $C_D$ is about 0.65 $C_D$ for the standard case and about 0.8 $C_D$ for the stage (iii) configuration. It should be remembered that these results are not only significant in terms of incremental drag. They represent equally significant reductions in the total aircraft + stores drag. As noted earlier (3.1.2), at quite moderate subsonic Mach numbers, $\Delta C_D$ due to such installations can be greater than $C_D$ for the clean aircraft.

The drag reductions achieved by removing the excrescences from a similar loaded triple carrier assembly when installed underwing are shown on figure 23. (This represents a feasible improvement of an existing carrier rather than the extensive redesign which 'staggering' would require). $\sum C_{D_{COMP}}$ for the removed excrescences is also shown. As for the isolated assembly, the installed drag reduction at Mach numbers up to about $M = 0.8$ is considerably greater than $\sum C_{D_{COMP}}$ for the excrescences, illustrating again the adverse interference within the assembly due to the excrescences. Also shown is the large variation in $\Delta C_D$ with $C_L$ at the lower Mach numbers indicating that the interference drag of the assembly may be further magnified by store-pylon-wing interference.

### 5.4. Favourable Aircraft-Store Interference

Examples of the very low values of $K_S$ achieved at both low and high subsonic Mach numbers with multiple arrays of small diameter stores closely packed beneath a flat underfuselage surface have already been discussed (3.2). Various extensions of this application of favourable aircraft-store viscous interference have been considered recently. In one method, known as conformal packaging[17], the use of a matrix of rectangular or cylindrical stores packed between suitable nose and tail fairings is proposed. Significant drag savings are claimed for this arrangement underfuselage, compared with current multiple store installations. Satisfactory jettison of the fairings might be required however, to avoid the probable high incremental drag in the absence of the packaged stores. A further possibility is to half submerge the stores in cavities in the underfuselage surface (semi-submerged stores). Lower installed drag increments would certainly be expected for such installations compared with conventional carriage. Unfortunately the drag increment due to the cavities, after store release, has been found in some cases to be larger than that due to the stores. Also the cavities have to be tailored to the shape of the stores, which may place restrictions on the range of stores carried by the aircraft. These objections might be overcome if jettisonable 'false bottom' type fairings for the stores could be devised. The safe jettison of such a fairing, as in the case of packaged stores, would however in itself be a difficult aerodynamic design problem. Another interesting proposed solution[18] is the use of lifting half-body store shapes. Reductions in incremental drag of the order 25%, compared with equivalent 'whole' shapes, were demonstrated in wind tunnel tests, at subsonic and supersonic Mach numbers, on half bombs and pods mounted on a flat underfuselage surface. Clean store separation characteristics were also demonstrated for these shapes. Recent studies of the aerodynamics of lifting bodies should provide sufficient data to at least investigate the feasibility or otherwise of such shapes as air launched weapons.

## 6. CONCLUDING REMARKS

The severe aerodynamic penalties which can be imposed by external store carriage have been noted and the large contribution made by some typical store installations to the total drag of strike aircraft has been emphasised. It has been shown that for many simple installations with single stores on well spaced pylons and with well behaved flow on the local parent aircraft surfaces, the interference between the aircraft and stores at low speed is of a potential flow type, with effective cancellation of the buoyancy drag forces on the separate components giving installation factors near unity. With a knowledge of the aircraft flow field and the geometry of the store-pylon installation, such conditions should be readily identified. For this type of installation, the variation of $\Delta C_D$ with Mach number correlates fairly well with the freestream drag characteristics of the store assembly and this form of correlation has been used in tentative empirical procedures proposed for the estimation of $\Delta C_D$ due to simple underfuselage assemblies and $\Delta C_{D_{MIN}}$ for single underwing stores. The variation of $\Delta C_D$ with $C_L$ at low to moderate $C_L$ for underwing stores is strongly influenced by the parent wing aerodynamic characteristics. For multiple installations involving significant viscous and compressibility effects in the interference within the assembly and between the aircraft and the stores, a wide range of values of the installation factor can occur and in these cases the prospects for predicting $\Delta C_D$ are remote. However the possibilities for reducing $\Delta C_D$ are more encouraging. The scope for drag reduction and for low drag designs is implied by the wide variation in $K_S$ between different installations. The examples quoted of modifications to current installations and of new types of installation indicate that potentially large drag reductions can be achieved by applying simple well established aerodynamic principles in practice, rather than from any radically new methods. While it is recognised that a degree of compromise is required between drag and the many other factors involved in the design of store installations, it must be stressed that it would require much greater effort to obtain such large percentage reductions in the drag of loaded strike aircraft from any other source. The proportion of the total drag due to external stores may well increase in the future, since advances in wing design could lead to the design of smaller aircraft for given missions and load carrying ability. A flexible and radical approach is required at the project design stage, which ideally should integrate the aerodynamic design of the aircraft and stores. Certainly if stores are to continue to be carried underwing, then this should be reflected in the future research programme on wing design for combat and strike aircraft.

## REFERENCES

| | | |
|---|---|---|
| 1. | PUGH, P.G.<br>HUTTON, P.G. | The Drag of Externally Carried Stores - Its Prediction and Alleviation.<br>AGARD C.P.124 PAPER NO.19. (April 1973). |
| 2. | BERRY, J.B. | Examples of Airframe-Store Interference.<br>AGARD C.P.71 PAPER NO.27. (September 1970). |
| 3. | ALFORD, W.J. Jr. | Theoretical and Experimental Investigation of the Subsonic-Flow Fields beneath Swept and Unswept Wings with Tables of Vortex-Induced Velocities.<br>N.A.C.A. REPORT 1327. (1957). |
| 4. | PALLISTER, K.C.<br>EVANS, M.J. | Unpublished A.R.A. Paper. |
| 5. | PALLISTER, K.C.<br>BERRY, J.B. | Measurement of the Drag Increments for a Range of Wing Mounted Store Installations on a 1/12 scale Model of the H.S.Buccaneer S.Mk.2 at Mach Numbers from 0.5 to 0.9.<br>UNPUBLISHED A.R.A. PAPER. |
| 6. | PALLISTER, K.C. | The Isolated Drag of Single and Multiple 1000 lb. MK.10 Bomb Installations.<br>UNPUBLISHED A.R.A. PAPER. |
| 7. | HESS, J.L.<br>FAULKNER, S.M. | Determination of Low Speed Interference Effects by Superposition.<br>AGARD C.P.71. PAPER NO.24. (September 1970). |
| 8. | LOEVE, W.<br>SLOOF, J.W. | On the use of "Panel Methods" for Predicting Subsonic Flow about Aerofoils and Aircraft Configurations.<br>N.L.R. MP 71018 U (October 1971). |
| 9. | EMINTON, E. | On the Minimisation and Numerical Evaluation of Wave Drag.<br>R.A.E. REPORT AERO 2564. (1955). |
| 10. | BERRY, J.B. | The Drag of Single Underwing Stores - An Approximate Empirical Method for Predicting the Variation of the Minimum Drag Increment with Mach Number at Subsonic Speeds.<br>UNPUBLISHED A.R.A. PAPER. |
| 11. | GAUDET, L.<br>JOHNSON, P. | Measurement of the Drag of Various 2-Dimensional Excrescences Immersed in Turbulent Boundary Layers at Mach Numbers between 0.2 and 0.8.<br>R.A.E. T.R.70190. (October 1970). |
| 12. | GAUDET, L.<br>JOHNSON, P. | Measurements of the Drag of Excrescences Immersed in Turbulent Boundary Layers at Mach Numbers between 0.2 and 2.8: Circular holes.<br>R.A.E. T.R.71181. (September 1971). |
| 13. | SIMPER, J.I.<br>HUTTON, P.G. | Formulae and Proposed Layout of Graphs for the Application of R.A.E. 8' x 8' Tunnel Results to the Rapid Estimation of Excrescence Drag.<br>A.R.A. MEMO NO.133. (1972). |
| 14. | PUGH, P.G.<br>WARD, L.C.<br>PETO, J.W. | Unpublished R.A.E. Work. |
| 15. | DROUGGE, G. | An Experimental Investigation of the Interference between Two Bodies of Revolution at Transonic Speeds with Special Reference to the Sonic and Supersonic Area Rules.<br>F.F.A. REPORT 83. (1959). |
| 16. | PUGH, P.G.<br>WARD, L.C.<br>PETO, J.W. | Unpublished R.A.E. Work. |

| | | |
|---|---|---|
| 17. | MARTIN, C.J. | Unpublished work. |
| 18. | FUREY, R.J.<br>MARTIN, C.J. | A Study of Captive Flight Drag and Separation Characteristics of Lifting Body (Half-Bomb and Half-Pod) Store Configurations. AGARD C.P.71. Paper No.34. (September 1970). |

## ACKNOWLEDGEMENTS

The author wishes to acknowledge the helpful comments of colleagues at A.R.A., upon whose work he has drawn in the preparation of this paper. The support of the Procurement Executive, Ministry of Defence for much of the work described is also acknowledged.

# APPENDIX A

## ESTIMATION PROCEDURE FOR THE LOW SPEED ZERO LIFT DRAG OF A STORE ASSEMBLY IN A FREE STREAM

### A.1. Bodies

(a) Bodies with small bases $\left[\frac{S_b}{S_m} \leq 0.2\right]$

$$\frac{D}{q} = \lambda\, C_f\, S_{WET}$$

$$\text{where } \lambda = \frac{C_{D_o}\left(\frac{d_m}{\ell_e}\right)}{C_{D_o}\left(\frac{d_m}{\ell} = 0\right)}$$

$\ell_e$ = $\ell$ or $\ell_f + \ell_a + 2d_m$ (see Fig.A.1)

whichever is less

$S_{WET}$ = wetted area of body excluding any base area

$C_f = f\,(R_\ell, x_t)$ = skin friction coefficient for a smooth flat plate with turbulent boundary layer from $x_t$, at $M = 0$, obtained from the charts of Ref A.1 (based on Prandtl-Schlichting)

$C_D\left(\frac{d_m}{\ell}\right)$ = $f\,(R_\ell, x_t)$ obtained from R.Ae.S.Data Sheets Bodies 02.04

(b) Bodies with significant base area (Fig.A.1).

The zero lift drag is split up as follows:

(i) Profile drag of ABDEG with no boat tail increment

$$\text{viz } \left(\frac{D}{q}\right)_1 = \lambda_1\, C_f\, S_{WET}$$

$$\text{where } \lambda_1 = \left[\frac{C_D\left(\frac{d_m}{\ell_e}\right)}{C_D\left(\frac{d_m}{\ell} = 0\right)} - 1\right]\frac{1}{2} + 1$$

and $\ell_e = 2\,\ell_f + \ell_m$ or $2\left[\ell_f + d_m\right]$ whichever is less.

This assumes that the form drag term $(\lambda_1 - 1)$ for the closed body ABCD'FG (a body with an imaginary afterbody CD'F of the same length and fineness ratio as the forebody ABG) is made up of equal contributions from the forebody and the afterbody.

Note that $C_D\left(\frac{d_m}{\ell}\right)$, $C_f$ and $S_{WET}$ are obtained as in A.1. (a) with $R_\ell$ based on total length $\ell$ as in A.1 (a).

(ii) Boat-tail drag $\frac{D_\beta}{q}$ (on CDEF) and base drag $\frac{D_b}{q}$

McDonald and Weir[A.2] give a correlation of data at $M = 0.90$ for both curved and conical afterbodies, based on the parameters; boat-tail angle ($\beta$) and base to body maximum diameter ratio. Honeywell[A.3] gives the empirical expression

$$C_{D_b} = 0.115 + (10M - 2)^3 \times 10^{-4} \quad \text{for } 0 < M < 1.0$$

based on the correlation of a large amount of experimental data for bodies without boat-tailing. Using Ref.A.2 values of boat-tail drag $\frac{D_\beta}{q}$ and base drag $\frac{D_b}{q}$ are found at $M = 0.9$. Honeywell's $C_{D_b} - M$ relationship is then used to factor $\frac{D_b}{q}$ for the appropriate Mach number:

$$\frac{D_b}{q}(M) = \frac{D_b}{q}(M = 0.9) \times \frac{C_{D_b}(M)}{C_{D_b}(M = 0.9)}$$

Then $\frac{D_a}{q} = \frac{D_\beta}{q} + \frac{D_b}{q}(M)$

This includes no Mach number effect on $\frac{D_\beta}{q}$.

McDonald and Weir found no significant Mach number effect however, at Mach numbers up to 0.9 in the data used for their correlation.

For a body without boat-tailing at $M = 0.9$, the two methods give values of base drag $\frac{D_b}{q}$ in very close agreement.

For any particular configuration it is advisable to consult other sources of information e.g. Refs. A.4. to A.7. in order to obtain an idea of the probable accuracy of prediction. In particular, Hart[A.6] shows the effect of tail fins on $C_{D_b}$.

(c) Bodies of non circular cross section.

These may often be treated as equivalent bodies of revolution. When these are slender shapes the method is as in A.1.(a) and (b). Certain types of launcher, strakes and fairings can be dealt with in this way.

For bluff bodies Hoerner[A.8.] gives values of $\Delta C_D$ due to nose bluntness, which can be used in conjunction with A.1.(a) and (b); and values of total $C_D$ for bodies of constant diameter. Data on the effect of rounded corners is also presented. Refs.A.9. and A.10. also contain data on the effect of nose shape on $C_D$.

Tests at A.R.A. which investigated the effect of slight nose "blunting" ( $\frac{\ell_f}{d}$ reduced from 3.5 to 3.3) on the installed drag of a store, showed no significant change in either the installed store axial force or the overall store drag increment at subsonic speeds.

(d) Excrescences.

Hoerner[A.8.] is used as a guide when allowing for the effects of lugs, brackets etc. It is hoped that improved estimates for some components will be possible following the recent R.A.E. programme of research on excrescence drag[A.11].

## A.2. Wings, fins, pylons

### (a) Profile Drag

$$\frac{D}{q} = 2n \int_{root}^{tip} \lambda \cdot c \cdot C_f \cdot dy$$

where n = number of wings or fins (e.g. 4 for cruciform layout).

There is no allowance for aspect ratio effects in this expression. This may be an important omission in the case of store pylons and, strictly, excludes the highly swept, low aspect ratio surfaces typical of missiles. However, at zero lift, it is in common use as a first approximation for missile wings and fins and can certainly be justified for the present purpose, since these contribute only a small proportion of the total store drag. For this case it is usual to simplify the expression for $\frac{D}{q}$ to:

$$\frac{D}{q} = n\,S_{WET} \cdot \lambda \cdot C_f$$

where $C_f$ is obtained as in A.1.(a) and

$\lambda = f$ (type of section; t/c; $x_t$)

$R_c$ and t/c are based on the mean chord.

The R.Ae.S. Data Sheets Wings 02.04 are used in determining $\lambda$. For store wings and fins no sweep factor is applied, but for pylons $\lambda$ is modified to

$$\lambda_{(SWEPT)} = 1 + (\lambda_{UNSWEPT} - 1)\cos^2\Lambda$$

where $\Lambda$ = mid chord sweep angle.

(b) 2-D Base drag

Store pylons with thick trailing edges can give rise to a considerable base drag contribution. For "slab sided" pylons with no boat-tailing, such as are often used on small scale wind tunnel models, the results obtained by Nash, Quincey and Callinan[A.12], who measured the base pressure on a 2-D section of this type at Mach numbers up to 1.1, are applicable. Nash[A.13] gives a prediction method and examples of the effects of boat-tailing on $C_{D_b}$ at $M = 0$; which may be used in conjunction with the results of Ref.A.12 for pylons with more conventional sections.

On some wind tunnel models, pylons having half round trailing edge sections have been used. These cases are treated as normal thick trailing edges for drag estimation. It is apparent, however, from the results in Ref. A.12 that this type of trailing edge could produce considerably higher drag at certain conditions of Reynolds number and Mach number.

## A.3. Total Freestream Drag

No allowance is made for mutual interference between the components or for junction drag. The total drag $\sum\left({}^{D}/_{q}\right)_{COMP}$ is obtained by simply summing the drags of the various components, e.g. for 4 missiles with cruciform control surfaces, bluff noses and bases and launchers, mounted in pairs on a carrier and pylon beneath each wing of an aircraft.

$$\sum\left({}^{D}/_{q}\right)_{COMP} = 4\sum\left({}^{D}/_{q}\right)_{BODY,LAUNCHER,CONTROLS} + 2\sum\left({}^{D}/_{q}\right)_{CARRIER,PYLON}$$

where $\sum\left({}^{D}/_{q}\right)_{BODY} = \lambda_1 C_f S_{WET} + \left(\frac{Da}{q}\right) + \left(\frac{\Delta D}{q}\right)_{NOSE} + \left(\frac{\Delta D}{q}\right)_{EXCRESCENCES}$

and so on for the other components.

## REFERENCES

A.1. CLUTTER, D.W. Charts for Determining Skin Friction Coefficients on Smooth and on Rough Flat Plates at Mach Numbers up to 5.0 with and without Heat Transfer. DOUGLAS REPORT ES 29074. (1959).

A.2. McDONALD, H. WEIR, J. A Correlation of Afterbody Drag at Subsonic Speeds. A.R.C. 24,625. (1962).

A.3. HONEYWELL, E.E. Compilation of Power-off Base Drag Data and Empirical Methods for Predicting Power-off Base Drag. CONVAIR REPORT T.M.334-337. (1959).

A.4. KELL, C. Free-flight Measurements of Pressure Distribution at Transonic and Supersonic Speeds on Bodies of Revolution having Parabolic Afterbodies. R.A.E. REPORT AERO.2605. (1958).

A.5. KURN, A.G. Drag Measurements on a Series of Afterbodies at Transonic Speeds showing the Effect of Sting Interference. R.A.E. T.R.66298. (1966).

A.6. HART, R.G. Effects of Stabilising Fins and a Rear-Support Sting on the Base Pressures of a Body of Revolution in Free Flight at Mach Numbers from 0.7 to 1.3. NACA R.M. L52E06. (1952).

A.7. SILHAN, F.V. CUBBAGE, J.M. Drag of Conical and Circular-arc boat-tail Afterbodies at Mach Numbers from 0.6 to 1.3. NACA R.M. L56K22. (1957).

A.8. HOERNER, S.F. Fluid-dynamic Drag. (1958).

A.9. STONEY, E.W. Collection of Zero-lift Drag Data on Bodies of Revolution from Free-flight Investigations. NASA TR R-100. (1961).

A.10. DUDLEY, R. LAWRENCE, T. Measurements of the Drag of Bombs at Transonic Speeds by the Ground-launched Rocket-boosted Model Technique. R.A.E. TECH.NOTE AERO.2150. (1952).

A.11. SIMPER, J.I.; HUTTON, P.G. Formulae and Proposed Layout of Graphs for the Application of R.A.E. 8' x 8' Tunnel Results to the Rapid Estimation of Excrescence Drag. A.R.A. MEMO NO. 133 (1972).

A.12. NASH, J.F.; QUINCEY, V.G.; CALLINAN, J. Experiments on Two-dimensional Base Flow at Subsonic and Transonic Speeds. A.R.C. 25,070. (1963).

A.13. NASH, J.F. An Approximate Method for the Prediction of the Zero-Lift Pressure Distribution and Drag of Symmetrical Blunt-trailing-edge Aerofoil Sections at Subsonic Speeds, in the absence of a Vortex Street. A.R.C. 26,117. (1964).

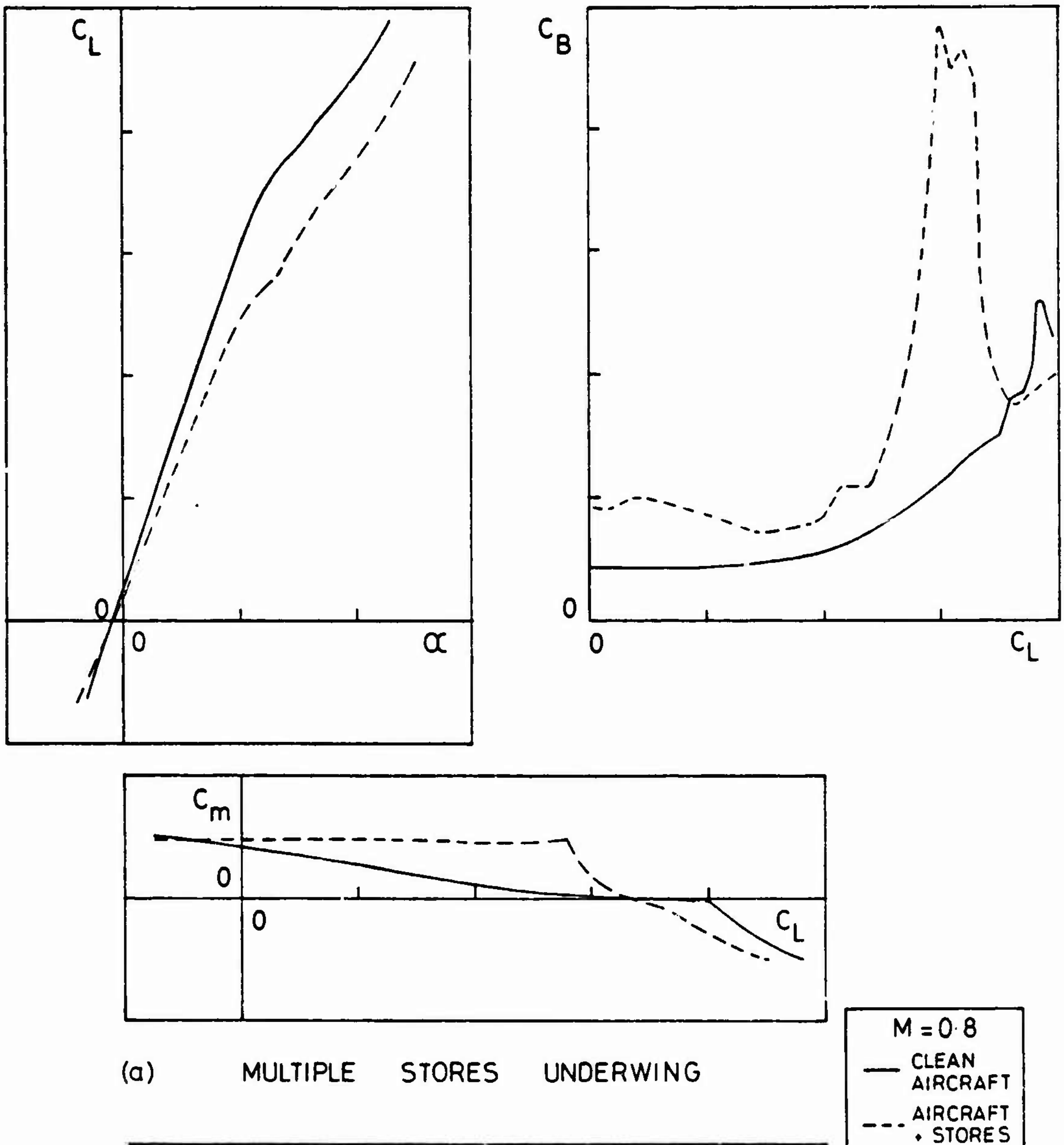

(a) MULTIPLE STORES UNDERWING

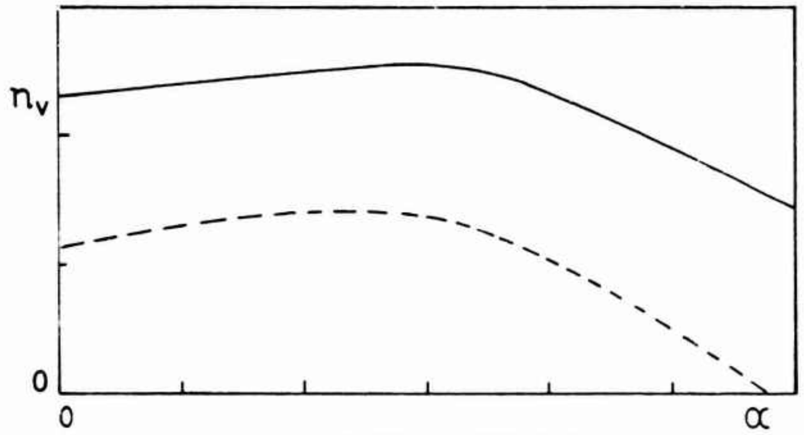

(b) LARGE STORE UNDERFUSELAGE

FIG.1 EFFECTS OF EXTERNAL STORES ON LONGITUDINAL AND LATERAL STABILITY

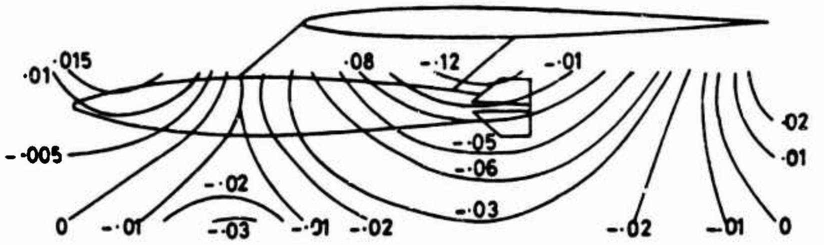

·01
·015
·08
-·12
-·01
·02
·01
-·005
-·05
-·06
-·02
-·03
0
-·01
-·03
-·01
-·02
-·02
-·01
0

STREAMLINED STORE LOCATED IN WING PRESSURE FIELD
($C_p$ VALUES AT $\alpha = 0$ ; FROM REF. 3)

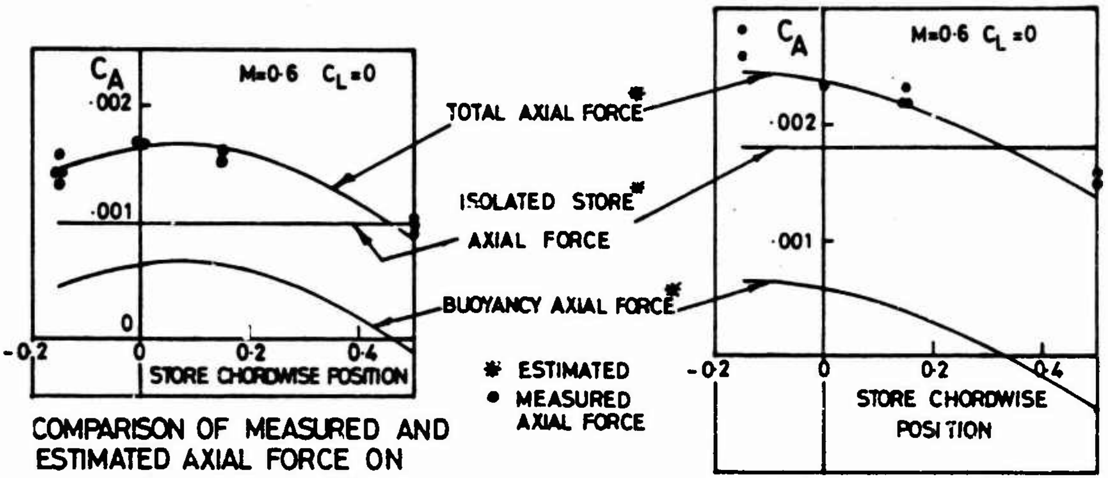

COMPARISON OF MEASURED AND ESTIMATED AXIAL FORCE ON STREAMLINED STORE

COMPARISON OF MEASURED AND ESTIMATED AXIAL FORCE ON FLAT BASED WINGED STORE

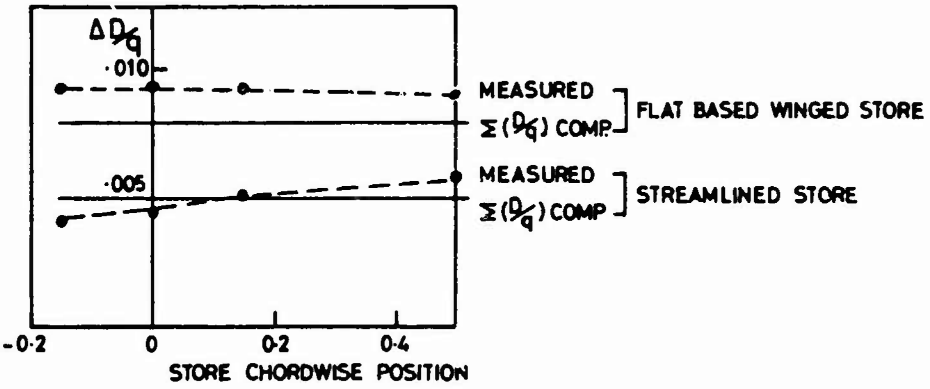

COMPARISON OF MEASURED $\Delta D/q$ AND ESTIMATED $\Sigma(D/q)$ COMP

FIG. 2. BUOYANCY EFFECT ON UNDERWING STORES

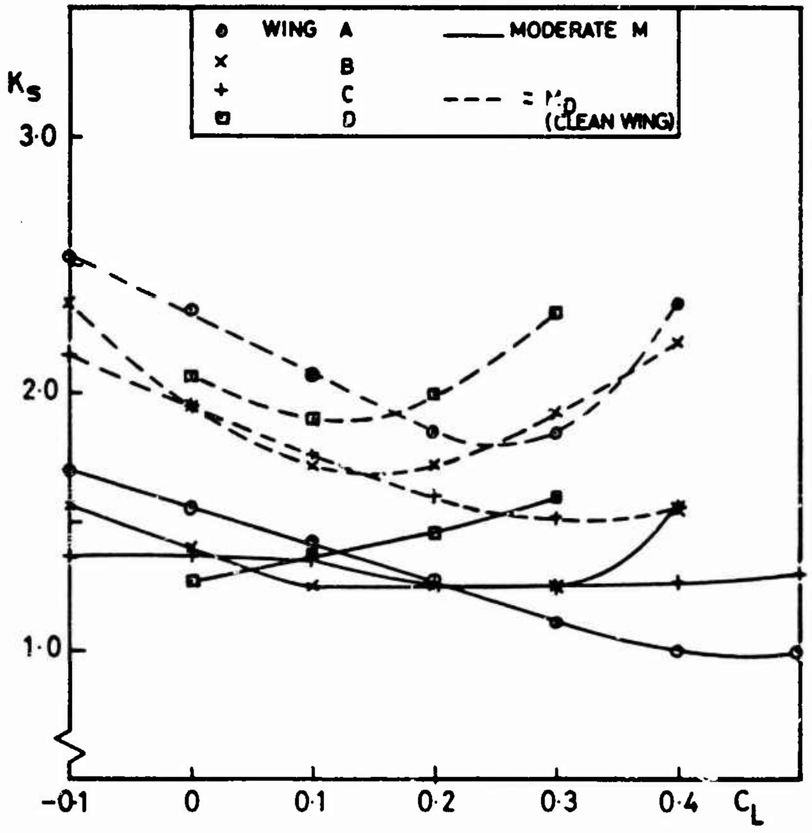

FIG.3 VARIATION OF INSTALLATION FACTOR WITH $C_L$

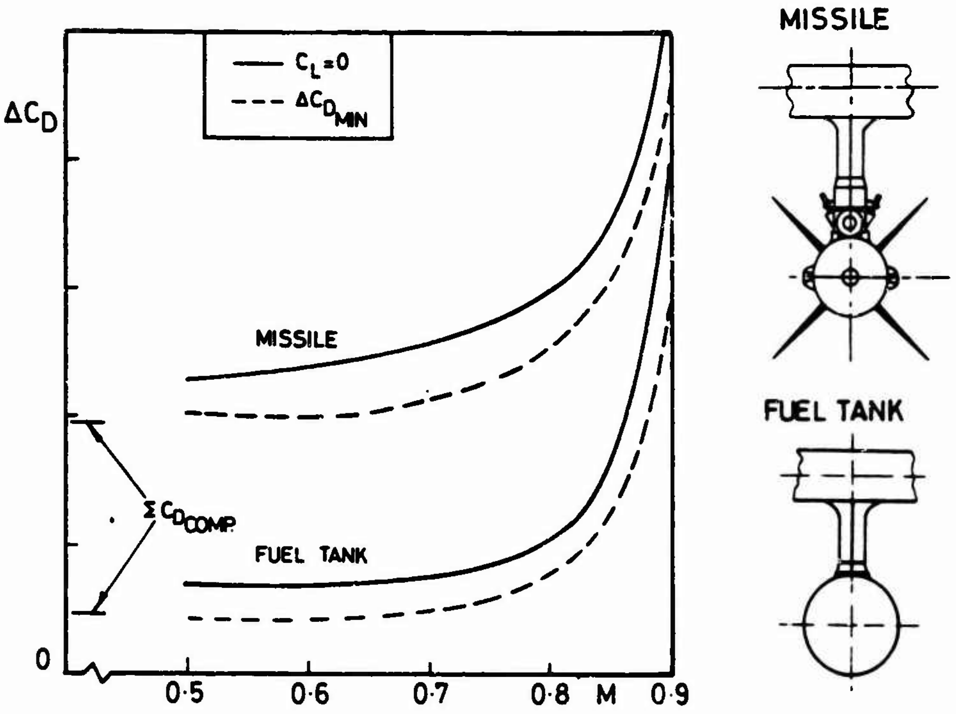

EFFECT OF STORE SHAPE

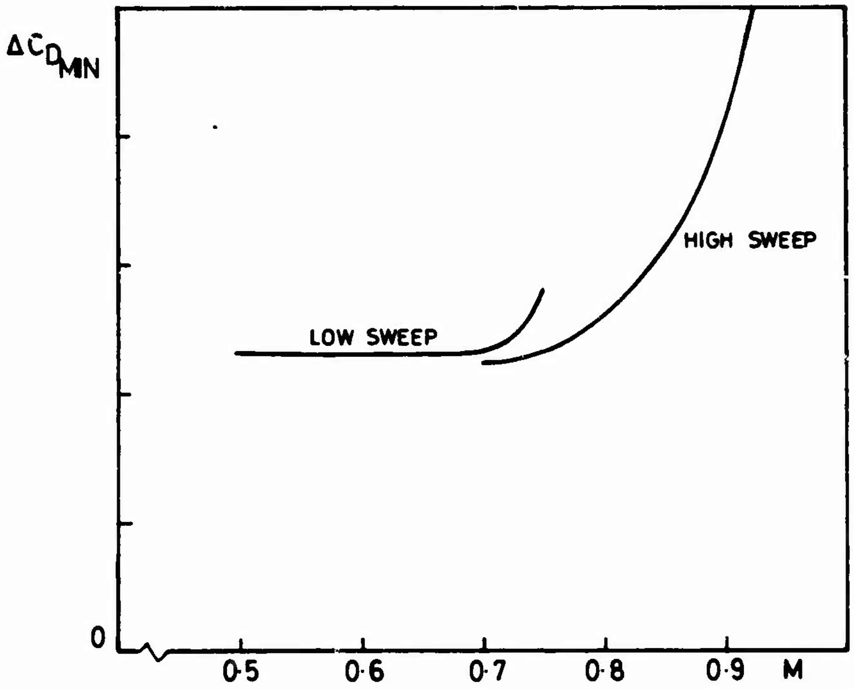

EFFECT OF WING SWEEP

FIG. 4 VARIATION OF $\Delta C_D$ WITH M

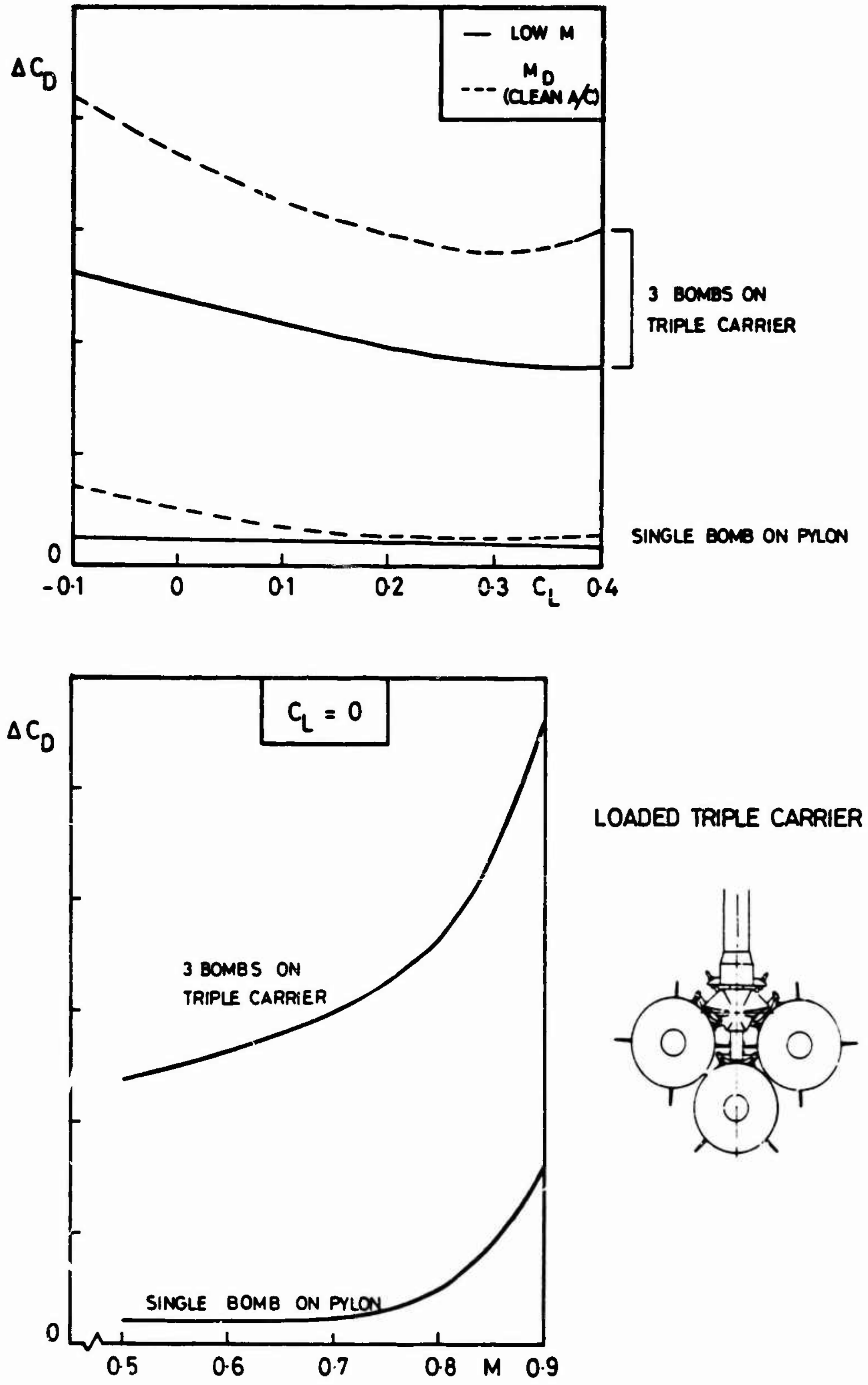

FIG.5. COMPARISON OF $\Delta C_D$ FOR MULTIPLE AND SINGLE UNDERWING INSTALLATIONS

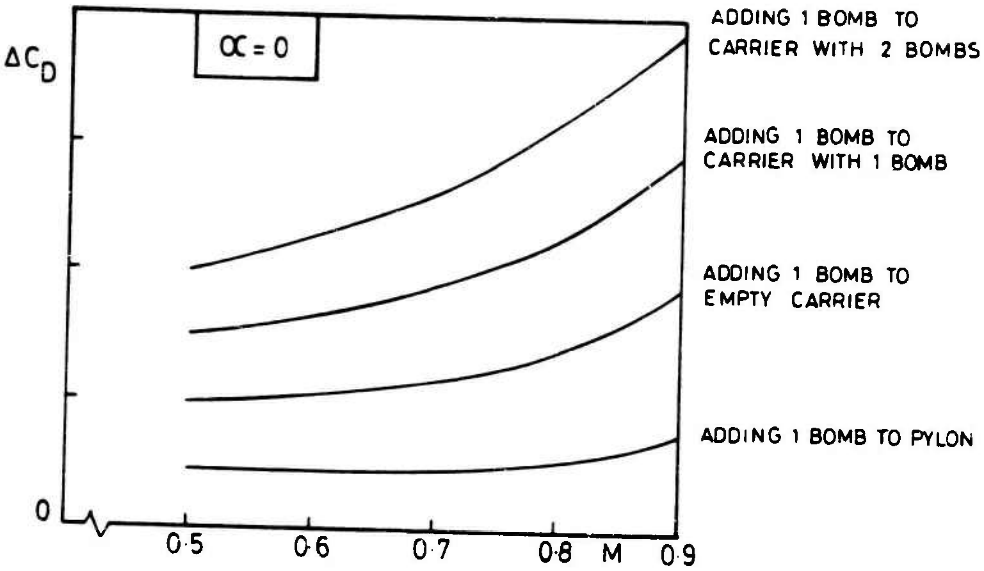

FIG. 6 EFFECT OF INTERFERENCE BETWEEN STORES IN A MULTIPLE ASSEMBLY

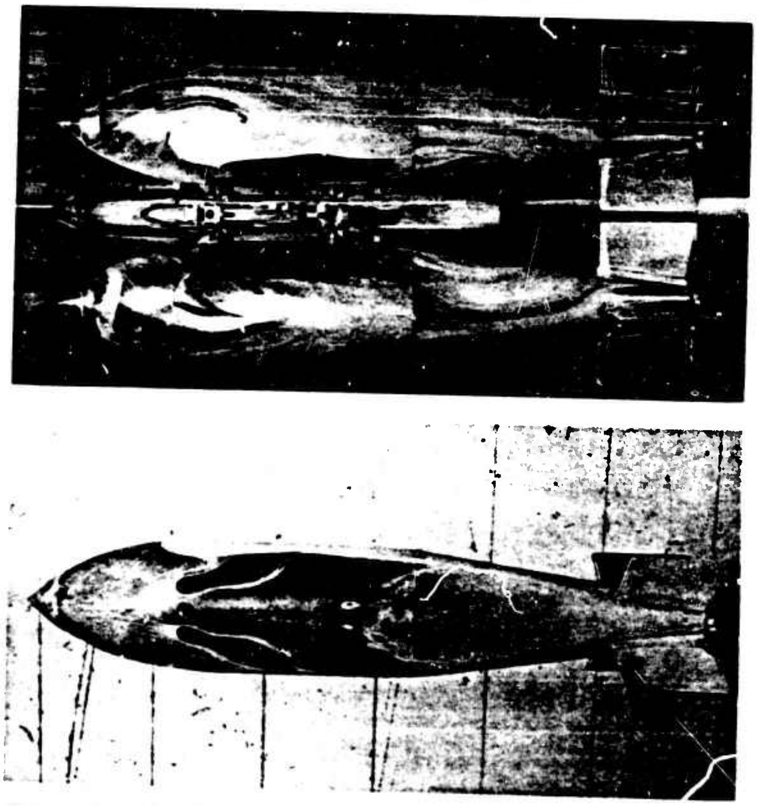

FIG. 7. OIL FLOW ON BOMBS ON TRIPLE CARRIER AT M = 0·75.

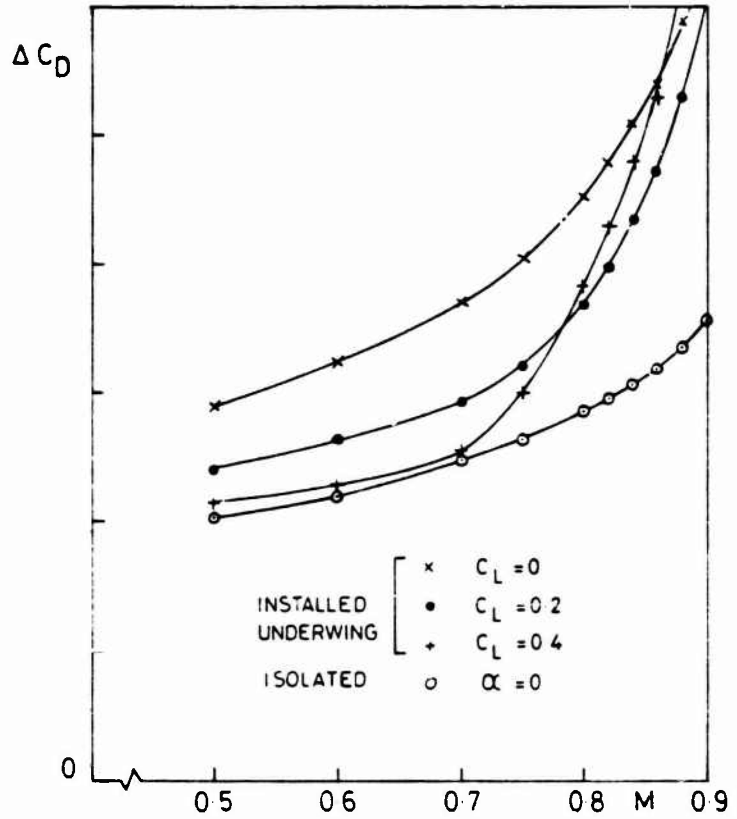

FIG. 8 COMPARISON OF ISOLATED DRAG WITH INSTALLED DRAG INCREMENT ~ 3 BOMBS ON TRIPLE CARRIER

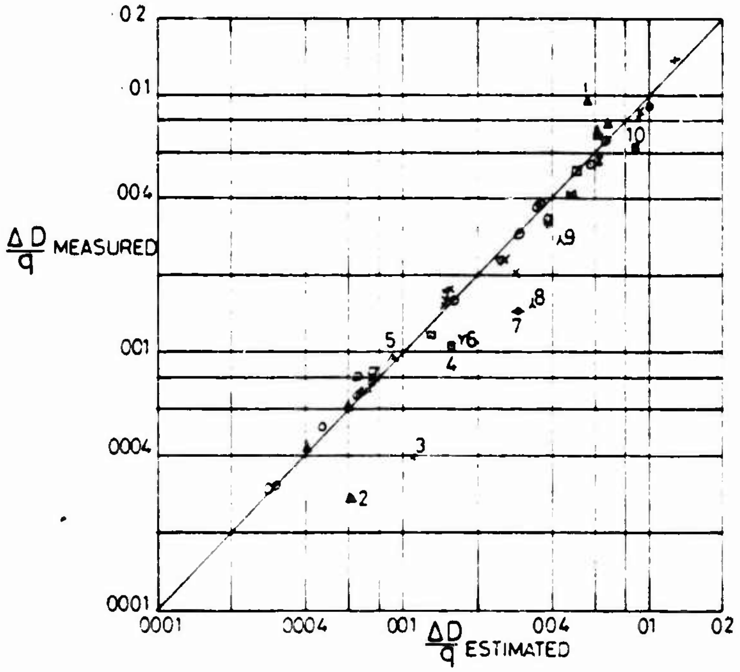

FIG. 9 LOW SPEED DRAG INCREMENTS UNDERFUSELAGE STORE INSTALLATIONS

4 BOMBS ON 2 PYLONS

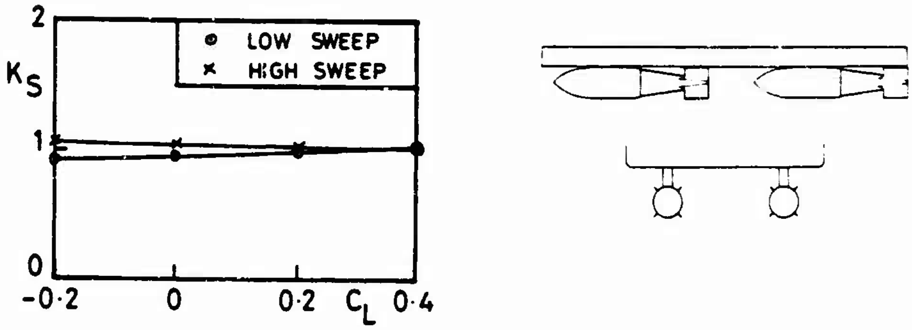

$K_S \sim C_L$ AT LOW M

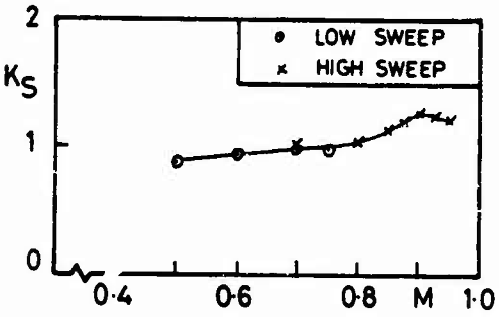

$K_S$ ~ M AT $C_L$ = 0

8 BOMBS ON 2 PYLONS

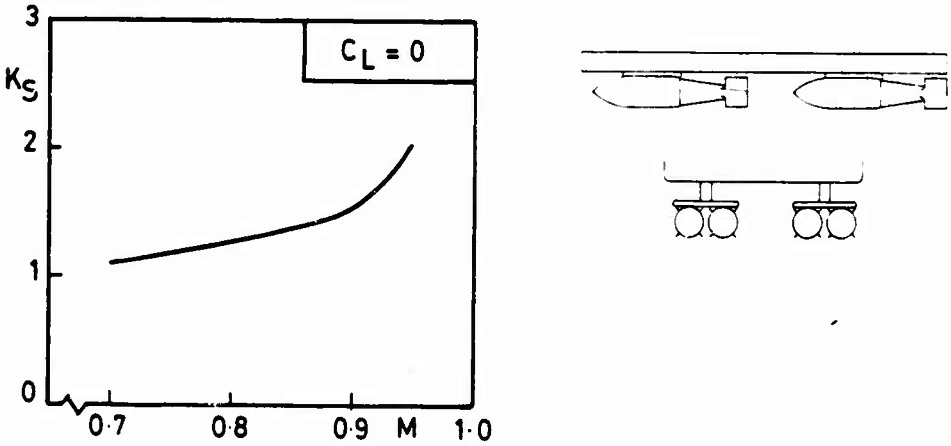

FIG.10. INSTALLATION FACTORS FOR UNDERFUSELAGE STORES

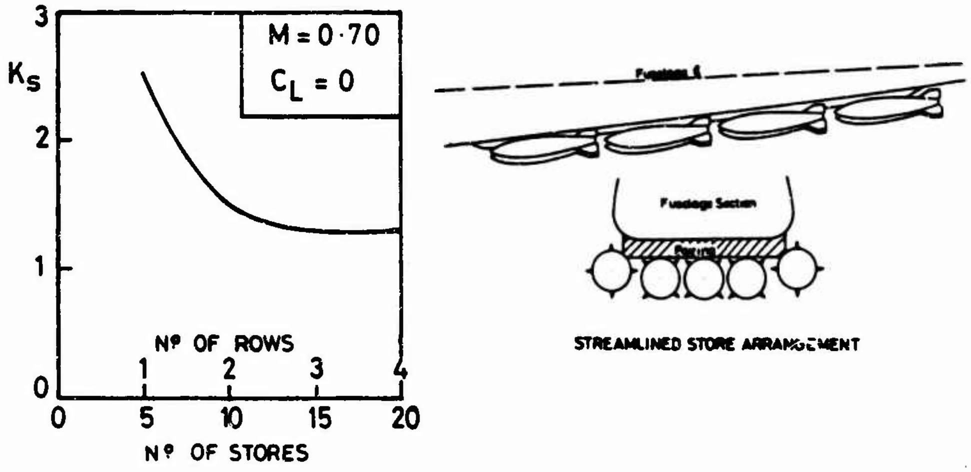

FIG. 11. INSTALLATION FACTORS FOR MULTIPLE UNDERFUSELAGE STORES

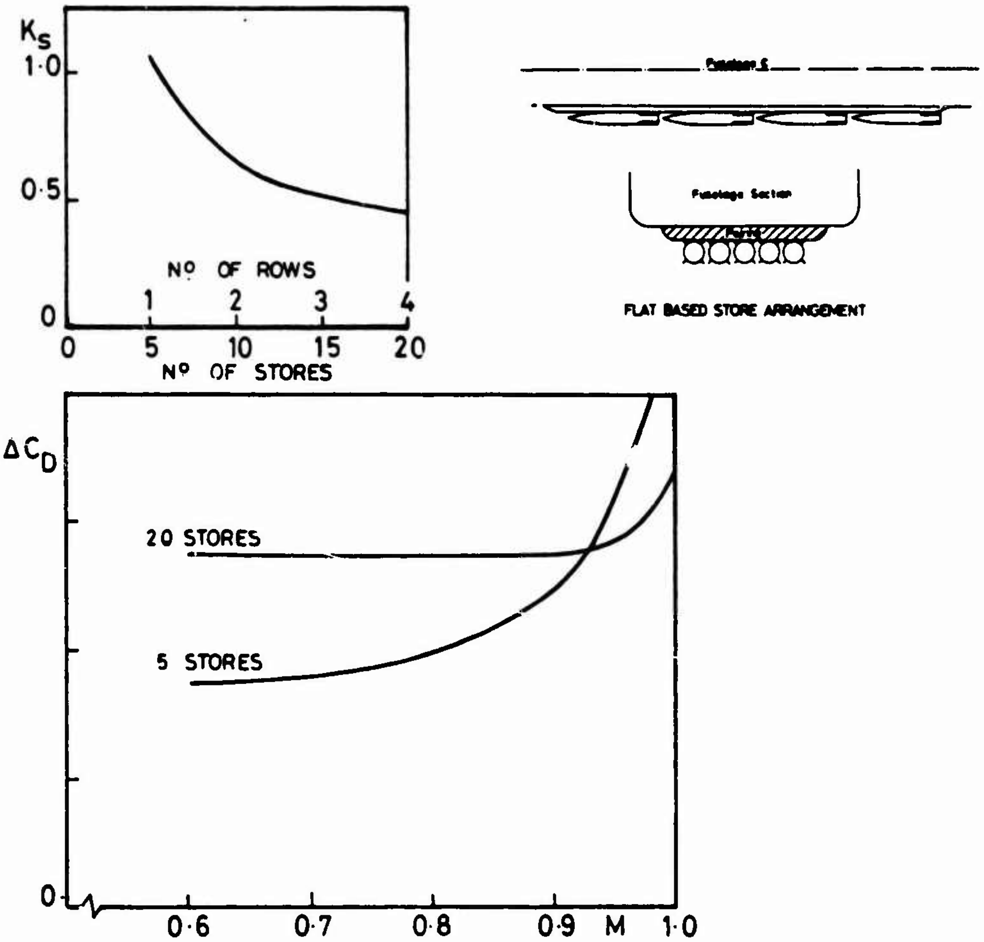

FIG. 12. FAVOURABLE INTERFERENCE WITH UNDERFUSELAGE STORES

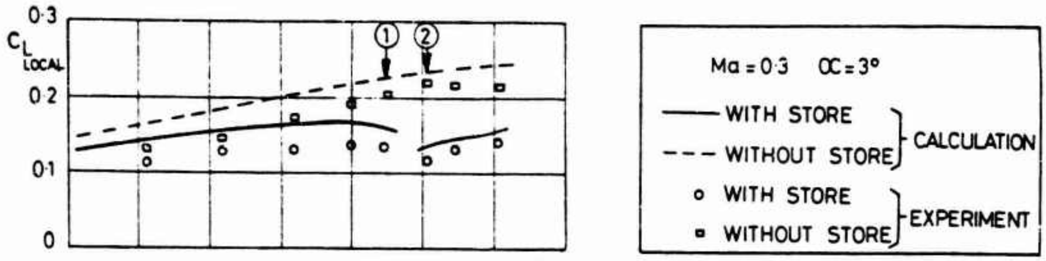

SPANWISE LIFT DISTRIBUTION

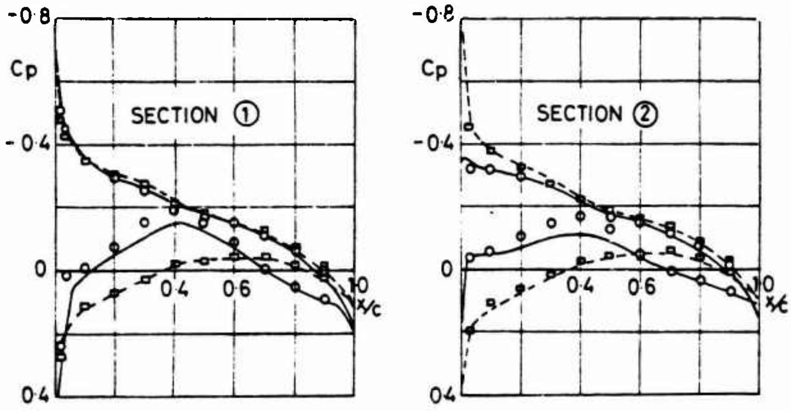

CHORDWISE PRESSURE DISTRIBUTIONS

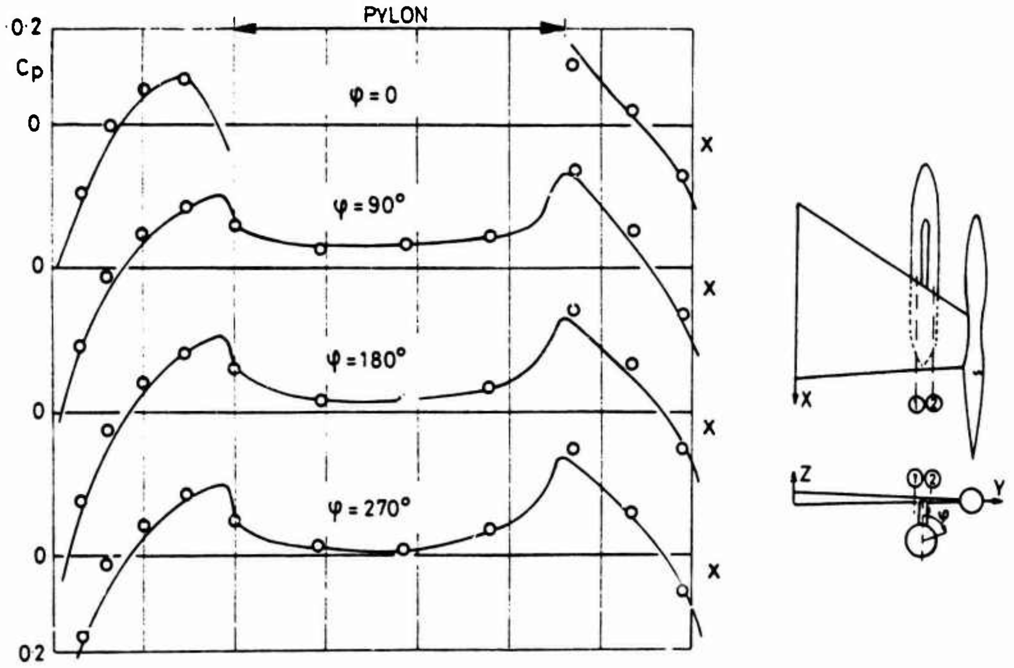

PRESSURE DISTRIBUTIONS ON STORE

FIG.13. CALCULATED AND EXPERIMENTAL PRESSURE DISTRIBUTIONS ON A WING-STORE COMBINATION (FROM REF. 8.)

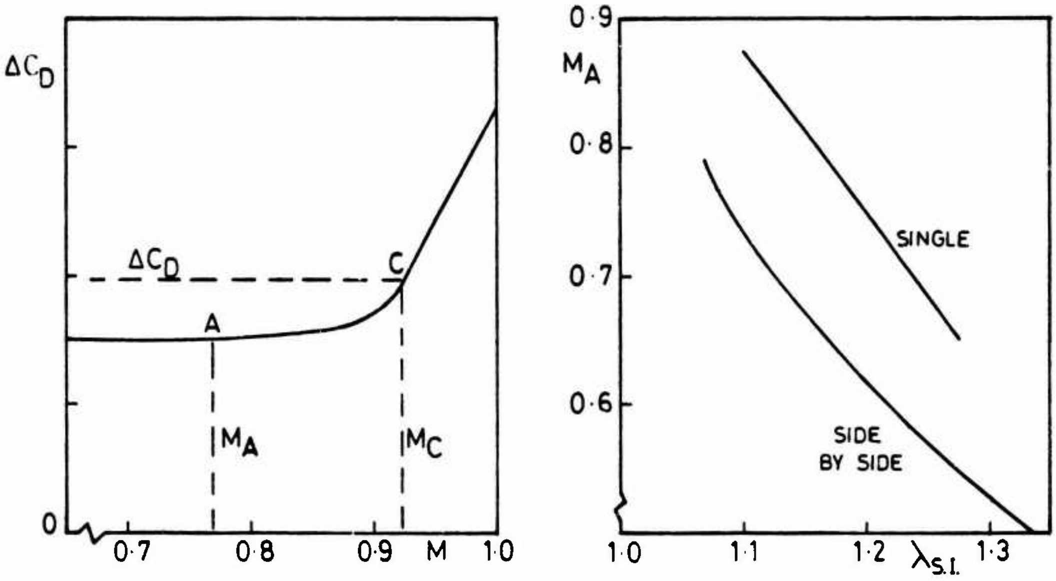

(a) $\Delta C_D \sim M$ FRAMEWORK

(b) CORRELATION OF $M_A$

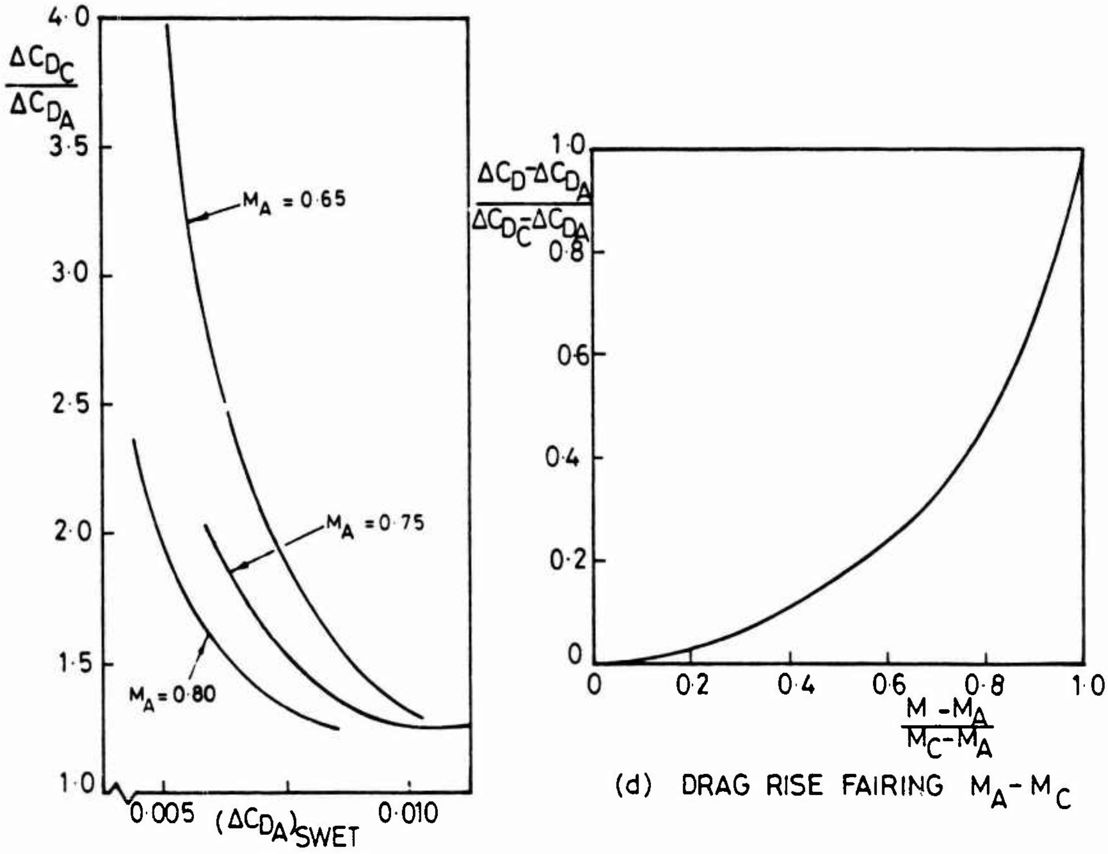

(d) DRAG RISE FAIRING $M_A - M_C$

(c) CORRELATION OF $\Delta C_{D_C}$

FIG. 14. EMPIRICAL ESTIMATION OF $\Delta C_D$ FOR UNDERFUSELAGE STORES

1. $\Sigma\left(\frac{D}{q}\right)_{COMP} = 0{\cdot}009874$

   $K_S = 1 \quad \therefore \Delta C_{D_A} = \underline{0{\cdot}00795}$

2. $\lambda_{SI}$ (SEE TEXT) $= 1{\cdot}124$

   FOR SIDE BY SIDE CASE $M_A = \underline{0{\cdot}705}$

3. $(\Delta C_{D_A})_{SWET} = 0{\cdot}00854;\ M_A = 0{\cdot}705$

   THEN $\Delta C_{D_C} = \underline{0{\cdot}01161}$

4. $M_c = 0{\cdot}92$

5.

| $\frac{M - M_A}{M_C - M_A}$ | $M$ | $\Delta C_D$ |
|---|---|---|
| 0·2 | 0·748 | 0·00806 |
| 0·4 | 0·791 | 0·00837 |
| 0·6 | 0·834 | 0·00883 |
| 0·8 | 0·877 | 0·00967 |

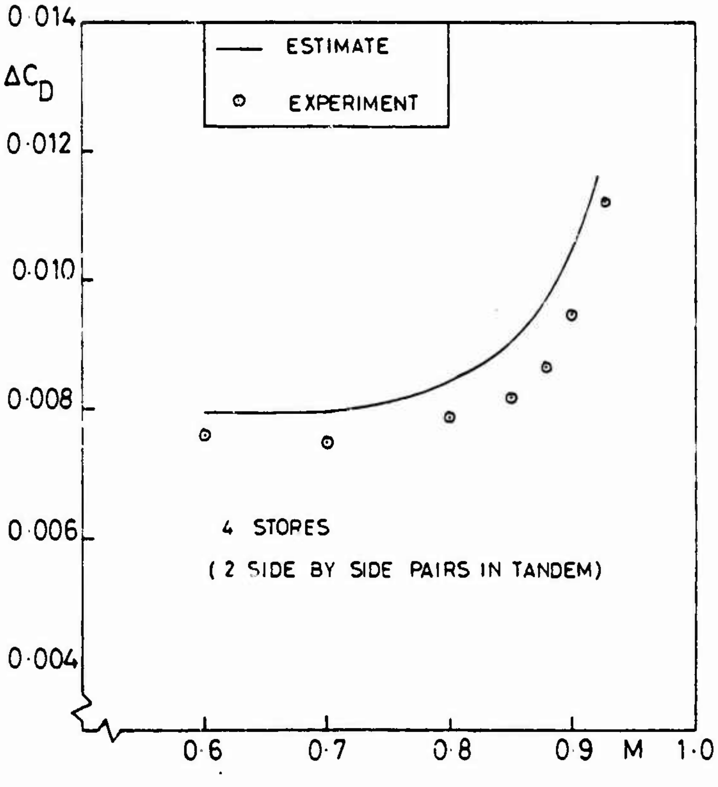

FIG.15. COMPARISON OF ESTIMATED AND MEASURED DRAG INCREMENTS FOR UNDERFUSELAGE STORES

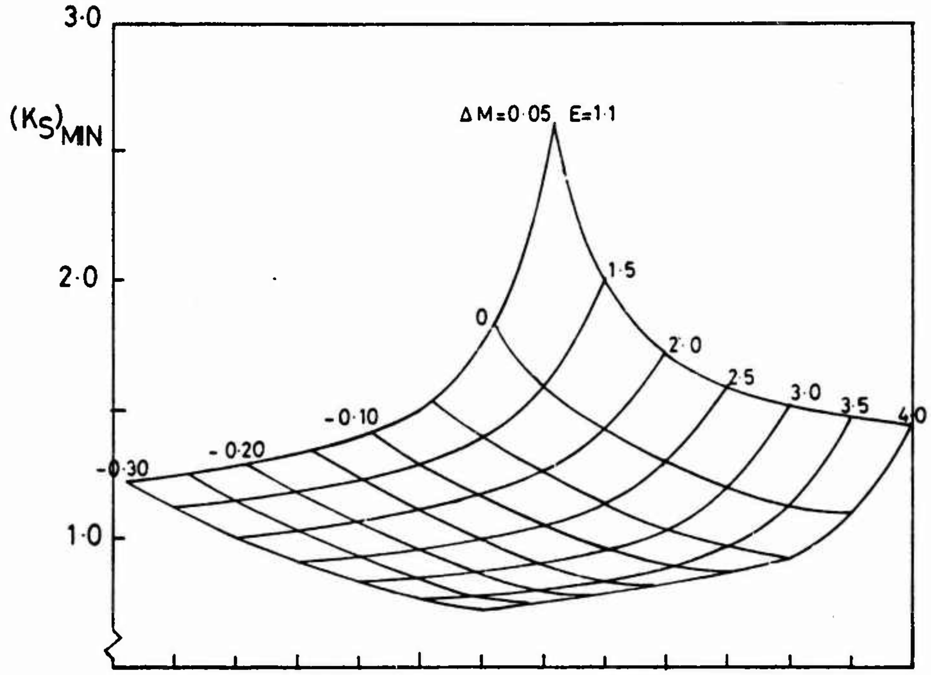

FIG.16. EMPIRICAL ESTIMATION $(K_S)_{MIN}$ FOR UNDERWING STORES

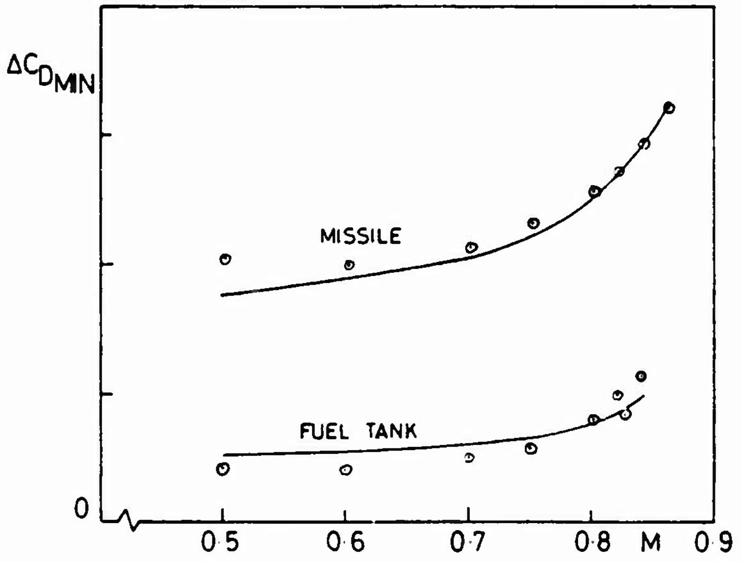

FIG. 17. COMPARISON OF ESTIMATED AND MEASURED $\Delta C_{D_{MIN}}$ FOR UNDERWING STORES

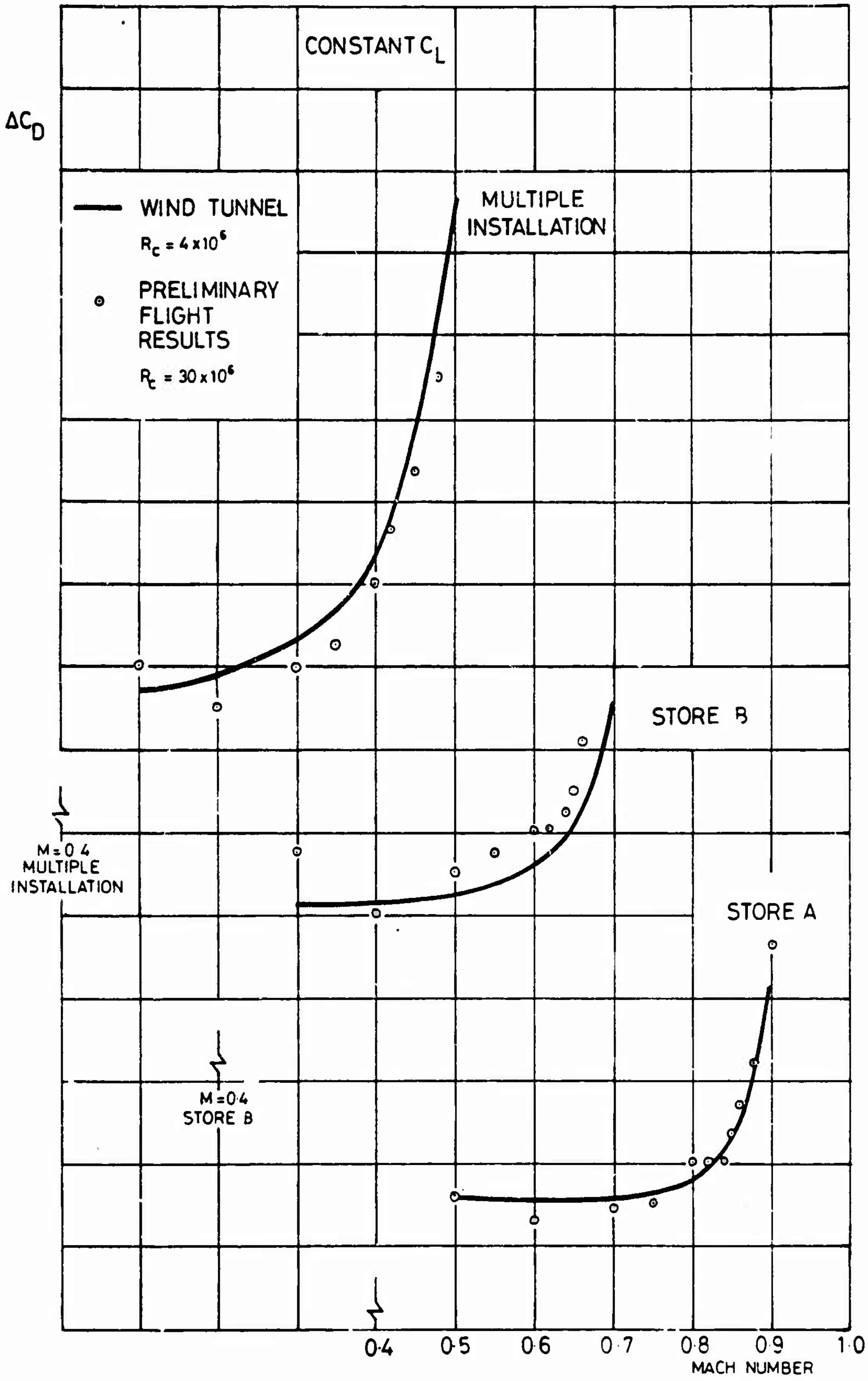

FIG. 18 WIND TUNNEL-FLIGHT COMPARISON

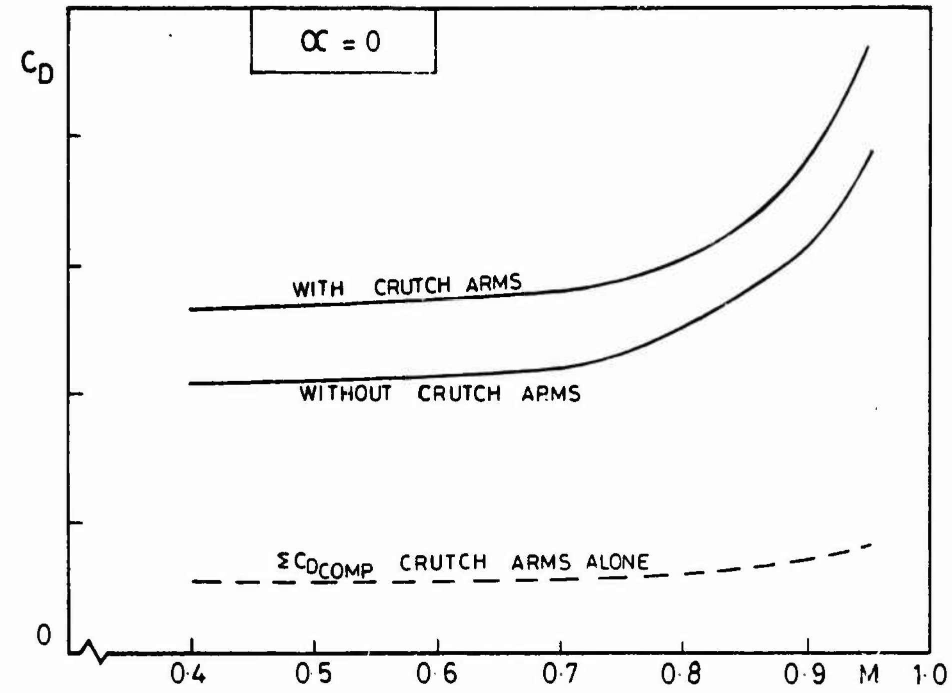

(a) SINGLE STORE – PYLON ASSEMBLY

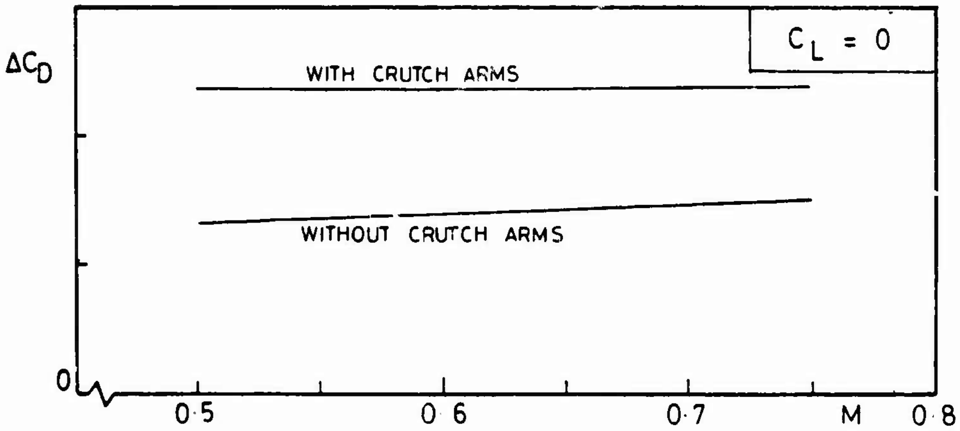

(b) 4 STORES ON 2 PYLONS UNDERFUSELAGE

FIG.19 REDUCTION OF DRAG DUE TO REMOVAL OF CRUTCH ARMS

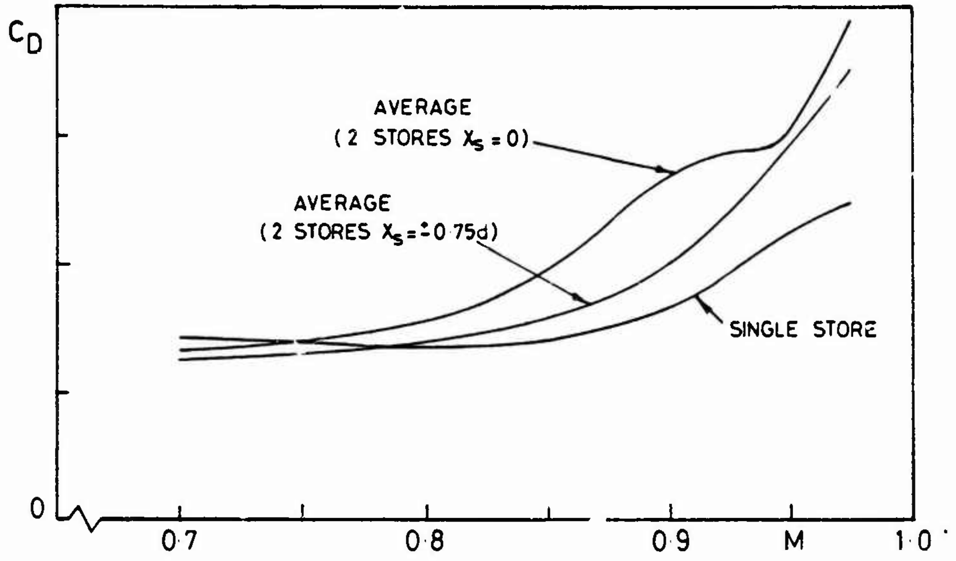

FIG. 20. REDUCTION OF DRAG BY AXIAL STAGGER OF SIDE BY SIDE STORES

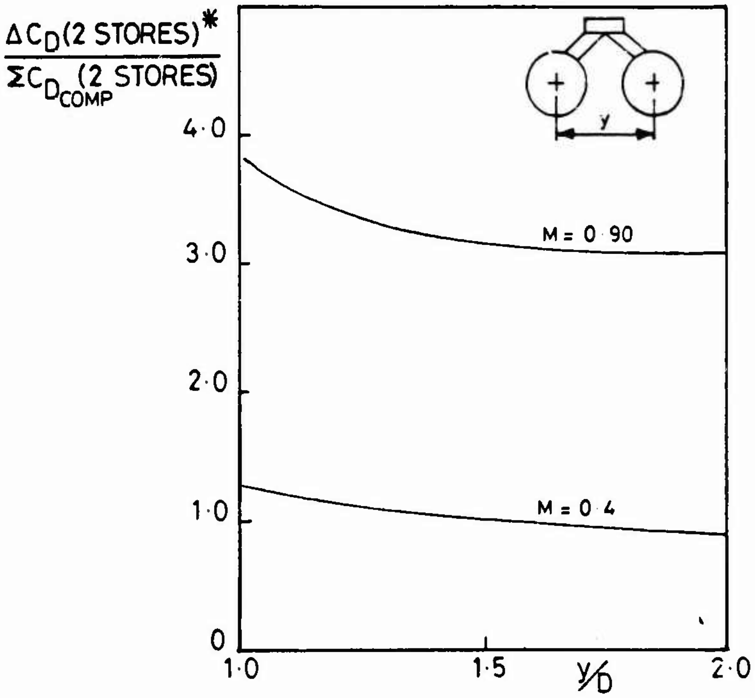

$*\Delta C_D$ (2 STORES) = $\Delta C_D$ (CARRIER + STORES) - $\Sigma C_{D_{COMP}}$ (CARRIER)

FIG. 21. REDUCTION OF DRAG BY INCREASED LATERAL SPACING BETWEEN STORES

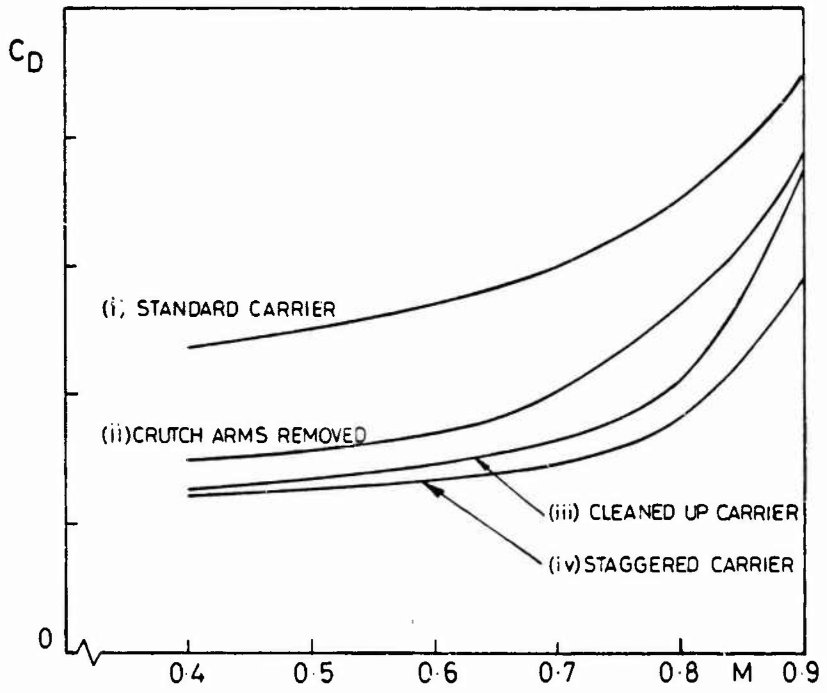

FIG. 22. REDUCTION OF DRAG OF LOADED TRIPLE CARRIER 'ASSEMBLY' BY REMOVING EXCRESCENCES AND STAGGERING BOMBS

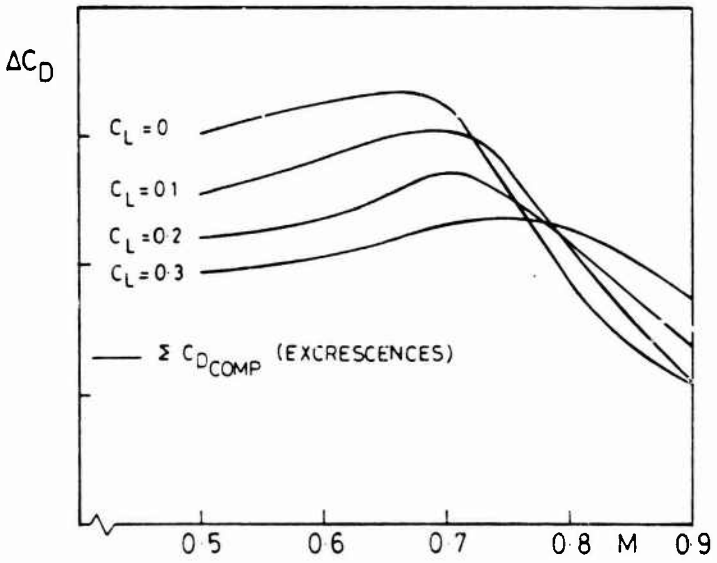

FIG. 23. REDUCTION OF DRAG OF LOADED TRIPLE CARRIER 'INSTALLATION' BY REMOVING EXCRESCENCES

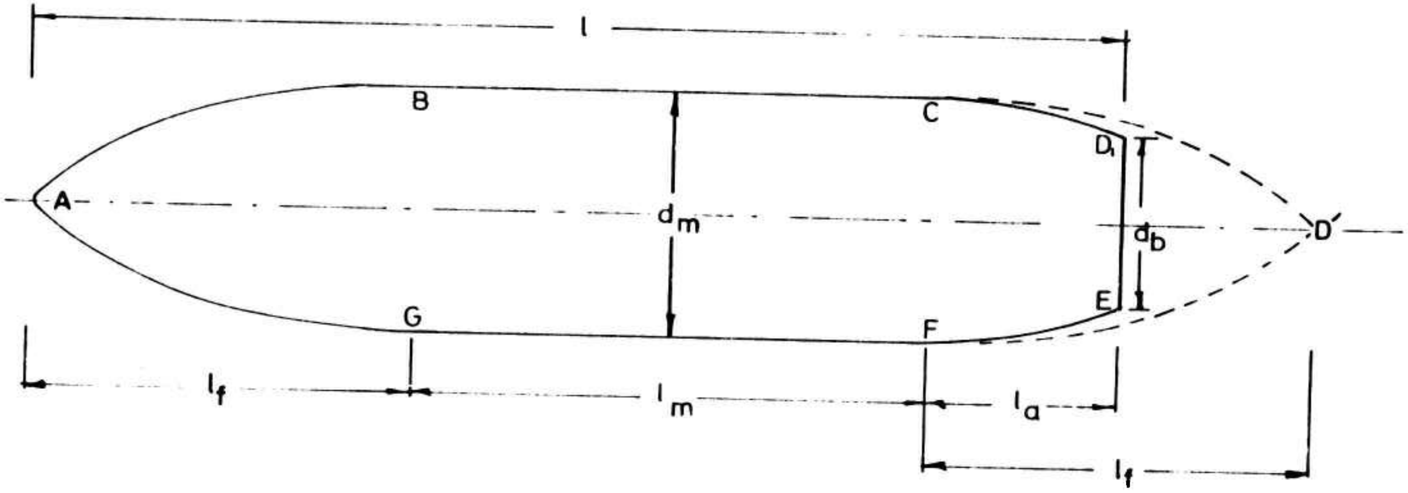
l
B
C
$D_1$
A
$d_m$
$d_b$
D′
G
E
F
$l_f$
$l_m$
$l_a$
$l_f$

FIG. A.1. NOTATION USED IN DRAG ESTIMATION FOR BODIES

Provisional Summary for

# STABILITY AND CONTROL IMPLICATIONS ON AIRCRAFT PERFORMANCE PREDICTION AND OPTIMIZATION

by

J E JENKINS

Air Force Flight Dynamics Laboratory, Wright Patterson Air Force Base, USA

Traditionally the stability and control considerations in preliminary design are restricted to the sizing of control and stabilizing surfaces and establishment of center-of-gravity limits. However, there are advantages to performing more comprehensive stability and control analyses in preliminary design because early consideration would permit better optimization through appropriate trade-offs. For example, trades between inherent airframe characteristics and flight control system complexity (CCV) offer potential performance benefits. Early consideration of stability and control characteristics can also help alleviate potentially serious problems such as pitch-up and roll coupling. Low cost digital computer techniques in both the aerodynamic and the dynamic-response areas are now available to permit the required analyses to be accomplished in a timely and cost-effective manner.

The interfaces between stability and control and other technical disciplines are briefly reviewed to identify the primary ways in which stability and control can influence the design. Not all of the possible interactions can or should be analyzed in preliminary design; rather, the preliminary design objective should be to seek an early definition of the requirements which will be levied on the flight control system (FCS) so that trades between FCS complexity and performance can be properly considered.

Two aspects of stability and control interactions with performance optimization are then discussed. These are (1) optimization with respect to the primary mission profile and (2) the impact of "off-design" operation.

Next, data requirements from the stability and control viewpoint are compared to the capabilities of available tools (Digital Datcom and Flexstab). Desirable features of automated prediction methods for design applications are discussed in addition to the method's limitations in accuracy and applicability.

Finally, a brief review of some CCV research program results is given to illustrate the potential performance benefits available through this approach.

Not Available for Publication

N74-26455

Supplementary Contribution on

# AIRCRAFT PERFORMANCE CONSIDERATIONS FOR NOISE REDUCTION

by

JOHN WILLIAMS

(Lecture Series Director)

## INTRODUCTION AND SUMMARY

During the next decade at least, the aircraft designer is faced with the problem of achieving much lower noise levels outside airport boundaries (10-20 PNdB reduction), while at the same time predicting and guaranteeing the noise field from future aircraft projects to a much greater accuracy than hitherto (say within $\pm 1$ dB). This applies primarily to civil transport operations, but similar reductions are also desirable for some military operations; not merely for transports, but also for low-level search, reconnaissance and transport aircraft. Moreover, such noise improvements are demanded with minimum penalties on aerodynamic, structural and propulsive efficiency. In fact, continuing improvements in airfield performance and en-route performance are likely to be expected, particularly in view of rising fuel costs and environmental constraints, with the associated penalties on operating costs.

Fortunately, there has been a rapid evolution already of gas-turbine engines for subsonic transport operation:

from early turbo-jets (BPR = 0),

through low BPR fan units (BPR = $\frac{1}{2}$ to 2),

to modern high BPR fan engines (BPR = 3 to 8)

This has yielded not only improvements in engine sfc and static/cruise thrust-ratio but also substantial reductions in noise. It can be argued that the penalties for the lower noise level of the latest generation of turbo-fan engines are relatively small, being associated with only a modest amount of absorptive treatment of the engine ducts.

However, the designers of the next generation of even quieter transport aircraft with minimum economic penalties need to exploit not only further improvements offered by the engine designer. The aircraft performance characteristics, the airframe design and airframe-engine aero-acoustic interference have also to be integrated and biased towards noise reduction. As I shall attempt to illustrate, there is now a necessity to analyse various aircraft design and performance features and to synthesise carefully the engine and airframe combination in respect of noise; as well as to satisfy the more conventional demands of operating performance, handling, and safety.

The development of even quieter engines will be essential of course and is already projected through the choice of appropriate thermodynamic cycles, designing components so as to minimise noise generation at source, and more elaborate use of acoustic treatment. All such steps will be conditioned by the avoidance of excessive penalties as regards installed mass performance, maintenance and cost.

The aircraft performance characteristics themselves, while satisfying the mission requirements, may also be exploited for noise reduction, for example in the following ways:-

Minimisation of TOL Thrust - less noise generated at source.

Steeper TOL Flight Paths - greater separation from ground.

Shorter Field Length - shorter footprint and less duration of noise.

En-Route Requirements - engine/airframe requirements.

Particular aircraft design features can also be significant either indirectly or directly, eg by:-

The appropriate optimisation of aerodynamic/structural parameters such as wing aspect-ratio and sweep, and the high-lift device arrangements; in particular to reduce thrust required and to allow steeper gradients.

The minimisation of airframe self-noise particularly with the high-lift devices and undercarriage deployed; since this may limit the aircraft noise floor attainable as the engine noise is further reduced.

Airframe shielding of engine noise sources, taking account of edge-diffraction effects.

Airframe flow-field influence on the propagation of engine noise through refraction or other effects.

The aero-acoustic interference between engine-flow and neighbouring airframe surfaces must also be taken into account, eg:-

Airframe surface interaction with engine flow development, thus modifying the engine noise sources.

Engine flow interaction with airframe surface, causing excess airframe noise.

This supplementary contribution to the Lecture Series will discuss such relevant aspects of aircraft performance and aero-acoustics, in relation to external noise prediction and reduction.

Supplementary Contribution on

# APPLICATION OF GROUND FACILITIES FOR FLIGHT AERODYNAMIC PERFORMANCE PREDICTION

by

Ph POISSON-QUINTON

Adjoint au Directeur Scientifique Central, (ONERA, France)

## SUMMARY

Within the scope of this seminar which ends the Lecture Series, an attempt is made firstly to extract some general conclusions in the light of the preceding lectures during which the problems of using ground facilities for the prediction of aircraft performance have been discussed.

The three regimes of a flight mission will therefore be examined:-

(a) Take-off/Climb and Approach/Landing,
(b) Cruise (subsonic and supersonic),
(c) Limits of the Manoeuvre flight envelope;

with a view to finding out to what measure present facilities are adequate for providing useful aerodynamic data for the prediction of actual flight conditions. In fact, in every case, the aircraft designer must make corrections to the results of his wind-tunnel tests based both on calculations and on his previous experience of flight/tunnel comparisons. For his part, the test engineer must effect corrections based on the particular conditions of each wind-tunnel test; wall and support-system corrections, exact localisation of transition on the model to permit the correction of the friction term, correction for the limited simulation of propulsion, etc.

Finally, reference will be made to the principal recommendations put forward by the AGARD/LaWs Working Group, charged recently with the task of making a study of prospective new test facilities (for development in Europe) capable of an optimal approach to the conditions of actual flight, particularly in the transonic and low-speed flow domains. In conclusion, it seems that a considerable effort must be made, not only to develop test facilities of better performance, but also to improve methods of measurement and analysis in the laboratory, in close conjunction with theoretical treatments.